

Chemistry of Secondary Organic Aerosol Formation

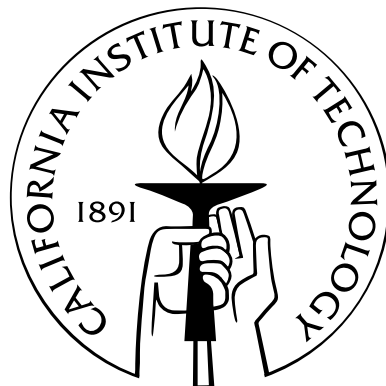
Thesis by

Lindsay Diana Yee

In Partial Fulfillment of the Requirements

for the Degree of

Doctor of Philosophy



California Institute of Technology

Pasadena, California

2013

(Submitted April 4, 2013)

© 2013

Lindsay Diana Yee

All Rights Reserved

To my grandparents, Cheung Boo and Soo Jin Yee, and Sidney and Susan Seid, for providing me the opportunity of a U.S. education, and to my parents, Thomas and Nana Yee, for instilling in me the value of life-long learning.

Acknowledgments

This thesis is more than a mere representation of some of my research activities at Caltech. Embedded within are memories and reminders of how my time at Caltech has been blessed by the support and love of many people.

I am grateful for the professors that served on my candidacy and thesis committees. This includes John Seinfeld, my advisor, Paul Wennberg, Rick Flagan, and Michael Hoffmann (candidacy) and Mitchio Okumura (thesis).

I thank my advisor, John Seinfeld, for inspiring me to pursue graduate studies in atmospheric chemistry. I saw for the first time the seminal figure on the uncertain role of aerosols on radiative forcing from the IPCC 2007 report in John's seminar at UC Riverside during my senior year of college. I remember leaving that seminar charged with the motivation to better understand aerosol chemistry, and it served as motivation in my successful research proposal for a National Science Foundation Graduate Research Fellowship that supported me while at Caltech. Since being at Caltech, I have appreciated John's advising, as I recall key moments when he took the initiative to address many of my concerns before I had to state them. He has shaped the way I look at and approach scientific problems, and I have always valued his professional mentorship.

Thanks to Paul Wennberg for the many chemistry discussions we had when looking at CIMS data and his genial nature that encouraged me through first-year classes.

I have always admired his keen sense of how to examine data in a way that answers compelling science questions, and I appreciate that he has imparted this perspective to me. Paul has fostered a knowledgeable and friendly research group (Andreas Kürten, Alan Kwan, Melinda Beaver, Nathan Eddingsaas, John Crounse, and Jason St. Clair) that has supported me throughout my work employing CIMS.

Rick Flagan's willingness to sit down with me to sketch diagrams, write out governing equations, and go over design aspects of the instrumentation I was building for the lab was invaluable to my Ph.D. experience. Rick played a central role in my design of an electrostatic precipitator and my gaining of an understanding of ionization and charger design. I had the opportunity to do a teaching assistantship with him for aerosol physics and my learning only continued.

I am grateful for Mike Hoffmann's support, as I remember several impromptu hallway discussions that he and I had about science and the Ph.D. process. I left those discussions feeling very lucky to be able to converse with so many professors at Caltech without hindrance from innate borders and restrictions across departmental lines. I enjoyed very much the latest Informal Symposium on Kinetics and Photochemical Processes in the Atmosphere (ISKPPA) held at Caltech and organized by Mitchio Okumura, Stan Sander, and Paul Wennberg. The atmospheric chemistry community has been so collaborative and good-natured, that I have appreciated being a part of this field, represented by individuals such as Mitchio who exemplify this spirit.

This spirit has also been experienced in my recent collaborations with Paul Ziemann at UC Riverside (3/4 of my thesis chapters!). Discussions with Paul regarding alkanes and particle-phase chemistry inspired many of my scientific interests that I will pursue in the future. I appreciate that he made the time to meet with me on several occasions to draw out chemical structures and potential electron impact

fragmentation patterns to help me better understand the chemistry I was studying.

Good science does not evolve in the microcosm of one brain. For this reason, I am thankful to have had many labmates to go through the pangs of data analysis and to discuss science with. Working on my first paper with Jill Craven was a pivotal moment during my Ph.D. work, and I will cherish good memories of us working late in the office discussing chemical mechanisms and ion assignments. The variety of skill sets in the Seinfeld group are phenomenal, and I am fortunate to have been able to learn from all the members. I got insight into the modeler's world having had many conversations with Joey Ensberg, Manabu Shiraiwa, and Andi Zuend. Having helped run many chamber experiments, it was nice being able to rely on Arthur Chan, Puneet Chhabra, Matt Coggon, Jill Craven, Beth Kautzman, Christine Loza, Katherine Schilling, Becky Schwantes, and Xuan Zhang.

I appreciate the members of the Caltech Community for their friendship and mentorship. Special thanks to the ChEESE(G)PSer group, consisting of Chemical Engineering, Environmental Science and Engineering, Geology, and Planetary Science graduate students from my year as well as others. We faithfully maintained weekly lunches for about four years since having core classes together during first year. This allowed me to share the results of "stress baking" with the group, and lunches always guaranteed a good laugh. Our summer softball team did too.

The Caltech Center for Diversity, and in particular, the Women Mentoring Women program, supported my time at Caltech in such a positive way. My mentor, Maggie Osburn, and I were matched my first year here, and I am grateful that she has served as my mentor for all five years. The match was perfect. Maggie helped me navigate many rough moments, and I am glad that she is willing to continue serving as a mentor to me even as we move on to our next professional steps. I also received great mentorship from Melinda Beaver, Beth Kautzman, Xerxes Lopez-Yglesias, Andrew

Metcalf, Havala Pye, Jason St. Clair, and Jason Surratt, whom I am grateful to have met at Caltech. Special thanks to Xerxes for being a loyal friend. Our raquetball sessions forced me to get out of lab, and the stresses of the day would make for good competition on the court. Beth led the methoxyphenols project, resulting in my first set of CIMS data requiring in-depth analyses and quite a chemistry challenge. She served as a good role model, and I appreciated working with her as I transitioned to project roles requiring more extensive leadership.

The value of sustained mentorship has been obvious to me via continued support from UCR professors, Sharon Walker, and my undergraduate research advisor, David Cocker. Working in David's laboratory inspired me to pursue graduate research. I am thankful that we have been able to catch up at annual AAAR meetings and that he has continued supporting me through reference letters and valuable discussions on professional development. I received fundamental research training from the graduate students, staff scientists, and professors at UCR CE-CERT that carried into my research at Caltech.

There are so many staff at Caltech that go above and beyond to help make life as a graduate student easier. I highlight thanks to Karen Baumgartner, Nathan Dalleska, Yvette Grant, Haick Issaian, André Jefferson, Fran Matzen, Nora Oshima, Megan Schmid, and Mike Vondrus for supporting my research needs.

Thanks to the greater community of Pasadena, as embodied by the people I have met through (a)Spire Ministry. I came to (a)Spire at a time when I did not expect there was a personal need for such a community, but I was empowered by my experiences and realized that in fact, it was something I yearned for but had not recognized until I stumbled upon it. Andy Schwiebert was central in supporting my involvement in (a)Spire. There is so much beauty in the making of new friends, and I am grateful I had the opportunity to do so in this community.

Lastly, I would like to thank my family. If it were not for them, I would not have ended up at Caltech for my graduate studies. If it were not for my father, Thomas Yee, I would not have been inspired to pursue a career in science and engineering. I thank my mother, Nana Yee, for providing a listening ear throughout my Ph.D. process as I navigated the growing pains of research and graduate study. I also thank my siblings: Christopher, Shelley, and Stefanie Yee for making me laugh and reminding me of the strength of family as modelled by our grandmother. She passed away during my second year here and has always been a constant inspiration for my internalization of gratitude, love, and family. I was lucky to have my dog Scamper move out to Pasadena with me for a few years, and she has been a significant source of calm and balance through "fuzz therapy" sessions and her mandate that I leave the lab every so often to walk her.

Finally, I would like to thank new family. I am so grateful for Christopher Lew's love and support, who from Riverside and then Minneapolis, managed to always put us first. Maintaining a long-distance relationship amidst a 24/7 chamber operation was never easy, and I thank him for accommodating my Ph.D. schedule into his postdoc schedule. We have been hoping to be in the same city for five years now, and that time is finally near!

Abstract

The photooxidation of volatile organic compounds (VOCs) in the atmosphere can lead to the formation of secondary organic aerosol (SOA), a major component of fine particulate matter. Improvements to air quality require insight into the many reactive intermediates that lead to SOA formation, of which only a small fraction have been measured at the molecular level. This thesis describes the chemistry of secondary organic aerosol (SOA) formation from several atmospherically relevant hydrocarbon precursors. Photooxidation experiments of methoxyphenol and phenolic compounds and C₁₂ alkanes were conducted in the Caltech Environmental Chamber. These experiments include the first photooxidation studies of these precursors run under sufficiently low NO_x levels, such that RO₂ + HO₂ chemistry dominates, an important chemical regime in the atmosphere. Using online Chemical Ionization Mass Spectrometry (CIMS), key gas-phase intermediates that lead to SOA formation in these systems were identified. With complementary particle-phase analyses, chemical mechanisms elucidating the SOA formation from these compounds are proposed.

Three methoxyphenol species (phenol, guaiacol, and syringol) were studied to model potential photooxidation schemes of biomass burning intermediates. SOA yields (ratio of mass of SOA formed to mass of primary organic reacted) exceeding 25% are observed. Aerosol growth is rapid and linear with the organic conversion, consistent with the formation of essentially non-volatile products. Gas and

aerosol-phase oxidation products from the guaiacol system show that the chemical mechanism consists of highly oxidized aromatic species in the particle phase. Syringol SOA yields are lower than that of phenol and guaiacol, likely due to unique chemistry dependent on methoxy group position.

The photooxidation of several C₁₂ alkanes of varying structure (*n*-dodecane, 2-methylundecane, cyclododecane, and hexylcyclohexane) were run under extended OH exposure to investigate the effect of molecular structure on SOA yields and photochemical aging. Peroxyhemiacetal formation from the reactions of several multifunctional hydroperoxides and aldehyde intermediates was found to be central to organic growth in all systems, and SOA yields increased with cyclic character of the starting hydrocarbon. All of these studies provide direction for future experiments and modeling in order to lessen outstanding discrepancies between predicted and measured SOA.

Contents

Acknowledgments	iv
Abstract	ix
1 Introduction	1
2 Secondary organic aerosol formation from biomass burning intermediates: phenol and methoxyphenols	4
3 Secondary organic aerosol formation from low- NO_x photooxidation of dodecane: evolution of multigeneration gas-phase chemistry and aerosol composition	42
4 Analysis of secondary organic aerosol formation and aging using positive matrix factorization of high-resolution aerosol mass spectra: application to the dodecane low- NO_x system	63
5 Effect of chemical structure on secondary organic aerosol formation from C_{12} alkanes	87
6 Conclusions and future work	123

A Application of the Statistical Oxidation Model (SOM) to Secondary Organic Aerosol formation from photooxidation of C12 alkanes	126
B α-pinene photooxidation under controlled chemical conditions - Part 1: Gas-phase composition in low- and high-NO_x environments	143
C α-Pinene photooxidation under controlled chemical conditions - Part 2: SOA yield and composition in low- and high-NO_x environments	160
D Chemical aging of m-xylene secondary organic aerosol: laboratory chamber study	176
E Yields of oxidized volatile organic compounds during the OH radical initiated oxidation of isoprene, methyl vinyl ketone, and methacrolein under high-NO_x conditions	194
F Analysis of photochemical and dark glyoxal uptake: implications for SOA formation	207
G Role of aldehyde chemistry and NOx concentrations in secondary organic aerosol formation	213

List of Figures

Figure 2.1 Growth curves of guaiacol aerosol	33
Figure 2.2 Growth curves of syringol aerosol	33
Figure 2.3 Phenol low-NO _x gas-phase and particle-phase development.....	34
Figure 2.4 Proposed pathway for gas-phase production of C6 carboxylic acids in the phenol low-NO _x system	35
Figure 2.5 Selected phenol low-NO _x gas-phase acids	36
Figure 2.6 Proposed mechanism for guaiacol low-NO _x oxidation	37
Figure 2.7 Selected traces in guaiacol low-NO _x gas-phase and particle-phase development	38
Figure 2.8 Common chemical routes in the phenol and guaiacol low-NO _x systems	39
Figure 2.9 Selected traces in syringol low-NO _x gas-phase and particle-phase development	40
Figure 2.10 Possible routes of methoxy loss in syringol gas-phase chemistry	41
Figure 3.1 Dodecane low-NO _x mechanism	46
Figure 3.2 Simulated (curves) and observed (open circles) time evolutions of various gas-phase species from OH-initiated photooxidation of dodecane	48
Figure 3.3 Carboxylic acids	52
Figure 3.4 Acids (hydroxycarboxylic/peracid) or hydroperoxides	52
Figure 3.5 Span of O:C values versus log of the pure subcooled liquid vapor pressures in units of $\mu\text{g m}^{-3}$ (C _i) for predicted compounds from dodecane low-NO _x photooxidation ..	55
Figure 3.6 Scheme for forming five types of PHAs from reaction of an aldehyde of carbon length n, with various hydroperoxy compounds	56
Figure 3.7 Aerosol growth occurs between formation of the carbonyl hydroperoxide (CARBROOH) and the onset of acid formation (observations in teal squares and simulated result, p(jCARBROOH), in teal) in the gas-phase	57

Figure 3.8 AMS high-resolution fragments and possible characteristic fragments of the hydroperoxide derived PHA	58
Figure 3.9 Rough estimate of total organic mass attributed to gas-to- particle phase partitioning from select semivolatiles as compared to the AMS organic trace	60
Figure 4.1 Total organic aerosol mass and O : C and H : C elemental ratios for experiment 2	67
Figure 4.2 Simplified chemical mechanism for dodecane photooxidation under low-NO _x , adapted from Yee et al. (2012)	68
Figure 4.3 Time series of ions and the raw data for “early growth” and “most oxidized growth” for <i>m/z</i> 183	69
Figure 4.4 Time series of ions and the raw data for “early growth” and “most oxidized growth” for <i>m/z</i> 215	69
Figure 4.5 C ₁₂ backbone ions with varying contributions of oxygen have distinct time trends over the duration of the experiment	70
Figure 4.6 Three-factor PMF solution, total organic mass, and O : C ratio	70
Figure 4.7 The 3-factor mass spectra profiles in terms of their families	71
Figure 4.8 Factor time series with the top three highest Pearson’s r correlating HR-ToF-AMS ions	72
Figure 4.9 Mass spectrum of octadecane condensing onto the seed before irradiation, and the relative mass spectrum just after lights on	74
Figure 4.10 Particle-phase HR-ToF-AMS factor time series with gas-phase CIMS time traces	74
Figure 4.11 Factor time series with MOVI-HRToF-CIMS heating-mode, aerosol-phase traces	75
Figure 4.12 Tracer ions for the carbonyl hydroperoxide increase while the bulk organic trace decreases when the 600 °C HR-ToF-AMS heater is turned off	76
Figure 4.13 The aerosol mass distribution grows from smaller diameter sizes to larger diameter sizes with increasing OH exposure (purple is low OH exposure, red is high OH exposure)	76
Figure 4.14 Mass distributions and time series of total organic mass broken down into 2 factors	77
Figure 4.15 Van Krevelen diagram for low-NO _x photooxidation of dodecane	78

Figure 5.1 General mechanism for alkanes under low-NO _x conditions	112
Figure 5.2 General mechanism for particle-phase chemistry involving PHA formation (right-hand side) and potential isomerization (left-hand side) from higher functionalized products formed along Channel 2 in Figure 1	113
Figure 5.3 Gas-phase trends of major species formed in the first three generations of photooxidation.....	114
Figure 5.4 High-resolution mass spectrum of SOA formed from n-dodecane at initial organic growth, midexperiment, and end of experiment.....	115
Figure 5.5 High-resolution mass spectrum of SOA formed from 2-methylundecane at initial organic growth, midexperiment, and end of experiment	116
Figure 5.6 High-resolution mass spectrum of SOA formed from hexylcyclohexane at initial organic growth, midexperiment, and end of experiment	117
Figure 5.7 High-resolution mass spectrum of SOA formed from cyclododecane at initial organic growth, midexperiment, and end of experiment	118
Figure 5.8 Gas-phase trends of the (a) n-dodecane, (b) 2-methylundecane, (c) hexylcyclohexane, and (d) cyclododecane generated carbonyl hydroperoxide (CARBROOH) and C6 carboxylic acid as monitored by the CIMS and the CARBROOH and its derived PHA in the particle phase	119
Figure 5.9 Characteristic ions in (a) n-dodecane, (b) 2-methylundecane, (c) hexylcyclohexane, and (d) cyclododecane aerosol measured by the AMS	120
Figure 5.10 Fraction of organic attributed to the corresponding ROO ⁺ PHA tracer ion for (top) carbonyl hydroperoxide PHA (CARBROOH PHA), (middle) dicarbonyl hydroperoxide (DICARBROOH), and (bottom) hydroxycarbonyl hydroperoxide (OHCARBROOH).	121
Figure 5.11 Van Krevelen diagram for low-NO _x photooxidation of n-dodecane, 2-methylundecane, hexylcyclohexane, and cyclododecane.	122

List of Tables

Table 2.1 Chemical properties.....	27
Table 2.2 Experimental conditions.....	28
Table 2.3 Proposed structures for CIMS ions in the phenol low-NO _x system	29
Table 2.4 Proposed structures for CIMS ions in the guaiacol low-NO _x system.....	30
Table 2.5 SOA products observed in UPLC/(-)ESI-TOFMS offline filter analysis for the guaiacol low-NO _x system.....	31
Table 2.6 Proposed structures for CIMS ions in the syringol low-NO _x system	32
Table 2.4 Proposed structures for CIMS ions in the guaiacol low-NO _x system.....	30
Table 3.1 Dodecane low-NO _x experiments.....	45
Table 3.2 Reactions included in the gas-phase photochemical model	47
Table 3.3 Signals monitored by CIMS and their suggested assignments	51
Table 4.1 Experimental conditions for dodecane low-NO _x photooxidation	66
Table 4.2 Ion fragments	72
Table 4.3 HR-ToF-AMS ions with highest Pearson's r values for fpeak = 0.2 solution	73
Table 4.4 Distinct ions present in early C ₁₈ SOA formation.....	79
Table 5.1 C ₁₂ compounds studied	107
Table 5.2 Experimental conditions.....	107
Table 5.3 Selected ions monitored by the CIMS for <i>n</i> -dodecane and 2-methylundecane	108
Table 5.4 Selected ions monitored by the CIMS for hexylcyclohexane and cyclododecane	108
Table 5.5 Selected ions monitored by the AMS in the <i>n</i> -dodecane and 2-methylundecane systems	109

Table 5.6 Selected ions monitored by the AMS in the hexylcyclohexane system	110
Table 5.7 Selected ions monitored by the AMS in the cyclododecane system	111

Chapter 1

Introduction

There are $\sim 10^{44}$ molecules in Earth's atmosphere, yet it is the trace gases making up $<1\%$ of the volume that are important for atmospheric chemistry. Volatile organic compounds (VOCs) are the most complex and elusive subset of the trace gases. While the origins of some VOCs are known (e.g. anthropogenic vs. biogenic), their chemical fate in the atmosphere has yet to be understood. Approximately 10^3 - 10^4 specific organic compounds have been directly measured in the atmosphere, yet emission inventories used to drive atmospheric chemistry models typically only use on the order of 20 major compound groups. Thus, the majority of VOCs are chemical intermediates, part of a photochemical cascade that ensues when precursors react in the atmosphere. Many of these intermediates are of low enough volatility that they partition into the particle phase, forming secondary organic aerosol (SOA). SOA is well known to have adverse human health effects and contribute to photochemical smog. In addition, SOA cause a net cooling effect on climate, the extent of which is perhaps the most uncertain radiative forcing in current global climate models. This stems mainly from not understanding how SOA chemistry affects cloud formation. Addressing these issues requires deeper insights into complex VOC and SOA chemistry.

This thesis focuses on the controlled study of SOA formation from atmospherically relevant volatile organic compounds in the Caltech Environmental Chambers. Chamber studies are used to simulate photochemical processes in a controlled manner, such that focused atmospheric chemistry problems can be studied. Key to this endeavor is the use of a suite of analytical instruments that monitors the chemical development of the gas and particle phases over time. Instrumentation that monitors product distributions at the molecular level is prime in identifying key gas-phase intermediates contributing to SOA formation. In the presented studies, the use of a Chemical Ionization Mass Spectrometer (CIMS) achieves this end. Complementary analyses from an online Aerodyne High-Resolution Time-of-Flight Aerosol Mass Spectrometer (HR-ToF-AMS) allows for insight into the particle-phase evolution and composition via elemental analyses (e.g. O:C and H:C ratios) and the use of ion tracers (i.e. characteristic fragments of certain functional groups/chemical species). Further, the analyses of offline filter measurements provide molecular level speciation of compounds found in the aerosol. Together, these techniques shed light on the chemistry of secondary organic aerosol formation.

The gas-phase oxidation steps leading to SOA formation from several biogenic (methoxyphenols) and anthropogenic (alkanes) hydrocarbons are elucidated. Methoxyphenols are aromatic compounds with phenolic and methoxy substituent groups. These compounds are intermediates derived from the combustion of lignin and are emitted into the atmosphere during the burning of biomass. Little is known about the gas-phase oxidation of such compounds and their role in SOA formation once emitted. Alkanes comprise an important contribution to the Unresolved Complex Mixture (UCM), a region in chromatograms that results from insufficient separation of chemically similar compounds. This phenomenon is observed looking at most vehicular fuel samples. This mixture consists of many isomers of the C₁₂ to C₂₄ alkanes of

which upwards of 10^{19} constitutional isomers for each carbon length can exist. C₁₂ alkanes, as studied here, are good candidates for exploring the SOA formation potential from intermediate volatility organic compounds (IVOCs) and semi-volatile organic compounds (SVOCs). SVOCs are those VOCs that exist in both the gas and particle phase, a volatility class to which many components of diesel fuel belong. Thus, the photooxidation of several C₁₂ alkanes of varying structure (*n*-dodecane, 2-methylundecane, cyclododecane, and hexylcyclohexane) were run under extended oxidation periods to investigate the effect of molecular structure on SOA yields and in photochemical aging.

Parameterizations of chamber data, such as those obtained here, can be implemented into atmospheric chemistry models to better understand regional and global air quality issues. While chamber studies do not simulate all the complexities in the atmosphere, they provide a focused approach for understanding some atmospheric observations. These three approaches (modeling, laboratory studies, and field measurements) are akin to a system of checks and balances. They are iterative, provide validation, and are informative for how each approach should be adjusted to address outstanding problems in atmospheric chemistry. This concerted approach ultimately informs policy makers on needs for future air-quality regulations and improves our understanding of global biogeochemical cycles, imperative for assessing future environmental sustainability.

Chapter 2

Secondary organic aerosol formation from biomass burning intermediates: phenol and methoxyphenols¹

¹This chapter is reproduced by permission from "Secondary organic aerosol formation from biomass burning intermediates: phenol and methoxyphenols," by L. D. Yee, K. E. Kautzman, C. L. Loza, K. A. Schilling, M. M. Coggon, P. S. Chhabra, M. Chan, A. W. H. Chan, S. P. Hersey, J. D. Crounse, P. O. Wennberg, R. C. Flagan, and J. H. Seinfeld., *Atmospheric Chemistry and Physics Discussions*, 13, 3485–3532, doi:10.5194/acpd-13-3485-2013, 2013. Copyright 2013 Authors. This work is licensed under a Creative Commons License.

Manuscript prepared for Atmos. Chem. Phys.
with version 4.2 of the L^AT_EX class copernicus.cls.
Date: 25 January 2013

Secondary organic aerosol formation from biomass burning intermediates: phenol and methoxyphenols

L. D. Yee¹, K. E. Kautzman^{2,*}, C. L. Loza², K. A. Schilling², M. M. Coggon², P. S. Chhabra^{2, **}, M. N. Chan^{1,***}, A. W. H. Chan^{2,****}, S. P. Hersey¹, J. D. Crounse³, P. O. Wennberg^{1,3}, R. C. Flagan^{2,1}, and J. H. Seinfeld^{2,1}

¹Division of Engineering and Applied Science, California Institute of Technology, Pasadena, CA, USA

²Division of Chemistry and Chemical Engineering, California Institute of Technology, Pasadena, CA, USA

³Division of Geological and Planetary Sciences, California Institute of Technology, Pasadena, CA, USA

* now at: Department of Chemistry, Towson University, Towson, MD, USA

** now at: Aerodyne Research Inc., Billerica MA, USA

*** now at: Chemical Sciences Division, Lawrence Berkeley National Laboratory, Berkeley, CA, USA

**** now at: Department of Environmental Science, Policy and Management, University of California, Berkeley, Berkeley, CA

Correspondence to: J. H. Seinfeld

(seinfeld@caltech.edu)

Abstract. The formation of secondary organic aerosol from oxidation of phenol, guaiacol (2-methoxyphenol), and syringol (2,6-dimethoxyphenol), major components of biomass burning, is described. Photooxidation experiments were conducted in the Caltech laboratory chambers under low-NO_x (< 10 ppb) conditions using H₂O₂ as the OH source. Secondary organic aerosol (SOA)

5 yields (ratio of mass of SOA formed to mass of primary organic reacted) greater than 25% are observed. Aerosol growth is rapid and linear with the primary organic conversion, consistent with the formation of essentially non-volatile products. Gas- and aerosol-phase oxidation products from the guaiacol system provide insight into the chemical mechanisms responsible for SOA formation. Syringol SOA yields are lower than those of phenol and guaiacol, likely due to novel methoxy group chemistry that leads to early fragmentation in the gas-phase photooxidation. Atomic oxygen to carbon (O:C) ratios calculated from high-resolution-time-of-flight Aerodyne Aerosol Mass Spectrometer (HR-ToF-AMS) measurements of the SOA in all three systems are ~0.9, which represent among the highest such ratios achieved in laboratory chamber experiments and are similar to that of aged atmospheric organic aerosol. The global contribution of SOA from intermediate volatility and 10 semivolatile organic compounds has been shown to be substantial (Pye and Seinfeld, 2010). An approach to representing SOA formation from biomass burning emissions in atmospheric models could involve one or more surrogate species for which aerosol formation under well-controlled conditions 15 has been quantified. The present work provides data for such an approach.

1 Introduction

20 Biomass burning is a major source of atmospheric organic aerosol (OA), with contributions from both anthropogenic (biofuel, deforestation, etc.) as well as natural sources such as wildfires. Aerosol produced from biomass burning has been estimated to account for 90% of all primary organic carbon emitted globally from combustion sources (Ito and Penner, 2005). Bond et al. (2004) estimated global annual emissions of carbonaceous aerosol due to combustion as 8.0 Tg for black carbon (BC) 25 and 33.9 Tg organic carbon (OC). Biofuel and open burning were estimated by these authors to account, respectively, for 20% and 42% of BC, and 19% and 74%, of OC. The amount and composition of organic aerosol formed from these sources vary widely based on combustion conditions and fuel type. Measured wood smoke emissions from fireplaces, for example, depend strongly on the type of fuel consumed and can vary in magnitude by a factor of five for different fuel sources 30 and sampling techniques (Fine et al., 2001). Particulate matter from biomass burning, including wildfires, residential wood burning, and deforestation is also of major concern for visibility, climate change and health effects (Naehler et al., 2007).

The pyrolysis of lignin, the second most abundant polymer on Earth comprising the secondary cell wall of plants, produces phenols. Hawthorne et al. (1989) showed that phenols and methoxyphenols 35 account for a significant fraction of particulate matter derived from wood smoke, constituting 21% and 45% by mass of total aerosol, respectively. Emission rates for methoxyphenol species from biomass burning have been estimated to range from 420-900 mg/kg fuel (Hawthorne et al., 1989; Hawthorne et al., 1992; Schauer et al., 2001). In addition to the significant emission factors of these compounds, guaiacol, which is emitted from both hard and soft wood combustion, and syringol, 40 which is emitted primarily from soft woods, have been proposed as aerosol markers for wood combustion as well as biomarkers to determine human exposure levels (Dills et al., 2001; Simpson and Naehler, 2010).

Here we investigate the aerosol-forming potential of phenol and two of the most abundant methoxyphenol species, guaiacol and syringol (Table 1). Both guaiacol and phenol are intermediate volatility 45 organic compounds; syringol has a vapor pressure 100 times less than those of phenol and guaiacol. The molecular structures are shown in Table 1 along with vapor pressures and reaction rate constants with OH. Here we determine the fractional yield of secondary organic aerosol (SOA) from photooxidation of phenol, guaiacol, and syringol by OH in laboratory chamber studies under low- NO_x (<10 ppb) conditions. In addition, we present analyses of the gas- and particle-phase constituents in guaiacol photooxidation to elucidate the chemical mechanism involved in guaiacol SOA formation. We 50 qualitatively compare the chemistry of the test compounds to explore why syringol results in lower SOA yield compared to phenol and guaiacol. A further motivation for this work is the potential use of phenol, guaiacol, and syringol as compounds to represent biomass burning emissions in atmospheric models of organic aerosol formation. SOA products identified in the laboratory studies may 55 also serve as markers for biomass burning in ambient aerosols.

2 Experimental section

2.1 Chamber experiments

All experiments were carried out in the Caltech dual 28 m³ Teflon chambers. Details of the facilities have been described previously (Cocker et al., 2001; Keywood et al., 2004). Before each experiment, 60 the chambers were flushed with dried purified air for > 24 h, until the particle number concentration was < 100 cm⁻³ and the volume concentration was < 0.1 $\mu\text{m}^3 \text{ cm}^{-3}$. In all yield experiments, ammonium sulfate seed aerosol was used to promote condensation of low volatility oxidation products. The seed aerosol was generated by atomization of a 0.015 M aqueous ammonium sulfate solution. Following atomization, the size distribution of the seed particles peaked at ~56 nm with an average 65 number concentration of ~2700 cm⁻³, and a total seed volume concentration of 10-15 $\mu\text{m} \text{ cm}^{-3}$ was achieved. The hydrocarbon was introduced into the chamber by injecting a known volume of pure hydrocarbon into a glass bulb and flowing purified air over the hydrocarbon at 5 L min⁻¹ until the hydrocarbon had fully vaporized.

For these low-NO_x experiments, hydrogen peroxide (H₂O₂) was used as the OH precursor. Prior 70 to atomization of the ammonium sulfate seed, H₂O₂ was introduced by flowing 5 L min⁻¹ of purified air through a glass trap containing 280 μL of a 50% aqueous H₂O₂ solution. The glass trap was submerged in a warm water bath maintained at 35-38 °C. This resulted in an approximate concentration of 4 ppm H₂O₂ in the chamber.

The aerosol number concentration and size distribution were measured by a differential mobility 75 analyzer (DMA, TSI model 3081) coupled with a condensation nuclei counter (TSI, CNC-3760). After allowing all concentrations to stabilize, irradiation was initiated. The temperature (*T*), relative humidity (*RH*), and concentrations of O₃, NO, and NO_x were continuously monitored. Experiments were run at temperatures ranging 20-26 °C and varied within ± 2 °C. *RH* remained below 10%. Table 2 summarizes the experimental conditions for the series of methoxyphenol oxidation 80 experiments conducted.

2.2 Gas-phase measurements

2.2.1 Gas Chromatography/Flame-Ionization Detection (GC/FID)

The hydrocarbon concentration was continuously monitored by GC/FID in the phenol experiments. Chamber air was sampled into a 10 mL injection loop and injected onto a HP5 15 m × 0.53 mm 85 ID × 1 μm thickness column installed on a 6890 Agilent GC. The GC response was calibrated by dissolving a known mass of the hydrocarbon in methanol and then vaporizing a known volume of that solution into a 55 L Teflon chamber. Guaiacol and syringol measurements obtained using the GC/FID were unreliable due to condensation loss in the sample loop; thus, the hydrocarbon concentration during these experiments was monitored using Chemical Ionization Mass Spectrometry

90 (CIMS) in negative mode operation.

2.2.2 Chemical Ionization Mass Spectrometry (CIMS)

Monitoring of gas-phase oxidation products was carried out in real time by the use of a CIMS instrument. The details of this instrument are described elsewhere (St. Clair et al., 2010). The instrument operates in both negative mode, using CF_3O^- as a reagent ion, and in positive proton transfer reaction (PTR)-MS mode. Negative mode is found to be more selective towards the detection of hydroperoxides and polar molecules, particularly acids, while positive mode detects a broader range of organic compounds. Analytes in negative mode can be monitored as the cluster product $[\text{R} \cdot \text{CF}_3\text{O}]^-$ and/or as the transfer product if it is more strongly acidic $[\text{R} \cdot \text{F}]^-$, where R is the analyte. Analytes in positive mode cluster as $[\text{R} \cdot (\text{H}_2\text{O})_n]^+$. Mass scans covering masses 50-300 amu for negative mode, and 50-200 amu for positive mode, with a total scan time of ~6 min were continuously repeated over the course of each experiment. Guaiacol was monitored at the fluoride transfer product ($[\text{M} + 19]^-$), m/z 143, and the cluster product ($[\text{M} + 85]^-$), m/z 209, in negative mode operation. Syringol was also monitored at the fluoride transfer product, m/z 173, and the cluster product, m/z 239.

105 **2.3 Particle-phase measurements**

2.3.1 Chamber filter sample collection, extraction, and off-line chemical characterization

A detailed description of the aerosol filter sample collection and extraction protocol for the Caltech laboratory chambers has been previously published (Surratt et al., 2008). Aerosol samples were collected on Teflon filters (PALL Life Sciences, 47-mm diameter, 1.0- μm pore size, teflomembrane). 110 Filter samplers employed for aerosol filter sample collection used a front and back-up filter sampling approach, in which back-up filters were collected in order to examine if aerosol breakthrough from the front filter occurred or whether evaporation of semivolatiles from the front filter occurred during sampling. In all experiments, no SOA constituents were detected on the back-up filters. Filter sampling was initiated when the aerosol volume reached its maximum (constant) value, as determined 115 by the DMA. Depending on the total volume concentration of aerosol in the chamber, the duration of filter sampling was 1.8 - 2.1 h, which resulted in 2.0 - 2.9 m^3 of total chamber air sampled. Teflon filter extraction protocols in high-purity methanol (LC-MS CHROMASOLV-Grade, Sigma-Aldrich) have been described previously (Surratt et al., 2008). The resultant filter extracts were then analyzed by a Waters ACQUITY ultra performance liquid chromatography (UPLC) system, coupled with a 120 Waters LCT Premier TOF mass spectrometer equipped with an ESI source, allowing for accurate mass measurements by UPLC/ESI-TOFMS to be obtained for each ion (Surratt et al., 2008).

Selected filter extracts from experiments were also analyzed by a Thermo Finnigan Surveyor high performance liquid chromatography (HPLC) system (pump and autosampler) coupled to a Thermo

Finnigan LCQ ion trap mass spectrometer (ITMS) equipped with an ESI source, allowing for tandem MS measurements to be obtained. Data were acquired and processed using Xcalibur version 1.3 software. A Waters Atlantis T3 column ($3 \mu\text{m}$ particle size; $2.1 \times 150 \text{ mm}$) was employed, which is similar to the Water ACQUITY UPLC HSS column used for the UPLC/ESI-TOFMS analysis. The mobile phases consisted of 0.1% acetic acid in water (A) and 0.1% acetic acid in methanol (B). The applied 45 min gradient elution program was as follows: the concentration of eluent B was kept at 3% for 4 min, then increased to 100% in 21 min, holding at 100% for 10 min, then decreased to 3% in 5 min, and kept at 3% for 5 min. The injection volume and flow rate were $10 \mu\text{L}$ and 0.2 mL min^{-1} , respectively. The ion trap mass analyzer was operated under the following conditions: sheath gas flow (N_2), 65 arbitrary units; auxiliary gas flow (N_2), 3 arbitrary units; source voltage, 4.5 kV; capillary voltage, 14.5 V; tube lens offset, 7 V; capillary temperature, 200°C ; and maximum ion injection time, 200 ms. Two scan events were used during each chromatographic run; scan event 1 was the full scan mode in which data were collected from m/z 120 to 600 in the negative ionization mode and scan event 2 was the MS2 mode in which product ions were generated from significant base peak ions observed in scan event 1. For MS2 experiments, an isolation width of $2.5 m/z$ units and a normalized collision energy level of 35% were applied. The $[\text{M}-\text{H}]^-$ ion signal optimization was carried out by introducing a 1 mg mL^{-1} malic acid standard solution. Due to the on-axis ESI source that is characteristic of the LCQ ITMS instrument, a solvent delay time of 3.5 min (which diverted the column effluent from the ESI source to waste) was employed to prevent clogging by nonvolatile salts at the entrance of the capillary.

2.3.2 High-Resolution Time-of-Flight Aerosol Mass Spectrometry (HR-ToF-AMS)

Real-time aerosol mass spectra were obtained using an Aerodyne HR-ToF-AMS (DeCarlo et al., 2006). The HR-ToF-AMS was operated in a lower resolution, higher sensitivity V-mode, and a high-resolution W mode, switching between modes once every minute. The V-mode data were analyzed to extract sulfate, ammonium, and organic spectra according to procedures in Allan et al. (2004). Calculation of the SOA densities were achieved by comparing the particle mass distributions obtained using the particle ToF mode and the volume distributions obtained by the DMA (Bahreini et al., 2005) in nucleation (seed-free) experiments. O : C, N : C, and H : C ratios were determined from W mode data using the APES toolbox and applying the procedures outlined in Aiken et al. (2007) and Aiken et al. (2008). The particle-phase signal of CO^+ and the organic contribution to H_xO^+ ions were estimated as described in Aiken et al. (2008). Particle-into-Liquid Sampler/Ion Chromatography (PILS/IC) was also employed as described in Kautzman et al. (2010) for the guaiacol experiments, though we find that $< \text{C}_6$ diacids do not constitute an important fraction of the SOA formed.

3 SOA yields and growth curves

The formation of secondary organic aerosol (SOA) results from the gas-particle partitioning of low-vapor-pressure products formed in the oxidation of volatile organic compounds (VOCs). The time-dependent aerosol growth curves permit analysis of the equilibrium and kinetic roles involved in SOA formation (Chan et al., 2007; Kroll and Seinfeld, 2005). The SOA yield is defined as the ratio of mass of organic aerosol formed, ΔM_o , to the mass of the parent organic species consumed, ΔOrg , $Y = \Delta M_o / \Delta \text{Org}$. The SOA yields for all experiments are summarized in Table 2. To calculate the mass concentration of the SOA, the SOA volumes established by DMA measurements are wall-loss corrected and then multiplied by the SOA density, as determined by the AMS in seed-free (nucleation) experiments. A density of $1.65 \mu\text{g cm}^{-3}$ was determined for phenol. Guaiacol and syringol densities were determined to be $1.45 \mu\text{g cm}^{-3}$ and $1.49 \mu\text{g cm}^{-3}$, respectively. The O : C was calculated at time of maximum SOA growth for these systems and were reported in Chhabra et al. (2011). O : C values of 0.88 ± 0.27 , 0.89 ± 0.28 , and 0.97 ± 0.30 were calculated for the phenol, guaiacol, and syringol systems, respectively.

About 80% of the initial phenol was reacted in these experiments. SOA yields for phenol range 25-44% under the experimental conditions. For phenol, the hydrocarbon measurement obtained from all gas-phase instruments displayed interferences under low- NO_x conditions, leading to a wider spread and greater uncertainty in the yield and growth curve parameters. Still, the measured yields under low- NO_x conditions overlap with the range of 38-45% reported by Nakao et al. (2011).

Characteristic growth curves for guaiacol are shown in Figure 1. Greater than 90% of the initial guaiacol was consumed over the course of all experiments except for the higher guaiacol loading 1/29 experiment as noted in Table 2. SOA yields from guaiacol photooxidation, based on the final aerosol volume achieved, range 44-50%. Aerosol growth curves under these conditions for all initial guaiacol and seed concentrations fall on a line (Figure 1), consistent with the formation of essentially non-volatile products.

Aerosol growth curves for syringol are shown in Figure 2. Within six hours of irradiation, the syringol levels are lower than the limit of detection. The SOA yields for syringol are less than those of guaiacol, ranging 25-37%. This range overlaps yields of 10-36% reported for syringol photooxidation under high- NO_x (approaching 10 ppm NO) conducted by Lauraguais et al. (2012) using CH_3ONO as the OH source. The SOA yields from the photooxidation of syringol are substantially lower than those of phenol and guaiacol, even though the boiling point and vapor pressure of syringol suggest it might have greater potential to form SOA. We further explore the chemical basis for this after examining the gas-phase chemistry.

In this low- NO_x regime, the aerosol growth curves overlap within a system, regardless of initial organic loading. Most methoxyphenol experiments ended shortly after the hydrocarbon decay was complete. Though, even 4 h after 109 ppb syringol was completely reacted in the 3/29 experiment, there was no additional SOA growth. The type of growth observed here is typified by

195 a mechanism involving oxidation to form SOA either from first-generation products or sufficiently rapid low-volatility product formation over the course of the experiment from further generation reactions (Chan et al., 2007; Ng et al., 2006). We believe it to be the latter explanation in the case of methoxyphenol systems. The high-level of oxidation determined from the measured O : C ratios of the SOA are indicative of multi-generation products, which is consistent with the identified gas and
 200 aerosol products discussed below.

4 SOA formation chemistry

We present in this section an analysis of the gas-phase mechanistic chemistry involved in SOA formation based on the CIMS traces for each system along with SOA mass growth over time. All ions unless otherwise noted were monitored during negative mode operation. CIMS signals are plotted
 205 in arbitrary units (a.u.). Discussion is focused on the guaiacol system since the offline aerosol filter analyses complement the gas-phase data. Chemical parallels are drawn between the three systems.

4.1 Gas-phase oxidation

Substituent groups such as -OH and -OCH₃ activate more strongly the aromatic ring towards electrophilic addition of OH compared to the -CH₃ group. Of these groups, activation potential of the
 210 ring increases in order of -CH₃ < -OCH₃ < -OH. Thus, as predicted, methoxyphenol compounds react faster with OH than their methyl or unsubstituted equivalents (Coeur-Tourneur et al., 2010). Methoxy and hydroxy substituent groups tend to make OH-attack favorable at positions *ortho* and *para* to the substituents, so structures for the measured *m/z*'s are proposed from chemical mechanisms assuming one of these positions of initial OH-attack. H-atom abstraction from the methoxy
 215 group is expected to be small, as this path was determined to contribute < 4% in the case of methoxybenzene (Coeur-Tourneur et al., 2010).

A generation is defined as the OH-initiated reaction of a stable (non-radical) species, and the OH exposure is calculated as the product of the OH concentration (inferred from the parent hydrocarbon decay) and the hours of irradiation. Each *m/z* is the sum of the signal from all isomeric structures detected by the CIMS at that ion, but are not shown explicitly in the abbreviated mechanisms and tables presented. However, from the chemical ionization method employed, we expect certain common chemical features of the proposed structures. For example, many of the transfer [M+19]⁻ products are likely acidic, containing carboxylic acid groups and/or sufficient acidic hydroxyl groups.

4.2 Phenol chemistry

225 Initial steps of the phenol gas-phase mechanism have been elucidated elsewhere (Olariu et al. 2002, Berndt and Boge 2003). Phenol + OH proceeds primarily with *ortho*- OH addition to the ring, O₂ addition, followed by elimination of HO₂ to form 1,2-dihydroxybenzene (catechol). In the low-NO_x

phenol experiments, CIMS ions are tracked that show successive OH adduct product formation up to three generations. Quinone products are also likely, though these are not detected in negative mode operation of the current CIMS technique unless they are additionally functionalized. A list of ions monitored in this system is presented in Table 3. Representative data for the phenol low- NO_x system are shown in Figure 3. Phenol, $\text{C}_6\text{H}_6\text{O}$, is monitored at m/z 179, a cluster product. We do not include m/z 113, the fluoride transfer product, because this signal includes interference from another compound (likely a small acid) that grows in over time. Dihydroxybenzene, $\text{C}_6\text{H}_6\text{O}_2$, is observed primarily as the fluoride transfer product m/z 129 (DHB) with less signal observed at the m/z 195 cluster product. A trace at m/z 211 indicates a third OH addition to the ring to form trihydroxybenzene (THB), $\text{C}_6\text{H}_6\text{O}_3$. These time profiles are shown along with SOA growth and phenol decay for the first nine hours of irradiation (Figure 3). SOA growth occurs coincident with the growth of m/z 211 (THB), indicating that the transition to lower volatility products to form SOA likely occurs along the 3rd addition of OH just after $\sim 1 \times 10^6$ molec cm^{-3} h of OH exposure. This is the approximate equivalent of one hour of photooxidation in the atmosphere assuming an ambient OH concentration of $\sim 1 \times 10^6$ molec cm^{-3} . There was very little signal at m/z 227, presumably $\text{C}_6\text{H}_6\text{O}_4$ (4HB) and a minor amount at m/z 229, the hydroperoxide $\text{C}_6\text{H}_8\text{O}_4$.

Figure 3 also shows that the SOA is in equilibrium with m/z 185, which we propose to be the ring fragment $\text{C}_4\text{H}_4\text{O}_3$, a carboxylic acid that forms from the decomposition of the bicyclic radical from phenol + OH. Another carboxylic acid, $\text{C}_4\text{H}_4\text{O}_4$, is monitored at m/z 135, which could be the analogous ring fragment from dihydroxybenzene + OH. These acids approach the high O:C ratios characteristic of the SOA in this system. Comparisons of the CIMS gas-phase traces and the offline filter analyses from similar experiments performed by Nakao et al. (2011) provide additional insights. Nakao et al. (2011) utilized electrospray ionization and atmospheric pressure chemical ionization mass spectrometry (ESI/APCI-TOFMS) as well as PILS-ESI-TOFMS for analysis, though Nakao et al. (2011) noted that the PILS-ESI-TOFMS spectra may include water soluble gas-phase species because a denuder was not used. While Nakao et al. (2011) observed an exact mass match that corresponds with the bicyclic hydroperoxide from phenol ($\text{C}_6\text{H}_8\text{O}_6$) and another compound with a suggested formula $\text{C}_6\text{H}_8\text{O}_7$ using both techniques, we do not observe these products in the gas-phase with the CIMS. It is possible that these compounds are of sufficiently low volatility at this point that they are not measurable in the gas phase. The CIMS does detect ions corresponding to several $< \text{C}_6$ products seen in Nakao et al. (2011), including: $\text{C}_4\text{H}_4\text{O}_3$ at m/z 185, $\text{C}_4\text{H}_4\text{O}_4$ at m/z 's 135 and 201, and $\text{C}_3\text{H}_4\text{O}_3$ at m/z 107.

Nakao et al. (2011) also observed a series of oxygen additions, from $\text{C}_6\text{H}_6\text{O}_2$ to $\text{C}_6\text{H}_6\text{O}_5$, which are interpreted to possibly be a series of OH adduct products. Another structural possibility is that these are C_6 retaining, but ring-opened carboxylic acids that would correspond to large signals in the CIMS as transfer products: m/z 's 145, 161, and 177. From the time profiles of these CIMS ions, we predict that they are likely carboxylic acids even though the proposed chemical formulae are isomeric

265 to the aromatic OH adducts. The prevalence of these products may explain the absence of a strong signal from a hydroperoxide $C_6H_8O_4$ at m/z 229. The alkylperoxy radical preferentially isomerizes to form the bicyclic peroxide radical and decomposes to $<C_6$ fragments as mentioned above, or it may participate in chemistry that regenerates OH and opens the ring (Birdsall et al., 2010). Figure 4 outlines a potential mechanism similar to that presented in Birdsall et al. (2010) to form these
 270 multifunctional C_6 carboxylic acids from phenol, dihydroxybenzene, and trihydroxybenzene. OH regeneration could also come from photolysis of a hydroperoxide producing a favorable alkoxy radical for ring opening, though we would not expect this to be significant on such a quick timescale that is consistent with negligible signal from the hydroperoxide. All CIMS traces for proposed ring opening acids (ACID) and ring fragments (FRAG) are presented in Figure 5. They all share a similar
 275 trend of constant linear growth over time.

4.3 Guaiacol chemistry

Figure 6 presents proposed oxidation pathways for the guaiacol system under low- NO_x conditions. Solid boxed structures indicate that the expected m/z from the chemical ionization reactions in the CIMS for that compound was detected. The m/z monitored is indicated, as are proposed $C_xH_yO_z$
 280 formulas and molecular weights. A list of ions monitored in this system is presented in Table 4. Chemical formulas shown in red indicate correspondence with a suggested $C_xH_yO_z$ for accurate mass observations in filter data (Table 5). The particular structures in Figure 6 indicate potential structures for the accurate mass suggested chemical formulae and the mechanism does not explicitly present all potential isomeric structures. The boxed colors correspond with the colors used for ion time traces as measured by the CIMS and included in Figure 7.

Guaiacol gas-phase oxidation proceeds with OH addition to the ring, followed by reaction with oxygen to form an organic peroxy radical. Under the experimental conditions, the fate of this RO_2 radical is reaction with HO_2 to form a hydroperoxide (Figure 6, Pathway 1), elimination of HO_2 to retain aromaticity (Figure 6, Pathway 2), or isomerization to the bicyclic radical (Figure 6, Pathway
 290 3).

4.3.1 Pathway 1: $RO_2 + HO_2$

Despite predominant conditions of $RO_2 + HO_2$ chemistry, we do not observe strong signals in the CIMS measurements for potential hydroperoxides, as is similar to the case of phenol. A small trace at m/z 259 suggests that there is slight production of the hydroperoxide $C_7H_{10}O_5$. The offline filter
 295 analysis does reveal a small contribution from a corresponding accurate mass measurement (Table 5). More significant signals in the CIMS are presented in Figure 7, demonstrating that the preferred routes are to preserve aromaticity or involve isomerization to the bicyclic radical. This observation is consistent with previous studies on aromatic systems (Calvert et al. 2002; Bloss et al. 2005; Johnson et al. 2005; Birdsall et al. 2010).

300 **4.3.2 Pathway 2: Continuous OH addition to ring**

The general chemical development of the consecutive OH addition pathways in the guaiacol low-
NO_x system are tracked in Figure 7. Figure 6, Pathway 2 is marked by *m/z* 225 on the CIMS, a
cluster product for the guaiacol OH-adduct product, C₇H₈O₃ and denoted as G + OH. Successive
OH addition products are monitored at 16 amu increments at *m/z*'s 241 and 257, for C₇H₈O₄ denoted
305 as G + 2OH and C₇H₈O₅ denoted as G + 3OH, respectively. The third OH adduct can be tracked
at both the transfer and the cluster products, *m/z* 191 and *m/z* 257, respectively. However, *m/z* 257
includes the combined signal of rapid epoxide formation and the later formed third generation OH
adduct. A signal at *m/z* 191 is predominantly the third generation OH adduct during the first 8 h
until another product (likely an acid) grows in at this *m/z*. The first OH-adduct product (*m/z* 225)
310 is short-lived due to further activation of the ring by the additional hydroxy group. Formation of
C₇H₈O₄ monitored at *m/z* 241 follows promptly. The signal at *m/z* 191 (not shown) was observed
to follow after *m/z* 241, indicating that third OH addition is achieved. C₇H₈O₅ is also a proposed
chemical formula for a product observed in the filter analysis (Table 5), suggesting that the third OH
adduct is of sufficiently low volatility to partition to the particle phase.

315 **4.3.3 Pathway 3: Isomerization to bicyclic radical**

The bicyclic peroxy radical can react with HO₂ to form the bicyclic hydroperoxide C₇H₁₀O₇ (Figure
6, Pathway 3ai), however no evidence exists for this product in the CIMS. This is analogous with
the bicyclic hydroperoxide from the phenolic case. However, if this product is formed, it already
has a low vapor pressure and an O : C of 1, and would likely partition into the aerosol phase. Filter
320 data also indicate the presence of C₇H₁₀O₇ in the particle-phase (Table 5). The majority of the filter
data guaiacol products exhibit O : C ratio >0.7, and the average bulk O : C ratio as measured by
the AMS is 0.89, so it is likely these hydroperoxide species may immediately partition and become
further processed in the particle phase.

Alternatively, the bicyclic radical can rearrange, breaking the oxygen bridge to form an epoxide
325 and open the ring (Figure 6, Pathway 3aiii). There is evidence of a significant epoxide (EPOX) route
that grows in early with the dihydroxybenzene route (Figure 7). The epoxide is monitored at *m/z*
257, the cluster product of C₇H₈O₅ (Figure 7), though there is some later contribution from the third
generation OH adduct, as mentioned earlier. The epoxide will continue to react with OH to generate
more functionalized molecules that will likely contribute to SOA formation.

330 The bicyclic radical can also decompose to several fragments as shown in the box in Figure 6,
Pathway 3aiii. A major fragment is observed at *m/z* 149, which could be the methoxy analog to
the phenolic fragment, hydroxy-butenedial (C₄H₄O₃) at *m/z* 185. We propose that *m/z* 149 is a
methoxy-hydroxy-butenedial fragment, C₅H₆O₄. C₅H₆O₄ is also an accurate mass assignment for
a product observed in the filter data (Table 5). The *m/z* 149 trace has a similar profile to the SOA

335 mass curve, indicating that it is in equilibrium with the particle phase (Figure 7). Other possible fragments are observed at m/z 's indicated in the mechanism. The $<C_4$ fragments approach O : C values >1 , and the C_4 and C_5 fragments would likely undergo further oxidation in the gas phase and then possibly contribute to the particle phase. The fate of butenedial ($C_4H_4O_2$) has been described elsewhere (Calvert et al. 2002; Bloss et al. 2005).

340 **4.3.4 Pathway 4: Methoxy loss route**

The early growth of a strong signal at m/z 129 (Figure 7) and a matching time profile at m/z 195 upon irradiation suggests that dihydroxybenzene ($C_6H_6O_2$) is somehow formed from guaiacol ($C_7H_8O_3$) + OH in the gas phase. This is further supported by matching time profiles from the guaiacol and phenol systems for dihydroxybenzene (DHB) and its oxidation to trihydroxybenzene (THB) in 345 Figure 8A, as well as growth of the proposed C_6 ring opening acids (Figure 8B). In the guaiacol system, the raw signal at m/z 211 includes contributions from the ^{18}O natural isotope peak of the guaiacol cluster product and trihydroxybenzene. The signal at m/z 211 has been corrected to reflect only the contribution from trihydroxybenzene (G-THB). There is negligible signal at m/z 227 in the 350 guaiacol system, indicating that the dihydroxybenzene that is formed proceeds only to one more step of oxidation before the carbon along this route is incorporated into pathways besides continuous OH adduct formation. Rather, the carbon likely ends up in production of ring-opened acids as shown in Figure 8B.

A trace at m/z 243 is present in the guaiacol system, though because there is negligible signal at m/z 227, it is unlikely that this ion is part of the OH adduct series from dihydroxybenzene as 355 $C_6H_6O_5$. Still, an exact mass match for $C_6H_6O_5$ is the fourth highest product (in terms of area counts) of constituents identified in the filter data, and m/z 243 follows the SOA trace indicating that it may be an important contributor to the particle phase. In the event that radical placement occurs on the carbon containing the methoxy group during formation of the bicyclic radical, carbon loss may occur by removal of a methyl radical. This leads to formation of a C_6 bicyclic ketone product 360 as outlined in Pathway 3b of Figure 6.

4.3.5 Guaiacol aerosol-phase products

The offline filter analysis suggests that there are additional chemical pathways for this system than those inferred from the gas-phase CIMS measurements. The top fifteen ions (by highest peak area) are presented in Table 5 along with measured masses and suggested corresponding chemical formulae. Of the suggested chemical formulae, the O : C ranges from 0.67 to 1.5. The $<C_7$ components are likely ring fragments that have undergone further oxidation to achieve such high O:C compared to those shown in Figure 6, Pathway 3aiii. Of the C_7 retaining products listed in Table 5, all suggested chemical formulae except $C_7H_5O_5$ can be explained by first-generation products along pathways 1, 2, 3ai, and 3aii (Figure 6) and the analogous pathways in higher generation chemistry from the OH

370 adducts. Similar structures to those proposed here have been observed previously in EI-MS analyses (Justesen, 2001). However, since many corresponding signals are not observed in the CIMS, it is also possible that a number of these highly oxygenated ($> O_5$) species may be formed in the particle phase.

4.4 Syringol chemistry

375 The chemistry of syringol under low- NO_x conditions leads to rapid formation of a rich diversity of gas-phase products and SOA growth. Whereas at least two generations of OH oxidation of phenol are required to generate SOA, guaiacol and syringol produce SOA in the first generation. This is clear when comparing the SOA mass curves between systems in Figures 3, 7, and 9. As expected, syringol is more reactive than guaiacol because of its additional methoxy group. Syringol is detected 380 primarily at the transfer $[M+19]^-$, m/z 173, with some signal at the cluster product $[M+85]^-$, m/z 239. This is the opposite of guaiacol, the signal of which is found predominantly at the cluster product. This suggests that the extra methoxy group on syringol compared to guaiacol leads to an enhancement towards greater acidity to be seen predominantly at the transfer product. This shift is observed for many of the ions in the syringol case that are analogous to the guaiacol system. CIMS 385 ions monitored in this system are presented in Table 6.

Syringol oxidation chemistry seems to undergo similar routes as guaiacol with analogous ions monitored by the CIMS for the following pathways: 1) hydroperoxide formation, 2) OH adduct formation up to two to three generations, and 3) epoxide and $<C_8$ ring fragment formation from decomposition of the bicyclic radical. These pathways are highlighted in Figure 9A by selected ions 390 at m/z 's 189 and 271 for OH adducts $C_8H_{10}O_4$ ($S + OH$) and $C_8H_{10}O_5$ ($S + 2OH$), respectively, m/z 287 for the $C_8H_{10}O_6$ syringol epoxide (SEPOX), and a $C_6H_8O_5$ ring fragment (FRAG) at m/z 245. A minor contribution from the $C_8H_{12}O_6$ syringol hydroperoxide at m/z 289 was observed in the CIMS spectra and is not shown.

These routes seem to be minor, however, in comparison to those that favor immediate scission 395 of the C_8 backbone (Figure 9). Many of the higher signals in the CIMS are at m/z values that can only be reasonably explained by $<C_8$ molecular formulas. For example, major traces are from ions at m/z 275 (Figure 9B), likely $C_7H_{10}O_6$. A signal was also observed in the CIMS spectra at m/z 291, possibly $C_7H_{10}O_7$, and is not shown. There is also evidence of methoxy and hydroxy exchanges and eliminations, providing even more diversity of masses in the CIMS spectra from 400 syringol photooxidation. More detailed analyses on chemical structure would be required to confirm precise mechanisms.

For syringol, the immediate loss of carbon through novel chemical pathways (methoxy group elimination or exchange with hydroxy) is more evident in multiple routes than was observed in the case of guaiacol. Figure 10 proposes several possibilities of syringol conversion to compounds 405 with fewer methoxy groups. Each of these pathways has representative ions that also appear in the

guaiacol case, though they are not necessarily the same mechanistically.

Analogous to the formation of dihydroxybenzene in the case of guaiacol + OH, the early growth of m/z 225 (presumably $C_7H_8O_3$) suggests that hydroxy guaiacol (G + OH) may form from syringol + OH (Figures 9B, 10, Pathway a). Another possibility is the complete exchange of both methoxy groups for hydroxy groups, resulting in trihydroxybenzene (THB) monitored at m/z 211 (Figures 9B, 10, Pathway b). Formation of guaiacol is also evident by matching time profiles growing in at m/z 143 and 209 (Figures 9B, 10, Pathway c). Growth of dihydroxybenzene (DHB) at m/z 129 and m/z 195 is observed later in the experiment, likely from conversion of guaiacol (Figure 10, Pathway d). Observation of signal at m/z 257 (the guaiacol epoxide and third OH adduct) supports that there is a guaiacol channel in syringol photooxidation, and is not shown. Though a guaiacol channel exists, the coincident formation of m/z 225 (G + OH) and m/z 211 (THB) with that of guaiacol at m/z 209 is consistent with their direct formation from syringol + OH.

4.5 Novel chemical pathways for loss of carbon in methoxyphenol systems

We observe evidence that guaiacol and syringol OH-initiated photooxidation leads to loss of carbon, likely due to unique chemistry involving the methoxy group. While gas-phase aromatic chemistry is not completely understood (Calvert et al., 2002), we propose possible explanations for these novel carbon loss pathways that seem specific to the methoxyphenols. Aihara et al. (1993) studied two pathways in which 1,2-dihydroxybenzene (catechol) forms from *o*-methoxyphenols using a copper (II) - ascorbic acid -dioxygen system: hydroxyl radical attack *ipso* to the methoxy containing carbon, and H-abstraction from the methoxy group. Hydroxyl radical attack *ipso* to the methoxy containing carbon allows for loss of the methoxy (-OCH₃) group in the form of methanol (CH₃OH), removing a C atom from the parent molecule. During H-abstraction from the methoxy group, Aihara et al. (1993) propose that the OCH₂ radical reacts with the OH radical and then elimination of formaldehyde (HCHO) ensues. In isotopically labeled studies, Aihara et al. (1993) observed transformation of guaiacol to catechol and syringol to hydroxy guaiacol. They also measure yields of these products that might imply *ipso* addition of OH being a more important route than previously considered compared to *ortho*- and *para*- OH addition to the ring. This route could serve as explanation of the observed hydroxy substitutions of methoxy groups in the current systems, but they cannot be verified without measurements of methanol and formaldehyde.

While we see ions indicating that methoxy groups may convert to hydroxyl groups, we do not see evidence supporting the addition of or reversible exchange of methoxy groups to the ring. Methoxy radicals may be formed from photolysis of the C–OCH₃ bond, if we assume that this bond energy can be proxied by the bond in dimethylether (CH₃–OCH₃). This bond energy, 351.9 kJ/mole (Luo, 2007), translates to an approximate wavelength of 340 nm, exactly where the irradiance spectrum of the light source in our atmospheric chambers peaks. In the event that methoxy radicals are formed, though, it seems unlikely that methoxy radical reaction with the methoxyphenols results

in methoxy addition to the ring or replacement of a hydroxy group, especially compared to rapid reaction with O_2 . Gomez et al. (2001) studied the reaction rate constants for methoxy radical with cyclohexane, cyclohexene, and 1,4-cyclohexadiene. It was found that methoxy radical reaction with 445 these compounds is likely to result in preferential H abstraction with minor routes of addition to cyclohexene and 1,4-cyclohexadiene. This corroborates the absence of $>C_7$ species in the guaiacol case and $>C_8$ species in the syringol case.

Thermodynamic evaluation of the substituent group effects in methoxyphenols can also provide some insight. The following discussion is based on the work presented in Varfolomeev et al. 450 (2010) that examines pairwise substitution effects, and inter- and intramolecular hydrogen bonds in methoxyphenols and dimethoxybenzenes. Varfolomeev et al. (2010) show that intramolecular hydrogen bonding plays a significant role on *ortho*-methoxy substituted phenols. This leads to *o*-methoxyphenols having a lower phenolic O–H bond dissociation energy (BDE) compared to *meta* isomers and higher than *para* isomers. This means that the phenolic O–H BDE increases in order 455 the order 4-methoxyphenol < 2-methoxyphenol < 3-methoxyphenol. From the ab initio calculations of Varfolomeev et al. (2010), the enthalpy of formation for 2-methoxyphenol (guaiacol) is expressed below:

$$\Delta_f H_m^\circ(2\text{-methoxyphenol}) = \Delta_f H_m^\circ(\text{B}) + \Delta H(\text{H} \rightarrow \text{OH}) + \Delta H(\text{H} \rightarrow \text{OCH}_3) + (\text{ortho-OH-OCH}_3),$$

where $\Delta_f H_m^\circ(\text{B})$ = enthalpy of formation of benzene,

460 $\Delta H(\text{H} \rightarrow \text{OH}) = -179.0 \text{ kJ mol}^{-1}$, the increment in enthalpy for substitution of an H atom by -OH,

$\Delta H(\text{H} \rightarrow \text{OCH}_3) = -150.5 \text{ kJ mol}^{-1}$, the increment in enthalpy for substitution of an H atom by -OCH₃, and

465 $(\text{ortho-OH-OCH}_3) = 4.5 \text{ kJ mol}^{-1}$, the increment in enthalpy for the pairwise interactions of -OH and -OCH₃ *ortho* to one another.

The enthalpy of formation expression begins with the base enthalpy of formation from benzene, then adds the effects of hydroxy or methoxy substitution to the ring. Finally, the pairwise interactions are added, reflecting the stabilizing intramolecular H bonding and destabilizing effect from sterics in the *ortho*-OH–OCH₃ configuration. From comparison of the substitution effects alone, this 470 suggests that H→OH is slightly more favorable than H→OCH₃. For example, this might support substitution of a methoxy group by a hydroxy group in the guaiacol system, as the pairwise *ortho* effect is minimal.

Assuming that the Varfolomeev et al. (2010) formulation can be extended to the case of a trisubstituted benzene, we can write an analogous expression for the case of syringol (2,6-dimethoxyphenol):

475 $\Delta_f H_m^\circ(2,6\text{-dimethoxyphenol}) = \Delta_f H_m^\circ(\text{B}) + \Delta H(\text{H} \rightarrow \text{OH}) + 2 \times \Delta H(\text{H} \rightarrow \text{OCH}_3) + 2 \times (\text{ortho-OH-OCH}_3) + (\text{meta-OCH}_3\text{-OCH}_3),$

where $(\text{meta-OCH}_3\text{-OCH}_3) = 0.1 \text{ kJ mol}^{-1}$ from Varfolomeev et al. (2010).

After writing a similar expression for 3-methoxybenzene-1,2-diol (hydroxyguaiacol), the differ-

ence between the substituent effects for hydroxyguaiacol and syringol is -30 kJ mol^{-1} , in slight favor of hydroxyguaiacol. The pairwise effect of (*ortho*-OH-OH) was not calculated by Varfolomeev et al. (2010), but assuming that it is less sterically hindered compared to (*ortho*-OH-OCH₃) and is stabilized by intramolecular hydrogen bonding similar to 1,2-dimethoxybenzene, we assume it to be $< 4.5 \text{ kJ mol}^{-1}$. Due to the combined favorability of energetics for the substituent effects and the pairwise effects, this can help explain why some of the syringol rapidly converts to hydroxyguaiacol and even trihydroxybenzene.

The "phenolic route," involving OH addition at the *ortho* position to the main electron-donating substituent group has been cited as being the main channel responsible for SOA formation in many aromatic systems (Calvert et al. 2002; Johnson et al. 2005; Nakao et al. 2011). However, with the additional methoxy groups, OH attack alpha to the methoxy groups becomes competitive and changes the potential for maintaining aromaticity in the methoxyphenol systems. It is possible that the extra methoxy group in syringol inhibits OH attack that is typically favored *ortho* to the hydroxyl substituted carbon in other systems that generate SOA via this route. For the other compounds, in order to achieve the degree of oxidation of the aerosol, it appears that at least two steps of reaction are needed, but that these steps occur fairly rapidly. If subsequent OH reactions are even slower due to the extra methoxy group in the case of syringol, then conversion to SOA may not be as complete as with the other two compounds over the duration of the experiments reported here.

4.6 Chemical basis for observed yields

The AMS high-resolution spectra for the methoxyphenol systems are distinct. Initial aerosol growth in the guaiacol system is marked by the exact mass ion C₄H₃O₂⁺. Later the aerosol growth is characterized by the ions C₂H₃O⁺, and C₂H₅O₂⁺. In the case of syringol, initial growth is characterized by C₅H₂O₂⁺ and C₇H₉O₃⁺ ions, followed by C₅H₅O₄⁺, and then by C₅H₂O₄⁺ and C₂H₄O₃⁺. This suggests that guaiacol SOA is characterized by smaller carbon number and less oxygenated fragments than the case of syringol.

The characteristic ions from the AMS spectra for syringol SOA seem counter-intuitive for understanding why the syringol SOA yield is lower than that of guaiacol. Syringol has more carbon and oxygen to begin with and these ions are larger, more oxygenated fragments than in guaiacol. However, if we return to the gas-phase comparison of the characteristic trends in the guaiacol (Figure 7) and syringol (Figure 9) systems, one notes that many of the major products from syringol photooxidation peak later than their analogs in the guaiacol system. Further, there is no analogous peak in the guaiacol system to the *m/z* 275 unique to the syringol system. Since this is a major product of gas-phase syringol photooxidation and it peaks $> 4 \times 10^6 \text{ molec cm}^{-3} \text{ h}$ of OH exposure compared to guaiacol ions that peak generally within $3 \times 10^6 \text{ molec cm}^{-3} \text{ h}$, it acts like a gas-phase carbon reservoir. That is, the signal at *m/z* 275 is much more significant than the more efficient SOA formers at *m/z* 129 (dihydroxybenzene, not shown) and *m/z* 209 (guaiacol) in Figure 9B.

515 AMS elemental analyses of SOA from these systems as reported in Chhabra et al. (2011) suggest
 that the majority of oxygenation is derived from organic acid functionalities: 77% for phenol, 61%
 for guaiacol, and 59% for syringol. This is consistent with the necessity of further oxidation of
 acidic fragments to explain the presence of highly oxidized species observed in the guaiacol filter
 analyses. The decrease in oxygenation derived from organic acid functionalities from phenol to
 520 the methoxphenol systems may reflect the oxygen reserved in OH adduct and aromatic retaining
 pathways, especially in the case of syringol (Figure 10). This may also partially explain why the
 syringol SOA yield is lower if acid formation drives the SOA growth. At similar OH exposures, the
 syringol system still has not developed an acid signal that tracks well with the SOA growth, as *m/z*
 525 185 does in the phenol system (Figure 3) and *m/z* 149 does in the guaiacol system (Figure 7). The
m/z 245 fragment lags the SOA growth in the syringol system (Figure 9A). This could be due to
 the lack of OH addition to the ring on syringol in critical positions that lead to SOA formation via
 ring-opening acid formation.

5 Atmospheric relevance

530 While the current experiments were conducted without the addition of NO_x , the chemistry elucidated
 under these low- NO_x conditions is expected to be relevant for typical atmospheric conditions. For
 phenol photooxidation in the presence of NO_x , Olariu et al. (2002) measured yields of 0.8 catechol
 (1,2-dihydroxybenzene), 0.037 1,4-benzoquinone, and 0.058 2-nitrophenol. However, according
 to kinetic data and yield comparisons for nitrophenol presented in Berndt and Boge (2003), it is
 likely that this nitro-product formation can be biased due to sufficiently high NO_2 ($\lesssim 800$ ppb)
 535 concentrations. Berndt and Boge (2003) point out that for atmospheric conditions with NO_2 of
 approximately 20 ppb, it is probable that phenoxy radicals also react with O_3 as well as NO and
 NO_2 . This would result in more minor nitrophenol yields in the atmosphere.

540 Thus, because OH addition dominates over H abstraction, and subsequent O_2 addition to the OH
 radical adduct is rapid, it is more likely that in the atmosphere, SOA primarily forms via pathways
 involving higher-generation OH adducts and their respective routes to oxygenated fragments. This
 is consistent with the chemistry presented in this work. Though we did not observe appreciable
 evidence of gas-phase hydroperoxides, they may be rapidly incorporated into the particle phase and
 contribute to peroxide formation, as postulated by Johnson et al. (2005) and observed by Sato et al.
 545 (2007) for the case of toluene photooxidation. Sato et al. (2007) also find similar species in the
 particle-phase under $[\text{NO}]_0 = 0.2$ and 1 ppm, still citing O_2 addition to the OH-aromatic adduct as
 the major channel contributing to SOA formation.

In the presence of moderate NO_x , we would expect the major gas-phase species to be the same as
 those presented here, with only a minor contribution from nitrogen-containing products. Still, for the
 studied compounds, novel routes of reaction of alkylperoxy radicals under these low- NO_x conditions

550 may still result in product distributions expected under higher NO_x conditions. First, the aromatic peroxy radicals in the studied systems may preferentially decompose to regenerate OH via novel $\text{RO}_2 + \text{HO}_2$ chemistry (Birdsall et al., 2010). This is a possible explanation for the observation of ring-opened acids in phenol and guaiacol. Second, generation of carbonyls via novel rearrangements of ether peroxy radicals (Orlando and Tyndall, 2012), relevant for guaiacol and syringol, would
555 further make the product distributions less distinct from alkoxy radical pathways expected under high- NO_x chemistry.

These observations warrant caution when conducting experiments in the presence of NO_x for aromatic compounds, as derived aerosol yields may be based on chemistry non-representative of the atmosphere. Klotz et al. (2002) found that at high- NO_x conditions (hundreds of ppb to ppm)
560 one must also start to consider reactions of NO_x with the hydroxy radical adduct. At sufficiently high NO_x concentrations, the gas-phase chemistry can generate higher yields of nitroaromatics as compared to the OH aromatic adduct (Koch et al., 2007; Nishino et al., 2008). Nitroaromatics can serve to enhance aerosol yields if sufficient nitro-containing functionalities are achieved or to act as gas-phase carbon reservoirs and depress aerosol yields. Hydroxyl groups will lead to a vapor
565 pressure lowering more than that associated with nitro groups, but sufficient nitro groups could lead to incorporation to the particle phase. Owing to the lower OH reactivity of the molecule containing a nitro group as compared to the comparable molecule containing a hydroxyl group (Kwok and Atkinson, 1995), one might also find that more OH is necessary in the presence of NO_x to attain further gas-phase development to more highly oxidized species that contribute to SOA formation.

570 While the OH-initiated photooxidation of aromatics in general is complex (Calvert et al., 2002), methoxyphenols seem to follow some steps of the general mechanism developed for simpler aromatics. We have qualitatively presented gas-phase trends that give some insight into the chemistry of SOA formation. Though, more complete mechanism development would be enhanced by the availability of authentic standards to solidify mass assignments and more detailed structural information.
575 For example, the structural identity of the ion at m/z 275 in the syringol system remains elusive. Calculation of quantitative gas-phase yields would benefit from additional kinetic data pertaining to some of the complex intermediates.

Carbon loss via the methoxy groups in guaiacol and syringol appears to be a feasible route to describe the gas-phase product distributions. While the chemistry of syringol is complex, this compound
580 may be a better model system to represent the mixture of methoxy and phenolic compounds since it displays chemistry from both classes. Syringol, however, does not generate as much SOA as these other systems. This may be a result of the unique $\text{OCH}_3-\text{OH}-\text{OCH}_3$ pairwise effects that hinder the typical phenolic pathway responsible for SOA formation.

Future studies to investigate this effect might start with methoxyphenols of different substituted
585 positions relative to the hydroxy group to see the effect on SOA yields. For example, using a methoxyphenol where at least one or two methoxy groups are not *ortho* to the hydroxy group would

serve to further investigate the importance of OH addition *ortho* to the hydroxy group in these compounds, as 1,2-dihydroxybenzene is the major gas-phase product and SOA fomer from phenol. Also, 2,5-dimethoxyphenol might also indicate if OH attack is preferred at the 6-position, again *ortho* to the hydroxy group. Such studies would require more detailed analyses that provide greater structural analysis for the gas-phase products as well as unique tracers for fragmentation patterns that would clarify the chemistry.

Detailed study of the gas-phase products from the OH-initiated photooxidation of methoxybenzene might also be informative for understanding the proposed carbon loss associated with methoxy groups in the guaiacol and syringol systems. If phenol is a major product, this has implications on understanding the chemical fate of methoxyphenol-like compounds in the atmosphere. For example, Lauraguais et al. (2012) suggest that syringol is too reactive with OH (1.8 h) to be a relevant tracer in the atmosphere for woodsmoke emissions and that it results in a very minor SOA yield. However, the chemical analyses presented in this study suggest that syringol can efficiently convert to guaiacol and hydroxylated benzenes that are longer lived in the atmosphere and potentially have larger SOA yields. This can be analogous to the isoprene photochemical cascade, where it is the products of isoprene photooxidation that have greater SOA forming potential (Kroll et al., 2006). The syringol conversion to guaiacol also has implications for using these compounds as specific tracers for fuel type (hardwood vs. softwood). Thus, care must be taken in selecting one or more surrogate species for use in modeling aerosol yields from biomass burning emissions in the atmosphere.

Acknowledgements. This work was supported by the US Department of Energy grants DE-FG02-05ER63983 and DE-SC 0006626 and US Environmental Protection Agency (EPA) STAR Research Agreement No. RD-833749.

References

610 Aihara, K., Urano, Y., Higuchi, T., and Hirobe, M.: Mechanistic studies of selective catechol formation from o-methoxyphenols using a copper(II) ascorbic-acid dioxygen system, *J. Chem. Soc. Perk. T. 2*, pp. 2165–2170, doi:10.1039/p29930002165, 1993.

Aiken, A. C., DeCarlo, P. F., and Jimenez, J. L.: Elemental analysis of organic species with electron ionization high-resolution mass spectrometry, *Anal. Chem.*, 79, 8350–8358, 2007.

615 Aiken, A. C., DeCarlo, P. F., Kroll, J. H., Worsnop, D. R., Huffman, J. A., Docherty, K. S., Ulbrich, I. M., Mohr, C., Kimmel, J. R., Sueper, D., Sun, Y., Zhang, Q., Trimborn, A., Northway, M., Ziemann, P. J., Canagaratna, M. R., Onasch, T. B., Alfarra, M. R., Prevot, A. S. H., Dommen, J., Duplissy, J., Metzger, A., Baltensperger, U., and Jimenez, J. L.: O/C and OM/OC ratios of primary, secondary, and ambient organic aerosols with high-resolution time-of-flight aerosol mass spectrometry, *Environ. Sci. Technol.*, 42, 4478–4485, 2008.

620 Allan, J. D., Delia, A. E., Coe, H., Bower, K. N., Alfarra, M. R., Jimenez, J. L., Middlebrook, A. M., Drewnick, F., Onasch, T. B., Canagaratna, M. R., Jayne, J. T., and Worsnop, D. R.: A generalised method for the extraction of chemically resolved mass spectra from Aerodyne aerosol mass spectrometer data, *J. Aerosol Sci.*, 35, 909–922, 2004.

Bahreini, R., Keywood, M. D., Ng, N. L., Varutbangkul, V., Gao, S., Flagan, R. C., Seinfeld, J. H., Worsnop, D. R., and Jimenez, J. L.: Measurements of secondary organic aerosol from oxidation of cycloalkenes, terpenes, and m-xylene using an Aerodyne aerosol mass spectrometer, *Environ. Sci. Technol.*, 39, 5674–5688, 2005.

Berndt, T. and Boge, O.: Gas-phase reaction of OH radicals with phenol, *Phys. Chem. Chem. Phys.*, 5, 342–350, doi:10.1039/b208187c, 2003.

630 Birdsall, A. W., Andreoni, J. F., and Elrod, M. J.: Investigation of the role of bicyclic peroxy radicals in the oxidation mechanism of toluene, *J. Phys. Chem. A*, 114, 10 655–10 663, doi:10.1021/jp105467e, 2010.

Bloss, C., Wagner, V., Bonzanini, A., Jenkin, M. E., Wirtz, K., Martin-Reviejo, M., and Pilling, M. J.: Evaluation of detailed aromatic mechanisms (MCMv3 and MCMv3.1) against environmental chamber data, *Atmos. Chem. Phys.*, 5, 623–639, doi:10.5194/acp-5-623-2005, 2005.

635 Bond, T. C., Streets, D. G., Yarber, K. F., Nelson, S. M., Woo, J. H., and Klimont, Z.: A technology-based global inventory of black and organic carbon emissions from combustion, *J. Geophys. Res.-Atmos.*, 109, 43, 2004.

Calvert, J. G., Atkinson, R., Becker, K. H., Kamens, R. M., Seinfeld, J. H., Wallington, T. J., and Yarwood, G.: The Mechanisms of Atmospheric Oxidation of Aromatic Hydrocarbons, Oxford University Press, Inc, New York, USA, 2002.

640 Chan, A. W. H., Kroll, J. H., Ng, N. L., and Seinfeld, J. H.: Kinetic modeling of secondary organic aerosol formation: effects of particle- and gas-phase reactions of semivolatile products, *Atmos. Chem. Phys.*, 7, 4135–4147, 2007.

Chhabra, P. S., Ng, N. L., Canagaratna, M. R., Corrigan, A. L., Russell, L. M., Worsnop, D. R., Flagan, R. C., and Seinfeld, J. H.: Elemental composition and oxidation of chamber organic aerosol, *Atmos. Chem. Phys.*, 11, 8827–8845, doi:10.5194/acp-11-8827-2011, 2011.

Cocker, D. R., Flagan, R. C., and Seinfeld, J. H.: State-of-the-art chamber facility for studying atmospheric aerosol chemistry, *Environ. Sci. Technol.*, 35, 2594–2601, 2001.

Coeur-Tourneur, C., Cassez, A., and Wenger, J. C.: Rate coefficients for the gas-phase reaction of hydroxyl radicals with 2-Methoxyphenol (guaiacol) and related compounds, *J. Phys. Chem. A*, 114, 11 645–11 650, doi:10.1021/jp1071023, 2010.

650 DeCarlo, P. F., Kimmel, J. R., Trimborn, A., Northway, M. J., Jayne, J. T., Aiken, A. C., Gonin, M., Fuhrer, K., Horvath, T., Docherty, K. S., Worsnop, D. R., and Jimenez, J. L.: Field-deployable, high-resolution, time-of-flight aerosol mass spectrometer, *Anal. Chem.*, 78, 8281–8289, 2006.

655 Dills, R. L., Zhu, X. Q., and Kalman, D. A.: Measurement of urinary methoxyphenols and their use for biological monitoring of wood smoke exposure, *Environ. Res.*, 85, 145–158, 2001.

Fine, P. M., Cass, G. R., and Simoneit, B. R. T.: Chemical characterization of fine particle emissions from fireplace combustion of woods grown in the northeastern United States, *Environ. Sci. Technol.*, 35, 2665–2675, 2001.

660 Gomez, N., Henon, E., Bohr, F., and Devolder, P.: Rate constants for the reactions of CH₃O with cyclohexane, cyclohexene, and 1,4-cyclohexadiene: Variable temperature experiments and theoretical comparison of addition and H-abstraction channels, *J. Phys. Chem. A*, 105, 11 204–11 211, doi:10.1021/jp010204h, 2001.

Hawthorne, S. B., Krieger, M. S., Miller, D. J., and Mathiason, M. B.: Collection and quantitation of methoxylated phenol tracers for atmospheric-pollution from residential wood stoves, *Environ. Sci. Technol.*, 23, 665 470–475, 1989.

Hawthorne, S. B., Miller, D. J., Langenfeld, J. J., and Krieger, M. S.: PM-10 high-volume collection and quantification of semivolatile and nonvolatile phenols, methoxylated phenols, alkanes, and polycyclic aromatic hydrocarbons from winter urban air and their relationship to wood smoke emmisions, *Environ. Sci. Technol.*, 26, 2251–2262, 1992.

670 Ito, A. and Penner, J. E.: Historical emissions of carbonaceous aerosols from biomass and fossil fuel burning for the period 1870-2000, *Global Biogeochem. Cy.*, 19, 14, 2005.

Johnson, D., Jenkin, M., Wirtz, K., and Martin-Reviejo, M.: Simulating the formation of secondary organic aerosol from the photooxidation of aromatic hydrocarbons, *Environ. Chem.*, 2, 35–48, doi:10.1071/EN04079, 2005.

675 Justesen, U.: Collision-induced fragmentation of deprotonated methoxylated flavonoids, obtained by electrospray ionization mass spectrometry, *J. Mass Spectrom.*, 36, 169–178, doi:10.1002/jms.118, 2001.

Kautzman, K. E., Surratt, J. D., Chan, M. N., Chan, A. W. H., Hersey, S. P., Chhabra, P. S., Dalleska, N. F., Wennberg, P. O., Flagan, R. C., and Seinfeld, J. H.: Chemical composition of gas- and aerosol-phase products from the photooxidation of naphthalene, *J. Phys. Chem. A*, 114, 913–934, 2010.

680 Keywood, M. D., Varutbangkul, V., Bahreini, R., Flagan, R. C., and Seinfeld, J. H.: Secondary organic aerosol formation from the ozonolysis of cycloalkenes and related compounds, *Environ. Sci. Technol.*, 38, 4157–4164, 2004.

Klotz, B., Volkamer, R., Hurley, M., Andersen, M., Nielsen, O., Barnes, I., Imamura, T., Wirtz, K., Becker, K., Platt, U., Wallington, T., and Washida, N.: OH-initiated oxidation of benzene - Part II. influence of elevated NO_x concentrations, *Phys. Chem. Chem. Phys.*, 4, 4399–4411, doi:10.1039/b204398j, 2002.

685 Koch, R., Knispel, R., Elend, M., Siese, M., and Zetzsch, C.: Consecutive reactions of aromatic-OH adducts with NO, NO₂ and O₂: benzene, naphthalene, toluene, m- and p-xylene, hexamethylbenzene, phenol, m-cresol and aniline, *Atmos. Chem. Phys.*, 7, 2057–2071, doi:10.5194/acp-7-2057-2007, 2007.

Kroll, J. H. and Seinfeld, J. H.: Representation of secondary organic aerosol laboratory chamber data for the interpretation of mechanisms of particle growth, *Environ. Sci. Technol.*, 39, 4159–4165, 2005.

Kroll, J. H., Ng, N. L., Murphy, S. M., Flagan, R. C., and Seinfeld, J. H.: Secondary organic aerosol formation from isoprene photooxidation, *Environ. Sci. Technol.*, 40, 1869–1877, doi:10.1021/es0524301, 2006.

Kwok, E. S. and Atkinson, R.: Estimation of hydroxyl radical reaction rate constants for gas-phase organic compounds using a structure-reactivity relationship: An update, *Atmos. Environ.*, 29, 1685 – 1695, doi:10.1016/1352-2310(95)00069-B, 1995.

Lauraguais, A., Coeur-Tourneur, C., Cassez, A., and Seydi, A.: Rate constant and secondary organic aerosol yields for the gas-phase reaction of hydroxyl radicals with syringol (2,6-dimethoxyphenol), *Atmos. Environ.*, 55, 43 – 48, doi:10.1016/j.atmosenv.2012.02.027, 2012.

Luo, Y. R.: *Comprehensive Handbook of Chemical Bond Energies*, CRC Press, Boca Raton, FL, 2007.

Naeher, L. P., Brauer, M., Lipsett, M., Zelikoff, J. T., Simpson, C. D., Koenig, J. Q., and Smith, K. R.: Woodsmoke health effects: A review, *Inhal. Toxicol.*, 19, 67–106, 2007.

Nakao, S., Clark, C., Tang, P., Sato, K., and Cocker III, D.: Secondary organic aerosol formation from phenolic compounds in the absence of NO_x , *Atmos. Chem. Phys.*, 11, 10 649–10 660, doi:10.5194/acp-11-10649-2011, 2011.

Ng, N. L., Kroll, J. H., Keywood, M. D., Bahreini, R., Varutbangkul, V., Flagan, R. C., Seinfeld, J. H., Lee, A., and Goldstein, A. H.: Contribution of first- versus second-generation products to secondary organic aerosols formed in the oxidation of biogenic hydrocarbons, *Environ. Sci. Technol.*, 40, 2283–2297, 2006.

Nishino, N., Atkinson, R., and Arey, J.: Formation of nitro products from the gas-phase OH radical-initiated reactions of toluene, naphthalene, and biphenyl: effect of NO_2 concentration, *Environmental Science & Technology*, 42, 9203–9209, doi:10.1021/es802046m, 2008.

Olariu, R. I., Klotz, B., Barnes, I., Becker, K. H., and Mocanu, R.: FTIR study of the ring-retaining products from the reaction of OH radicals with phenol, o-, m-, and p-cresol, *Atmos. Environ.*, 36, 3685–3697, 2002.

Orlando, J. J. and Tyndall, G. S.: Laboratory studies of organic peroxy radical chemistry: an overview with emphasis on recent issues of atmospheric significance, *Chem. Soc. Rev.*, 41, 6294–6317, doi:10.1039/c2cs35166h, 2012.

Pye, H. O. T. and Seinfeld, J. H.: A global perspective on aerosol from low-volatility organic compounds, *Atmos. Chem. Phys.*, 10, 4377–4401, 2010.

Sato, K., Hatakeyama, S., and Immamura, T.: Secondary organic aerosol formation during the photooxidation of toluene: NO_x dependence of chemical composition, *J. Phys. Chem. A*, 111, 9796–9808, doi:10.1021/jp071419f, 2007.

Schauer, J. J., Kleeman, M. J., Cass, G. R., and Simoneit, B. R. T.: Measurement of emissions from air pollution sources. 3. C-1-C-29 organic compounds from fireplace combustion of wood, *Environ. Sci. Technol.*, 35, 1716–1728, 2001.

Simpson, C. D. and Naeher, L. P.: Biological monitoring of wood-smoke exposure, *Inhal. Toxicol.*, 22, 99–103, 2010.

St. Clair, J. M., McCabe, D. C., Crounse, J. D., Steiner, U., and Wennberg, P. O.: Chemical ionization tandem mass spectrometer for the in situ measurement of methyl hydrogen peroxide, *Rev. Sci. Instrum.*, 81, 094 102, 2010.

Surratt, J. D., Gómez-González, Y., Chan, A. W. H., Vermeylen, R., Shahgholi, M., Kleindienst, T. E., Edney,
730 E. O., Offenberg, J. H., Lewandowski, M., Jaoui, M., Maenhaut, W., Claeys, M., Flagan, R. C., and Seinfeld,
J. H.: Organosulfate formation in biogenic secondary organic aerosol, *J. Phys. Chem. A*, 112, 8345–8378,
2008.

Varfolomeev, M. A., Abaidullina, D. I., Solomonov, B. N., Verevkin, S. P., and Emelyanenko, V. N.: Pairwise
735 substitution effects, inter- and intramolecular hydrogen bonds in methoxyphenols and dimethoxybenzenes.
thermochemistry, calorimetry, and first-principles calculations, *J. Phys. Chem. B*, 114, 16 503–16 516, doi:
10.1021/jp108459r, 2010.

Table 1. Chemical Properties

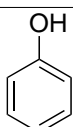
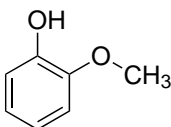
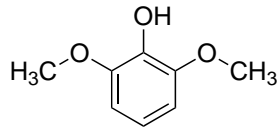
Compound	Structure	Boiling Pt. (°C)	V.P. @ 25°C (mm Hg)	$k_{OH} \times 10^{-11}$ (molec cm ⁻³ s ⁻¹)
Phenol		182	0.351	2.7 ± 0.25 at 25 °C (Calvert et al., 2002)
Guaiacol		205	0.13	7.53 ± 0.41 at 21 ± 2 °C (Coeur-Tourneur et al., 2010)
Syringol		260	0.0062	9.66 ± 1.11 at 21 ± 2 °C (Lauraguais et al., 2012)

Table 2. Experimental Conditions

Date (2010)	Organic	[Org] ₀ (ppb)	[Org] _f (ppb)	[NO ₂] ₀ (ppb)	[NO] ₀ (ppb)	V ₀ μm ³ /cm ³	V _f μm ³ /cm ³	Yield
1/29	guaiacol	66.3	13.4	< LDL ^a	< LDL ^a	18.2	120.0	0.49
2/2	guaiacol	5.9	< LDL ^a	< LDL ^a	< LDL ^a	16.4	25.0	0.46
2/4	guaiacol	12.4	< LDL ^a	< LDL ^a	< LDL ^a	13.6	31.0	0.44
2/6	guaiacol	45.5	4.1	< LDL ^a	5	12.9	85.0	0.50
2/11	phenol	47.6	9.9	< LDL ^a	6	16.0	58.0	0.44
2/15	phenol	10.0	2.1	< LDL ^a	5	11.4	20.0	0.40
2/17	phenol	73.9	14.4	< LDL ^a	< LDL ^a	12.0	44.0	0.25
2/20	phenol	101.9	18.8	< LDL ^a	5	10.0	69.0	0.24
3/10	syringol	185.1	< LDL ^a	7	< LDL ^a	11.0	325.0	0.37
3/15	syringol	49.5	< LDL ^a	< LDL ^a	< LDL ^a	14.2	67.0	0.25
3/29	syringol	112.9	< LDL ^a	9	< LDL ^a	11.7	174.0	0.34

^a below lower detection limit

Table 3. Proposed structures for CIMS ions in the phenol low- NO_x system. C and T indicate the cluster and transfer product, respectively.

Observed m/z	Product	Chemical Formula	Proposed Structure (one isomer shown)	Chemical Pathway
179	C	$\text{C}_6\text{H}_6\text{O}$		phenol
129	T ^a	$\text{C}_6\text{H}_6\text{O}_2$		$\text{DHB} = \text{phenol} + \text{OH}$
211	C	$\text{C}_6\text{H}_6\text{O}_3$		$\text{THB} = \text{DHB} + \text{OH}$
227	C	$\text{C}_6\text{H}_6\text{O}_4$		$4\text{HB} = \text{THB} + \text{OH}$
145	T	$\text{C}_6\text{H}_6\text{O}_3$		ring opening acid
161	T	$\text{C}_6\text{H}_6\text{O}_4$		ring opening acid
177	T	$\text{C}_6\text{H}_6\text{O}_5$		ring opening acid
185	C ^b	$\text{C}_4\text{H}_4\text{O}_3$		ring fragment
135	T ^c	$\text{C}_4\text{H}_4\text{O}_4$		ring fragment
107	T	$\text{C}_3\text{H}_4\text{O}_3$		ring fragment

^a m/z 195 is also present as $\text{C}_6\text{H}_6\text{O}_2$, but is lower signal than at m/z 129.

^b The transfer product at $\text{C}_4\text{H}_4\text{O}_3$ is at m/z 119, which is not monitored in low- NO_x conditions because it is the cluster product of H_2O_2 .

^c m/z 201 is also present as $\text{C}_4\text{H}_4\text{O}_4$, but is lower signal than at m/z 135.

Table 4. Proposed structures for CIMS ions in the guaiacol low- NO_x system. C and T indicate the cluster and transfer product, respectively.

Observed m/z	Product	Chemical Formula	Proposed Structure (one isomer shown)	Chemical Pathway ^a
209	C ^b	C ₇ H ₈ O ₂		guaiacol
259	C	C ₇ H ₁₀ O ₅		1) hydroperoxide
225	C	C ₇ H ₈ O ₃		2) G + OH = guaiacol + OH
241	C	C ₇ H ₈ O ₄		2) G + 2OH = guaiacol + 2OH
191	T ^c	C ₇ H ₈ O ₅		2) G + 3OH = guaiacol + 3OH
175	T	C ₇ H ₈ O ₄		ring opening acid
257	C ^d	C ₇ H ₈ O ₅		3aiii) EPOX and 2) G + 3OH
149	T	C ₅ H ₆ O ₄		3aiii) ring fragment
187	C	C ₄ H ₆ O ₃		3aiii) ring fragment
199	C	C ₃ H ₄ O ₃		3aiii) ring fragment
107	T	C ₃ H ₄ O ₃		3aiii) ring fragment
189	C	C ₃ H ₄ O ₄		3aiii) ring fragment
243	T	C ₆ H ₆ O ₅		3b) C ₆ bicyclic ketone
129	T ^e	C ₆ H ₆ O ₂		4) Methoxy Loss

^a Numbers indicate correspondence with pathways outlined in mechanism (Figure 6).

^b m/z 143 is also present as C₇H₈O₂, but is lower signal than at m/z 209.

^c Also includes signal from C₇H₈O₅ ring opening acid.

^d Includes contributions from G + 3OH along pathway 2 in Figure 6

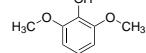
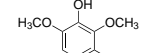
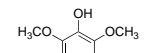
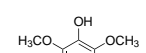
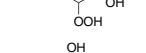
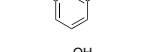
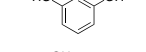
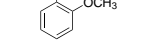
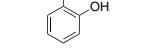
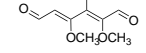
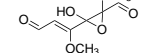
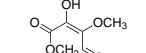
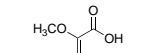
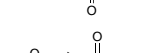
^e m/z 195 is also present as C₆H₆O₂, but is lower signal than at m/z 129.

Table 5. SOA products observed in UPLC/(-)ESI-TOFMS offline filter analysis for the guaiacol low- NO_x system.

[M-H] ⁻	Meas. Mass	Suggested Chemical Formula (M)	Error ^a (mDa)
189	189.0378	C ₇ H ₁₀ O ₆	-2.1
219	219.014	C ₇ H ₈ O ₈	-0.1
147	147.0266	C ₅ H ₈ O ₅	-2.6
157	157.0113	C ₆ H ₆ O ₅	-2.4
133	133.0133	C ₄ H ₆ O ₅	-2.4
149	149.0072	C ₄ H ₆ O ₆	-1.4
205	205.0327	C ₇ H ₁₀ O ₇	2.1
145	145.048	C ₆ H ₁₀ O ₄	-2.1
163	163.0233	C ₅ H ₈ O ₆	-1
203	203.0177	C ₇ H ₈ O ₇	-1.5
171	171.0279	C ₇ H ₈ O ₅	-1.4
169	169.0124	C ₇ H ₆ O ₅	-1.3
173	173.0428	C ₇ H ₁₀ O ₅	-2.2
115	115.0004	C ₄ H ₄ O ₄	-2.7
129	129.0175	C ₅ H ₆ O ₄	-1.3

^a The error in the accurate mass measurements is the difference between the theoretical mass of the suggested molecular formulae of the parent molecule (M) and the measured mass of the ion.

Table 6. Proposed structures for CIMS ions in the syringol low- NO_x system. C and T indicate the cluster and transfer product, respectively.

Observed m/z	Product	Chemical Formula	Proposed Structure (one isomer shown)	Chemical Pathway ^a
173	T ^b	C ₈ H ₁₀ O ₃		syringol
189	T	C ₈ H ₁₀ O ₄		S + OH = syringol + OH
271	C	C ₈ H ₁₀ O ₅		S + 2OH = syringol + 2OH
289	C	C ₈ H ₁₂ O ₆		hydroperoxide
225	C	C ₇ H ₈ O ₃		a) G + OH = guaiacol + OH
211	C	C ₆ H ₆ O ₃		b) THB = DHB + OH
209	C	C ₇ H ₈ O ₂		c) guaiacol
129	T ^c	C ₆ H ₆ O ₂		d) DHB = phenol + OH
205	T ^d	C ₈ H ₁₀ O ₅		ring opening acid
287	C	C ₈ H ₁₀ O ₆		SEPOX
245	C	C ₆ H ₈ O ₅		ring fragment
149	T	C ₅ H ₆ O ₄		ring fragment
185	C	C ₄ H ₄ O ₃		ring fragment
203	C	C ₄ H ₆ O ₄		ring fragment
275	C	C ₇ H ₁₀ O ₆	none proposed	C ₈ scission
291	C	C ₇ H ₁₀ O ₇	none proposed	C ₈ scission

^a Letters indicate correspondence with pathways outlined in mechanism (Figure 10).

^b m/z 239 is also present as C₈H₁₀O₃, but is lower signal than at m/z 173.

^c m/z 195 is also present as C₆H₆O₂, but is lower signal than at m/z 129.

^d Includes contributions from S + 2OH as well as ring opening acid.

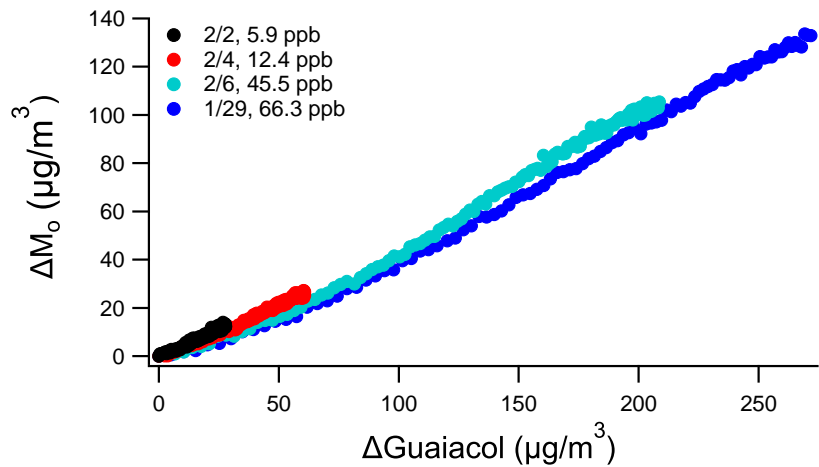


Fig. 1. Growth curves of guaiacol aerosol.

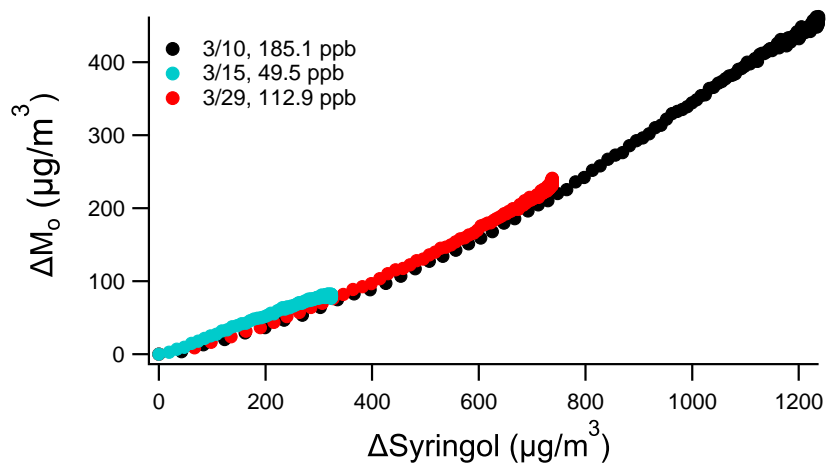


Fig. 2. Growth curves of syringol aerosol.

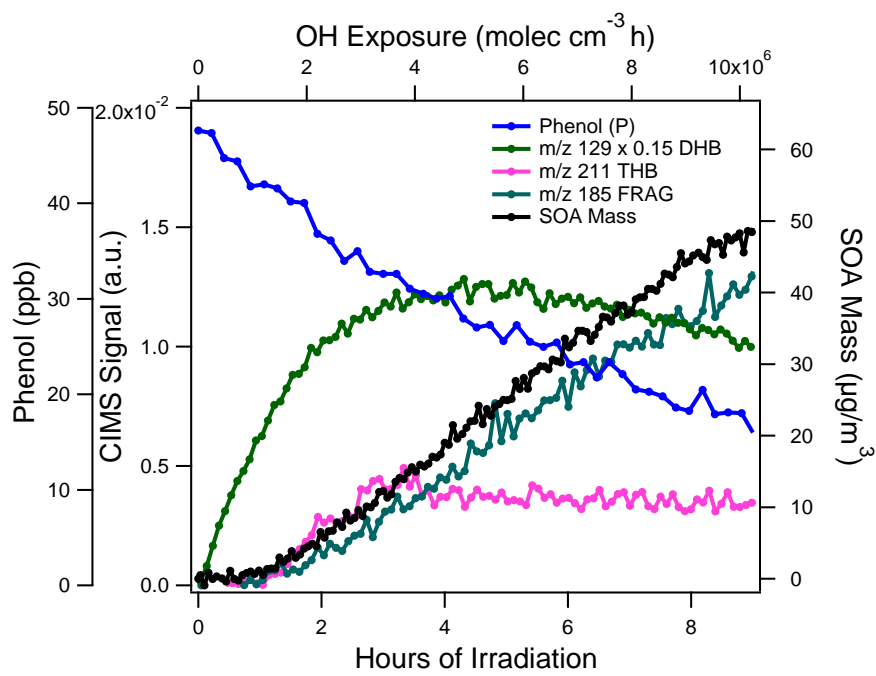


Fig. 3. Phenol low- NO_x gas-phase and particle-phase development.

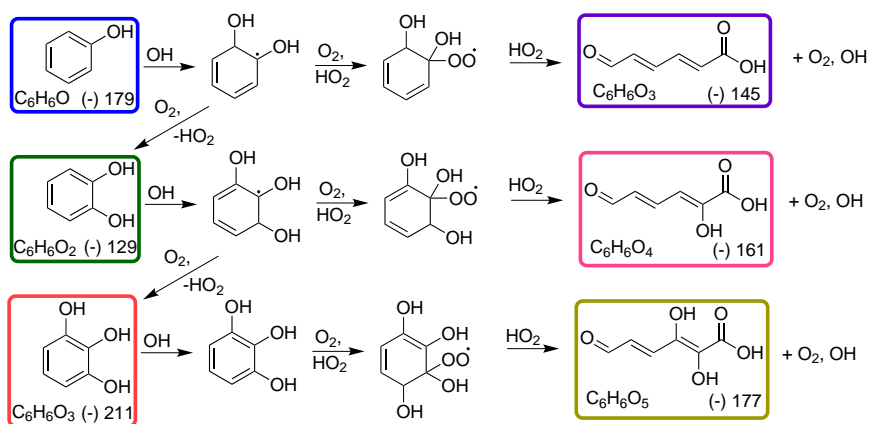


Fig. 4. Proposed pathway for gas-phase production of C₆ carboxylic acids in the phenol low-NO_x system. Boxed structures indicate that the expected *m/z* from the chemical ionization reactions in the CIMS for that compound was detected.

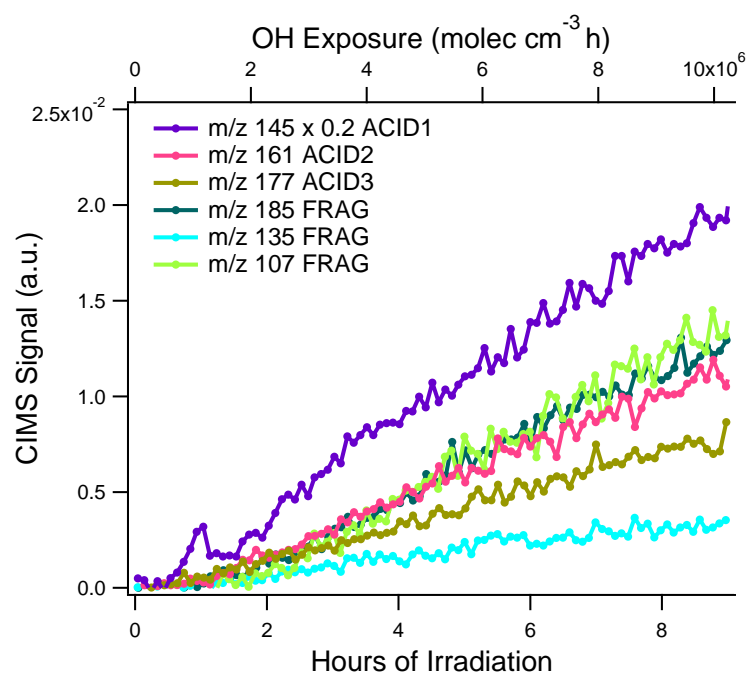


Fig. 5. Selected phenol low- NO_x gas-phase acids.

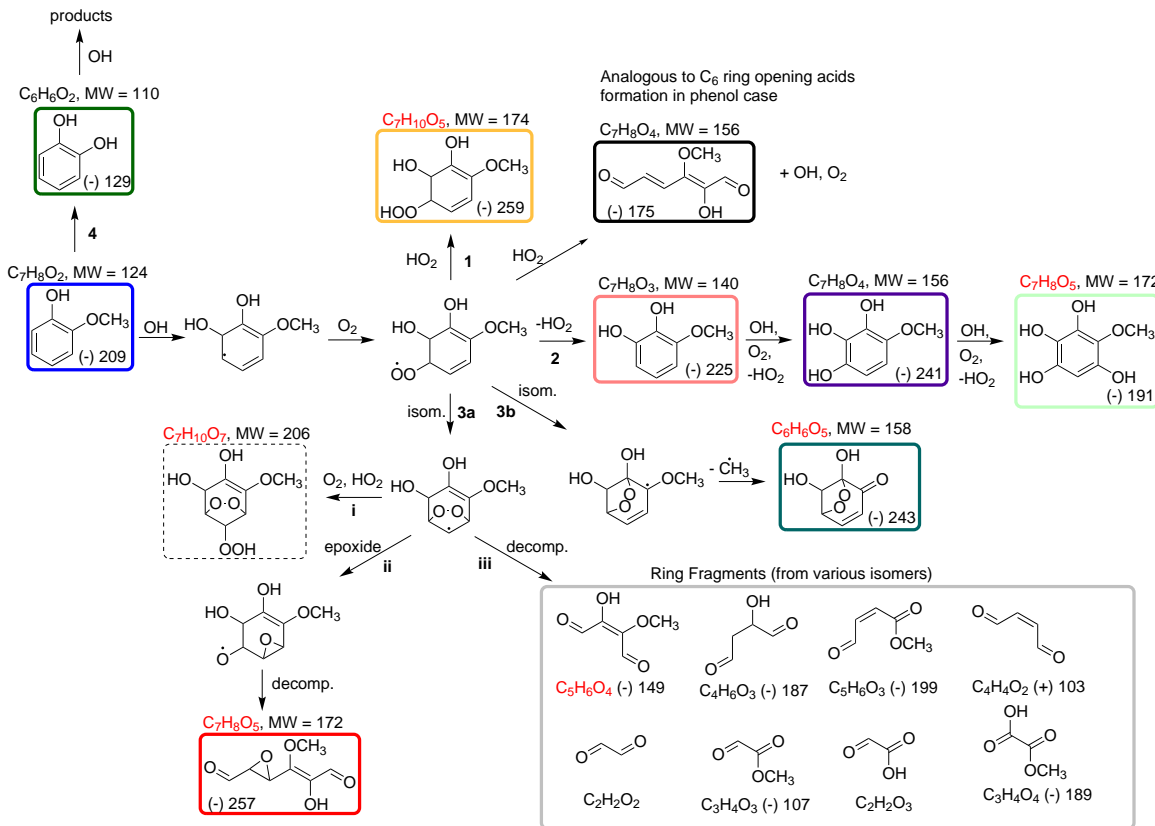


Fig. 6. Proposed mechanism for guaiacol low-NO_x oxidation. Boxed structures indicate that the expected m/z from the chemical ionization reactions in the CIMS for that compound was detected. Chemical formulae in red correspond with those proposed for the filter accurate mass aerosol measurements.

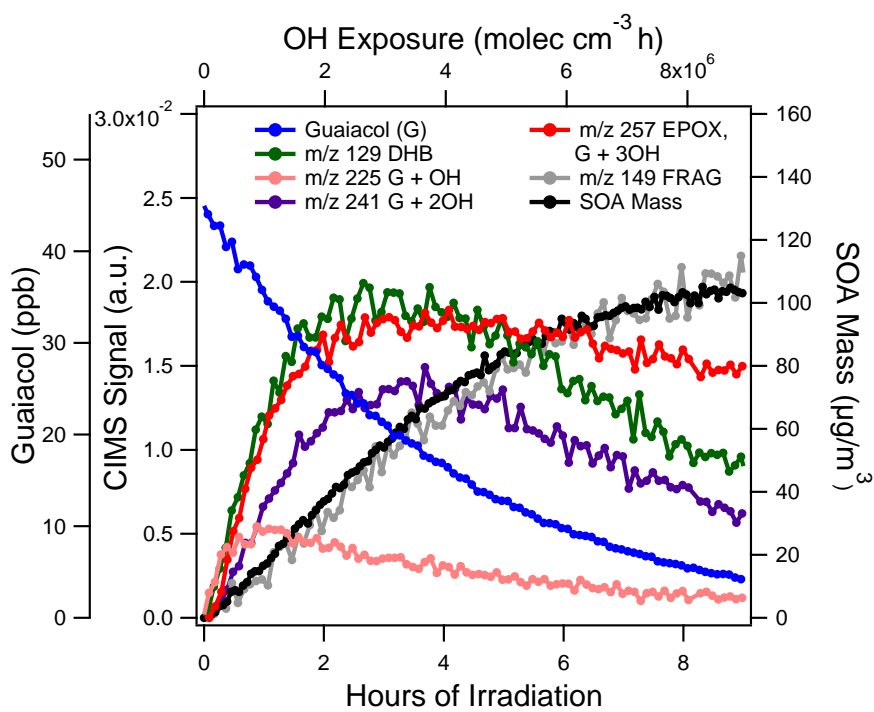


Fig. 7. Selected traces in guaiacol low- NO_x gas-phase and particle-phase development.

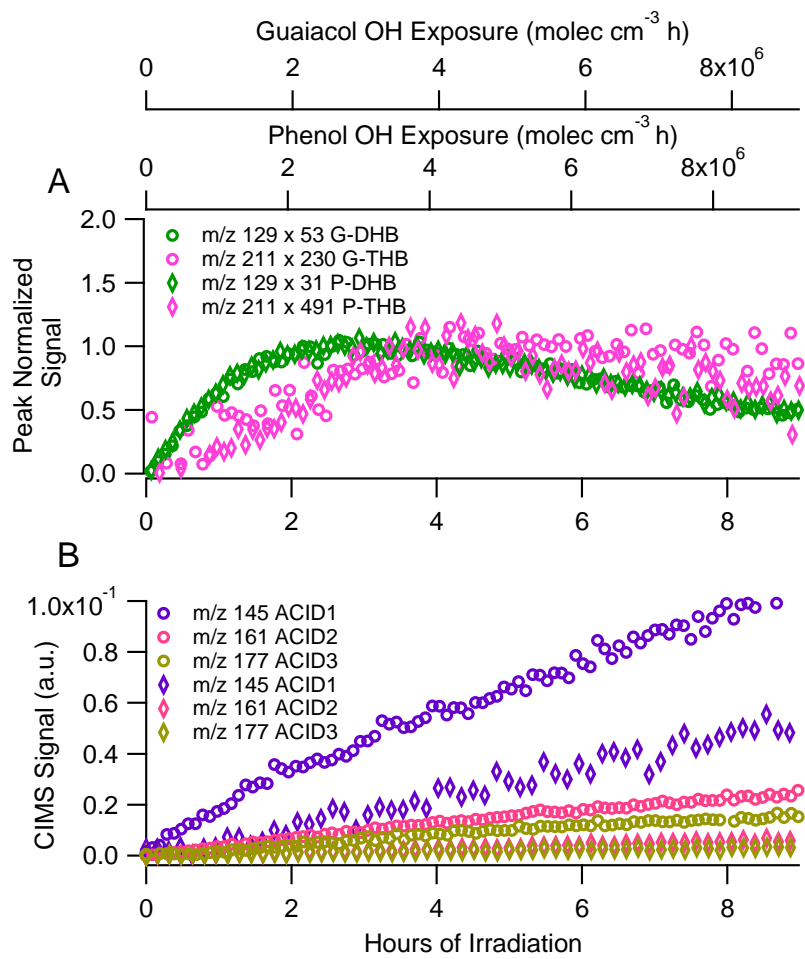


Fig. 8. Common chemical routes in the phenol and guaiacol low- NO_x systems. (A) Dihydroxybenzene routes in phenol (diamonds) and guaiacol (open circles). Each CIMS trace is normalized by the peak value. (B) Common acids in phenol (diamonds) and guaiacol (open circles).

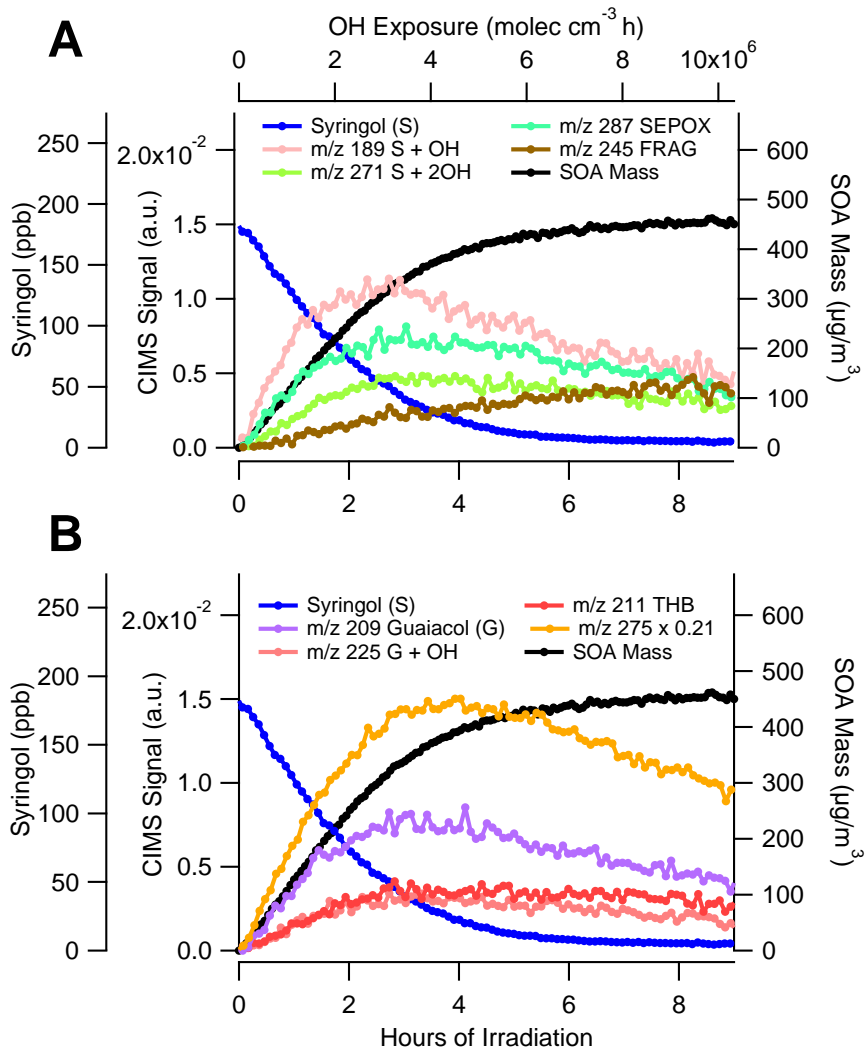


Fig. 9. Selected traces in syringol low- NO_x gas-phase and particle-phase development. (A) OH addition pathways. (B) Traces indicating methoxy loss pathways.

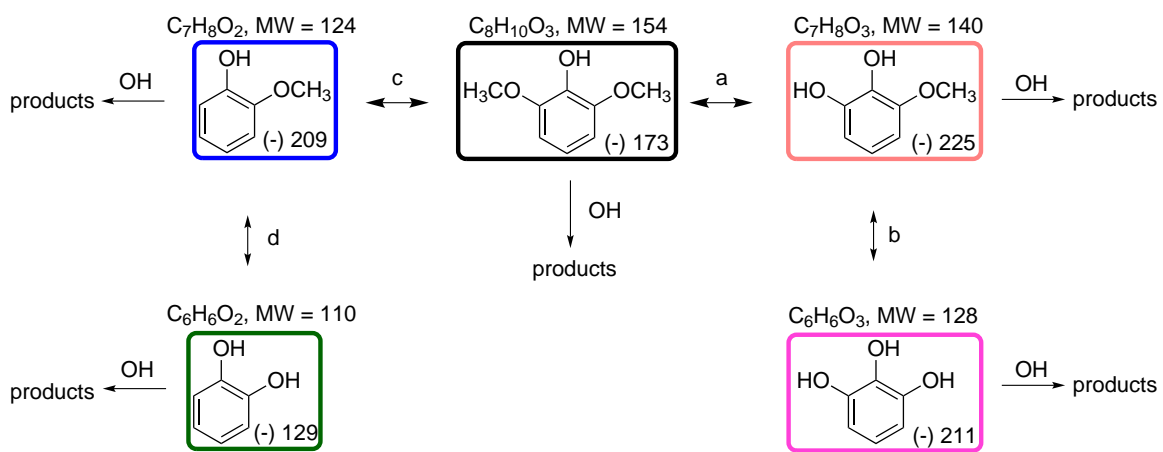


Fig. 10. Possible routes of methoxy loss in syringol gas-phase chemistry.

Chapter 3

Secondary organic aerosol formation from low- NO_x photooxidation of dodecane: evolution of multigeneration gas-phase chemistry and aerosol composition¹

¹This chapter is reproduced by permission from "Secondary Organic Aerosol Formation from Low- NO_x Photooxidation of Dodecane: Evolution of Multigeneration Gas-Phase Chemistry and Aerosol Composition," by Lindsay D. Yee, Jill S. Craven, Christine L. Loza, Katherine A. Schilling, Nga Lee Ng, Manjula R. Canagaratna, Paul J. Ziemann, Richard C. Flagan, and John H. Seinfeld, *Journal of Physical Chemistry A*, 116, 6211 – 6230, dx.doi.org/10.1021/jp211531h, 2012. Copyright 2006 American Chemical Society

Secondary Organic Aerosol Formation from Low- NO_x Photooxidation of Dodecane: Evolution of Multigeneration Gas-Phase Chemistry and Aerosol Composition

Lindsay D. Yee,[†] Jill S. Craven,[‡] Christine L. Loza,[‡] Katherine A. Schilling,[‡] Nga Lee Ng,[§] Manjula R. Canagaratna,^{||} Paul J. Ziemann,[†] Richard C. Flagan,^{†,‡} and John H. Seinfeld*,^{†,‡}

[†]Division of Engineering and Applied Science, California Institute of Technology, Pasadena, California 91125, United States

[‡]Division of Chemistry and Chemical Engineering, California Institute of Technology, Pasadena, California 91125, United States

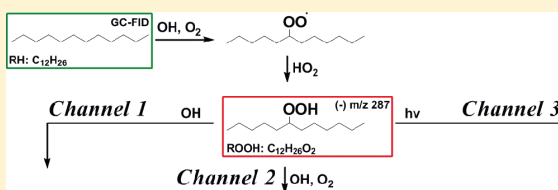
[§]School of Chemical and Biomolecular Engineering and School of Earth and Atmospheric Sciences, Georgia Institute of Technology, Atlanta, Georgia 30332, United States

^{||}Aerodyne Research, Inc., Billerica, Massachusetts 01821, United States

^{*}Air Pollution Research Center, Department of Environmental Sciences and Environmental Toxicology Graduate Program, University of California, Riverside, California 92521, United States

Supporting Information

ABSTRACT: The extended photooxidation of and secondary organic aerosol (SOA) formation from dodecane ($\text{C}_{12}\text{H}_{26}$) under low- NO_x conditions, such that $\text{RO}_2 + \text{HO}_2$ chemistry dominates the fate of the peroxy radicals, is studied in the Caltech Environmental Chamber based on simultaneous gas and particle-phase measurements. A mechanism simulation indicates that greater than 67% of the initial carbon ends up as fourth and higher generation products after 10 h of reaction, and simulated trends for seven species are supported by gas-phase measurements. A characteristic set of hydroperoxide gas-phase products are formed under these low- NO_x conditions. Production of semivolatile hydroperoxide species within three generations of chemistry is consistent with observed initial aerosol growth. Continued gas-phase oxidation of these semivolatile species produces multifunctional low volatility compounds. This study elucidates the complex evolution of the gas-phase photooxidation chemistry and subsequent SOA formation through a novel approach comparing molecular level information from a chemical ionization mass spectrometer (CIMS) and high m/z ion fragments from an Aerodyne high-resolution time-of-flight aerosol mass spectrometer (HR-ToF-AMS). Combination of these techniques reveals that particle-phase chemistry leading to peroxyhemiacetal formation is the likely mechanism by which these species are incorporated in the particle phase. The current findings are relevant toward understanding atmospheric SOA formation and aging from the “unresolved complex mixture,” comprising, in part, long-chain alkanes.



INTRODUCTION

Atmospheric chemical transformations occur through mechanisms involving free radical reactions, sunlight, and reactions in or on condensed media.¹ The formation of secondary organic aerosol (SOA) involves the multigeneration oxidation of a parent organic molecule leading to product molecules that partition between the gas and particle phases. As the parent organic is consumed, usually by reaction with the hydroxyl (OH) radical, subsequent products may also react with OH, giving rise to an evolving product distribution. As products become more functionalized with oxygen-containing moieties, their volatility decreases, and their propensity to partition into the particle phase increases.² In the gas-phase chemical cascade, both functionalization and fragmentation (C–C bond scission) reactions occur, and the interplay between these two general types of reactions, together with the progressive decrease in volatility accompanying the addition of oxygen atoms to the

parent backbone, defines the SOA formation process for a particular parent organic.³ As the SOA formation process evolves, a competition ensues between the rate of production of lower volatility species with increasing oxygen-to-carbon (O:C) atomic ratio and the increase in the SOA mass; as the mass of SOA increases, the partitioning of gas-phase products with somewhat higher volatility and somewhat lower O:C ratio is enhanced. The mass of SOA can, in some cases, reach a maximum and decrease as gas-phase fragmentation reactions convert lower volatility species into higher volatility species, leading to evaporation of the lower volatility particle-phase species in an attempt to maintain gas-particle equilibrium. In

Special Issue: A. R. Ravishankara Festschrift

Received: November 30, 2011

Revised: March 16, 2012

Published: March 16, 2012

short, the rate at which oxygens are added via successive gas-phase reactions, the relative importance of fragmentation versus functionalization reactions, and the specific decrease in volatility attending the formation of oxidized species govern the evolution of the SOA mass.

Long-chain alkanes represent an especially important class of organics with respect to SOA formation. The so-called unresolved complex mixture (UCM) is likely an important source of unaccounted for SOA formation in the atmosphere,⁴ and alkanes are a major component of that mixture.^{5,6} Low-volatility vapors from the UCM are a source of “untraditional” SOA, as they evaporate from primary organic aerosol emissions upon dilution and undergo subsequent oxidation to form SOA.⁴ Quantifying the SOA formation from long-chain alkanes will undoubtedly aid in closing the gap between observed atmospheric organic aerosol and that predicted by atmospheric models based on traditional biogenic and anthropogenic SOA precursors. SOA formation from alkane photooxidation has received study.^{7–12} Alkane–OH reaction kinetics^{13,14} and gas-phase chemistry in the presence of NO_x exhibit a product distribution that can lead to highly oxidized products.^{7,9,10} Studies of alkane oxidation under low- NO_x conditions have also been carried out.¹⁵ Importantly, owing to the relatively long lifetimes against OH reaction at typical ambient OH concentrations (on the order of 12 h to several days) and to a relatively rich information base on the kinetics and mechanisms of alkane oxidation reactions, long-chain alkanes represent an especially important class of compounds with respect to SOA formation. Finally, it is crucial to develop detailed chemical databases on the explicit pathways of SOA formation for classes of parent organics, which can serve as benchmarks for evaluation of empirical/statistical models of SOA formation.

The present work represents the first report on a comprehensive series of laboratory chamber experiments on SOA formation from long-chain alkanes. We focus here on SOA formation from dodecane under low- NO_x conditions. The low- NO_x regime of atmospheric chemistry is particularly important in the regional to remote atmosphere and is especially relevant to the chemical aging that is intrinsic to SOA formation. The key to atmospheric photooxidation chemistry is the fate of the alkyl peroxy radical (RO_2) formed after OH attack and O_2 addition. RO_2 can react with HO_2 , RO_2 , or NO_x , the distribution of which is critical for understanding radical propagation and sinks, as well as the pathways that lead eventually to SOA.^{16,17} In atmospheric regions of low NO_x levels, the RO_2 radical will react preferentially with HO_2 and RO_2 . In such regions, HO_2 concentrations are on the order of 10^9 molecules cm^{-3} ,^{18–20} and the $\text{RO}_2\text{–HO}_2$ reaction is competitive with the reaction of RO_2 with NO_x . Generally, under such atmospheric conditions, the $\text{RO}_2\text{–HO}_2$ reaction, which leads to hydroperoxides, dominates over RO_2 self-reaction. We present here the first experimental study of SOA formation from dodecane oxidation in the regime in which the fate of the dodecane peroxy radical is dominated by the $\text{RO}_2 + \text{HO}_2$ regime of alkyl peroxy radical chemistry. The particular focus of the present work is the multigeneration gas-phase chemistry of dodecane oxidation that leads to SOA formation. We employ chemical ionization mass spectrometry (CIMS) to track the evolution of the gas-phase oxidation products. We develop a gas-phase mechanism to describe the low- NO_x regime of chemistry. The mechanism is used to explicitly simulate four generations of gas-phase chemistry. By combining

CIMS and high-resolution time-of-flight aerosol mass spectrometer (HR-ToF-AMS) measurements, we are able to simultaneously track several semivolatile oxidation products in the gas and particle phases. Together, these measurements provide evidence of particle-phase formation of peroxyhemiacetals (PHAs).

EXPERIMENTAL SECTION

Instrumentation. Experiments were conducted in the dual 28 m³ Teflon reactors in the Caltech Environmental Chamber described elsewhere.^{21,22} The reactors are flushed with clean, dry air for 24 h before a new experiment. A suite of online gas- and particle-phase instruments was used to monitor the development of the chemistry from dodecane photooxidation. The dodecane decay was monitored by taking hourly samples at 0.13 LPM of chamber air over 10 min (1.3 L total sample volume) onto a Tenax adsorbent. This was then loaded into the inlet of a gas chromatograph with flame ionization detection (GC/FID, Agilent 6890N), desorbed, and then injected onto an HP-5 column (15 m × 0.53 mm ID × 1.5 μm thickness, Hewlett-Packard). Desorption was at 270 °C for 15 min onto the column held at 30 °C. Next the oven was ramped from 30 to 280 °C at 10 °C/min and held at 280 °C for 5 min. The mass response of the detector was calibrated by spiking the Tenax cartridges with 0.5 μL of standard solution and analyzing them following the previously described method. Standard solutions of 25 mL volume each with concentrations ranging from 1 mM to 11 mM of dodecane in cyclohexane were prepared for these calibrations. The O_3 and NO_x were monitored using a standard UV absorption O_3 analyzer (Horiba, APOA 360) and a chemiluminescence NO_x analyzer (Horiba, APNA 360). During the injection period and before lights on, the temperature was around 293–294 K. After lights on, the temperature for all experiments ranged between 296 and 298 K, and relative humidity levels remained <5%.

The gas-phase chemistry was tracked using measurements from a CIMS, consisting of a modified Varian 1200 quadrupole mass spectrometer to accommodate a custom ionization region. The general operation and details of the instrument have been discussed previously.^{23–25} In negative mode operation, the use of CF_3OOCF_3 reagent gas makes the instrument ideal for measuring hydroperoxide containing compounds and acidic species, as described in studies of CF_3OOCF_3 chemistry.²⁶ For a more strongly acidic species [H-X], the transfer product is formed during ionization [H-X-F][–], resulting in a nominal mass-to-charge ratio, m/z , of [M+19][–], where M is the molecular weight of the analyte. For less acidic species and hydroperoxides [R], the cluster product forms [R- CF_3O][–], or m/z = [M+85][–]. Carboxylic acids such as acetic and formic acids tend to have equal contributions to the transfer and cluster product, in which case the overall signal of a compound is considered as the sum of the two product channels. In positive mode operation, an analyte R can undergo proton transfer reaction generating an ion of the form [R-H]⁺ and/or react with n positively charged water clusters to form a cluster in the form of [(H₂O)_n·R-H]⁺. Hydroperoxide species tend to undergo dehydration after protonation, and are thus monitored at nominal m/z = [M-17]⁺.²⁷ Unfortunately, due to mass tuning shifts midproject, the positive mode m/z 's reported do not reflect the expected m/z from the clustering theory, but use of this mode of the CIMS was essential for tracking less polar compounds such as the carbonyl and, in some instances, where product m/z 's were out of range for the mass scan in negative

Table 1. Dodecane Low- NO_x Experiments

expt date	hrs of photooxidation	initial HC (ppb)	$[\text{NO}]_0$ (ppb)	$[\text{NO}_x]_0$ (ppb)	$[\text{O}_3]_0$ (ppb)	initial seed vol. ($\mu\text{m}^3\text{cm}^{-3}$)	ΔHC (ppb)	peak organic ^a ($\mu\text{g cm}^{-3}$)
1/16/2011	18	34.2 \pm 1.6	<LDL	<LDL	2.7	9.1 \pm 0.3	32.0 \pm 2.1	54.6
3/13/2011	36	34.9 \pm 1.6	<LDL	<LDL	2.6	11.4 \pm 1.5	33.6 \pm 2.1	62.8
3/16/2011	18	33.0 \pm 1.6	<LDL	<LDL	3.3	12.0 \pm 1.2	32.3 \pm 2.1	51.3

^aNot corrected for particle wall loss.

mode operation. The positive mode m/z 's are reported as monitored during the experiment, but suggested assignments were made using a back calibration of the shift of m/z , generally upward by five atomic mass units (amu) in the m/z range of interest from 200 to 220. While the CIMS is capable of measuring a diverse array of chemical species, specificity is challenged when isomers or different compounds with the same nominal MW contribute to the same m/z signal, which has unit mass resolution. In this study, many isomers are formed because there are many possible locations of hydroxyl radical attack on the starting chain. The CIMS signal at one m/z represents the summed contribution of all the isomers. Isomeric compounds in this study were mostly problematic for distinguishing the acids, in that one cannot fully distinguish the difference between a C_n peracid, C_n hydroxycarboxylic acid, and a C_{n+1} hydroperoxide, as discussed in the results section on acid formation.

Particle size distribution and number concentration measurements are made with a cylindrical differential mobility analyzer (DMA; TSI Model 3081) coupled to a condensation particle counter (TSI Model 3010). A logarithmic scan from a mobility diameter of 10 nm to 1 μm is completed every 90 s. Sheath and excess flows of 2.5 LPM were used, with a 5:1 flow rate ratio of sheath-to-aerosol (i.e., a resolving power of 5). An Aerodyne HR-ToF-AMS,^{28–30} hereafter referred to as the AMS, continuously measured submicrometer nonrefractory aerosol composition at 1 min resolution switching between the higher resolution, lower sensitivity W mode and the lower resolution, higher sensitivity V mode. A detailed discussion of the AMS method for the automated m/z calibration, mass accuracy, mass resolution of V and W modes, the high-resolution ion fitting algorithm, and ion signal integrations at the same integer mass is presented in previous work.²⁹ The AMS ions (organic) are reported with a relative ionization efficiency of 1.4.³⁰

Experimental Protocols. To maximize total OH exposure, a set of experiments was designed following phased instrument sampling protocols similar to those used in the work of Loza et al.³¹ to capture 36 h of total photooxidation while preserving reactor volume. In this study, the 36 h time series is achieved by combining data from an 18 h experiment during which all instruments are online and a 36 h experiment during which all instruments but the AMS are offline during the first 20 h of oxidation. Relative humidity and temperature were monitored for the full 36 h. Thus, the concatenated time series for many instruments (i.e., the CIMS, DMA, NO_x , and O_3 analyzers) is that of the 18 h experiment and the last 16 h of the 36 h experiment. A list of the experiments used for this study are in Table 1. The March experiments used another DMA with a lower total effective flow rate. General consistency between the AMS and CIMS measurements across the two 18 h experiments is observed (see Supporting Information, Figure S1). In the 18 h January experiment, CIMS traces for negative mode ions at $m/z > 300$ were included; the mass scan was reduced to $m/z \leq 300$ in the March experiments. The January

experiment also provided evidence for supporting alternate positive mode m/z 's used for monitoring select hydroperoxide species in the March experiments, which would otherwise be best monitored by the negative mode in the m/z range >300 (see Supporting Information, Figure S2).

Injection protocols were the same for all experiments. Two-hundred eighty microliters of a 50% by weight solution of hydrogen peroxide in water was measured using a glass syringe and injected into a glass trap. The trap was submerged in a warm water bath (~ 35 – 38 °C) while 5 LPM of the purified injection air flowed through the trap and into the chamber evaporating the hydrogen peroxide over approximately 90 min. This results in an approximate starting hydrogen peroxide concentration of 4 ppm. Next a 0.015 M aqueous ammonium sulfate solution was atomized into the chambers providing ~ 11 $\mu\text{m}^3/\text{cm}^3$ volume concentration of seed prior to lights on, as measured by the chamber DMA. Finally, 9 μL of dodecane (Sigma-Aldrich, 98% purity) was injected into a glass bulb and connected within six inches to a reactor injection port via 1/4" o.d. polytetrafluoroethylene (PTFE) tubing. This led to a 10 inch line of 1/4" o.d. PTFE internal to the reactor from the injection port to ensure injection would not be directly to the reactor wall. Using a heat gun with gentle heat, the dodecane evaporated into a flow of 5 LPM of purified injection air going into the chamber. This injection method was performed as close to the chamber as possible to prevent losses of the parent hydrocarbon during line transfer. The resulting dodecane concentration in the chamber was about 34 ppb. Each experiment's starting concentration is listed in Table 1. After loading the reactors, an hour period elapsed to allow for mixing. Then, the blacklights were turned on initiating generation of the OH radical from H_2O_2 photolysis.

Experimental Controls. A thorough discussion on characterizations of the particle-phase wall loss for longer experiments in the Caltech Environmental Chamber appears elsewhere.³¹ For this study, we estimate that by 18 and 36 h of oxidation, approximately 15% and finally 28% of the particle volume has been lost to the walls when comparing DMA suspended volume and wall loss corrected particle volume. A diagnostic dark vapor-phase wall-loss experiment was performed by injecting 60 ppb 2-dodecanone into the chamber and monitoring its decay in the dark over 22 h. Although there was an observed loss of 14% CIMS dodecanone signal over 22 h from its initial signal after injection, one cannot eliminate the possibility of immediate wall-loss or transfer loss during the injection and mixing period (~ 75 min total). Because handling of the standard proved difficult for establishing a confident calibration curve for the CIMS, this could not be verified. No appreciable formation of $> \text{C}_3$ acids and hydroperoxide species above the background noise from the CIMS measurements was observed, and no aerosol volume above the limit of detection ($\sim 0.6 \mu\text{m}^3 \text{cm}^{-3}$) was produced by 22 h as measured by the DMA. Further investigation would be necessary for the goal of mass closure. In order to verify the fragmentation pattern of

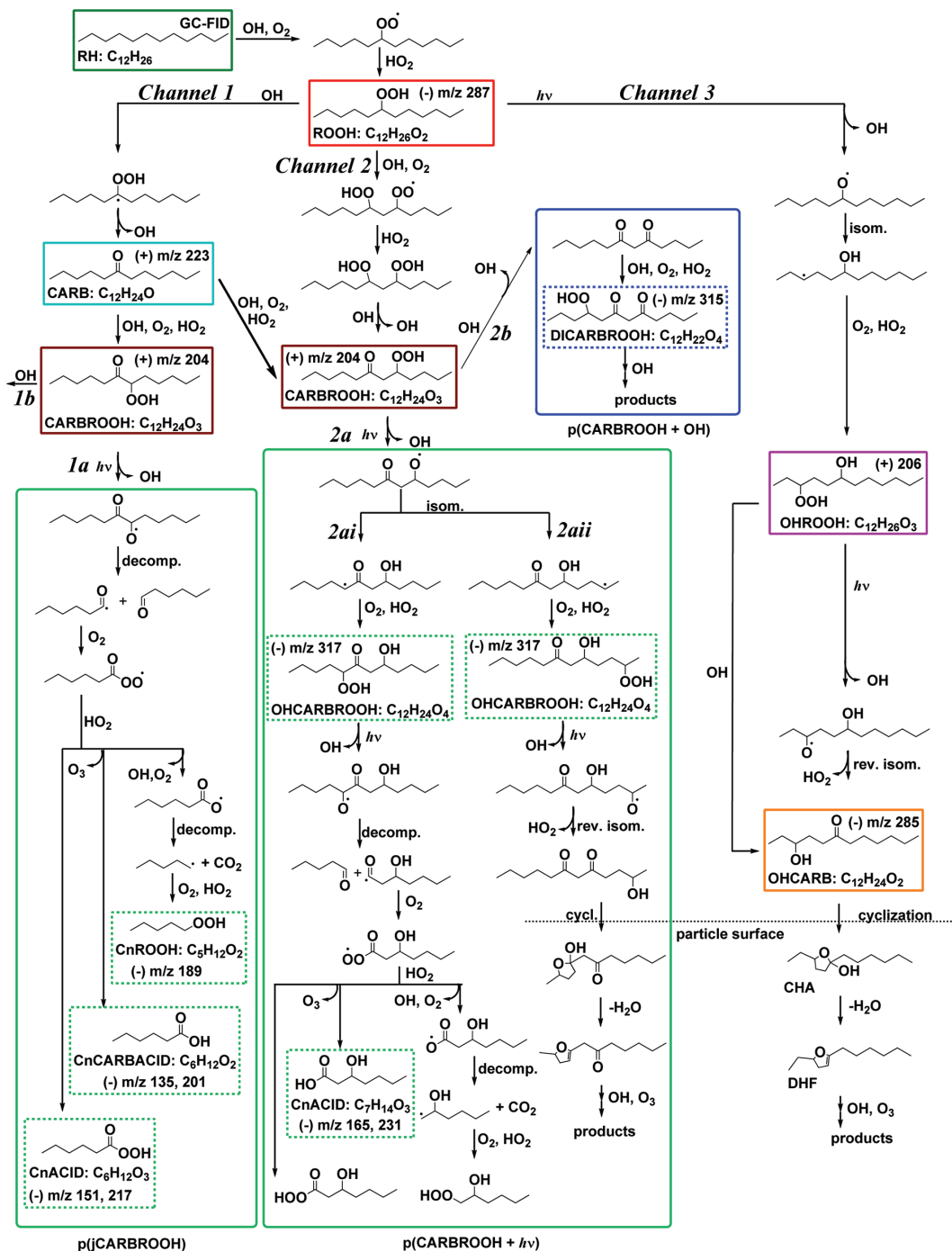


Figure 1. Dodecane low- NO_x mechanism. This scheme explicitly shows OH attack at the C₆ position; however, abstraction of other hydrogens on secondary carbons can also occur. Reaction of dodecane with OH forms a hydroperoxide (ROOH). The hydroperoxide undergoes successive reactions to generate the carbonyl hydroperoxide (CARBROOH, Channel 1 and Channel 2) or photolyzes to form the hydroxy hydroperoxide (OHROOH, Channel 3). The solid colored boxes indicate compounds or reaction pathways photochemically simulated. CIMS monitored species have *m/z* noted. Dashed colored boxes indicate compounds monitored by CIMS, but not explicitly simulated in the photochemical mechanism. The gray dashed line denotes a gas-particle interface where 1,4-hydroxycarbonyl (OHCARB)-like compounds reactively uptake onto the particle and cyclize to form a cyclic hemiacetal (CHA).

Table 2. Reactions Included in the Gas-Phase Photochemical Model

rxn #	reaction	k	ref.
1	$\text{H}_2\text{O}_2 + h\nu \rightarrow 2\text{OH}$	$j_{\text{H}_2\text{O}_2} = 2.87 \times 10^{-6} \text{ s}^{-1}$	JPL ³⁷ + chamber irradiance data
2	$\text{H}_2\text{O}_2 + \text{OH} \rightarrow \text{HO}_2 + \text{H}_2\text{O}$	$k_1 = 1.8 \times 10^{-12} \text{ cm}^3 \text{ molecule}^{-1} \text{ s}^{-1}$	JPL ³⁷
3	$\text{RH} + \text{OH} \rightarrow \text{RO}_2 + \text{H}_2\text{O}$	$k_2 = k_{\text{OH}} = 13.2 \times 10^{-12} \text{ cm}^3 \text{ molecule}^{-1} \text{ s}^{-1}$	Atkinson, 1997 ¹⁴
4	$\text{RO}_2 + \text{RO}_2 + \text{M} \rightarrow \text{pRO}_2\text{RO}_2 + \text{M}$	$k_3 = 5 \times 10^{-15} \text{ cm}^3 \text{ molec}^{-1} \text{ s}^{-1}$	Atkinson, 1997 ¹⁴
5	$\text{RO}_2 + \text{HO}_2 \rightarrow \text{ROOH} + \text{O}_2$	$k_4 = 2.16 \times 10^{-11} \text{ cm}^3 \text{ molecule}^{-1} \text{ s}^{-1}$	MCM 3.2
6	$\text{HO}_2 + \text{HO}_2 \rightarrow \text{H}_2\text{O}_2 + \text{O}_2$	$k_5 = 1.5 \times 10^{-12} \text{ cm}^3 \text{ molec}^{-1} \text{ s}^{-1}$	JPL ³⁷
7	$\text{OH} + \text{HO}_2 \rightarrow \text{H}_2\text{O} + \text{O}_2$	$k_6 = 1.1 \times 10^{-10} \text{ cm}^3 \text{ molecule}^{-1} \text{ s}^{-1}$	JPL ³⁷
8	$\text{OH} + \text{OH} \rightarrow \text{H}_2\text{O}_2$	$k_7 = 6.28 \times 10^{-12} \text{ cm}^3 \text{ molec}^{-1} \text{ s}^{-1}$	JPL ³⁷
9	$\text{ROOH} + \text{OH} \rightarrow \text{CARB}$	$k_8 = 7.4 \times 10^{-12} \text{ cm}^3 \text{ molecule}^{-1} \text{ s}^{-1}$	JPL ³⁷
10	$\text{ROOH} + h\nu \rightarrow \text{RO} + \text{OH}$	$j_{\text{ROOH}} = 2.30 \times 10^{-6} \text{ s}^{-1}$	MCM 3.2 + chamber irradiance data
11	$\text{RO} + \text{O}_2 \rightarrow \text{OHRO}_2$	$k_9 = 2.59 \times 10^{-6} \text{ cm}^3 \text{ molecule}^{-1} \text{ s}^{-1}$	MCM 3.2
12	$\text{OHRO}_2 + \text{HO}_2 \rightarrow \text{OHROOH} + \text{O}_2$	$k_{10} = k_4$	MCM 3.2
13	$\text{CARB} + \text{OH} \rightarrow \text{CARBRO}_2 + \text{H}_2\text{O}$	$k_{11} = 1.49 \times 10^{-11} \text{ cm}^3 \text{ molecule}^{-1} \text{ s}^{-1}$	MCM 3.2
14	$\text{CARBRO}_2 + \text{HO}_2 \rightarrow \text{CARBROOH}$	$k_{12} = k_4$	MCM 3.2
15	$\text{CARB} + h\nu \rightarrow \text{pjCARB}$	$j_{\text{CARB}} = 3.32 \times 10^{-7} \text{ s}^{-1}$	MCM 3.2 + chamber irradiance data
16	$\text{CARBROOH} + \text{OH} \rightarrow \text{p(CARBROOH + OH)}$	$k_{13} = 9.10 \times 10^{-11} \text{ cm}^3 \text{ molecule}^{-1} \text{ s}^{-1}$	MCM 3.2
17	$\text{CARBROOH} + h\nu \rightarrow \text{p(jCARBROOH), aka p(CARBROOH + h\nu)}$	j_{ROOH}	MCM 3.2 + chamber irradiance data
18	$\text{OHROOH} + \text{OH} \rightarrow \text{OHCARB}$	$k_{14} = 4.97 \times 10^{-11} \text{ cm}^3 \text{ molecule}^{-1} \text{ s}^{-1}$	MCM 3.2 + chamber irradiance data
19	$\text{OHROOH} + h\nu \rightarrow \text{pjOHROOH}$	$k_{15} = 2.83 \times 10^7 \text{ cm}^3 \text{ molecule}^{-1} \text{ s}^{-1}$	MCM 3.2
20	$\text{pjOHROOH} \rightarrow \text{OHCARB} + \text{HO}_2$	$k_{16} = 9.04 \times 10^{-12} \text{ cm}^3 \text{ molecule}^{-1} \text{ s}^{-1}$	MCM 3.2
21	$\text{RO}_2 + \text{NO} \rightarrow 0.56 \text{ RO} + 0.44 \text{ pRONO}_2$	$k_{17} = k_{16}$	MCM 3.2
22	$\text{OHRO}_2 + \text{NO} \rightarrow 0.176 \text{ OHRO} + 0.824 \text{ pOHRONO}_2$	$k_{18} = k_{16}$	MCM 3.2
23	$\text{CARBRO}_2 + \text{NO} \rightarrow \text{CARBRO}$	$k_{19} = k_3$	MCM 3.2
24	$\text{OHRO}_2 + \text{RO}_2 \rightarrow \text{pOHRO}_2\text{RO}_2$	$k_{20} = k_3$	MCM 3.2
25	$\text{CARBRO}_2 + \text{RO}_2 \rightarrow \text{pCARBRO}_2\text{RO}_2$	$k_{21} = 9.0 \times 10^{-12} \text{ cm}^3 \text{ molecule}^{-1} \text{ s}^{-1}$	JPL ³⁷
26	$\text{RO}_2 + \text{NO}_2 \rightarrow \text{pRO}_2\text{NO}_2$	$k_{22} = k_{21}$	JPL ³⁷
27	$\text{OHRO}_2 + \text{NO}_2 \rightarrow \text{pOHRO}_2\text{NO}_2$	$k_{23} = k_{21}$	JPL ³⁷
28	$\text{CARBRO}_2 + \text{NO}_2 \rightarrow \text{pCARBRO}_2\text{NO}_2$		

hydroperoxide species in the AMS spectrum, a seeded photooxidation experiment was run with a target injection of 300 ppb octadecane ($\text{C}_{18}\text{H}_{38}$) using the experimental protocols discussed earlier. The first generation hydroperoxide ($\text{C}_{18}\text{H}_{38}\text{O}_2$) immediately partitions to the particle-phase, and a distinct AMS ion at nominal $m/z = 253$ ($\text{C}_{18}\text{H}_{37}^+$) appeared after lights on, suggesting that hydroperoxide species fragment to form ions of the form $[\text{M}-33]^+$, where M is the molecular weight of the hydroperoxide species.

DODECANE LOW- NO_x GAS-PHASE MECHANISM

The OH-initiated photooxidation of *n*-alkanes has been studied previously, providing a framework of well-known chemical reactions under varying NO_x conditions^{14,15} that can be extended to the case of dodecane. Such reactions are also included in the Master Chemical Mechanism 3.2 (MCM 3.2) via Web site: <http://mcm.leeds.ac.uk/MCM>.^{32,33} The reactions proposed in such previous studies in conjunction with gas-phase measurements from this study afforded the development of a mechanism for the photooxidation of dodecane under low- NO_x conditions where $\text{RO}_2 + \text{HO}_2$ chemistry dominates (see Figure 1). Reaction pathways past the carbonyl hydroperoxide (CARBROOH) along Channel 1a and Channel 2b are not included in the MCM 3.2 for dodecane. For clarity, colored boxed molecules with simple labels are those that were explicitly simulated in the photochemical mechanism and are represented in the reactions of Table 2, consistent with the color scheme comparing CIMS measurements and simulated output in Figure 2 (RH, ROOH, CARB, CARBROOH, OHROOH, and OHCARB). In some cases, a group of products was not modeled explicitly, so a reaction pathway is

boxed and labeled (p(jCARBROOH), p(CARBROOH + $h\nu$), and p(CARBROOH + OH)). Boxed molecules with a dashed border indicate those that have been monitored by the CIMS including the m/z that was monitored, but they were not explicitly modeled in the photochemical mechanism (CnROOH, CnCARBACID, CnACID, OHCARBROOH, and DICARBROOH). Reaction channels are noted with alphanumeric labels, and the labels for molecules or product channels of interest are referred to throughout the text. OH attack is explicitly shown at the C_6 carbon, although it is expected that any of the hydrogens on secondary carbons will be similarly vulnerable to abstraction by the OH radical. Using estimated structure activity relationship reaction rate constants,³⁴ OH abstraction of the hydrogens on the primary carbons would only represent two percent of the overall reaction rate of dodecane with OH. Five generations of chemistry are represented in the reaction pathways of Figure 1, with a generation defined as the OH-initiated or photolysis reaction of a stable (nonradical) compound. The mechanism provides an overview of the types of products generated from the alkyl peroxy radical RO_2 exclusively reacting with HO_2 to generate hydroperoxides, which then react with OH or undergo photolysis. While a wide variety of compounds are included in the mechanism shown in Figure 1, this mechanism is by no means exhaustive of all possible compounds formed in terms of functional group placement and molecular structure.

Low- NO_x Conditions. Under conditions in which $[\text{HO}_2] \gg [\text{RO}_2]$, and in which NO_x levels are very low, RO_2 can be expected to react exclusively with HO_2 . For the experimental conditions, the HO_2 is calculated by a photochemical model. The HO_2 concentration ($\sim 1 \times 10^{10}$ molecules cm^{-3}) exceeds

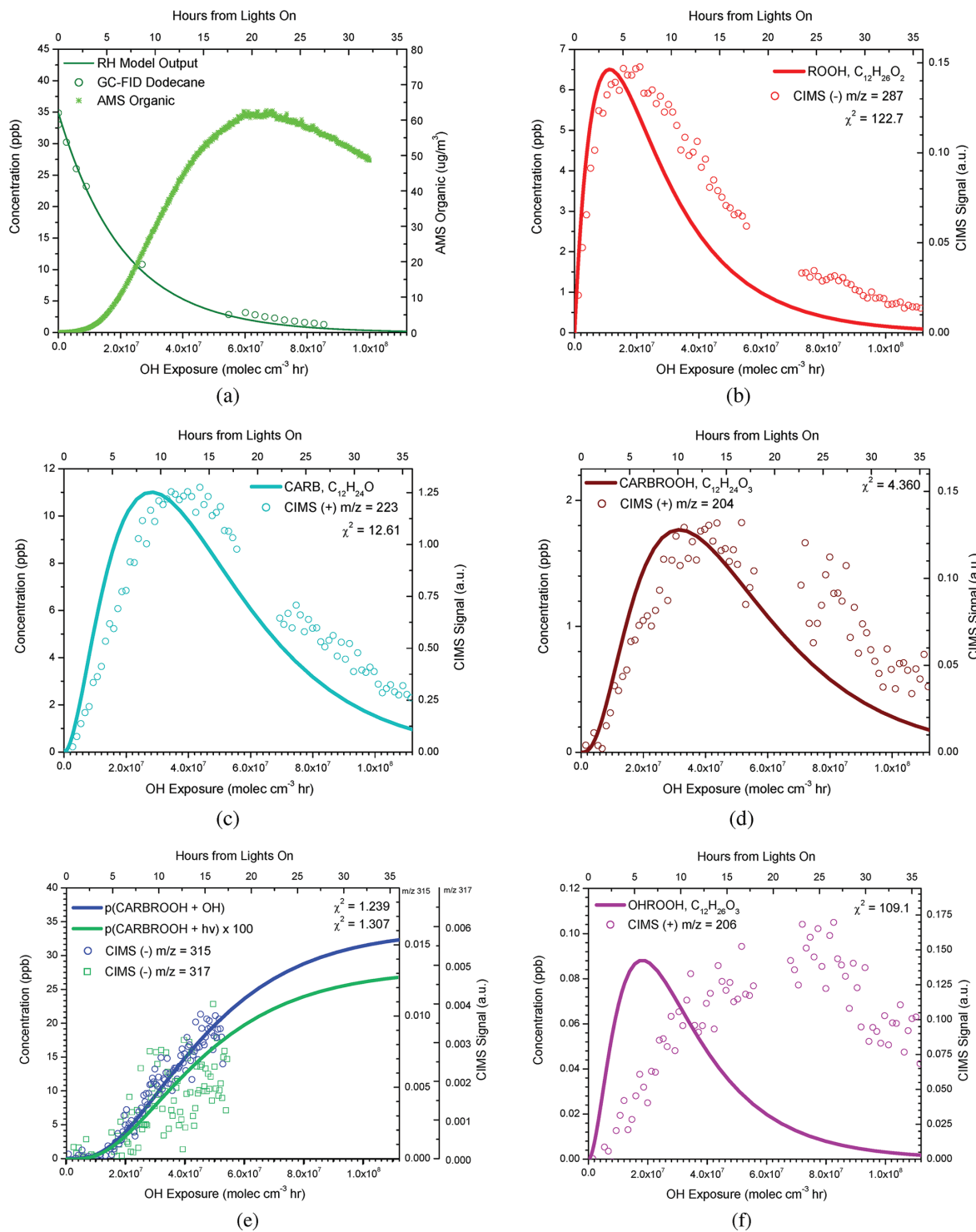


Figure 2. continued

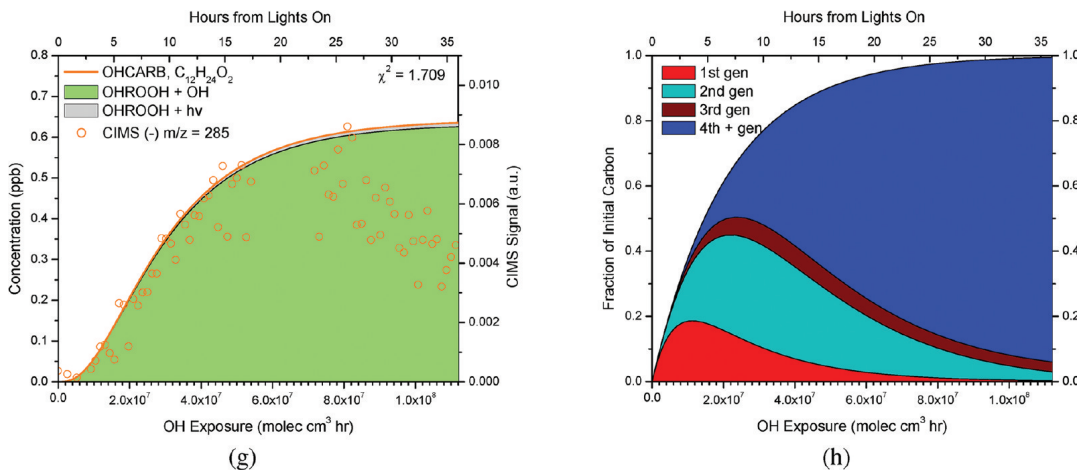


Figure 2. Simulated (curves) and observed (open circles) time evolutions of various gas-phase species from OH-initiated photoxidation of dodecane. Colors used match species outlined in the gas-phase mechanism. (a) Decay of dodecane parent hydrocarbon with suspended organic growth. (b) First-generation formation of the hydroperoxide (ROOH) monitored at (−) m/z 287. (c) Second-generation formation of the ketone (CARB) monitored at (+) m/z 223. (d) Third-generation formation of the carbonyl hydroperoxide (CARBROOH) monitored at (+) m/z 204. (e) Simulated output of remaining carbon from further oxidation of the carbonyl hydroperoxide p(CARBROOH + OH) as (−) m/z 315 or photolysis p(CARBROOH + $h\nu$) as (−) m/z 317. (f) Photolysis of the hydroperoxide (ROOH) leads to formation of a hydroxy hydroperoxide (OHROOH) monitored at (+) m/z 206. (g) Formation of the hydroxycarbonyl (OHCARB) from two sources: (1) photolysis of the hydroxy hydroperoxide (OHROOH + $h\nu$) and (2) OH reaction with the hydroxy hydroperoxide (OHROOH + OH). (h) Simulated fraction of initial carbon in the gas-phase by generation over the course of the experiment.

that of RO_2 ($\sim 1 \times 10^8$ molecules cm^{-3}) by 2 orders of magnitude. The dominant route of RO_2 chemistry is reaction with HO_2 to form hydroperoxide compounds. It is important to note that what determines low- NO_x or high- NO_x conditions is not merely dependent on the HO_2 concentration itself; rather, the conditions are defined by the dynamics of NO and RO_2 and the various reaction rate constants. For example, the reaction rate constants for CH_3O_2 with HO_2 , CH_3O_2 , NO, and NO_2 at 298 K are 5.2×10^{-12} cm^3 molecule⁻¹ s^{-1} , 3.7×10^{-13} cm^3 molecule⁻¹ s^{-1} , $6.5-7.8 \times 10^{-12}$ cm^3 molecule⁻¹ s^{-1} , and 3.9×10^{-12} cm^3 molecule⁻¹ s^{-1} , respectively.¹⁴ On the basis of these rate constants, CH_3O_2 lifetime against reaction with these species increases in the order of NO, HO_2 , NO_2 , and CH_3O_2 . However, sufficient concentrations of HO_2 and/or CH_3O_2 as compared with NO would shift the conditions to an effectively low- NO_x regime of chemistry, in which the relative concentrations of HO_2 and CH_3O_2 would then determine whether the low- NO_x regime is dominated by $\text{CH}_3\text{O}_2 + \text{HO}_2$ or shared with $\text{CH}_3\text{O}_2 + \text{CH}_3\text{O}_2$.

Without any addition of NO_x , a small amount of NO_x , presumably from residual nitrogen-containing acids (e.g., HONO or HNO_3) on the chamber walls, is generated upon irradiation. This phenomenon of “ NO_x offgassing”^{35,36} is a common observation among environmental chambers.^{35,36} In the chamber experiments to be described, the NO concentration is below the limit of detection (~ 5 ppb), and the NO_2 generated is <5 ppb. While the total generated NO_x is primarily in the form of NO_2 , NO_2 cannot be calibrated directly with this technique, and there are fewer calibration points at this lower range leading to some uncertainty in the measurement. Low- NO_x conditions in the chamber are further verified by CIMS measurements of HO_2NO_2 pernitric acid (PNA), the formation of which is highly sensitive to the $\text{HO}_2:\text{NO}_2$ ratio. Using the CIMS sensitivity to PNA,²⁴ the PNA concentration generated upon lights on is <350 pptv. As discussed in the work of Paulot

et al.,²⁴ it is likely that the sensitivity to PNA is overestimated due to ligand exchange of H_2O_2 with the reagent ion. Using the expected HO_2 concentration generated upon irradiation, and the equilibrium constant for $\text{HO}_2 + \text{NO}_2 \rightleftharpoons \text{HO}_2\text{NO}_2$, 1.6×10^{-11} cm^3 molec⁻¹,³⁷ the predicted NO_2 residual concentration is <1.2 ppb.

To explore possible effects of residual NO_x , the chemistry was simulated with initial concentrations of NO at 0.1 ppb, 2 ppb, and constant NO at 0.1 ppb, using all reactions in Table 2. Under these varying NO_x conditions, we estimate that $<1\%$, $<10\%$, and $<19\%$, respectively, of the dodecane reacts via $\text{RO}_2 + \text{NO}_x$ reactions. Relative lifetimes of RO_2 against reaction with RO_2 , HO_2 , NO, and NO_2 for these varying NO_x conditions are provided in the Supporting Information, Table S1. The two species, the 1,4-hydroxycarbonyl (OHCARB, Figure 1) and the hydroxy hydroperoxide (OHROOH, Figure 1) that would be most affected by the presence of NO_x are shown based on NO concentration and provided in the Supporting Information, Figure S3. At NO concentration greater than 0.1 ppb, the delay seen in the CIMS measurement of the 1,4-hydroxycarbonyl is not reproduced (Supporting Information, Figure S3a). The 1,4-hydroxycarbonyl is an important intermediate in SOA formation in the presence of NO_x ,^{12,38} so the presence of NO should enhance its production and contribute to initial organic growth. The observed delay in the organic growth as measured by the AMS is consistent with the absence of any appreciable NO_x in the system. Further, the presence of NO should accelerate formation of the hydroxy hydroperoxide (OHROOH) (Supporting Information, Figure S3b), causing the simulations to further deviate from the observed gas-phase measurements. These analyses support the fact that residual NO_x does not play a significant role in the overall chemistry represented and that the majority of alkoxy radical formation is not a result of $\text{RO}_2 + \text{NO}$ chemistry. In addition, CIMS spectra show no evidence of nitrate compounds formed. Thus, the

photochemical mechanism used in the remainder of this study excludes the presence of NO_x .

Hydroperoxide Photolysis. The OH-initiated reaction of dodecane results in the formation of the peroxy radical which, upon reaction with HO_2 , rapidly produces the hydroperoxide ($\text{C}_{12}\text{H}_{26}\text{O}_2$, ROOH in Figure 1). The hydroperoxide can undergo further reaction with OH or photolysis. In the absence of an explicit photolysis rate, following MCM 3.2, the methyl hydroperoxide photolysis rate is used as a proxy for the photolysis rate of hydroperoxide species. Using absorption cross sections and quantum yields for methyl hydroperoxide (CH_3OOH)^{39,40} with the actinic flux calculated from spectral irradiance measurements in the chamber using a LICOR spectroradiometer, the expected photolysis rate constant of methyl hydroperoxide is calculated to be $j = 2.30 \times 10^{-6} \text{ s}^{-1}$. Under these experimental conditions, the C_{12} hydroperoxide is simulated in the mechanism to react with OH and undergo photolysis in branching ratios of 86% and 14%, respectively. The most likely route of photolysis is to sever the O–OH bond rather than the C–OOH bond in the hydroperoxy group,⁴¹ resulting in the formation of an alkoxy radical. In the domain of $\text{RO}_2 + \text{HO}_2$ chemistry, alkoxy radicals can be generated only via photolysis of a hydroperoxy group; there is no formation of simple alcohols, which is the same when NO_x is present.^{9,11,14,15} Along Channel 3 of the mechanism in Figure 1, the hydroperoxide photolyses to generate the alkoxy radical. Due to the length of the carbon chain, isomerization through a 1,5-hydride shift will occur,^{9,11,15} generating a hydroxy group and leaving a radical on a secondary carbon. Reaction of this radical with O_2 followed by reaction with HO_2 leads to the hydroxy hydroperoxide ($\text{C}_{12}\text{H}_{26}\text{O}_3$) referred to as OHROOH in Figure 1, which can undergo photolysis or further reaction with OH. Under photolysis, the same reverse isomerization of the resulting hydroxy alkoxy radical occurs to form a 1,4-hydroxycarbonyl ($\text{C}_{12}\text{H}_{24}\text{O}_2$)^{9,11} referred to as OHCARB in Figure 1. On the basis of the calculated photolysis rate constant of methyl hydroperoxide as a proxy and the OH concentration lumped reaction rate constant, $k_{\text{OH}} = 9.94 \times 10^{-5} \text{ s}^{-1}$, generation of the 1,4-hydroxycarbonyl (OHCARB) via reaction with OH is the preferred pathway. The 1,4-hydroxycarbonyl is estimated to react with OH and undergo photolysis in branching ratios of 98% and 2%, respectively, according to the photochemical simulation. In the case of reaction with OH, the positions of the carbonyl and hydroxy groups would be switched from what is shown in the mechanism. This formation mechanism of the 1,4-hydroxycarbonyl (OHCARB) is also distinct from the predominant reverse isomerization mechanism when in the presence of NO_x .^{9,11,14,15} Still, an even quicker route of formation is through alkyl peroxy radical isomerization with an extrapolated isomerization rate constant of 0.03 s^{-1} at 298 K, which is applicable to the conditions of $[\text{RO}_2] < 6 \times 10^{12} \text{ molecules cm}^{-3}$ and $[\text{NO}] < 3 \times 10^9 \text{ molecules cm}^{-3}$.^{15,42,43} Since the NO concentration is only confidently known to be <5 ppb or $1 \times 10^{11} \text{ molecules cm}^{-3}$ (the lower detection limit of our NO_x analyzer), the alkyl peroxy radical isomerization route is unconfirmed.

Hydroperoxide + OH. The hydroperoxide primarily reacts with OH, in which abstraction of the hydrogen from the hydroperoxy-containing carbon is favored.⁴¹ This leads to decomposition of the hydroperoxy group to form a carbonyl ($\text{C}_{12}\text{H}_{24}\text{O}$), resulting in recycling of OH radical (Channel 1, CARB in Figure 1). In the case in which the OH attacks another secondary carbon along the hydroperoxide chain, a

dihydroperoxide, $\text{C}_{12}\text{H}_{26}\text{O}_4$, (Channel 2 in Figure 1) may be formed. Reaction of the carbonyl or the dihydroperoxide with OH would generate the third-generation carbonyl hydroperoxide (CARBROOH), with chemical formula $\text{C}_{12}\text{H}_{24}\text{O}_3$. OH reaction with the carbonyl generally favors attack at a carbon beta from the existing carbonyl group;³⁴ however, a small fraction could occur at the α position. Depending on the relative positions of the carbonyl and hydroperoxy group, fragmentation or functionalization will occur. In the case of Channel 1, the carbonyl and hydroperoxy groups are on adjoining carbons, such that when photolysis of the hydroperoxy group generates the alkoxy radical, scission of this C–C bond is favored. Products along Channel 1a are referred to as p(jCARBROOH) in reaction 17 of Table 2. Decomposition of the carbonyl alkoxy radical leads to an acyl radical and an aldehyde. The eventual fate of the acyl radical is reaction with O_2 to generate an acyl peroxy radical, which reacts with HO_2 to generate acids (Channel 1a, CnCARBACID and CnACID) and eventually a shorter chain hydroperoxide (Channel 1a, CnROOH). While the formation of aldehydes and acids is reliant upon the formation of a less abundant form of the carbonyl hydroperoxide and its photolysis, Channel 1a serves an important role in generating aldehydes in a system with hydroperoxide species. These aldehydes can react in the particle phase to form PHAs, to be discussed later in the paper.

In the case of the carbonyl and hydroperoxy groups located beta to one another (Channel 2), photolysis (Channel 2a) or reaction with OH (Channel 2b) leads to more highly functionalized compounds than if the C_{12} backbone is fragmented as in Channel 1a. Products along Channel 2a are collectively referred to as p(CARBROOH + $\text{h}\nu$) in reaction 17 (Table 2), and products along Channel 2b are referred to as p(CARBROOH + OH) in reaction 16 (Table 2). In chemistry analogous to the photolysis route (Channel 3) of the initial hydroperoxide (ROOH), functionalization is achieved by gain of a hydroxy group through isomerization, leading to a multifunctional compound containing carbonyl, hydroxy, and hydroperoxide groups (Channel 2a). Again, the relative positions of these functional groups lead to hydroxy acids formation through photolysis (Channel 2ai, CnACID) or a 1,4-hydroxycarbonyl with an additional keto group (Channel 2aii). Consecutive OH reaction with the carbonyl hydroperoxide (CARBROOH) would lead to multiple keto groups forming from the previous hydroperoxide group (Channel 2b). However, the competitive photolysis of hydroperoxy groups leads to the variety in functionalization as in Channel 2a. Although the fate of the carbonyl hydroperoxide (CARBROOH) is likely to channel more carbon through reaction with OH (pCARBROOH + OH), (Channel 2b), the gas-phase chemistry in Channel 1a becomes important for SOA growth and will be discussed subsequently.

■ COMPARISON OF GAS-PHASE MECHANISM AND MEASUREMENTS

The dodecane–OH mechanism derived from the MCM 3.2^{32,33} (Table 2) was used to simulate the first four generations of chemistry. The simulated hydrocarbon decay agrees with GC-FID measurements of dodecane in Figure 2a. The photolysis rate for H_2O_2 was calculated using the absorption cross section and quantum yield^{39,40} with the chamber actinic flux, analogous to the calculation done for hydroperoxide species. The simple labels for compounds in Figure 1 are also used in the legend entries for the photochemical mechanism

and CIMS measurements comparisons throughout Figure 2. CIMS traces are referred to with a polarity as “(+)” or “(−)” preceding the m/z solely to indicate the ionization mode used, positive or negative, respectively. Table 3 provides a summary of the monitored CIMS ions and their suggested assignments.

Table 3. Signals Monitored by CIMS and Their Suggested Assignments

mode	m/z (s)	assignment	molecular formula
(−)	287	ROOH	$C_{12}H_{26}O_2$
(+)	223	CARB	$C_{12}H_{24}O$
(+)/−	204/301 ^a	CARBROOH	$C_{12}H_{24}O_3$
(+)/−	206/303 ^a	OHROOH	$C_{12}H_{26}O_3$
(−)	285	OHCARB	$C_{12}H_{24}O_2$
(−)	315 ^a	DICARBROOH	$C_{12}H_{22}O_4$
(−)	317 ^a	OHCARBROOH	$C_{12}H_{24}O_4$
(−)	187	C5CARBACID	$C_5H_{10}O_2$
(−)	135/201	C6CARBACID	$C_6H_{12}O_2$
(−)	149/215	C7CARBACID	$C_7H_{14}O_2$
(−)	163/229	C8CARBACID	$C_8H_{16}O_2$
(−)	177/243	C9CARBACID	$C_9H_{18}O_2$
(−)	191/257	C10CARBACID	$C_{10}H_{20}O_2$
(−)	205/271	C11CARBACID	$C_{11}H_{22}O_2$
(−)	203	C5ACID/C6ROOH	$C_5H_{10}O_3/C_6H_{14}O_2$
(−)	151/217	C6ACID/C7ROOH	$C_6H_{12}O_3/C_7H_{16}O_2$
(−)	165/231	C7ACID/C8ROOH	$C_7H_{14}O_3/C_8H_{18}O_2$
(−)	245	C8ACID/C9ROOH	$C_8H_{16}O_3/C_9H_{20}O_2$
(−)	193/259	C9ACID/C10ROOH	$C_9H_{18}O_3/C_{10}H_{22}O_2$

^aDenotes negative mode ions at $m/z > 300$ monitored in the January 18 h experiment. All other m/z 's were monitored in the January and March experiments.

The mechanism was used primarily for evaluating time profiles of expected products in the CIMS measurements. The scales for the CIMS signal and the simulated output have been adjusted for peak matching to compare the trends in Figure 2. Reduced χ^2 values are given for the fit of the simulated trace and the CIMS measurements using the maximum value for the first 18 h as the normalization parameter. The χ^2 for the simulated and measured 1,4-hydroxycarbonyl (OHCARB) is for the first 18 h since the measurement decays, but the simulation does not include a reactive sink. Vapor-phase wall loss is not treated here in the photochemical model or in correcting the gas-phase observations (for reasons described in the Experimental Section), although it is likely to play a role affecting the more highly oxidized lower volatility products formed as in other chamber studies.^{44,45} While the gas-phase chemistry represented in the mechanism generally describes the gas-phase CIMS trends for many species such as the hydroperoxide (ROOH), carbonyl (CARB), and carbonyl hydroperoxide (CARBROOH), the hydroxy hydroperoxide (OHROOH) may be subject to greater vapor-phase wall loss, contributing to some of the discrepancy between the simulated and measured trace in the beginning of the experiment. This effect is discussed further in the following section.

Mechanism and Measurement Comparison of Hydroperoxide + OH. Mechanism predictions of the hydroperoxide (ROOH) capture the trend of the CIMS measurements for the hydroperoxide (−) $m/z = 287$ (Figure 2b). At its peak, the hydroperoxide is simulated to represent about 20% of the initial carbon. While the hydroperoxide production rate is captured by the ROOH photochemical mechanism, the simulated loss is

overestimated. The loss processes for the hydroperoxide include ROOH + OH and ROOH + $h\nu$. As noted, the MCM 3.2 gives an explicit reaction rate constant for a C_{12} hydroperoxide with OH, but utilizes the photolysis rate of CH_3OOH as a general photolysis rate for all hydroperoxide species. Extrapolating the photolysis rate from a C_1 to a C_{12} hydroperoxide is a source of uncertainty in the simulated trace. The simulated chemistry is more rapid than the measurements, consistent with a faster than measured production rate of the carbonyl.

The MCM 3.2 mechanism for dodecane does not include explicit reactions for formation of the dihydroperoxide (Channel 2), although evidence exists in the CIMS data at (−) $m/z = 319$ (CF_3O^- cluster) that suggests formation. The possibility of alkyl peroxy radical isomerization⁴⁶ was also considered, but this is unlikely under these experimental conditions because the $[HO_2]$ and $[OH]$ are not low enough to extend the lifetime of the alkyl peroxy radical for it to isomerize. Because the carbonyl (CARB) is not sufficiently polar to be detected in the negative mode ionization, it was monitored in positive mode at (+) $m/z = 223$. The carbonyl measurements also track the mechanism simulations, although with a slight lag (Figure 2c). The carbonyl (CARB) forms quickly, simultaneously with the hydroperoxide generation, so its peak just after 10 h represents almost a third of the initial carbon. The carbonyl hydroperoxide (CARBROOH) monitored at (+) $m/z = 204$ also times well with the model output during growth, but the gas-phase concentration remains low overall because of its many reactive sinks.

Owing to the complexity of the many later generation products, these are not represented explicitly in the mechanism, and the simulation terminates with the remaining carbon represented in further reaction of the carbonyl hydroperoxide. This includes three possible routes as discussed previously and seen in Figure 1: (1) photolysis and subsequent decomposition if the carbonyl and hydroperoxy group are vicinal (Channel 1a), (2) photolysis of the hydroperoxy group beta to the carbonyl (Channel 2a), and subsequent decomposition products (Channel 2ai) or C_{12} retaining products (Channel 2aii), and (3) continued OH reaction and functionalization of the C_{12} molecule (Channel 2b). The respective photolysis of the α -carbonyl hydroperoxide (Channel 1a) and the β -carbonyl hydroperoxide photolysis (Channel 2a) or reaction with OH (Channel 2b) are represented in the mechanism scheme in Figure 1. However, the MCM 3.2 makes no distinction between reaction rates for isomers of the carbonyl hydroperoxide, so the sum of the α -carbonyl hydroperoxide (Channel 1) and the β -carbonyl hydroperoxide (Channel 2) are implemented in the photochemical simulation as (CARBROOH). Thus, the subsequent photolysis product from the α -carbonyl hydroperoxide (Channel 1a) and the β -carbonyl hydroperoxide (Channel 2a), respectively, will produce the same time trend from the photochemical simulation (Table 2, Reaction 17), although we distinguish the alpha photolysis products (Channel 1a) as $p(j)CARBROOH$ and the beta photolysis products (Channel 2a) as $p(CARBROOH + h\nu)$ for relevant discussion on a distinct set of products formed from photolysis of each isomer. That is, acid formation (Figures 3b and 4b) is considered as $p(j)CARBROOH$, and the multifunctional formed via Channel 2a is considered as $p(CARBROOH + h\nu)$ in Figure 2e.

Note that photolysis of the β -carbonyl hydroperoxide (Channel 2ai) produces a hydroxy carbonyl hydroperoxide

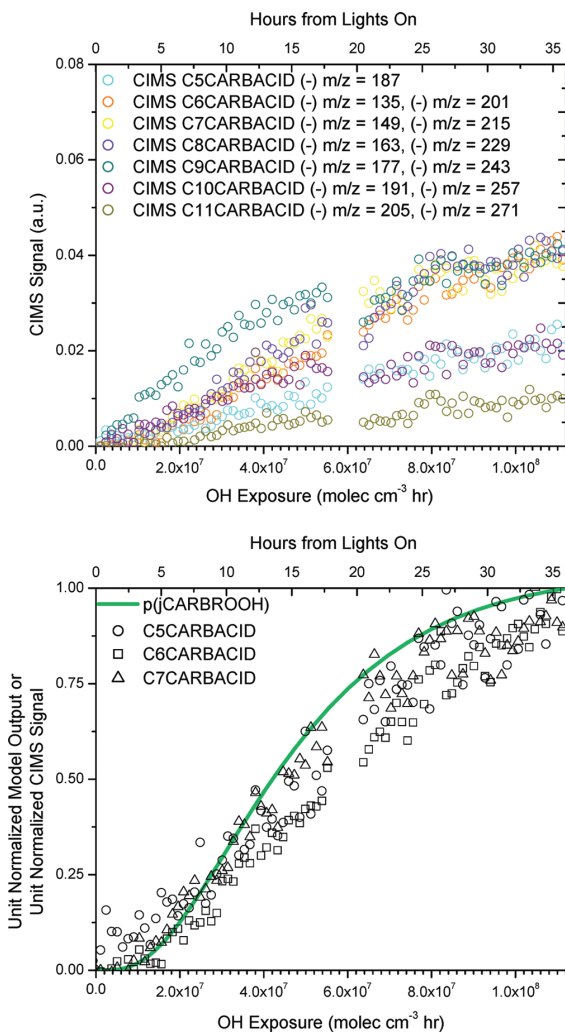


Figure 3. Carboxylic acids. (a) Series of suggested C₅ through C₁₁ carboxylic acid traces and the ions measured in CIMS negative mode ionization. (b) Representative C₅ through C₇ carboxylic acid traces on a unit normalized scale trend with modeled results for photolysis of the carbonyl hydroperoxide.

(OHCARBROOH) with the carbonyl and hydroperoxide groups vicinal. Photolysis of this multifunctional compound shows a parallel decomposition route to Channel 1a leading to hydroxy acids. Channel 2aii retains the C₁₂ backbone, because, although it also starts with a hydroxy carbonyl hydroperoxide (OHCARBROOH), the carbonyl and hydroxy functional groups are nonvicinal to the -OOH group. Analogous to the treatment of the two carbonyl hydroperoxide (CARBROOH) isomers, these two hydroxy carbonyl hydroperoxide (OHCARBROOH) isomers are also not distinguished in the photochemical simulation; they are shown as p(CARBROOH + hν). That is, Figure 2e compares the simulated output of p(CARBROOH + hν) to the CIMS measured ion suggested for the multifunctional compound (presumably OHCARBROOH, C₁₂H₂₄O₄) at (-) m/z = 317 to represent Channel 2a. Products of the continued OH oxidation of the β-carbonyl

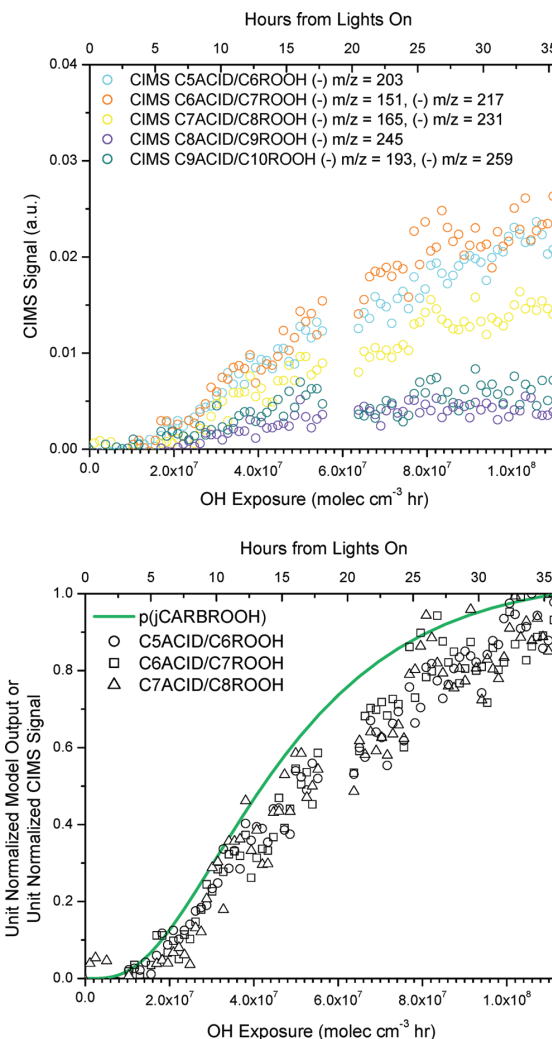


Figure 4. Acids (hydroxycarboxylic/peracid) or hydroperoxides. (a) Series of suggested C₅ through C₉ peracid and hydroxy carboxylic acid, and C₆ through C₁₀ hydroperoxide traces. Since the peracid and hydroxy carboxylic acid are the same molecular weight as a hydroperoxide with one additional carbon, the ions measured by the CIMS may have contributions from all three species. (b) Example unit normalized trends of C₅ through C₇ peracids and hydroxycarboxylic acids, and C₆ through C₈ hydroperoxides that trend with the product of carbonyl hydroperoxide photolysis from the mechanism.

hydroperoxide (Channel 2b) are simulated under p(CARBROOH + OH), which has a distinct output from that of the carbonyl hydroperoxide photolysis, represented identically in p(CARBROOH + hν) and p(j)CARBROOH. Production of a possible dicarbonyl hydroperoxide (presumably DICARBROOH, C₁₂H₂₂O₄), monitored at (-) m/z = 315, represents this channel in the mechanism (Channel 2b). Note that the signals at (-) m/z = 317 and (-) m/z = 315 do not extend the full 36 h because they were not monitored for a full 36 h as described in the Experimental Section. More detailed treatment of Channel 1a is discussed subsequently relative to acid formation.

Mechanism and Measurement Comparison of Hydroperoxide Photolysis. The hydroxy hydroperoxide measurements exhibit the largest deviation of all CIMS traces from the simulated hydroxy hydroperoxide (OHROOH) (Figure 2f). While we cannot fully account for this discrepancy at the present time, it could be possible that (1) the hydroxy hydroperoxide formation is in fact slower than predicted by using the photolysis rate of a C₁ hydroperoxide for the C₁₂ hydroperoxide and (2) the hydroxy hydroperoxide (OHROOH) has sufficiently low volatility that it may be lost to the chamber walls more quickly than other gas-phase compounds. We observe that the chemistry in general is actually slower than the simulation. That is, the simulated hydroperoxide (ROOH) exhibits a faster decay than that of the measurement (Figure 2b) and subsequent products (CARB, CARBROOH, and OHROOH) are simulated to rise more quickly than their individual measurements (Figure 2c,d,f). Hence, we do expect that OHROOH's actual rise will come later than that simulated. If gas-to-wall partitioning is responsible for the discrepancy, the walls may first act as a reservoir but subsequently release the hydroxy hydroperoxide back to the gas-phase as it is removed by secondary reactions, shifting the trend of the gas-phase measurement from the simulated trend. We return to the hydroxy hydroperoxide sinks in the SOA Growth section.

The 1,4-hydroxycarbonyl (OHCARB, Figure 2g) is generated from the hydroxy hydroperoxide (OHROOH, Figure 2f) in greater concentration than its precursor. As discussed earlier, the 1,4-hydroxycarbonyl may be formed via photolysis of the hydroxy hydroperoxide (OHROOH + $h\nu$) or via hydroxyl radical reaction with the hydroxy hydroperoxide (OHROOH + OH). The relative contributions from these sources to 1,4-hydroxycarbonyl (OHCARB) formation are shown in Figure 2g. The CIMS measurement of the 1,4-hydroxycarbonyl at (−) m/z = 285 follows the simulated production despite discrepancy in the simulation and measurement for its precursor, the hydroxy hydroperoxide (OHROOH). This may suggest that the true time profile for OHROOH is not captured by the measurement. The vapor pressure of OHROOH is about 2 orders of magnitude lower than OHCARB, so one hypothesis is that the early losses of OHROOH are due to vapor-phase wall loss to the reactor walls and reaction with OH to form OHCARB. Mass closure is needed to confirm whether the measurements match the expected OHROOH distribution among losses to the wall and its oxidation to OHCARB, but it is possible that if the OHROOH is converted quickly to OHCARB via reaction with OH (lifetime ~ 2.8 h), then the trend in the CIMS measurement for OHCARB would still agree with the simulation early on as observed (Figure 2g). Although there is no explicitly simulated sink for the 1,4-hydroxycarbonyl (OHCARB), the measurement peaks sometime after 18 h. It is expected that from the difference between the gas-phase and mechanism trends, roughly 0.3 ppb of it exists in this sink.

Mechanism and Measurement Comparison of Acid Formation. Acidic species are expected to form from photolysis of a hydroperoxy group that is vicinal to another oxygen containing carbon. Photolysis of the hydroperoxy group results in an alkoxy radical vicinal to another oxygen containing carbon so decomposition ensues (see Figure 1, Channels 1a and 2ai). Depending on where in the molecule the C–C bond is severed, varying carbon length carboxylic acids (Channel 1a, CnCARBACID, C_nH_{2n}O₂), peracids (Channel 1a, CnACID,

C_nH_{2n}O₃), hydroxycarboxylic acids, (Channel 2ai, CnACID C_nH_{2n}O₃), and hydroxyperacids (Channel 2ai) result. Such compounds in the CIMS may appear as both the transfer (m/z = [M + 19][−]) and the cluster product (m/z = [M + 85][−]), so the traces shown are the sum of these two ions (see Figure 3 and Figure 4). In some cases, like the C₅ carboxylic acid, there were additional contributions to the cluster product ion (m/z = 253), so it is omitted. The C₉ carboxylic acid likely has contributions from an unidentified mass interferent since its time profile is slightly different than the others. The overall time profiles and their relative abundances are consistent with expectations that C₁₁ acid production is least likely to form, as tertiary H abstraction at the end carbons is slower.³⁴ Still, distribution by carbon number would need to be confirmed after full mass quantification. When unit normalized, the carboxylic acid traces (CnCARBACID) collapse to a distinct time profile consistent with the modeled trace representing the photolysis products of the carbonyl hydroperoxide p(jCARBROOH) in Figure 3b.

The formation of a peracid (Channel 1a, CnACID) of the same carbon number as a hydroxy carboxylic acid (Channel 2ai, CnACID) is difficult to discern, as they are isomers. Thus, these two types of acids have been referred to generally as CnACID, and this is separate from the carboxylic acids referred to as CnCARBACID. Other isomers include a hydroperoxide (Channel 1a, CnROOH) with an additional carbon. Hence, the ions monitored are generally assigned as a C_n acid or a C_{n+1} hydroperoxide in Figure 4. Still, it is more likely that the majority initial contribution to these ions stems from the peracid, as the hydroxycarboxylic acid (Channel 2ai, CnACID) is a higher generation product. Further, resulting branching ratios for the products of the acyl peroxy radical reaction with HO₂, as discussed in Hasson et al.⁴⁷ for the case of acetyl peroxy radical (CH₃C(O)O₂), would tend to favor peracid (via R(O)O₂ + HO₂ → R(O)OOH) and carboxylic acid formation (via R(O)O₂ + HO₂ → R(O)OH + O₃) routes over generation of another alkoxy radical (leading to the eventual < C₁₂ hydroperoxides of Channel 1a in the dodecane case). Again, on a unit normalized basis, these ion traces collapse onto the unit normalized mechanism prediction for the products of carbonyl hydroperoxide photolysis, p(jCARBROOH), consistent with this identification as peracids accompanying carboxylic acid formation (Figure 4b). While the decomposition products (i.e., acyl radical and aldehyde) in Channel 1a preceding acid formation are not explicitly modeled, the reaction of the acyl radical with O₂ is considered instantaneous, and the lifetime of an acyl peroxy radical with HO₂ is expected to be 3.7 s under low-NO_x conditions. Thus, comparison of the acid traces with p(jCARBROOH) is sufficiently close for comparison to the trend in the gas-phase measurements. While the aldehydes could not be explicitly monitored by the CIMS, the acid traces are confirmation of aldehyde formation in the gas-phase. The aldehyde will be seen to be an important gas-phase intermediate, for its role in PHA formation.

Carbon Balance. Now we discuss the fate of the initial mass of dodecane distributed among the various reaction channels in the mechanism and compare to the gas-phase measurements. More reactions are represented in the mechanism scheme of Figure 1 than are implemented in the photochemical simulation (Table 2). While the distinct product distribution from photolysis of the two isomers of the carbonyl hydroperoxide (CARBROOH) matters for the gas-phase chemistry and SOA formation, the alpha isomer is not

considered in MCM 3.2, although reactions along Channel 2a including the formation and fate of a hydroxy carbonyl hydroperoxide (OHCARBROOH) are included. As is, the photolysis rates of the carbonyl hydroperoxide (CARBROOH) isomers would be treated the same, so $p(j\text{CARBROOH})$ and $p(j\text{CARBROOH} + h\nu)$ are simulated to be the same (Table 2, Reaction 17). This prevents further explicit extension of the photochemical simulation for products along Channel 1a without further approximation of reaction rate coefficients. For carbonyl hydroperoxide (CARBROOH) reaction with OH, MCM 3.2 ends with production of the carbonyl hydroperoxy radical (CARBRO₂ in reactions 13 and 14 of Table 2); CARBRO₂ then goes back to the carbonyl hydroperoxide (CARBROOH) after reaction with HO₂ for these experimental conditions. That is, MCM 3.2 does not suggest further oxidation of CARBROOH to a dicarbonyl or to a threecfunctionalized chain (DICARBROOH), as supported by the CIMS trace monitored at (−) $m/z = 315$ (DICARBROOH). Effectively, this route (Channel 2b) becomes a large carbon sink without further explicit treatment of the products. With the limitation of measurable gas-phase species beyond this point, extension of the photochemical simulation is not attempted, although the further extent of oxidation is of interest, as it will play a role in the volatilities of products and contribution to particle growth.

The simulated fraction of initial carbon over time in the various generations of products is shown in Figure 2h. After sufficient time, the majority of the carbon resides in fourth and later generation products. While fourth and later generation products represent over half of the initial carbon, the major development of this chemistry becomes apparent after the third and earlier generations peak around 2.3×10^7 molecules cm^{-3} h of total OH exposure (~10 h). This would correspond to almost a day of atmospheric aging, assuming an ambient OH concentration of $\sim 10^6$ molecules cm^{-3} . Thus, dodecane and other alkanes that have similarly long OH-reactive lifetimes have the potential for generating multifunctional semivolatile species over the course of a few days.

Although CIMS sensitivities to each individual compound could not be determined (see Experimental Section), we used previously determined sensitivities for compounds with similar functionality as proxies for the sensitivity of species in this mechanism. We used the previously measured sensitivity of methyl hydroperoxide (CH_3OOH)²³ for the C_{12} hydroperoxide monitored at (−) $m/z = 287$, and the previously measured sensitivity of hydroxyacetone ($\text{C}_3\text{H}_6\text{O}_2$)⁴⁸ for the acids and multifunctional compounds. At the end of 18 h, it is estimated that roughly 13 ppb within a factor of 2 of the simulated 31 ppb of dodecane reacted is accounted for by the CIMS negative mode ions measured. All CIMS traces shown in Figure 2 were included, except the carbonyl (CARB, Figure 2c), as it could only be monitored in positive mode, and signal intensities of this mode are not comparable to that of negative mode. Although the carbonyl hydroperoxide (CARBROOH, Figure 2d) and the hydroxy hydroperoxide (OHROOH, Figure 2f) are tracked in positive mode over 36 h, we used the signals at (−) $m/z = 301$ and (−) $m/z = 303$, respectively, from the 18 h January experiment for a rough carbon balance at 18 h. The acid traces shown in Figure 3a and Figure 4a were also included, although there is likely a great deal of carbon still unaccounted for in $< \text{C}_5$ acids. Other remaining carbon not accounted for by the CIMS measurements include vapor-phase wall loss (though it is expected to be small), aldehyde

formation from Channel 1a of the mechanism, and the many later generation products along Channel 2 that are not explicitly monitored by the CIMS.

■ SOA GROWTH

Organic growth as measured by the AMS is shown versus the dodecane decay in Figure 2a. The AMS organic trace is not corrected for particle wall-loss. The onset of growth occurs coincident with the peak of the hydroperoxide, indicating aerosol formation from higher generation oxidation products. The total suspended particle organic peaked at approximately $63 \mu\text{g m}^{-3}$ around hour 20, consistent with the development of fourth-generation gas-phase chemistry. Peak particle diameter grew from 58 nm (seed diameter) to 190 nm at the point of maximum concentration, and then to 200 nm by the end of the experiment as measured by the DMA. Further analyses and consideration of heterogeneous chemistry provide more insight into the dynamics of the aerosol growth.

Vapor Pressure Estimation. To better constrain the expected aerosol chemical makeup, vapor pressures at 298 K were estimated for an array of compounds listed in Table S2 of the Supporting Information section using the EVAPORATION (Estimation of Vapor Pressure of ORganics, Accounting for Temperature, Intramolecular, and Nonadditivity effects) method.⁴⁹ The method predicts the (subcooled) liquid pure compound vapor pressure, p^0 , taking into account intramolecular effects from the positions of functional groups on a compound. For example, the predicted p^0 for the α -carbonyl hydroperoxide is 6.58×10^{-8} atm, more than twice that of the β -carbonyl hydroperoxide, $p^0 = 2.45 \times 10^{-8}$ atm. Conversion of the pure component liquid vapor pressure to a value of C_i^0 in units of $\mu\text{g m}^{-3}$ (also in Table S2, Supporting Information) can be used to classify compounds according to previously defined volatility classes.⁵⁰ These classes in order of increasing volatility include extremely low volatility organic compounds (ELVOCs) with $C_i^* < 3 \times 10^{-4} \mu\text{g m}^{-3}$, low volatility organic compounds (LVOCs) with $3 \times 10^{-4} < C_i^* < 0.3 \mu\text{g m}^{-3}$, semivolatile organic compounds (SVOCs) with $0.3 < C_i^* < 300 \mu\text{g m}^{-3}$, intermediate volatility organic compounds (IVOCs) with $300 < C_i^* < 3 \times 10^6 \mu\text{g m}^{-3}$, and finally volatile organic compounds (VOCs) with $C_i^* > 3 \times 10^6 \mu\text{g m}^{-3}$. These volatility regimes are provided for reference in Figure 5. Note that the calculated values presented here are not the conventionally used C_i^* , since values for the activity coefficients, γ_i , are not estimated and experimental volatility measurements were not made. C_i^* is related to C_i^0 through the activity coefficient, $C_i^* = \gamma_i C_i^0$.⁵⁰

O:C Values. The O:C values for each molecule are included in the Supporting Information section, Table S2. To view the progression of the oxidation, each compound is shown in the O:C versus $\log C_i^0$ space (Figure 5). The marker colors indicate the gas-phase generation of the compound. Black markers are reserved specifically for those compounds that may participate in heterogeneous chemistry. Each compound has a letter assigned label, corresponding to the key used in Table S2. A general upward trend to the left indicates lower volatility and increasing oxygenation over time. Exceptions do occur where there is formation of second generation compounds, like the hydroxy hydroperoxide and the dihydroperoxide, of a higher O:C and lower volatility compared to later generation products. AMS measurements show that within the first 10 h of early growth, the O:C stabilizes at 0.22, after which it steadily increases to 0.30 by the end of the experiment. O:C measurements are estimated to have an uncertainty of 30%,⁵¹

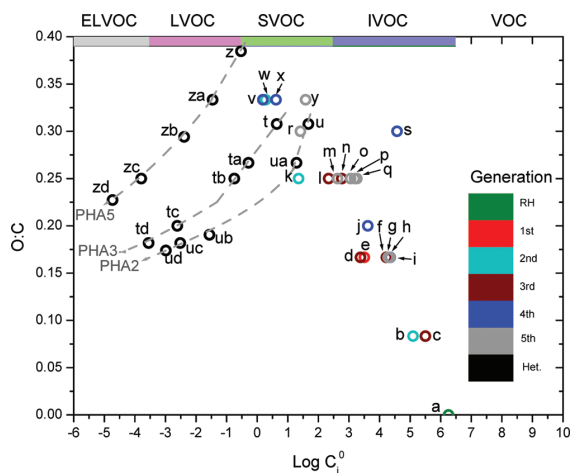


Figure 5. Span of O:C values versus log of the pure subcooled liquid vapor pressures in units of $\mu\text{g m}^{-3}$ (C_i^0) for predicted compounds from dodecane low- NO_x photoxidation. Colored markers indicate the product generation, and black markers indicate compounds thought to participate in heterogeneous chemistry. Letter data labels correspond with the compounds listed in Table S2. Regions of volatility previously defined⁵⁰ are denoted along the top axis for reference. The overall progression is upward to the left; vapor pressure drops from the starting dodecane, “a”, at $\log(C_i^0) = 6.3$ to $\log(C_i^0) = 0.19$ for $\text{C}_{12}\text{H}_{24}\text{O}_4$, “v”, and O:C increases to a max at 0.33. AMS measured O:C of 0.22–0.30 during the experiment. The gray dashed lines indicate the progression of increasing carbon length on the aldehyde that reacts with a hydroperoxy compound to form PHAs. PHA2 represents formation of the carbonyl hydroperoxide (CARBROOH) derived PHA, γ -keto- α -alkyl- α' -hydroxyalkyl peroxide (KAHAP); PHA3 the hydroxy hydroperoxide (OHROOH) derived PHA, δ -hydroxy- α -alkyl- α' -hydroxyalkyl peroxide (HAHAP); and PHA5 the hydroxycarbonyl hydroperoxide derived PHA, ϵ -hydroxy- γ -keto- α -alkyl- α' -hydroxyalkyl peroxide (HKAHAP). Increasing carbon length leads to convergence to a lower O:C and lower vapor pressure approaching the ELVOC region.

and the species shown in Figure 5 fall within the measured O:C range. The fifth-generation compounds in gray markers represent an increase in vapor pressure, owing to the formation of the hydroxy acids (Channel 2ai) and conversion of hydroperoxy groups to carbonyl groups. Only C_{10} acids are shown to condense the space and represent the bulk aerosol character. With estimated volatilities of expected gas-phase products and the measured O:C range, we investigate further the role of the semivolatiles on SOA growth.

Peroxyhemiacetal Formation. Many of the semivolatiles in Figure 5 are hydroperoxide species including (1) the second-generation hydroxy hydroperoxide (OHROOH, Channel 3; Figure 5 “k”), (2) the third-generation carbonyl hydroperoxide (CARBROOH, Channels 1 and 2; Figure 5 “n” and “l”), (3) the fourth-generation hydroxycarbonyl hydroperoxide (OH-CARBROOH, Channel 2a; Figure 5, “v” and “x”), and (4) the fifth-generation dicarbonyl hydroperoxide (DICARBROOH, Channel 2b; Figure 5, “y”). Once these semivolatiles have partitioned into the particle phase, reaction with aldehydes generated from decomposition of the photolyzed α -carbonyl hydroperoxide (Channel 1a) can occur to form PHAs. A general mechanism summarizing some possible reactions for the current system is shown in Figure 6. If the first-generation hydroperoxide (ROOH) reacts with an aldehyde, an α -alkyl- α' -

hydroxyalkyl peroxide (hereafter referred to as AHAP) will be generated. If the β -carbonyl hydroperoxide (CARBROOH) reacts with an aldehyde, a γ -keto- α -alkyl- α' -hydroxyalkyl peroxide is formed (hereafter referred to as KAHAP). Similarly, if a hydroxy hydroperoxide (OHROOH) reacts with an aldehyde, a δ -hydroxy- α -alkyl- α' -hydroxyalkyl peroxide (hereafter referred to as HAHAP) will be formed. If a dicarbonyl hydroperoxide (DICARBROOH) reacts with an aldehyde, a ϵ - γ -diketo- α -alkyl- α' -hydroxyalkyl peroxide is formed (hereafter referred to as DKAHAP). Finally, if a hydroxycarbonyl hydroperoxide (OHCARBROOH) reacts with an aldehyde, a ϵ -hydroxy- γ -keto- α -alkyl- α' -hydroxyalkyl peroxide is formed (hereafter referred to as HKAHAP). There is also the possibility of cyclization of the KAHAP, DKAHAP, or HKAHAP because of the carbonyl groups, similar to the mechanisms proposed in previous studies,^{52–54} although being isomers the cyclic and noncyclic forms would be hard to distinguish. Of course, alternative functional group placement on the compounds presented in Figure 6 is expected, and the compounds shown are examples.

PHA volatility will depend on the length of the aldehyde that originally reacted with the particle-phase incorporated hydroperoxide. Progression of the O:C and volatility of three select PHAs with increasing length of the aldehyde is marked by the series of “t” through “td” markers for HAHAP, “u” through “ud” for KAHAP, and “z” through “zd” for HKAHAP in Figure 5. The gray dotted lines are intended to guide the eye along these progressions toward lower O:C and lower vapor pressure, labeled “PHA2” for the KAHAP, “PHA3” for the HAHAP, and “PHAS” for the HKAHAP for visual clarity. PHA formation effectively converts semivolatiles into lower volatility products that approach the ELVOC region.

Evidence of PHA Formation Comparing Gas-Phase and Particle-Phase Mass Spectra. PHA formation is complex, as it involves reaction of a fourth-generation aldehyde (of varying carbon length) with second- to fifth-generation but lower vapor pressure hydroperoxy compounds at/in the particle. Figure 7 shows that aerosol growth follows after gas-phase formation of the carbonyl hydroperoxide (CARBROOH, Channels 1 and 2), but more importantly it is delayed until photolysis of the carbonyl hydroperoxide, p(jCARBROOH). The aldehydes could not be measured directly with CIMS because of their nonpolar nature, but the simulated p(jCARBROOH) can be used as a proxy for their expected formation according to Channel 1a in the mechanism. The aldehydes would precede acid formation, which is very quick after photolysis of the carbonyl hydroperoxide, when comparing the $\text{C}_6\text{CARBACID}$ trace with the p(jCARBROOH) trace in Figure 7. From the trends presented in Figure 7, it appears that aerosol growth is timed with aldehyde formation, making PHA formation a potential mechanism for aerosol growth. This is further supported in species-specific comparisons of the CIMS and AMS.

Comparisons of the gas-phase mechanism predictions and CIMS traces were made with selected ion fragments from the HR-ToF-AMS mass spectra. The AMS utilizes vaporization and electron impact (EI) ionization resulting in fragmentation of aerosol species, but the prevalence of high m/z ($m/z > 100$) in the spectra suggests that some stable high MW ions retain more of the original backbone and functionality of the initial product molecule. The selected ions discussed are those that would result from a PHA severed at either C–O bond of the peroxide $\text{RC}_1\text{--OO--C}_2\text{R}$. Scission at $\text{C}_1\text{--O}$ results in the ion RC_1^+ .

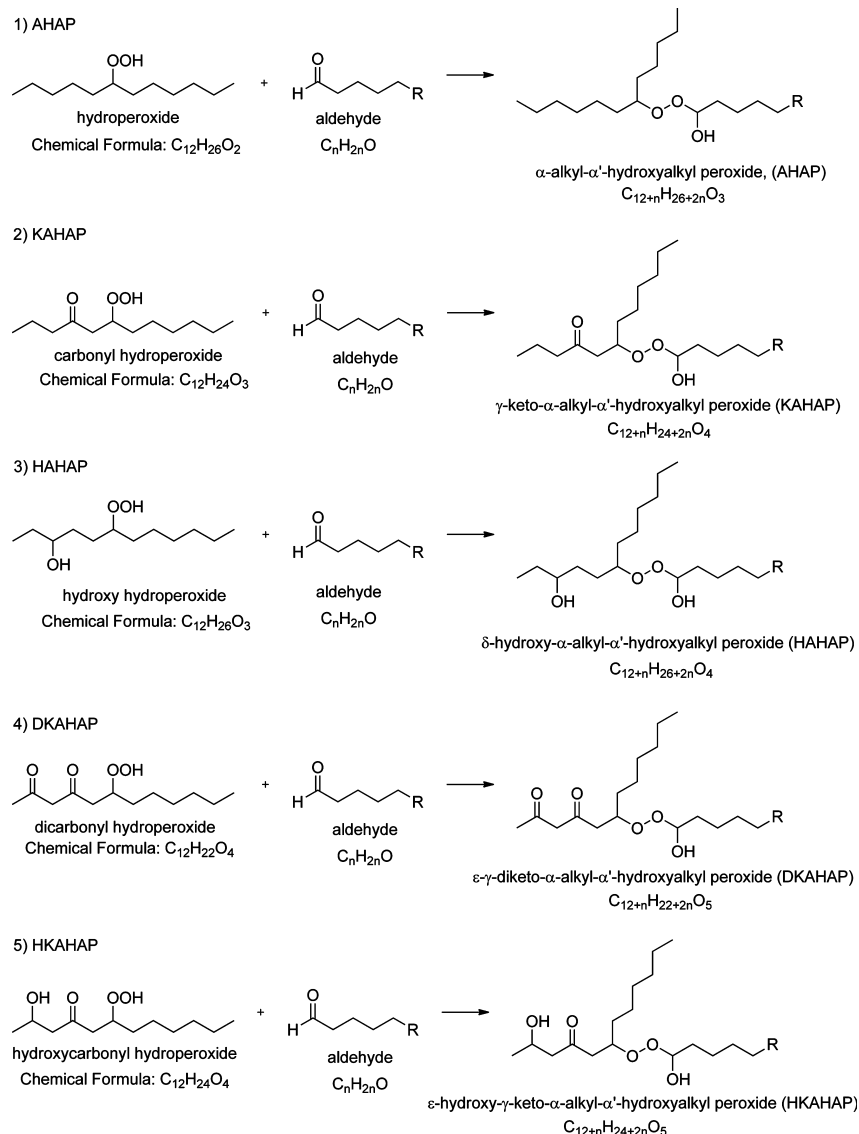


Figure 6. Scheme for forming five types of PHAs from reaction of an aldehyde of carbon length n , with various hydroperoxy compounds. (1) Reaction with a hydroperoxide generates an AHAP. (2) Reaction with a β -carbonyl hydroperoxide forms a KAHAP. (3) Reaction with a hydroxy hydroperoxide generates a HAHAP. (4) Reaction with a dicarbonyl hydroperoxide forms a DKAHAP. (5) Reaction with a hydroxycarbonyl hydroperoxide forms a HKAHAP.

Scission at $\text{C}_2\text{-O}$ results in the ion RC_1OO^+ , 32 amu greater than the RC_1^+ ion. The RC_1^+ ion was observed in previous studies of α -substituted hydroperoxide-derived PHAs,^{52,55} although not the RC_1OO^+ , which we propose for the PHAs in this study. The hydroperoxides we discuss in this study are not α -substituted, which may be cause for the different fragmentation pattern. Note that the RC_1^+ ion would be the equivalent ion generated from a hydroperoxide compound, $\text{RC}_1\text{-OOH}$, by loss of the hydroperoxy group to generate the $m/z = [\text{M}-33]^+$ ion, where M = mass of the hydroperoxide, also previously observed.^{52,55} This fragmentation pathway was observed in identifying the C_{18} hydroperoxide during the standard experiment described previously in the Experimental

section. Examination of $[\text{M}-33]^+$ ions and their exact masses from this fragmentation pathway alone suggests incorporation of the gas-phase carbonyl hydroperoxide (CARBROOH), hydroxy hydroperoxide (OHROOH), and other multifunctional long chains (OHCARBROOH, DICARBROOH) into the aerosol phase. However, the predominance of their respective RC_1^+ ions trending closely with their respective RC_1OO^+ ions strongly supports that these compounds are incorporated into the aerosol phase via PHA formation. The following discussion focuses on the pairing of $m/z < 200$ ions and their $m/z > 200$ (+ 32 amu) counterparts. For simplicity, we refer to the nominal mass of an ion rather than its exact

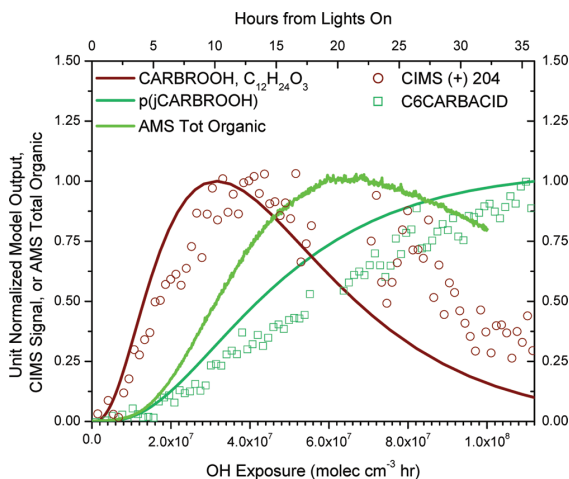


Figure 7. Aerosol growth occurs between formation of the carbonyl hydroperoxide (CARBROOH) and the onset of acid formation (observations in teal squares and simulated result, $p(j)$ CARBROOH, in teal) in the gas-phase. It is likely that initial aerosol growth can be supported by PHA formation since hydroperoxide containing species in the gas phase form within 5 h of lights on, and aldehyde formation will precede acid formation after photolysis of the carbonyl hydroperoxide.

mass, but the exact mass was used to obtain the chemical formula of the ion.

The AMS ions at $m/z = 183$ ($C_{12}H_{23}O^+$) and $m/z = 215$ ($C_{12}H_{23}O_3^+$) dominate the early SOA growth, suggesting that they may be characteristic fragments of the carbonyl hydroperoxide (CARBROOH)-derived PHA (KAHAP in Figure 6). Comparison of the simulated and measured gas-phase carbonyl hydroperoxide and AMS ions $m/z = 183$ and $m/z = 215$ is shown in Figure 8a along with the simulated gas-phase trend for photolysis of the carbonyl hydroperoxide, $p(j)$ CARBROOH in Channel 1a. The growth of these ions in the aerosol phase is delayed from the onset of the carbonyl hydroperoxide formation in the gas phase until aldehyde formation begins, as proxied by the simulated $p(j)$ CARBROOH trace in teal representing Channel 1a of the mechanism in Figure 1. As further reactions of the carbonyl hydroperoxide dominate, the gas-phase trace peaks and decays, followed as well by a decrease in these characteristic ions in the AMS mass spectrum. An analysis of the dynamics of the particle-phase AMS spectra will be addressed in a subsequent study.

AMS ions consistent with hydroxy hydroperoxide (OH-ROOH)-derived PHAs (HAHAP in Figure 6) at $m/z = 185$ ($C_{12}H_{25}O^+$) and $m/z = 217$ ($C_{12}H_{25}O_3^+$) grow in similarly with $m/z = 183$ and $m/z = 215$, although they peak later with their corresponding gas-phase trace (See Figure 8a and Figure 8b). Again, the appearance of these hydroxy hydroperoxide-derived PHA ions are contingent upon aldehyde formation as represented by the simulated $p(j)$ CARBROOH trace in Figure 8b. If gas-to-particle partitioning was partially responsible for the simulated versus measured discrepancy for hydroxy hydroperoxide (OH-ROOH) Figure 2f, we would expect to see the $m/z = 185$ ion grow into the aerosol-phase before $m/z = 217$ and before aldehyde formation. That is, $m/z = 185$ growing in earlier to the aerosol-phase would indicate uptake of the hydroxy hydroperoxide (OH-ROOH) itself without

conversion to PHA. With little SOA at this time and no aldehyde formation, partitioning of the hydroxy hydroperoxide early on is unlikely to account for this model-measurement discrepancy. It is possible that the hydroxy hydroperoxide lingers in the gas phase before aldehyde formation and undergoes vapor-phase wall loss as discussed previously.

The incorporation of the dicarbonyl hydroperoxide (DICARBROOH, $C_{12}H_{22}O_4$) into the particle phase is tracked with the AMS ion fragment at $m/z = 197$ ($C_{12}H_{21}O_5^+$) paired with $m/z = 229$ ($C_{12}H_{21}O_4^+$) in Figure 8c but after aldehyde formation. Note that, on a unit normalized scale, the $p(j)$ CARBROOH overlaps the $p(CARBROOH + OH)$ trend. This implies that dicarbonyl hydroperoxide (DICARBROOH) formation is practically simultaneous with aldehyde formation, although not necessarily in the same amount. The other threecfunctionalized chain, a hydroxycarbonyl hydroperoxide (OH-CARBROOH, $C_{12}H_{24}O_4$) is tracked with AMS ion fragments $m/z = 199$ ($C_{12}H_{23}O_2^+$) and $m/z = 231$ ($C_{12}H_{23}O_4^+$). The ion trace at $m/z = 199$ is within the variation of the noisy CIMS marker at $(-) m/z = 317$ (Figure 8d).

Thus far, we observe that in the progression of increasing oxygenation (decreasing volatility) of the starting hydroperoxide there is less time between the gas-phase formation of a species and its incorporation into the particle phase. For example, there are a few hours between carbonyl hydroperoxide (CARBROOH) formation in the gas-phase measured by the CIMS at $(+)$ $m/z = 204$ and the growth of the derived PHA AMS ions at m/z 's 183 and 215 (Figure 8a). This is partially due to the delay in aldehyde formation. Still, once aldehyde is present, this time is significantly reduced for the delay between the hydroxy hydroperoxide (OH-ROOH) growth in the gas-phase measurement and its derived PHA ions (Figure 8b). While this also holds for the dicarbonyl hydroperoxide (DICARBROOH) in Figure 8c and the hydroxycarbonyl hydroperoxide (OH-CARBROOH) in Figure 8d, there is a delay in the appearance of the AMS ions expected from their derived PHAs. That is, even though aldehyde is present and the threecfunctionalized compounds have been produced in the gas-phase, their incorporation as PHAs to the aerosol-phase is not timed with aldehyde formation as is the case for CARBROOH- and OH-ROOH-derived PHAs. This lag may be due to limiting reactant effects. That is, although the unit normalized simulations in Figure 8c suggest that DICARBROOH and aldehyde formation are practically simultaneous, it may be that the aldehyde produced is in lower quantity than the stoichiometric amount needed for reaction compared to the total semivolatile hydroperoxides available. Another possibility may be decreased reactivity of the dicarbonyl hydroperoxide (DICARBROOH) with another aldehyde since it already contains two carbonyl groups that may compete for or deactivate reaction with the hydroperoxy group, depending on their placement. Cyclization of carbonyl containing α -substituted hydroperoxides via intramolecular reaction of the carbonyl with the hydroperoxy group has been observed, setting up potential competition between cyclization and PHA formation.⁵² Further study would be required to test for deactivation effects. Steric effects due to intramolecular hydrogen bonding⁵⁶ may also play a role for compounds like the hydroxy carbonyl hydroperoxide (OH-CARBROOH). A previous study on the kinetics of α -hydroxy peroxides ($RCH(OH)OOR$) in solution noted that tetratin hydroperoxide is more reactive to acetaldehyde over cumene

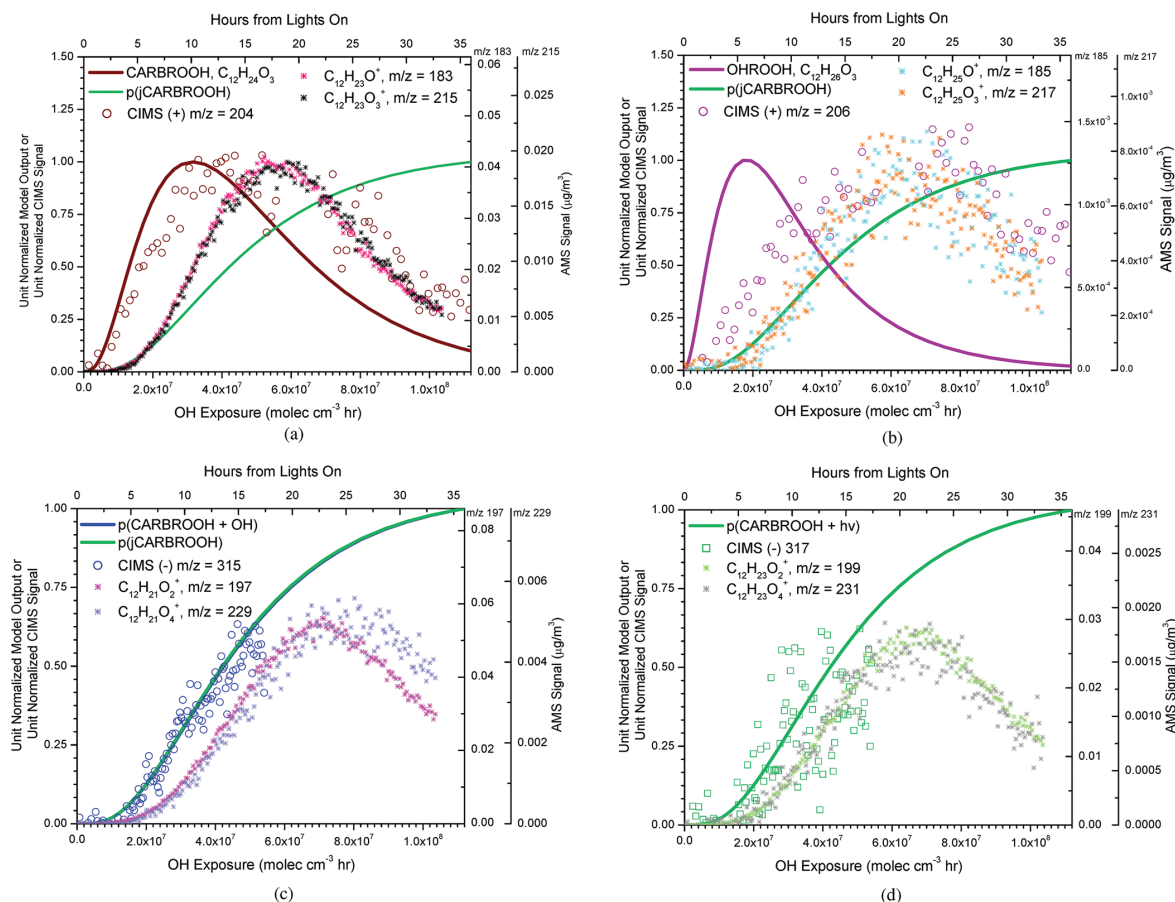


Figure 8. (a) AMS high-resolution fragments at $m/z = 183$ and $m/z = 215$ are possible characteristic fragments of the carbonyl hydroperoxide (CARBROOH)-derived PHA. (b) AMS high-resolution fragments at $m/z = 185$ and $m/z = 217$ are possible characteristic fragments of the hydroxy hydroperoxide (OHROOH)-derived PHA. (c) AMS high-resolution fragments at $m/z = 197$ and $m/z = 229$ are possible characteristic fragments of a multifunctional compound, dicarbonyl hydroperoxide (DICARBROOH)-derived PHA. (d) AMS high-resolution fragments at $m/z = 199$ and $m/z = 231$ are possible characteristic fragments of a multifunctional compound, hydroxycarbonyl hydroperoxide (OHCARBROOH) and its derived PHA.

hydroperoxide and other hydroperoxides because the peroxy group is surrounded by α -hydrogens.⁵⁶

We note that the $m/z = 183$ and $m/z = 185$ (Figure 8a,b) ion fragments may be derived from other molecules containing similar functionalities to the carbonyl hydroperoxide (CARBROOH) and hydroxy hydroperoxide (OHROOH). For example, the fourth-generation hydroxycarbonyl hydroperoxide multifunctional (OHCARBROOH, Channel 2a) shares two of its functional groups with the carbonyl hydroperoxide (CARBROOH) and two with the hydroxy hydroperoxide (OHROOH), suggesting that there may be contributions to these ion signals from later incorporation of this multifunctional compound into the particle. This is similar to the case of the dicarbonyl hydroperoxide (DICARBROOH, Channel 2b) sharing two functionalities with the carbonyl hydroperoxide (CARBROOH), so it may contribute to the signal at $m/z = 183$. However, because the $m/z = 183$ and $m/z = 185$ ions are distinct and dominant components of the initial organic growth, and since their trends do not deviate from their respective $+32$ amu ion partners ($m/z = 215$, $m/z = 217$) with later incorporation of the suggested ions for the multifunc-

tions (m/z 's 197, 199, 229, and 231), they are still likely representative ion fragments from the carbonyl hydroperoxide-derived PHA (KAHAP) and the hydroxy hydroperoxide-derived PHA (HAHAP).

Particle-Phase Peroxyhemiacetal Formation. The surface matrix of an aerosol particle probably enhances PHA generation by lowering energetic barriers or chemically catalyzing the reaction at the surface,⁵⁵ similar to dihydrofuran (DHF) formation.³⁸ Still, a lower energy barrier was not sufficient to see evidence of AHAP formed from the second-generation hydroperoxide (ROOH) in the AMS spectra. Its higher vapor pressure, further reaction with OH or photolysis, as well as the delay to aldehyde formation are all likely reasons why the fate of the ROOH is purely gas-phase oxidation. The nature of the particle interface and bulk are difficult to establish when considering such heterogeneous processes in the current study, but some insights into the chemistry behind PHA formation come from the study by Antonovskii and Terent'ev.⁵⁶ First, they find that aldehydes are more likely than ketones to participate in α -hydroxy peroxide formation because they exhibit greater polarity and polarizability in their

$\text{C}=\text{O}$ containing π bond. Hence, PHA formation from the second-generation carbonyl is not considered for this discussion. Second, they observed that the forward reaction to α -hydroxy peroxide dominated over backward dissociation when run in polar solvents (chloroform, diisopropyl ether, or hexanol). Considering earlier discussion on the characteristic of the aerosol chemistry, PHA formation may be hindered if the aerosol matrix is not sufficiently polar, as there is a large mass fraction of organic described by CH family ions. Lastly, Antonovskii and Terent'ev observed stable α -hydroxy peroxides at 20 and 40 °C, but they note that α -hydroxy peroxides are less thermally stable than the hydroperoxide. This could mean the peroxides do not survive well through the thermal vaporization (600 °C) and ionization process in the techniques here. This may possibly explain the small mass concentrations for the characteristic PHA ions relative to the total organic mass. Still, in this study we keep in mind that the aldehyde formation relies on photolysis of a well-positioned α -carbonyl hydroperoxide. So, concentration, timing, and chemistry of the aerosol all have to be in harmony to facilitate PHA formation.

Cyclic Hemiacetal Formation. The 1,4-hydroxycarbonyl (OHCARB) has been theorized³⁸ and found experimentally to heterogeneously react, isomerizing to a cyclic hemiacetal (CHA) in the particle^{9,11} or on chamber walls in an acid-catalyzed process.¹⁵ These heterogeneous reactions have been found to happen within a time frame of approximately 1 h.^{9,11,15} Conversion of the CHA to a DHF is sensitive to water vapor;⁵⁷ under low relative humidity environments, it will dehydrate to form a higher vapor pressure DHF compound that can partition back to the gas-phase and undergo further reaction with OH or O_3 . A summary of these reactions is shown in Channel 3, Figure 1. Higher relative humidity conditions will slow the dehydration process, and OH reaction with the 1,4-hydroxycarbonyl (OHCARB) will more likely be its fate.⁵⁸ Under the current experimental conditions, DHF reaction with O_3 is expected to dominate after 2.5 h of irradiation when O_3 produced over time surpasses 5 ppb, the limit at which reaction with O_3 is competitive with reaction of the available OH radical ($\sim 2 \times 10^6$ molecules cm^{-3}). This is based on reaction rate coefficients available in the literature on 4,5-dihydro-2-methylfuran, using $k_{\text{DHF}-\text{OH}} = 2.18 \times 10^{-10}$ molecules $\text{cm}^{-3} \text{s}^{-1}$ and $k_{\text{DHF}-\text{O}_3} = 3.49 \times 10^{-15}$ molecules $\text{cm}^{-3} \text{s}^{-1}$.⁵⁹ This provides an interesting problem to consider when thinking of the true lifecycle of the starting alkane and its ultimate generation of a higher vapor pressure unsaturated compound susceptible to oxidation and relevant for further SOA formation. Kinetic study of this heterogeneous conversion under OH radical initiated photoxidation of C_{11} – C_{17} alkanes in the presence of NO_x suggests that the conversion to the CHA is fast in dry air, while the dehydration of the CHA to the DHF occurs on the order of ~ 15 min.¹²

CHA formation may be possible via the photolysis of the hydroperoxide (ROOH) in Channel 3 or through a fifth-generation multifunctional compound analogously cyclizing (Channel 2aii), though the resulting CHA has an extra carbonyl group as seen in Figure 1. Sufficient evidence does not exist to confirm CHA formation for this study despite low relative humidity experimental conditions. If the CHA is formed as $\text{C}_{12}\text{H}_{24}\text{O}_2$, an AMS fragment at $m/z = 183$ ($\text{C}_{12}\text{H}_{23}\text{O}^+$) generated from loss of the $-\text{OH}$ group⁹ is possible. However, this fragment is more appropriately assigned as a characteristic ion of the carbonyl hydroperoxide (CARBROOH)-derived

PHA instead as discussed earlier. In experiments carried out in the presence of NO_x , which are not reported here, the $m/z = 183$ ion is observed distinctly and does not pair with $m/z = 215$, making the current assignment consistent with the expected gas-phase mechanism under low- NO_x conditions. Since a distinct time trend indicating formation of the CHA in the particle-phase is not yet fully distinguished from the nominal mass at $m/z = 183$, the kinetics under the current experimental conditions cannot be modeled. On another note, the nature of the particle acidity is different than that of previous studies, as it is thought that adsorbed HNO_3 on the particle surface catalyzed the heterogeneous conversion to the DHF.^{11,12} Under these low- NO_x conditions, HNO_3 formation is not considered. While the particle character shows enhancement of acidity as tracked by the AMS ion CO_2^+ at $m/z = 44$, there is still a large mass fraction described by the CH family ions, consistent with the many reduced fragments that could be derived from these long chain products. Considering that the simulated production of the 1,4-hydroxycarbonyl is only around 0.6 ppb in the gas-phase (without sinks) and the unclear nature of the particle acidity, if the cyclization and dehydration to the DHF does occur, the amount that formed was probably small, indiscernible in the AMS signal.

Heterogeneous Chemistry versus Gas-Phase Oxidation. We have currently considered two routes to formation of SOA through heterogeneous reactions. We see evidence of PHA formation derived from many semivolatile hydroperoxide species formed in all reaction channels, but we cannot confirm formation of the CHA from the 1,4-hydroxycarbonyl (OHCARB) at this time. Furthermore, the contributions to the SOA mass from pure gas-particle partitioning and heterogeneous chemistry of the hydroperoxide compounds to the SOA mass are unclear. To explore this, we roughly estimate the mass contributions of organic from five select semivolatiles that have been highlighted in a previous discussion: (1) carbonyl hydroperoxide (CARBROOH), (2) hydroxy hydroperoxide (OHROOH), (3) hydroxycarbonyl hydroperoxide (OHCARBROOH), (4) dicarbonyl hydroperoxide (DICARBROOH) and (5) 1,4-hydroxycarbonyl (OHCARB). Using the roughly estimated gas-phase concentrations of these species as monitored by the CIMS, the subcooled pure component liquid vapor pressure estimates (C_i^0), and the organic mass concentration from the AMS (as shown in Figure 2a), we assume that gas-particle equilibrium is established quickly so that the instantaneous contribution of each compound in the particle-phase is calculated by eq 1:

$$C_{\text{pi}} = \frac{C_{\text{org}} C_{\text{gi}}}{\gamma_i C_i^0} \quad (1)$$

where C_{pi} is the mass concentration of species i in the particle phase [$\mu\text{g m}^{-3}$], C_{org} is the mass concentration of organic aerosol in [$\mu\text{g m}^{-3}$], C_{gi} is the mass concentration of species i in the gas phase [$\mu\text{g m}^{-3}$], γ_i is the activity coefficient of species i in the bulk aerosol solution (assumed as 1 here), and C_i^0 is the subcooled pure component liquid vapor pressure of species i [$\mu\text{g m}^{-3}$].

The result of this analysis is presented in Figure 9. Note that we estimate the organic mass only up to 18 h because we utilized species monitored at $m/z \geq 300$, available only from the January experiment. We see that just under $10 \mu\text{g m}^{-3}$ of organic is expected each from the dicarbonyl hydroperoxide (DICARBROOOH), carbonyl hydroperoxide (CARBROOH),

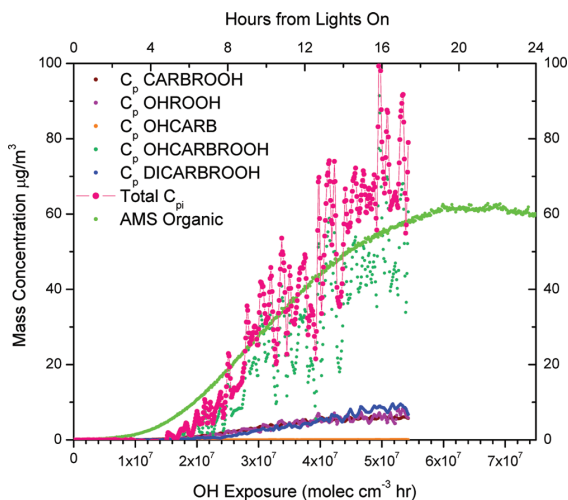


Figure 9. Rough estimate of total organic mass attributed to gas-to-particle phase partitioning from select semivolatiles (pink circles with line) as compared to the AMS organic trace (bright green). Individual contributions from each species are shown: (1) carbonyl hydroperoxide (CARBROOH, wine-colored circles), (2) hydroxy hydroperoxide (OHROOH, purple circles), (3) 1,4-hydroxycarbonyl (OHCARB, orange circles), (4) hydroxycarbonyl hydroperoxide (OHCARBROOH, teal circles), and (5) dicarbonyl hydroperoxide (DICARBROOH, blue circles).

and the hydroxy hydroperoxide (OHROOH). The 1,4-hydroxycarbonyl (OHCARB) makes negligible mass, and this is consistent with the small amount expected to form from the gas-phase chemistry and the absence of an AMS ion for the CHA. The hydroxycarbonyl hydroperoxide (OHCARBROOH) is expected to make up the majority of the organic mass ($\sim 60 \mu\text{g m}^{-3}$). The total contributions of these species to organic mass is $C_{\text{tot}} = \sum_i C_{\text{pi}}$. Thus, partitioning from just four semivolatile hydroperoxides could explain the majority of the organic growth observed after 5 h of irradiation. However, a small amount of organic was formed previously and is not fully described by equilibrium partitioning of these semivolatiles.

The uncertainty in the estimated gas-phase concentrations could resolve the appearance of organic growth prior to significant contributions from partitioning, but based on the well-paired $m/z < 200$ and $m/z > 200$ ions that differ by 32 amu, it is overwhelmingly likely that the fragments come from the same compound (their respective PHA). These ions also begin to appear prior to 5 h with aldehyde formation in the case of the carbonyl hydroperoxide (CARBROOH) and the hydroxy hydroperoxide (OHROOH) (see Figure 8a,b). So the early gap between the measurement and estimated organic mass may be due to PHA formation initiating aerosol growth. In light of the AMS measurements of characteristic PHA ions and the estimated mass from partitioning of the same hydroperoxide semivolatiles, it is difficult to tell whether these semivolatiles would be completely in the particle-phase as PHAs or in molecular form. In addition, later more functionalized compounds may partition in without conversion to PHA formation right away, as in the lag between gas-phase aldehyde formation and PHA ion appearance observed for the hydroxycarbonyl hydroperoxide (OHCARBROOH) and for that of the dicarbonyl hydroperoxide (DICARBROOH). However, since aldehyde formation is fairly coincident with

most of the higher generation multifunctionals (OHCARBROOH, DICARBROOH) in the gas-phase, PHA formation as a mechanism for their incorporation into the particle phase cannot be ruled out. Full treatment of the kinetics of the heterogeneous chemistry require mass closure on the contribution of PHA mass to the organic present. While the AMS ions presented support PHA formation, their mass concentration signals do not account for the total mass of the derived PHA in the particle phase. Recall that the ions discussed do not include the side of the molecule that contains varying carbon lengths from the aldehyde that reacted with the hydroperoxide species. This provides a multitude of possible PHA structures. Second, being such a large molecule, PHA mass would certainly be distributed in the AMS spectrum among many possible fragmentation pathways. To truly understand these aspects, synthesis of these compounds would be required as an AMS standard to understand the full spectrum distribution.

ATMOSPHERIC IMPLICATIONS

Presented here is the first experimental study of SOA formation from the long-chain alkanes under low- NO_x conditions, such that $\text{RO}_2 + \text{HO}_2$ chemistry dominates the fate of the RO_2 radical. This regime of chemistry is typical of a region relatively isolated from NO_x sources and where trace VOC concentrations are too low to sustain RO_2 self-reaction. It is a challenge to simulate this chemistry in most laboratory chambers under atmospherically pristine conditions at which NO_x levels are typically tens to low hundreds of pptv. The gas-phase measurements of this study are consistent with chemistry expected for NO_x levels toward this range. Further, a regime of “slow” chemistry that lengthens the RO_2 lifetime sufficiently to allow for alkyl peroxy radical rearrangement through a 1,6-H shift is relevant to pristine conditions (ppt levels of NO_x , HO_2 , and low $[\text{OH}] \sim 1.2 \times 10^5 \text{ molecules cm}^{-3}$).⁴⁶ Achieving such conditions further challenges the design of environmental chamber studies. Although many challenges remain in simulating and spanning the range of “atmospherically relevant” conditions using environmental chambers, fundamental studies such as that described here address the fundamental chemistry in a regime relevant for closing the gap in the VOC and SOA budgets.

A myriad of compounds is formed in long-chain alkane photooxidation via functionalization and fragmentation pathways in the gas phase. For dodecane, 19 gas-phase species were monitored by the CIMS, and many compared well to a simulation with an abbreviated chemical mechanism based on the MCM 3.2. The gas-phase mechanism generally captures the observations only using four generations of explicit chemistry. Further work on empirical quantification and branching ratios of the gas-phase routes in the mechanism is needed, but was hindered for this study due to the lack of available standards and difficulties associated with experimental handling. Nonetheless, this study fundamentally captures the chemical framework representative of low initial organic loading of a longer-lived species (in terms of reaction with OH) while in the relative absence of NO_x that can be extended to alkanes of different lengths and structures. Current work is ongoing to understand the chemistry of SOA formation from other C_{12} alkanes of branched and cyclic conformations.

Mechanisms of particle formation emerge from comparison of the gas-phase mechanism and known heterogeneous chemistry. While there is evidence supporting the formation

of PHAs, confirmation of the heterogeneous conversion of the 1,4-hydroxycarbonyl to the CHA is lacking, but the amount that formed was probably small. A powerful approach to confirming direct partitioning of specific gas-phase compounds is through comparison of CIMS gas-phase time trends and corresponding characteristic ion fragments from the AMS. The paired (32 amu difference) high $m/z > 100$ AMS fragments identified were instrumental in deriving more molecular structure information in support of PHA formation. Comparisons of time trends provide insight into the chemistry of the partitioning, as seen, for example, with the decreasing delay between appearance of characteristic AMS ions and gas-phase product growth with increasing oxidation of the parent molecule. A rough estimate shows that much of the organic growth can be described by theoretical partitioning estimates of select semivolatile hydroperoxides. Still, better mass closure on the semivolatiles in the system in the gas and particle-phases could provide greater insight into the kinetic and equilibrium effects on SOA formation from dodecane.

The degree of generational development in the gas-phase photooxidation of this long-chain alkane over the extended chamber experiments is quite remarkable. While the majority of the gas-phase product distribution (almost two-thirds of the carbon) is developed within the first 20 h of photooxidation, SOA formation clearly involves the further oxidation of the third-generation carbonyl hydroperoxide, which peaks about 8 h earlier. This chemical development occurs much later than typical experimental time scales for chamber experiments, which highlights the need for simulating extended oxidation to truly capture the SOA formation process.

While the chemical composition of the gas and aerosol phases was well resolved with the techniques used in this study, challenges still exist in understanding the nature of the particle phase, as this can have profound effects on the further chemical aging of the particles.⁶⁰ This aging could be manifested in the formation of alkane-derived PHAs. In regards to time scale, the current work focuses on oxidative processes in the gas phase affecting the chemical development of the particle phase, although the possibility of photolysis or reactions with OH of the aerosol products may become more important under extended photooxidation time scales. A better understanding of these and other factors that potentially affect SOA chemical evolution might address issues such as the observed "glassy" nature of some SOA.^{61,62} Extrapolating the present study to the atmosphere suggests that (1) hydroperoxide and PHA species are likely to be in the particle phase for alkane-derived aerosol under low- NO_x conditions, and (2) with the possibility of viscous phases that affect further chemical aging in the aerosol phase, the lifetimes of these products could be extended, lending themselves to long-range transport and a more complicated assessment of the SOA life cycle.

ASSOCIATED CONTENT

Supporting Information

The Supporting Information includes (1) A table with calculated lifetimes of RO_2 with RO_2 , HO_2 , NO , and NO_2 under varying NO_x conditions, (2) table of O:C and volatility, (3) figures on AMS and CIMS measurements across all experiments, (4) alternative positive mode ions for CIMS negative mode ions, and (5) simulations of varying NO concentration. This information is available free of charge via the Internet at <http://pubs.acs.org>.

AUTHOR INFORMATION

Corresponding Author

*E-mail: seinfeld@caltech.edu.

Notes

The authors declare no competing financial interest.

ACKNOWLEDGMENTS

This work was supported by the Office of Science (Biological and Environmental Research), U.S. Department of Energy Grant (DE-SC 0006626), and National Science Foundation Grants AGS-1057183 and ATM-0650061. We acknowledge John D. Crounse and Jason M. St. Clair for helpful discussions on CIMS data analysis, Reddy L. N. Yatavelli and ManNin Chan for useful discussions, and Andreas Zuend, Xuan Zhang, and Steve Compernolle for assistance with the vapor-pressure estimations. L.D.Y., J.S.C., and C.L.L. were supported by National Science Foundation Graduate Research Fellowships.

REFERENCES

- (1) Ravishankara, A. R. *Chem. Rev.* **2003**, *103*, 4505–4508.
- (2) Jimenez, J. L.; Canagaratna, M. R.; Donahue, N. M.; Prevot, A. S. H.; Zhang, Q.; Kroll, J. H.; DeCarlo, P. F.; Allan, J. D.; Coe, H.; Ng, N. L.; et al. *Science* **2009**, *326*, 1525–1529.
- (3) Kroll, J. H.; Donahue, N. M.; Jimenez, J. L.; Kessler, S. H.; Canagaratna, M. R.; Wilson, K. R.; Altieri, K. E.; Mazzoleni, L. R.; Wozniak, A. S.; Bluhm, H.; et al. *Nat. Chem.* **2011**, *3*, 133–139.
- (4) Robinson, A. L.; Donahue, N. M.; Shrivastava, M. K.; Weitkamp, E. A.; Sage, A. M.; Grieshop, A. P.; Lane, T. E.; Pierce, J. R.; Pandis, S. N. *Science* **2007**, *315*, 1259–1262.
- (5) Schauer, J. J.; Kleeman, M. J.; Cass, G. R.; Simoneit, B. R. T. *Environ. Sci. Technol.* **1999**, *33*, 1578–1587.
- (6) Schauer, J. J.; Kleeman, M. J.; Cass, G. R.; Simoneit, B. R. T. *Environ. Sci. Technol.* **2002**, *36*, 1169–1180.
- (7) Presto, A. A.; Miracolo, M. A.; Kroll, J. H.; Worsnop, D. R.; Robinson, A. L.; Donahue, N. M. *Environ. Sci. Technol.* **2009**, *43*, 4744–4749.
- (8) Presto, A. A.; Miracolo, M. A.; Donahue, N. M.; Robinson, A. L. *Environ. Sci. Technol.* **2010**, *44*, 2029–2034.
- (9) Lim, Y. B.; Ziemann, P. J. *Environ. Sci. Technol.* **2005**, *39*, 9229–9236.
- (10) Lim, Y. B.; Ziemann, P. J. *Environ. Sci. Technol.* **2009**, *43*, 2328–2334.
- (11) Lim, Y. B.; Ziemann, P. J. *Aerosol Sci. Technol.* **2009**, *43*, 604–619.
- (12) Lim, Y. B.; Ziemann, P. J. *Phys. Chem. Chem. Phys.* **2009**, *11*, 8029–8039.
- (13) Talukdar, R. K.; Mellouki, A.; Gierczak, T.; Barone, S. *Int. J. Chem. Kinet.* **1994**, *26*, 973–990.
- (14) Atkinson, R. *J. Phys. Chem. Ref. Data* **1997**, *26*, 215–290.
- (15) Atkinson, R.; Arey, J.; Aschmann, S. M. *Atmos. Environ.* **2008**, *42*, 5859–5871.
- (16) Tyndall, G. S.; Cox, R. A.; Granier, C.; Lesclaux, R.; Moortgat, G. K.; Pilling, M. J.; Ravishankara, A. R.; Wallington, T. J. *J. Geophys. Res.* **2001**, *106*, 12157–12182.
- (17) Kroll, J. H.; Seinfeld, J. H. *Atmos. Environ.* **2008**, *42*, 3593.
- (18) Lelieveld, J.; Butler, T. M.; Crowley, J. N.; Dillon, T. J.; Fischer, H.; Ganzeveld, L.; Harder, H.; Lawrence, M. G.; Martinez, M.; Taraborrelli, D.; et al. *Nature* **2008**, *452*, 737–740.
- (19) Ren, X.; Olson, J. R.; Crawford, J. H.; Brune, W. H.; Mao, J.; Long, R. B.; Chen, Z.; Chen, G.; Avery, M. A.; Sachse, G. W.; et al. *J. Geophys. Res.* **2008**, *113*, D05310.
- (20) Wolfe, G. M.; Thornton, J. A.; Bouvier-Brown, N. C.; Goldstein, A. H.; Park, J.-H.; McKay, M.; Matross, D. M.; Mao, J.; Brune, W. H.; LaFranchi, B. W.; et al. *Atmos. Chem. Phys.* **2011**, *11*, 1269–1294.
- (21) Cocker, D. R.; Flagan, R. C.; Seinfeld, J. H. *Environ. Sci. Technol.* **2001**, *35*, 2594–2601.

(22) Keywood, M. D.; Varutbangkul, V.; Bahreini, R.; Flagan, R. C.; Seinfeld, J. H. *Environ. Sci. Technol.* **2004**, *38*, 4157–4164.

(23) St Clair, J. M.; McCabe, D. C.; Crounse, J. D.; Steiner, U.; Wennberg, P. O. *Rev. Sci. Instrum.* **2010**, *81*, 6.

(24) Paulot, F.; Crounse, J. D.; Kjaergaard, H. G.; Kroll, J. H.; Seinfeld, J. H.; Wennberg, P. O. *Atmos. Chem. Phys.* **2009**, *9*, 1479–1501.

(25) Crounse, J. D.; McKinney, K. A.; Kwan, A. J.; Wennberg, P. O. *Anal. Chem.* **2006**, *78*, 6726–6732.

(26) Huey, L. G.; Villalta, P. W.; Dunlea, E. J.; Hanson, D. R.; Howard, C. J. *J. Phys. Chem.* **1996**, *100*, 190–194.

(27) Crutzen, P.; Williams, J.; Pöschl, U.; Hoor, P.; Fischer, H.; Warneke, C.; Holzinger, R.; Hansel, A.; Lindinger, W.; Scheeren, B.; Lelieveld, J. *Atmos. Environ.* **2000**, *34*, 1161–1165.

(28) Jayne, J. T.; Leard, D. C.; Zhang, X.; Davidovits, P.; Smith, K. A.; Kolb, C. E.; Worsnop, D. R. *Aerosol Sci. Technol.* **2000**, *33*, 49–70.

(29) DeCarlo, P. F.; Kimmel, J. R.; Trimborn, A.; Northway, M. J.; Jayne, J. T.; Aiken, A. C.; Gonin, M.; Fuhrer, K.; Horvath, T.; Docherty, K. S.; et al. *Anal. Chem.* **2006**, *78*, 8281–8289.

(30) Canagaratna, M.; et al. *Mass Spectrom. Rev.* **2007**, *26*, 185–222.

(31) Loza, C. L.; Chhabra, P. S.; Yee, L. D.; Craven, J. S.; Flagan, R. C.; Seinfeld, J. H. *Atmos. Chem. Phys. Disc.* **2011**, *11*, 24969–25010.

(32) Jenkin, M. E.; Saunders, S. M.; Pilling, M. J. *Atmos. Environ.* **1997**, *31*, 81–104.

(33) Saunders, S. M.; Jenkin, M. E.; Derwent, R. G.; Pilling, M. J. *Atmos. Chem. Phys.* **2003**, *3*, 161–180.

(34) Kwok, E. S.; Atkinson, R. *Atmos. Environ.* **1995**, *29*, 1685–1695.

(35) Carter, W. P.; Cocker, D. R. I.; Fitz, D. R.; Malkina, I. L.; Bumiller, K.; Sauer, C. G.; Pisano, J. T.; Bufalino, C.; Song, C. *Atmos. Environ.* **2005**, *39*, 7768–7788.

(36) Wang, J.; Doussin, J. F.; Perrier, S.; Perraudin, E.; Katrib, Y.; Pangui, E.; Picquet-Varrault, B. *Atmos. Meas. Tech.* **2011**, *4*, 2465–2494.

(37) Sander, S. P.; Abbatt, J.; Barker, J. R.; Burkholder, J. B.; Friedl, R. R.; Golden, D. M.; Huie, R. E.; Kolb, C. E.; Kurylo, M.; Moortgat, G. K.; et al., Chemical kinetics and photochemical data for use in atmospheric studies, Evaluation No. 17. JPL Publication 10-6, 2011; <http://jpldataeval.jpl.nasa.gov>.

(38) Dibble, T. S. *Chem. Phys. Lett.* **2007**, *447*, 5–9.

(39) Vaghjiani, G.; Ravishankara, A. *J. Geophys. Res.* **1989**, *94* (D3), 3487–3492.

(40) Vaghjiani, G. L.; Ravishankara, A. R. *J. Chem. Phys.* **1990**, *92*, 996–1003.

(41) Baasandorj, M.; Papanastasiou, D. K.; Talukdar, R. K.; Hasson, A. S.; Burkholder, J. B. *Phys. Chem. Chem. Phys.* **2010**, *12*, 12101–12111.

(42) Atkinson, R. *J. Phys. Chem. Ref. Data, Monogr.* **1994**, *2*, 1–216.

(43) Atkinson, R.; Arey, J. *Chem. Rev.* **2003**, *103*, 4605–4638.

(44) Matsunaga, A.; Ziemann, P. J. *Aerosol Sci. Technol.* **2010**, *44*, 881–892.

(45) Loza, C. L.; Chan, A. W. H.; Galloway, M. M.; Keutsch, F. N.; Flagan, R. C.; Seinfeld, J. H. *Environ. Sci. Technol.* **2010**, *44*, 5074–5078.

(46) Crounse, J. D.; Paulot, F.; Kjaergaard, H. G.; Wennberg, P. O. *Phys. Chem. Chem. Phys.* **2011**, *13*, 13607–13613.

(47) Hasson, A. S.; Tyndall, G. S.; Orlando, J. J. *J. Phys. Chem. A* **2004**, *108*, 5979–5989.

(48) Spencer, K. M.; Beaver, M. R.; Clair, J. M. S.; Crounse, J. D.; Paulot, F.; Wennberg, P. O. *Atmos. Chem. Phys. Disc.* **2011**, *11*, 23619–23653.

(49) Compernolle, S.; Ceulemans, K.; Müller, J.-F. *Atmos. Chem. Phys.* **2011**, *11*, 9431–9450.

(50) Donahue, N. M.; Kroll, J. H.; Pandis, S. N.; Robinson, A. L. *Atmos. Chem. Phys. Disc.* **2011**, *11*, 24883–24931.

(51) Aiken, A. C.; DeCarlo, P. F.; Jimenez, J. L. *Anal. Chem.* **2007**, *79*, 8350–8358.

(52) Ziemann, P. J. *J. Phys. Chem. A* **2003**, *107*, 2048–2060.

(53) Matsunaga, A.; Docherty, K. S.; Lim, Y. B.; Ziemann, P. J. *Atmos. Environ.* **2009**, *43*, 1349–1357.

(54) Kern, W.; Spitteler, G. *Tetrahedron* **1996**, *52*, 4347–4362.

(55) Tobias, H. J.; Ziemann, P. J. *Environ. Sci. Technol.* **2000**, *34*, 2105–2115.

(56) Antonovskii, V. L.; Terent'ev, V. A. *J. Org. Chem. U.S.S.R. (Engl. Transl.)* **1967**, *3*, 972.

(57) Holt, T.; Atkinson, R.; Arey, J. *J. Photochem. Photobiol. A* **2005**, *176*, 231–237.

(58) Aschmann, S. M.; Arey, J.; Atkinson, R. *J. Atmos. Chem.* **2003**, *45*, 289–299.

(59) Martin, P.; Tuazon, E. C.; Aschmann, S. M.; Arey, J.; Atkinson, R. *J. Phys. Chem. A* **2002**, *106*, 11492.

(60) Ziemann, P. J. *Faraday Discuss.* **2005**, *130*, 469–490.

(61) Virtanen, A.; Joutsensaari, J.; Koop, T.; Kannisto, J.; Yli-Pirila, P.; Leskinen, J.; Makela, J. M.; Holopainen, J. K.; Poschl, U.; Kulmala, M.; et al. *Nature* **2010**, *467*, 824–827.

(62) Vaden, T. D.; Imre, D.; Beránek, J.; Shrivastava, M.; Zelenyuk, A. *Proc. Natl. Acad. Sci. U. S. A.* **2011**, *108*, 2190–2195.

Chapter 4

Analysis of secondary organic aerosol formation and aging using positive matrix factorization of high-resolution aerosol mass spectra: application to the dodecane low- NO_x system¹

¹This chapter is reproduced by permission from “Analysis of secondary organic aerosol formation and aging using positive matrix factorization of high-resolution aerosol mass spectra: application to the dodecane low- NO_x system,” by J. S. Craven, L. D. Yee, N. L. Ng, M. R. Canagaratna, C. L. Loza, K. A. Schilling, R. L. N. Yatavelli, J. A. Thornton, P. J. Ziemann, R. C. Flagan, and J. H. Seinfeld, *Atmospheric Chemistry and Physics*, 12, 11795 –11817, doi:10.5194/acp-12-11795-2012, www.atmos-chem-phys.net/12/11795/2012/, 2012. Copyright 2012 Authors. This work is licensed under a Creative Commons License.



Analysis of secondary organic aerosol formation and aging using positive matrix factorization of high-resolution aerosol mass spectra: application to the dodecane low-NO_x system

J. S. Craven¹, L. D. Yee², N. L. Ng⁶, M. R. Canagaratna³, C. L. Loza¹, K. A. Schilling¹, R. L. N. Yatavelli^{4,*}, J. A. Thornton⁴, P. J. Ziemann⁵, R. C. Flagan^{1,2}, and J. H. Seinfeld^{1,2}

¹Division of Chemistry and Chemical Engineering, California Institute of Technology, Pasadena, California, USA

²Division of Engineering and Applied Science, California Institute of Technology, Pasadena, California, USA

³Aerodyne Research, Inc., Billerica, Massachusetts, USA

⁴Department of Atmospheric Sciences, University of Washington, Seattle, Washington, USA

⁵Air Pollution Research Center, Department of Environmental Sciences, and Environmental Toxicology Graduate Program, University of California, Riverside, California, USA

⁶School of Chemical and Biomolecular Engineering and School of Earth and Atmospheric Sciences, Georgia Institute of Technology, Atlanta, Georgia, USA

* current address: Cooperative Institute for Research in Environmental Sciences (CIRES), University of Colorado, Boulder, Colorado, USA

Correspondence to: J. H. Seinfeld (seinfeld@caltech.edu)

Received: 7 June 2012 – Published in Atmos. Chem. Phys. Discuss.: 6 July 2012

Revised: 26 October 2012 – Accepted: 4 December 2012 – Published: 17 December 2012

Abstract. Positive matrix factorization (PMF) of high-resolution laboratory chamber aerosol mass spectra is applied for the first time, the results of which are consistent with molecular level MOVI-HRToF-CIMS aerosol-phase and CIMS gas-phase measurements. Secondary organic aerosol was generated by photooxidation of dodecane under low-NO_x conditions in the Caltech environmental chamber. The PMF results exhibit three factors representing a combination of gas-particle partitioning, chemical conversion in the aerosol, and wall deposition. The slope of the measured high-resolution aerosol mass spectrometer (HR-ToF-AMS) composition data on a Van Krevelen diagram is consistent with that of other low-NO_x alkane systems in the same O : C range. Elemental analysis of the PMF factor mass spectral profiles elucidates the combinations of functionality that contribute to the slope on the Van Krevelen diagram.

1 Introduction

The processes by which the atmospheric oxidation of volatile organic compounds (VOCs) leads to low volatility products that partition into the aerosol phase, forming Secondary Organic Aerosol (SOA), are complex and not thoroughly understood. Gas-phase oxidation processes are key in SOA formation, but there is increasing evidence that chemistry occurring in the particle phase, as well, may be important in producing the low-volatility, oxygenated compounds that characterize SOA. Laboratory chamber studies are essential to understand the lifecycle of organics involved in the formation of SOA. In such chamber experiments, measurements of both gas- and particle-phase chemical composition provide a window into the complex chemistry of SOA formation. While measurement of the complete suite of compounds involved in SOA formation is generally not feasible, key observations can provide considerable insight into the nature of the multi-generation gas-phase oxidation that characterizes SOA formation. High-Resolution Time-of-Flight

Aerosol Mass Spectrometer (HR-ToF-AMS) measurements of aerosol composition enable derivation of a number of key SOA properties; these include the atomic oxygen-to-carbon and hydrogen-to-carbon ratios (O : C and H : C), from which one can infer the overall oxidation state of the aerosol. The full HR-ToF-AMS spectrum, over the course of SOA formation and evolution, comprises a large number of mass-to-charge ratios (m/z), which contain time-dependent information on the overall processes occurring. Positive Matrix Factorization (PMF) has proved to be a powerful procedure for analyzing HR-ToF-AMS spectra in terms of the evolution of major mass spectral factors (Lanz et al., 2007; Ulbrich et al., 2009; Aiken et al., 2009; Ng et al., 2010; Hersey et al., 2011; Fry et al., 2011). The factor profile extracts the contributions from a number of masses that are co-correlated, providing information on the time evolution of the aerosol composition that is not immediately evident from the complex aerosol spectrum. We present here the first application of PMF to HR-ToF-AMS spectra obtained in a laboratory chamber investigation of SOA formation.

The present study is part of a comprehensive investigation of SOA formation from large alkanes. Historically, alkanes have been considered a significant atmospheric component of the unresolved complex mixture (UCM) of organics (Schauer et al., 2001, 2002). With the advent of a recently developed soft ionization gas chromatography technique, the unresolved complex mixture has been characterized at the molecular level to contain *n*-alkanes, cycloalkanes, bicycloalkanes, tricycloalkanes, and steranes (Isaacman et al., 2012). Pye and Pouliot (2012) predict from the Community Multiscale Air Quality (CMAQ) model the SOA yield from alkanes and PAHs to be 20 to 30 % of that from anthropogenic hydrocarbons. In particular, the linear alkane is predicted to dominate the SOA yield for the C₁₂ alkanes. This first phase of the comprehensive investigation of alkanes focuses on high-resolution HR-ToF-AMS spectra of dodecane (C₁₂H₂₆) SOA. In conjunction with Chemical Ionization Mass Spectrometer (CIMS) measurements, and Micro-Orifice Volatilization Impactor Coupled to a Chemical Ionization Mass Spectrometer (MOVI-HRToF-CIMS), the application of PMF provides insight into the multi-generational and multi-phase processes involved in SOA formation and aging.

2 Experimental

Experiments were carried out in the Caltech environmental chamber facility, which is comprised of dual 28 m³ teflon chambers (Table 1, Cocker et al., 2001). Experiments were carried out in a low-NO_x environment with hydrogen peroxide (H₂O₂) photolysis as the OH source. For each experiment, 280 µl of 50 % wt aqueous H₂O₂ solution was evaporated into the chamber, followed by atomization of 0.015 M aqueous ammonium sulfate (AS) solution for seed particles,

which were subsequently dried. Finally, the specific volume of liquid dodecane necessary to achieve the desired gas-phase concentration was evaporated into the chamber. The oxidant, seed, and hydrocarbon mixed for 1 h prior to irradiation.

2.1 High-resolution time-of-flight aerosol mass spectrometer

In the Aerodyne high-resolution time-of-flight aerosol mass spectrometer (HR-ToF-AMS), aerosol is sampled at atmospheric pressure through an aerodynamic lens into a particle time-of-flight chamber, at the end of which the particles impact a 600 °C heater and 70 eV filament assembly where they are vaporized and ionized. The aerosol ion fragments are then orthogonally extracted into the ion time-of-flight chamber where they are sampled in either V (higher signal) or W (higher resolution) mode. For these experiments, both modes were utilized at a 1 min sequential sampling rate. The V-mode was utilized for PMF analysis, as the higher m/z values exhibit a more favorable signal-to-noise ratio; the W-mode was used for ion identification, clarification, and elemental analysis. The V-mode and W-mode can be set to measure bulk aerosol composition in which all of the particles within the transmission of the instrument (60–600 nm with 100 % transmission efficiency) are measured. This is commonly referred to as mass spec.-mode (MS-mode). The HR-ToF-AMS can also measure size-resolved chemistry by employing the particle time-of-flight-mode (PTOF-mode) in which the aerosol beam is chopped in the particle time-of-flight chamber and single particles are sized and sampled. All HR-ToF-AMS data were processed with “Squirrel”, the ToF-AMS Unit Resolution Analysis Toolkit (<http://cires.colorado.edu/jimenez-group/ToFAMSResources/ToFSoftware/index.html>), in Igor Pro Version 6.22A (Wavemetrics, Lake Oswego, OR). Adjustments to the fragmentation table were made to correct for air interferences based on measurements made at the beginning of each experiment with a particle filter in-line with the chamber sample line and the HR-ToF-AMS (Allan et al., 2004). The ToF-AMS High Resolution Analysis software tool PIKA (Peak Integration by Key Analysis) was employed for high-resolution analysis (DeCarlo et al., 2006). Elemental ratios were calculated using the technique outlined by Aiken et al. (2008) and Chhabra et al. (2010).

2.2 Chemical Ionization Mass Spectrometer

A Chemical Ionization Mass Spectrometer (CIMS) was employed for the measurement of gas-phase photooxidation products, including key intermediates contributing to the particle phase. The CIMS consists of a Varian 1200 triple quadrupole mass spectrometer that has been modified to accommodate a custom ionization region. Sample air from the environmental chamber flows at 190 sccm into a glass flow

Table 1. Experimental conditions for dodecane low-NO_x photooxidation.

Exp #	duration (h)	initial hydrocarbon conc. (ppb)	seed type	initial seed volume ($\mu\text{m}^3 \text{cm}^{-3}$)	HR-ToF-AMS mode
1	18	34	AS	9.1	MS-mode, (V and W)
2	34	34	AS	11.4	(MS-mode (V and W))
3	18	33	AS	12.0	(MS-mode (V and W))
4	18	50	AS	14.1	MS-mode (V and W), PTOF-mode (V)
5	18	300	AS	34.7	MS-mode (V and W), turned heater off

tube, where it is diluted by a factor of nine with N₂ gas. It then enters the chemical ionization region. The CIMS uses CF₃OOCF₃ reagent gas, generating cluster products at [X.CF₃O]⁺ and fluoride transfer products at [X.F][−], where X is the analyte. Hydroperoxide-containing species are detected as a cluster product, and strongly acidic species are primarily detected as the transfer product. More weakly acidic species can be detected as both a cluster and transfer product. In these experiments, such products were tracked with the CIMS as discussed previously (Yee et al., 2012). Additional details of the instrument and its general operation have been described elsewhere (St. Clair et al., 2010; Paulot et al., 2009; Crounse et al., 2006).

2.3 Micro-orifice volatilization impactor coupled to a high-resolution time-of-flight chemical ionization mass spectrometer

A micro-orifice volatilization impactor coupled to a high-resolution time-of-flight chemical-ionization mass spectrometer (MOVI-HRToF-CIMS) was employed. Analysis in the MOVI-HRToF-CIMS is a two-step cycle in which (i) gas-phase compounds are measured by the high-resolution TOFMS while aerosols are collected, and (ii) collected aerosols are then thermally vaporized with composition measured by the spectrometer. Chemical ionization (CI) preserves the parent ion in most cases, which, when combined with a high-resolution TOF analyzer, allows determination of the elemental composition of the molecular ions in the mass range of 17–550 m/z with a mass resolution of 4500 for mass to charge > 100 (Yatavelli and Thornton, 2010; Yatavelli et al., 2012).

2.4 Positive Matrix Factorization (PMF)

Positive Matrix Factorization (PMF) has emerged as a powerful technique for source apportionment of HR-ToF-AMS measurements of ambient aerosol (Paatero and Tapper, 1994; Jimenez et al., 2009; Lanz et al., 2007; Ulbrich et al., 2009; Aiken et al., 2009; Hersey et al., 2011; Ng et al., 2010; Allan, 2003; Zhang et al., 2011). Here, the application of PMF to HR-ToF-AMS spectra to investigate SOA formation in a laboratory chamber is reported for the first time. The factors are groups of ions (or fractions of ions) that

vary together in time. For chamber experiments, this variation could result from processes such as gas-particle partitioning, chemical conversion in the aerosol, or wall loss of either individual molecules, or more likely a group of molecules with similar chemical character, such as the gas-phase products from a specific generation of gas-phase oxidation. Gas-phase measurements support and the dodecane low-NO_x mechanism predicts the multi-generation production of increasingly oxidized gas-phase products, which are expected to condense at different times. The AMS-PMF time series results are compared with molecular level detail of the CIMS gas-phase and MOVI-HRToF-CIMS aerosol-phase measurements, linking the HR-ToF-AMS high time-resolution electron impact ion information to the complex aerosol molecular level composition. The PMF results are explored using the PMF Evaluation Tool Version 2.04 in Igor Pro (http://cires.colorado.edu/jimenez-group/wiki/index.php/PMF-AMS_Analysis_Guide, Ulbrich et al., 2009). The details of implementing PMF are given in the Appendix A.

3 Results

SOA formation and aging comprise a number of atmospheric processes: (1) gas-phase reactions involving the primary organic and its oxidation products that involve functionalization and fragmentation; (2) gas-particle partitioning of lower volatility products; (3) chemical reactions in the aerosol phase that can lead to even lower volatility compounds or, in some cases, fragmentation and return to the gas phase. In interpreting the results of laboratory chamber experiments, one must also consider the effect of deposition of gases and particles to the chamber walls. In the present study we seek, via a combination of HR-ToF-AMS and CIMS measurements, to evaluate both gas- and particle-phase routes to formation of oxidized compounds.

3.1 Elemental ratios

Figure 1 shows the evolution of total organic aerosol mass during the longer experiment (Table 1). The O : C and H : C elemental ratios of the aerosol provide information on the bulk chemical evolution over the course of the experiment.

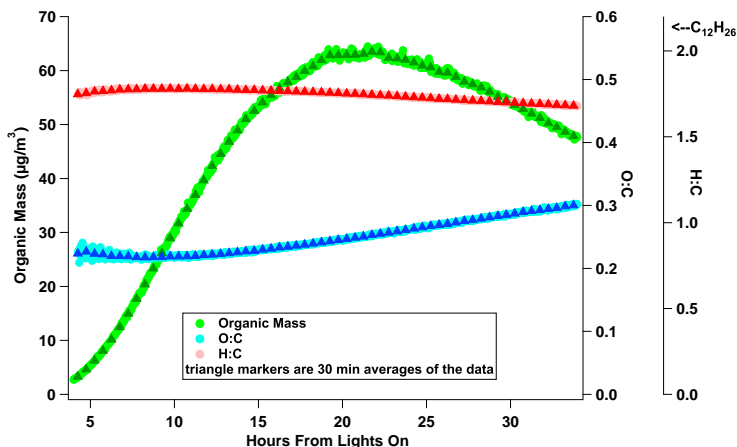


Fig. 1. Total organic aerosol mass and O:C and H:C elemental ratios for experiment 2. The C_2H_4^+ ion has been removed from the mass spectra due to its interference with the large signal from the N_2^+ ion. The triangles are 30 min averages of the data.

The first reliable O:C measurement yields a value near 0.22, which is consistent with the predicted early aerosol product, the C_{12} carbonyl hydroperoxide (product formula of $\text{C}_{12}\text{H}_{24}\text{O}_3$, O:C of 0.25). Upon further OH exposure, the O:C ratio grows to about 0.3. The H:C ratio is initially at 1.7, reflecting the oxidized nature of the aerosol composition at a relatively early stage of formation. The H:C ratio then increases after early growth to 1.79 and then decreases to 1.69 at 34 h. Dodecane itself has an H:C of 2.17 and an O:C of 0, so the initially high H:C and low O:C reflect the early oxidation stage of aerosol. The C_2H_4^+ ion was removed from the mass spectra owing to large interference with the N_2^+ ion, but with little effect on the absolute value and time trend of the elemental ratios. Individual high resolution ions provide further information on those masses in the spectrum that are driving the evolution of the aerosol chemical composition.

3.2 High-resolution ion analysis

The higher mass ions ($>m/z$ 100) in the HR-ToF-AMS spectrum provide key information regarding the low-volatility SOA constituents. Owing to the fragmentation caused by electron impact ionization, numerous ion combinations contribute to each nominal mass; the larger the mass, the greater the potential information regarding molecular detail, but the greater challenge in extracting that information. An explicit chemical mechanism of dodecane oxidation is critical in identifying individual ions, as well as patterns in the HR-ToF-AMS spectrum. A simplified schematic of the low- NO_x mechanism presented by Yee et al. (2012) is shown in Fig. 2.

At early growth, m/z 183 and m/z 215 dominate the signal for $m/z > 100$ (Figs. 3 and 4). At the outset, the only apparent ion at m/z 183 is $\text{C}_{12}\text{H}_{23}\text{O}^+$, but by the end of oxidation, $\text{C}_{10}\text{H}_{15}\text{O}_3^+$ has clearly grown in as a “left-side” neighbor to the original ion. This same type of behavior occurs for m/z 215 and, indeed, for almost all of the other masses in the spectrum. These developing patterns allow for a systematic identification of the ions at each mass. In each case, the later neighboring ion(s) have fewer carbons and more oxygens, as expected from continuous multi-generation oxidation. The unit mass resolution signals of m/z 183 and m/z 215, shown in Figs. 3 and 4, emphasize the difference in information between the unit mass and high-resolution analysis. The high resolution ions well past m/z 100 provide ion trend information (see Sect. 3.3), even if these ions do not influence the overall H:C and O:C ratios owing to small mass contributions.

3.3 Varying time trends for C_{12} ion fragments

The ions at higher m/z provide unique time traces from which inferences about the aerosol composition can be drawn. For example, the time series of C_{12} fragments in Fig. 5 shows distinct maxima during the course of the experiment. Since the parent hydrocarbon is a C_{12} molecule, the fragments shown in Fig. 5 are close to molecular level detail. The steady increase in signal of the less oxidized ion $\text{C}_{12}\text{H}_{23}\text{O}^+$ at m/z 183, followed by the increase of $\text{C}_{12}\text{H}_{21}\text{O}_2^+$ at m/z 197, and then $\text{C}_{12}\text{H}_{19}\text{O}_3^+$ at m/z 211 reflect the incorporation of increasingly oxidized products to the aerosol. The processes by which each ion reaches a maximum and then decreases are more challenging to infer. Deposition of aerosol to the chamber walls will cause the ion

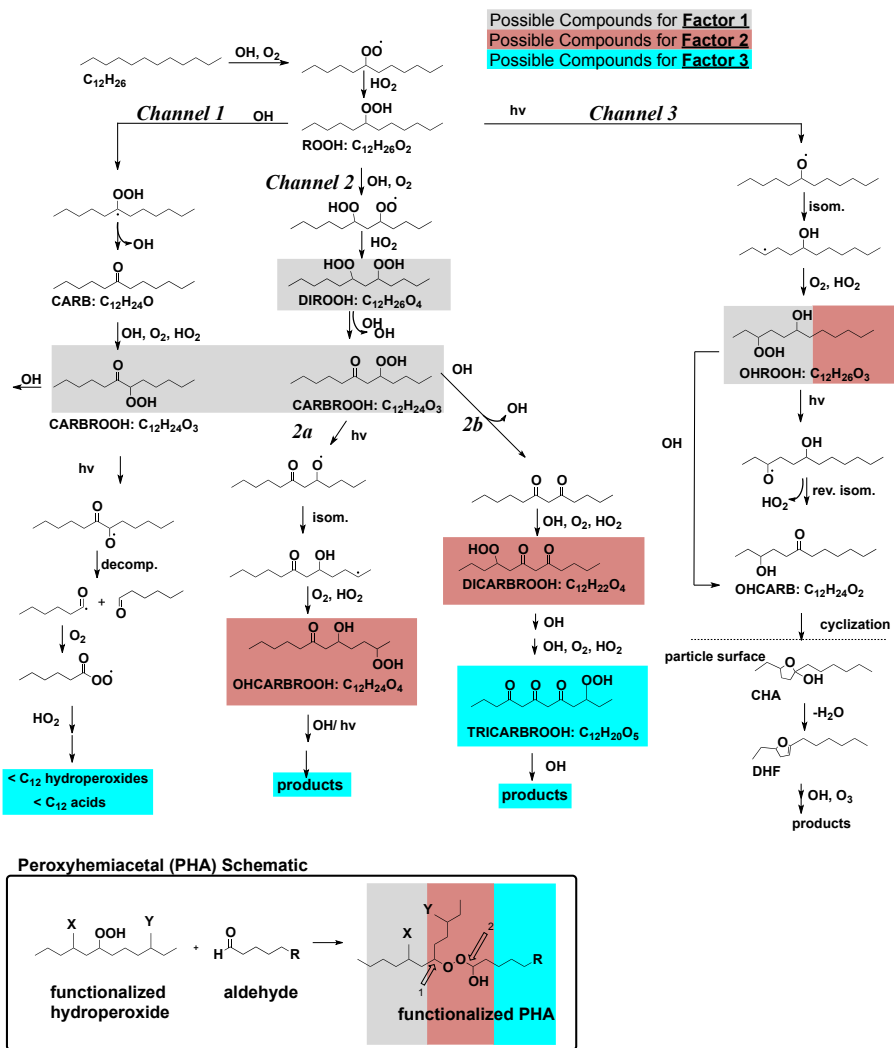


Fig. 2. Simplified chemical mechanism for dodecane photooxidation under low- NO_x , adapted from Yee et al. (2012). Shaded portions of the mechanisms are possible assignments for the PMF factors 1, 2 and 3, as discussed in Sects. 3.4 and 3.5.

signals to decrease (Sect. 3.6). A decreasing trend could also be the result of partitioning of products back to the gas-phase as their gas-phase equivalent reacts. Then, upon further oxidation in the gas-phase, the product re-condenses as a more oxidized species. Chemical conversion of the condensed products would provide another explanation for some ions to be decreasing, at the same time other ions are increasing. In electron impact ionization a particular ion fragment can be produced from two different compounds. This effect is magnified in the smaller m/z 's, for example, the C_2H_3^+ ion

at m/z 27, which is dominant throughout the entire experiment and a common fragment for alkyl molecules.

The ions identified in the HR-ToF-AMS spectra are a linear combination of the molecules in the aerosol; positive matrix factorization is well suited for long-duration chamber experiments, especially with ions that have unique time trends. The PMF results are an attempt to rebuild the molecular trend information that is lost from electron impact ionization in the HR-ToF-AMS. The less harsh ionization methods of both the heating mode of the MOVI-HRToF-CIMS and gas-phase measurements from the CIMS provide molecular

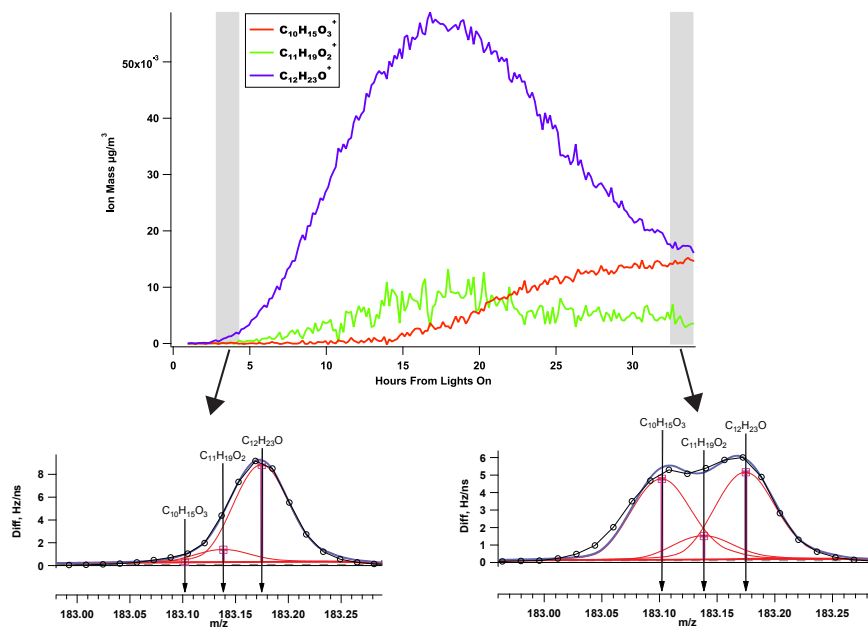


Fig. 3. Time series of ions and the raw data for “early growth” and “most oxidized growth” for m/z 183.

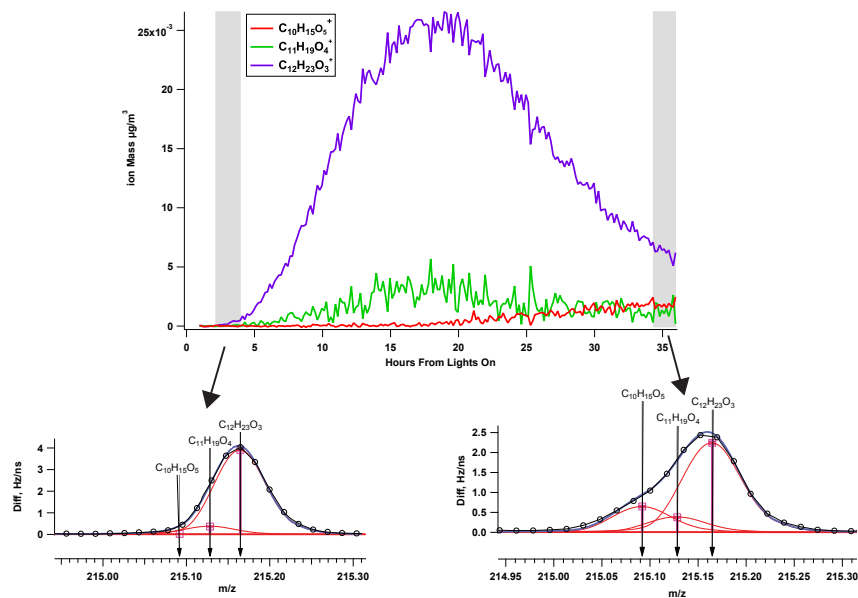


Fig. 4. Time series of ions and the raw data for “early growth” and “most oxidized growth” for m/z 215.

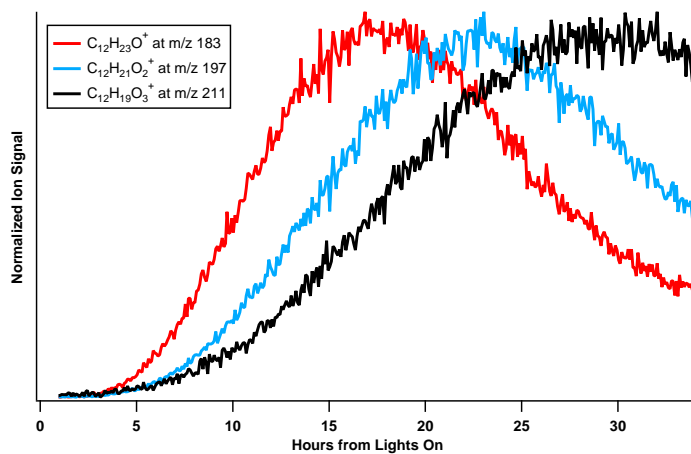


Fig. 5. C₁₂ backbone ions with varying contributions of oxygen have distinct time trends over the duration of the experiment.

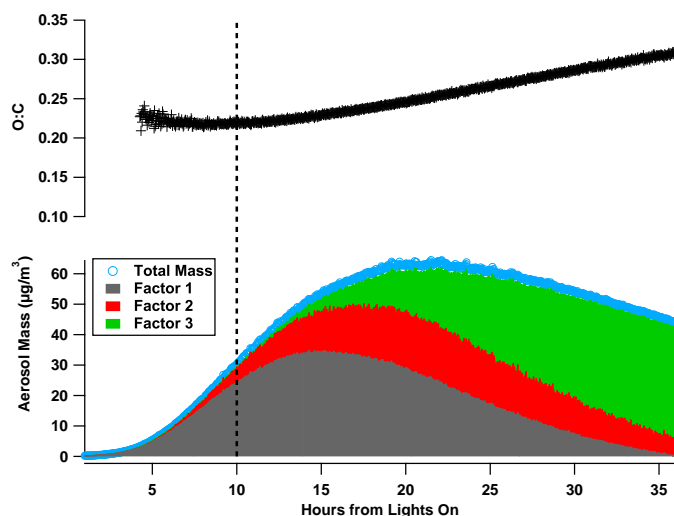


Fig. 6. Three-factor PMF solution, total organic mass, and O : C ratio. The dashed line denotes the point at which factor 3 grows in and the O : C begins to rise appreciably.

level information that the HR-ToF-AMS is unable to obtain, but to which the PMF results show similarity. From this comparison, molecular information can be inferred about the HR-ToF-AMS spectra, and how compounds fragment in the HR-ToF-AMS. Moreover, PMF results can be applied to obtain insight into the partitioning of the populations of oxidized molecules and the aerosol composition that evolves with continued oxidation.

3.4 Three-factor PMF solution

The PMF results for low-NO_x SOA formation from dodecane oxidation exhibit three distinct time traces with their correlating factor mass spectral profiles (Figs. 6 and 7). The three factor time series, shown in Fig. 6, are overlaid with the total organic loading to emphasize the relationship of each factor to the total SOA mass. The O : C ratio traces the overall oxidation state in the aerosol, and the PMF factors help explain that behavior. Factor 1, in grey, is dominant in the early aerosol growth and contains the least oxidized ions

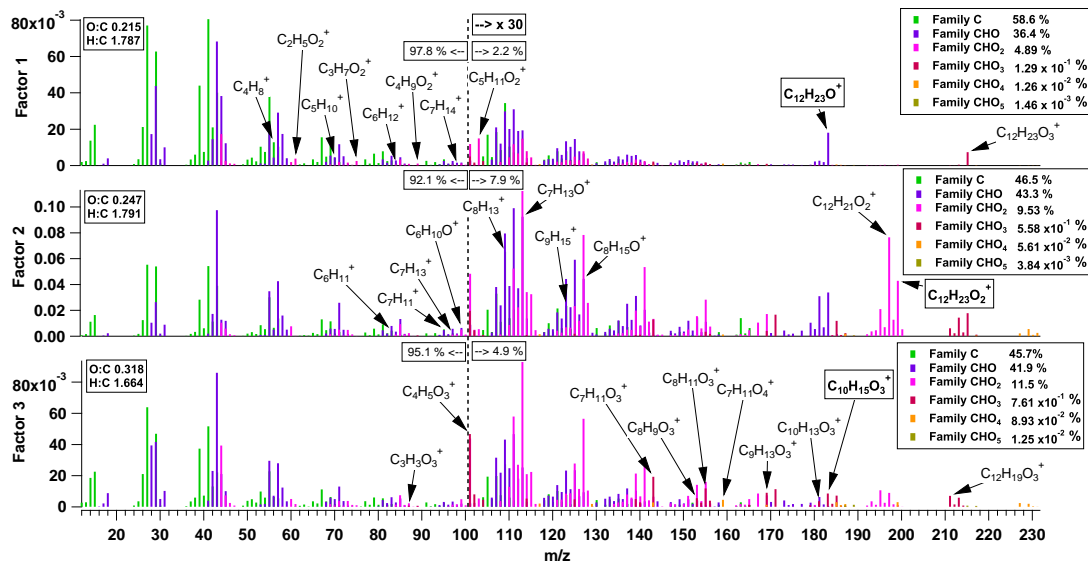


Fig. 7. The 3-factor mass spectra profiles in terms of their families. The ions past m/z 100 are multiplied by 30 to amplify signal strength.

(has the highest H:C ratio) of the factors. Factor 2 grows in next, peaks after factor 1, and then decreases. Factor 3 contains the highest contribution to the CO^+ and CO_2^+ ions and other O_2 , O_3 , O_4 , and O_5 – containing ions, explaining the steady increase in O:C over the course of the experiment. The CO_2^+ ion is the tracer for carboxylic acid in the HR-ToF-AMS (Aiken et al., 2008), which could explain the increase in O:C; however, the existence of the > 2 oxygen ion fragments indicates the O:C ratio increase could also be due to highly functionalized compounds, and not solely carboxylic acids, an observation supported by the chemical mechanism (Fig. 2) and the Van Krevelen Diagram (Sect. 3.7).

The mass spectral profiles of the factors are presented in Fig. 7, in which ions with different oxygen contents (different ion families) are highlighted by different colors. The mass percentage of each family to the total factor is presented in each factor's legend. Each factor profile has distinct, unique masses in the $> m/z$ 100 range. While it is difficult to identify an ion unique to one factor, certain ions have a higher contribution to one factor than another. Pearson's r correlation of each ion in the spectrum to each factor time series was used to identify which unique ions contribute the most to each factor. The 10 ions with the highest correlation in time with the factor profiles are tagged in the figure, with the top ion surrounded by a box. These are also listed in Table 3. The time trends of the top 3 ions correlating with each factor are displayed in Fig. 8. These ions provide the basis for identifying HR-ToF-AMS tracer ions for different generations of oxidation products. The interpretation of these factor time series and mass spectral profiles is aided by a chemical mech-

anism of dodecane oxidation, as well as comparison of time series to CIMS and MOVI-HRToF-CIMS data and individual HR-ToF-AMS ions.

3.5 Chemical interpretation of PMF solution

Factor 1 mass spectra and time series correlations with CIMS (Fig. 10) and MOVI-HRToF-CIMS (Fig. 11) ion time traces suggest that factor 1 could be C_{12} carbonyl hydroperoxide or C_{12} dihydroperoxide gas-to-particle partitioning (CARBROOH or DIROOH, Fig. 2, see grey shaded box) and possibly peroxyhemiacetal formation (see inset from Fig. 2). A $\text{C}_{18}\text{H}_{38}$ low- NO_x photooxidation experiment was carried out to produce a hydroperoxide standard and to understand the hydroperoxide fragmentation pattern in the HR-ToF-AMS (Fig. 9 and Table 4). The first product from $\text{C}_{18}\text{H}_{38}$ low- NO_x photooxidation is the hydroperoxide, which because of its long carbon chain, is expected to condense immediately onto the aerosol. Removal of HO_2 from the C_{18} hydroperoxide is supported by the $\text{C}_{18}\text{H}_{37}^+$ ion in the HR-ToF-AMS spectrum; this ion is considered a tracer for the C_{18} hydroperoxide. Fraser et al. (1970) also saw alkyl ions with 70 eV electronic impact ionization mass spectrometry measurements of alkyl hydroperoxides and attributed these peaks to HO_2 elimination from the hydroperoxide. The $\text{C}_3\text{H}_7\text{O}_2^+$ ion is also considered to be a tracer for the hydroperoxide-like compound since it has the highest percent difference between the $\text{C}_{18}\text{H}_{38}$ condensation spectrum before irradiation and the mass spectrum immediately after irradiation.

For dodecane, we do not expect the C_{12} hydroperoxide to partition to the particle phase, but we do expect the C_{12}

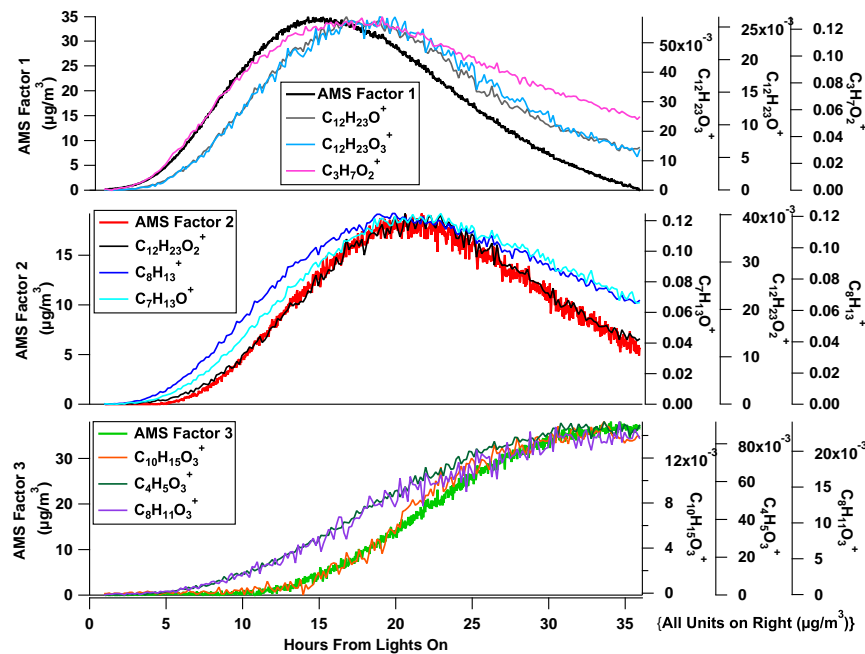


Fig. 8. Factor time series with the top three highest Pearson's r correlating HR-ToF-AMS ions.

Table 2. Ion fragments.

<i>m/z</i>	Ion	possible identification
169	$\text{C}_{12}\text{H}_{25}^+$	hydroperoxide, hydroperoxide-peroxyhemiacetal
201	$\text{C}_{12}\text{H}_{25}\text{O}_2^+$	hydroperoxide-peroxyhemiacetal
185	$\text{C}_{12}\text{H}_{25}\text{O}^+$	hydroxy hydroperoxide, hydroxy hydroperoxide-peroxyhemiacetal
217	$\text{C}_{12}\text{H}_{25}\text{O}_3^+$	hydroxy hydroperoxide-peroxyhemiacetal
183	$\text{C}_{12}\text{H}_{23}\text{O}^+$	carbonyl hydroperoxide, carbonyl hydroperoxide-peroxyhemiacetal
215	$\text{C}_{12}\text{H}_{23}\text{O}_3^+$	carbonyl hydroperoxide-peroxyhemiacetal
197	$\text{C}_{12}\text{H}_{21}\text{O}_2^+$	dicarbonyl hydroperoxide, dicarbonyl hydroperoxide-peroxyhemiacetal
229	$\text{C}_{12}\text{H}_{21}\text{O}_4^+$	dicarbonyl hydroperoxide-peroxyhemiacetal
199	$\text{C}_{12}\text{H}_{23}\text{O}_2^+$	hydroxy carbonyl hydroperoxide, hydroxy carbonyl hydroperoxide-peroxyhemiacetal
231	$\text{C}_{12}\text{H}_{23}\text{O}_4^+$	hydroxy carbonyl hydroperoxide-peroxyhemiacetal
211	$\text{C}_{12}\text{H}_{19}\text{O}_3^+$	tricarbonyl hydroperoxide, tricarbonyl hydroperoxide-peroxyhemiacetal
243	$\text{C}_{12}\text{H}_{19}\text{O}_5^+$	tricarbonyl hydroperoxide-peroxyhemiacetal

carbonyl hydroperoxide to partition (Yee et al., 2012). The presence of ion fragment $\text{C}_{12}\text{H}_{23}\text{O}^+$ at *m/z* 183 supports this explanation (Fig. 3). The $\text{C}_{12}\text{H}_{23}\text{O}_3^+$ ion at *m/z* 215 (a 32 *m/z* and O_2^+ difference from the carbonyl hydroperoxide ion) trends with the $\text{C}_{12}\text{H}_{23}\text{O}^+$ ion with a Pearson's *r* of 0.986 and is the ion with the highest correlation in the entire spectrum to $\text{C}_{12}\text{H}_{23}\text{O}^+$. A possible assignment of $\text{C}_{12}\text{H}_{23}\text{O}_3^+$

in correlation with $\text{C}_{12}\text{H}_{23}\text{O}^+$ is the peroxyhemiacetal corresponding to the carbonyl hydroperoxide (possible fragmentation at site 2 of peroxyhemiacetal, see inset in Fig. 2). Although the fragmentation of a peroxyhemiacetal standard in the HR-ToF-AMS can not be confirmed, the chemical mechanism prediction of aldehyde formation in the gas-phase and evidence for hydroperoxides in the gas- and particle-phase

Table 3. HR-ToF-AMS ions with highest Pearson's r values for $f_{\text{peak}} = 0.2$ solution.

Pearson's r with factor 1	Ion Formula	Ion Mass ($\mu\text{g m}^{-3}$)	Pearson's r with factor 2	Ion Formula	Ion Mass ($\mu\text{g m}^{-3}$)	Pearson's r with factor 3	Ion Formula	Ion Mass ($\mu\text{g m}^{-3}$)
0.888964	$\text{C}_{12}\text{H}_{23}\text{O}$	183.175	0.992157	$\text{C}_{12}\text{H}_{23}\text{O}_2$	199.17	0.978408	$\text{C}_{10}\text{H}_{15}\text{O}_3$	183.102
0.858995	$\text{C}_{12}\text{H}_{23}\text{O}_3$	215.165	0.975248	C_8H_{13}	109.102	0.970308	$\text{C}_4\text{H}_5\text{O}_3$	101.024
0.854958	$\text{C}_3\text{H}_7\text{O}_2$	75.0446	0.973654	$\text{C}_7\text{H}_{13}\text{O}$	113.097	0.95434	$\text{C}_8\text{H}_{11}\text{O}_3$	155.071
0.851494	C_6H_{12}	84.0939	0.973188	C_7H_{13}	97.1017	0.953511	$\text{C}_5\text{H}_7\text{O}_3$	115.039
0.835077	$\text{C}_5\text{H}_{11}\text{O}_2$	103.076	0.972338	$\text{C}_8\text{H}_{15}\text{O}$	127.112	0.949821	$\text{C}_9\text{H}_{13}\text{O}_3$	169.087
0.830188	$\text{C}_4\text{H}_9\text{O}_2$	89.0603	0.972216	C_7H_{11}	95.0861	0.947504	$\text{C}_7\text{H}_{11}\text{O}_3$	143.071
0.83002	C_5H_{10}	70.0782	0.970214	$\text{C}_{12}\text{H}_{21}\text{O}_2$	197.154	0.94481	$\text{C}_{12}\text{H}_{19}\text{O}_3$	211.133
0.819021	C_7H_{14}	98.1096	0.969585	C_9H_{15}	123.117	0.943721	$\text{C}_{10}\text{H}_{16}\text{O}_3$	184.11
0.812879	$\text{C}_2\text{H}_5\text{O}_2$	61.0289	0.969189	C_6H_{11}	83.0861	0.941672	$\text{C}_{10}\text{H}_{13}\text{O}_3$	181.087
0.775934	C_4H_8	56.0626	0.968232	$\text{C}_6\text{H}_{11}\text{O}$	99.081	0.939138	$\text{C}_3\text{H}_3\text{O}_3$	87.0082

suggest that peroxyhemiacetal formation or other oligomerization processes are possible.

Figure 8 shows the PMF factor time series with the top 3 correlating HR-ToF-AMS ions. The $\text{C}_3\text{H}_7\text{O}_2^+$ ion at m/z 75, which is a suggested hydroperoxide tracer (Table 4), nearly overlaps factor 1 for the first 15 h, after which the time trend of $\text{C}_3\text{H}_7\text{O}_2^+$ decays more slowly than factor 1; this is because the hydroperoxide functionalization could also have a contribution to factor 2, or later generations of oxidation products. $\text{C}_{12}\text{H}_{23}\text{O}^+$ at m/z 183 and $\text{C}_{12}\text{H}_{23}\text{O}_3^+$ at m/z 215 also have a high correlation, although these ions grow in slightly after the hydroperoxide ion at m/z 75. The difference between the individual ions trends and the PMF time trace is expected since the PMF factor represents the bulk variation of the aerosol composition over time and is not necessarily expected to exactly overlap with individual ion trends. Additionally, due to the fragmentation in the HR-ToF-AMS, single ions can contribute to multiple factors. The top 10 ions with the highest Pearson's r values for each factor show this effect (Fig. A1). The chemical interpretation of factor 1 is also supported by comparison to the CIMS gas-phase measurement of positive mode m/z 204, the suggested product being the carbonyl hydroperoxide (Fig. 10, Yee et al., 2012) as well as the MOVI-HRToF-CIMS heating-mode measurement of the $\text{C}_{12}\text{H}_{21}\text{O}_3^+$ ion, which is likely the chemical ionization product of a C_{12} dihydroperoxide (Fig. 11).

HR-ToF-AMS, CIMS, and MOVI-HRToF-CIMS measurements suggest that factor 2 represents the gas-phase partitioning of tri-functionalized products and their corresponding peroxyhemiacetals (see pink shaded boxes in Fig. 2). Factor 2 correlates highly with HR-ToF-AMS ion $\text{C}_{12}\text{H}_{23}\text{O}_2^+$ at m/z 199, which is the suggested ion tracer for the hydroxy carbonyl hydroperoxide (OHCARBROOH). Factor 2 also correlates well with the CIMS gas-phase positive mode m/z 219, which is the suggested dicarbonyl hydroperoxide product (Fig. 10) and the MOVI-HRToF-CIMS heating-mode ion $\text{C}_9\text{H}_{15}\text{O}_4^+$ (Fig. 11). The MOVI-HRToF-CIMS ion has higher oxygen content than ions trending with factor 1,

which could suggest an additional functional group from further oxidation.

Factor 3 is likely the gas-particle partitioning of multi-functional (4 or more functional groups) products, as indicated by HR-ToF-AMS ion $\text{C}_{10}\text{H}_{15}\text{O}_3^+$ at m/z 183 and $\text{C}_{12}\text{H}_{19}\text{O}_3^+$ at m/z 211 (Fig. 7), which could be the tri-carbonyl hydroperoxide product (TRICARBROOH). MOVI-HRToF-CIMS data also support the addition of a highly oxidized product to the aerosol with the ion $\text{C}_{10}\text{H}_{15}\text{O}_3^+$ trend (Fig. 11). Although the CIMS did not measure in the high m/z range necessary for identifying greater than tri-functionalized gas-phase products, the CIMS gas-phase C_8 carboxylic acid trace shows continual increase. This is consistent with factor 3 growth, the potential for acid formation in the chemical mechanism, and HR-ToF-AMS CO_2^+ ion, which could be from either acid formation or multifunctional products (Fig. 10). These results support factor 3 containing highly functionalized compounds, and acidic compounds, either from gas-to-particle partitioning of highly oxidized products or possibly from condensed chemical conversion from products in factors 1 and 2.

Factors 1 and 2 both exhibit a maximum with respect to time. A decrease after the maximum owing to wall deposition alone, addressed in Sect. 3.6, does not fully explain the decrease of these factors. The extent of evaporation of aerosol products is difficult to interpret from the gas-phase data. Other processes, such as cyclization or peroxyhemiacetal oligomerization, are possible (Tobias and Ziemann, 2000; Ziemann, 2003) but cannot be established unequivocally from HR-ToF-AMS data, as the fragments resulting from oligomerization are not unique. Masses greater than m/z 300 are observed in the MOVI-HRToF-CIMS spectra, which although difficult to assign exact elemental formulas, may suggest that products greater than C_{12} exist in the aerosol. Chemical conversion likely contributes to the decrease in factors 1 and 2 and increase in factor 3 (although gas-phase partitioning of highly oxidized compounds could also be contributing to the increase in factor 3). The percentages of mass greater than m/z 100 for factors 2 and 3 are

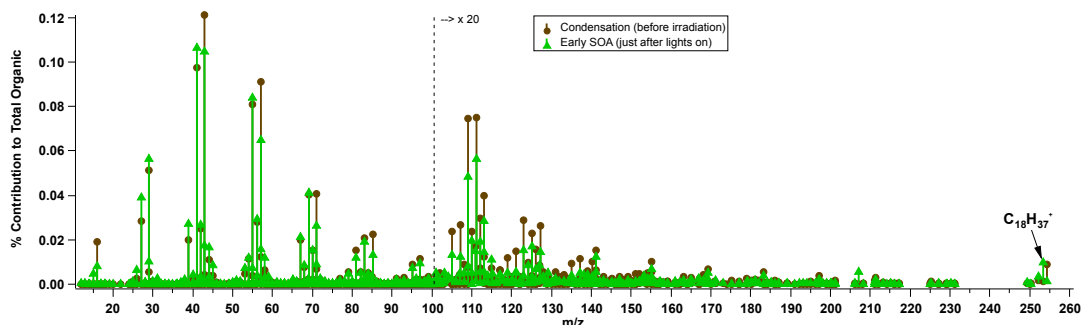


Fig. 9. Mass spectrum of octadecane condensing onto the seed before irradiation, and the relative mass spectrum just after lights on. The hypothesized octadecane-equivalent hydroperoxide fragment is marked at m/z 253.

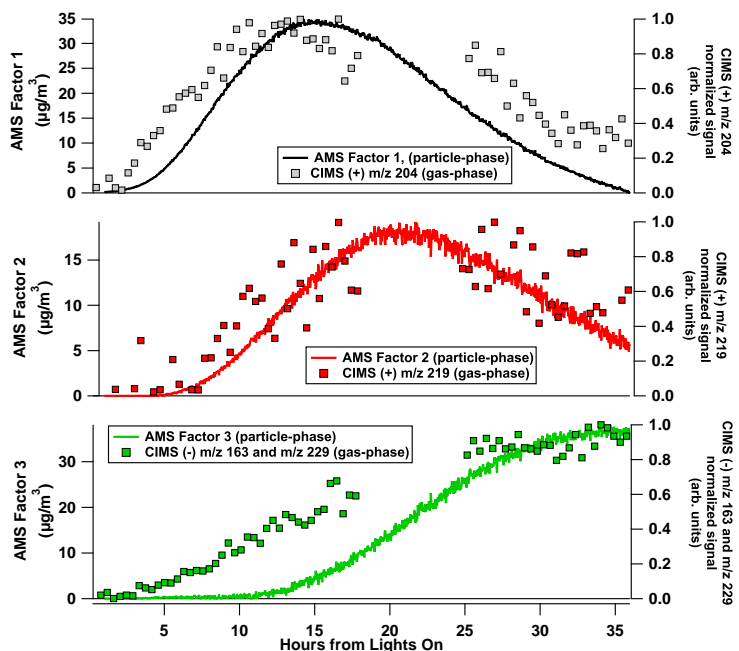


Fig. 10. Particle-phase HR-ToF-AMS factor time series with gas-phase CIMS time traces.

8 % and 5 %, respectively. The decrease of mass concentration of ions correlating with factor 2 may be a result of fragmentation in the aerosol. Molecular level identification of individual species from further MOVI-HRToF-CIMS analysis would be necessary to confirm this.

Other HR-ToF-AMS ions with 32 m/z difference that support a C_{12} functionalized hydroperoxide reacting with an aldehyde to form peroxyhemiacetal are listed in Table 2. Other 32 m/z pairs with fewer than 12 carbons exist, and may come from hydroperoxide formation in Channel 1 of the

mechanism containing fragmentation of carbon chains fewer than 12.

The proposed peroxyhemiacetal tracer ions behave differently under reduced HR-ToF-AMS temperature. In experiment 5 in Table 1, the HR-ToF-AMS 600 °C heater was turned off and only ionization (no vaporization) was used to sample the aerosol. During the time when the heater was turned off, the bulk of the organic ions decreased, since the ionization of the aerosol is contingent upon its vaporization. However, signal generated by the ions for the hypothesized

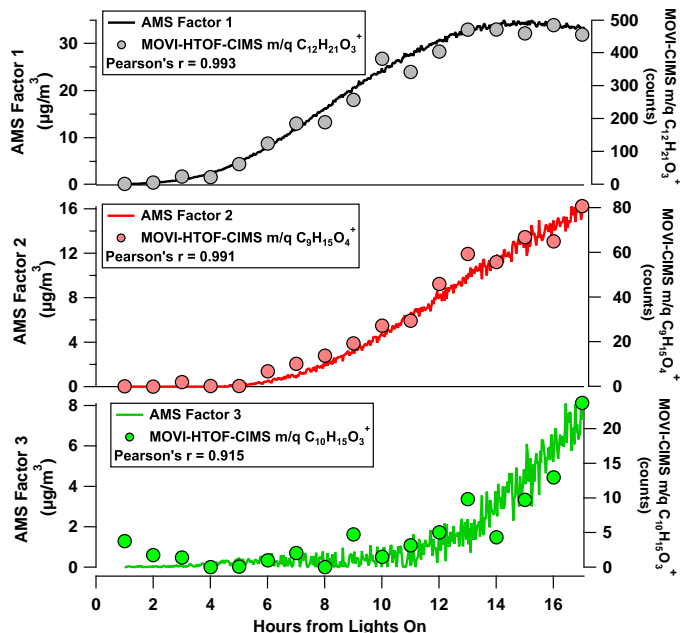


Fig. 11. Factor time series with MOVI-HRToF-CIMS heating-mode, aerosol-phase traces. Only the first 18 h of data is available for the MOVI-HRToF-CIMS data.

peroxyhemiacetal actually increased (Fig. 12). Since peroxyhemiacetals are unstable at high temperature, the decrease in temperature would stabilize peroxyhemiacetal, allowing the molecules to be more available for ionization.

It is important to note that the latter half of experiment 2 provides useful information in interpreting the chemistry of the aerosol. In the first 17 h, all of the factors show only an increase (see Figs. 11 and A1). The time trends of factors 2 and 3 look very similar in the first 17 h, but distinction becomes possible in the latter half of the experiment in which factor 2 decreases and factor 3 increases (Fig. 6). This explains perhaps why in a shorter experiment, two factors explain the data better (see Appendix A for further explanation on the effect of PMF on different lengths of experiment).

3.6 Chamber processes

Deposition of aerosol to the chamber walls decreases the suspended aerosol mass. PTOF-mode data are not available for the 34 h experiment discussed above. Experiment 4 was carried out, with a similar initial dodecane concentration, to explore the contribution from wall loss to the decrease in mass of the PMF factor time series. As expected, the average diameter of the aerosol mass distribution grew with increasing OH exposure (Fig. 13 and panel a1, a2 and a3 in Fig. 14). Since the wall loss rate is a function of diameter (Fig. 13, Loza et al., 2012), the size of the aerosol and composition

at that size are important for factor dependent wall-loss corrections. Panel b of Fig. 14 shows the PMF factors (only 2 for a shorter experiment, see Sect. A2) as a function of time. “Time 1” is early in the experiment when the mass distribution is expected to have a major contribution from factor 1. “Time 2” is at maximum growth in time of factor 1 and a large contribution from factor 2, and “Time 3” is when factor 2 has passed factor 1 in overall mass. The PMF results for the mass distributions (diameter is the independent variable now instead of time) are shown with the overall organic mass distribution to emphasize the contribution from factors 1 and 2 to each size bin (panel a1, a2, and a3 with b on Fig. 14). Since factor 1 is the first to condense onto the aerosol, some of its mass is lost more rapidly than factor 2, which condenses later onto larger particles (which are lost by deposition at a slower rate). The mass fractions of factors 1 and 2 were calculated for each size bin for 12 mass distributions; this information was used to adapt the wall deposition calculations carried out by Loza et al. (2012) for individual factor wall loss corrections.

Even with wall loss correction, factor 1 shows a decrease, while factor 2 shows an increase; the cumulative mass loss by wall deposition for factor 1 at the end of the experiment is $18 \mu\text{g m}^{-3}$, which accounts for approximately 50 % of the decrease in mass from the peak of factor 1 (panel c from Fig. 14). These results further support the hypothesis that the mass in the aerosol is undergoing chemical conversion. It is

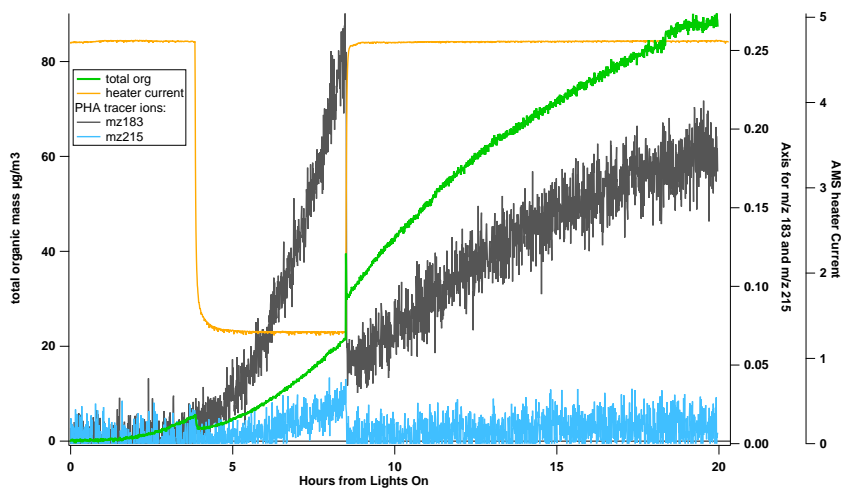


Fig. 12. Tracer ions for the carbonyl hydroperoxide increase while the bulk organic trace decreases when the 600 °C HR-ToF-AMS heater is turned off.

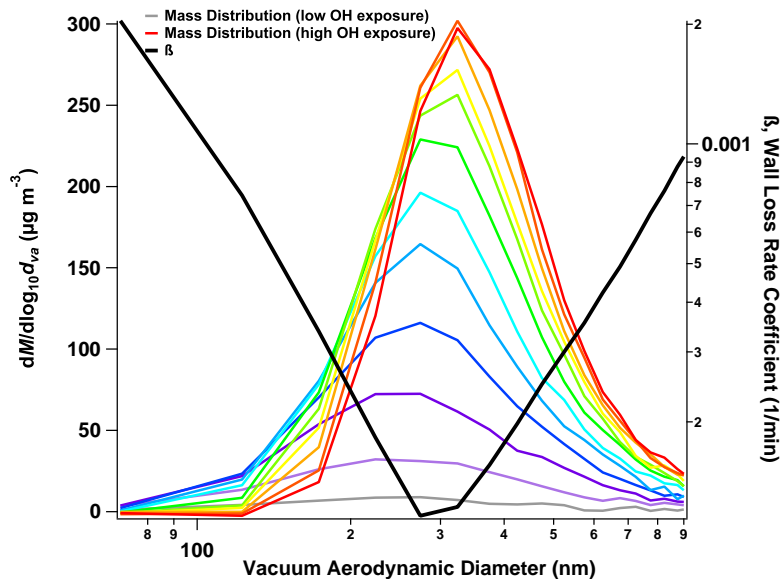


Fig. 13. The aerosol mass distribution grows from smaller diameter sizes to larger diameter sizes with increasing OH exposure (purple is low OH exposure, red is high OH exposure). The wall deposition rate coefficient is overlaid for comparison.

also important to note that the effects of wall loss on factors 1 and 2 differ as a result of the size distribution of the aerosol when the factor emerges.

3.7 Van Krevelen diagram

The Van Krevelen diagram has been used to represent the evolution of HR-ToF-AMS elemental ratios, H:C vs. O:C, for both ambient and chamber-generated organic aerosols (Heald et al., 2010; Ng et al., 2011; Chhabra et al., 2011; Lambe et al., 2011, 2012). A slope of 0 on the diagram is

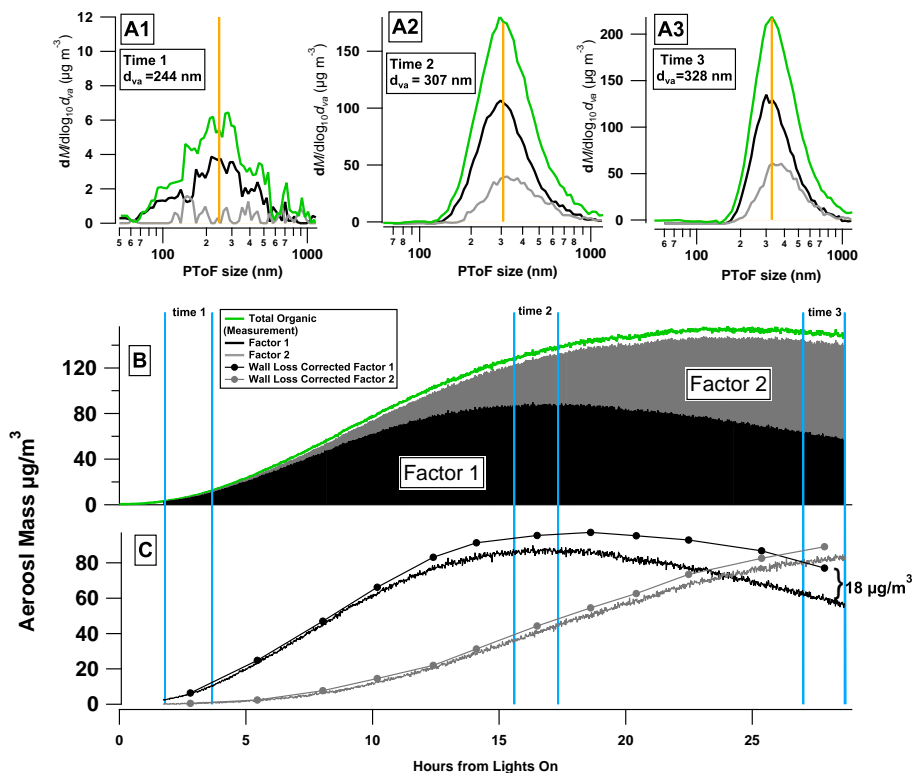


Fig. 14. Mass distributions (A1, A2 and A3) and time series (B) of total organic mass (green) broken down into 2 factors (black and grey). The average diameter for each mass distribution is highlighted by the yellow bar, and the time associated with each distribution is outlined with the two blue bars on the time series graphs. The wall-loss corrected versions of the individual factor time series are also shown (C).

consistent with peroxide or alcohol functionalization without carbon chain fragmentation. A slope of -1 is consistent with carboxylic acid or ketone/aldehyde and alcohol addition on the same carbon chain, and a slope of -2 is consistent with ketone/aldehyde addition (Van Krevelen, 1950; Heald et al., 2010). Lambe et al. (2012) report the slopes for low- NO_x photooxidation of long chain alkanes (C_{10} , C_{15} , and C_{17}) in a PAM reactor in two regimes in terms of the $\text{O} : \text{C}$ ratio. For $\text{O} : \text{C} < 0.3$, the slope is relatively steep (-1.3 ± 0.2), while for $\text{O} : \text{C} > 0.3$ the slope becomes less negative (-0.7 ± 0.1). Lambe et al. (2012) attribute this change in slope to a transition from functionalization to fragmentation dominated reactions. The dodecane aerosol composition data presented here lie primarily in the regime where $\text{O} : \text{C} < 0.3$, with a slope of -1.16 that is consistent with Lambe et al. (2012) in this $\text{O} : \text{C}$ range.

As discussed by Ng et al. (2011) and Lambe et al. (2012), the slope on a Van Krevelen diagram can represent a combination of several functionalities and generally requires molecular level information for further interpretation. The

PMF analysis links the HR-ToF-AMS aerosol spectrum to molecular level detail when compared to measurements from CIMS and MOVI-HRToF-CIMS. Concurrent with our chemical understanding, over 34 h of oxidation, the dodecane low- NO_x system is characterized by the addition of peroxides and ketone/aldehyde functionalization, as opposed to solely carboxylic acid formation. PMF factor 1 (black marker in Fig. 15) overlaps the bulk composition data (grey markers) near the initial growth at low OH exposure. Factor 2 (red marker in Fig. 15) has a similar H : C ratio as factor 1, but higher O : C ratio. The slope between factors 1 and 2, $m_{12} = 0.12$, is characteristic of either hydroxy or peroxide addition. We have already shown that factor 2 describes the gas-phase partitioning of hydroperoxide species (Sect. 3.5). The addition of hydroperoxide functional groups is not obvious from the bulk H : C and O : C ratios (slope = -1.16), but only from the PMF factor elemental ratios. The H:C and O : C ratios of factor 3 (green marker in Fig. 15) overlaps the data (grey markers) at the end of the experiment. The slope from factor 2 to 3, $m_{23} = -1.78$, is characteristic of

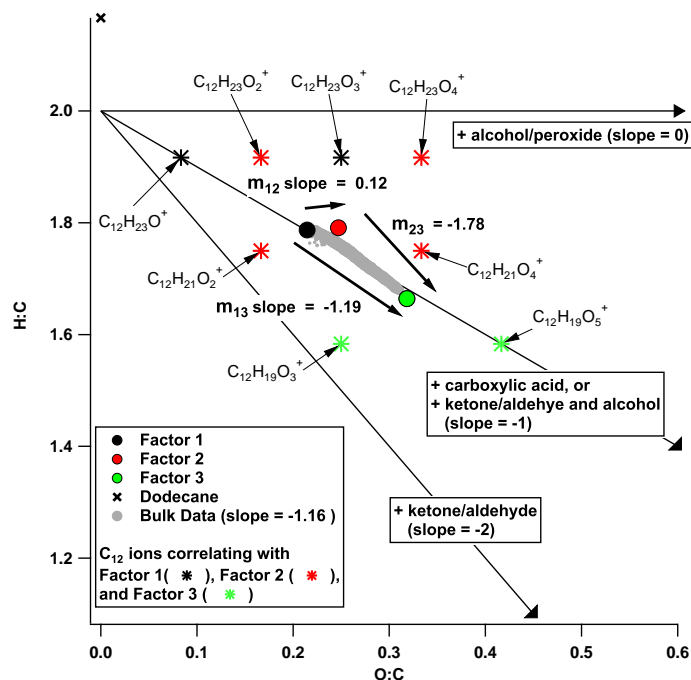


Fig. 15. Van Krevelen diagram for low- NO_x photooxidation of dodecane. HR-ToF-AMS bulk composition data are indicated by the grey markers and PMF factors 1–3 are shown by the black, red, and green circle markers. C_{12} ions, which are the ions retaining the most molecular-level detail, with high correlation to each factor are also displayed by the black, red, and green star markers.

the addition of products with carbonyl or ketone functionalization. The slope between factor 1 and 3, $m_{13} = -1.19$, is consistent with either carboxylic acid formation or ketone/aldehyde and alcohol addition to a product in factor 1. The slopes between the factor elemental ratios help indicate the combinations of functionality in the aerosol, with more clarity than one slope from the bulk elemental analysis. The C_{12} ion fragments correlating the highest with each factor and hypothesized to be mono-, di-, or tri- functionalized C_{12} hydroperoxides and/or functionalized peroxyhemiacetals are also displayed on Fig. 15.

4 Conclusions

In the present work, PMF has been applied to high-resolution chamber HR-ToF-AMS mass spectra to deduce the chemical and physical processes associated with low- NO_x dodecane SOA formation and aging. PMF untangles some of the complexity of SOA mass spectra by providing a mass spectral signature, with ion tracers, associated with a group of molecules at a distinct oxidation level. Factor 1 represents the gas-phase partitioning of initial oxidation products with two functional groups, factor 2 is the further oxidized, tri-

functionalized products incorporating into the particle phase, and factor 3 is the partitioning of extended oxidation products quadruply functionalized. All three factors could also include oligomerization processes and contributions from wall-loss.

An octadecane low- NO_x photooxidation experiment was conducted to develop a hydroperoxide standard for the HR-ToF-AMS, from which the alkyl-ion $C_{18}\text{H}_{37}^+$ at m/z 253 and $C_3\text{H}_7\text{O}_2^+$ at m/z 75 were identified as hydroperoxide ion tracers. With the PMF factor results, in combination with the SOA mechanism, CIMS, and MOVI-HRToF-CIMS measurements, the peroxyhemiacetal ion tracers were proposed, such as the $C_{12}\text{H}_{23}\text{O}^+$ at m/z 183 and $C_{12}\text{H}_{23}\text{O}_3^+$ at m/z 215 for the carbonyl hydroperoxide-peroxyhemiacetal.

The Van Krevelen diagram of the data, supported by the chemical interpretation of the dodecane low- NO_x oxidation, is consistent with the addition of peroxides and ketone/aldehyde functionalization rather than solely carboxylic acids. While the bulk experimental elemental ratios exhibit a slope of -1.16 , the change in H:C and O:C ratios from factors 1 to 2 reveals a slope of 0.12 , strongly indicating hydroperoxide addition to the aerosol. The elemental ratios between factors 2 and 3 have a slope of -1.78 , indicating adding of aldehyde/carbonyl functionalization, and the slope between factor 1 and 3 is -1.19 , indicating either

Table 4. Distinct ions present in early C₁₈ SOA formation.

Ion Formula	Exact Mass	% Difference from C ₁₈ Condensation MS*	Mass Fraction in SOA Spectrum
C ₃ H ₇ O ₂	75.0446	0.99	0.0005
CO	27.9949	0.99	0.0007
CO ₂	43.9898	0.99	0.0007
C	12.0000	0.99	0.0006
C ₂ H ₂ O	42.0106	0.99	0.0017
CHO ₂	44.9977	0.99	0.0006
CH	13.0078	0.99	0.0006
CH ₃	15.0235	0.99	0.0048
C ₅ H ₃	63.0235	0.99	0.0006
C ₁₈ H ₃₇	253.2900	0.98	0.0005
C ₅ H ₇ O	83.0497	0.98	0.0024
C ₄ H ₆ O	73.0653	0.98	0.0014
C ₂ H ₃ O	43.0184	0.97	0.0174
C ₆ H ₆	78.0470	0.96	0.0014
CH ₃ O	31.0184	0.95	0.0027
C ₂ H ₂	26.0156	0.95	0.0066
C ₃ H ₇ O	59.0497	0.95	0.0036
C ₂ H ₅ O	45.0340	0.94	0.0084
C ₃ H	37.0078	0.94	0.0008
C ₄ H ₂	50.0157	0.94	0.0009
C ₃ H ₃ O	55.0184	0.94	0.0072
CHO	29.0027	0.93	0.0103
C ₄ H ₄	52.0313	0.93	0.0012
C ₂ H ₅ O ₂	61.0289	0.93	0.0007
C ₃ H ₆ O	58.0419	0.93	0.0118
C ₃ H ₄ O	56.0262	0.93	0.0010
C ₅ H ₅ O	81.0340	0.92	0.0010
C ₄ H ₅	53.0391	0.92	0.0074
C ₃ H ₄	40.0313	0.92	0.0041
C ₅ H ₁₀ O	86.0732	0.92	0.0005
C ₅ H ₁₁ O	87.0810	0.92	0.0005
C ₉ H ₇	115.0550	0.92	0.0006
C ₄ H ₆ O	70.0419	0.92	0.0019
C ₂ H ₄ O	44.0262	0.92	0.0167
C ₆ H ₈	80.0626	0.92	0.0013
C ₃ H ₂	38.0157	0.91	0.0020
C ₂ H ₃	27.0235	0.91	0.0390
C ₅ H ₅	65.0391	0.91	0.0020
C ₆ H ₁₁ O	99.0810	0.91	0.0015
C ₄ H ₇ O	71.0497	0.91	0.0089
C ₃ H ₃	39.0235	0.91	0.0271
C ₄ H ₃	51.0235	0.91	0.0016
C ₃ H ₅ O	57.0340	0.90	0.0158

* Early Oxidation MS-Condensation MS)/Condensation MS

carboxylic acid formation or aldehyde/ketone and alcohol addition. With the aid of the PMF results, the experimental data displayed on the Van Krevelen diagram can be broken down into contributions from different types of functionality.

Size-dependent composition was utilized to determine the extent of wall-loss deposition affecting factors 1 and 2. The wall deposition contributed differently to each factor, but does not entirely explain the factor mass decrease; the decrease unexplained by wall loss deposition is attributed to chemical aging of the aerosol.

The chamber photooxidation HR-ToF-AMS PMF results facilitate the interpretation of SOA chemical and physical processes by linking the bulk AMS aerosol composition data to molecular level information provided by CIMS and MOVI-HRToF-CIMS measurements.

Appendix A

SOA formation from a single source in a laboratory is characterized by smooth aerosol growth (Fig. A1); the well-behaved nature of ion signals and their associated errors is ideal for application of PMF. The size of the organic signal input matrix for PMF of experiment 2 in Table 1 is 1050 × 325. The columns of the matrix correspond to individual identified ions. High resolution stick intensities for identified ions at fractional *m/z*'s from 12–300 were used. AMS ion identification in the *m/z* 101–300 range was aided by the dodecane low-NO_x chemical mechanism, CIMS gas-phase measurements, and MOVI-CIMS aerosol measurements. Not all of the individual ions identified were included in PMF analysis, due to *S/N* constraints.

The ions included in PMF analysis and the solution justification are discussed here. The organic matrix was calculated using PIKA's "Open" minus "Closed" option for high-resolution ions with an average signal-to-noise ratio (*S/N*) greater than 0.2. Signals with a *S/N* between 0.2 and 2 were down-weighted by a factor of 3, as recommended by Paatero and Hopke (2003). The error matrix was calculated in PIKA in the standard way using "Open" minus "Closed" errors. The errors (σ) normalize the residuals (e) for the minimization function routine of PMF, Q ; therefore, good quantification of errors is needed. For an input matrix of $n \times m$, the PMF minimization function from Ulbrich et al. (2009), is:

$$Q = \sum_{i=1}^n \sum_{j=1}^m (e_{ij} / \sigma_{ij})^2 \quad (\text{A1})$$

Careful consideration was given when choosing the ions for PMF. Even though the ion may appear to be present in the ion fitting window in PIKA, sometimes the time trend of this ion is too noisy for PMF. Noisiness in the time trend can be introduced when there are: (a) ions that are in the shoulder of a larger ion at the same nominal mass (i.e., C₃H₃O₅⁺ is in the shoulder of the much larger ion C₈H₇O⁺ at *m/z* 119), (b) ions that are in the valley of two larger ions at the same nominal mass (i.e., the C₃H₇⁺ ion is in-between C₃H₃O₃⁺ and C₄H₇O₂⁺ at *m/z* 87), (c) ions that exhibit a strong signal in the closed spectra, but only a small signal in the difference spectra (i.e., C₁₀H₇⁺ at *m/z* 127), and/or (d) an ion is coincident with another ion that is expected to be there (i.e., the isotope of N₂⁺ ion and CHO⁺ ion are extremely close in exact mass). If ions like the ones mentioned above are included in PMF, then there is considerable noise in the time trend

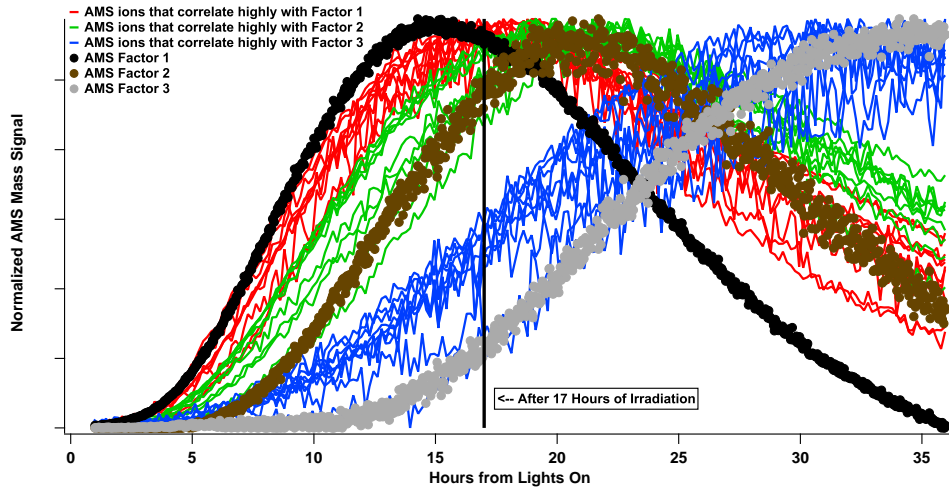


Fig. A1. Normalized mass signals from the AMS PMF factor time series are plotted with the AMS ions that have the highest correlations with those factors (ions listed in Table 3).

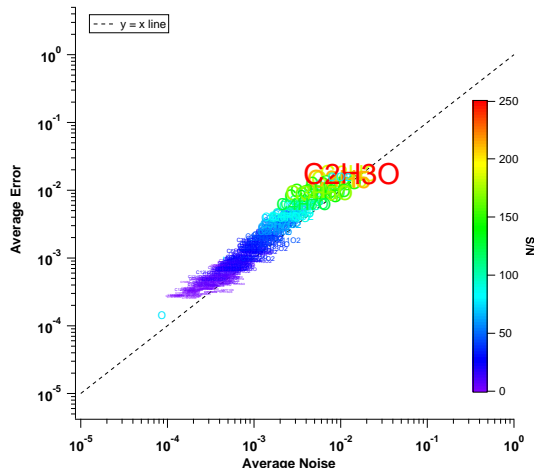


Fig. A2. Average error vs. the average noise for each ion is plotted along with the $y = x$ line. The marker is labeled by the ion it represents and is colored and sized by the S/N ratio of that ion. If the marker lies directly on the $y = x$ line, this means the calculated errors have captured the noise in the ion signal, which is critical for PMF analysis.

of Q/Q_{expected} . This noisiness results from peak fitting ions that experience large interference from other (often larger) ions, and should not be considered for PMF. An effective diagnostic to determine which ions to exclude from PMF is to calculate the S/N of each ion using the errors generated in PIKA (S/N_{error}), and then compare that to the S/N using the

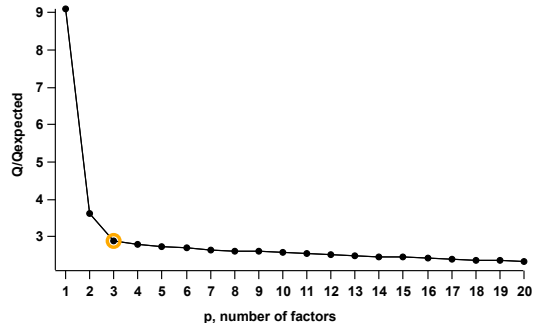


Fig. A3. Q/Q_{exp} vs. p , number of factors. The solution chosen is highlighted by the yellow circle.

observed noise (S/N_{noise}). The observed noise is calculated by smoothing the data using the binomial smoothing function in Igor (order of smoothing is chosen by user) and then subtracting the data from the smoothed data at each time point. Since the equation for errors in PIKA does not consider noise introduced by ion fitting (in the a., b., c., and d. scenarios described above), the S/N_{noise} is a good way to assess how well the ion is quantified. If S/N_{error} is much different than the S/N_{noise} , then either the ion should not be fit because it is a minor ion, or it is an ion described by a., b., c., or d. above, and should be removed from PMF analysis. Figure A2 shows the time-averaged error vs. time-averaged noise for each ion. The marker is labeled by the ion it represents and is sized and colored by its S/N . A marker lying on the $y = x$ line means that the calculated errors in PIKA captured the noisiness of

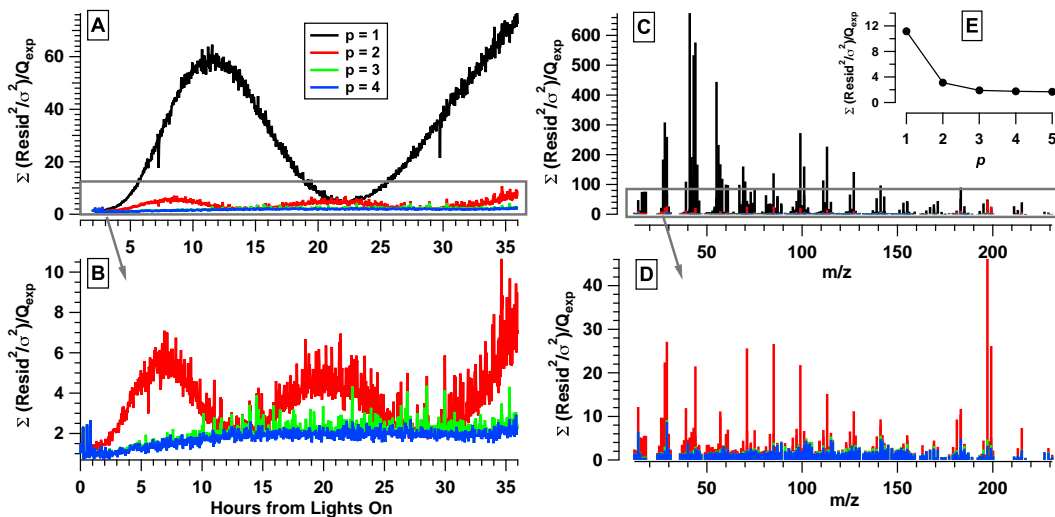


Fig. A4. The ratio of Q/Q_{expected} for $p = 1, 2, 3$, and 4 is used as a diagnostic in determining the number of factors in PMF analysis. Time series trend of Q/Q_{expected} for $p = 1$ through $p = 4$ solutions (A) and (B) clearly show that at least three factors are needed to describe the solution. The difference between the $p = 3$ and 4 solutions is minor, with the $p = 4$ solution having the same trend as the $p = 3$, but with less noise. The Q/Q_{expected} at each m/z for $p = 1$ through $p = 4$ solutions and (C) and (D) show similar results, just for the m/z dependence. The overall time trend and m/z contributions to the Q/Q_{expected} at each factor are also presented (E).

the ion, which is essential for PMF analysis. The noisiness in the Q/Q_{expected} time trend results from some noisy ions that were selected to remain in the input PMF analysis because the time trend of the ions, albeit noisy, appears to contain useful time trend information. This must be decided by the user for each system analyzed with PMF. No smoothed or averaged data were used for PMF, albeit averaging is recommended for future chamber PMF studies (Paatero, 2012).

The optimization function, Q , for PMF involves the minimization of the scaled residual at each mass over time (Ulbrich et al., 2009). Figure A3 shows the initial decrease in Q/Q_{expected} with the addition of one factor from $p = 1$ to $p = 2$, which is expected for any data set with enough variability to run PMF. And then there is a slight decrease between $p = 2$ and $p = 3$. After $p = 3$, the decrease in Q/Q_{expected} is small and continues to decrease by the same amount with each increase in p and never flattens out. At $p = 3$, the solution has reached a point at which no additional information is gained in adding another factor. It is useful to remember that in PMF, the factor mass spectral profiles are constant, and so one has to assume that the same is true for the actual SOA. The numerous processes associated with continuous oxidation of the gas and aerosol phase may invalidate this assumption, and so this may be why the Q/Q_{expected} never flattens out. This behavior can make it difficult to select a solution. A good strategy is to examine how both specific ions and the majority of the ions are reconstructed by the fac-

torization and if individual high m/z ions (tracer ions) trend with each factor time series (see Fig. 8).

The time series of the sum of the residuals and the Q/Q_{expected} is also useful in determining a solution. Any major structure in either of these parameters would suggest that additional factors are needed to describe the data. Figure A4 shows these two parameters for the $p = 1, p = 2, p = 3$ and $p = 4$ solution for the all ion iteration of PMF. There is clear structure in both the $p = 1$ and $p = 2$ solutions, whereas the $p = 3$ and $p = 4$ solutions have a flat sum of residuals and a relatively flat and small Q/Q_{expected} . There is little difference between the $p = 3$ and $p = 4$ solutions, so the addition of another factor would not enhance the information learned from the factorization from a residual point of view. The reason why the Q/Q_{expected} has a slightly curved shape for both the $p = 3$ and $p = 4$ solutions arises from variability in the mass spectra that is beyond what is explained by the input noise. This may be a consequence of the composition of the aerosol becoming more complex, combined with the assumption of PMF that the factor must have a constant mass spectral profile (which does not hold with these systems).

Map plots were made for the $p = 2$ and $p = 3$ solutions (Figs. A5 and A6). In these plots, a red dot indicates the $\text{residual}_{ij} > \text{error}_{ij}$, a blue dot is where $\text{residual}_{ij} < -\text{error}_{ij}$, and a white dot is where $-\text{error}_{ij} < \text{residual}_{ij} < \text{error}_{ij}$. For a two factor solution (Fig. A5) there is clearly a non-random

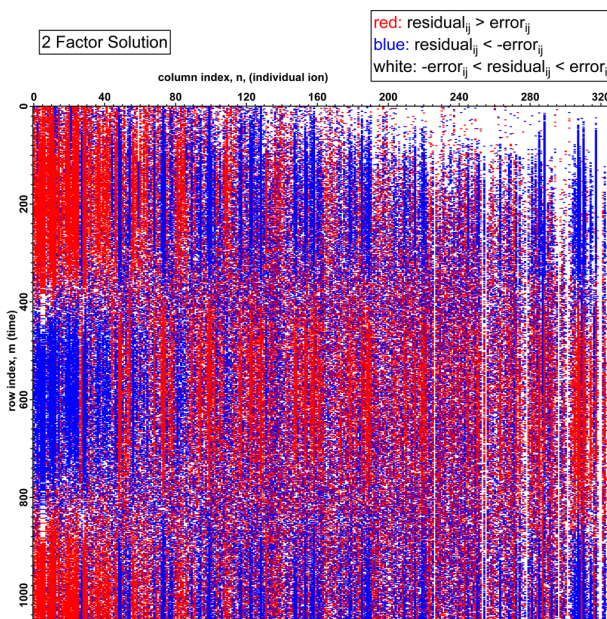


Fig. A5. The map plot for the two factor solution displays a red dot where the $\text{residual}_{ij} > \text{error}_{ij}$, a blue dot where $\text{residual}_{ij} < -\text{error}_{ij}$, and a white dot where $-\text{error}_{ij} < \text{residual}_{ij} < \text{error}_{ij}$. For a two-factor solution there is clearly a non-random pattern, indicating two factors do not adequately describe the data.

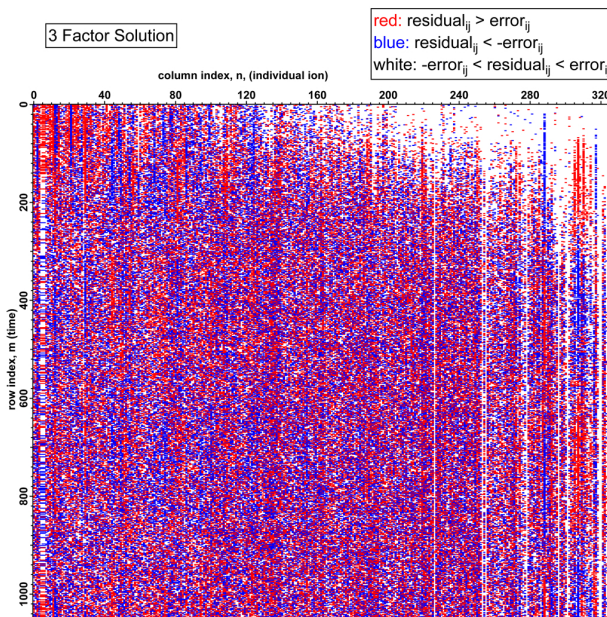


Fig. A6. The map plot, as described in Fig. A5 is shown for 3 factors. The pattern is random, indicating 3 factors describe the data variation well.

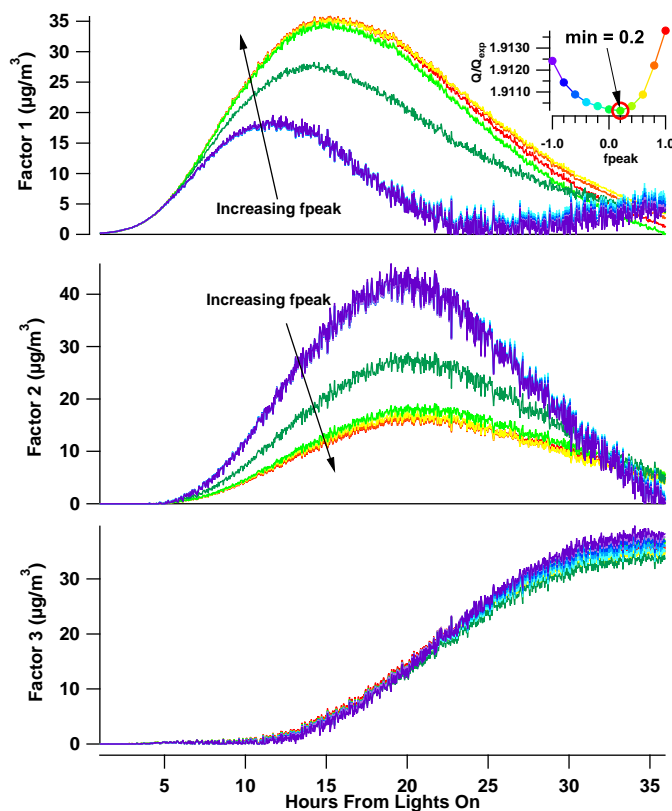


Fig. A7. The change in f_{peak} affects factors 1 and 2 more than factor 3. The increase in factor 1 explains the decrease in factor 2 when f_{peak} changes from 0 to 1. The same effect occurs when the f_{peak} changes from 0 to -1. There is a small change in factor 3, but overall trend and magnitude remain the same for factor 3. The minimum in Q is associated with an f_{peak} of 0.2.

pattern, whereas for the 3 factor solution (Fig. A6), the pattern is random. This further supports a three factor solution.

The solution was chosen by running several iterations of PMF on the same dataset. As explained by Ulbrich et al. (2009), the PMF solution can be systematically explored by varying p , the factor number, and two other parameters, the seeds and the f_{peaks} . The 3-factor solution was uniform across many seeds, but not across f_{peaks} . Figure A7 shows the effect of f_{peak} for the three factor solution. Factor 3 shows little difference for varying solutions, however factors 1 and 2 seem to trade off mass between the different types of solutions. The minimum of Q/Q_{expected} which occurs at $f_{\text{peak}} = 0.2$ (see inset of Fig. A7) was chosen as the solution. This solution had good agreement with the time series comparison with high m/z HR-ToF-AMS molecular ion tracers (Fig. 8) and with the CIMS and MOVI-HRTof-CIMS measurements (Fig. 10). However, as emphasized by Ulbrich et al. (2009), f_{peak} does not explore all possible rotations (Paatero et al., 2002). In the current experiment, it is possible

that factor 1 time trend goes to zero, however, as indicated by the positive f_{peaks} (Fig. A7), the factor 1 decrease could also taper toward the end of 34 h and perhaps not reach zero. A longer experiment may have clarified this ambiguity, and/or comparison with aerosol molecular-level information out at this time range. If an external comparison (i.e. MOVI-CIMS molecular trace) for factor 1 did not go to zero, then it would be necessary to pull up the last few elements of the time trend of factor 1. If the increase in factor 1 at the end of the experiment did not increase Q too intensely, then the desired rotation would have been found (Paatero, 2012). Although not reported here, a full exploration of rotational ambiguity requires induced rotations, such as the example just described, by explicitly pulling individual factor elements in desired directions. For PMF2, this is described in Paatero et al. (2002).

The solution of PMF will only be as descriptive as the data matrix itself. In a chamber experiment, the initial mass spectra reflect the chemistry of early aerosol formation and are not necessarily the same as those later in the oxidation.

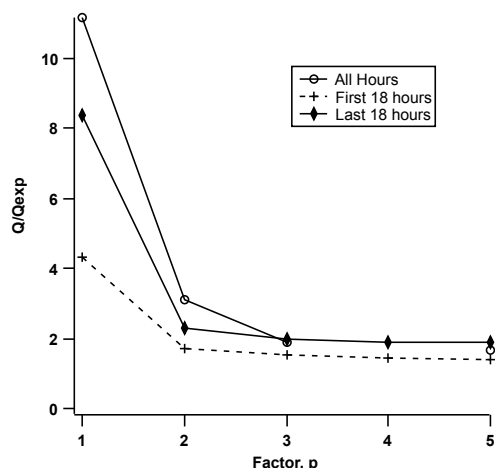


Fig. A8. Q/Q_{exp} vs. p for 3 types of solutions.

Figure A8 shows the Q/Q_{expected} versus factor number, p , for the 1 seed solution from experiment 2 for “all h”, “first 18 h”, and the “last 18 h”. For the 1 factor solution ($p = 1$), the “first 18 h” solution has the lowest Q/Q_{expected} , the “all h” solution has the highest Q/Q_{expected} , and the “last 18 h” is in between. This trend is the same for $p = 2$. The first 18 h solution is lower than the last 18 h because chemically the mass spectra are less complex at the beginning of the experiment, and $p = 1$ or $p = 2$ describes much of the data (there is less variability earlier on, in comparison to the full 34 h solution). As the oxidation progresses, the aerosol composition becomes more complex, as higher m/z oxygen-containing ions appear in the mass spectra, in addition to those observed at initial aerosol growth. For the same Q/Q_{expected} value, the last 18 h (and all h) requires more factors to describe the data to the same degree as the “first 18 h”. Three factors best describe the “all h” solution and the “last 18 h” solution since the third factor grows in at about 18 h. The “first 18 h” solution, would not “see” this third factor (since it covers only the first 18 h), so only 2 factors are necessary to describe the variability in the input data matrix.

Acknowledgements. This work was supported by US Department of Energy grant DE-SC 000 6626. Analysis of the MOVI-HRToF-CIMS data is supported by a grant to J. A. T. from the US Department of Energy (DOE-ER65318).

Edited by: M. C. Facchini

References

Aiken, A. C., DeCarlo, P. F., Kroll, J. H., Worsnop, D. R., Huffman, J. A., Docherty, K. S., Ulbrich, I. M., Mohr, C., Kimmel, J. R., Sueper, D., Sun, Y., Zhang, Q., Trimborn, A., Northway, M., Ziemann, P. J., Canagaratna, M. R., Onasch, T. B., Alfarra, M. R., Prevot, A. S. H., Dommen, J., Duplissy, J., Metzger, A., Baltensperger, U., and Jimenez, J. L.: O/C and OM/OC Ratios of Primary, Secondary, and Ambient Organic Aerosols with High-Resolution Time-of-Flight Aerosol Mass Spectrometry, *Environ. Sci. Technol.*, 42, 4478–4485, 2008.

Aiken, A. C., Salcedo, D., Cubison, M. J., Huffman, J. A., DeCarlo, P. F., Ulbrich, I. M., Docherty, K. S., Sueper, D., Kimmel, J. R., Worsnop, D. R., Trimborn, A., Northway, M., Stone, E. A., Schauer, J. J., Volkamer, R. M., Fortner, E., de Foy, B., Wang, J., Laskin, A., Shutthanandan, V., Zheng, J., Zhang, R., Gaffney, J., Marley, N. A., Paredes-Miranda, G., Arnott, W. P., Molina, L. T., Sosa, G., and Jimenez, J. L.: Mexico City aerosol analysis during MILAGRO using high resolution aerosol mass spectrometry at the urban supersite (T0) – Part 1: Fine particle composition and organic source apportionment, *Atmos. Chem. Phys.*, 9, 6633–6653, doi:10.5194/acp-9-6633-2009, 2009.

Allan, J. D.: Quantitative sampling using an Aerodyne aerosol mass spectrometer 1. Techniques of data interpretation and error analysis, *J. Geophys. Res.*, 108, 4090, doi:10.1029/2002JD002358, 2003.

Allan, J. D., Delia, A. E., Coe, H., Bower, K. N., Alfarra, M. R., Jimenez, J. L., Middlebrook, A. M., Drewnick, F., Onasch, T. B., Canagaratna, M. R., Jayne, J. T., and Worsnop, D. R.: A generalised method for the extraction of chemically resolved mass spectra from Aerodyne aerosol mass spectrometer data, *J. Aerosol Sci.*, 35, 909–922, 2004.

Chhabra, P. S., Flagan, R. C., and Seinfeld, J. H.: Elemental analysis of chamber organic aerosol using an aerodyne high-resolution aerosol mass spectrometer, *Atmos. Chem. Phys.*, 10, 4111–4131, doi:10.5194/acp-10-4111-2010, 2010.

Chhabra, P. S., Ng, N. L., Canagaratna, M. R., Corrigan, A. L., Russell, L. M., Worsnop, D. R., Flagan, R. C., and Seinfeld, J. H.: Elemental composition and oxidation of chamber organic aerosol, *Atmos. Chem. Phys.*, 11, 8827–8845, doi:10.5194/acp-11-8827-2011, 2011.

Cocker, D. R., Flagan, R. C., and Seinfeld, J. H.: State-of-the-Art Chamber Facility for Studying Atmospheric Aerosol Chemistry, *Environ. Sci. Technol.*, 35, 2594–2601, 2001.

Crounse, J. D., McKinney, K. A., Kwan, A. J., and Wennberg, P. O.: Measurement of Gas-Phase Hydroperoxides by Chemical Ionization Mass Spectrometry, *Anal. Chem.*, 78, 6726–6732, 2006.

DeCarlo, P. F., Kimmel, J. R., Trimborn, A., Northway, M. J., Jayne, J. T., Aiken, A. C., Gonin, M., Fuhrer, K., Horvath, T., Docherty, K. S., Worsnop, D. R., and Jimenez, J. L.: Field-Deployable, High-Resolution, Time-of-Flight Aerosol Mass Spectrometer, *Anal. Chem.*, 78, 8281–8289, 2006.

Fraser, R. T. M., Paul, N. C., and Phillips, L.: Mass spectrometry of some alkyl peroxides, *J. Chem. Soc. B*, 1970, 1278–1280, doi:10.1039/J29700001278, 1970.

Fry, J. L., Kiendler-Scharr, A., Rollins, A. W., Brauers, T., Brown, S. S., Dorn, H.-P., Dubé, W. P., Fuchs, H., Mensah, A., Rohrer, F., Tillmann, R., Wahner, A., Wooldridge, P. J., and Cohen, R. C.: SOA from limonene: role of NO_3 in its generation and degradation, *Atmos. Chem. Phys.*, 11, 3879–3894, doi:10.5194/acp-11-

3879–2011, 2011.

Heald, C. L., Kroll, J. H., Jimenez, J. L., Docherty, K. S., DeCarlo, P. F., Aiken, A. C., Chen, Q., Martin, S. T., Farmer, D. K., and Artaxo, P.: A simplified description of the evolution of organic aerosol composition in the atmosphere, *Geophys. Res. Lett.*, **37**, L08803, doi:10.1029/2010GL042737, 2010.

Hersey, S. P., Craven, J. S., Schilling, K. A., Metcalf, A. R., Sorooshian, A., Chan, M. N., Flagan, R. C., and Seinfeld, J. H.: The Pasadena Aerosol Characterization Observatory (PACO): chemical and physical analysis of the Western Los Angeles basin aerosol, *Atmos. Chem. Phys.*, **11**, 7417–7443, doi:10.5194/acp-11-7417-2011, 2011.

Isaacman, G., Chan, A. W. H., Nah, T., Worton, D. R., Ruehl, C. R., Wilson, K. R., and Goldstein, A. H.: Heterogeneous OH Oxidation of Motor Oil Particles Causes Selective Depletion of Branched and Less Cyclic Hydrocarbons, *Environ. Sci. Technol.*, **46**, 10632–10640, 2012.

Jimenez, J. L., Canagaratna, M. R., Donahue, N. M., Prévôt, A. S. H., Zhang, Q., Kroll, J. H., DeCarlo, P. F., Allan, J. D., Coe, H., Ng, N. L., Aiken, A. C., Docherty, K. S., Ulbrich, I. M., Grieshop, A. P., Robinson, A. L., Duplissy, J., Smith, J. D., Wilson, K. R., Lanz, V. A., Hueglin, C., Sun, Y. L., Tian, J., Laaksonen, A., Raatikainen, T., Rautiainen, J., Vaattovaara, P., Ehn, M., Kulmala, M., Tomlinson, J. M., Collins, D. R., Cubison, M. J., E., Dunlea, J., Huffman, J. A., Onasch, T. B., Alfarra, M. R., Williams, P. I., Bower, K., Kondo, Y., Schneider, J., Drewnick, F., Borrmann, S., Weimer, S., Demerjian, K., Salcedo, D., Cottrell, L., Griffin, R., Takami, A., Miyoshi, T., Hatakeyama, S., Shimono, A., Sun, J. Y., Zhang, Y. M., Dzepina, K., Kimmel, J. R., Sueper, D., Jayne, J. T., Herndon, S. C., Trimborn, A. M., Williams, L. R., Wood, E. C., Middlebrook, A. M., Kolb, C. E., Baltensperger, U., and Worsnop, D. R.: Evolution of Organic Aerosols in the Atmosphere, *Science*, **326**, 1525–1529, 2009.

Lambe, A. T., Onasch, T. B., Massoli, P., Croasdale, D. R., Wright, J. P., Aherne, A. T., Williams, L. R., Worsnop, D. R., Brune, W. H., and Davidovits, P.: Laboratory studies of the chemical composition and cloud condensation nuclei (CCN) activity of secondary organic aerosol (SOA) and oxidized primary organic aerosol (OPOA), *Atmos. Chem. Phys.*, **11**, 8913–8928, doi:10.5194/acp-11-8913-2011, 2011.

Lambe, A. T., Onasch, T. B., Croasdale, D. R., Wright, J. P., Martin, A. T., Franklin, J. P., Massoli, P., Kroll, J. H., Canagaratna, M. R., Brune, W. H., Worsnop, D. R., and Davidovits, P.: Transitions from Functionalization to Fragmentation Reactions of Laboratory Secondary Organic Aerosol (SOA) Generated from the OH Oxidation of Alkane Precursors, *Environ. Sci. Technol.*, **46**, 5430–5437, 2012.

Lanz, V. A., Alfarra, M. R., Baltensperger, U., Buchmann, B., Hueglin, C., and Prévôt, A. S. H.: Source apportionment of sub-micron organic aerosols at an urban site by factor analytical modelling of aerosol mass spectra, *Atmos. Chem. Phys.*, **7**, 1503–1522, doi:10.5194/acp-7-1503-2007, 2007.

Loza, C. L., Chhabra, P. S., Yee, L. D., Craven, J. S., Flagan, R. C., and Seinfeld, J. H.: Chemical aging of *m*-xylene secondary organic aerosol: laboratory chamber study, *Atmos. Chem. Phys.*, **12**, 151–167, doi:10.5194/acp-12-151-2012, 2012.

Ng, N. L., Canagaratna, M. R., Zhang, Q., Jimenez, J. L., Tian, J., Ulbrich, I. M., Kroll, J. H., Docherty, K. S., Chhabra, P. S., Bahreini, R., Murphy, S. M., Seinfeld, J. H., Hildebrandt, L., Donahue, N. M., DeCarlo, P. F., Lanz, V. A., Prévôt, A. S. H., Dinar, E., Rudich, Y., and Worsnop, D. R.: Organic aerosol components observed in Northern Hemispheric datasets from Aerosol Mass Spectrometry, *Atmos. Chem. Phys.*, **10**, 4625–4641, doi:10.5194/acp-10-4625-2010, 2010.

Ng, N. L., Canagaratna, M. R., Jimenez, J. L., Chhabra, P. S., Seinfeld, J. H., and Worsnop, D. R.: Changes in organic aerosol composition with aging inferred from aerosol mass spectra, *Atmos. Chem. Phys.*, **11**, 6465–6474, doi:10.5194/acp-11-6465-2011, 2011.

Paatero, P.: Interactive comment on *Atmos. Chem. Phys. Discuss.*, **12**, 16647, 2012.

Paatero, P. and Hopke, P. K.: Discarding or downweighting high-noise variables in factor analytic models, *Anal. Chim. Acta*, **490**, 277–289, 2003.

Paatero, P. and Tapper, U.: Positive Matrix Factorization – a Nonnegative Factor Model with Optimal Utilization of Error-Estimates of Data Values, *Environmetrics*, **5**, 111–126, 1994.

Paatero, P., Hopke, P. K., Song, X. H., and Ramadan, Z.: Understanding and controlling rotations in factor analytic models, *Chemometr. Intell. Lab.*, **60**, 253–264, 2002.

Paulot, F., Crouse, J. D., Kjaergaard, H. G., Kroll, J. H., Seinfeld, J. H., and Wennberg, P. O.: Isoprene photooxidation: new insights into the production of acids and organic nitrates, *Atmos. Chem. Phys.*, **9**, 1479–1501, doi:10.5194/acp-9-1479-2009, 2009.

Pye, H. O. T. and Pouliot, G. A.: Modeling the Role of Alkanes, Polycyclic Aromatic Hydrocarbons, and Their Oligomers in Secondary Organic Aerosol Formation, *Environ. Sci. Technol.*, **46**, 6041–6047, 2012.

Schauer, J. J., Kleeman, M. J., Cass, G. R., and Simoneit, B. R. T.: Measurement of Emissions from Air Pollution Sources. 3. C1–C29 Organic Compounds from Fireplace Combustion of Wood, *Environ. Sci. Technol.*, **35**, 1716–1728, 2001.

Schauer, J. J., Kleeman, M. J., Cass, G. R., and Simoneit, B. R. T.: Measurement of Emissions from Air Pollution Sources. 5. C1–C32 Organic Compounds from Gasoline-Powered Motor Vehicles, *Environ. Sci. Technol.*, **36**, 1169–1180, 2002.

St. Clair, J. M., McCabe, D. C., Crouse, J. D., Steiner, U., and Wennberg, P. O.: Chemical ionization tandem mass spectrometer for the in situ measurement of methyl hydrogen peroxide, *Rev. Sci. Instrum.*, **81**, 094102, doi:10.1063/1.3480552, 2010.

Tobias, H. J. and Ziemann, P. J.: Thermal Desorption Mass Spectrometric Analysis of Organic Aerosol Formed from Reactions of 1-Tetradecene and O₃ in the Presence of Alcohols and Carboxylic Acids, *Environ. Sci. Technol.*, **34**, 2105–2115, 2000.

Ulbrich, I. M., Canagaratna, M. R., Zhang, Q., Worsnop, D. R., and Jimenez, J. L.: Interpretation of organic components from Positive Matrix Factorization of aerosol mass spectrometric data, *Atmos. Chem. Phys.*, **9**, 2891–2918, doi:10.5194/acp-9-2891-2009, 2009.

Van Krevelen, D. W.: Graphical-statistical method for the study of structure and reaction processes of coal, *Fuel*, **24**, 269–284, 1950.

Yatavelli, R. L. N. and Thornton, J. A.: Particulate Organic Matter Detection Using a Micro-Orifice Volatilization Impactor Coupled to a Chemical Ionization Mass Spectrometer (MOVI-CIMS), *Aerosol Sci. Tech.*, **44**, 61–74, 2010.

Yatavelli, R. L. N., Lopez-Hilfiker, F. D., Wargo, J., Kimmel, J. R., Cubison, M. J., Bertram, T. H., Jimenez, J. J., Gonin, M., Worsnop, D. R., and Thornton, J. A.: Analysis of Gas and Particle-phase

Organic Matter Using a Chemical Ionization High-Resolution Time-of-Flight Mass Spectrometer (HTOF-CIMS) Coupled to a Micro Orifice Volatilization Impactor (MOVI), *Aerosol Sci. Tech.*, 46, 1313–1327, doi:10.1080/02786826.2012.712236, 2012.

Yee, L. D., Craven, J. S., Loza, C. L., Schilling, K. A., Ng, N. L., Canagaratna, M. R., Ziemann, P. J., Flagan, R. C., and Seinfeld, J. H.: Secondary Organic Aerosol Formation from Low-NO_x Photooxidation of Dodecane: Evolution of Multi-Generation Gas-Phase Chemistry and Aerosol Composition, *J. Phys. Chem. A*, 116, 6211–6230, 2012.

Zhang, Q., Jimenez, J. L., Canagaratna, M. R., Ulbrich, I. M., Ng, N. L., Worsnop, D. R., and Sun, Y.: Understanding atmospheric organic aerosols via factor analysis of aerosol mass spectrometry: a review, *Anal. Bioanal. Chem.*, 401, 3045–3067, 2011.

Ziemann, P. J.: Formation of Alkoxyhydroperoxy Aldehydes and Cyclic Peroxyhemiacetals from Reactions of Cyclic Alkenes with O₃ in the Presence of Alcohols, *J. Phys. Chem. A*, 107, 2048–2060, 2003.

Chapter 5

Effect of chemical structure on secondary organic aerosol formation from C₁₂ alkanes¹

¹This chapter has been prepared for submission to *Atmospheric Chemistry and Physics*

Manuscript prepared for Atmos. Chem. Phys.
 with version 4.2 of the L^AT_EX class *copernicus.cls*.
 Date: 4 April 2013

Effect of chemical structure on secondary organic aerosol formation from C₁₂ alkanes

L. D. Yee¹, J. S. Craven², C. L. Loza², K. A. Schilling², N. L. Ng³, M. R. Canagaratna⁴, P. J. Ziemann⁵, R. C. Flagan^{2,1}, and J. H. Seinfeld^{2,1}

¹Division of Engineering and Applied Science, California Institute of Technology, Pasadena, CA, USA

²Division of Chemistry and Chemical Engineering, California Institute of Technology, Pasadena, CA, USA

³School of Chemical and Biomolecular Engineering and School of Earth and Atmospheric Sciences, Georgia Institute of Technology, Atlanta, Georgia

⁴Aerodyne Research, Inc., Billerica, Massachusetts

⁵Air Pollution Research Center, Department of Environmental Sciences, and Environmental Toxicology Graduate Program, University of California, Riverside, California

Correspondence to: J. H. Seinfeld
 (seinfeld@caltech.edu)

Abstract. The SOA formation from four C₁₂ alkanes (*n*-dodecane, 2-methylundecane, hexylcyclohexane, and cyclododecane) is studied in the Caltech Environmental Chamber under low-NO_x conditions, in which the principal fate of the peroxy radical formed in the initial OH reaction is re-

action with HO₂. Simultaneous gas- and particle-phase measurements elucidate the effect of alkane structure on the chemical mechanisms underlying SOA growth. Reaction of branched structures leads to fragmentation and more volatile products, while cyclic structures are subject to faster oxidation and lead to less volatile products. Product identifications reveal that particle-phase reactions involving peroxyhemiacetal formation from several multi-functional hydroperoxide species initiate SOA growth in all four systems. The continued chemical evolution of the particle-phase is structure-dependent, with 2-methylundecane SOA formation exhibiting the least extent of chemical processing and cyclododecane SOA achieving sustained growth with the greatest variety of chemical pathways. The extent of chemical development is not necessarily reflected in the oxygen to carbon (O:C) ratio of the aerosol as cyclododecane achieves the lowest O:C, just above 0.2, by the end of the experiment and hexylcyclohexane the highest, approaching 0.35.

15 1 Introduction

Long-chain alkanes constitute a significant component of the unresolved complex mixture (UCM) in motor vehicle fuel sources and its combustion products (Schauer et al., 1999, 2002) and are a potential source of atmospheric secondary organic aerosol (SOA) formation (Robinson et al., 2007).

However, the extent of SOA formation from atmospheric alkane photooxidation remains uncertain
 20 (Bahreini et al., 2012; Gentner et al., 2012). Each fuel type (e.g. gasoline vs. diesel) has different distributions of alkane chain length and structure in terms of straight-chain, branched, cyclic, and cyclic + branched conformations (Schauer et al., 1999, 2002; Isaacman et al., 2012; Gentner et al., 2012). This variety in structure leads to chemical differences in the processes leading to SOA formation, which have been the subject of extensive laboratory studies (Lim and Ziemann, 2005; Lipsky and Robinson, 2006; Lim and Ziemann, 2009a,b,c; Presto et al., 2009, 2010; Nakao et al., 2011; Lambe et al., 2012; Tkacik et al., 2012) and modeling efforts (Jordan et al., 2008; Pye and Pouliot, 2012; Zhang and Seinfeld, 2012; Cappa et al., 2013).

Gas-phase chemical mechanisms for the OH-initiated oxidation of alkanes in the presence of NO_x have been studied (Atkinson, 1994, 1997; Atkinson and Arey, 2003; Atkinson et al., 2008).
 30 Many aspects of key particle-phase reactions for these species have also been explored (Aschmann et al., 2003; Dibble, 2007; Lim and Ziemann, 2009c). The prevailing level of NO_x is fundamental in atmospheric oxidation chemistry, as it controls, among other steps, the fate of the alkyl peroxy radical (RO₂) formed in the initial OH-organic reaction. The designation, high- and low-NO_x, refer to conditions in which the RO₂ fate is predominantly RO₂ + NO and RO₂ + HO₂, respectively.
 35 These cases represent idealizations of actual atmospheric conditions, but they allow isolation of the mechanistic pathways leading to SOA formation in the two cases.

We focus here on the low-NO_x oxidation mechanisms of four C₁₂ alkanes (*n*-dodecane, 2-methylundecane, hexylcyclohexane, and cyclododecane) (Table 1). The C₁₂ alkane system is a prototype for relatively long alkanes, which are characterized by side chains and cyclic structure in addition to a linear structure.
 40 The distribution of oxidation products comprise a variety of functionalizations (hydroperoxy, hydroxyl, ketone, aldehyde, carboxylic acid, and peracid). Detailed study of the C₁₂ system affords insight into the effect of alkane structure on SOA composition and yield.

This study builds on the previous work on the *n*-dodecane low-NO_x system (Yee et al., 2012; Craven et al., 2012) employing complementary gas- (chemical ionization mass spectrometry) and
 45 particle-phase measurements (Aerodyne high-resolution time-of-flight aerosol mass spectrometry). We focus on the effect of alkane structure on the multi-generation gas-phase oxidation and particle-phase chemistry that leads to SOA formation. Of special interest is the identification of and incorporation of multi-functional hydroperoxides in the aerosol via accretion reactions in the form of peroxyhemiacetal (PHA) formation as well as the chemical evolution of the aerosol as it ages.

50 2 Experimental Section

2.1 Chamber experiments

The experiments in this study were conducted using the experimental protocols and controls as discussed in Yee et al. (2012) and Craven et al. (2012). The experiments and conditions are given

in Table 2. The *n*-dodecane experiments are the same as those presented in Yee et al. (2012) and Craven et al. (2012), and are used here for additional analyses and comparisons to the other C₁₂ structures.

Experiments were conducted in the dual 28 m³ Caltech Environmental Chambers (Cocker et al., 2001; Keywood et al., 2004). The chambers were flushed for at least 24 h with dry purified air between experiments, resulting in particle number and volume concentrations < 100 cm⁻³ and < 0.1 μm³ cm⁻³, respectively. Particle number concentration and size distributions were measured using a coupled differential mobility analyzer (DMA, TSI model 3081) and condensation particle counter (TSI Model 3010). Hydroxyl radicals were generated by photolysis of H₂O₂. Experiments began with slow injection of 280 μL of a 50% aqueous H₂O₂ solution in a glass trap submerged in a warm water bath at 35-38 °C, via a 5 L min⁻¹ flow of pure air. The chamber was then seeded with atomized 0.015 M aqueous ammonium sulfate solution to achieve a target initial seed volume of ~ 10-15 μm cm⁻³. Subsequently, the hydrocarbon was injected by delivering the appropriate liquid volume or solid mass amount for the desired chamber concentration into a glass bulb, gently heating the glass bulb, and flowing 5 L min⁻¹ of pure air over the hydrocarbon until evaporation was complete.

Temperature (T), relative humidity (RH), and concentrations of O₃, NO, and NO_x were continuously monitored. Experiments were run at temperatures ranging from 23-26 °C after an initial rise from 20 °C upon irradiation. RH remained below 10% for all experiments except for the cyclododecane 36 h experiment in which RH rose to about 20% in the last six hours. NO levels remained below the 5 ppb_v lower detection limit of the analyzer (Horiba, APNA 360) and measured NO₂ levels remained below 7 ppb_v after irradiation began.

2.2 Gas- and particle-phase measurements

Hydrocarbon concentration was continuously monitored by GC-FID by taking 1.3 L samples of chamber air on Tenax adsorbent. The cartridge was loaded into the GC-FID (Agilent 6890N), desorbed, and injected onto an HP-5 column (15 m x 0.53 mm ID x 1.5 μm thickness, Hewlett-Packard).

Gas-phase oxidation products were monitored using a Chemical Ionization Mass Spectrometer (CIMS), consisting of a custom-modified Varian 1200 triple quadrupole mass spectrometer (Crounse et al., 2006; Paulot et al., 2009; St. Clair et al., 2010). Briefly, the instrument was operated in negative mode with CF₃OOCF₃ reagent gas, generating cluster products from the analyte at [X · CF₃O]⁻ and F transfer products at [X · F]⁻. The cluster product tends to occur when the analyte, X, is a hydroperoxide or weakly acidic compound. The transfer product dominates for more strongly acidic compounds. Several carboxylic acids are present in both ionizations, and are therefore reported as the sum of the two products when used. The negative mode mass scan ranged from *m/z* 50-300. Positive mode ionization utilizes water as the reagent gas and results in ion clusters of the form [X · (H₂O)_n]⁺. The positive mode mass scan ranged from *m/z* 50-200.

90 Due to mid-project tuning shifts in the positive mode operation, the ions monitored were not those
 expected from the ionization of proposed products. The reported ions are those as monitored during
 the project, though the proposed ion assignments are reported taking the tuning shift into account. A
 back-calibration was performed to verify the shift in peak-centering, which typically resulted in an
 upwards shift by 5 amu in the range of 200-220 amu during positive mode operation. To distinguish
 95 between ions monitored in the different modes of the instrument a (+) or (-) is indicated in front of
 the m/z monitored for ions monitored in positive and negative mode operation, respectively.

100 An Aerodyne high-resolution time-of-flight aerosol mass spectrometer (DeCarlo et al., 2006),
 hereafter referred to as the AMS, was operated at 1 min resolution switching between the lower
 resolution, higher sensitivity “V-mode”, and the high-resolution “W-mode”. Data analysis and cal-
 ibrations were performed according to procedures previously described (Allan et al., 2004; Aiken
 et al., 2007, 2008; Canagaratna et al., 2007). HR-ToF-AMS data were processed with Squirrel, the
 ToF-AMS Unit Resolution Analysis Toolkit and PIKA (Peak Integration by Key Analysis, DeCarlo
 et al. (2006)), the high-resolution analysis software tool ([http://cires.colorado.edu/jimenez-group/](http://cires.colorado.edu/jimenez-group/ToFAMSResources/ToFSoftware/index.html)
 ToFAMSResources/ToFSoftware/index.html), in Igor Pro Version 6.22A (Wavemetrics, Lake Os-
 105 wego, OR). At the beginning of each experiment, an AMS sample was taken with a particle filter
 in-line to the chamber sample line to make corrections for air interferences (Allan et al., 2004). The
 adjustments to the fragmentation table proposed by Aiken et al. (2008) for organic mass at m/z 18
 and m/z 28 were included. Elemental ratios were calculated using the technique outlined by Aiken
 et al. (2007, 2008). The $C_2H_4^+$ ion at m/z 28 was not fit in PIKA due to strong interference from N_2^+ ,
 110 and was therefore not included in the elemental ratio calculations.

115 Photochemical simulations of each system were performed based on that of *n*-dodecane used in
 Yee et al. (2012) to further define the level of NO. An initial NO level of ≤ 1 ppb_v is consistent with
 $\leq 10\%$ of reactions of RO₂ being due to reaction with NO_x. This NO concentration is also consistent
 with the trends observed for NO_x-sensitive species such as the first generation hydroperoxide and
 the 1,4-hydroxycarbonyl. Multi-functional nitrate species in the CIMS spectra were not significant,
 supporting that the RO₂ + NO_x channels are not significant in these experiments.

3 SOA formation chemistry

3.1 Chemical mechanism leading to SOA formation

120 A generalized mechanism for the photooxidation of alkanes under low-NO_x conditions (i.e. RO₂
 reacts exclusively with HO₂) is presented in Figure 1. This scheme is based on the *n*-dodecane
 photooxidation mechanism developed in Yee et al. (2012) generalized to the C₁₂ structures studied
 here. R₁ and R₂ represent alkyl groups. In the case of *n*-dodecane, R₁ and R₂ are any straight-chain
 alkyl groups that sum to C₇H₁₆. For 2-methylundecane, R₁ and R₂ are also alkyl groups that make
 up C₇H₁₆, though one side contains a methyl branch at the number 2 carbon atom. For hexylcyclo-

125 hexane, R₁ is C₆H₅ and R₂ is CH₃. While the sites of oxidation are shown in the mechanism to occur between R₁ and R₂, oxidation can also occur on the R₁ and R₂ groups including the C₆H₅ ring in hexylcyclohexane. In the case of cyclododecane, R₁ and R₂ are bonded together, indicated as R in the sidebar denoted by an asterisk. Structures in a solid box indicate one isomer of a product identified by the CIMS in the gas phase or the AMS in the particle phase. Colors of boxes containing 130 compounds are consistent with those used when comparing trends of species in later plots within a compound system. Product names within the boxes will continue to be referenced in the following discussion, tables of identified products, and figures.

135 Photooxidation begins with H-abstraction by OH from the parent alkane (RH) to form an alkylperoxy radical (RO₂). Under the experimental conditions, the fate of the RO₂ radical is dominated by reaction with HO₂ radical ($\geq 90\%$), to form the 1st-generation hydroperoxide (ROOH). The hydroperoxide (ROOH) can then undergo reaction with OH (Channels 1 and 2) or photolysis (Channel 3). Along Channel 1, a 2nd-generation carbonyl (CARB) is formed, followed by continued oxidation to form a 3rd-generation carbonyl hydroperoxide (CARBROOH). This CARBROOH can also be generated via Channel 2, in which ROOH undergoes reaction with OH to generate a dihydroperoxide (DIROOH). In the case of Channel 1 where the carbonyl hydroperoxide forms such that the functional groups are on adjacent carbons (α -CARBROOH), photolysis of the hydroperoxy group (Channel 1a) results in formation of an aldehyde (ALD) and several <C₁₂ fragments: peracid (C_nPACID), carboxylic acid (C_nCARBACID), and hydroperoxides (C_nROOH).

140 Along Channel 2, the carbonyl hydroperoxide (CARBROOH) can undergo photolysis (Channel 2a) analogous to the reactions outlined in Channel 3, or react with OH (Channel 2b). Channels 2a and 2b both lead to higher functionalized products. There is potential for tri-functionalized compounds (not shown) to form, a hydroxy carbonyl hydroperoxide (OHCARBROOH) to be formed along Channel 2a and a dicarbonyl hydroperoxide (DICARBROOH) along Channel 2b. Additional oxidation (not shown) can lead to a tricarbonyl hydroperoxide (TRICARBROOH) and hydroxy di-145 carbonyl hydroperoxide (OHDICARBROOH). The carbonyl hydroperoxide (CARBROOH), has a pure liquid vapor pressure ranging from 6.14×10^{-9} to 6.6×10^{-8} atm depending on structure, as estimated using the EVAPORATION method (Compernolle et al., 2011). This intermediate volatility/semi-volatile organic is one of the first products that can partition to the particle phase, Channel 2c.

155 In Channel 3, photolysis of the 1st-generation hydroperoxide produces an alkoxy radical RO. The C₁₂ alkoxy radical will undergo 1,4-isomerization according to well-established mechanisms (Atkinson, 1997; Lim and Ziemann, 2005, 2009a,b). This results in the formation of a 1,4-hydroxy hydroperoxide (OHROOH) which has sufficiently low volatility to partition into the particle-phase or undergo reaction with OH or photolyze to generate a 1,4-hydroxy carbonyl (OHCARB). The 160 1,4-hydroxy carbonyl is known to undergo cyclization under an acid-catalyzed process on the particle surface to generate a cyclic hemiacetal (CHA) and dehydrate to form a dihydrofuran (DHF),

which can then return to the gas phase to become further oxidized (Aschmann et al., 2003; Lim and Ziemann, 2009c).

In the case of cyclododecane where the ring strain is high enough (Benson, 1976; Lim and Ziemann, 2009a), the alkoxy radical can decompose to generate an aldehydic alkyl radical and a hydroperoxy aldehyde according to the starred scheme to the side (Figure 1). Though a C₆ ring is not considered to have ring strain (Benson, 1976; Lim and Ziemann, 2009a), hexylcyclohexane may also undergo ring opening in an analogous process depending on the extent and position of functionalization on the ring and its alkyl chain during continued oxidation. By structure activity estimations (Kwok and Atkinson, 1995), initial H-absraktion by OH should primarily take place at the secondary carbons over the branching point in an approximate 80% to 20% ratio. Continued oxidation will tend to favor these secondary carbon sites over the branching point, though eventually fragmentation may be induced.

Several multi-functional hydroperoxides can potentially react with the aldehydes generated in Channel 1a to form peroxyhemiacetals. The carbonyl hydroperoxide PHA (CARBROOHPHA) is explicitly shown in the mechanisms (Figures 1 and 2, Scheme 1), and was proposed as a key component of the initial SOA growth in the case of *n*-dodecane (Yee et al., 2012). Multi-functional PHAs are represented generally in Figure 1, where Y is any functional group (-hydroxyl, -carbonyl, -hydroperoxy). The more explicit representation of expected higher functionalized products along Channel 2, and their potential to form PHAs is represented along the right-hand side of Figure 2. One isomer is shown with the expected functionalization. PHA formation from DIROOH (Figure 1, Channel 2) and OHROOH (Figure 1, Channel 3) is not explicitly shown since these tracer ions are relatively small signals compared to those of other multi-functional hydroperoxides in the AMS. Of note is the potential to generate a 2nd-generation C₁₂ hydroperoxy aldehyde in the case of cyclododecane, which is a likely candidate for participating in peroxyhemiacetal formation. Under Channels 1 and 2, the CARBROOH is a 3rd-generation product, though continued reaction with OH in these channels may compete with one generation of OH reaction and photolysis to form the hydroperoxy aldehyde.

3.2 Gas- and particle-phase product identification using CIMS and AMS

Ions monitored by the CIMS and the AMS and their proposed compound assignments by system are presented in Tables 3-7. Note that because hexylcyclohexane and cyclododecane differ by one degree of unsaturation from that of 2-methylundecane and *n*-dodecane, many of the ions monitored across sytems for analogous products differ by just 2 amu.

3.2.1 Gas-phase mechanism comparison

Assuming that the CIMS sensitivity to certain functionalized species within the same mode of operation are comparable despite difference in structure (straight, branched, cyclic + branched, cyclic),

comparisons of the several analogous gas-phase species help elucidate the chemical development by structure. These CIMS signals are normalized by the total reacted hydrocarbon to account for differences in initial hydrocarbon loading and represented along an OH exposure time scale for 200 comparison of the different systems (Figure 3). While there are slight differences in magnitude of the curves presented, gas-phase yields are not inferred from these figures as slight variations in the CIMS sensitivity based on structure may account for this effect.

The OH exposure in the system is defined as the product of the concentration of OH (molec cm^{-3}) and the hours of irradiation. The OH concentration is inferred from the initial hydrocarbon 205 decay using the known reaction rate coefficient with OH. The OH concentration over the course of an experiment is constant ($\sim 2 \times 10^6$ molec cm^{-3}). Total OH exposure ranges from $\sim 8 \times 10^7$ molec cm^{-3} h to $\sim 1 \times 10^8$ molec cm^{-3} h for these experiments.

The 1st-generation hydroperoxides (ROOH) trends across systems are shown in Figure 3, top 210 panel. Under similar OH exposures the hexylcyclohexane hydroperoxide peaks slightly earlier than those of *n*-dodecane and cyclododecane. This is consistent with a slightly faster reaction rate coefficient for hexylcyclohexane. The 2nd-generation carbonyl (CARB) formation is compared across the systems in Figure 3, middle panel. The trends are consistent with faster gas-phase oxidation for hexylcyclohexane.

Most of the intermediate hydroperoxide species are best monitored in negative mode operation 215 of the CIMS, but due to the mass scan range ending at 300 amu, alternative ions in positive mode were used to track development of some expected products. Major products such as the carbonyl hydroperoxide (CARBROOH) for the 2-methylundecane and *n*-dodecane systems were monitored at (+) m/z 204 for this reason (Table 3), while for hexylcyclohexane and cyclododecane CARBROOH was monitored at (-) m/z 299 (Table 4). Note that signal intensities should not be compared across 220 positive and negative mode operation of the CIMS, as the sensitivities differ. The CARBROOH trends in Figure (3, bottom panel) show similar trends, though the signals are more noisy as this hydroperoxide is expected to be the first species with sufficiently low volatility to partition into the particle phase.

Many of the semi-volatile, higher functionalized products (OHROOH, OHCARBROOH, and DI- 225 CARBROOH) while observed in Yee et al. (2012), were of too low signal to report for hexylcyclohexane and cyclododecane. A small signal with a trend consistent with the expected kinetics for the DICARBROOH in the 2-methylundecane system exists, indicating that this system does achieve this extent of oxidation in the gas-phase. However, the lack of expected signals in the gas-phase for all systems besides *n*-dodecane is likely a result of several factors. First, these multi-functional 230 species are of sufficiently low vapor pressure to partition into the particle phase. Second, the experimental design utilized lower initial hydrocarbon loadings (to achieve comparable organic growth) moving towards the more cyclic structure of the studied compounds, lowering the overall production of such species in the gas-phase compared to their more straight-chain analogs. Finally, compounds

like 2-methylundecane and hexylcyclohexane may undergo more fragmentation processes leading to
235 scission of the C₁₂ chain and thereby less C₁₂ multi-functional products owing to the potential to
form tertiary alkoxy radicals.

3.2.2 Particle-phase composition

Mass spectra (1-2 h averages) from the AMS at the time of initial growth, a period mid-experiment, and at experiment end for each system, along with a difference spectrum from end and initial growth,
240 are presented in Figures 4-7. The initial growth spectrum is taken at the point where the organic mass rises above the limit of detection. The limit of detection is defined as 3 standard deviations above the signal during the filter period taken before photooxidation begins. The mid-experiment average spectrum is taken at the point where the suspended organic is the highest, typically coincident with the peak of one or more AMS ion tracers of interest. The peak in suspended organic is consistent
245 with the effects of particle wall loss and unlikely due to evaporation as the size distribution remains the same. The end spectrum is the average of the spectra during the last 1-2 h of photooxidation. The C_xH_yO_z chemical formulas corresponding with the dominant exact masses are labeled in the mass spectra. Unit mass *m/z* is denoted here for brevity, but the reported ion chemical formulas are determined from the exact mass ions.

250 A few observations of the spectra are noted here. The mass spectrum from the hexylcyclohexane system (Figures 6) between *m/z* 100-200 amu is less discretely structured as compared to the other compounds (Figure 4, 5, 7). Since hexylcyclohexane exhibits alkyl, cyclic, and branched features in its structure, this may be realized as a unique “chaos” from this hybrid of chemical features in the aerosol spectrum. Overall, the difference spectra in the *m/z* 100-300 amu region are all positive,
255 indicating the incorporation of higher molecular weight species. The only negative differences in signal are in the *m/z* < 100 range and are the result of alkyl ion fragments decreasing in the particle phase. Several ions in the >150 amu range have been proposed as tracers for particle-phase chemistry, as, though low in signal, they retain more molecular information. The chemical processes by which these >150 amu ions are generated may be analogous across all systems, as the structure of
260 the spectra in this range are generally the same. That is, the prominent ions in hexylcyclohexane correspond to the prominent ions in the *n*-dodecane and 2-methylundecane cases, but tend to have one additional degree of unsaturation. This is consistent with the difference in degrees of unsaturation between the parent compounds. However, the cyclododecane peaks in this high amu region tend to be two degrees of unsaturation lower than those of *n*-dodecane. This could indicate chemical processing that results in more carbonyl group formation for the case of cyclododecane. This type of functionalization is relevant for cyclododecane along Channel 3 in the gas-phase mechanism (Figure 1), as cyclododecane can ring-open early on, generating an aldehyde. This also means that cyclododecane can form a lower vapor pressure C₁₂ aldehyde that can participate in particle-phase reactions as discussed in Lim and Ziemann (2009a,b), whereas other systems form a <C₁₂ aldehyde

270 along Channel 1a (Figure 1).

3.2.3 Indicators of particle-phase chemistry: peroxyhemiacetal (PHA) formation

Yee et al. (2012) and Craven et al. (2012) proposed that several ion tracers in the $m/z > 150$ amu region differing by 32 amu could be used to track a variety of potential peroxyhemiacetals (PHAs) formed in the particle-phase. Craven et al. (2012) established that general hydroperoxides (ROOH) 275 could be monitored in the AMS at ions consistent with an $m/z [M-33]^+$, where M is the molecular weight of the hydroperoxide. This ion will be hereafter referred to as R^+ . However, the distinct pattern of similarly trending ions > 150 amu that are 32 amu apart suggests that this mass difference may result from the peroxide O–O bond of a peroxyhemiacetal. We refer to this ion as ROO^+ for the following discussions. These ions are listed in tables of ions monitored in the AMS along 280 with their proposed product assignments (Tables 5–7). Since these initial studies, another *n*-dodecane experiment (not presented here) involved intentional injection of tridecanal in the dark after an initial period of dodecane photooxidation and SOA formation to induce peroxyhemiacetal formation. Upon tridecanal injection, a corresponding decrease in signal of several hydroperoxide species occurred 285 in the gas-phase (as monitored by the CIMS) accompanied by a corresponding increase in the 32 amu difference ion pairs in the AMS, consistent with the proposed attribution to particle-phase chemistry involving peroxyhemiacetal formation.

The formation of fragments along Channel 1a, specifically carboxylic acids tracked by the CIMS, 290 is the key proxy for the presence of aldehyde in the system (since the aldehyde is not directly measured). The presence of gas-phase acid indicates that peroxyhemiacetal formation may commence, as observed in Yee et al. (2012) for *n*-dodecane. Hence, a key comparison of the gas and particle-phase measurements includes the time trend comparison between gas-phase acid production and particle-phase ion markers for PHA formation. In each system, the CARBROOH PHA ions grow in the particle phase when gas-phase acid forms, as indicated by the C_6 carboxylic acid, C6CARBACID, in Figure 8. The initial growth of organic in each of these systems is also characterized by the respective CARBROOH and CARBROOH PHA tracer ions in the AMS mass spectra. 295 In Figures 4 and 5, $C_{12}H_{23}O^+$ at m/z 183 and $C_{12}H_{23}O_3^+$ at m/z 215 are the dominant ions at initial growth of *n*-dodecane and 2-methylundecane SOA. For hexylcyclohexane (Figure 6) and cyclododecane (Figure 7), the ion at $C_{12}H_{21}O_3^+$ at m/z 213 is characteristic of initial growth. Note that there are different right hand axes and scales for the R^+ and ROO^+ ion tracers in Figure 8.

300 3.2.4 Effect of structure on PHA formation

The general particle-phase development is shown in terms of the multi-functional hydroperoxide/PHA R^+ and PHA ROO^+ proposed ion tracers for all systems (Figures 9). All ion signals have been normalized by the suspended organic to account for effects on the ion signal trend due to particle wall loss. This normalization results in large noise at periods $< OH$ exposure of 2×10^7 molec cm^{-3} h,

305 owing to low and noisy ion and organic signals before this time. The same tracer ions are present in both the *n*-dodecane and 2-methylundecane systems (Figures 9a and 9b). $C_{12}H_{19}O_5^+$ is of low signal in the 2-methylundecane and *n*-dodecane AMS spectra, though there is a greater contribution from this ion in *n*-dodecane SOA. All of these ions can potentially be explained by multi-functional hydroperoxide compounds that can carry up to four sites of functionalization and three degrees of
 310 unsaturation relative to the parent (See PHA schemes in Figure 2 for proposed multi-functional structures and AMS ions assignments in Table 5). Generally, the CARBROOH is initially incorporated, followed by the DICARBROOH ($C_{12}H_{21}O_2^+$ at *m/z* 197) and the OHCARBROOH ($C_{12}H_{23}O_2^+$ at *m/z* 199). Additional chemical processing leads to incorporation of a potential OHDICARBROOH ($C_{12}H_{21}O_3^+$ at *m/z* 213) and a TRICARBROOH ($C_{12}H_{19}O_3^+$ at *m/z* 211). The $C_{12}H_{19}O_5^+$ at *m/z*
 315 245 is possibly the OHDICARBROOH PHA ROO^+ ion, though the signal at this *m/z* is not sufficiently high to be plotted on the same scale as the R^+ ions here. The DIROOH and OHROOH tracer ions are also not included for this reason, although tracer ions are identified in the mass spectra. Of note is the relatively earlier peaking (in terms of OH exposure) and lower relative contribution of these ions in the 2-methylundecane system as compared to their analogs in the *n*-dodecane system.
 320 This may be a result of fragmentation processes relevant for 2-methylundecane gas-phase oxidation that begin to dominate. The lower relative contribution of $C_{12}H_{19}O_5^+$ for 2-methylundecane SOA as compared to *n*-dodecane SOA is also consistent with less chemical development due to gas-phase fragmentation dominating over functionalization, as well as potentially slower gas-phase oxidation since 2-methylundecane has a lower k_{OH} than that of *n*-dodecane.

325 For hexylcyclohexane, there is noticeably more simultaneous incorporation in the aerosol phase of such species as the CARBROOH ($C_{12}H_{21}O^+$ at *m/z* 181), DICARBROOH ($C_{12}H_{19}O_2^+$ at *m/z* 195), OHCARBROOH ($C_{12}H_{21}O_2^+$ at *m/z* 197), and their respective PHAs (Figure 9c, Table 6). There is also significant contribution from an ion at $C_{12}H_{19}O^+$, not explained by the PHA tracer fragmentation pattern. The presence of the $C_{12}H_{19}O^+$ ion may be a result of forming an analogous
 330 hydroperoxy dihydrofuran product (Figure 2, Scheme 3) via the OHCARBROOH undergoing 1,4 cyclization and dehydration. This ion is unique to hexylcyclohexane SOA (in terms of degrees of unsaturation achieved with little oxygen in the ion formula and prominence of the ion). The proposed reaction is consistent with the hexylcyclohexane structure affording another 1,4-cyclization due to its C₆ branch. This also forms a dihydrofuran-like structure of higher volatility. This prominent
 335 route may therefore limit formation of lower volatility oxidation products during hexylcyclohexane oxidation. The peak of the suspended organic (Figure 9c, OH exposure $\sim 5 \times 10^6$ molec cm⁻³ h) does follow the peak of this ion and those of the DICARBROOH, OHCARBROOH, consistent with limitations of the growth. At this point the rate of particle wall loss dominates over the rate of continued growth.

340 Tracer ions for these products are followed by further chemical processing leading also to the OHDICARBROOH and its PHA ($C_{12}H_{19}O_3^+$ at *m/z* 211) and the OHDICARBROOH PHA ($C_{12}H_{19}O_5^+$

at m/z 243). The m/z 243 ion is not shown due to low signal. The ion at m/z 227 $\text{C}_{12}\text{H}_{19}\text{O}_4^+$ corresponds to the ROO^+ ion for DICARBROOH PHA, though the time trend does not follow that of the R^+ ion as closely, and may indicate another species (in combination) being responsible for the signal here. For example, in Figure 2, Scheme 5, the OHDICARBROOH may isomerize (left reaction) via cyclization between a carbonyl and hydroperoxy group to form this ion as well. It may also undergo 1,4-cyclization involving the hydroxy and ketone groups. This presents two potentially competitive fates for the OHDICARBROOH, one to PHA formation (Scheme 5, right reaction) and cyclization (Scheme 5, left and bottom reaction). Cyclization of alkoxy hydroperoxy aldehydes has been observed to be potentially competitive with PHA formation in the case of cyclic alkenes ozonolysis in the presence of alcohols (Ziemann, 2003). A similar cyclization reaction for the multi-functional carbonyl hydroperoxides can explain the presence of additional ions not expected from PHA formation.

For cyclododecane, at least two “waves” of chemical development exist in the particle phase (Figure 9d). Initially, R^+ ions associated with the CARBROOH, OHCARBROOH, and DICARBROOH grow in. Then, a series of ions with formulae of the form $\text{C}_{12}\text{H}_y\text{O}_3^+$, with $y = 19, 17$, and 15 grow in consecutively. $\text{C}_{12}\text{H}_{19}\text{O}_3^+$ at m/z 211 and $\text{C}_{12}\text{H}_{17}\text{O}_3^+$ at m/z 209 could correspond with the OHDICARBROOH and TRICARBROOH R^+ ions, respectively. Note that the $\text{C}_{12}\text{H}_{19}\text{O}_3^+$ ion can also result from a ring-opened TRICARBROOH (same as in the linear case), but where at least one of the carbonyl groups is presumably an aldehyde. The $\text{C}_{12}\text{H}_{15}\text{O}_3^+$ at m/z 207 implies yet another step achieving one fewer degree of saturation. This was characteristic of many of the ions in the cyclododecane AMS mass spectra achieving one additional degree of unsaturation compared to that of hexylcyclohexane and two compared to the non-cyclic systems. This ion assignment is uncertain, though it could correspond with a structure containing a hydroxy, four ketone groups, and a hydroperoxy group with the ring intact (OH4CARBROOH). There may be additional cyclizations or dehydration reactions in the particle phase and/or additional ionization patterns in the AMS that may more feasibly explain the presence of this ion. This is especially relevant when considering the ions of the form $\text{C}_{12}\text{H}_y\text{O}_z^+$, with $y = 19, 17$, and 15 and $z = 3, 4, 5$. For the OH4CARBROOH, TRICARBROOH, and OHDICARBROOH the mass spectrum (Figure 7) indicates a greater fraction of organic due to the corresponding $z = 4$ ions compared to the $z = 5$ ions. This may indicate competitive cyclization over PHA formation as shown in Schemes 4 (TRICARBROOH) and 5 (OHDICARBROOH) of Figure 2.

Common for all four systems, three ions that enter the particle phase early on (within 2×10^7 molec $\text{cm}^{-3} \text{ h}$ OH exposure) are attributed to their respective CARBROOH, OHCARBROOH, and DICARBROOH. While the R^+ ions can come from both the hydroperoxide itself and its derived PHA, the ROO^+ ion is considered to arise mostly from PHA. To understand the effect of structure on PHA formation, time trends of the fraction of the organic attributed to ROO^+ PHA tracer ions can be compared across parent structures. These analyses assume that the ionization probability and

fragmentation pattern in the AMS are relatively consistent for PHAs of analogous functionality.
 380 For example, the CARBROOH PHA ionization probability is similar across the four C₁₂ alkanes studied. Also, this currently assumes that there is only one hydroperoxide and its PHA (regardless of the aldehyde variety) contributing to the ROO⁺.

Figure 10 shows that the relative fraction of organic attributed to the CARBROOH PHA is approximately similar for *n*-dodecane and hexylcyclohexane, followed by 2-methylundecane and cyclododecane (top panel). For the DICARBROOH PHA (middle panel) and OHCARBROOH PHA (bottom panel), a greater fraction of the organic is attributed to PHAs in hexylcyclohexane SOA, followed by *n*-dodecane. Smaller contributions are made for the PHAs from 2-methylundecane and cyclododecane. Generally, the fraction of organic attributed to the cyclododecane-derived PHAs is lower compared to the other systems, indicating that there may be structural biases in PHA formation.
 385 Since PHA formation relies on the intermolecular reaction of two condensing species, aldehyde and a hydroperoxide, it may be that the cyclic structure of cyclododecane is less apt for this reaction. There is also trend information in Figure 8d that shows that the R⁺ and ROO⁺ ions for CARBROOH PHA in cyclododecane do not trend together as tightly as compared to the other systems (Figures 8a-8c). The ROO⁺ ion lags slightly, indicating that PHA formation from the CARBROOH
 390 in cyclododecane may not form immediately with the condensation of CARBROOH.
 395

While signal at the ROO⁺ ion for CARBROOH PHA can also potentially be derived from the OHCARBROOH cyclizing as in Figure 2, Scheme 3, the tight correlation of the R⁺ and ROO⁺ ions for *n*-dodecane and 2-methylundecane suggests less of a contribution from competing cyclization. Since the R⁺ ions cannot be derived from the competitive cyclization products, the majority of the
 400 signal at the ROO⁺ ion is attributed to the CARBROOH PHA form. For hexylcyclohexane and cyclododecane, however, there is slightly more deviation of the R⁺ and ROO⁺ ion trends. This may suggest that these structures may undergo intramolecular reactions that result in the variety of ions and chemical development as discussed earlier.

3.2.5 AMS Elemental Ratios

405 The Van Krevelen diagram, originally used for showing how O:C and H:C elemental ratios change during coal formation (Van Krevelen, 1950), has been recently utilized with HR-TOF-AMS data to aid in the interpretation of elemental ratio changes in organic aerosol formation (Heald et al., 2010; Ng et al., 2011; Chhabra et al., 2011; Lambe et al., 2011, 2012). The slopes on the diagram of O:C versus H:C can provide insight into the chemical evolution of the aerosol in terms of functional
 410 group changes. A slope of -1 for ambient and laboratory data is consistent with carboxylic acid groups without fragmentation (Heald et al., 2010). Ng et al. (2011), showed that for aged ambient organic aerosol, the slope of -0.5 is consistent with carboxylic acid addition with fragmentation. Both of these results highlighted aerosol that was already quite oxidized, with most of the O:C values greater than 0.30. Lambe et al. (2012) presented SOA results from a Potential Aerosol Mass

415 (PAM) chamber in which long-chain alkane SOA O:C extended from a value of 0 to close to 1.4. The Van Krevelen slope from an O:C of 0 to approximately 0.3 was -1.3, and for O:C values greater than 0.3 the slope became less negative with a value of -0.7. Lambe et al. (2012) attribute this change in slope to a transition from a functionalized- to fragment-dominated regime.

420 The elemental ratios from the current study are shown in Figure 11. The experimental progression for all four systems is from upper left to lower right across the Van Krevelen space. All of the compounds have O:C < 0.3, except for the end of the hexylcyclohexane experiment. In increasing order, the slopes are -1.73, -1.35, -1.19, and -1.14 for cyclododecane, 2-methylundecane, dodecane, and hexylcyclohexane. The higher O:C achieved for hexylcyclohexane may be a result of the generally faster chemistry seen in both the gas-phase oxidation and the particle-phase development, in which 425 initial key ions in the particle phase (Figure 9c) peak earlier in terms of OH exposure $< 5 \times 10^7$ molec $\text{cm}^{-3} \text{ h}$ as compared to those of the other systems. This could be a result of fragmentation processes increasing the O:C or oxygenation achieved from continued oxidation.

430 *n*-Dodecane achieves the next highest O:C for the OH exposures in this study, and while the progression of key >150 amu ions in this system (Figure 9a) is more gradual, there is continued oxygenation, as observed by the presence of the $\text{C}_{12}\text{H}_{19}\text{O}_5^+$ ion. Yee et al. (2012) also found the O:C range to be consistent with the O:C of several of the multi-functional hydroperoxides and their derived PHAs. 2-methylundecane SOA exhibits a lower O:C than that from *n*-dodecane, supported by the lower fraction of total organic attributed to oxidized ions, compared to *n*-dodecane.

435 Finally, cyclododecane SOA has the slope closest to -2, indicating a greater contribution from ketone and aldehyde groups. This is consistent with the $\text{C}_{12}\text{H}_y\text{O}_3^+$ ion series in Figure 9d and the relatively higher degrees of unsaturation in the cyclododecane AMS mass spectrum (Figure 7) as compared to the other systems.

4 Conclusions

We address here the mechanisms of formation of SOA in alkane systems under low- NO_x conditions.

440 Special attention is given to the effect of alkane structure on SOA formation and to the molecular identifications of the oxidation products responsible for SOA growth. Aerosol formation from the photooxidation of *n*-dodecane, 2-methylundecane, hexylcyclohexane, and cyclododecane under low- NO_x conditions, is initiated by the partitioning of a 2nd-generation product, the carbonyl hydroperoxide (CARBROOH), to the particle phase. It appears that this hydroperoxide is incorporated 445 with simultaneous formation of a peroxyhemiacetal. Several other multi-functional hydroperoxides are proposed to explain characteristic ions in the AMS mass spectra for each system, suggesting that at least three additional degrees of unsaturation might be achieved for cyclododecane while functionalizing primarily via ketone/aldehyde addition. Evidence for additional particle-phase reactions including cyclization of multi-functional hydroperoxides exists. Intramolecular cyclization of multi-

450 functional hydroperoxides can be competitive with the intermolecular reaction of multi-functional hydroperoxides with aldehydes to form PHAs.

2-methylundecane exhibits the least extent of chemical processing relative to the other systems, likely a result of gas-phase fragmentation that leads to a product distribution consisting of relatively higher volatility intermediates. Hexylcyclohexane exhibits rapid gas-phase oxidation and particle-phase processing reflected in the highest achieved O:C (verging on 0.4). Of the systems studied, 455 hexylcyclohexane behaves in terms of SOA chemistry somewhere between 2-methylundecane and cyclododecane. It exhibits the rapid formation of functionalized semi- and low-volatility species that contribute to the particle phase, but then fragmentation processes (attributable to the branching) start to dominate and lower the relative particle mass due to C₁₂ oxygenates. Cyclization processes 460 analogous to cyclic hemiacetal and higher volatility dihydrofuran formation can also contribute to limitations in particle growth.

While the >150 amu tracer ions in the AMS help to identify potential species involved in particle-phase chemistry like PHA formation, the more oxidized and functionalized the ion, the greater potential exists for multiple ionization and fragmentation schemes in the AMS. Ideally, standards of 465 different structure, but analogous functionality would be necessary to better understand the mass spectra in this region. Ionization schemes that include possibilities of cyclic and/or cyclization followed by dehydration of compounds in the particle phase are necessary. Such schemes were proposed here to explain additional ions in the AMS not expected purely from PHA formation. This is relevant for determining the molecular identity of some of the highly oxygenated (>O₃⁺) ions that 470 grow in the particle phase at extended OH exposures.

For the functional groups presumed to be incorporated via the gas-phase mechanism, ketone (some aldehyde for cyclododecane), hydroperoxy, and hydroxyl, it is very likely these functional groups undergo intramolecular, as well as intermolecular, reactions (including oligomer formation) depending on their relative positions on the C₁₂ backbone. This may be highly relevant for hexylcyclohexane 475 in which the alkyl branch is sufficiently long to still cyclize and result in a bicyclic structure. Cyclododecane may ring open to form functionalized aldehydes and then cyclize again (not necessarily returning to a C₁₂ ring).

The systematic study of these C₁₂ structures lays a chemical groundwork for understanding the dynamics of particle growth concerted with particle-phase reactions (e.g. PHA formation) and 480 sustained growth via semi-volatile and low-volatile product partitioning, followed by additional particle-phase oxidation if unhampered by fragmentation processes. Further study of the C₁₂ system should include additional isomeric configurations of branching and cyclic + branched structures to understand better the spectrum of oxidation pathways between 2-methylundecane and hexylcyclohexane and between hexylcyclohexane and cyclododecane. These structural dependencies will 485 certainly impact the mechanisms of SOA formation and SOA yields, which can affect the representation of SOA formation from alkanes.

Acknowledgements. This work was supported by the Office of Science (Biological and Environmental Research), U. S. Department of Energy Grant (DE-SC 0006626), and National Science Foundation Grants AGS-1057183 and ATM-0650061. The authors acknowledge helpful discussions with John D. Crounse and Jason M. 490 St. Clair regarding treatment of CIMS data and gas-phase data, as well as experimental assistance and discussions with Reddy L. N. Yatavelli and ManNin Chan. L. D. Yee, J. S. Craven, and C. L. Loza were supported by National Science Foundation Graduate Research Fellowships.

References

Aiken, A. C., DeCarlo, P. F., and Jimenez, J. L.: Elemental analysis of organic species with electron ionization
495 high-resolution mass spectrometry, *Anal. Chem.*, 79, 8350–8358, 2007.

Aiken, A. C., Decarlo, P. F., Kroll, J. H., Worsnop, D. R., Huffman, J. A., Docherty, K. S., Ulbrich, I. M., Mohr,
C., Kimmel, J. R., Sueper, D., Sun, Y., Zhang, Q., Trimborn, A., Northway, M., Ziemann, P. J., Canagaratna,
M. R., Onasch, T. B., Alfarra, M. R., Prevot, A. S. H., Dommen, J., Duplissy, J., Metzger, A., Baltensperger,
U., and Jimenez, J. L.: O/C and OM/OC ratios of primary, secondary, and ambient organic aerosols with
500 high-resolution time-of-flight aerosol mass spectrometry, *Environ. Sci. Technol.*, 42, 4478–4485, 2008.

Allan, J. D., Delia, A. E., Coe, H., Bower, K. N., Alfarra, M. R., Jimenez, J. L., Middlebrook, A. M., Drewnick,
F., Onasch, T. B., Canagaratna, M. R., Jayne, J. T., and Worsnop, D. R.: A generalised method for the
extraction of chemically resolved mass spectra from aerodyne aerosol mass spectrometer data, *J. Aerosol
Sci.*, 35, 909–922, 2004.

505 Aschmann, S. M., Arey, J., and Atkinson, R.: Kinetics and products of the gas-phase reaction of OH radicals
with 5-hydroxy-2-pentanone at 296 2 k, *J. Atmos. Chem.*, 45, 289–299, doi:10.1023/A:1024216900051,
2003.

Atkinson, R.: Gas-phase tropospheric chemistry of organic compounds, *J. Phys. Chem. Ref. Data, Monogr.*, 2,
1–216, 1994.

510 Atkinson, R.: Gas-phase tropospheric chemistry of volatile organic compounds. 1. Alkanes and alkenes, *J.
Phys. Chem. Ref. Data*, 26, 215–290, 1997.

Atkinson, R. and Arey, J.: Atmospheric degradation of volatile organic compounds, *Chem Rev.*, 103, 4605–
4638, doi:10.1021/cr0206420, 2003.

Atkinson, R., Arey, J., and Aschmann, S. M.: Atmospheric chemistry of alkanes: Review and recent develop-
515 ments, *Atmos. Environ.*, 42, 5859 – 5871, doi:10.1016/j.atmosenv.2007.08.040, 2008.

Bahreini, R., Middlebrook, A. M., de Gouw, J. A., Warneke, C., Trainer, M., Brock, C. A., Stark, H., Brown,
S. S., Dube, W. P., Gilman, J. B., Hall, K., Holloway, J. S., Kuster, W. C., Perring, A. E., Prevot, A. S. H.,
Schwarz, J. P., Spackman, J. R., Szidat, S., Wagner, N. L., Weber, R. J., Zotter, P., and Parrish, D. D.:
Gasoline emissions dominate over diesel in formation of secondary organic aerosol mass, *Geophys. Res.
Lett.*, 39, doi:10.1029/2011GL050718, 2012.

Benson, S. W.: Thermochemical kinetics, Wiley, second edn., 1976.

520 Canagaratna, M., Jayne, J., Jimenez, J., Allan, J., Alfarra, M., Zhang, Q., Onasch, T., Drewnick, F., Coe, H.,
Middlebrook, A., Delia, A., Williams, L., Trimborn, A., Northway, M., DeCarlo, P., Kolb, C., Davidovits,
P., and Worsnop, D.: Chemical and microphysical characterization of ambient aerosols with the Aerodyne
aerosol mass spectrometer, *Mass Spectrom. Rev.*, 26, 185–222, doi:10.1002/mas.20115, 2007.

Cappa, C. D., Zhang, X., Loza, C. L., Craven, J. S., Yee, L. D., and Seinfeld, J. H.: Application of the statistical
oxidation model (SOM) to secondary organic aerosol formation from photooxidation of C₁₂ alkanes, *Atmos.
Chem. Phys.*, 13, 1591–1606, doi:10.5194/acp-13-1591-2013, 2013.

Chhabra, P. S., Ng, N. L., Canagaratna, M. R., Corrigan, A. L., Russell, L. M., Worsnop, D. R., Flagan, R. C.,
530 and Seinfeld, J. H.: Elemental composition and oxidation of chamber organic aerosol, *Atmos. Chem. Phys.*,
11, 8827–8845, doi:10.5194/acp-11-8827-2011, 2011.

Cocker, D. R., Flagan, R. C., and Seinfeld, J. H.: State-of-the-art chamber facility for studying atmospheric

aerosol chemistry, *Environ. Sci. Technol.*, 35, 2594–2601, 2001.

Compernolle, S., Ceulemans, K., and Müller, J.-F.: EVAPORATION: a new vapour pressure estimation method-
535 for organic molecules including non-additivity and intramolecular interactions, *Atmos. Chem. Phys.*, 11, 9431–9450, doi:10.5194/acp-11-9431-2011, 2011.

Craven, J. S., Yee, L. D., Ng, N. L., Canagaratna, M. R., Loza, C. L., Schilling, K. A., Yatavelli, R. L. N., Thornton, J. A., Ziemann, P. J., Flagan, R. C., and Seinfeld, J. H.: Analysis of secondary organic aerosol formation and aging using positive matrix factorization of high-resolution aerosol mass spectra: application to
540 the dodecane low- NO_x system, *Atmos. Chem. Phys.*, 12, 11 795–11 817, doi:10.5194/acp-12-11795-2012, 2012.

Crounse, J. D., McKinney, K. A., Kwan, A. J., and Wennberg, P. O.: Measurement of gas-phase hydroperoxides by chemical ionization mass spectrometry, *Anal. Chem.*, 78, 6726–6732, 2006.

DeCarlo, P. F., Kimmel, J. R., Trimborn, A., Northway, M. J., Jayne, J. T., Aiken, A. C., Gonin, M., Fuhrer,
545 K., Horvath, T., Docherty, K. S., Worsnop, D. R., and Jimenez, J. L.: Field-deployable, high-resolution, time-of-flight aerosol mass spectrometer, *Anal. Chem.*, 78, 8281–8289, 2006.

Dibble, T. S.: Cyclization of 1,4-hydroxycarbonyls is not a homogenous gas phase process, *Chem. Phys. Lett.*, 447, 5 – 9, doi:10.1016/j.cplett.2007.08.088, 2007.

Gentner, D. R., Isaacman, G., Worton, D. R., Chan, A. W. H., Dallmann, T. R., Davis, L., Liu, S., Day,
550 D. A., Russell, L. M., Wilson, K. R., Weber, R., Guha, A., Harley, R. A., and Goldstein, A. H.: Elucidating secondary organic aerosol from diesel and gasoline vehicles through detailed characterization of organic carbon emissions, *Proc. Natl. Acad. Sci. U. S. A.*, doi:10.1073/pnas.1212272109, 2012.

Heald, C. L., Kroll, J. H., Jimenez, J. L., Docherty, K. S., DeCarlo, P. F., Aiken, A. C., Chen, Q., Martin, S. T., Farmer, D. K., and Artaxo, P.: A simplified description of the evolution of organic aerosol composition in
555 the atmosphere, *Geophys. Res. Lett.*, 37, L08 803, doi:10.1029/2010GL042737, 2010.

Isaacman, G., Wilson, K. R., Chan, A. W. H., Worton, D. R., Kimmel, J. R., Nah, T., Hohaus, T., Gonin, M., Kroll, J. H., Worsnop, D. R., and Goldstein, A. H.: Improved resolution of hydrocarbon structures and constitutional isomers in complex mixtures using gas chromatography-vacuum ultraviolet-mass spectrometry, *Anal. Chem.*, 84, 2335–2342, doi:10.1021/ac2030464, 2012.

Jenkin, M. E., Saunders, S. M., and Pilling, M. J.: The tropospheric degradation of volatile organic compounds: a protocol for mechanism development, *Atmos. Environ.*, 31, 81 – 104, doi:10.1016/S1352-2310(96)00105-7, 1997.

Jordan, C. E., Ziemann, P. J., Griffin, R. J., Lim, Y. B., Atkinson, R., and Arey, J.: Modeling SOA formation from OH reactions with C8-C17 n-alkanes, *Atmos. Environ.*, 42, 8015–8026, doi:10.1016/j.atmosenv.2008.
565 06.017, 2008.

Keywood, M. D., Varutbangkul, V., Bahreini, R., Flagan, R. C., and Seinfeld, J. H.: Secondary organic aerosol formation from the ozonolysis of cycloalkenes and related compounds, *Environ. Sci. Technol.*, 38, 4157–4164, 2004.

Kwok, E. S. and Atkinson, R.: Estimation of hydroxyl radical reaction rate constants for gas-phase organic
570 compounds using a structure-reactivity relationship: An update, *Atmos. Environ.*, 29, 1685 – 1695, doi:10.1016/1352-2310(95)00069-B, 1995.

Lambe, A. T., Onasch, T. B., Massoli, P., Croasdale, D. R., Wright, J. P., Ahern, A. T., Williams, L. R.,

Worsnop, D. R., Brune, W. H., and Davidovits, P.: Laboratory studies of the chemical composition and cloud condensation nuclei (CCN) activity of secondary organic aerosol (SOA) and oxidized primary organic aerosol (OPOA), *Atmos. Chem. Phys.*, 11, 8913–8928, doi:10.5194/acp-11-8913-2011, 2011.

575 Lambe, A. T., Onasch, T. B., Croasdale, D. R., Wright, J. P., Martin, A. T., Franklin, J. P., Massoli, P., Kroll, J. H., Canagaratna, M. R., Brune, W. H., Worsnop, D. R., and Davidovits, P.: Transitions from functionalization to fragmentation reactions of laboratory secondary organic aerosol (SOA) generated from the OH oxidation of alkane precursors, *Environ. Sci. Technol.*, 46, 5430–5437, doi:10.1021/es300274t, 2012.

580 Lim, Y. B. and Ziemann, P. J.: Products and mechanism of secondary organic aerosol formation from reactions of n-alkanes with OH radicals in the presence of NO_x , *Environ. Sci. Technol.*, 39, 9229–9236, doi:10.1021/es051447g, 2005.

585 Lim, Y. B. and Ziemann, P. J.: Effects of molecular structure on aerosol yields from OH radical-initiated reactions of linear, branched, and cyclic alkanes in the presence of NO_x , *Environ. Sci. Technol.*, 43, 2328–2334, doi:10.1021/es803389s, 2009a.

590 Lim, Y. B. and Ziemann, P. J.: Chemistry of secondary organic aerosol formation from OH radical-initiated reactions of linear, branched, and cyclic alkanes in the presence of NO_x , *Aerosol Sci. Technol.*, 43, 604–619, doi:10.1080/02786820902802567, 2009b.

595 Lim, Y. B. and Ziemann, P. J.: Kinetics of the heterogeneous conversion of 1,4-hydroxycarbonyls to cyclic hemiacetals and dihydrofurans on organic aerosol particles, *Phys. Chem. Chem. Phys.*, 11, 8029–8039, doi:10.1039/B904333K, 2009c.

Lipsky, E. M. and Robinson, A. L.: Effects of dilution on fine particle mass and partitioning of semivolatile organics in diesel exhaust and wood smoke, *Environ. Sci. Technol.*, 40, 155–162, 2006.

595 Nakao, S., Shrivastava, M., Nguyen, A., Jung, H., and Cocker, D.: Interpretation of secondary organic aerosol formation from diesel exhaust photooxidation in an environmental chamber, *Aerosol Sci. Technol.*, 45, 964–972, doi:10.1080/02786826.2011.573510, 2011.

Ng, N. L., Canagaratna, M. R., Jimenez, J. L., Chhabra, P. S., Seinfeld, J. H., and Worsnop, D. R.: Changes in organic aerosol composition with aging inferred from aerosol mass spectra, *Atmos. Chem. Phys.*, 11, 6465–6474, doi:10.5194/acp-11-6465-2011, 2011.

600 Paulot, F., Crounse, J. D., Kjaergaard, H. G., Kroll, J. H., Seinfeld, J. H., and Wennberg, P. O.: Isoprene photooxidation: new insights into the production of acids and organic nitrates, *Atmos. Chem. Phys.*, 9, 1479–1501, 1680–7316, 2009.

605 Presto, A. A., Miracolo, M. A., Kroll, J. H., Worsnop, D. R., Robinson, A. L., and Donahue, N. M.: Intermediate-volatility organic compounds: a potential source of ambient oxidized organic aerosol, *Environ. Sci. Technol.*, 43, 4744–4749, doi:10.1021/es803219q, 2009.

Presto, A. A., Miracolo, M. A., Donahue, N. M., and Robinson, A. L.: Secondary organic aerosol formation from high- NO_x photo-oxidation of low volatility precursors: n-alkanes, *Environ. Sci. Technol.*, 44, 2029–2034, doi:10.1021/es903712r, 2010.

610 Pye, H. O. T. and Pouliot, G. A.: Modeling the role of alkanes, polycyclic aromatic hydrocarbons, and their oligomers in secondary organic aerosol formation, *Environ. Sci. Technol.*, 46, 6041–6047, doi:10.1021/es300409w, 2012.

Robinson, A. L., Donahue, N. M., Shrivastava, M. K., Weitkamp, E. A., Sage, A. M., Grieshop, A. P., Lane,

T. E., Pierce, J. R., and Pandis, S. N.: Rethinking organic aerosols: Semivolatile emissions and photochemical aging, *Science*, 315, 1259–1262, 2007.

615 Schauer, J. J., Kleeman, M. J., Cass, G. R., and Simoneit, B. R. T.: Measurement of emissions from air pollution sources. 2. C1 through C30 organic compounds from medium duty diesel trucks, *Environ. Sci. Technol.*, 33, 1578–1587, doi:10.1021/es980081n, 1999.

Schauer, J. J., Kleeman, M. J., Cass, G. R., and Simoneit, B. R. T.: Measurement of emissions from air pollution sources. 5. C1-C32 organic compounds from gasoline-powered motor vehicles, *Environ. Sci. Technol.*, 36, 620 1169–1180, doi:10.1021/es0108077, 2002.

St. Clair, J. M., McCabe, D. C., Crounse, J. D., Steiner, U., and Wennberg, P. O.: Chemical ionization tandem mass spectrometer for the in situ measurement of methyl hydrogen peroxide, *Rev. Sci. Instrum.*, 81, 094 102, 2010.

Tkacik, D. S., Presto, A. A., Donahue, N. M., and Robinson, A. L.: Secondary organic aerosol formation from 625 intermediate-volatility organic compounds: cyclic, linear, and branched alkanes, *Environ. Sci. Technol.*, 46, 8773–8781, doi:10.1021/es301112c, 2012.

Van Krevelen, D. W.: Graphical-statistical method for the study of structure and reaction processes of coal, *Fuel*, 24, 269–284, 1950.

Yee, L. D., Craven, J. S., Loza, C. L., Schilling, K. A., Ng, N. L., Canagaratna, M. R., Ziemann, P. J., Flagan, 630 R. C., and Seinfeld, J. H.: Secondary organic aerosol formation from low- NO_x photooxidation of dodecane: evolution of multigeneration gas-phase chemistry and aerosol composition, *J. Phys. Chem. A*, 116, 6211–6230, doi:10.1021/jp211531h, 2012.

Zhang, X. and Seinfeld, J. H.: A functional group oxidation model (FGOM) for SOA formation and aging, *Atmos. Chem. Phys. Disc.*, 12, 32 565–32 611, doi:10.5194/acpd-12-32565-2012, 2012.

635 Ziemann, P. J.: Formation of alkoxyhydroperoxy aldehydes and cyclic peroxyhemiacetals from reactions of cyclic alkenes with O_3 in the presence of alcohols, *J. Phys. Chem. A*, 107, 2048–2060, doi:10.1021/jp022114y, 2003.

Table 1. C₁₂ compounds studied

Compound	Structure	V.P. ^a @ 25 °C (atm)	$k_{\text{OH}} \times 10^{12b}$ (molec cm ⁻³ s ⁻¹)
<i>n</i> -dodecane		2.59×10^{-4}	13.9
2-methylundecane		4.1×10^{-4}	13.1
hexylcyclohexane		2.59×10^{-4}	17.4
cyclododecane		1.64×10^{-4}	14.7

^a Using EVAPORATION (Compernolle et al., 2011)^b Calculated using relative rate from *n*-dodecane k_{OH} in MCM (Jenkin et al., 1997)**Table 2.** Experimental conditions

Expt	Organic	Duration of photooxidation (h)	Initial HC (ppb _v)	[NO] ₀ (ppb _v)	[NO _x] ₀ (ppb _v)	[O ₃] ₀ (ppb _v)	Initial Seed Vol. μm ³ /cm ³	Δ HC (ppb _v)	Peak Organic ^a μg/m ³
1	<i>n</i> -dodecane	18	33.0	< LDL ^b	< LDL ^b	3.3	12.0	32.3	51.3
2	<i>n</i> -dodecane	36	34.9	< LDL ^b	< LDL ^b	2.6	11.4	33.6	62.8
3	2-methylundecane	18	27.3	< LDL ^b	< LDL ^b	4.0	16.3	22.4	not available ^c
4	2-methylundecane	36	28.9	< LDL ^b	< LDL ^b	4.2	13.6	27.6	45.6
5	hexylcyclohexane	18	16.2	< LDL ^b	< LDL ^b	2.4	10.5	15.2	34.8
6	hexylcyclohexane	36	14.9	< LDL ^b	< LDL ^b	3.8	4.2	14.4	34.4
7	cyclododecane	18	10.1	< LDL ^b	< LDL ^b	2.0	24.4	9.2	19.5 ^d
8	cyclododecane	36	11.0	< LDL ^b	< LDL ^b	3.1	14.1	10.6	30.8

^a Not corrected for particle wall loss^b Below lower detection limit (5 ppb_v)^c AMS not sampling^d Reported for end of experiment, though growth had not peaked

Table 3. Selected ions monitored by the CIMS for *n*-dodecane and 2-methylundecane

Mode	Observed <i>m/z</i>	Chemical Formula	Assignment
(-)	287	C ₁₂ H ₂₆ O ₂	ROOH
(+)	223	C ₁₂ H ₂₄ O	CARB
(+)	204	C ₁₂ H ₂₄ O ₃	CARBROOH
(-)	285	C ₁₂ H ₂₄ O ₂	OHCARB
(-)	135/201	C ₆ H ₁₂ O ₂	C ₆ CARBACID

Table 4. Selected ions monitored by the CIMS for hexylcyclohexane and cyclododecane

Mode	Observed <i>m/z</i>	Chemical Formula	Assignment
(-)	285	C ₁₂ H ₂₄ O ₂	ROOH
(+)	221	C ₁₂ H ₂₂ O	CARB
(-)	299	C ₁₂ H ₂₂ O ₃	CARBROOH
(-)	283	C ₁₂ H ₂₂ O ₂	OHCARB
(-)	135/201	C ₆ H ₁₂ O ₂	C ₆ CARBACID

Table 5. Selected ions monitored by the AMS in the *n*-dodecane and 2-methylundecane systems

Observed <i>m/z</i>	Exact mass ion formula	Proposed assignment
183	$C_{12}H_{23}O^+$	CARBROOH + CARBROOH PHA
215	$C_{12}H_{23}O_3^+$	CARBROOH PHA
185	$C_{12}H_{25}O^+$	OHROOH + OHROOH PHA
217	$C_{12}H_{25}O_3^+$	OHROOH PHA
197	$C_{12}H_{21}O_2^+$	DICARBROOH + DICARBROOH PHA
229	$C_{12}H_{21}O_4^+$	DICARBROOH PHA + CYC. OHDICARBROOH
199	$C_{12}H_{23}O_2^+$	OHCARBROOH + OHCARBROOH PHA
231	$C_{12}H_{23}O_4^+$	OHCARBROOH PHA
201	$C_{12}H_{25}O_2^+$	DIROOH
211	$C_{12}H_{19}O_3^+$	TRICARBROOH + TRICARBROOH PHA
243	$C_{12}H_{19}O_5^+$	TRICARBROOH PHA
213	$C_{12}H_{21}O_3^+$	OHDICARBROOH + OHDICARBROOH PHA
245	$C_{12}H_{21}O_5^+$	OHDICARBROOH PHA

Table 6. Selected ions monitored by the AMS in the hexylcyclohexane system

Observed <i>m/z</i>	Exact mass ion formula	Proposed assignment
179	$C_{12}H_{19}O^+$	OHCARBROOH DHF
181	$C_{12}H_{21}O^+$	CARBROOH + CARBROOH PHA
213	$C_{12}H_{21}O_3^+$	CARBROOH PHA
183	$C_{12}H_{23}O^+$	OHROOH + OHROOH PHA
215	$C_{12}H_{23}O_3^+$	OHROOH PHA
195	$C_{12}H_{19}O_2^+$	DICARBROOH + DICARBROOH PHA
227	$C_{12}H_{19}O_4^+$	DICARBROOH PHA + CYC. OHDICARBROOH
197	$C_{12}H_{21}O_2^+$	OHCARBROOH + OHCARBROOH PHA
229	$C_{12}H_{21}O_4^+$	OHCARBROOH PHA
199	$C_{12}H_{23}O_2^+$	DIROOH
209	$C_{12}H_{17}O_3^+$	TRICARBROOH + TRICARBROOH PHA
211	$C_{12}H_{19}O_3^+$	OHDICARBROOH + OHDICARBROOH PHA
243	$C_{12}H_{19}O_5^+$	OHDICARBROH PHA

Table 7. Selected ions monitored by the AMS in the cyclododecane system

Observed <i>m/z</i>	Exact mass ion formula	Proposed assignment
181	$C_{12}H_{21}O^+$	CARBROOH + CARBROOH PHA
213	$C_{12}H_{21}O_3^+$	CARBROOH PHA
183	$C_{12}H_{23}O^+$	OHROOH + OHROOH PHA
215	$C_{12}H_{23}O_3^+$	OHROOH PHA
195	$C_{12}H_{19}O_2^+$	DICARBROOH + DICARBROOH PHA
227	$C_{12}H_{19}O_4^+$	DICARBROOH PHA
197	$C_{12}H_{21}O_2^+$	OHCARBROOH + OHCARBROOH PHA
229	$C_{12}H_{21}O_4^+$	OHCARBROOH PHA
199	$C_{12}H_{23}O_2^+$	DIROOH
207	$C_{12}H_{15}O_3^+$	OH4CARBROOH
223	$C_{12}H_{15}O_4^+$	CYC. OH4CARBROOH
209	$C_{12}H_{17}O_3^+$	TRICARBROOH/4CARBROOH Ring Opened
225	$C_{12}H_{17}O_4^+$	CYC. TRICARBROOH
211	$C_{12}H_{19}O_3^+$	OHDICARBROOH/TRICARBROOH Ring Opened

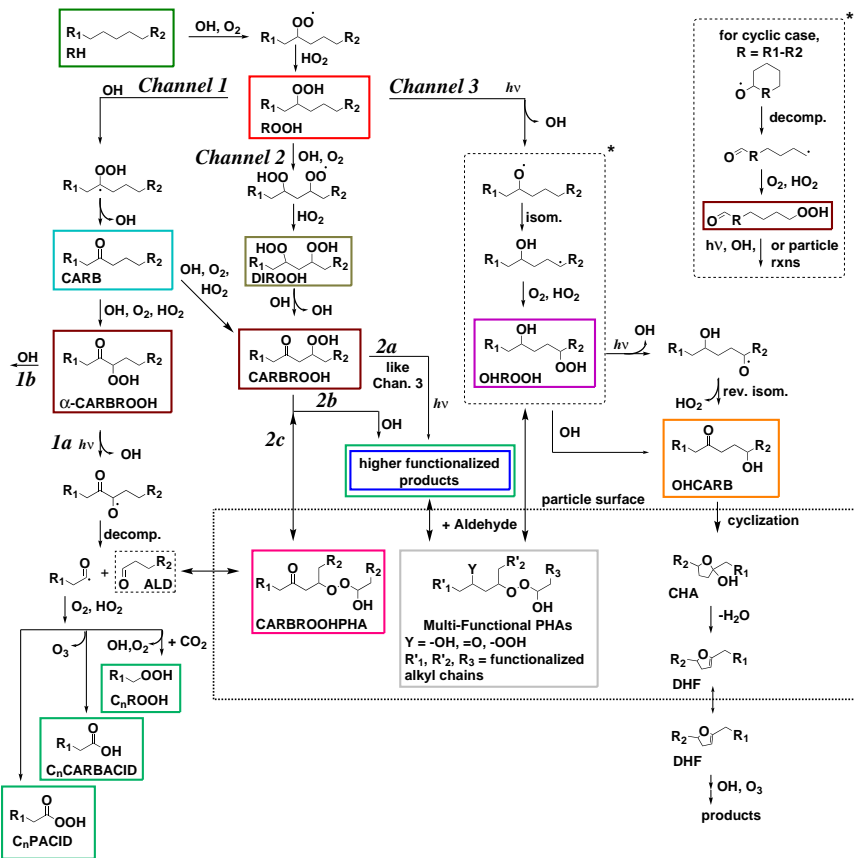


Fig. 1. General mechanism for alkanes under low- NO_x conditions. R_1 and R_2 are alkyl groups. Solid boxed compounds indicate proposed structures monitored by the CIMS in the gas-phase and/or the AMS in the particle-phase. Pathway in upper right with asterisk denotes alternative pathway for the cyclic case (R_1 and R_2 are bonded together as R).

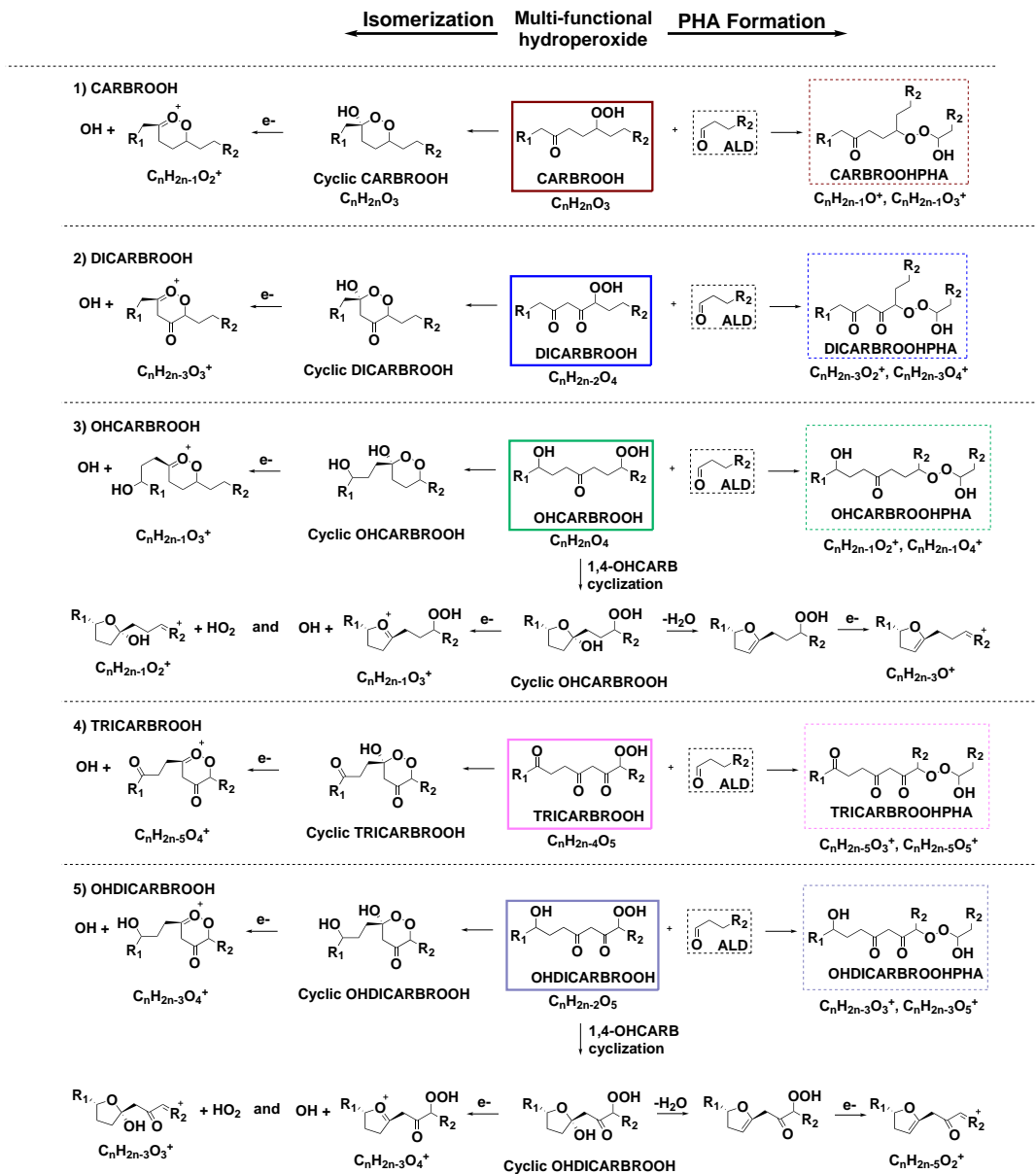


Fig. 2. General mechanism for particle-phase chemistry involving PHA formation (right-hand side) and potential isomerization (left-hand side) from higher functionalized products (solid boxed) formed along Channel 2 in Figure 1. R_1 and R_2 are alkyl groups. One isomer shown. Dashed boxed compounds indicate PHA structures for which AMS ion tracers exist. General chemical and ion formulae for multi-functional hydroperoxides and proposed PHA and isomerization products shown, where $n=12$. Analogous products for hexylcyclohexane and cyclododecane would have an additional degree of unsaturation.

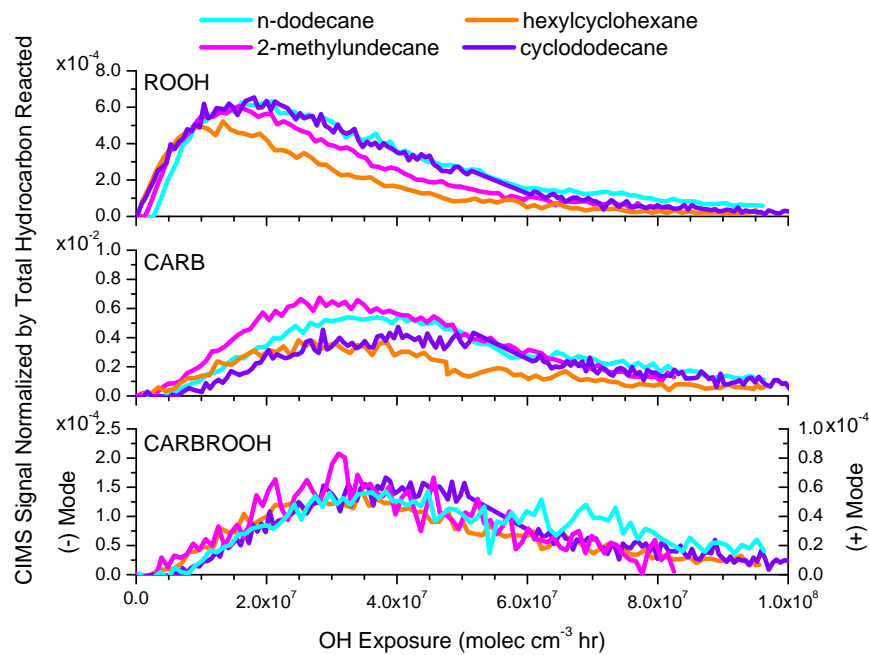


Fig. 3. Gas-phase trends of major species formed in the first three generations of photooxidation. Top Panel: First-generation hydroperoxide (ROOH), Middle Panel: Second-generation carbonyl (CARB), and Bottom Panel: Third-generation carbonyl hydroperoxide (CARBROOH). Note that the CARBROOH was monitored in positive mode for *n*-dodecane and 2-methylundecane (the right side axis) and in negative mode for hexylcyclohexane and cyclododecane (the left side axis).

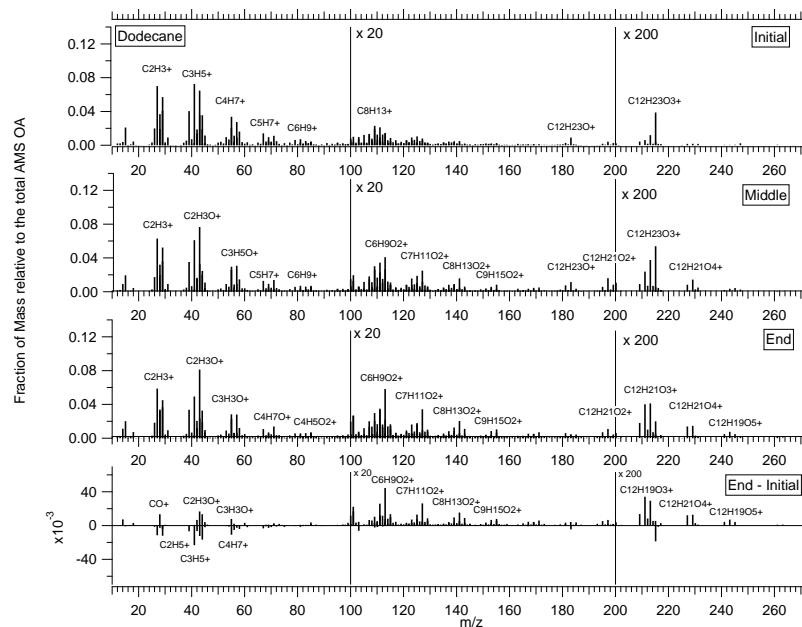


Fig. 4. High-resolution mass spectrum of SOA formed from *n*-dodecane at initial organic growth, mid-experiment, and end of experiment. The difference spectrum is also shown. m/z 's 101 - 200 are multiplied by 20, and m/z 's 201 - 300 are multiplied by 200 for visual clarity. Ions with high signal are labeled.

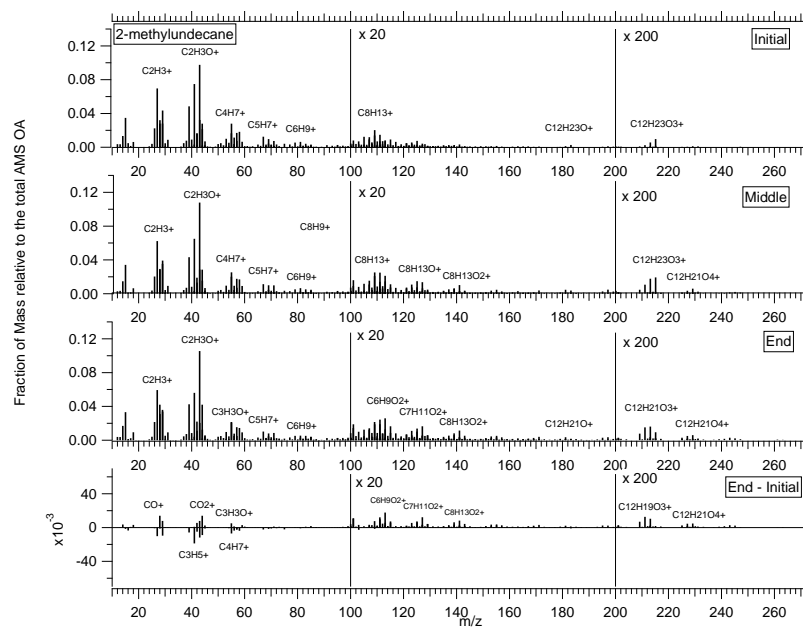


Fig. 5. High-resolution mass spectrum of SOA formed from 2-methylundecane at initial organic growth, mid-experiment, and end of experiment. The difference spectrum is also shown. m/z 's 101 - 200 are multiplied by 20, and m/z 's 201 - 300 are multiplied by 200 for visual clarity. Ions with high signal are labeled.

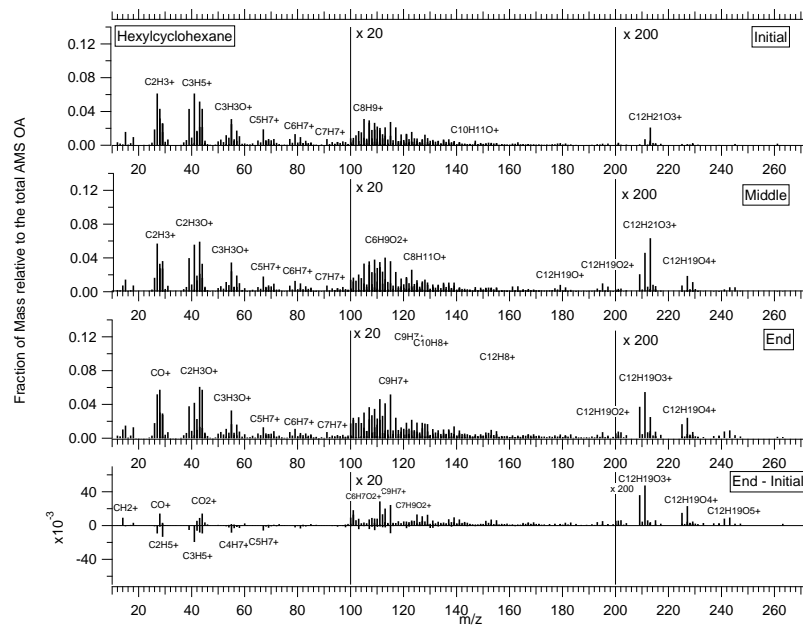


Fig. 6. High-resolution mass spectrum of SOA formed from hexylcyclohexane at initial organic growth, mid-experiment, and end of experiment. The difference spectrum is also shown. m/z 's 101 - 200 are multiplied by 20, and m/z 's 201 - 300 are multiplied by 200 for visual clarity. Ions with high signal are labeled.

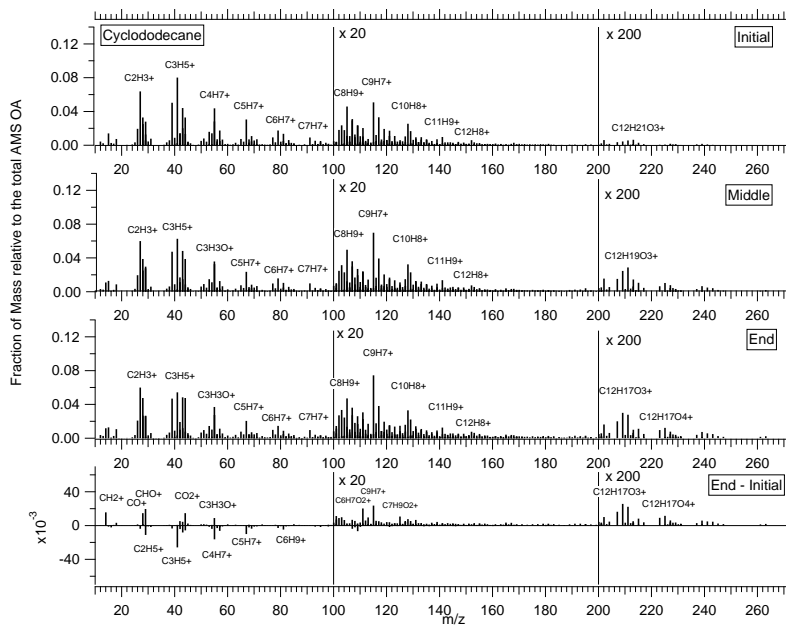


Fig. 7. High-resolution mass spectrum of SOA formed from cyclododecane at initial organic growth, mid-experiment, and end of experiment. The difference spectrum is also shown. m/z 's 101 - 200 are multiplied by 20, and m/z 's 201 - 300 are multiplied by 200 for visual clarity. Ions with high signal are labeled.

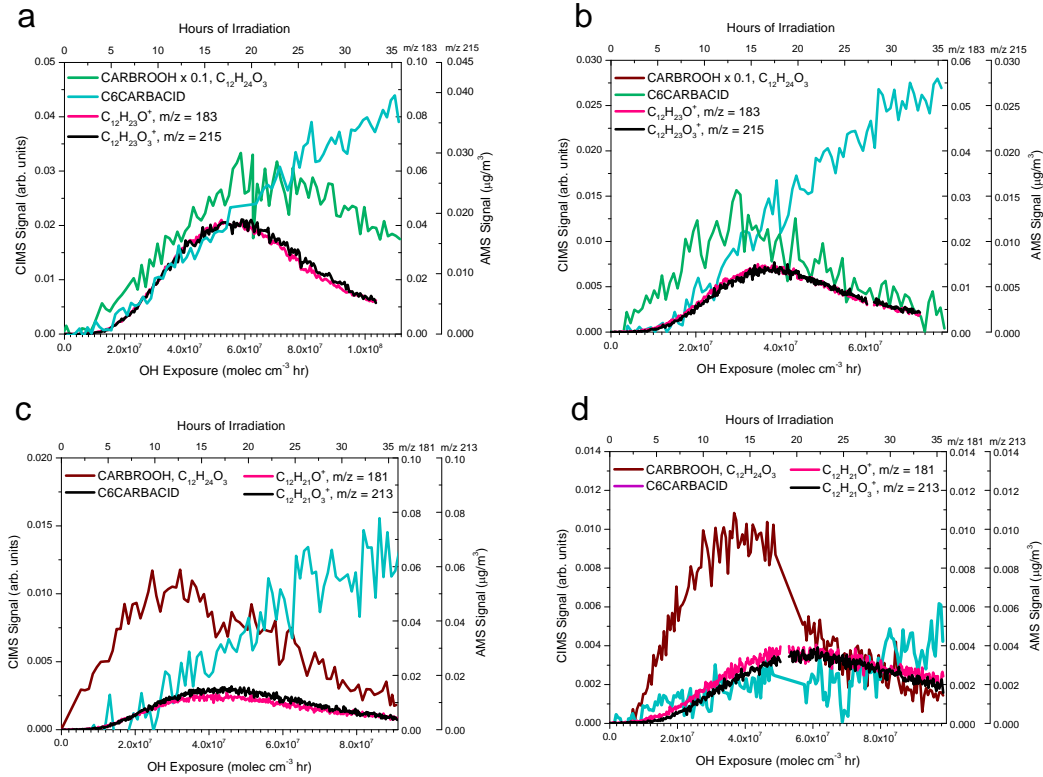


Fig. 8. Gas-phase trends of the (a) *n*-dodecane, (b) 2-methylundecane, (c) hexylcyclohexane, and (d) cyclododecane generated carbonyl hydroperoxide (CARBROOH) and C₆ carboxylic acid as monitored by the CIMS and the CARBROOH and its derived PHA in the particle phase. CARBROOH and its PHA are tracked by AMS ions C₁₂H₂₃O⁺ and C₁₂H₂₃O₃⁺ for *n*-dodecane and 2-methylundecane, and by C₁₂H₂₁O⁺ and C₁₂H₂₁O₃⁺ for hexylcyclohexane and cyclododecane.

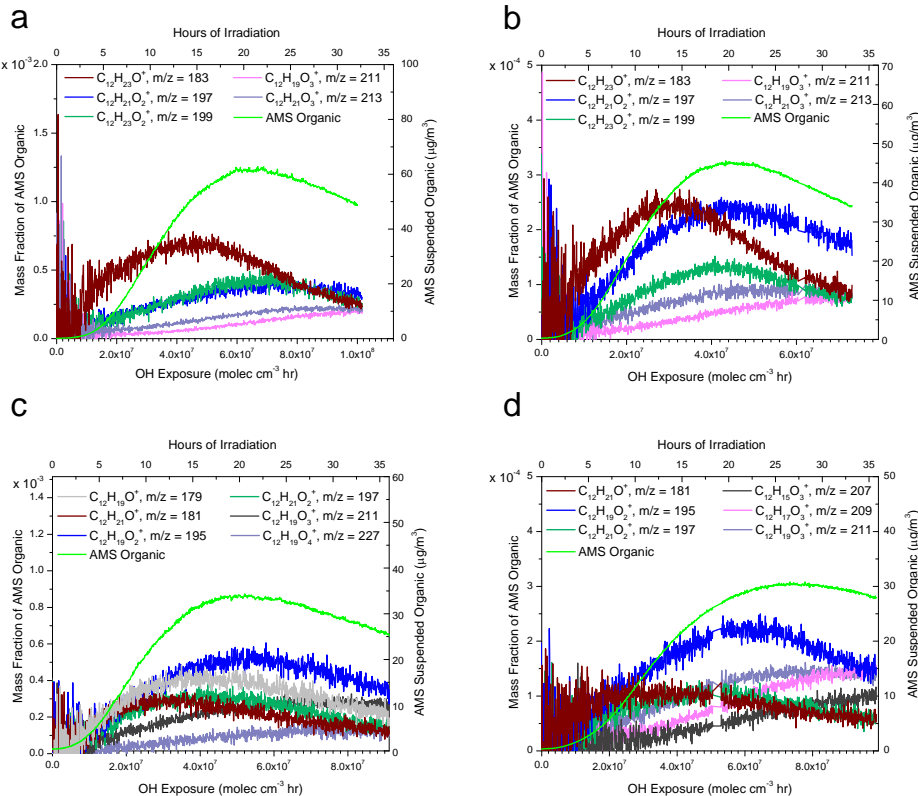


Fig. 9. Characteristic ions in (a) *n*-dodecane, (b) 2-methylundecane, (c) hexylcyclohexane, and (d) cyclododecane aerosol measured by the AMS.

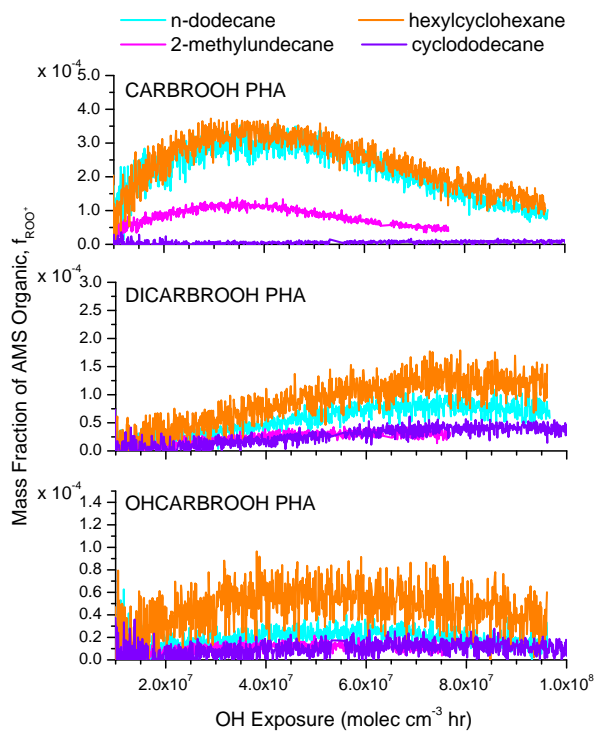


Fig. 10. Fraction of organic attributed to the corresponding ROO^+ PHA tracer ion for (top) carbonyl hydroperoxide PHA (CARBROOH PHA), (middle) dicarbonyl hydroperoxide (DICARBROOH), and (bottom) hydroxycarbonyl hydroperoxide (OHCARBROOH).

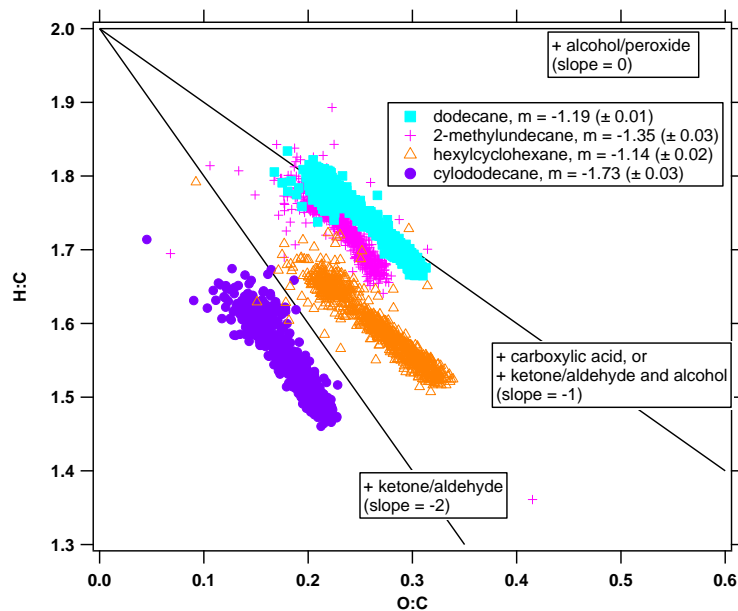


Fig. 11. Van Krevelen diagram for low- NO_x photooxidation of *n*-dodecane, 2-methylundecane, hexylcyclohexane, and cyclododecane.

Chapter 6

Conclusions and future work

The chamber studies conducted here emphasize the importance of structure-dependent chemistry affecting SOA formation. For the methoxyphenols study, syringol resulted in a lower aerosol yield than guaiacol and phenol under the experimental conditions. This is non-intuitive considering that syringol has a lower vapor pressure than guaiacol and phenol, but the rapid conversion of syringol to guaiacol and phenolic products suggests that there is potential to form more aerosol via these more efficient SOA formers, but under extended periods of OH exposure. For the C₁₂ alkanes, cyclododecane exhibits continued organic growth compared to the straight-chain, branched, and cyclic branched structures. This is a result of several factors including: 1) for the analogous products across the systems, cyclododecane products will tend to have a lower vapor pressure due to the C₁₂ ring structure, 2) if the C₁₂ ring opens, an aldehydic hydroperoxide is generated which can immediately participate in oligomer and accretion reactions (e.g. peroxyhemiacetal formation), and 3) continued functionalization of the molecule dominates over fragmentation, whereas branching leading to fragmentation for the cases of 2-methylundecane and hexylcyclohexane limits their potential for organic growth. *n*-dodecane exhibits less fragmentation than hexylcyclohexane, but as observed in the characteristic time

trends of the chemical development across systems, it also does not functionalize as quickly as hexylcyclohexane. Thus, these structure-dependent oxidation processes explain why SOA yield increases from branched, straight-chain, cyclic branched, to cyclic.

These findings have implications for the field of atmospheric chemistry in many ways. First, these results imply that atmospheric chemistry models that employ model compounds as surrogates to represent SOA formation from a related class of compounds (e.g. methoxyphenols or alkanes), must be chosen with care. The conversion of syringol to guaiacol and phenol suggests that selecting any one of the test compounds to represent SOA formation from biomass burning could underscore the true fate of related compounds in the atmosphere. It also shows that while syringol and guaiacol are considered to be relatively unique tracers for different wood/fuel types, the conversion of syringol to guaiacol means that they are no longer unique tracers as measured in situ. Similarly for alkanes, the relative amount of each structure type in currently used fuels is important to know to implement accurate emission inventories as well as their respective known structure-based SOA yields into atmospheric models.

The current work motivates future exploration of additional details of the gas- and particle-phase chemistry of these compounds and their role in SOA formation. The methoxyphenols studies present the need for additional experiments where methoxy group placement is varied to determine the influence on position of initial OH attack, product distributions, and the eventual effect on SOA yield. Analytical techniques that can isolate the position of functional groups on the ring during chemical development will also be necessary for understanding preferred routes in oxidation leading to SOA formation. These compounds contain the functional groups that make them good candidates for further studies into aqueous-phase processing (experiments run

in the presence of humidity), in an effort to explore radiative effects of brown carbon. Brown carbon is formed during biomass burning events and has grown of increasing importance to understand aerosol radiative effects.

The alkanes studies provided a unique opportunity to delve into particle-phase chemistry affecting SOA formation. In the case of *n*-dodecane, strong evidence from the complementary gas-phase and particle-phase measurements supports that under the experimental conditions, SOA growth is initiated by accretion reactions driving semi- and intermediate volatility organic compounds into the particle phase. Purely based on vapor pressure and equilibrium partitioning theory, many of the early measured multi-generational hydroperoxides would not be expected to contribute significantly to organic growth at the time of initial growth. However, the enhancement due to kinetic growth processes such as accretion reactions involving reactive carbonyls (e.g. aldehydes) is important to understand for representing these processes in the atmosphere. Future work includes further exploration into the environmental factors affecting these routes to SOA formation, as these reactions are often surface and/or acid catalyzed, and the presence of water and the chemical state of the particle phase may shift the equilibrium under which these products are stable. This work provides a basis for ongoing modeling studies that focus on understanding the kinetic and thermodynamic effects at play. Current atmospheric models do not implement schemes for particle-phase chemistry and phase effects, though they have become of increasing importance to our understanding of aerosol chemistry.

Appendix A

Application of the Statistical Oxidation Model (SOM) to Secondary Organic Aerosol formation from photooxidation of C12 alkanes¹

¹This chapter is reproduced by permission from "Application of the Statistical Oxidation Model (SOM) to Secondary Organic Aerosol formation from photooxidation of C12 alkanes," by C. D. Cappa, X. Zhang, C. L. Loza, J. S. Craven, L. D. Yee, and J. H. Seinfeld, *Atmospheric Chemistry and Physics*, 13, 1591 –1606, doi:10.5194/acp-13-1591-2013, www.atmos-chem-phys.net/13/1591/2013/, 2013. Copyright 2013 Authors. This work is licensed under a Creative Commons License.



Application of the Statistical Oxidation Model (SOM) to Secondary Organic Aerosol formation from photooxidation of C₁₂ alkanes

C. D. Cappa¹, X. Zhang², C. L. Loza³, J. S. Craven³, L. D. Yee², and J. H. Seinfeld^{2,3}

¹Department of Civil and Environmental Engineering, University of California, Davis, CA, 95616, USA

²Division of Engineering and Applied Science, California Institute of Technology, Pasadena, CA, 91125, USA

³Division of Chemistry and Chemical Engineering, California Institute of Technology, Pasadena, CA, 91125, USA

Correspondence to: C. D. Cappa(ccdcappa@ucdavis.edu) and J. H. Seinfeld (seinfeld@caltech.edu)

Received: 14 September 2012 – Published in Atmos. Chem. Phys. Discuss.: 15 October 2012

Revised: 23 January 2013 – Accepted: 25 January 2013 – Published: 8 February 2013

Abstract. Laboratory chamber experiments are the main source of data on the mechanism of oxidation and the secondary organic aerosol (SOA) forming potential of volatile organic compounds. Traditional methods of representing the SOA formation potential of an organic do not fully capture the dynamic, multi-generational nature of the SOA formation process. We apply the Statistical Oxidation Model (SOM) of Cappa and Wilson (2012) to model the formation of SOA from the formation of the four C₁₂ alkanes, dodecane, 2-methyl undecane, cyclododecane and hexylcyclohexane, under both high- and low-NO_x conditions, based upon data from the Caltech chambers. In the SOM, the evolution of reaction products is defined by the number of carbon (N_C) and oxygen (N_O) atoms, and the model parameters are (1) the number of oxygen atoms added per reaction, (2) the decrease in volatility upon addition of an oxygen atom and (3) the probability that a given reaction leads to fragmentation of the molecules. Optimal fitting of the model to chamber data is carried out using the measured SOA mass concentration and the aerosol O:C atomic ratio. The use of the kinetic, multi-generational SOM is shown to provide insights into the SOA formation process and to offer promise for application to the extensive library of existing SOA chamber experiments that is available.

1 Introduction

Organic aerosol (OA) comprises a major fraction of the atmospheric sub-micron aerosol burden (Zhang et al., 2007; Jimenez et al., 2009), and the dominant portion of OA is

formed from condensation of oxidation products of gas-phase reactions of volatile organic compounds, termed secondary organic aerosol (SOA). The extent to which a given parent organic compound forms SOA depends on a variety of factors, including the carbon chain length, structure and reactivity, as well as external factors such as temperature, the abundance of NO_x (=NO + NO₂) and the identity of the oxidant (OH, O₃, NO₃) (Kanakidou et al., 2005). Additionally, the properties of the SOA, e.g. hygroscopicity, volatility and atomic composition, depend on all of the above factors (Jimenez et al., 2009).

Understanding SOA formation via photooxidation (i.e. reactions with OH) presents a unique challenge in that not only is the precursor SOA species (i.e. the parent organic) reactive towards OH, but so are the oxidation products. The extent to which each generation of products contributes directly to SOA formation depends intimately on the details of the atmospheric chemistry for the particular organic. Laboratory chamber experiments are the main source of data on the mechanism of oxidation and the SOA forming potential of a parent organic. Because SOA forms via gas-particle partitioning, the amount of SOA depends on the mass of absorbing material in the aerosol phase, in addition to the unique chemistry. For comparison of SOA formation from different organics, especially in atmospheric models, an SOA model is required. Traditional methods of representing the SOA formation potential, or yield, of an organic do not fully capture the dynamic, multi-generational nature of photooxidation, as they generally treat SOA formation as a one-step process from precursor to products. This includes both the 2-product model (Odum et al., 1996) and static volatility

Table 1. Experimental conditions and results from photooxidation experiments.

Alkane	[HC] ₀ (ppbv)	[OH] ^a (molecules cm ⁻³)	<i>C</i> _{OA} ($\mu\text{g m}^{-3}$)	Yield ^b (%)	Yield ^c (%)	O:C max	O:C min
Low NO_x							
dodecane	34.0	2.5×10^6	21.6	10.3	6.1	0.28	0.21
2-methylundecane	28.1	2.4×10^6	18.1	10.8	7.2	0.28	0.20
hexylcyclohexane	15.6	2.95×10^6	28.9	29.6	15.4	0.32	0.22
cyclododecane	9.8	2.7×10^6	15.8	24.4	17.2	0.24	0.15
High NO_x							
dodecane	32.2	$4.5 \times 10^7 / 1.85$	10.6	6.8	6.2	0.33	0.33
2-methylundecane	72.4	$3.3 \times 10^7 / 1.85$	23.5	7.8	5.1	0.26	0.26
hexylcyclohexane	22.1	$4.1 \times 10^7 / 1.7$	17.5	16.4	12.3	0.32	0.32
cyclododecane	13.8	$2.7 \times 10^7 / 0.92$	29.5	41.5	38.3	0.27	0.27

^a For high-NO_x conditions, [OH] is time dependent and has the form $[\text{OH}]_t = [\text{OH}]_{t=0} \exp(-kt)$, where *t* is the time elapsed (in hours) and *k* is the decay constant. The $[\text{OH}]_{t=0}$ and *k* values are reported in the table.

^b *C*_{OA} and yield values are reported after 15 h (low-NO_x) and 3 h (high-NO_x) of reaction, respectively.

^c Yield values are reported for *C*_{OA} = 10 $\mu\text{g m}^{-3}$.

basis-set (Donahue et al., 2006). Recently, methodologies have been developed that represent photooxidation and subsequent SOA formation within more dynamic frameworks (Aumont et al., 2005; Robinson et al., 2007; Lane et al., 2008; Barsanti et al., 2011; Valorso et al., 2011; Cappa and Wilson, 2012; Donahue et al., 2012). Depending on the specific methodology employed, these models allow for reaction of the first (and later) generation oxidation products, fragmentation and tracking of the detailed composition of the particle and gas-phase.

Here, we apply the Statistical Oxidation Model (SOM) of Cappa and Wilson (2012) to model the formation of SOA from the photooxidation of a series of C₁₂ alkanes of varying structure, two of which are linear (dodecane and 2-methyl undecane) and two of which have ring structures (cyclododecane and hexylcyclohexane). Experiments were conducted under both high- and low-NO_x conditions to explore the important influence of NO_x on the SOA formation. The best-fit model is found to capture the time-evolution of the observed SOA mass concentration and, to a reasonable extent, the O:C atomic ratio under both high- and low-NO_x conditions. Best-fit SOM parameters are reported, and indicate that, per reaction with OH, photooxidation leads to more rapid oxygen addition under high-NO_x conditions than low-NO_x conditions. Despite the more rapid oxygen addition under high-NO_x conditions, the nature of the functional groups added lead to a smaller decrease in volatility (per oxygen added) than under low-NO_x conditions. The success of fitting the SOM to these alkane SOA formation data offers promise to apply the SOM to the extensive library of existing chamber experiments that is available.

2 Experimental methods

Experiments were conducted in the Caltech dual 28-m³ Teflon chambers. Details of the facility have been described previously (Cocker et al., 2001). Prior to each experiment, the chambers were flushed with dried, purified air for >24 h, until the particle concentration was <100 cm⁻³ and the volume concentration was <0.1 $\mu\text{m}^3 \text{m}^{-3}$.

For all experiments, neutral ammonium sulfate seed aerosol was used to provide surface area for condensation of the semi-volatile oxidation products. Particle size distributions were measured using a differential mobility analyser (DMA, TSI, 3081) coupled with a condensation particle counter (CPC, TSI, CNC-3760).

Photooxidation experiments were run under both high and low-NO_x conditions. Low-NO_x (<1 ppb) experiments were conducted using photolysis of H₂O₂ as the OH radical source. High-NO_x experiments were conducted using photolysis of HONO as the OH radical source. The primary NO_x source is direct photolysis of HONO, although some NO and NO₂ formed as part of the HONO preparation. The gas-phase concentration of the SOA precursor was measured throughout the experiments. Initial concentrations are given in Table 1. Four alkanes are considered here, each with 12 carbon atoms: dodecane (C₁₂H₂₆), 2-methyl undecane (C₁₂H₂₆), hexylcyclohexane (C₁₂H₂₄) and cyclododecane (C₁₂H₂₄).

Photooxidation was initiated by irradiating the chamber with blacklights. Output from the lights is between 300 and 400 nm, with a maximum at 354 nm. Importantly, HONO photolysis is efficient in this wavelength range, and thus the concentration of HONO (and OH) decays towards zero over a period of ~3 h once the lights are turned on. H₂O₂ photolysis is comparably much slower, which facilitates operation at

a nearly constant [OH] throughout the low-NO_x experiments. To access long oxidation times (up to 32 h) in the low-NO_x experiments, the methodology set out by Loza et al. (2012) was followed. As a result, the time series of OA mass concentrations (C_{OA}) under low-NO_x conditions have a “gap” of ~ 6 h (typically from hours 18–24).

Chemically-resolved aerosol mass concentrations were measured using an Aerodyne high-resolution time-of-flight aerosol mass spectrometer (HR-ToF-AMS, henceforth referred to as AMS). Real-time mass spectra of the particles were collected alternating between “V-mode” and “W-mode”. The “V-mode” provides higher sensitivity while the “W-mode” provides higher resolution. The “W-mode” data were analysed using the software toolboxes PIKA (DeCarlo et al., 2006) and APES (Aiken et al., 2007; Aiken et al., 2008; Chhabra et al., 2010). Through consideration of ions with specific molecular formulas, as determined from the “W-mode” spectra, the elemental composition of the SOA can be determined (in particular, the O:C and H:C atomic ratios). The estimated uncertainty in the O:C is ± 30 % and in the H:C is 10 %.

A correction for wall loss needs to be applied to determine the SOA mass concentration. Two limiting assumptions can be employed to bound the interactions between particles deposited to the wall and vapors in the chamber. Here we use a lower bound, in which particles deposited on the wall are assumed to cease interaction with suspended vapors after deposition (Loza et al., 2012). The total organic mass deposited to the wall was calculated based on the particle number-weighted size distribution. The wall loss rates for particles of different sizes are obtained from separate characterization experiments. The deposited particle number distribution is added to the suspended particle number distribution to give a wall-loss corrected number distribution, which is then converted to a volume concentration and then mass concentration, assuming spherical particles. For the low-NO_x experiments reported on here, wall loss corrections at long times require extrapolation of the C_{OA} across the “gap”, which decreases the certainty of the correction and, as a result, the accuracy of the wall-loss corrected C_{OA} values after the gap. Thus, only the pre-gap C_{OA} data are used quantitatively here.

3 Statistical Oxidation Model

The statistical oxidation model (SOM) simulates the oxidation of a parent hydrocarbon and its reaction products in time, and is described in detail in Cappa and Wilson (2012). In the SOM, the evolution of the gas and particle phase composition is followed through a space in which all product species are defined solely by their number of carbon (N_C) and oxygen (N_O) atoms. Equilibrium partitioning between the gas and particle phases is assumed to hold at each time-step of the model (~ 1 –2 min) (Pankow, 1994). It is assumed that the properties of each species (i.e. N_C/N_O pair) can be repre-

sented by some mean values that account for the actual distribution of functional groups within the group of molecules that make up an SOM species. There are a few adjustable parameters within the SOM: (1) the number of oxygen atoms added per reaction, which is represented as an array of probabilities of adding 1, 2, 3 or 4 oxygen atoms, termed P_{func} , (2) the decrease in volatility upon addition of an oxygen atom, termed ΔLVP , which is the difference in the log of the saturation concentration, C_{sat} , per oxygen added, or

$$\Delta LVP = \log \left[\frac{C_{sat, N_O}}{C_{sat, N_O + 1}} \right] \quad (1)$$

and (3) the probability that a given reaction leads to fragmentation of the product molecule into two smaller molecules, termed P_{frag} . Note that positive values of ΔLVP correspond to a decrease in vapour pressure upon oxygen addition. These parameters can be adjusted to determine a best fit of the model to the observations. The SOM also includes heterogeneous reactions with OH radicals (Cappa and Wilson, 2012). It is assumed that each heterogeneous OH reaction leads to the addition of one oxygen atom, that the fragmentation probability is assumed equivalent to the gas-phase, and that the reactive uptake coefficient is unity. The model additionally requires as input the initial concentration of the parent hydrocarbon, $[HC]_0$, and the (potentially time-dependent) oxidant concentration. In this study, for the low-NO_x experiments the [OH] was constant (or nearly constant) throughout, while for the high-NO_x experiments the [OH] decayed rapidly. In either case, the model [OH] was specified so that the observed temporal decay of [HC] was reproduced (see Table 1).

It is not yet clear what the most appropriate functional form is for the fragmentation probability, P_{frag} . Therefore, two parameterizations are considered here: $P_{frag}(O:C) = (O:C)^{m_{frag}}$ and $P_{frag}(N_O = c_{frag} N_O)$, where m_{frag} and c_{frag} are adjustable parameters, and there is an upper limit of $P_{frag} = 1$. Smaller values of m_{frag} and larger values of c_{frag} indicate more extensive fragmentation, respectively. It is assumed that the generated fragments are randomly distributed in terms of where the carbon bond scission occurs.

Best-fit values for P_{func} , ΔLVP and P_{frag} are determined by simultaneously fitting the time-dependent model predictions to observations of wall-loss corrected organic aerosol mass concentrations (C_{OA}) and O:C for each system (in this case, C₁₂ compounds reacting with OH radicals under high- or low-NO_x conditions). Alternatively, the SOM was fit only to the C_{OA} observations. The data fitting was performed using the Levenberg-Marquardt algorithm built into the data analysis program Igor. Uncertainties in the measured C_{OA} were assumed to be the larger of $0.5 \mu\text{g m}^{-3}$ or 10 %. Uncertainties in the O:C were ± 30 %. An upper limit of $\Delta LVP = 2.2$ was applied. The functional group that contributes most to the decrease of vapour pressure per O atom added is the –OH group. The EVAPORATION model (Compernolle et al., 2011) predicts that ΔLVP upon addition of –OH to primary, secondary and tertiary C is 2.23,

1.70 and 1.16, respectively, whereas the SIMPOL.1 model (Pankow and Asher, 2008) predicts 2.76, 2.10 and 1.49, respectively. Here we take the average between the two vapour pressure models as the upper limit to ΔLVP . For low-NO_x experiments, which have a gap in the C_{OA} data from ~ 18 –24 h of reaction, the data are fit only prior to this gap. As noted above, the reason for this is that the uncertainty in the wall-loss correction across the gap leads to larger uncertainty in the C_{OA} after the gap.

Variation in the H:C atomic ratio with oxidation is characterized within the SOM by specifying the average number of hydrogen atoms lost per oxygen atom added, which is equal to the negative slope in a Van Krevelen diagram (a graph of H:C vs. O:C) (Heald et al., 2010). Here, the H-loss-per-O-added is specified a priori based on the observed Van Krevelen slope, although it should be noted that the specification of this relationship has a negligible influence on the evolution of either the C_{OA} or O:C.

Condensed phase reactions (besides heterogeneous OH reactions) are not explicitly accounted for in the SOM. Thus, to the extent that condensed phase reactions (e.g. oligomerization, dehydration, cyclization) alter the observed SOA properties, this will be reflected in the best-fit model parameters.

4 Results

4.1 Low-NO_x conditions

The time-evolution of the observed wall-loss corrected SOA mass concentrations (C_{OA}) and the particle-phase O:C atomic ratios are shown in Fig. 1, along with the tuned model results obtained using both P_{frag} parameterizations and after fitting simultaneously to both C_{OA} and O:C. In general, as oxidation proceeds, the observed C_{OA} increases until the parent [HC] decays to around 10 % of its initial value (which occurs around 15–20 h of oxidation). After this point, the C_{OA} starts to level off, or even decrease slightly, even though there is still OH present in the system. The observed SOA O:C atomic ratio at early times tends to decrease slightly until the parent [HC] decays to around 30 % of its initial value (at 5–10 h of oxidation), after which time it begins to slowly increase. Aerosol mass yields for the two ring-containing compounds are larger than for the non-ring containing compounds (Table 1), consistent with previous results from Lim and Ziemann (2009).

The SOM, after fitting, captures the general time-dependent behaviour of the observed C_{OA} , with the model C_{OA} exhibiting a levelling off or slight decrease at long times for many of the simulations (Fig. 1). The exact time-dependence of the model C_{OA} depends somewhat on the assumed fragmentation parameterization and method. In general, the $P_{frag}(N_O)$ parameterization tends to show a more pronounced turnover in the C_{OA} at long times than the $P_{frag}(O:C)$ parameterization. The $P_{frag}(N_O)$ results appear

slightly more consistent with the observations, which is an unexpected result given that the more physically intuitive behavior is that the probability of fragmentation for a given molecule should depend on the relative oxygen abundance (i.e. O:C) rather than the absolute oxygen abundance (i.e. N_O). However, the uncertainty in the observed C_{OA} after the data gap limits our ability to definitively make this assessment.

The SOM captures the general shape of the observed O:C time-dependence, with the model O:C typically first decreasing before increasing with time, similar to the experimental results (Fig. 1). Despite the satisfactory shape of the model O:C time-dependence, for all of the hydrocarbons considered the absolute value of the model O:C is somewhat greater than the observed O:C, although typically within the experimental uncertainty. Cyclododecane is the notable exception, with a model O:C that is substantially higher than the observed value (although the shape of the calculated and observed time-dependencies are quite similar). The over-prediction is, in part, a consequence of setting an upper limit for $\Delta LVP = 2.2$ during fitting; allowing for larger values of ΔLVP can lead to better model/measurement agreement for most compounds (although not for cyclododecane) and can still allow for a good fit to the observed C_{OA} . The $P_{frag}(N_O)$ parameterization generally yields somewhat lower absolute O:C values compared to $P_{frag}(O:C)$. An additional reason for the over-prediction of the model O:C relative to the observations could be that the HR-ToF-AMS underestimates the oxygen derived from hydroperoxides, with these species instead detected with the –OOH removed (Craven et al., 2012). This would lead to a measured O:C that is somewhat lower than the actual O:C, with the extent of this disparity potentially dependent upon the hydroperoxide fraction of the oxygenated functional groups.

When the model is fit to both the C_{OA} and O:C, the best-fit ΔLVP is 2.2 for all compounds, i.e. the imposed upper-limit (Fig. 2 and Table 2). This is not surprising given that the model O:C is particularly sensitive to the ΔLVP parameter (Cappa and Wilson, 2012). When the model is fit to only the C_{OA} data, the best-fit values remain high, with $2 < \Delta LVP < 2.2$. For all compounds considered, the addition of 1 oxygen atom per reaction was most probable, with some smaller fraction of reactions requiring the addition of 2, 3 or 4 oxygen atoms (Fig. 2 and Table 2). The model results indicate that fragmentation is extensive, and the non-ring-containing compounds have larger c_{frag} and smaller m_{frag} values compared to the ring-containing compounds, suggesting more extensive fragmentation of the non-ring containing compounds. For all compounds, the c_{frag} values (for $P_{frag}(N_O)$) were ≥ 0.33 , which indicates that any molecule already containing 3 or more oxygen atoms will exclusively fragment upon reaction. Note that this does not preclude formation of species with > 3 oxygen atoms because some reactions add more than 1 oxygen atom and because fragmentation also leads to oxygen addition. It does, however, limit the rate and overall extent

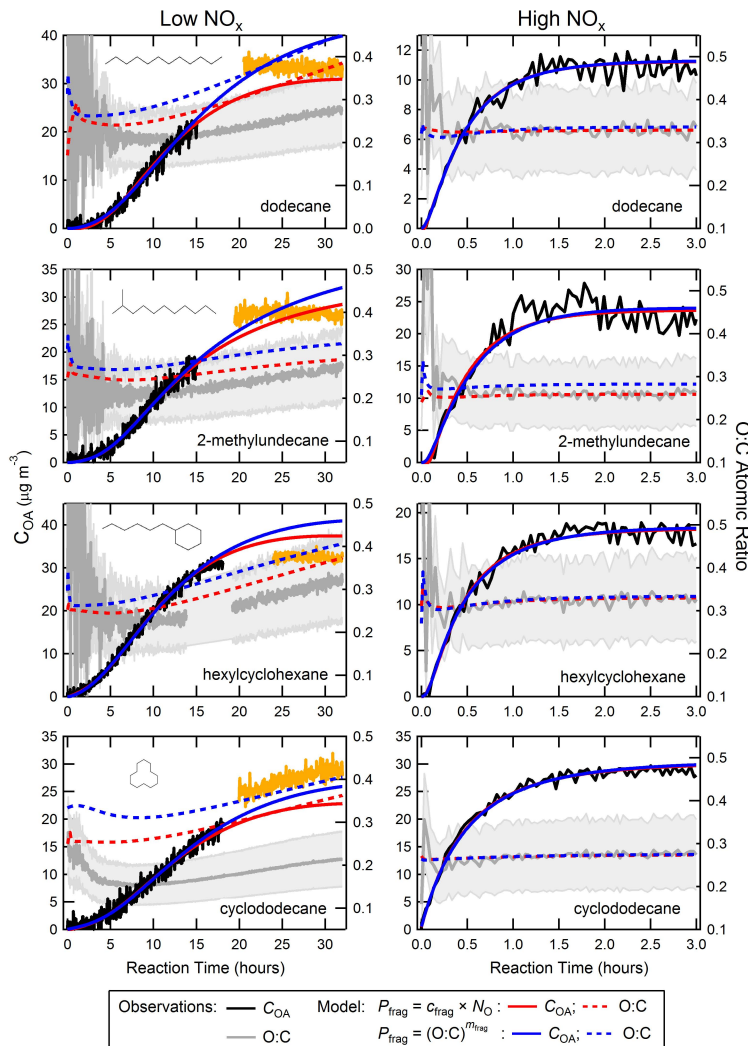


Fig. 1. Evolution of the SOA mass concentration, C_{OA} , (black lines, left axes) and O:C atomic ratio (gray lines, right axes) for low- NO_x (left panels) and high- NO_x (right panels) for dodecane, 2-methylundecane, hexylcyclohexane and cyclododecane (top-to-bottom). The light gray bands on the O:C indicate the estimated uncertainty range ($\pm 30\%$). The model results using $P_{frag}(NO)$ and $P_{frag}(O:C)$ are shown as red and blue lines, respectively. Solid lines are model fits for C_{OA} and dashed lines for O:C. The model has been fit simultaneously to the C_{OA} and O:C data for $t < 15$ h (low- NO_x , black lines) or $t < 3$ h (high- NO_x). For the low- NO_x conditions, the orange lines correspond to data collected after a pause in sampling (indicated by a gap in the C_{OA} time series).

to which such highly oxygenated species can form. Similar conclusions are reached if the $P_{frag}(O:C)$ parameterization is instead considered, although the exact details are changed somewhat due to the different functional form of the parameterization.

The observed co-variation of H:C with O:C, shown as a Van Krevelen diagram, indicates that the number of H atoms lost per O atom added, or the negative slope on the graph,

ranges from 1.45 to 2.2 (Fig. 3); this parameter is specified within the SOM so as to match the model to the observations. The model aerosol exhibits a continuous evolution of the H:C and O:C throughout the reaction, consistent with the observations, which is indicated by the wide range of values that fall along a line with a constant slope (Fig. 3).

The distribution of molecules in N_C/N_O space at the end of the dodecane + OH reaction is shown for both P_{frag}

Table 2. Statistical oxidation model best-fit parameters when fit to both C_{OA} and O:C.

Alkane	ΔLVP	c_{frag} or m_{frag}	Oxygen Addition Probabilities ^a
Low-NO _x ; $P_{\text{frag}} = c_{\text{frag}} N_{\text{O}}$			
dodecane	2.20 ^b	0.423	[0.57, 0.12, 0.00, 0.31]
2-methylundecane	2.20 ^b	0.455	[0.79, 0.00, 0.10, 0.11]
hexylcyclohexane	2.20 ^b	0.333	[0.80, 0.05, 0.12, 0.03]
cyclododecane	2.20 ^b	0.333	[0.86, 0.02, 0.12, 0.0]
Low-NO _x ; $P_{\text{frag}} = (\text{O:C})^m \text{ frag}$			
dodecane	2.20 ^b	0.077	[0.79, 0.17, 0.03, 0.0]
2-methylundecane	2.20 ^b	0.110	[0.96, 0.0, 0.04, 0.0]
hexylcyclohexane	2.20 ^b	0.214	[0.75, 0.17, 0.08, 0.0]
cyclododecane	2.20 ^b	0.250	[0.88, 0.0, 0.0, 0.11]
High-NO _x ; $P_{\text{frag}} = c_{\text{frag}} N_{\text{O}}$			
dodecane	1.46	0.279	[0.31, 0.41, 0.07, 0.19]
2-methylundecane	1.68	0.397	[0.24, 0.50, 0.27, 0.0]
hexylcyclohexane	1.54	0.233	[0.0, 0.50, 0.43, 0.06]
cyclododecane	2.01	0.279	[0.0, 0.0, 0.73, 0.26]
High-NO _x ; $P_{\text{frag}} = (\text{O:C})^m \text{ frag}$			
dodecane	1.69	0.105	[0.26, 0.38, 0.31, 0.05]
2-methylundecane	1.80	0.113	[0.30, 0.57, 0.13, 0.0]
hexylcyclohexane	1.67	0.191	[0.18, 0.23, 0.59, 0.0]
cyclododecane	2.06	0.251	[0.0, 0.0, 0.88, 0.12]

^a The relative probabilities of adding 1, 2, 3 or 4 oxygen atoms per reaction.^b Constrained as an upper limit.

parameterizations (Fig. 4a,b). Overall, the OA is dominated by compounds that have $N_{\text{C}} = 12$ (Fig. 4e), although there are interestingly contributions from compounds with as few as 2 carbons at the 0.1 % level. Although the two P_{frag} parameterizations give generally similar results with respect to the temporal variation in the C_{OA} and O:C, the distribution of molecules that make up the OA differ. The $P_{\text{frag}}(\text{O:C})$ parameterization allows for a fragmentation probability that asymptotically approaches 1 (at O:C = 1), and thus it is possible to produce molecules with $N_{\text{C}} = 12$ and with a relatively large number of oxygen atoms, although the contribution of species with $N_{\text{O}} > 3$ to the total OA mass is small. For the $P_{\text{frag}}(N_{\text{O}})$ parameterization the probability of fragmentation linearly varies with N_{O} and, given $c_{\text{frag}} = 0.42$ coupled with a P_{func} array dominated by 1 oxygen per reaction, there is similarly not substantial production of $N_{\text{C}} = 12$ species with $N_{\text{O}} > 3$.

4.2 High-NO_x conditions

The observed variations in wall-loss corrected C_{OA} and O:C with reaction time for high-NO_x conditions for each of the alkanes considered are shown in Fig. 1. It is important to note that the OH concentration during these experiments was time

dependent and decayed rapidly from $> 10^7$ molecules cm⁻³ to zero (by around 3 h). This is in contrast to the low-NO_x experiments, where the OH concentration was constant at around 3×10^6 molecules cm⁻³. The time-dependence of the [OH] was accounted for in the SOM fit to the observations. The observed C_{OA} in each experiment rapidly increased before reaching a plateau by around 2–3 h. Unlike the low-NO_x experiments, this plateau behaviour results primarily from the loss of OH radicals and the cessation of photochemical reactions and not from an evolution in the distribution of gas-phase photooxidation products. The observed SOA O:C were essentially constant with time. Aerosol mass yields were larger for the ring-containing compounds (Table 1).

The SOM reproduces the observed time-dependent behaviour of the C_{OA} and O:C, both in terms of shape and absolute magnitude. Note that the close match between the observed and predicted O:C is different than for the low-NO_x conditions, where O:C was over-predicted. Fitting to either C_{OA} and O:C simultaneously or only to C_{OA} gave generally similar results. The best-fit ΔLVP values ranged from 1.46 to 2.06 (Fig. 2 and Table 2) and are overall substantially lower compared to the low-NO_x systems, with the exception of cyclododecane. Under high-NO_x conditions the optimal fit of the SOM indicates that the majority of reactions

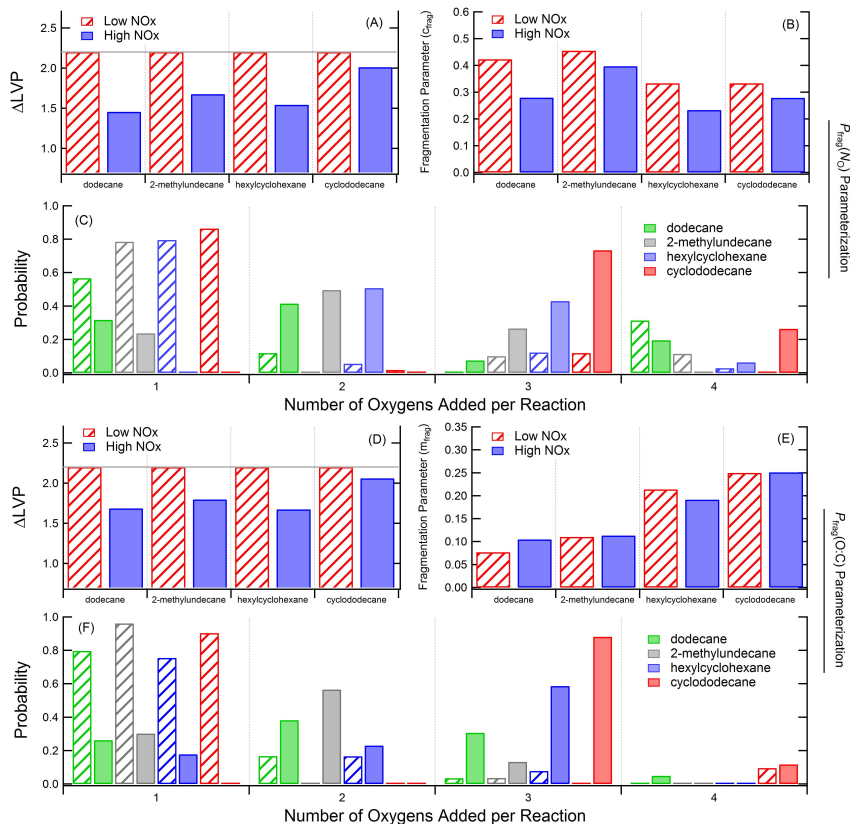


Fig. 2. Best-fit SOM parameters for dodecane, 2-methylundecane, hexylcyclohexane, and cyclododecane under low-NO_x (hatched) and high-NO_x (solid) conditions for different parameterizations for fragmentation: (A–C) used $P_{\text{frag}}(N_O)$ while (D–F) used $P_{\text{frag}}(O:C)$. Results are shown for ΔLVP (A and D), the fragmentation parameter (B and E) and the oxygen addition array (C and F). The model was fit simultaneously to the observed C_{OA} and O:C. The two fragmentation parameterizations give generally similar results. Note that for the fragmentation parameter, larger values of c_{frag} correspond to greater fragmentation while smaller values of m_{frag} correspond to greater fragmentation. The grey line in (A) and (D) indicates the upper-limit constraint on ΔLVP .

added 2 to 4 oxygen atoms per reaction, with the exact probability distribution varying for each alkane considered and some probability of adding 1 oxygen per reaction (with the exception of cyclododecane). This is in distinct contrast to the low-NO_x systems, where predominantly only 1 oxygen is predicted to be added per reaction. The P_{func} distributions are generally similar between the two fragmentation parameterizations. In general, the non-ring-containing compounds require larger c_{frag} (or smaller m_{frag}) than the ring-containing compounds, indicating more extensive fragmentation. Additionally, the best-fit c_{frag} values are generally larger (and the m_{frag} smaller) under high-NO_x conditions than under low-NO_x conditions for a given compound, although the extent to which the values differ depends on the specific alkane and whether c_{frag} or m_{frag} is considered; in some cases the differences are slight (Fig. 2 and Table 2).

The observed co-variation of H:C with O:C indicates that the number of H atoms lost per O atom added ranges from 1.25 to 1.83, which is slightly less than for low-NO_x conditions (Fig. 3). The SOM captures the observed behaviour (after specifying the H-per-O relationship), namely that the H:C and O:C are both nearly constant throughout the reaction, unlike the low-NO_x systems (Fig. 3).

The distribution of molecules in N_C/N_O space at the end of the reaction is shown for dodecane (Fig. 4c,d). As in the low-NO_x systems, the overall SOA composition is dominated by compounds with $N_C = 12$ (Fig. 4e), although the fractional contribution of compounds with $N_C < 12$ is less than in the low-NO_x experiments. This is likely the result of a greater number of oxygen atoms being added per reaction for the high- vs. low-NO_x case. This predicts that compounds with $N_C = 12$ more rapidly add oxygen, leading to a volatility

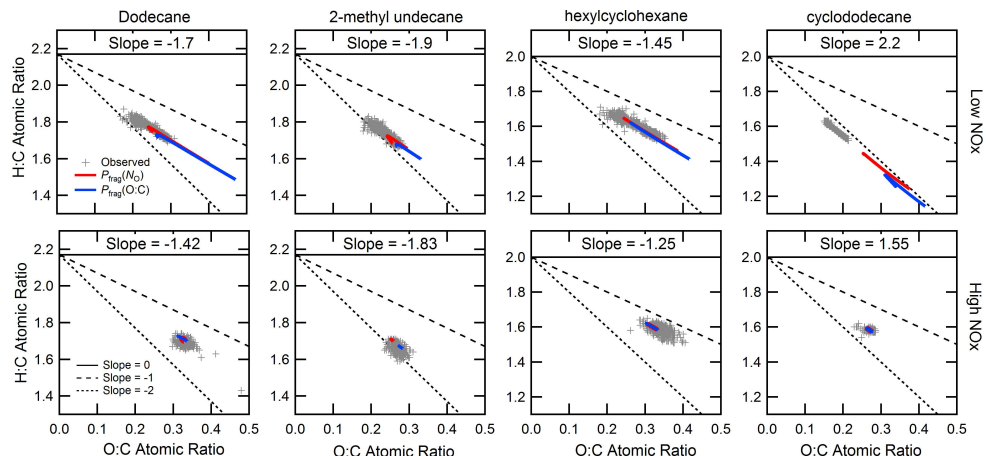


Fig. 3. Van Krevelen diagrams (H:C vs. O:C) for the observed SOA (gray points) and the model SOA using the $P_{\text{frag}}(N_{\text{O}})$ (red lines) and $P_{\text{frag}}(\text{O:C})$ (blue lines) fragmentation parameterizations. The top row shows results for low- NO_x conditions and the bottom row for high- NO_x conditions. The Van Krevelen slopes (defined according to the parent hydrocarbon y-intercept) are given in each panel.

sufficiently low that condensation is efficient even though the ΔLVP tends to be smaller for the high- NO_x mechanisms.

5 Discussion

The observations indicate that aerosol mass yields, defined as $C_{\text{OA}}/\Delta\text{HC}$ (where ΔHC is the amount of precursor reacted), are larger for the ring-containing compounds than for the non-ring-containing compounds for both high- and low- NO_x conditions (Table 1). For equivalent amounts of aerosol formed (specifically, 10 $\mu\text{g m}^{-3}$), the mass yields for each species under high- and low- NO_x conditions are reasonably similar, with the exception of cyclododecane, for which the high- NO_x yield is greater (Table 1). Low- NO_x conditions typically have greater H-loss per O-added (i.e. more negative Van Krevelen slopes) than high- NO_x conditions and also exhibit a more continuous evolution through the Van Krevelen space as the reactions proceed. Considering the model results, the SOM indicates that the decrease in volatility per oxygen added is substantially larger for low- NO_x vs. high- NO_x conditions. The magnitude of the fragmentation parameter, c_{frag} , is generally larger (and m_{frag} smaller) for low- vs. high- NO_x . Under high- NO_x conditions a greater number and broader distribution of oxygen atoms are added, on average, per reaction. Low- NO_x conditions lead to a slightly broader distribution of compounds with $N_{\text{C}} < 12$ in the particle phase compared to high- NO_x conditions.

To facilitate further comparison between the low- NO_x and high- NO_x experiments, which were conducted using different $[\text{OH}]$ temporal profiles and different $[\text{HC}]_0$, time-dependent SOA growth simulations were run under the same reaction conditions using the best-fit parameters determined

above (Fig. 5). Specific reaction conditions and model inputs were: $[\text{OH}] = 2.5 \times 10^6$ molecules cm^{-3} , $[\text{HC}]_0 = 33.5$ ppb, the $P_{\text{frag}}(N_{\text{O}})$ parameterization was used and the model was run for 32 h of oxidation. For all except 2-methylundecane, the C_{OA} formed after a given reaction time is initially somewhat greater for the high- NO_x conditions, but with an eventual cross-over to where the C_{OA} becomes larger for the low- NO_x conditions, often substantially so, at long times. For 2-methylundecane the yield under low- NO_x conditions is always greater than under high- NO_x conditions, with the difference growing with time.

For high- NO_x conditions there tends to be a more pronounced turnover in the C_{OA} with time and with the turnover occurring at shorter times compared to low- NO_x conditions. The overall time-dependent evolution of the gas + particle system reflects the combined influence of all of the parameters (P_{frag} and P_{func} and ΔLVP). Thus, the observed NO_x -dependence on the time-dependent aerosol yields can be understood through the influence of NO_x on both the probabilities of fragmentation vs. functionalization reactions and on the nature of the functional groups formed, specifically the decrease in volatility that occurs upon functional group addition.

There are no clear, systematic differences in the evolution of the O:C with oxidation between the low- and high- NO_x cases, although O:C tends to be slightly higher for high- NO_x . In general, for low- NO_x the O:C first decreases then increases, consistent with the experiments (which were conducted under similar conditions as these simulations). For high- NO_x , both 2-methylundecane and hexylcyclohexane exhibit a noticeable increase in the O:C with oxidation, similar to the low- NO_x cases, whereas dodecane and

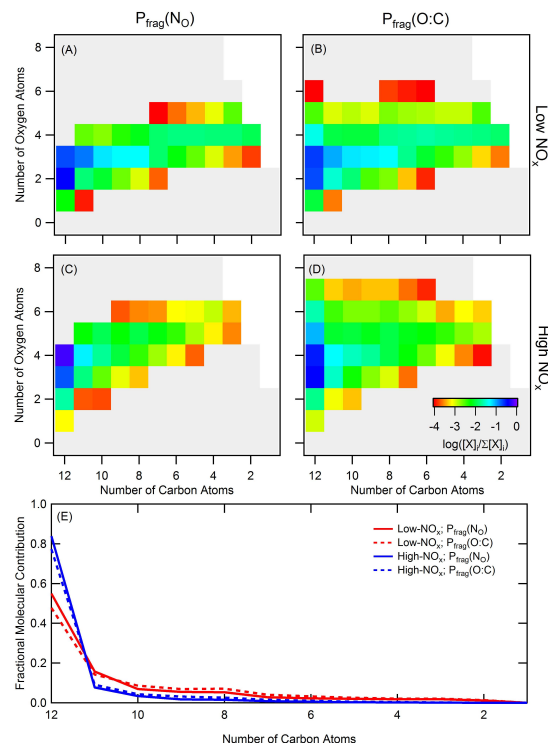


Fig. 4. Distribution of molecules comprising the model dodecane SOA at the end of the experiment for low-NO_x (**A**, **B**) and high-NO_x (**C**, **D**) for the $P_{\text{frag}}(N_{\text{O}})$ (**A**, **C**) and $P_{\text{frag}}(O:\text{C})$ (**B**, **D**) parameterizations. The colors correspond to the log of the fractional molecular abundance, i.e. $\log([X]_j/\sum[X]_j)$, with a lower-limit of -4 ($=0.01\%$). (**E**) The distributions, binned by N_{C} , for low-NO_x (red) and high-NO_x (blue).

cyclododecane exhibit comparably small variations in O:C with oxidation.

5.1 Time-evolution of individual SOA species

The SOM can be used to follow the time-evolution of the individual species (i.e. $N_{\text{C}}/N_{\text{O}}$ pairs) that comprise the model SOA. Tracking of each SOM species can help to understand which species contribute most to the SOA mass at any given time during the experiment, and thus how the composition is evolving. An example of such a time-trace is shown for the low-NO_x dodecane system using the $P_{\text{frag}}(N_{\text{O}})$ parameterization, where the individual species have been normalized to their maximum concentration (Fig. 6). It can be seen that there is some clustering of different species with respect to their specific time-evolution, and species that exhibit similar time-dependent behaviour have been colored similarly. The $N_{\text{C}}=12$ species with 1 and 2 oxygen atoms have unique time-profiles while the $N_{\text{C}}=8$ to 11 species with 1 or 2 oxy-

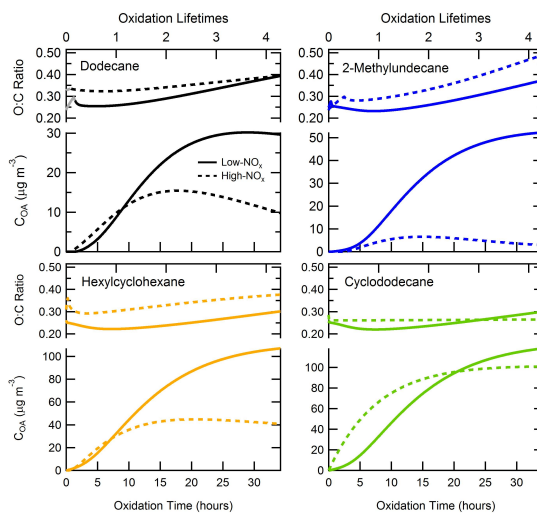


Fig. 5. Simulated time-evolution of CO_A and O:C for each of the parent alkanes using the same reaction conditions but with compound-specific best-fit SOM parameters. Results are shown for low-NO_x (solid) and high-NO_x (dashed), assuming $[OH]=2.5 \times 10^6$ molecules cm^{-3} and $[HC]_0=33.5$ ppb.

gens cluster together into one predominant mode. Similarly, there is a clustering of species with $N_{\text{C}}=6$ –7 and $N_{\text{O}}=2$ –3, and of species with $N_{\text{C}}=8$ –12 with $N_{\text{O}}=3$. Finally, species with $N_{\text{O}} \geq 4$ cluster together nearly independent of N_{C} . This type of clustering behaviour is consistent with the identification of unique “factors” associated with the formation and ageing of low-NO_x dodecane SOA (Craven et al., 2012). In general, the concentrations of individual particle-phase species with greater numbers of oxygen atoms and smaller carbon atom numbers peak later in time, consistent with their formation occurring only after many generations of oxidation. (Note that the assumption of random fragmentation and the use of a single SOM “grid” preclude direct, quantitative connections between N_{C} , N_{O} and generation number to be made.) The clustering of particular species in terms of their particle-phase concentrations is related to the combined influence of gas-phase formation rates and the volatility of each species.

It is also important to consider the actual time-dependent contributions from each species to the total SOA mass, as the above discussion (which uses normalized traces) might place undue focus on species that contribute negligibly to the SOA mass. Figure 7a shows the actual time-evolution of the particle phase mass concentration for each SOM species, and Fig. 7b–d show snapshots of the concentrations of each species after 5 h, 15 h and 25 h of reaction, normalized to the total particle mass at that time. It is evident that at early times the SOA is dominated by the $N_{\text{C}}=12$, $N_{\text{O}}=2$ species and the cluster of $N_{\text{C}}=8$ –12, $N_{\text{O}}=3$ species. As the

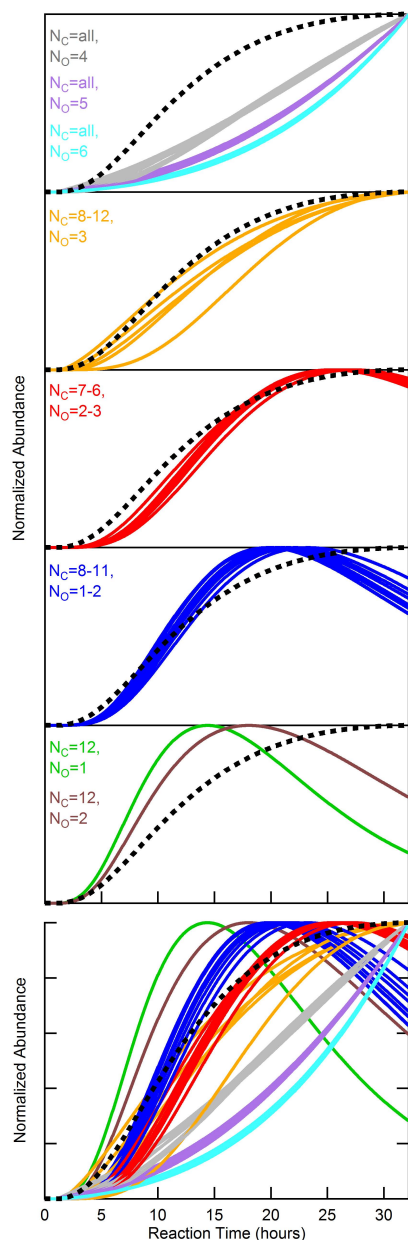


Fig. 6. Simulated time-evolution of each SOM species (i.e. N_C/N_O pair) during the low- NO_x photooxidation of dodecane. Species that exhibit a similar temporal dependence have been grouped into “clusters” and are shown in individual panels with the same color; the N_C and N_O of the species that belong to each “cluster” for each panel are indicated as labels. Each species profile has been normalized to its maximum concentration. For reference, the dashed black trace in each panel shows the time-evolution of the normalized total SOA mass. The bottom panel shows all traces together so that the time-evolution of the various clusters can be compared.

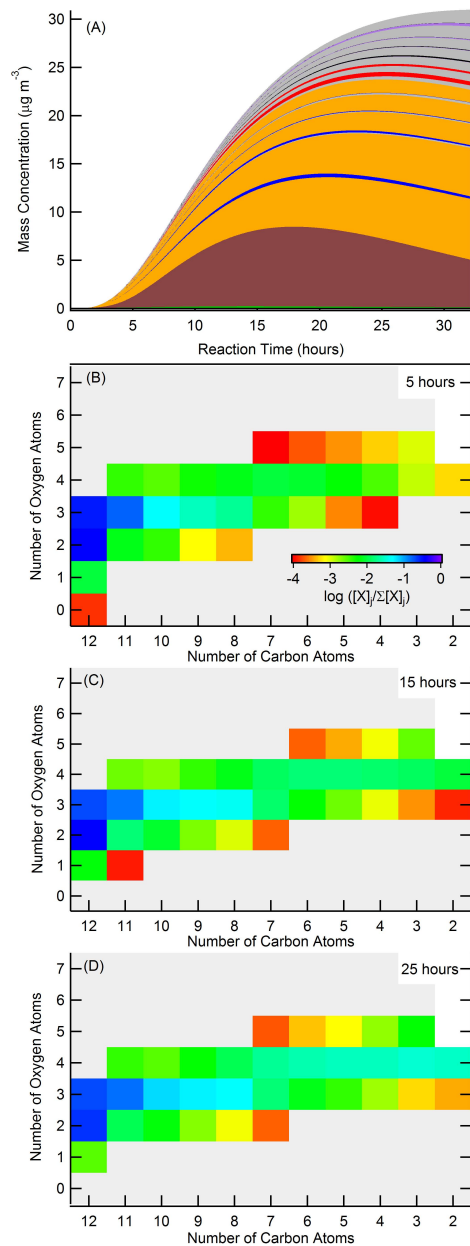


Fig. 7. (A) Simulated mass concentrations of each SOM species, with each species stacked on the previous. The colors correspond to those in Fig. 6 and indicate species of a particular “cluster”. (B), (C) and (D) show snapshots at 5, 15 and 25 hours of reaction, respectively, of the normalized mass concentration of all SOM species on an oxygen/carbon grid, with concentration indicated by the color of each cell in the grid (see legend). For each snapshot, the mass concentration of each species is normalized by the total SOA mass concentration as in Fig. 4; species with a normalized abundance $<10^{-4}$ are shown as gray and species with $O:C > 2$ are shown as white.

reaction progresses, the cluster of $N_O = 4$ species begins to contribute significantly while the abundance of the $N_C = 12$, $N_O = 2$ species decreases as it is converted into more oxidized species. This illustrates the dynamic nature of the SOA composition as it forms and ages.

5.2 Relationship of ΔLVP and oxygen addition

In principle, the addition of different functional groups corresponds to different values for ΔLVP in the SOM. For example, the SIMPOL model of Pankow and Asher (2008) suggests the following: $\Delta LVP(\text{alcohol}) \sim 2.23$; $\Delta LVP(\text{ketone}) \sim 0.94$; $\Delta LVP(\text{aldehyde}) \sim 1.35$; $\Delta LVP(\text{nitrile}) \sim 0.74$; $\Delta LVP(\text{hydroperoxide}) \sim 1.24$. (Recall that ΔLVP is defined on a per-oxygen basis.)

Under low- NO_x reaction conditions, likely products from gas-phase pathways are hydroperoxides, carbonyl hydroperoxides, hydroxyl hydroperoxides, carboxylic acids, hydroxylcarboxylic acids, hydroxyperacids and hydroxyl carbonyls (Yee et al., 2012). For the low- NO_x systems the best-fit SOM ΔLVP values are all >2 , which would suggest the addition of predominately hydroxyl ($-\text{OH}$) functional groups. However, addition only of alcohols seems unlikely, both from a mechanistic perspective (Yee et al., 2012) and from consideration of the observed H-loss per O-added (or Van Krevelen slope). Strict alcohol addition would correspond to a Van Krevelen slope of 0, which can be compared with the addition of a ketone or aldehyde (slope = -2) or hydroperoxide (slope = 0). The observed low- NO_x Van Krevelen slopes ranged from -1.45 to -2.2 . Such values are more suggestive of substantial ketone or aldehyde addition, as opposed to addition of alcohols, ketones and hydroperoxides as suggested by Yee et al. (2012). Thus, there appears to be some inconsistency between the model ΔLVP values, the observed Van Krevelen slopes and the expected products.

One potential reconciliation between these differing indications of functional group addition is the presence of condensed phase reactions. The above functional group/ ΔLVP relationships do not account for condensed phase reactions that can alter the nature of the functional groups comprising the SOA (and thus the H:C and O:C relationship) and the apparent volatility of the condensed-phase compounds. Importantly, certain condensed phase reactions involve a change in the Van Krevelen slope while others preserve the slope. Dehydration reactions involve loss of water molecules and lead to a change in the observed H:C vs. O:C slope, moving it towards steeper values. For example, ester formation, typically from the reaction of a carboxylic acid and alcohol, involves loss of a water molecule:



Assuming that this water does not influence the SOA O:C measurement, esterification leads to an overall Van Krevelen slope of -2 relative to the unreacted hydrocarbon and, by forming a longer-chain species (i.e. an oligomer), a de-

crease in vapour pressure despite the loss of functional group (the magnitude of this vapour pressure decrease will depend on the carbon chain length of the molecules involved). Cyclization reactions of hydroxycarbonyl species to form cyclic hemiacetals followed by dehydration to form a dihydrofuran also involve loss of water molecules, again leading to a shift in the Van Krevelen slope towards steeper values. However, such reactions do not lead to oligomerization, and thus the volatility of the dihydrofuran product may be substantially higher than the cyclic hemiacetal. The increased vapour pressure could lead to evaporation of the dihydrofuran, which could undergo further gas-phase processing and, potentially, re-condensation as a more oxidized species. Ultimately, if the dihydrofuran does not remain or end up back in the particle, the Van Krevelen slope of the SOA will be unaffected. It is worth noting that such dehydration reactions will lead to a decrease in the observed SOA O:C, and could provide an explanation for the model over-estimate. Altogether, consideration of the observations and the model results suggest that condensed-phase reactions occur that alter not only the apparent volatility of the SOA species, but also their atomic composition. However, it is possible that a bias against detection of hydroperoxides could also have influenced the observed Van Krevelen slope. Addition of hydroperoxides should yield a slope of 0. Thus, if hydroperoxides are primarily detected following loss of $-\text{OOH}$, the observed slope would be shifted towards more negative values. To the extent that this occurs, the need to invoke condensed phase reactions to explain the differing indications of functional group addition would be lessened.

Under high- NO_x conditions, the model ΔLVP values ranged from 1.46 to 2.06 (or 1.46 to 1.80 if cyclododecane is excluded). Interestingly, these values are significantly larger than that associated with organonitrate addition ($\Delta LVP = 0.74$) even though the best-fit P_{func} array indicates a substantial fraction of reactions add up to 3 or 4 oxygen atoms per reaction, which is consistent with nitrate addition. The mean H-loss-per-O added ranged from 1.25 to 1.83, also significantly larger than expected if nitrate functional group addition dominates (-0.33). Again, these results suggest that condensed phase reactions are altering the observed SOA properties, and thus the interpretation of the SOM best-fit parameters. As with the low- NO_x case, condensed phase reactions that make the Van Krevelen slope more negative (steeper) are suggested to reconcile the observations, expected mechanism and SOM results. In the condensed phase, organonitrates can undergo hydration reactions followed by acid-catalyzed nitrate loss to form alcohols. However, such reactions are unlikely under the very low RH conditions of these experiments, and furthermore would move the slope in the wrong direction (i.e. towards zero). Esterification (dehydration) reactions may also be occurring in the high- NO_x particles, moving the slope towards more negative values and, likely, decreasing the apparent volatility of the condensed species. Taken together, the low and high- NO_x

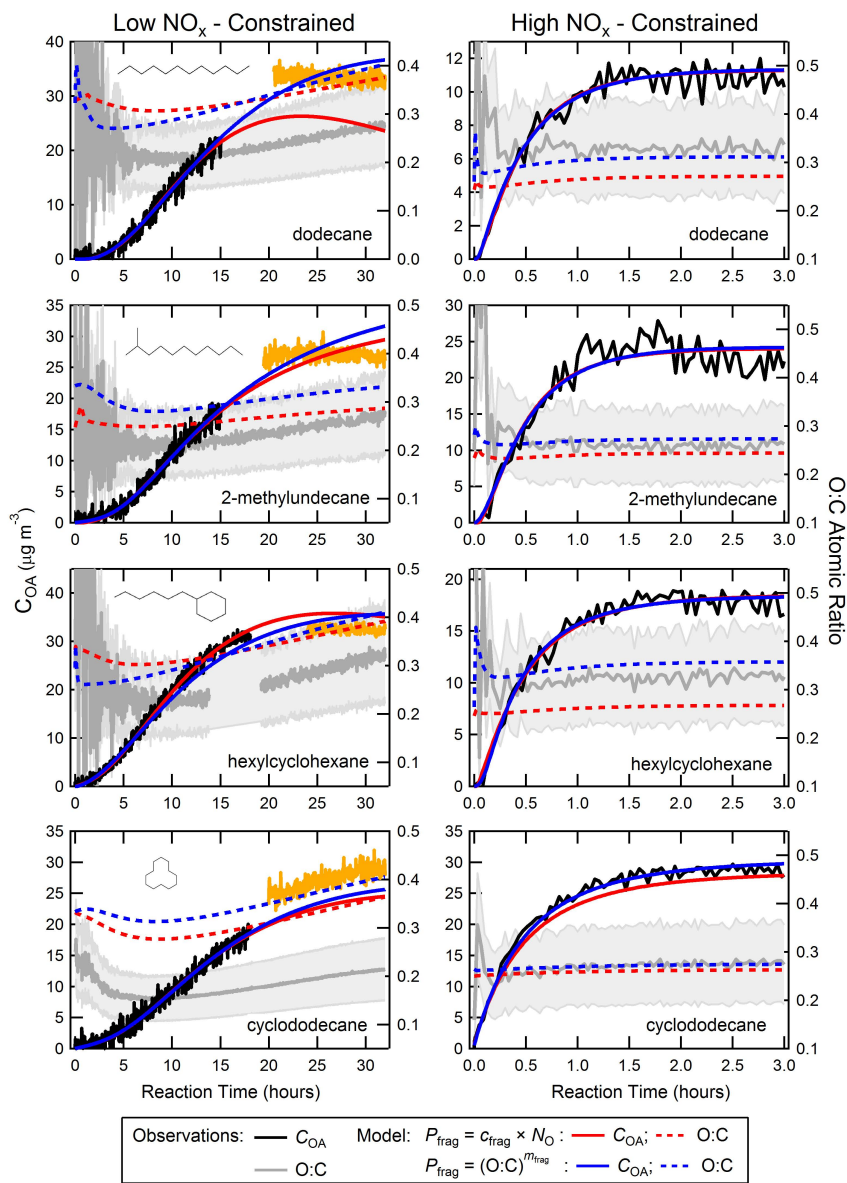


Fig. 8. Same as Fig. 1, but where the high-NO_x and low-NO_x c_{frag} and m_{frag} parameters have been constrained; see text for details.

results illustrate the broader point that interpretation of Van Krevelen diagrams in terms of how the SOA composition relates to the associated gas-phase composition is not necessarily straightforward since the measurements may likely be affected by condensed phase reactions. This conclusion is consistent with the findings of Craven et al. (2012), who determined that movement between the different identified SOA “factors” occurs along multiple Van Krevelen slopes.

When interpreting the best-fit SOM parameters in terms of chemical mechanisms, as above, it is important to consider the robustness of the fit parameters. This is examined here by re-fitting the SOM to observations of COA only (as opposed to C_{OA} and O:C), but where the P_{frag} parameters (i.e. c_{frag} and m_{frag}) for the high-NO_x reactions are constrained to be equal to the best-fit values from the low-NO_x reactions, and vice versa. The extent to which the constrained c_{frag} and

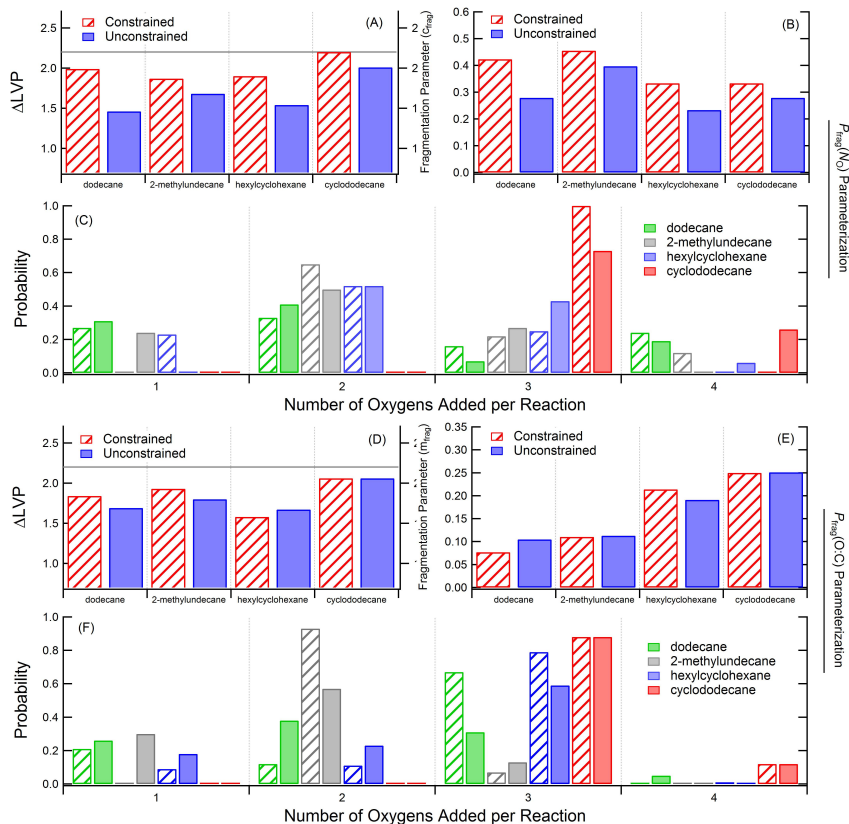


Fig. 9. Best-fit SOM parameters for dodecane, 2-methylundecane, hexylcyclohexane, and cyclododecane under high-NO_x conditions for both the overall best-fit (solid bars, as in Fig. 2) and the best-fit when the c_{frag} and m_{frag} parameters are constrained to be equal to the low-NO_x overall best-fit values (hatched bars). Results are shown for both the $P_{\text{frag}}(N_{\text{O}})$ (**A**–**C**) and $P_{\text{frag}}(\text{O:C})$ (**D**–**F**) parameterizations and include (**A** and **D**) ΔLVP , (**B** and **E**) the fragmentation parameter, and (**C** and **F**) the oxygen addition array. The constrained model was fit only to the observed C_{OA} . The grey line in (**A**) and (**D**) indicates the upper-limit constraint on ΔLVP .

m_{frag} values differ from the best-fit values differ for each alkane, although in general the constrained high-NO_x c_{frag} is larger (and m_{frag} smaller) compared to the overall best-fit, while for low-NO_x reactions the opposite is true (Table 2). In most cases, it is still possible to fit the SOM to the observed C_{OA} growth, although there are a few exceptions where the C_{OA} is under-predicted after fitting (Fig. 8). In general, the extent to which the best-fit ΔLVP and P_{frag} array differ between the constrained and overall fit depends on how different the c_{frag} and m_{frag} parameters are. For the high-NO_x reactions, many of the resulting ΔLVP values for the constrained fits are increased to offset the greater fragmentation, while, importantly, the oxygen distributions are reasonably similar between the constrained and overall best-fit (Fig. 9). The predicted O:C for the constrained fit does not match the observations quite as well as the overall best-fit (although remaining within the $\pm 30\%$ uncertainty for all cases; Fig. 8). For the

low-NO_x reactions, some of the resulting ΔLVP values for the constrained fits are decreased, although for many cases the differences are small, while the oxygen distributions are generally unchanged (Fig. 10). This comparison illustrates that the ΔLVP and P_{frag} parameters can have compensating effects, which indicates that care must be taken in their interpretation. Nonetheless, the results from the constrained and overall best-fits are sufficiently similar that the general conclusions reached above are unchanged.

6 Summary and conclusions

For a comprehensive series of SOA formation experiments from photooxidation of four $N_{\text{C}} = 12$ alkanes, two straight chain and two ring-containing, observations indicate that the SOA yield is larger for these compounds under low- vs. high-NO_x conditions, with the exception of cyclododecane. The

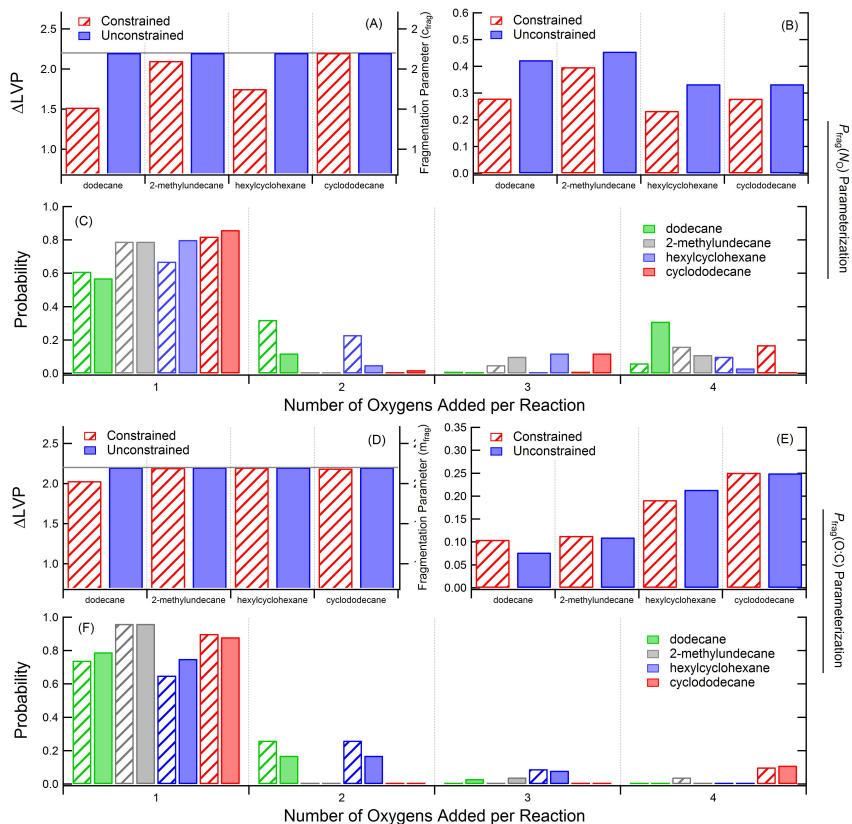


Fig. 10. Best-fit SOM parameters for dodecane, 2-methylundecane, hexylcyclohexane, and cyclododecane under low-NO_x conditions for both the overall best-fit (solid bars, as in Fig. 2) and the best-fit when the c_{frag} and m_{frag} parameters are constrained to be equal to the high-NO_x overall best-fit values (hatched bars). Results are shown for both the $P_{\text{frag}}(N_{\text{O}})$ (A–C) and $P_{\text{frag}}(\text{O:C})$ (D–F) parameterizations and include (A and D) ΔLVP , (B and E) the fragmentation parameter, and (C and F) the oxygen addition array. The constrained model was fit only to the observed C_{OA} . The grey line in (A) and (D) indicates the upper-limit constraint on ΔLVP .

O:C atomic ratio is generally similar between high- and low-NO_x, although the low-NO_x experiments exhibit a continuous increase in O:C as oxidation proceeds. This difference results primarily from the differing oxidation conditions: the [OH] during low-NO_x experiments was approximately constant around 2×10^6 molecules cm⁻³, whereas the [OH] during high-NO_x experiments started higher but rapidly decayed due to efficient photolysis of the OH precursor (HONO).

The observed C_{OA} temporal growth curves have been fit to the statistical oxidation model (Cappa and Wilson, 2012) to derive values for the mean decrease in volatility per oxygen added (ΔLVP), the probability of fragmentation and the distribution of oxygens added per reaction. In general, there is excellent model/measurement agreement in terms of the time-evolution of the C_{OA} . This work demonstrates that the use of a kinetic, multi-generation model to represent SOA formation during photooxidation can provide insights into

the SOA formation process and facilitate the interpretation of smog chamber observations.

Acknowledgements. This work was supported by the National Science Foundation (ATM-1151062) and the Department of Energy (DE-SC0006626).

Edited by: F. Keutsch

References

Aiken, A. C., Decarlo, P. F., and Jimenez, J. L.: Elemental analysis of organic species with electron ionization high-resolution mass spectrometry, *Anal. Chem.*, 79, 8350–8358, doi:10.1021/ac071150w, 2007.
 Aiken, A. C., Decarlo, P. F., Kroll, J. H., Worsnop, D. R., Huffman, J. A., Docherty, K. S., Ulbrich, I. M., Mohr, C., Kimmel,

J. R., Sueper, D., Sun, Y., Zhang, Q., Trimborn, A., Northway, M., Ziemann, P. J., Canagaratna, M. R., Onasch, T. B., Alfarra, M. R., Prevot, A. S. H., Dommen, J., Duplissy, J., Metzger, A., Baltensperger, U., and Jimenez, J. L.: O/C and OM/OC ratios of primary, secondary, and ambient organic aerosols with high-resolution time-of-flight aerosol mass spectrometry, *Environ. Sci. Technol.*, 42, 4478–4485, doi:10.1021/es703009q, 2008.

Aumont, B., Szopa, S., and Madronich, S.: Modelling the evolution of organic carbon during its gas-phase tropospheric oxidation: development of an explicit model based on a self generating approach, *Atmos. Chem. Phys.*, 5, 2497–2517, doi:10.5194/acp-5-2497-2005, 2005.

Barsanti, K. C., Smith, J. N., and Pankow, J. F.: Application of the np+mP modeling approach for simulating secondary organic particulate matter formation from α -pinene oxidation, *Atmos. Environ.*, 45, 6812–6819, doi:10.1016/j.atmosenv.2011.01.038, 2011.

Cappa, C. D., and Wilson, K. R.: Multi-generation gas-phase oxidation, equilibrium partitioning, and the formation and evolution of secondary organic aerosol, *Atmos. Chem. Phys.*, 12, 9505–9528, doi:10.5194/acp-12-9505-2012, 2012.

Chhabra, P. S., Flagan, R. C., and Seinfeld, J. H.: Elemental analysis of chamber organic aerosol using an aerodyne high-resolution aerosol mass spectrometer, *Atmos. Chem. Phys.*, 10, 4111–4131, doi:10.5194/acp-10-4111-2010, 2010.

Cocker, D. R., Flagan, R. C., and Seinfeld, J. H.: State-of-the-art chamber facility for studying atmospheric aerosol chemistry, *Environ. Sci. Technol.*, 35, 2594–2601, doi:10.1021/es0019169, 2001.

Compernolle, S., Ceulemans, K., and Müller, J. F.: EVAPORATION: a new vapour pressure estimation method for organic molecules including non-additivity and intramolecular interactions, *Atmos. Chem. Phys.*, 11, 9431–9450, doi:10.5194/acp-11-9431-2011, 2011.

Craven, J. S., Yee, L. D., Ng, N. L., Canagaratna, M. R., Loza, C. L., Schilling, K. A., Yatavelli, R. L. N., Thornton, J. A., Ziemann, P. J., Flagan, R. C., and Seinfeld, J. H.: Analysis of secondary organic aerosol formation and aging using positive matrix factorization of high-resolution aerosol mass spectra: application to the dodecane low-NO_x system, *Atmos. Chem. Phys.*, 12, 11795–11817, doi:10.5194/acp-12-11795-2012, 2012.

DeCarlo, P. F., Kimmel, J. R., Trimborn, A., Northway, M. J., Jayne, J. T., Aiken, A. C., Gonin, M., Fuhrer, K., Horvath, T., Docherty, K. S., Worsnop, D. R., and Jimenez, J. L.: Field-deployable, high-resolution, time-of-flight aerosol mass spectrometer, *Anal. Chem.*, 78, 8281–8289, doi:10.1021/ac061249n, 2006.

Donahue, N. M., Robinson, A. L., Stanier, C. O., and Pandis, S. N.: Coupled partitioning, dilution, and chemical aging of semivolatile organics, *Environ. Sci. Technol.*, 40, 2635–2643, doi:10.1021/es052297c, 2006.

Donahue, N. M., Kroll, J. H., Pandis, S. N., and Robinson, A. L.: A two-dimensional volatility basis set – Part 2: Diagnostics of organic-aerosol evolution, *Atmos. Chem. Phys.*, 12, 615–634, doi:10.5194/acp-12-615-2012, 2012.

Heald, C. L., Kroll, J. H., Jimenez, J. L., Docherty, K. S., DeCarlo, P. F., Aiken, A. C., Chen, Q., Martin, S. T., Farmer, D. K., and Artaxo, P.: A simplified description of the evolution of organic aerosol composition in the atmosphere, *Geophys. Res. Lett.*, 37, L08803, doi:10.1029/2010gl042737, 2010.

Jimenez, J. L., Canagaratna, M. R., Donahue, N. M., Prevot, A. S. H., Zhang, Q., Kroll, J. H., DeCarlo, P. F., Allan, J. D., Coe, H., Ng, N. L., Aiken, A. C., Docherty, K. S., Ulbrich, I. M., Grieshop, A. P., Robinson, A. L., Duplissy, J., Smith, J. D., Wilson, K. R., Lanz, V. A., Hueglin, C., Sun, Y. L., Tian, J., Laaksonen, A., Raatikainen, T., Rautiainen, J., Vaattovaara, P., Ehn, M., Kulmala, M., Tomlinson, J. M., Collins, D. R., Cubison, M. J., Dunlea, E. J., Huffman, J. A., Onasch, T. B., Alfarra, M. R., Williams, P. I., Bower, K., Kondo, Y., Schneider, J., Drewnick, F., Borrmann, S., Weimer, S., Demerjian, K., Salcedo, D., Cottrell, L., Griffin, R., Takami, A., Miyoshi, T., Hatakeyama, S., Shimono, A., Sun, J. Y., Zhang, Y. M., Dzepina, K., Kimmel, J. R., Sueper, D., Jayne, J. T., Herndon, S. C., Trimborn, A. M., Williams, L. R., Wood, E. C., Middlebrook, A. M., Kolb, C. E., Baltensperger, U., and Worsnop, D. R.: Evolution of organic aerosols in the atmosphere, *Science*, 326, 1525–1529, doi:10.1126/science.1180353, 2009.

Kanakidou, M., Seinfeld, J. H., Pandis, S. N., Barnes, I., Dentener, F. J., Facchini, M. C., Van Dingenen, R., Ervens, B., Nenes, A., Nielsen, C. J., Swietlicki, E., Putaud, J. P., Balkanski, Y., Fuzzi, S., Horth, J., Moortgat, G. K., Winterhalter, R., Myhre, C. E. L., Tsigaridis, K., Vignati, E., Stephanou, E. G., and Wilson, J.: Organic aerosol and global climate modelling: a review, *Atmos. Chem. Phys.*, 5, 1053–1123, doi:10.5194/acp-5-1053-2005, 2005.

Lane, T. E., Donahue, N. M., and Pandis, S. N.: Simulating secondary organic aerosol formation using the volatility basis-set approach in a chemical transport model, *Atmos. Environ.*, 42, 7439–7451, doi:10.1016/j.atmosenv.2008.06.026, 2008.

Lim, Y. B. and Ziemann, P. J.: Effects of Molecular Structure on Aerosol Yields from OH Radical-Initiated Reactions of Linear, Branched, and Cyclic Alkanes in the Presence of NO_x, *Environ. Sci. Technol.*, 43, 2328–2334, doi:10.1021/es803389s, 2009.

Loza, C. L., Chhabra, P. S., Yee, L. D., Craven, J. S., Flagan, R. C., and Seinfeld, J. H.: Chemical aging of m-xylene secondary organic aerosol: laboratory chamber study, *Atmos. Chem. Phys.*, 12, 151–167, doi:10.5194/acp-12-151-2012, 2012.

Odum, J. R., Hoffmann, T., Bowman, F., Collins, D., Flagan, R. C., and Seinfeld, J. H.: Gas/particle partitioning and secondary organic aerosol yields, *Environ. Sci. Technol.*, 30, 2580–2585, doi:10.1021/es950943+, 1996.

Pankow, J. F.: An absorption-model of the gas aerosol partitioning involved in the formation of secondary organic aerosol, *Atmos. Environ.*, 28, 189–193, doi:10.1016/1352-2310(94)90094-9, 1994.

Pankow, J. F. and Asher, W. E.: SIMPOL.1: a simple group contribution method for predicting vapor pressures and enthalpies of vaporization of multifunctional organic compounds, *Atmos. Chem. Phys.*, 8, 2773–2796, doi:10.5194/acp-8-2773-2008, 2008.

Robinson, A. L., Donahue, N. M., Shrivastava, M. K., Weitkamp, E. A., Sage, A. M., Grieshop, A. P., Lane, T. E., Pierce, J. R., and Pandis, S. N.: Rethinking organic aerosols: Semivolatile emissions and photochemical aging, *Science*, 315, 1259–1262, doi:10.1126/science.1133061, 2007.

Valorso, R., Aumont, B., Camredon, M., Raventos-Duran, T., Mouchel-Vallon, C., Ng, N. L., Seinfeld, J. H., Lee-Taylor, J., and Madronich, S.: Explicit modelling of SOA formation from alpha-pinene photooxidation: sensitivity to vapour pressure esti-

mation, *Atmos. Chem. Phys.*, 11, 6895–6910, doi:10.5194/acp-11-6895-2011, 2011.

Yee, L. D., Craven, J. S., Loza, C. L., Schilling, K. A., Ng, N. L., Canagaratna, M. R., Ziemann, P. J., Flagan, R. C., and Seinfeld, J. H.: Secondary organic aerosol formation from Low-NO_x Photooxidation of Dodecane: Evolution of Multigeneration Gas-Phase Chemistry and Aerosol Composition, *J. Phys. Chem. A*, 116, 6211–6230, doi:10.1021/jp211531h, 2012.

Zhang, Q., Jimenez, J. L., Canagaratna, M. R., Allan, J. D., Coe, H., Ulbrich, I., Alfarra, M. R., Takami, A., Middlebrook, A. M., Sun, Y. L., Dzepina, K., Dunlea, E., Docherty, K., DeCarlo, P. F., Salcedo, D., Onasch, T., Jayne, J. T., Miyoshi, T., Shimojo, A., Hatakeyama, S., Takegawa, N., Kondo, Y., Schneider, J., Drewnick, F., Borrmann, S., Weimer, S., Demerjian, K., Williams, P., Bower, K., Bahreini, R., Cottrell, L., Griffin, R. J., Rautiainen, J., Sun, J. Y., Zhang, Y. M., and Worsnop, D. R.: Ubiquity and dominance of oxygenated species in organic aerosols in anthropogenically-influenced Northern Hemisphere midlatitudes, *Geophys. Res. Lett.*, 34, L13801, doi:10.1029/2007GL029979, 2007.

Appendix B

α -pinene photooxidation under controlled chemical conditions - Part 1: Gas-phase composition in low- and high- NO_x environments¹

¹This chapter is reproduced by permission from “ α -pinene photooxidation under controlled chemical conditions - Part 1: Gas-phase composition in low- and high- NO_x ,” by N. C. Eddingsaas, C. L. Loza, L. D. Yee, J. H. Seinfeld, and P. O. Wennberg, *Atmospheric Chemistry and Physics*, 12, 6489–6504, doi:10.5194/acp-12-6489-2012, 2012. Copyright 2012 Authors. This work is licensed under a Creative Commons License.



α -pinene photooxidation under controlled chemical conditions – Part 1: Gas-phase composition in low- and high- NO_x environments

N. C. Eddingsaas¹, C. L. Loza¹, L. D. Yee², J. H. Seinfeld^{1,2}, and P. O. Wennberg^{2,3}

¹Division of Chemistry and Chemical Engineering, California Institute of Technology, Pasadena, CA, USA

²Division of Engineering and Applied Science, California Institute of Technology, Pasadena, CA, USA

³Division of Geological and Planetary Sciences, California Institute of Technology, Pasadena, CA, USA

Correspondence to: N. C. Eddingsaas (eddingsaas@caltech.edu)

Received: 29 December 2011 – Published in *Atmos. Chem. Phys. Discuss.*: 1 March 2012

Revised: 21 June 2012 – Accepted: 1 July 2012 – Published: 25 July 2012

Abstract. The OH oxidation of α -pinene under both low- and high- NO_x environments was studied in the Caltech atmospheric chambers. Ozone was kept low to ensure OH was the oxidant. The initial α -pinene concentration was 20–50 ppb to ensure that the dominant peroxy radical pathway under low- NO_x conditions is reaction with HO_2 , produced from reaction of OH with H_2O_2 , and under high- NO_x conditions, reactions with NO. Here we present the gas-phase results observed. Under low- NO_x conditions the main first generation oxidation products are a number of α -pinene hydroxy hydroperoxides and pinonaldehyde, accounting for over 40 % of the yield. In all, 65–75 % of the carbon can be accounted for in the gas phase; this excludes first-generation products that enter the particle phase. We suggest that pinonaldehyde forms from $\text{RO}_2 + \text{HO}_2$ through an alkoxy radical channel that regenerates OH, a mechanism typically associated with acyl peroxy radicals, not alkyl peroxy radicals. The OH oxidation and photolysis of α -pinene hydroxy hydroperoxides leads to further production of pinonaldehyde, resulting in total pinonaldehyde yield from low- NO_x OH oxidation of ~33 %. The low- NO_x OH oxidation of pinonaldehyde produces a number of carboxylic acids and peroxyacids known to be important secondary organic aerosol components. Under high- NO_x conditions, pinonaldehyde was also found to be the major first-generation OH oxidation product. The high- NO_x OH oxidation of pinonaldehyde did not produce carboxylic acids and peroxyacids. A number of organonitrates and peroxyacetyl nitrates are observed and identified from α -pinene and pinonaldehyde.

1 Introduction

The emissions of biogenic volatile organic compounds (BVOCs) far outnumber those of anthropogenic VOCs (Guenther et al., 1995; Steinbrecher et al., 2009; Monks et al., 2009). Excluding methane, BVOCs are estimated to account for a flux of $\sim 1150 \text{ Tg C yr}^{-1}$, while anthropogenic VOCs account for only $\sim 140 \text{ Tg C yr}^{-1}$ (Guenther et al., 1995; Goldstein and Galbally, 2007). Important BVOCs include isoprene, (flux of $\sim 500 \text{ Tg C yr}^{-1}$) and the monoterpenes ($\sim 127 \text{ Tg C yr}^{-1}$) of which α -pinene accounts for $\sim 50 \text{ Tg C yr}^{-1}$ (Guenther et al., 1995; Chung and Seinfeld, 2002). Because they are unsaturated, these compounds are highly reactive towards OH, O_3 , and NO_3 and thus play an important role in tropospheric chemistry. The atmospheric oxidation of BVOCs also results in the formation of secondary organic aerosol (SOA). Monoterpenes are significant sources of SOA due to their large emission rate and high SOA yield (Hoffmann et al., 1997; Pye et al., 2010).

The gas-phase oxidation of simple alkanes and alkenes is well understood and most tropospheric chemical mechanisms use laboratory studies of reactions of these species to inform the parameterization of the atmospheric oxidation of VOCs. Many BVOCs, including isoprene, which has a conjugated double bond system, and α -pinene which is a bicyclic hydrocarbon with an endocyclic double bond, however, have much more complicated chemistry than the simple alkanes and alkenes. For example, recent experimental and theoretical studies with isoprene have shown that its atmospheric chemistry is not well modeled by the reactions of simple

Table 1. Experimental conditions.

Date	Hydrocarbon	Concentration (ppb)	OH Source	Aerosol seed ^a	Length of experiment (hours)
5 May 2010	α -pinene	45	H_2O_2	No seed	12
6 May 2010	α -pinene	50	HONO	No seed	10
7 May 2010	α -pinene	48	H_2O_2	AS	11
9 May 2010	α -pinene	52	HONO	AS	8
10 May 2010	α -pinene	47	H_2O_2	AS+SA	11
11 May 2010	α -pinene	46	HONO	AS+SA	10
12 May 2010	α -pinene	20	H_2O_2	No seed	19
13 May 2010	α -pinene	42	CH_3ONO	No seed	8
14 May 2010	α -pinene	47	H_2O_2	AS	12
17 May 2010	α -pinene	48	CH_3ONO	AS	8
18 May 2010	α -pinene	47	H_2O_2	AS+SA	12
19 May 2010	α -pinene	44	CH_3ONO	AS+SA	8
2 June 2010	α -pinene	45	H_2O_2	AS	12
3 June 2010	α -pinene	45	CH_3ONO	AS	8
4 June 2010	Pinonaldehyde	_b	H_2O_2	No Seed	9
8 Feb 2011	α -pinene	43	H_2O_2	No seed	8
14 Feb 2011	Pinonaldehyde	_b	H_2O_2	No seed	9
16 Feb 2011	α -pinene	31	CH_3ONO	No seed	3
17 Feb 2011	Pinonaldehyde	_b	CH_3ONO	No seed	4

^a AS: ammonium sulfate, AS+SA: ammonium sulfate and sulfuric acid.^b The initial concentration of pinonaldehyde was not determined.

alkenes, especially under low- NO_x (NO and NO_2) conditions (Paulot et al., 2009b; Peeters and Muller, 2010; Crounse et al., 2011).

α -pinene is a ten-carbon bicyclic hydrocarbon with an endocyclic double bond and, therefore, has the potential to react in ways not represented by simple alkenes. In addition, α -pinene is highly reactive with both O_3 and OH, reacting in the atmosphere with α -pinene nearly equally, adding to the richness of its atmospheric photochemistry (Capouet et al., 2008). Despite a number of studies of OH oxidation of α -pinene, large uncertainties in the identity and yields of its reaction products remain. For instance, the reported yield of pinonaldehyde from the photooxidation of α -pinene ranges from 28 to 87 % in the presence of NO_x and from 3 to 37 % in the absence of NO_x (Arey et al., 1990; Hatakeyama et al., 1991; Noziere et al., 1999; Jaoui and Kamens, 2001; Wisthaler et al., 2001; Aschmann et al., 2002; Lee et al., 2006). In addition, the molecular structures of major products identified by mass (e.g. 184 and 200 daltons) are subject to debate (Aschmann et al., 2002; Vereecken et al., 2007). The photooxidation product with molecular mass 184 has been assigned to an unsaturated hydroperoxy carbonyl (Vereecken et al., 2007) or a dihydroxy carbonyl (Aschmann et al., 2002). A better understanding of α -pinene gas-phase chemistry will increase the accuracy of α -pinene atmospheric chemistry models and provide insight into atmospheric photooxidation mechanisms in general.

In this study, we isolate the peroxy radical reaction pathways to investigate the photochemistry of α -pinene. We have

studied these reactions under low- NO_x conditions similar to those found in the atmosphere, where $\text{RO}_2 + \text{HO}_2$ is the dominant peroxy radical reaction, and other reactions are suppressed ($\text{RO}_2 + \text{RO}_2$ and reactions with O_3). We contrast these conditions with results from the gas-phase photooxidation of α -pinene under high- NO_x (with varied amounts of NO_2 to study both $\text{RO}_2 + \text{NO}$ and $\text{RO}_2 + \text{NO}_2$). We focus our analysis on low- NO_x rather than high- NO_x chemistry because the low- NO_x chemistry of α -pinene is less well-characterized yet it is more atmospherically-relevant (Pye et al., 2010). In a forthcoming paper, SOA yields and composition formed from the controlled chemical conditions described here will be presented.

2 Experimental

Photooxidation experiments of α -pinene were performed in the Caltech dual 28 m³ Teflon chambers. Details of the chamber facilities have been described elsewhere (Cocker et al., 2001; Keywood et al., 2004). A few photooxidation experiments were performed in a ~1 m³ bag enclosed in a small, black walled chamber with UV-lights lining one wall, as described by Crounse et al. (2011). 40 W black lights (Sylvania F40/350BL) with emission peak emission at 352 nm were used in both chambers. The light intensity as a function of wavelength (300–800 nm) was measured using a Licor (LI-1800) spectroradiometer. Prior to each run, the chamber was flushed for a minimum of 24 h with dry purified air. While

being flushed, the chamber was irradiated with the chamber lights for a minimum of six hours. The temperature, relative humidity (RH), and concentrations of O_3 , and NO_x (NO and NO_2) were continuously monitored. In all experiments the RH was kept below 10 %. Aerosol size distribution and number concentration were measured continuously by a differential mobility analyzer (DMA, TSI model 3081) coupled to a condensation nucleus counter (TSI model 3760). Information on aerosol measurements can be found in part 2, where aerosol formation, growth, and composition are discussed. Table 1 shows a list of conditions for all experiments used in this study. Experiments ran for 3 to 19 h. No gas phase losses to the chamber walls of either α -pinene prior to light irradiation or oxidation products after lights were extinguished was observed.

Experiments were performed under low- and high- NO_x conditions. Under low- NO_x conditions, photolysis of hydrogen peroxide (H_2O_2) was the OH source, while for the high- NO_x experiments the photolysis of nitrous acid (HONO) or methyl nitrite (CH_3ONO) produced OH. For low- NO_x experiments, 280 μ L of 50 wt % H_2O_2 was injected into the chamber resulting in an H_2O_2 concentration \sim 4 ppm. The two different OH sources used during the high- NO_x experiments provided the mechanism to vary the NO to NO_2 ratio, with a higher quantity of NO_2 in the CH_3ONO experiments. HONO was prepared daily by dropwise addition of 15 mL of 1 wt % $NaNO_2$ into 30 mL of 10 wt % H_2SO_4 in a glass bulb, and then introduced into the chamber with dry air. This process produces NO and NO_2 as side products, which are also introduced to the chamber. CH_3ONO was synthesized, purified, and stored according to the procedure outlined by Taylor et al. (1980). CH_3ONO was warmed from liquid nitrogen temperatures and vaporized into an evacuated 500 mL glass bulb and introduced into the chamber with an air stream of 5 L min $^{-1}$. After addition of CH_3ONO , 300–400 ppb of NO was added to the chamber to suppress the formation of O_3 . Determination of exact NO and NO_2 concentrations using the commercial NO_x monitor was precluded due to interferences by both HONO and CH_3ONO . At the start of all high- NO_x experiments the total NO_x reading (NO, NO_x , and interference from HONO or CH_3ONO) was 800 ppb and NO concentration throughout the experiments was such that the concentration of O_3 never exceeded 5 ppb.

α -pinene was added to the chamber to achieve a concentration of 20–50 ppb by passing dry air through a bulb containing a known volume of α -pinene. The mixing ratio of α -pinene was monitored by gas chromatography (Agilent 6890N) coupled with a flame ionization detector (GC-FID). The GC-FID was calibrated using a 55 L Teflon bag containing a known concentration of pure α -pinene. Gas phase photooxidation products were monitored using triple-quadrupole chemical ionization mass spectrometry (CIMS) (St. Clair et al., 2010).

Details of the operation of the CIMS can be found in a number of previous reports (Crounse et al., 2006; Paulot

et al., 2009a; St. Clair et al., 2010) and therefore only a brief description is presented here. The CIMS was operated in negative ion mode using CF_3O^- as the reagent ion, and in the positive ion mode using H_3O^+ for proton transfer mass spectrometry (PTR-MS). In negative mode, CF_3O^- is sensitive to the detection of polar and acidic compounds by either clustering with the analyte (R) resulting in an ion with a mass-to-charge ratio (m/z) $MW+85$ ($R \cdot CF_3O^-$) or via fluorine ion transfer resulting in m/z $MW+19$ ($HF \cdot R_{-H}^-$). The dominant ionization mechanism depends mostly on the acidity of the neutral species; highly acidic species such as nitric acid only form the fluorine transfer ion, while non-acidic species such as methyl hydrogen peroxide form only the cluster ion. This separation aids both in the determination of the structure of a molecule and in the identification of isomers. In negative mode, tandem mass spectrometry (MS/MS) was used to help identify functional groups of an analyte. In brief, a parent ion selected in the first quadrupole is exposed to an elevated pressure of N_2 resulting in collision-induced dissociation (CID) in the second quadrupole, and the resulting fragmentation ions are detected in the third quadrupole. Molecules with different functional groups have been shown to fragment differently by CID and thus the detection of certain fragment ions in quadrupole three can aid in the identification of an analyte. For instance, hydroperoxides form a characteristic fragment at m/z 63 (Paulot et al., 2009b).

Standards are not available for most of the VOCs described here and thus the sensitivity of the CIMS is related to the thermal capture rate and the binding energy of the cluster ($VOC \cdot CF_3O^-$). Details on calculating the sensitivity of the CIMS to a given analyte can be found in previous publications (Paulot et al., 2009a,b).

3 Results and discussion

The goal of this study is to determine the gas-phase reaction products and mechanism of the photooxidation of α -pinene by OH under both low- NO_x and high- NO_x conditions. In both cases, the experiment is designed such that α -pinene only reacts with OH and that a single peroxy radical reaction is dominant. Under ambient conditions, α -pinene reacts at an approximately equal rate with O_3 ($k_{O_3} = 9.0 \times 10^{-17} \text{ cm}^3 \text{ molecules}^{-1} \text{ s}^{-1}$) and OH ($k_{OH} = 5.3 \times 10^{-11} \text{ cm}^3 \text{ molecules}^{-1} \text{ s}^{-1}$) (Sander et al., 2006; Atkinson et al., 2006). To isolate the OH chemistry, the formation of O_3 was suppressed.

Under low- NO_x conditions, photolysis of H_2O_2 resulted in steady state OH concentration of $\sim 2 \times 10^6 \text{ cm}^{-3}$ and an HO_2 concentration $\sim 1 \times 10^{10} \text{ cm}^{-3}$. The OH and HO_2 concentrations were determined from a kinetic molecular model of α -pinene OH reaction which is described in detail in Sect. 3.2 and in the Supplement. In brief, OH is produced by the photolysis of H_2O_2 and is primarily consumed by reactions with VOCs in the chamber and with H_2O_2 . The reaction of OH

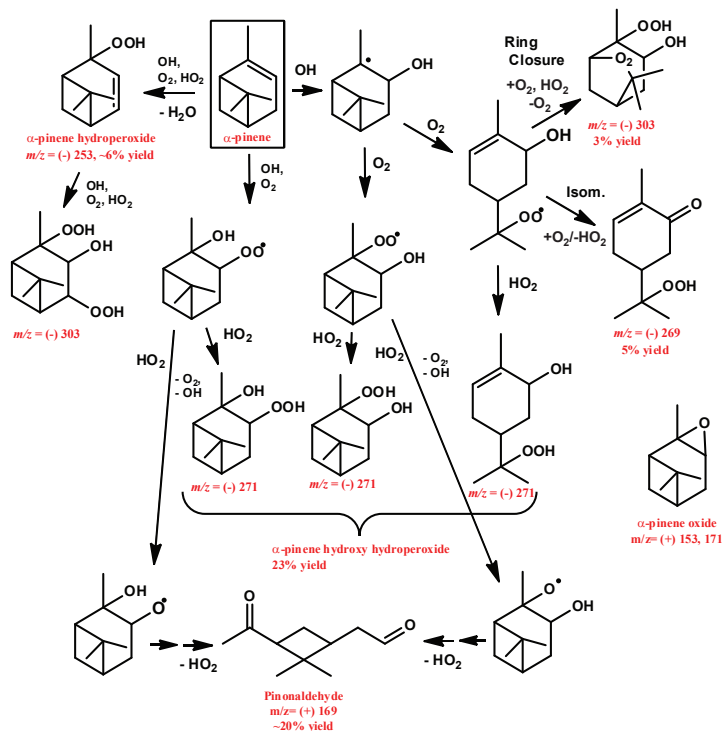


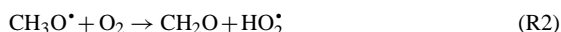
Fig. 1. Pathway of photooxidation of α -pinene under low- NO_x conditions. Species that were observed are labeled in red. The m/z of all species observed in the negative mode are of the complex with CF_3O^- (molecular mass + 85). Pinonaldehyde is observed at molecular mass + 1 in the positive mode and α -pinene oxide is observed at molecular mass + 1 and + 19. The observed percent yield for first-generation products is also indicated.

and H_2O_2 produces HO_2 . The photolysis rate of H_2O_2 used in the model and the OH concentration determined by the model were confirmed by comparison of the gas-phase concentrations of H_2O_2 and α -pinene from the experiment and the model (Fig. S1). These OH concentrations are similar to those observed in the troposphere; however, the HO_2 concentrations are about an order of magnitude greater than levels typically observed in rural or remote areas (Lelieveld et al., 2008; Ren et al., 2008; Wolfe et al., 2011). The O_3 concentration at the start of each experiment was <4 ppb and typically did not exceed 12 ppb over the course of an experiment (in one experiment, conducted for 20 h, the O_3 concentration increased nearly linearly from 4 to 25 ppb). Modeling of these oxidant concentrations indicated that reaction with O_3 accounted for <3 % of the α -pinene loss.

In the oxidation of α -pinene by OH , OH adds predominantly to the endocyclic double bond, followed by addition of O_2 to the resulting β -hydroxy alkyl radicals producing a number of hydroxy peroxy radicals. OH abstraction of a hydrogen from α -pinene occurs with a yield of ~ 12 %, resulting in a peroxy radical when O_2 reacts with the alkyl rad-

ical (Capouet et al., 2004). Under low- NO_x conditions the peroxy radicals can react with either HO_2 or with another RO_2 (self or cross-reactions). Here we seek to emulate atmospheric conditions where $\text{RO}_2 + \text{HO}_2$ dominates. To confirm that the $\text{RO}_2 + \text{HO}_2$ pathway dominated in our experiments, a kinetic model was constructed, as described in Sect. 3.2 and the Supplement. For the experimental conditions (with initial concentration of α -pinene of 20–50 ppb), the kinetic model indicates that less than 1 % of the peroxy radical reactions proceed via $\text{RO}_2 + \text{RO}_2$.

For high- NO_x photooxidation experiments, OH is generated from the photolysis of either HONO or methyl nitrite. When HONO is synthesized, NO and NO_2 are produced as side products, which are also introduced to the chamber when HONO is injected. Methyl nitrite is synthesized pure and upon photolysis eventually produces OH and NO_2 :



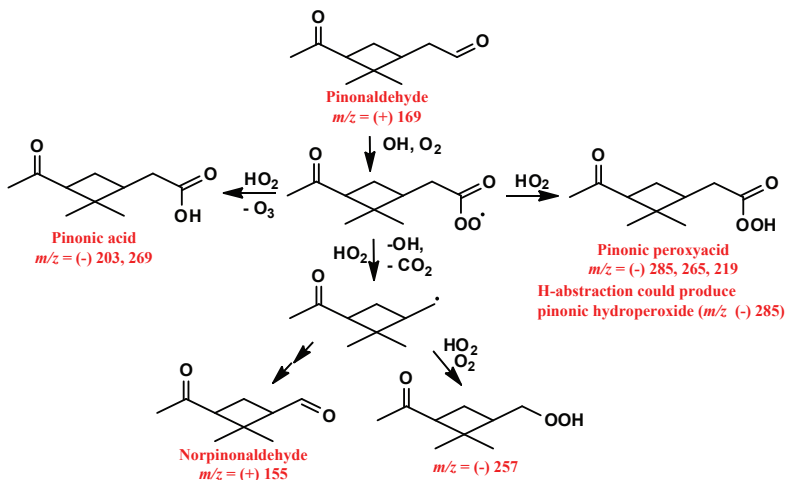


Fig. 2. Pathway of photooxidation of pinonaldehyde under low- NO_x conditions. Species that were observed are labeled in red. Pinonic acid and pinonic peracid were observed in the negative mode as both the transfer ion (molecular mass + 19) and the complex (molecular mass + 85), pinonic peracid is also observed as the complex minus HF (molecular mass + 65), norpinonaldehyde hydroperoxide was observed as the complex ion, pinonaldehyde and norpinonaldehyde are observed in the positive mode at their molecular mass +1.

When methyl nitrite was used as the OH source, 300 to 400 ppb of NO was added to suppress O_3 production. Under the conditions used, the peroxy radicals formed from the OH reaction of α -pinene react with NO and not RO_2 or HO_2 . This is confirmed by the lack of $\text{RO}_2 + \text{HO}_2$ or $\text{RO}_2 + \text{RO}_2$ reaction products during high- NO_x photooxidation. The exact ratio of NO to NO_2 is not known as both HONO and methyl nitrite interfere with the signals from the chemiluminescence NO_x instrument; however, it was determined that a higher NO_2 concentration exists during methyl nitrite photolysis due to the increased production of peroxyacetyl nitrates (PANs), as detected by CIMS in the negative mode, which result from the $\text{RO}_2 + \text{NO}_2$ reaction. More details on the detection of, as well as the specific PANs detected will be discussed in Sect. 3.3.

3.1 Gas phase composition from low- NO_x photooxidation of α -pinene

The principal first-generation oxidation products observed from the low- NO_x photooxidation of α -pinene were a number of α -pinene hydroxy hydroperoxides and pinonaldehyde. Production of α -pinene hydroperoxide from H-abstraction and α -pinene oxide are also observed (see Fig. 1 for proposed reaction mechanism for α -pinene and Fig. 2 for pinonaldehyde). The time traces from the CIMS are shown in Fig. 3 along with those from a number of the minor oxidation products. The identification of each of these signals is discussed below.

The α -pinene hydroxy hydroperoxides are observed at m/z (-)271 (molecular weight + CF_3O^-) by the CIMS. They

are expected to be a major products of the reaction channel of $\text{RO}_2 + \text{HO}_2$. Three different α -pinene hydroxy hydroperoxide isomers are formed; two β -hydroxy hydroperoxides and one ring opened hydroxy hydroperoxide containing a double bond (see Fig. 1). The subsequent reaction pathways of these three α -pinene hydroxy hydroperoxides are expected to be different and will lead to distinct reaction products, as discussed in Sect. 3.2. The overall estimated initial yield of the α -pinene hydroxy hydroperoxides is ~23 %. This estimate accounts for the small yield of pinic acid, which has the same molecular weight as these peroxides (MW = 186). Similar to other carboxylic acids, ionization of pinic acid by CF_3O^- yields approximately equal amounts of signal at m/z (-)271 and 205 (MW - H + HF). This allows us to use the signal at m/z (-)205 to insure that the pinic acid concentration does not significantly impact the hydroperoxide yield estimate.

Pinonaldehyde is neither acidic nor is the complex with CF_3O^- significantly strong to be detected in the negative mode and thus is observed only in the positive mode of the CIMS. Pinonaldehyde was synthesized to directly observe its OH oxidation; however, the synthesized sample was not of sufficient purity to calibrate the CIMS response. While we cannot report an absolute yield for pinonaldehyde, we observe that the yield under low- NO_x conditions is 2/3 of that under high- NO_x conditions. As pinonaldehyde is one of the main products of α -pinene oxidation by any atmospheric oxidant, it has been widely studied. Although the reported yield of pinonaldehyde under high- NO_x conditions varies widely from 27–87 % (Arey et al., 1990; Hatakeyama et al., 1991; Noziere et al., 1999; Wisthaler et al., 2001; Jaoui and Kamens, 2001; Aschmann et al., 2002; Lee et al., 2006),

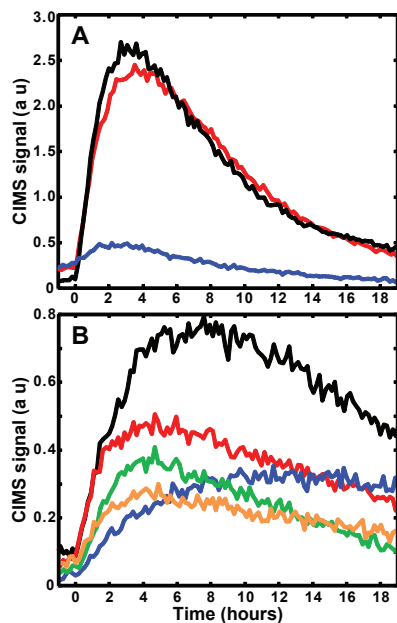
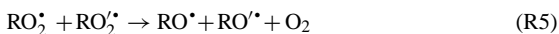
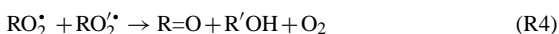


Fig. 3. CIMS time traces of a number of important low- NO_x photooxidation products of α -pinene. (A) Main first generation products, m/z (-)271 α -pinene hydroxy hydroperoxide (black), m/z (+)169 pinonaldehyde (red), m/z (-)253 α -pinene hydroperoxide (blue) (B) Signals of species that are formed in multiple generations m/z (-)285 (black), m/z (-)269 (red), m/z (-)303 (green), m/z (-)301 (orange), and purely second-generation m/z (-)203 pinonic acid (blue). The signal from m/z (+)169 is the only signal shown from the positive mode and the intensity was divided by 2 for clarity.

most of the measured yields are between 27–35 %. The very high yields were measured by FTIR which may be biased by interference from other carbonyls (Noziere et al., 1999; Hatakeyama et al., 1991). Assuming that under high- NO_x conditions the pinonaldehyde yield is between 27–35 %, we estimate that the low- NO_x yield is about 20 %.

Pinonaldehyde has been observed from the low- NO_x photooxidation of α -pinene previously; however, it is typically assigned as a product of $\text{RO}_2 + \text{RO}_2$ chemistry (Noziere et al., 1999; Larsen et al., 2001). In the present set of experiments, the chemistry is overwhelmingly dominated by $\text{RO}_2 + \text{HO}_2$ (i.e. low α -pinene concentration and relatively high HO_2 concentration). This is confirmed by the photooxidation products observed. The two main reaction channels for alkyl peroxy radicals with other RO_2 are:

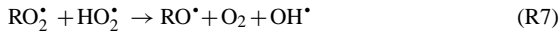


resulting in the formation of alcohols and carbonyls from Reaction (R4) and alkoxy radicals from Reaction (R5). In the case of α -pinene, these would be β -diols, β -hydroxy carbonyl, and hydroxy alkoxy radicals. The six membered ring of the hydroxy alkoxy radical will then open forming pinonaldehyde. There is no indication of either β -diols or β -hydroxy carbonyl being formed during the present experiments. In the case of alkyl peroxy radicals reacting with HO_2 , the main reaction channel is:



which forms hydroperoxides. For α -pinene, Reaction (R6) will produce the observed α -pinene hydroxy hydroperoxides. For many small alkyl peroxy radicals it has been shown to be the only channel (Hasson et al., 2004; Raventos-Duran et al., 2007; Noell et al., 2010).

If Reaction (R6) was the only channel, there would be no route to pinonaldehyde production. One possible route to pinonaldehyde is a radical channel (see Fig. 1):



similar to those known to be important for acetyl peroxy radicals (Hasson et al., 2004; Dillon and Crowley, 2008) and possibly for the reaction of OH with toluene (Birdsall et al., 2010). If this is the route to pinonaldehyde formation, an OH recycling channel would also be of importance in the reaction of OH with α -pinene under low- NO_x conditions.

α -pinene hydroperoxide and α -pinene oxide are also observed products of the OH oxidation of α -pinene under low- NO_x conditions. α -pinene hydroperoxide can be formed from H-abstraction by OH, which is estimated to account for about 12 % of the OH reaction with α -pinene (Capouet et al., 2004). Assuming similar CIMS sensitivity to α -pinene hydroperoxide and α -pinene hydroxy hydroperoxide, the yield of α -pinene hydroperoxide is estimated to be ~6 %. The remainder of the H-abstraction branching ratio cannot be accounted for at this time. α -pinene oxide is neither acidic nor is the complex with CF_3O^- significantly strong to be detected in the negative mode and thus is observed only in the positive mode at m/z (+)153 and 171 as confirmed by direct injection of α -pinene oxide into the chamber. Further evidence of α -pinene oxide formation is presented in part 2 of this series of paper where SOA composition is discussed. α -pinene oxide appears to be a minor product, and the mechanism for its formation by OH oxidation is not known. The mechanism for the formation from O_3 oxidation is known and yields of a few percent have been reported (Alvarado et al., 1998; Berndt et al., 2003); however, in the present experiments O_3 accounts for less than 3 % of the oxidation of α -pinene.

The oxidation products of pinonaldehyde have been shown to be important in the formation of SOA from the photooxidation of α -pinene. Specifically, pinonic acid, 10-hydroxy pinonic acid, and pinic acid have been observed in ambient SOA samples (Kavouras et al., 1998, 1999; Yu

et al., 1999; Laaksonen et al., 2008; Zhang et al., 2010) and in laboratory studies of α -pinene photooxidation (Larsen et al., 2001; Jaoui and Kamens, 2001; Librando and Tringali, 2005). The low- NO_x photooxidation of pinonaldehyde was carried out to determine the contribution of pinonaldehyde oxidation products to the gas and particle phases of α -pinene photooxidation.

Photooxidation of pinonaldehyde accounts for a number of the products observed from α -pinene photooxidation. OH oxidation of pinonaldehyde occurs by H-abstraction, typically from the aldehydic group (59–86 %) (Kwok and Atkinson, 1995; Vereecken and Peeters, 2002) forming an acyl peroxy radical after the addition of O_2 . The reaction of HO_2 with an acyl peroxy radical produces carboxylic acids, peroxyacids, and acetoxy radicals that will decompose to produce CO_2 and an alkyl radical. Hasson et al. (2004) have shown that these three pathways occur in roughly equal yields. The reaction pathways and products from pinonaldehyde are shown in Fig. 2. Pinonic acid is observed by the CIMS mostly by its transfer product ion (ratio of m/z (–)203 to m/z (–)269 is $\sim 9:1$), typical of acidic species, while the peroxyacid is observed more by its complex ion (ratio of m/z (–)219 to m/z (–)285 is $\sim 1:4$) (Fig. 4). In addition, we have observed, using synthesized peracetic acid, that peroxyacids are also observed in the negative mode as its molecular mass +65 (complex with $\text{CF}_3\text{O}^- - \text{HF}$) at 10–20 % that of the complex ion (+85). A signal at m/z (–)265, ~ 10 % the intensity of m/z (–)285, has been assigned to pinonic peroxyacid providing further evidence of its formation. These two products are formed in roughly equal yields. H-abstraction at carbons other than the aldehydic carbon could also form pinonaldehyde hydroperoxide which would also be detected at m/z (–)285, as would 10-hydroxy pinonic acid (product found in SOA). A signal at m/z (–)257 that has nine carbons was observed and has been assigned to the hydroperoxide formed from the alkyl radical formed from the decomposition of the acetoxy radical. The formation of norpinaldehyde was also detected. Pinic acid was observed in equal amounts at m/z (–)205 and m/z (–)271, but is a minor product.

Low- NO_x photooxidation of α -pinene also leads to the pinonaldehyde oxidation products (Fig. 4). Ions at m/z (–)203 and (–)219 assigned to the transfer ions of pinonic acid and pinonic peroxyacid are observed to be second generation products from α -pinene photooxidation, as would be expected arising from the oxidation of pinonaldehyde. The ion at m/z (–)257 assigned to the C₉ hydroperoxide produced from pinonaldehyde photooxidation is also observed to be second generation. Pinonic acid and pinonic peroxyacid are also observed as the complex ion at m/z (–)269 and (–)285 respectively. The time traces for m/z (–)269 and m/z (–)285 from the photooxidation of α -pinene are not purely from first or second generation products (see Figs. 3 and 4) but a combination of the two. The second generation products observed as these two ions are pinonic acid and pinonic peroxyacid, evident from their transfer ions, while

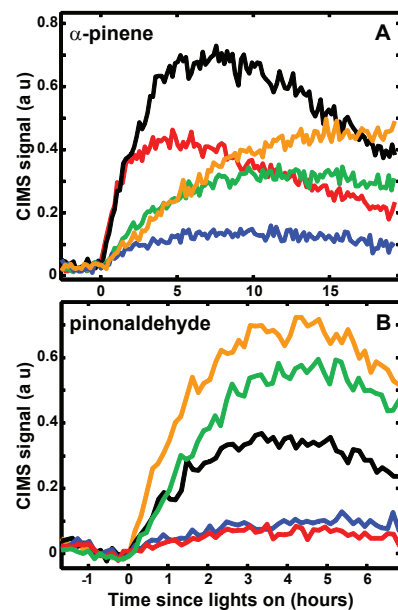


Fig. 4. Comparison of CIMS signals from low- NO_x photooxidation of (A) α -pinene and (B) pinonaldehyde; m/z (–)285 (black), m/z (–)269 (red), m/z (–)257 (orange), m/z (–)219 (blue), and m/z (–)203 (green). Pinonaldehyde photooxidation produces pinonic peroxyacid observed at both m/z (–)285 and (–)219, pinonic acid observed at both m/z (–)269 and (–)203, and a C₉ hydroperoxide observed at m/z (–)257. The pinonaldehyde photooxidation products are observed from α -pinene photooxidation along with additional first-generation signals at m/z (–)269 and (–)285 from first-generation photooxidation products.

the first generation products arise from the photooxidation of α -pinene. Oxidation products of these molecular mass (184 and 200) have been observed and theoretically proposed from the photooxidation of α -pinene in the presence of NO (Aschmann et al., 2002; Vereecken et al., 2007). Under high- NO_x conditions, Aschmann et al. (2002) observed molecules at these masses and assigned them to a dihydroxy carbonyl and a trihydroxy carbonyl that would be formed by a number of isomerization steps as well as multiple reactions of peroxy radicals with NO to form alkoxy radicals. Vereecken et al. (2007) indicate that molecules with these molecular weights could be formed by isomerization reactions after ring opening, while the molecule with MW = 200 is produced from a reaction of NO with the peroxy radical. In both mechanisms, alkoxy radicals are essential. Alkoxy radicals appear to form from the reaction of the initially formed α -pinene hydroxy peroxy radical intermediates with HO_2 , and this is a possible route; however, at this point, the structure of these molecules is unknown. These are, however, clearly polyoxygenated species formed from the primary oxidation

of α -pinene and their most likely molecular formulas are $C_{10}H_{16}O_3$ and $C_{10}H_{16}O_4$.

Highly oxidized species at m/z (–)301 and (–)303 are also observed as first generation products (see Fig. 3). Both signals decay similarly to the signals at m/z (–)269 and (–)285, indicating that they are also formed as later generation products. The most likely structure for the first-generation species at m/z (–)303 is an α -pinene hydroxy hydroperoxide with a bridging peroxy group that results from the ring closing channel of the ring opened hydroxy hydroperoxide as shown in Fig. 1. This mechanism has been postulated by Vereecken et al. (2007). The addition of one hydroxyl group and two hydroperoxyl groups decreases the vapor pressure about eight orders of magnitude making this product a likely aerosol phase component (Capouet and Müller, 2006). The photooxidation of α -pinene hydroperoxide will produce a hydroxy dihydroperoxide that will also be observed at m/z (–)303 thus accounting for the slow decay of the signal. We do not know the structure of the photooxidation product(s) at m/z (–)301. Given the molecular weight, the structure potentially includes one carbonyl and two hydroperoxyl groups. Whatever the structure, the vapor pressure will be greatly reduced from that of α -pinene, once again making it a potential SOA component.

Another route to the formation of the low vapor pressure oxidation products at m/z (–)301 and (–)303 is peroxy radical isomerization. Peroxy radical isomerization has recently been extensively studied for the isoprene system both theoretically (Peeters et al., 2009; da Silva et al., 2010; Nguyen et al., 2010) as well as experimentally (Crounse et al., 2011). It has been shown that peroxy radical isomerization most often occurs via a six or seven membered intermediate (Perriin et al., 1998; Blin-Simiand et al., 2001; Jorand et al., 2003). When OH adds to the tertiary carbon of the double bond the peroxy radical on the secondary carbon can form a seven membered ring with the hydrogen of either the secondary carbon in the four membered ring or one of primary carbons attached to the four membered ring. After isomerization, reaction with O_2 and HO_2 will result in the formation of α -pinene hydroxy dihydroperoxide which would be detected at m/z (–)303. See Fig. S2 in the Supplement for proposed mechanism. When OH adds to the secondary carbon of the double bond, a seven membered intermediate can form with the other tertiary carbon of the four membered ring ultimately forming α -pinene hydroxy dihydroperoxide. Similarly, the α -pinene hydroxy hydroperoxide peroxy radical formed from isomerization from the addition of OH to the secondary carbon can form a six membered ring with the hydrogen on the carbon α to the hydroxyl group. This isomerization would result in the formation of α -pinene carbonyl dihydroperoxide which would be observed at m/z (–)301. For the species observed at m/z (–)301 and (–)303 to be formed via isomerization, the rate of peroxy radical isomerization would have to be competitive with that of $RO_2 + HO_2$. In the present experiments $[HO_2] \sim 1 \times 10^{10}$ molecules cm^{-3} so

the rate of loss of α -pinene hydroxy radical by reaction with HO_2 is $\sim 0.2\text{ s}^{-1}$. In the atmosphere the HO_2 concentration is about an order of magnitude less, so for isomerization to be competitive (10 % of peroxy radical reaction) the rate would have to be $\sim 0.002\text{ s}^{-1}$. In the isoprene system the isomerization rate has been found to be 0.002 s^{-1} with conformer specific rates being much faster (Crounse et al., 2011). At this time there have been no experimental studies on the isomerization rate in the α -pinene system so it is unknown what the rate is and therefore its atmospheric relevance. If the rate of isomerization is competitive with reaction with HO_2 in the atmosphere, more low vapor pressure species capable of partitioning into the aerosol will be formed than were observed in this study.

3.2 Kinetic model of low- NO_x photooxidation of α -pinene

To gain a better understanding of the low- NO_x photooxidation of α -pinene, a kinetic model was assembled and compared to the time traces of α -pinene and the reaction products measured during the photooxidation of 19.8 ppb α -pinene and 4 ppm H_2O_2 . The kinetic model was constructed using Kintecus modeling software (Ianni, 2002). When available, rate constants from literature were used; however, a majority of the rate constants are not known. In these cases, reaction rates with respect to OH oxidation were estimated using the structural activity relationship derived by Kwok and Atkinson (Kwok and Atkinson, 1995). This method has been shown to predict rate constants to within a factor of two for most species (see Tables S1 and S2 for lists of photooxidation products, reactions, and reaction rates used in this model). The rate constants were then modified slightly to best fit the data. The rate constants for $RO_2 + HO_2$ and $RO_2 + RO_2$ were taken from the estimates used for the Master Chemical Mechanism (Saunders et al., 2003). Photolysis was included for hydrogen peroxide, the organic hydroperoxides, and for pinonaldehyde. The photodissociation frequencies (j) were determined from the spectral radiance measured from the chamber lights and the absorption cross sections reported in the literature for hydrogen peroxide and pinonaldehyde and estimated for the organic hydroperoxides from reported cross sections of similar hydroperoxides (Atkinson et al., 2006; Sander et al., 2006).

For the model to be accurate, the concentration of OH and HO_2 need to be correct. OH is produced from photolysis of H_2O_2 which initially reacts with hydrocarbons in the chamber as well as H_2O_2 . It is the reaction of OH with H_2O_2 that produces HO_2 . The value of $j_{H_2O_2}$ was confirmed by comparing the simulated loss of H_2O_2 (photolysis and reaction with OH) to the time trace observed from the CIMS (see SI Fig. S1). The comparison of the simulated loss of α -pinene, using the recommended rate constant for the reaction of α -pinene with OH from the IUPAC database (Atkinson et al., 2006), with the the observed loss of α -pinene also confirms

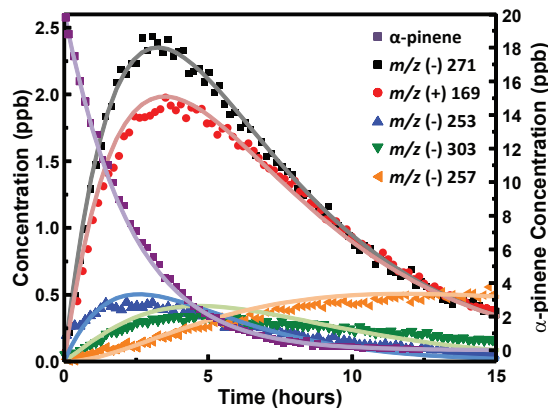


Fig. 5. Time-dependent observed (points) versus simulated (lines) concentrations from the photooxidation of 19.8 ppb of α -pinene. Represented are α -pinene (purple), α -pinene hydroxy hydroperoxide (black), pinonaldehyde (red), α -pinene hydroperoxide (blue), α -pinene hydroxy dihydroperoxide (green), and the C₉ hydroperoxide from pinonaldehyde (orange). See the Supplement for structural information and kinetic model.

the simulation produces the correct amount of OH (see Fig. S1 in the Supplement). The modeled OH concentration quickly reaches 2.2×10^6 molecules cm^{-3} and is approximately constant between $2.2\text{--}2.5 \times 10^6$ molecules cm^{-3} over the course of the experiment, while the HO₂ concentration rapidly plateaus at about 1×10^{10} molecules cm^{-3} . In addition, the rate constant of OH with pinonaldehyde was confirmed from the experiment where pinonaldehyde was directly injected into the chamber. Pinonaldehyde is lost by reaction with OH as well as photolysis ($\sim 10\%$ of overall reaction), and the best fit to the data is achieved with $k_{\text{pinonaldehyde}+\text{OH}} = 3.7 \times 10^{-11} \text{ cm}^3 \text{ molecules}^{-1} \text{ s}^{-1}$ (Fig. S3 in the Supplement). This rate constant is within the error recommended by the IUPAC database and the latest measurement of this reaction rate by Davis et al. (2007); Atkinson et al. (2006).

Figure 5 shows the time traces of α -pinene and several of the photooxidation products along with the simulated concentrations from the kinetic model. The oxidation products in Fig. 5 are representative of first-generation products (α -pinene hydroxy-hydroperoxides, pinonaldehyde, and α -pinene hydroperoxide) and a second-generation product (C₉ hydroperoxide from pinonaldehyde) (see Table S1 for structural information of each compound). The one exception is the highly oxygenated compound observed at m/z (–)303 (assigned to hydroxyl dihydroperoxide) that is both a first- and second-generation product, and due to its high degree of oxidation and low volatility is predicted to partition into the particle phase. As noted in Sect. 3.1, pinic acid is a minor second generation product that is observed at m/z (–)205 and m/z (–)271 in roughly equal amounts. This small yield was

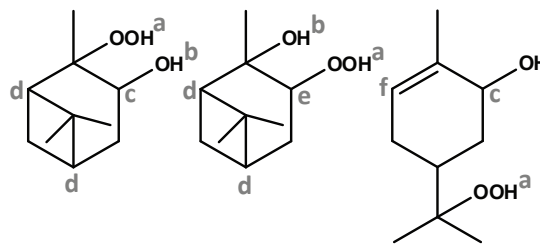


Fig. 6. Structure of the hydroxy hydroperoxides formed from the low-NO_x photooxidation of α -pinene, the most likely positions for reaction with OH are also shown; H-abstraction (a–e) and OH addition (f).

accounted for in determining the concentration of α -pinene hydroxy hydroperoxides. Using the fastest RO₂ + RO₂ rate constant for α -pinene hydroxy peroxy radicals from MCM, only 0.05 % of the peroxy radical is predicted to react through the RO₂ + RO₂ channel. Including all of the identified first-generation products (these presented here along with the products at m/z (–)269, 285, and 301), 65–75 % of the carbon can be accounted for, and this does not include compounds that are expected to partition into the aerosol phase.

Pinonaldehyde, in the present set of experiments, is formed from the RO₂ + HO₂ reaction channel of two of the α -pinene hydroxy peroxy radicals, and the reaction rate with OH has been well characterized. However, based on these formation and loss mechanisms for pinonaldehyde, the simulated pinonaldehyde decays far too quickly; therefore, pinonaldehyde must also be produced as a second-generation oxidation product. Of the first-generation products, the most likely candidates to produce pinonaldehyde from a reaction with OH are the α -pinene hydroxy hydroperoxides.

There are a number of paths by which the α -pinene hydroxy hydroperoxides will form pinonaldehyde. First of all, the hydroperoxide will not only react with OH but will also undergo photolysis. Photolysis cleaves the weak O–O bond of the hydroperoxide producing an alkoxy radical that will produce pinonaldehyde. We estimate, however, that photolysis represents $\sim 3\%$ of the α -pinene hydroxy hydroperoxide loss and thus does not provide mass closure between the data and the simulation.

Figure 6 shows the three hydroxy hydroperoxides that are formed from low-NO_x photooxidation of α -pinene, two β -hydroxy hydroperoxides and a ring-opened one that includes a double bond. The β -hydroxy hydroperoxides have a number of places where OH hydrogen abstraction could occur (Fig. 6), the carbon α to the alcohol; carbon α to the hydroperoxy group; either of the tertiary carbons; the alcoholic hydrogen; or the hydroperoxy hydrogen. Hydrogen abstraction from an alcohol will mostly occur from the α carbon which has been shown to result in the formation of a

carbonyl and HO_2 (Carter et al., 1979; Atkinson, 1986; Grosjean, 1997). Presumably this would form a hydroperoxy carbonyl, a mass analog of the known second-generation product pinonic acid. As there are first- and second-generation products with m/z (–)269, it is not clear how important this H-abstraction channel is. There have only been a few hydroperoxides whose H-abstraction reaction rates and product distributions have been studied: methyl, ethyl and tert-butyl (Vaghjiani and Ravishankara, 1989; Niki et al., 1983; Wang and Chen, 2008; Baasandorj et al., 2010). It has been shown that the OO-H bond is fairly labile and H-abstraction from both the hydroperoxide as well as the α -carbon will occur. H-abstraction from the hydroperoxyl group will result in reformation of the peroxy radical with the same branching ratio of products from the initial reaction forming, among other species, pinonaldehyde and hydroxy hydroperoxide. H-abstraction from the α -carbon of the hydroperoxy group would presumably form a hydroxy carbonyl, which is a mass analog of α -pinene hydroperoxide. In the model, the signal associated with α -pinene hydroperoxide is fit well with a production channel from α -pinene and a reaction rate with OH that is nearly as fast as α -pinene itself, suggesting that it is unlikely that there is a second-generation product formed at this mass. It is possible that following hydrogen abstraction, the ring is cleaved, ultimately resulting in the formation of pinonaldehyde. Finally, H-abstraction from either of the tertiary carbons will produce more highly oxygenated species, including a hydroxyl dihydroperoxide (m/z (–)303). Of these different H-abstraction pathways, those involving the hydroperoxide and carbons α to the hydroperoxy and hydroxyl groups are expected to dominate. The ring opened hydroxy hydroperoxide has a highly reactive double bond instead of one of the tertiary carbons. After addition of OH to the double bond, the reaction will most likely proceed in one of the following ways: formation of a dihydroxy dihydroperoxide or intermolecular reaction of the alkyl radical with the hydroperoxy group forming a ring with one oxygen and releasing OH. The former product has not been observed in the present experiments; however, this highly oxidized compound has a low vapor pressure and is expected to primarily reside in the particle phase. The later product is a mass analog of the hydroxy hydroperoxide, and the two species are indistinguishable by CIMS.

In the simulation, all the pathways for reaction of the α -pinene hydroxy hydroperoxides were considered and the contribution of each was varied until the simulation best fit the data based on a least-squares analysis of α -pinene hydroxy hydroperoxide and pinonaldehyde. The best fit results when 58 % of the reaction produces pinonaldehyde directly while another 25 % reforms the peroxy radical, resulting in a net ~33 % of α -pinene producing pinonaldehyde from low- NO_x photooxidation. This is important since the oxidation products of pinonaldehyde are main SOA components. There is need for further studies on the photooxidation of α -pinene hydroxy hydroperoxides to confirm these reaction pathways.

and branching ratios; however, the data and kinetic model strongly indicate that pinonaldehyde is produced from the OH oxidation of α -pinene hydroxy hydroperoxides under low- NO_x conditions.

3.3 Gas-phase composition from high- NO_x photooxidation of α -pinene

Figure 7 shows the proposed reaction mechanism of α -pinene photooxidation under high- NO_x conditions. This mechanism and the following discussion of the reaction products are not intended to be all-inclusive. The photooxidation of α -pinene under high- NO_x conditions produces a large variety of compounds through functionalization and fragmentation reactions. We observe signals at many masses but, for brevity, we only focus on those of the major products of α -pinene and pinonaldehyde high- NO_x OH oxidation.

In the presence of NO_x , the main photooxidation products of α -pinene are pinonaldehyde, organonitrates, and isomerization products from the alkoxy radical formed from the reaction of NO with the peroxy radical. The yield of pinonaldehyde is 1.5 times that formed in the absence of NO_x , and, as mentioned above, previous studies show that it is 27–35 %. Capouet et al. (2004) estimates α -pinene hydroxy nitrate yield to be ~15 %. Alkoxy radical isomerization products are observed at m/z (–)269 (MW 184) and m/z (–)285 (MW 200). These isomerization products have been observed previously and have been assigned to either a dihydroxy carbonyl and a trihydroxy carbonyl (Aschmann et al., 2002) or to ring opened substituted hydroperoxides (Vereecken et al., 2007). In the present study, the yield of the isomerization products was found to be less than 20 %. The OH addition to the double bond can also result in prompt ring opening of the four-membered ring. Further reactions of the ring-opened alkyl radical will result in fragmentation producing an alkyl radical and acetone (see Fig. 7). This is a minor pathway, as the total acetone yield observed was less than 10 %, including the production of acetone from the photooxidation of pinonaldehyde. Finally, there is a first-generation species observed at m/z (–)301, which was also present during low- NO_x photooxidation. A likely molecular formula is $\text{C}_{10}\text{H}_{16}\text{O}_5$, but the identity of this molecule is unknown. The same oxidation products were observed from high- NO_x photooxidation, regardless of OH source, HONO or methyl nitrite.

The photooxidation of pinonaldehyde was studied using methyl nitrite as the OH source. Figure 8 shows the proposed mechanism and products of this reaction. There have been two theoretical studies on the H-abstraction of pinonaldehyde (Kwok and Atkinson, 1995; Vereecken and Peeters, 2002). Kwok and Atkinson (1995) indicate that 86 % of the abstraction will occur at the aldehydic hydrogen, while Vereecken and Peeters (2002) determined that 59 % will be of the aldehydic hydrogen, 23 % from the carbon β to the aldehydic carbon, and 14 % from the tertiary carbons. The

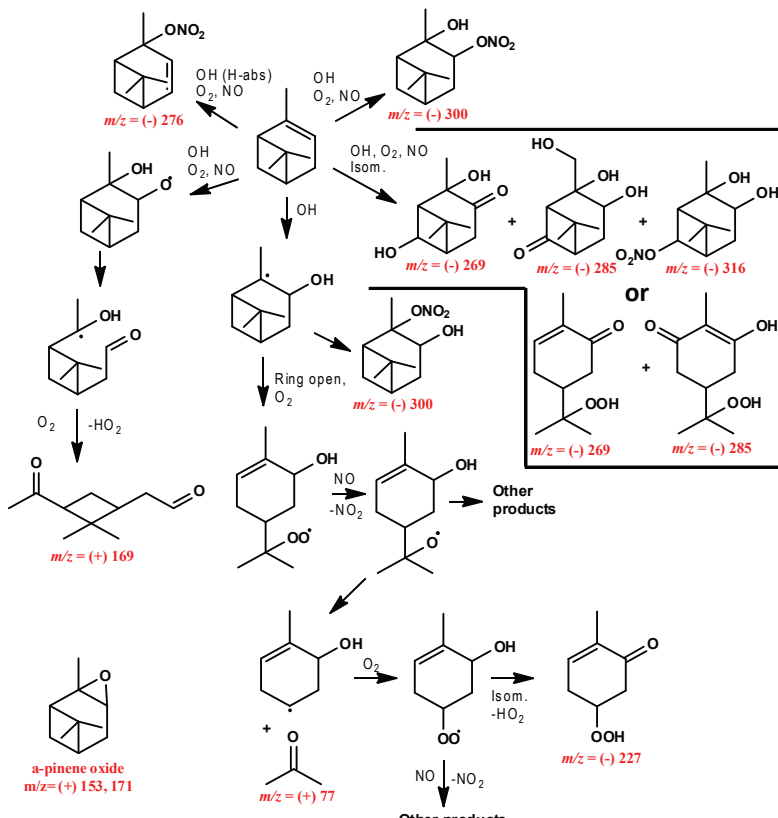


Fig. 7. Pathways of photooxidation of α -pinene under high- NO_x conditions, the structures for m/z (-)269 and (-)285 (MW 184 and 200) are those proposed by Aschmann et al. (2002) and Vereecken et al. (2007). Ion of compounds detected by CIMS are indicated in red.

products expected, and observed, of the primary channel (H-abstraction of the aldehydic hydrogen) are pinonaldehyde PAN, formed from reaction of the acyl peroxy radical with NO_2 or norpinonaldehyde, formed from reaction of the acyl peroxy radical with NO (see Fig. 8 for structures and mechanisms). H-abstraction from the carbon β to the aldehydic carbon produces either pinonaldehyde nitrate or norpinonaldehyde with the loss of CO. Finally, H-abstraction from the tertiary carbons produces pinonaldehyde nitrate or a tertiary alkoxy radical. One potential reaction pathway for the tertiary alkoxy radical is the decomposition to form acetone (see Fig. 8), which is observed in low yield from high- NO_x photooxidation of pinonaldehyde. Once formed, norpinonaldehyde will be oxidized in similar fashion to pinonaldehyde. The signal for pinonaldehyde PAN is 4–8 times that of pinonaldehyde nitrate (from all high- NO_x experiments, α -pinene and pinonaldehyde) depending on the NO_2 concentration relative to NO. The observed signal of the norpinonaldehyde PAN to norpinonaldehyde nitrate from the photooxidation of pinonaldehyde was greater than 14 to 1. Pinonaldehyde PAN

is formed from an acyl peroxy radical while pinonaldehyde PAN will be formed from an alkyl peroxy radical. The formation of an acyl peroxy radical is favored over the formation of an alkyl peroxy radical from H-abstraction of pinonaldehyde and thus the formation of pinonaldehyde PANs is expected to be formed in higher yield than pinonaldehyde nitrate. A quantitative yield of the PAN is not known because the CIMS has not been calibrated for these compounds. The product distribution from the photooxidation of pinonaldehyde indicates that it does not add much to the total organonitrate yield from the photooxidation of α -pinene. Pinonic acid and pinic acid were not observed in the gas phase from either α -pinene or pinonaldehyde photooxidation under high- NO_x conditions.

An array of organonitrates and PANs are observed from the photooxidation of α -pinene. In addition to those previously discussed, nitrates were observed at m/z (-)276, 316, 318, 320, and 332 as well as PANs at m/z (-)346 and (-)362 (most likely observed as the molecular complex ion MW + 85). The unidentified organonitrates and PANs are

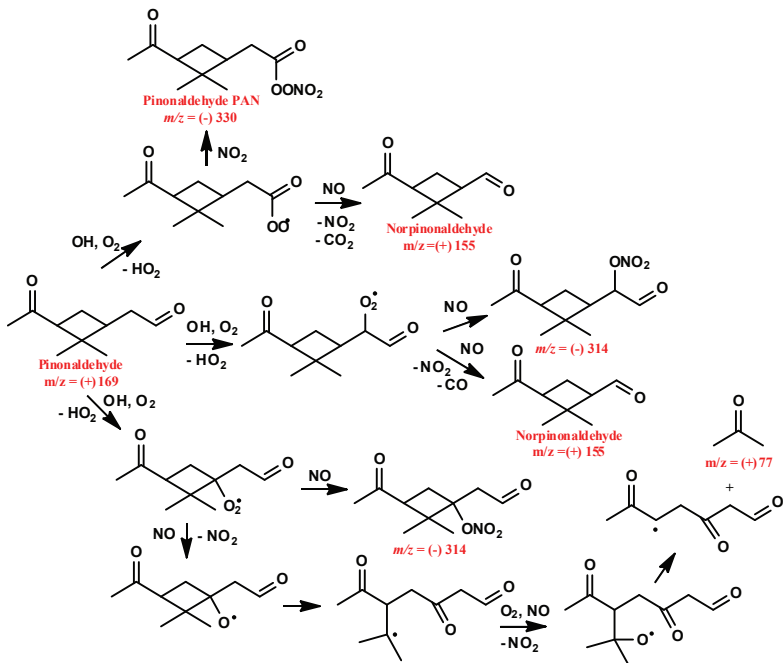


Fig. 8. Pathways of photooxidation of pinonaldehyde under high- NO_x conditions, H-abstraction by OH occurs predominantly at the aldehydic carbon. Ion of compounds detected by CIMS are indicated in red.

formed in much lower yields than those identified earlier. Nitrates and PANs are distinguished from each other by the nature of their decay. PANs thermally decompose so their gas-phase concentration will continue to decrease even after OH is no longer present. Norpinonaldehyde PAN is observed at m/z (-)316; however, comparing the time traces of this ion from pinonaldehyde photooxidation and α -pinene photooxidation, there appears to be a product formed from α -pinene as well. This could be the α -pinene dihydroxynitrate proposed by Aschmann et al. (2002). One interesting observation is that α -pinene hydroxy nitrate is lost from the gas phase at nearly an equal rate as pinonaldehyde. This is in contrast to the other organonitrates, whose signals are stable once they are formed.

The products of high- NO_x photooxidation of α -pinene are the same regardless of NO_2 level; however, there are a few differences in concentrations of certain species depending on the level of NO_2 . The most noticeable difference in the gas-phase composition depending on the $[\text{NO}_2]$ is the concentration of PANs, which are greater at high NO_2 (methyl nitrite photolysis). This is expected as the NO_2 concentration is higher in the methyl nitrite experiments resulting in a greater likelihood of NO_2 reacting with the acyl peroxy radicals produced from pinonaldehyde and norpinonaldehyde. The concentrations of isomerization products at m/z (-)269 and (-)285 showed a dependence on seed particle acidity when

HONO was used as the OH source but not when CH_3ONO was used as the OH source. In the case of the HONO source, the isomerization products were observed to be lower in the presence of an acidic seed. A discussion of why the products observed at m/z (-)269 and (-)285 are dependent on aerosol acidity only for the HONO case will be presented in part 2. The only other observed difference in the gas phase was the concentration of nitric acid, which was 1.5 times greater when methyl nitrite was the OH source than when HONO was the OH source.

4 Atmospheric implications

Under low- NO_x photooxidation of α -pinene, pinonaldehyde is produced by $\text{RO}_2 + \text{HO}_2$ chemistry in high yields. $\text{RO}_2 + \text{RO}_2$ chemistry is not the source, as is commonly assumed. While the atmospheric concentrations of HO_2 and RO_2 are similar, the rate constant of $\text{RO}_2 + \text{HO}_2$ is typically 1–4 orders of magnitude greater than $\text{RO}_2 + \text{RO}_2$. The further OH oxidation of pinonaldehyde produces a number of low volatility carboxylic acids and peroxyacids, which are important SOA components. While the only product with higher yield than pinonaldehyde is α -pinene hydroxy hydroperoxide, pinonaldehyde is also produced from the photolysis and OH oxidation of α -pinene hydroxy hydroperoxide. Including

the reaction channels of α -pinene hydroxy hydroperoxide that form pinonaldehyde (58 %) and assuming 19 % direct yield from α -pinene, the overall oxidation of α -pinene by OH under low- NO_x conditions has a pinonaldehyde yield of $\sim 33\%$.

Pinonic acid is an important tracer for SOA formed from α -pinene oxidation and is believed to be the precursor for other SOA tracers, such as 3-methyl-1,2,3-butanetricarboxylic acid (Szmigielski et al., 2007; Müller et al., 2012). Pinonic acid is not observed from the high- NO_x photooxidation of α -pinene, which is not surprising since there is no clear formation mechanism for it in the gas phase. Thus, observation of pinonic acid and the tracers derived from pinonic acid likely point to either low- NO_x oxidation of α -pinene by OH or ozonolysis under high- NO_x conditions. The aerosol-phase composition of these carboxylic acids as well as other carboxylic acids from α -pinene photooxidation will be discussed in detail in Part 2.

The gas-phase chemistry of α -pinene and its photooxidation products is complex and not well represented by the reactions of simple alkenes. By isolating the critical peroxy radical reactions, the products and branching ratios of a number of key reactions have been better constrained. Perhaps most importantly, we suggest that the formation of pinonaldehyde from low- NO_x photooxidation of α -pinene via $\text{RO}_2 + \text{HO}_2$ proceeds by the formation of an alkoxy radical and OH recycling. This reaction scheme has previously been shown to be important only for acyl peroxy radicals and possibly toluene. Unfortunately, the nature of the potential energy surface leading to radical recycling in the reactions of HO_2 with peroxy radicals has not been fully formulated. Is the OH recycling channel available due to the β hydroxyl group withdrawing electron density from the peroxy group, the bicyclic ring structure of α -pinene, or some other reason all together? To date, most of the detailed work on the reaction of alkyl peroxy radicals with HO_2 has focused on small, unsubstituted peroxy radicals; further work on a broader set of peroxy radicals, including atmospherically relevant VOCs such as monoterpenes and sesquiterpenes, is clearly needed to elucidate the physical chemistry. Finally, we suggest that there is a large secondary pinonaldehyde source from the photooxidation and/or photolysis of the three pinene hydroxy hydroperoxides produced from α -pinene.

Supplementary material related to this article is available online at: <http://www.atmos-chem-phys.net/12/6489/2012/acp-12-6489-2012-supplement.pdf>.

Acknowledgements. This work was supported in part by Department of Energy grant DE-SC0006626 and National Science Foundation grant AGS-1057183. N. Eddingsaas was supported by the Camille and Henry Dreyfus Postdoctoral Program in

Environmental Chemistry. C. Loza and L. Yee were supported by National Science Foundation Graduate Research Fellowships. The authors would like to thank John Crounse for helpful discussion.

Edited by: F. Keutsch

References

Alvarado, A., Tuazon, E. C., Aschmann, S. M., Atkinson, R., and Arey, J.: Products of the gas-phase reactions of $\text{O}(\text{P}^3)$ atoms and O_3 with alpha-pinene and 1,2-dimethyl-1-cyclohexene, *J. Geophys. Res.-Atmos.*, 103, 25541–25551, doi:10.1029/98JD00524, 1998.

Arey, J., Atkinson, R., and Aschmann, S. M.: Produt study of the gas-phase reactions of monoterpenes with the OH radical in the presence of NO_x , *J. Geophys. Res.*, 95, 18539–18546, doi:10.1029/JD095iD11p18539, 1990.

Aschmann, S. M., Atkinson, R., and Arey, J.: Products of reaction of OH radicals with alpha-pinene, *J. Geophys. Res.-Atmos.*, 107, D14, doi:10.1029/2001JD001098, 2002.

Atkinson, R.: Kinetics and mechanisms of the gas-phase reactions of the hydroxyl radical with organic compounds under atmospheric conditions, *Chem. Rev.*, 86, 69–201, 1986.

Atkinson, R., Baulch, D. L., Cox, R. A., Crowley, J. N., Hampson, R. F., Hynes, R. G., Jenkin, M. E., Rossi, M. J., Troe, J., and IUPAC Subcommittee: Evaluated kinetic and photochemical data for atmospheric chemistry: Volume II – gas phase reactions of organic species, *Atmos. Chem. Phys.*, 6, 3625–4055, doi:10.5194/acp-6-3625-2006, 2006.

Baasandorj, M., Papastasiou, D. K., Talukdar, R. K., Hasson, A. S., and Burkholder, J. B.: $(\text{CH}_3)_3\text{COOH}$ (tert-butyl hydroperoxide): OH reaction rate coefficients between 206 and 375 K and the OH photolysis quantum yield at 248 nm, *Phys. Chem. Chem. Phys.*, 12, 12101–12111, doi:10.1039/C0CP00463D, 2010.

Berndt, T., Boge, O., and Stratmann, F.: Gas-phase ozonolysis of alpha-pinene: gaseous products and particle formation, *Atmos. Environ.*, 37, 3933–3945, 2003.

Birdsall, A. W., Andreoni, J. F., and Elrod, M. J.: Investigation of the role of bicyclic peroxy radicals in the oxidation mechanism of toluene, *J. Phys. Chem. A*, 114, 10655–10663, 2010.

Blin-Simiand, N., Jorand, F., Sahetchian, K., Brun, M., Kerhoas, L., Malosse, C., and Einhorn, J.: Hydroperoxides with zero, one, two or more carbonyl groups formed during the oxidation of n-dodecane, *Combust. Flame*, 126, 1524–1532, doi:10.1016/s0010-2180(01)00264-4, 2001.

Capouet, M. and Müller, J.-F.: A group contribution method for estimating the vapour pressures of α -pinene oxidation products, *Atmos. Chem. Phys.*, 6, 1455–1467, doi:10.5194/acp-6-1455-2006, 2006.

Capouet, M., Peeters, J., Noziere, B., and Müller, J.-F.: Alpha-pinene oxidation by OH: simulations of laboratory experiments, *Atmos. Chem. Phys.*, 4, 2285–2311, doi:10.5194/acp-4-2285-2004, 2004.

Capouet, M., Mueller, J. F., Ceulemans, K., Compernolle, S., Vereecken, L., and Peeters, J.: Modeling aerosol formation in alpha-pinene photo-oxidation experiments, *J. Geophys. Res.-Atmos.*, 113, D02308, doi:10.1029/2007JD008995, 2008.

Carter, W. P. L., Darnall, K. R., Graham, R. A., Winer, A. M., and Pitts, J. N.: Reactions of C_2 and C_4 alpha-hydroxy radicals with

oxygen, *J. Phys. Chem.*, 83, 2305–2311, 1979.

Chung, S. H. and Seinfeld, J. H.: Global distribution and climate forcing of carbonaceous aerosols, *J. Geophys. Res.-Atmos.*, 107, doi:10.1029/2001JD001397, 2002.

Cocker, D. R. I., Flagan, R. C., and Seinfeld, J. H.: State-of-the-art chamber facility for studying atmospheric aerosol chemistry, *Environ. Sci. Technol.*, 35, 2594–2601, 2001.

Crounse, J. D., McKinney, K. A., Kwan, A. J., and Wennberg, P. O.: Measurement of gas-phase hydroperoxides by chemical ionization mass spectrometry, *Anal. Chem.*, 78, 6726–6732, 2006.

Crounse, J. D., Paulot, F., Kjaergaard, H. G., and Wennberg, P. O.: Peroxy radical isomerization in the oxidation of isoprene, *Phys. Chem. Chem. Phys.*, 13, 13607–13613, doi:10.1039/C1CP21330J, 2011.

da Silva, G., Graham, C., and Wang, Z.-F.: Unimolecular beta-Hydroperoxy Radical Decomposition with OH Recycling in the Photochemical Oxidation of Isoprene, *Environ. Sci. Technol.*, 44, 250–256, doi:10.1021/es900924d, 2010.

Davis, M. E., Talukdar, R. K., Notte, G., Ellison, G. B., and Burkholder, J. B.: Rate coefficients for the OH plus pinonaldehyde ($C_{10}H_{16}O_2$) reaction between 297 and 374 K, *Environ. Sci. Technol.*, 41, 3959–3965, 2007.

Dillon, T. J. and Crowley, J. N.: Direct detection of OH formation in the reactions of HO_2 with $CH_3C(O)O_2$ and other substituted peroxy radicals, *Atmos. Chem. Phys.*, 8, 4877–4889, doi:10.5194/acp-8-4877-2008, 2008.

Goldstein, A. H. and Galbally, I. E.: Known and unexplored organic constituents in the Earth's atmosphere, *Environ. Sci. Technol.*, 41, 1514–1521, 2007.

Grosjean, D.: Atmospheric chemistry of alcohols, *J. Braz. Chem. Soc.*, 8, 433–442, 1997.

Guenther, A., Hewitt, C. N., Erickson, D., Fall, R., Geron, C., Graedel, T., Harley, P., Klinger, L., Lerdau, M., McKay, W. A., Pierce, T., Scholes, B., Steinbrecher, R., Tallamraju, R., Taylor, J., and Zimmerman, P.: A global model of natural volatile organic compound emissions, *J. Geophys. Res.-Atmos.*, 100, 8873–8892, doi:10.1029/94JD02950, 1995.

Hasson, A. S., Tyndall, G. S., and Orlando, J. J.: A product yield study of the reaction of HO_2 radicals with ethyl peroxy ($C_2H_5O_2$), acetyl peroxy ($CH_3C(O)O_2$), and acetonyl peroxy ($CH_3C(O)CH_2O_2$) radicals, *J. Phys. Chem. A*, 108, 5979–5989, 2004.

Hatakeyama, S., Izumi, K., Fukuyama, T., Akimoto, H., and Washida, N.: Reactions of OH with alpha-pinene and beta-pinene in air – Estimate of global CO production from the atmospheric oxidation of terpenes, *J. Geophys. Res.-Atmos.*, 96, 947–958, 1991.

Hoffmann, T., Odum, J. R., Bowman, F., Collins, D., Klockow, D., Flagan, R. C., and Seinfeld, J. H.: Formation of organic aerosols from the oxidation of biogenic hydrocarbons, *J. Atmos. Chem.*, 26, 189–222, doi:10.1029/90JD02341, 1997.

Ianni, J. C.: Kintecus, Window v. 2.80, www.kintecus.com, 2002.

Jaoui, M. and Kamens, R. M.: Mass balance of gaseous and particulate products analysis from alpha-pinene/ NO_x /air in the presence of natural sunlight, *J. Geophys. Res.-Atmos.*, 106, 12541–12558, doi:10.1029/2001JD900005, 2001.

Jorand, F., Heiss, A., Perrin, O., Sahetchian, K., Kerhoas, L., and Einhorn, J.: Isomeric hexyl-ketohydroperoxides formed by reactions of hexoxy and hexylperoxy radicals in oxygen, *Int. J. Chem. Kinet.*, 35, 354–366, doi:10.1002/kin.10136, 2003.

Kavouras, I. G., Mihalopoulos, N., and Stephanou, E. G.: Formation of atmospheric particles from organic acids produced by forests, *Nature (London)*, 395, 683–686, 1998.

Kavouras, I. G., Mihalopoulos, N., and Stephanou, E. G.: Formation and gas/particle partitioning of monoterpenes photo-oxidation products over forests, *Geophys. Res. Lett.*, 26, 55–58, doi:10.1029/1998GL900251, 1999.

Keywood, M. D., Varutbangkul, V., Bahreini, R., Flagan, R. C., and Seinfeld, J. H.: Secondary organic aerosol formation from the ozonolysis of cycloalkenes and related compounds, *Environ. Sci. Technol.*, 38, 4157–4164, 2004.

Kwok, E. S. C. and Atkinson, R.: Estimation of hydroxyl radical reaction rate constants for gas-phase organic compounds using a structure-reactivity relationship: an update, *Atmos. Environ.*, 29, 1685–1695, 1995.

Laaksonen, A., Kulmala, M., O'Dowd, C. D., Joutsensaari, J., Vaattovaara, P., Mikkonen, S., Lehtinen, K. E. J., Sogacheva, L., Dal Maso, M., Aalto, P., Petäjä, T., Sogachev, A., Yoon, Y. J., Lihavainen, H., Nilsson, D., Facchini, M. C., Cavalli, F., Fuzzi, S., Hoffmann, T., Arnold, F., Hanke, M., Sellegrí, K., Umann, B., Junkermann, W., Coe, H., Allan, J. D., Alfarra, M. R., Worsnop, D. R., Riekkola, M.-L., Hytöläinen, T., and Viisanen, Y.: The role of VOC oxidation products in continental new particle formation, *Atmos. Chem. Phys.*, 8, 2657–2665, doi:10.5194/acp-8-2657-2008, 2008.

Larsen, B. R., Di Bella, D., Glasius, M., Winterhalter, R., Jensen, N. R., and Hjorth, J.: Gas-phase OH oxidation of monoterpenes: Gaseous and particulate products, *J. Atmos. Chem.*, 38, 231–276, 2001.

Lee, A., Goldstein, A. H., Kroll, J. H., Ng, N. L., Varutbangkul, V., Flagan, R. C., and Seinfeld, J. H.: Gas-phase products and secondary aerosol yields from the photooxidation of 16 different terpenes, *J. Geophys. Res.-Atmos.*, 111, D17305, doi:10.1029/2006JD007050, 2006.

Lelieveld, J., Butler, T. M., Crowley, J. N., Dillon, T. J., Fischer, H., Ganzeveld, L., Harder, H., Lawrence, M. G., Martinez, M., Taraborrelli, D., and Williams, J.: Atmospheric oxidation capacity sustained by a tropical forest, *Nature*, 452, 737–740, 2008.

Librando, V. and Tringali, G.: Atmospheric fate of OH initiated oxidation of terpenes. Reaction mechanism of alpha-pinene degradation and secondary organic aerosol formation, *J. Environ. Manage.*, 75, 275–282, 2005.

Monks, P. S., Granier, C., Fuzzi, S., Stohl, A., Williams, M. L., Akimoto, H., Amann, M., Baklanov, A., Baltensperger, U., Bey, I., Blake, N., Blake, R. S., Carslaw, K., Cooper, O. R., Dentener, F., Fowler, D., Frakou, E., Frost, G. J., Generoso, S., Ginoux, P., Grewe, V., Guenther, A., Hansson, H. C., Henne, S., Hjorth, J., Hofzumahaus, A., Huntrieser, H., Isaksen, I. S. A., Jenkin, M. E., Kaiser, J., Kanakidou, M., Klimont, Z., Kulmala, M., Laj, P., Lawrence, M. G., Lee, J. D., Lioussse, C., Maione, M., McFig-gans, G., Metzger, A., Mieville, A., Moussiopoulos, N., Orlando, J. J., O'Dowd, C. D., Palmer, P. I., Parrish, D. D., Petzold, A., Platt, U., Pöschl, U., Prevot, A. S. H., Reeves, C. E., Reimann, S., Rudich, Y., Sellegrí, K., Steinbrecher, R., Simpson, D., ten Brink, H., Theloke, J., van der Werf, G. R., Vautard, R., Vestreng, V., Vlachokostas, C., and von Glasow, R.: Atmospheric composition change – global and regional air quality, *Atmos. Environ.*, 43, 5268–5350, 2009.

Müller, L., Reinnig, M.-C., Naumann, K. H., Saathoff, H., Mentel, T. F., Donahue, N. M., and Hoffmann, T.: Formation of 3-methyl-1,2,3-butanetricarboxylic acid via gas phase oxidation of pinonic acid – a mass spectrometric study of SOA aging, *Atmos. Chem. Phys.*, 12, 1483–1496, doi:10.5194/acp-12-1483-2012, 2012.

Nguyen, T. L., Vereecken, L., and Peeters, J.: HO_x Regeneration in the Oxidation of Isoprene III: Theoretical Study of the key Isomerisation of the Z-delta-hydroperoxy-isoprene Radicals, *Chem. Phys. Chem.*, 11, 3996–4001, doi:10.1002/cphc.201000480, 2010.

Niki, H., Maker, P. D., Savage, C. M., and Breitenbach, L. P.: A Fourier transform infrared study of the kinetics and mechanism for the reaction hydroxyl + methyl hydroperoxide, *J. Phys. Chem.*, 87, 2190–2193, 1983.

Noell, A. C., Alconcel, L. S., Robichaud, D. J., Okumura, M., and Sander, S. P.: Near-Infrared kinetic spectroscopy of the HO₂ and C₂H₅O₂ self-reactions and cross reactions, *J. Phys. Chem. A*, 114, 6983–6995, 2010.

Noziere, B., Barnes, I., and Becker, K.-H.: Product study and mechanisms of the reactions of alpha-pinene and of pinonaldehyde with OH radicals, *J. Geophys. Res.-Atmos.*, 104, 23645–23656, doi:10.1029/1999JD900778, 1999.

Paulot, F., Crounse, J. D., Kjaergaard, H. G., Kroll, J. H., Seinfeld, J. H., and Wennberg, P. O.: Isoprene photooxidation: new insights into the production of acids and organic nitrates, *Atmos. Chem. Phys.*, 9, 1479–1501, doi:10.5194/acp-9-1479-2009, 2009a.

Paulot, F., Crounse, J. D., Kjaergaard, H. G., Kurten, A., St. Clair, J. M., Seinfeld, J. H., and Wennberg, P. O.: Unexpected epoxide formation in the gas-phase photooxidation of isoprene, *Science*, 325, 730–733, 2009b.

Peeters, J. and Muller, J. F.: HO_x radical regeneration in isoprene oxidation via peroxy radical isomerisations. II: experimental evidence and global impact, *Phys. Chem. Chem. Phys.*, 12, 14227–14235, doi:10.1039/C0CP00811G, 2010.

Peeters, J., Nguyen, T. L., and Vereecken, L.: HO_x radical regeneration in the oxidation of isoprene, *Phys. Chem. Chem. Phys.*, 11, 5935–5939, 2009.

Perrin, O., Heiss, A., Doumenc, F., and Sahetchian, K.: Homogeneous and heterogeneous reactions of the n-C₅H₁₁O, n-C₅H₁₀OH and OOC₅H₁₀OH radicals in oxygen. Analytical-steady state solution by use of the Laplace transform, *J. Chem. Soc. Faraday Trans. 2*, 94, 2323–2335, doi:10.1039/a803340d, 1998.

Pye, H. O. T., Chan, A. W. H., Barkley, M. P., and Seinfeld, J. H.: Global modeling of organic aerosol: the importance of reactive nitrogen (NO_x and NO₃), *Atmos. Chem. Phys.*, 10, 11261–11276, doi:10.5194/acp-10-11261-2010, 2010.

Raventos-Duran, M. T., Percival, C. J., McGillen, M. R., Hamer, P. D., and Shallcross, D. E.: Kinetics and branching ratio studies of the reaction of C₂H₅O₂ + HO₂ using chemical ionization mass spectrometry, *Phys. Chem. Chem. Phys.*, 9, 4338–4348, doi:10.1039/B703038J, 2007.

Ren, X., Olson, J. R., Crawford, J. H., Brune, W. H., Mao, J., Long, R. B., Chen, Z., Chen, G., Avery, M. A., Sachse, G. W., Barrick, J. D., Diskin, G. S., Huey, L. G., Fried, A., Cohen, R. C., Heikes, B., Wennberg, P. O., Singh, H. B., Blake, D. R., and Shetter, R. E.: HO_x chemistry during INTEX-A 2004: observation, model calculation, and comparison with previous studies, *J. Geophys. Res.-Atmos.*, 113, D05310, doi:10.1029/2007JD009166, 2008.

Sander, S. P., Finlayson-Pitts, B. J., Friedl, R. R., Golden, D. M., Huie, R. E., Kolb, C. E., Kurylo, M. J., Molina, M. J., Moortgat, G. K., Orkin, V. L., and Ravishankara, A. R.: Chemical kinetics and photochemical data for use in atmospheric studies, evaluation number 15, Tech. rep., Jet Propulsion Laboratory, 2006.

Saunders, S. M., Jenkin, M. E., Derwent, R. G., and Pilling, M. J.: Protocol for the development of the Master Chemical Mechanism, MCM v3 (Part A): tropospheric degradation of non-aromatic volatile organic compounds, *Atmos. Chem. Phys.*, 3, 161–180, doi:10.5194/acp-3-161-2003, 2003.

St. Clair, J. M., McCabe, D. C., Crounse, J. D., Steiner, U., and Wennberg, P. O.: Chemical ionization tandem mass spectrometer for the in situ measurement of methyl hydrogen peroxide, *Rev. Sci. Instrum.*, 81, 094102, doi:10.1063/1.3480552, 2010.

Steinbrecher, R., Smiatek, G., Koebel, R., Seufert, G., Theloke, J., Hauff, K., Ciccioli, P., Vautard, R., and Curci, G.: Intra- and inter-annual variability of VOC emissions from natural and semi-natural vegetation in Europe and neighbouring countries, *Atmos. Environ.*, 43, 1380–1391, 2009.

Szmiigelski, R., Surratt, J. D., Gomez-Gonzalez, Y., Van der Veken, P., Kourtchev, I., Vermeylen, R., Blockhuys, F., Jaoui, M., Kleindienst, T. E., Lewandowski, M., Offenberg, J. H., Edney, E. O., Seinfeld, J. H., Maenhaut, W., and Claeys, M.: 3-methyl-1,2,3-butanetricarboxylic acid: an atmospheric tracer for terpene secondary organic aerosol, *Geophys. Res. Lett.*, 34, L24811, doi:10.1029/2007GL031338, 2007.

Taylor, W. D., Allston, T. D., Moscato, M. J., Fazekas, G. B., Kozlowski, R., and Takacs, G. A.: Atmospheric photo-dissociation lifetimes for nitromethane, methyl nitrite, and methyl nitrate, *Int. J. Chem. Kinet.*, 12, 231–240, doi:10.1002/kin.550120404, 1980.

Vaghjiani, G. L. and Ravishankara, A. R.: Kinetics and mechanism of OH reaction with CH₃OOH, *J. Phys. Chem.*, 93, 1948–1959, 1989.

Vereecken, L. and Peeters, J.: Enhanced H-atom abstraction from pinonaldehyde, pinonic acid, pinic acid, and related compounds: theoretical study of C-H bond strengths, *Phys. Chem. Chem. Phys.*, 4, 467–472, doi:10.1039/B109370C, 2002.

Vereecken, L., Muller, J. F., and Peeters, J.: Low-volatility poly-oxygenates in the OH-initiated atmospheric oxidation of alpha-pinene: impact of non-traditional peroxy radical chemistry, *Phys. Chem. Chem. Phys.*, 9, 5241–5248, doi:10.1039/B708023A, 2007.

Wang, C. and Chen, Z.: An experimental study for rate constants of the gas phase reactions of CH₃CH₂OOH with OH radicals, O₃, NO₂ and NO, *Atmos. Environ.*, 42, 6614–6619, 2008.

Wisthaler, A., Jensen, N. R., Winterhalter, R., Lindinger, W., and Hjorth, J.: Measurements of acetone and other gas phase product yields from the OH-initiated oxidation of terpenes by proton-transfer-reaction mass spectrometry (PTR-MS), *Atmos. Environ.*, 35, 6181–6191, 2001.

Wolfe, G. M., Thornton, J. A., Bouvier-Brown, N. C., Goldstein, A. H., Park, J.-H., McKay, M., Matross, D. M., Mao, J., Brune, W. H., LaFranchi, B. W., Browne, E. C., Min, K.-E., Wooldridge, P. J., Cohen, R. C., Crounse, J. D., Faloona, I. C., Gilman, J. B., Kuster, W. C., de Gouw, J. A., Huisman, A., and Keutsch, F. N.: The Chemistry of Atmosphere-Forest Exchange (CAFE) Model – Part 2: Application to BEARPEX-2007 observations, *Atmos. Chem. Phys.*, 11, 1269–1294, doi:10.5194/acp-11-1269-2011, 2011.

Yu, J., Griffin, R. J., Cocker, David R., I., Flagan, R. C., Seinfeld, J. H., and Blanchard, P.: Observation of gaseous and particulate products of monoterpene oxidation in forest atmospheres, *Geophys. Res. Lett.*, 26, 1145–1148, doi:10.1029/1999GL900169, 1999.

Zhang, Y. Y., Müller, L., Winterhalter, R., Moortgat, G. K., Hoffmann, T., and Pöschl, U.: Seasonal cycle and temperature dependence of pinene oxidation products, dicarboxylic acids and nitrophenols in fine and coarse air particulate matter, *Atmos. Chem. Phys.*, 10, 7859–7873, doi:10.5194/acp-10-7859-2010, 2010.

Appendix C

α -Pinene photooxidation under controlled chemical conditions - Part 2: SOA yield and composition in low- and high- NO_x environments¹

¹This chapter is reproduced by permission from “ α -Pinene photooxidation under controlled chemical conditions-part 2: SOA yield and composition in low- and high- NO_x environments,” by N. C. Eddingsaas, C. L. Loza, L. D. Yee, M. Chan, K. A. Schilling, P. S. Chhabra, J. H. Seinfeld, and P. O. Wennberg, *Atmospheric Chemistry and Physics*, 12, 7413–7427, doi:10.5194/acp-12-7413-2012, 2012. Copyright 2012 Authors. This work is licensed under a Creative Commons License.



α -pinene photooxidation under controlled chemical conditions – Part 2: SOA yield and composition in low- and high- NO_x environments

**N. C. Eddingsaas¹, C. L. Loza¹, L. D. Yee², M. Chan², K. A. Schilling¹, P. S. Chhabra^{1,*}, J. H. Seinfeld^{1,2}, and
P. O. Wennberg^{2,3}**

¹Division of Chemistry and Chemical Engineering, California Institute of Technology, Pasadena, CA, USA

²Division of Engineering and Applied Science, California Institute of Technology, Pasadena, CA, USA

³Division of Geological and Planetary Sciences, California Institute of Technology, Pasadena, CA, USA

* now at: Aerodyne Research Inc, Billerica, MA, USA

Correspondence to: N. C. Eddingsaas (eddingsa@caltech.edu)

Received: 2 March 2012 – Published in Atmos. Chem. Phys. Discuss.: 4 April 2012

Revised: 26 July 2012 – Accepted: 30 July 2012 – Published: 16 August 2012

Abstract. The gas-phase oxidation of α -pinene produces a large amount of secondary organic aerosol (SOA) in the atmosphere. A number of carboxylic acids, organosulfates and nitrooxy organosulfates associated with α -pinene have been found in field samples and some are used as tracers of α -pinene oxidation. α -pinene reacts readily with OH and O_3 in the atmosphere followed by reactions with both HO_2 and NO. Due to the large number of potential reaction pathways, it can be difficult to determine what conditions lead to SOA. To better understand the SOA yield and chemical composition from low- and high- NO_x OH oxidation of α -pinene, studies were conducted in the Caltech atmospheric chamber under controlled chemical conditions. Experiments used low O_3 concentrations to ensure that OH was the main oxidant and low α -pinene concentrations such that the peroxy radical (RO_2) reacted primarily with either HO_2 under low- NO_x conditions or NO under high- NO_x conditions. SOA yield was suppressed under conditions of high- NO_x . SOA yield under high- NO_x conditions was greater when ammonium sulfate/sulfuric acid seed particles (highly acidic) were present prior to the onset of growth than when ammonium sulfate seed particles (mildly acidic) were present; this dependence was not observed under low- NO_x conditions. When aerosol seed particles were introduced after OH oxidation, allowing for later generation species to be exposed to fresh inorganic seed particles, a number of low- NO_x products partitioned to the highly acidic aerosol. This indicates that the effect of

seed acidity and SOA yield might be under-estimated in traditional experiments where aerosol seed particles are introduced prior to oxidation. We also identify the presence of a number of carboxylic acids that are used as tracer compounds of α -pinene oxidation in the field as well as the formation of organosulfates and nitrooxy organosulfates. A number of the carboxylic acids were observed under all conditions, however, pinic and pinonic acid were only observed under low- NO_x conditions. Evidence is provided for particle-phase sulfate esterification of multi-functional alcohols.

1 Introduction

Biogenically emitted monoterpenes are important to atmospheric organic aerosol concentration and composition due to their large emission rates and high secondary organic aerosol (SOA) yields (Guenther et al., 1995; Hoffmann et al., 1997; Chung and Seinfeld, 2002; Pye et al., 2010). Of the monoterpenes, α -pinene is the most abundantly emitted. Many carboxylic acids, organonitrates, and organosulfates associated with α -pinene have been observed in aerosols both in the field and from laboratory oxidation (Kavouras et al., 1998, 1999; Yu et al., 1999b; Jaoui and Kamens, 2001; Larsen et al., 2001; Librando and Tringali, 2005; Surratt et al., 2007, 2008; Laaksonen et al., 2008; Zhang et al., 2010). A number of carboxylic acids have been used as particle-phase

tracers of α -pinene oxidation, including pinonic acid, pinic acid, 10-hydroxypinonic acid, terpenylic acid, diaterpenylic acid acetate, and 3-methyl-1,2,3-butanetricarboxylic acid (3-MBTCA). For instance, pinonic and pinic acid have been observed to be in high concentration in aerosols collected in Portugal (accounting for 18–40 % of fine particle mass), in Greece (up to 26 % of fine particle mass), as well as in high yield in Finland (Kavouras et al., 1998, 1999; Anttila et al., 2005).

In the troposphere, α -pinene is oxidized approximately equally by OH and O_3 during the daytime (Capouet et al., 2008). During the nighttime, NO_3 is the most important oxidant of α -pinene worldwide and oxidation by NO_3 can be important during the daytime under conditions of elevated NO_x (Spittler et al., 2006). After reaction with the oxidant, the peroxy radicals that are formed can react with a number of species, including HO_2 , NO, NO_2 and other peroxy radicals (RO_2). Depending on the nature of the reactant with the peroxy radical, different oxidation products are produced in the gas phase. This was demonstrated in Part 1 of this series of papers (Eddingsaas et al., 2012). It was determined that pinonaldehyde is an important oxidation product under both low- and high- NO_x conditions. The formation of pinonaldehyde from low- NO_x OH oxidation implies that the reaction of α -pinene hydroxy hydroperoxy radical and HO_2 has a channel that produces an alkoxy radical and recycles OH. This type of reaction channel has been shown to be important only for acyl peroxy radicals and possibly toluene. In addition, it was demonstrated that number of organic acids formed from low- NO_x OH oxidation, including pinonic acid and pinonic peracid, are not formed from high- NO_x OH oxidation. From a modeling standpoint, it is of interest to understand how the different gas-phase reaction mechanisms influence the particle-phase composition and concentration. This understanding will improve the ability to accurately simulate the amount of aerosol produced in the oxidation of α -pinene.

In this study, we describe the SOA yield and particle phase composition from the photooxidation of α -pinene under conditions where the peroxy radical chemistry is known. We focus on OH photooxidation because particle-phase composition from ozonolysis of α -pinene has been extensively studied (Glasius et al., 1999; Yu et al., 1999a; Inuma et al., 2005; Presto et al., 2005; Ma et al., 2008; Shilling et al., 2009). The SOA composition from OH photooxidation has been much less studied and there are almost no studies examining low- NO_x conditions (Noziere et al., 1999; Ng et al., 2007a; Claeys et al., 2009). We discuss SOA composition focusing on several carboxylic acids which have been used as tracers of α -pinene oxidation. The formation of organosulfates and nitrooxy organosulfates formed from α -pinene photooxidation is also addressed. We compare SOA and gas-phase composition based on different peroxy radical reactants as well as different aerosol seed (i.e. no seed, ammonium sulfate (AS) seed, and ammonium sulfate and sulfuric acid (AS + SA) seed).

2 Experimental

Photooxidation experiments of α -pinene and pinonaldehyde were performed in the Caltech dual 28 m³ Teflon chambers. Details of the chamber facilities have been described elsewhere (Cocker et al., 2001; Keywood et al., 2004). Prior to each run, the chamber was flushed for a minimum of 24 h with dry purified air. While being flushed, the chamber was irradiated with the chamber lights for a minimum of six hours. The temperature, relative humidity, and concentrations of O_3 , NO, and NO_x (NO and NO_2) were continuously monitored. In all experiments the RH was kept below 10 %. Aerosol size distribution and number concentration were measured continuously by a differential mobility analyzer (DMA, TSI model 3081) coupled to a condensation nucleus counter (TSI model 3760). Aerosol growth data were corrected for size dependent wall-loss (Keywood et al., 2004; Ng et al., 2007b).

Experiments were performed under low- and high- NO_x conditions. Under low- NO_x conditions, photolysis of hydrogen peroxide (H_2O_2) was the OH source, while for the high- NO_x experiments the photolysis of nitrous acid (HONO) or methyl nitrite (CH_3ONO) produced OH. For low- NO_x experiments, 280 μ l of 50 wt % H_2O_2 was injected into the chamber, resulting in a concentration \sim 4 ppm. Using HONO and CH_3ONO allowed the ratio of NO to NO_2 to be varied, with a lower ratio in the CH_3ONO experiments. For the remainder of this paper, the use of HONO as the OH source will be referred to as high-NO and the use of methyl nitrite will be referred to as high- NO_2 to distinguish between the relative importance of NO and NO_2 .

HONO was prepared daily by dropwise addition of 15 ml of 1 wt % $NaNO_2$ into 30 ml of 10 wt % H_2SO_4 in a glass bulb, and then introduced into the chamber with dry air. This process produces NO and NO_2 as side products, which are also introduced to the chamber. CH_3ONO was synthesized, purified, and stored according to the procedure outlined by Taylor et al. (1980). CH_3ONO was warmed from liquid nitrogen temperatures and vaporized into an evacuated 500 ml glass bulb and introduced into the chamber with an air stream of 51 min⁻¹. After addition of CH_3ONO , 300–400 ppb of NO was added to the chamber to suppress the formation of O_3 . Determination of exact NO and NO_2 concentrations using the commercial NO_x monitor was precluded due to interferences by both HONO and CH_3ONO . While the exact NO and NO_2 concentration could not be determined, it was confirmed that greater NO_2 concentration and the ratio of NO_2 to NO is greater in the methyl nitrite experiments due to the increased gas-phase concentration of nitric acid and peroxyacetyl nitrates (PANs). The gas-phase concentration of nitric acid and PANs in the methyl nitrite experiments was 1.4–2 times that in similar HONO experiments. At the start of all high- NO_x experiments the total NO_x reading (NO, NO_x , and interference from HONO or CH_3ONO) was 800 ppb and NO

concentration throughout the experiments was such that the concentration of O_3 never exceeded 5 ppb.

Experiments were performed with either no aerosol seed present, ammonium sulfate seed (AS), or ammonium sulfate plus sulfuric acid (AS + SA). The AS + SA produced a much more acidic aerosol seed. When applicable, seed particles were added to the chamber after the addition of the oxidant. Aerosol seed particles were generated by atomizing an aqueous solution of 15 mM $(NH_4)_2SO_4$ (AS) or 15 mM $(NH_4)_2SO_4$ and 15 mM H_2SO_4 (AS + SA). Upon addition of an aerosol seed, the initial aerosol number concentration was $\sim 1.8 \times 10^4 \text{ cm}^{-3}$, with a mean diameter of $\sim 60 \text{ nm}$, resulting in the initial aerosol volume of $10\text{--}15 \mu\text{m}^3 \text{ cm}^{-3}$.

Once the aerosol seed was added and stable, α -pinene was added to the chamber by transferring a known amount of α -pinene from a small glass bulb to achieve a concentration of 20–50 ppb. The mixing ratio of α -pinene was monitored with a gas chromatograph (Agilent 6890N) coupled with a flame ionization detector (GC-FID). The GC-FID was calibrated for α -pinene using a standard prepared in a 551 Teflon bag. In photooxidation experiments where pinonaldehyde was the initial hydrocarbon, pinonaldehyde was introduced into the chamber by passing dry nitrogen over a liquid sample.

Gas-phase photooxidation products were monitored by a custom-modified Varian 1200 triple-quadrupole chemical ionization mass spectrometer (CIMS) (St. Clair et al., 2010). Details of the operation of the CIMS can be found in a number of previous reports (Crounse et al., 2006; Paulot et al., 2009a; St. Clair et al., 2010). The CIMS was operated in negative ion mode using CF_3O^- as the reagent ion, and in the positive ion mode using H_3O^+ for proton transfer mass spectrometry (PTR-MS). In negative mode, CF_3O^- is sensitive to polar and acidic compounds by either clustering with the analyte (R) resulting in an ion with a mass-to-charge ratio (m/z) $MW + 85 (R \cdot CF_3O^-)$ or via fluorine ion transfer resulting in $m/z MW + 19 (HF \cdot R_{-H}^-)$. The dominant ionization mechanism depends mostly on the acidity of the neutral species; highly acidic species such as nitric acid form only the fluorine transfer ion, while non-acidic species such as methyl hydrogen peroxide form only the cluster ion. This separation aids both in the determination of the structure of a molecule and in the identification of isomers. In negative mode, tandem mass spectrometry (MS/MS) was used to help identify functional groups of an analyte. In brief, a parent ion selected in the first quadrupole is exposed to an elevated pressure of N_2 resulting in collision-induced dissociation (CID) in the second quadrupole, and the resulting fragmentation ions are detected in the third quadrupole. Molecules with different functional groups have been shown to fragment differently by CID. For example, fragmentation of hydroperoxides form a characteristic anion at $m/z 63$ (Paulot et al., 2009b). Unfortunately, authentic standards for most compounds described here are not readily available, and thus the sensitivity of the CIMS cannot be experimentally determined. In the absence of such standards, we estimate that the sensitivity scales with

the thermal capture rate and the binding energy of the cluster ($VOC \cdot CF_3O^-$). Details on calculating the sensitivity of the CIMS to a given analyte can be found in previous publications (Paulot et al., 2009a,b).

Duplicate Teflon filters (PALL Life Sciences, 47 mm diameter, 1.0 μm pore size, Teflon membrane) were collected from each of the chamber experiments for off-line chemical analysis. Filter sampling was started when the aerosol volume reached a constant value. For the chemical analysis, each filter was extracted with methanol (LC-MS CHROMASOLV-grade, Sigma-Aldrich) under ultrasonication for 45 min. The extract was dried under ultrapure nitrogen gas, and the residue was reconstituted with a 50 : 50 (v/v) solvent mixture of methanol with 0.1 % acetic acid (LC-MS CHROMASOLV-grade, Sigma-Aldrich) and water with 0.1 % acetic acid (LC-MS CHROMASOLV-grade, Sigma-Aldrich). Filter sample extracts were analyzed by ultra-performance liquid chromatography/electrospray ionization-time-of-flight mass spectrometry (UPLC/ESI-TOFMS) operated in negative ion mode. Further details of the filter collection, sample preparation procedures, and UPLC/ESI-TOFMS analysis can be found in a previous publications (Surratt et al., 2008; Chan et al., 2010).

Products having either a carboxylic acid group or that are organosulfates can be ionized via deprotonation and are detected in the negative ion mode as $[M - H]^-$ ions. All accurate mass measurements were within $\pm 5 \text{ mDa}$ of the theoretical mass associated with the proposed chemical formula. From repeated UPLC/ESI-TOFMS measurements, the variations in the chromatographic peak areas are about 5 % (Chan et al., 2011). The concentrations are not corrected for extraction efficiencies.

High-resolution time-of-flight aerosol mass spectrometry (HR-ToF-AMS) spectra were obtained for one low- NO_x experiment with AS seed and one high- NO_x experiment with AS seed. The analysis of the data has previously been reported (Chhabra et al., 2011). Both high-resolution W-mode and higher sensitivity V-mode were taken, switching between the two modes every minute. The V-mode data were analyzed using a fragmentation table that enables separation of sulfate, ammonium, and organic components and to time-trace specific mass-to-charge ratios (m/z) (Allan et al., 2004). W-mode data were analyzed using the high-resolution spectra toolbox, PIKA, to determine the chemical formulas contributing to distinct m/z (DeCarlo et al., 2006).

3 Results and discussion

In Part 1 (Eddingsaas et al., 2012), the gas-phase composition of OH photooxidation of α -pinene under low- NO_x , high-NO ($HONO$ as the OH source), and high- NO_2 (methyl nitrite as the OH source) conditions was discussed. Under low- NO_x conditions, care was taken to ensure that reaction with HO_2 dominated the loss of the peroxy radicals. O_3 was suppressed

in all experiments so that the oxidation of α -pinene was completely dominated by OH oxidation. Here, the results of the aerosol phase growth, yield, and composition from these controlled experiments are discussed.

3.1 Aerosol growth and yield

Table 1 lists the experimental conditions of the studies, the SOA yields, and a number of other variables of interest. The SOA density used to calculate SOA mass and SOA yield were taken from previous results: 1.32 g cm^{-3} under low- NO_x conditions and 1.33 g cm^{-3} under high- NO_x conditions (Ng et al., 2007a). SOA yield is calculated cumulatively throughout the experiments as the ratio of SOA mass to the mass of α -pinene reacted. For this suite of experiments, we cannot directly relate the time-dependent aerosol growth curves (i.e. SOA mass as a function of experiment time) to yield because the OH concentration varied widely between the systems. For example, the initial OH concentration for the low- NO_x experiments was $\sim 2 \times 10^6 \text{ molecules cm}^{-3}$, while in the high-NO experiments the initial OH was approximately 3 times larger, and under high- NO_2 conditions the initial OH was an order of magnitude larger, thereby resulting in much faster oxidation of α -pinene and faster aerosol growth. In addition, under both high-NO and high- NO_2 conditions, the OH concentration declined significantly over time. The OH concentration through the experiments was determined by comparing the loss of α -pinene to a kinetic model of α -pinene OH oxidation under low- or high- NO_x conditions. Details of the model and gas phase measurements can be found in Part 1 (Eddingsaas et al., 2012). By using OH exposure (as units of OH concentration multiplied by reaction time in hours) as the coordinate system, a more direct comparison between different photooxidation systems is, however, possible.

Figure 1 shows SOA yield as a function of OH exposure from all experiments in the presence of AS seed particles. The overall yield was consistent between runs with the same OH source, but there is a systematic difference in SOA yield between the systems, decreasing as the concentration of NO increases. SOA growth under high- NO_2 conditions resembles low- NO_x SOA growth more than it does high-NO SOA growth, consistent with the hypothesis that reaction of the peroxy radicals with NO leads to reduced yields. Second, the SOA yield from high- NO_2 continued to increase after two α -pinene lifetimes. This is in contrast to the high-NO experiments where most of the aerosol growth is complete after one α -pinene lifetime. The SOA from low- NO_x photooxidation also continued to increase after two α -pinene lifetimes. This indicates that later generation oxidation products are important in determining the amount of SOA formed. As discussed in the gas-phase analysis (Eddingsaas et al., 2012), a distinct difference in the later generation oxidation products is the formation of carboxylic acids and peracids in the low- NO_x

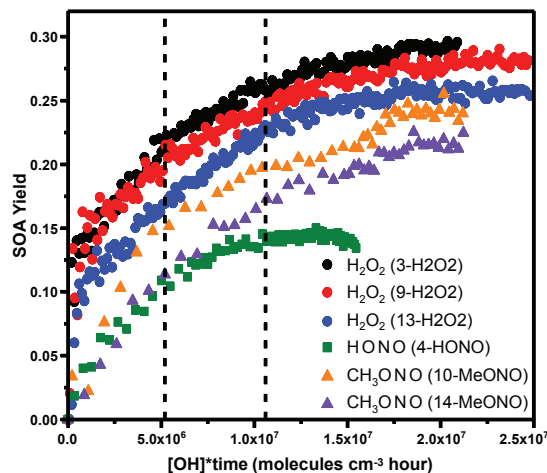


Fig. 1. SOA yield as a function of OH exposure of α -pinene from low- NO_x , high-NO, and high- NO_2 OH oxidation in the presence of ammonium sulfate seed particles. The vertical dashed lines represent one and two α -pinene lifetimes with respect to reaction with OH. The OH source and sample ID for each experiment is shown in the figure.

photooxidation. In the high- NO_2 cases, more PANs and nitric acid are formed compared to high-NO.

Illustrating that later generation oxidation products are important to SOA growth, the gas-phase time traces of first- and second-generation oxidation products are shown along with the SOA growth under all three conditions in the presence of ammonium sulfate seed in Fig. 2. Under all conditions, aerosol growth continues through the production of second-generation oxidation products. Under low- NO_x conditions, the signal for pinonaldehyde peracid and/or 10-hydroxy pinonic acid is lost from the gas phase faster than pinonic acid. This is likely due to greater partitioning into the aerosol phase as a result of its lower vapor pressure. In the presence of high- NO_2 , pinonaldehyde PAN is observed to be lost from the gas phase faster than SOA growth as a result of thermal decomposition. Pinonaldehyde nitrate is lost at a faster rate when methyl nitrite is the OH source. This could be due to either higher OH exposure or aerosol uptake.

The effect of the acidity of the seed particle on SOA yield was investigated. Figure 3 shows the SOA yield as a function of OH exposure with no seed, and in the presence of either AS seed (mildly acidic) or AS + SA seed (highly acidic) in low- NO_x , high-NO, and high- NO_2 OH oxidation. From low- NO_x photooxidation with initial α -pinene concentration of $\sim 50 \text{ ppb}$, there is no difference in the aerosol growth in the presence of no, AS, or AS + SA seed. This was expected as the only difference in the gas-phase composition is that α -pinene oxide is in lower concentration in the presence of an

Table 1. SOA yields from low- and high- NO_x photooxidation of α -pinene.

Sample ID	Oxidant	Seed	Temp. (°C)	HC (ppb)	Initial Vol. ($\mu\text{m}^3 \text{cm}^{-3}$)	ΔHC^a ($\mu\text{g m}^{-3}$)	$\Delta\text{M}_\text{O}^b$ ($\mu\text{g m}^{-3}$)	SOA Yield ^c (%)
1-H2O2	H_2O_2	no seed	20–23	45.0±1.0	0.9±0.3	250±6	66.8±6.0	26.7±2.5
2-HONO	HONO	no seed	20–23	50.1±1.1	0.3±2	260±6	20.0±2.3	7.7±0.9
3-H2O2	H_2O_2	AS	20–25	48.5±1.1	11.0±0.4	265±6	76.6±6.7	28.9±2.6
4-HONO	HONO	AS	20–23	52.4±1.2	12.0±0.7	258±7	37.2±3.0	14.4±1.1
5-H2O2	H_2O_2	AS + SA	20–25	46.9±1.1	9.3±0.58	264±6	72.9±7.0	27.6±2.8
6-HONO	HONO	AS + SA	20–23	45.5±1.0	16.0±1.1	225±6	39.6±4.5	17.6±1.9
7-H2O2	H_2O_2	no seed	20–25	19.8±0.5	0.5±0.2	109±3	40.0±3.1	36.7±3.0
8-MeONO	CH_3ONO	no seed	20–23	38.9±1.0	5.1±0.2	208±6	51.9±3.8	25.4±1.7
9-H2O2	H_2O_2	AS	20–25	46.8±1.1	9.4±0.4	254±6	71.6±6.2	28.2±2.5
10-MeONO	CH_3ONO	AS	20–23	47.9±1.1	10.5±0.5	249±6	60.3±4.9	24.2±1.9
11-H2O2	H_2O_2	AS + SA	20–25	46.8±1.1	8.5±0.4	256±6	70.4±6.2	27.5±2.5
12-MeONO	CH_3ONO	AS + SA	20–23	43.7	14	242	42.6	17.6
13-H2O2	H_2O_2	AS	20–25	45.0±1.0	13.7±0.6	247±6	63.5±5.6	25.7±2.3
14-MeONO	CH_3ONO	AS	20–23	44.9±1	15.4±0.6	250±6	54.0±4.3	21.6±1.8

^a ΔHC : mass concentration of α -pinene reacted.^b ΔM_O : mass concentration of SOA.^c SOA yield is maximum mass concentration of SOA formed by the mass concentration of α -pinene reacted.

acidic seed. α -pinene oxide is a minor product. This indicates that there is almost no reactive uptake occurring due to acid-catalyzed reactions and that if there are any changes in the aerosol composition, they occur within the particle phase. SOA yield was different when the initial α -pinene concentration was reduced to 20 ppb (37 % compared to 26–29 % when the initial concentration was 50 ppb). The cause of the increase in SOA yield with lower α -pinene concentration is not known.

As with low- NO_x photooxidation, there is no difference in aerosol growth under any seed conditions for high- NO_2 photooxidation. However, with high-NO, the yield does depend on seed conditions; yields increase from no seed to AS seed to AS + SA seed (increase of 22 % from AS to AS + SA seed). In the presence of AS+SA seed, the SOA yield was the same under high-NO and high- NO_2 conditions. This small increase with acidity is in contrast to low- NO_x photooxidation of isoprene where the SOA increased markedly (1000 %) (Surratt et al., 2010).

Self-nucleation under high-NO conditions did not occur until nearly one α -pinene lifetime. In contrast, nucleation occurred nearly immediately under both high- NO_2 and low- NO_x conditions. One possible explanation for the difference in behavior is that for the aerosols in the higher NO_2 case, the self-nucleated and AS seeded aerosols are more acidic than in the low- NO_2 case due to increased partitioning of nitric acid and possibly the PANs. This would result in an acidic aerosol under all conditions for the higher NO_2 experiments. When AS + SA seed is used, the particles have the same level of acidity and partitioning should be more similar. Analysis of the particle-phase composition provides more insight into the differences between the systems.

3.2 Aerosol chemical composition

Tables 2 and 3 list the UPLC peak areas for each of the carboxylic acids associated with atmospheric photooxidation of α -pinene under low- NO_x , high-NO, and high- NO_2 conditions, in the presence of either AS or AS + SA seed. Figure 4 shows the structures of the identified SOA components. The peak areas are presented both as the raw peak areas (Table 2) as well as peak areas scaled to the SOA mass loading of the low- NO_x AS seed run (Table 3), so that a weighted average of each component can be compared. Concentration calibrations were not performed and therefore the analysis is qualitative. Figure 5 shows the UPLC chromatograms from the filter samples from low- NO_x OH oxidation in the presence of AS or AS + SA seed particles along with the chromatogram from pinonaldehyde low- NO_x photooxidation, while Fig. 6 shows the UPLC chromatograms from high-NO and high- NO_2 OH oxidation in the presence of AS or AS + SA seed particles. The species of interest – pinonic acid, 10-hydroxy pinonic acid, pinic acid, terpenylic acid, 2-hydroxy terpenylic acid, diaterpenylic acid acetate, 3-MBCTA, the organosulfates and the nitrooxy organosulfates have previously been identified by UPLC/(-)ESI-TOFMS (Warnke et al., 2006; Szmiigelski et al., 2007; Claeys et al., 2009), and it is these identifications that are being used to confirm the presence or absence of each species.

3.2.1 Comparison of SOA composition between low- NO_x , high-NO, and high- NO_2 OH oxidation in the presence of ammonium sulfate seed

Pinonic acid, pinic acid, and 10-hydroxy pinonic acid are only observed in substantial quantities in the aerosol phase

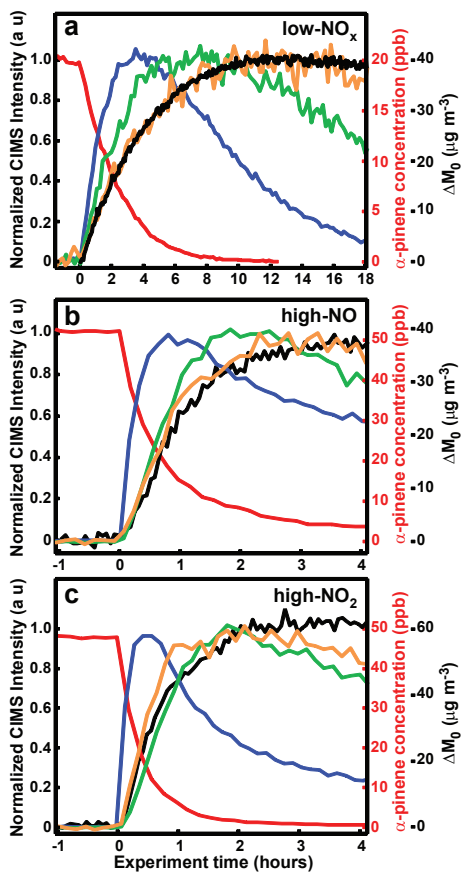


Fig. 2. Time evolution of SOA growth along with gas-phase time profile of first- and second-generation products of OH oxidation of α -pinene under (a) low- NO_x conditions (7-H₂O₂), (b) high-NO conditions (4-HONO), and (c) high- NO_2 conditions (10-MeONO). In all plots, the red line is α -pinene, blue line is pinonaldehyde, and black line is SOA growth. In (a) green is 10-hydroxy pinonic/pinonic peracid and orange is pinonic acid, (b, c) green is pinonaldehyde-PAN, and orange is pinonaldehyde nitrate.

from the low- NO_x photooxidation (Tables 2 and 3 and Fig. 5). This was expected as pinonic and 10-hydroxy pinonic acid were only observed in the gas-phase in the low- NO_x photooxidation (Eddingsaas et al., 2012). These species originate from the oxidation of pinonaldehyde as confirmed by the gas-phase data (Eddingsaas et al., 2012) as well as the UPLC chromatogram of the low- NO_x photooxidation of pinonaldehyde (Fig. 4c). Pinonic acid, pinic acid, and 10-hydroxy pinonic acid are also typical species found in SOA from the ozonolysis of α -pinene (Hoffmann et al., 1997; Ma et al., 2008; Camredon et al., 2010). Thus, it is likely that previous observation of pinonic acid, pinic acid, and 10-hydroxy

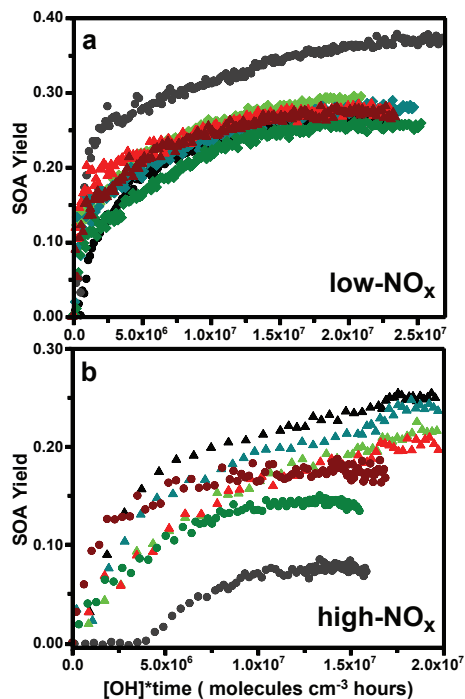


Fig. 3. SOA yield as a function of OH exposure of α -pinene OH oxidation in the presence of no (black, gray), neutral (shades of green), or acidic (shades of red) seed particles under (a) low- NO_x conditions and (b) high- NO_x conditions where photolysis of HONO (dots) or methyl nitrite (triangles) is the OH source. The sample IDs for each experiment are (a) black dots (1-H₂O₂), gray dots (7-H₂O₂), light green diamonds (3-H₂O₂), teal diamonds (9-H₂O₂), green diamonds (13-H₂O₂), red triangles (5-H₂O₂), dark red triangles (11-H₂O₂) (b) gray dots (2-HONO), black triangles (8-MeONO), green dots (4-HONO), light green triangles (10-MeONO), teal triangles (14-MeONO), dark red dots (6-HONO), and red triangles (12-MeONO). The low- NO_x experiment that resulted in greater SOA yield (gray points in panel a (7-H₂O₂)) is from 20 ppb of α -pinene, all other data is from the OH oxidation of \sim 50 ppb of α -pinene.

pinonic acid in studies of α -pinene high- NO_x photooxidation were a result of ozonolysis and not OH chemistry.

3-MBTCA is believed to be a tracer compound of α -pinene derived SOA (Szmigielski et al., 2007; Kourtchev et al., 2009; Zhang et al., 2010) and indeed it was observed here under all conditions (as well as from the low- NO_x photooxidation of pinonaldehyde). It has been proposed that 3-MBTCA is the result of further high- NO_x oxidation of pinonic acid in the gas phase (Szmigielski et al., 2007; Müller et al., 2012). A recent study by Müller et al. (2012) shows evidence of gas-phase formation of 3-MBTCA from the photooxidation of pinonic acid in the presence of NO.

Table 2. Raw peak areas from UPLC chromatograms of carboxylic acids, organosulfates, and nitrooxy organosulfates from the photooxidation of α -pinene.

SOA component ($[M - H]^-$)	H ₂ O ₂		HONO		MeONO	
	AS	AS + SA	AS	AS + SA	AS	AS + SA
2-Hydroxyterpenylic acid (187)	–	–	1918	824	2285	1509
Terpenylic acid (171)	2097	2522	911	933	1152	1255
3-methyl-1,2,3-butanetricarboxylic acid (3-MBTCA) (203)	458	702	307	337	910	1231
Diaterpenylic acid acetate (231)	318	763	1984	401	1658	1728
10-Hydroxypinonic acid (199)	2229	1760	361	426	314	662
Pinic acid (185)	1552	1469	–	–	–	–
Pinonic acid (183)	1155	1297	–	–	–	–
Sulfate of 10-hydroxy pinonic acid (279)	–	723	–	1185	–	1343
α -pinene hydroxy sulfate (249)	–	1692	–	1904	–	933
Ring opened carbonyl nitrate sulfate (310)	–	–	–	1744	–	1075
<i>m/z</i> 247.07 ($C_{10}H_{15}O_5S$)	–	–	–	3193	–	435
<i>m/z</i> 265.07 ($C_{10}H_{17}O_6S$)	–	–	–	219	–	229
<i>m/z</i> 294.06 ($C_{10}H_{16}NO_7S$)	–	–	–	1799	–	–
<i>m/z</i> 295.05 ($C_{10}H_{15}O_8S$)	–	–	–	494	–	–
<i>m/z</i> 296.04 ($C_{10}H_{14}NO_8S$)	–	–	–	108	–	–
<i>m/z</i> 328.07 ($C_{10}H_{18}NO_9S$)	–	–	–	345	–	–
<i>m/z</i> 342.05 ($C_{10}H_{16}NO_10S$)	–	–	–	110	–	–

Table 3. Peak areas scaled to low- NO_x AS seed SOA loading from UPLC chromatograms of carboxylic acids, organosulfates, and nitrooxy organosulfates from the photooxidation of α -pinene.

SOA component ($[M - H]^-$)	H ₂ O ₂		HONO		MeONO	
	AS	AS + SA	AS	AS + SA	AS	AS + SA
2-Hydroxyterpenylic acid (187)	–	–	4480	1426	3167	2617
Terpenylic acid (171)	2097	2451	2128	1615	1597	2177
3-methyl-1,2,3-butanetricarboxylic acid (3-MBTCA) (203)	458	682	717	583	1261	2135
Diaterpenylic acid acetate (231)	318	742	4635	695	2298	2997
10-Hydroxypinonic acid (199)	2229	1711	843	737	435	1148
Pinic acid (185)	1552	1428	–	–	–	–
Pinonic acid (183)	1155	1261	–	–	–	–
Sulfate of 10-hydroxy pinonic acid (279)	–	703	–	2051	–	2329
α -pinene hydroxy sulfate (249)	–	1645	–	3296	–	1618
Ring opened carbonyl nitrate sulfate (310)	–	–	–	3019	–	1865
<i>m/z</i> 247.07 ($C_{10}H_{15}O_5S$)	–	–	–	5527	–	755
<i>m/z</i> 265.07 ($C_{10}H_{17}O_6S$)	–	–	–	379	–	397
<i>m/z</i> 294.06 ($C_{10}H_{16}NO_7S$)	–	–	–	3114	–	–
<i>m/z</i> 295.05 ($C_{10}H_{15}O_8S$)	–	–	–	855	–	–
<i>m/z</i> 296.04 ($C_{10}H_{14}NO_8S$)	–	–	–	187	–	–
<i>m/z</i> 328.07 ($C_{10}H_{18}NO_9S$)	–	–	–	597	–	–
<i>m/z</i> 342.05 ($C_{10}H_{16}NO_10S$)	–	–	–	190	–	–

In the present study, however, 3-MBTCA is observed under high- NO and high- NO_2 conditions when pinonic acid is not observed and, in addition, 3-MBTCA is observed from low- NO_x photooxidation where peroxy radical reactions are dominated by reactions with HO_2 . The ratio of 3-MBTCA to pinic acid in low- NO_x oxidation of α -pinene is substantially greater than from pinonaldehyde photooxidation. This is in contrast to the ratios of pinic acid, pinonic acid, and

10-hydroxypinonic acids which are very similar regardless of which initial hydrocarbon was used under low- NO_x conditions.

Terpenylic acid and diaterpenylic acid were observed in filters from all α -pinene photooxidation mechanisms, while 2-hydroxy terpenylic acid was observed only in the presence of NO_x . Under low- NO_x photooxidation, terpenylic acid is the dominant peak and is observed only as a dimer (*m/z*

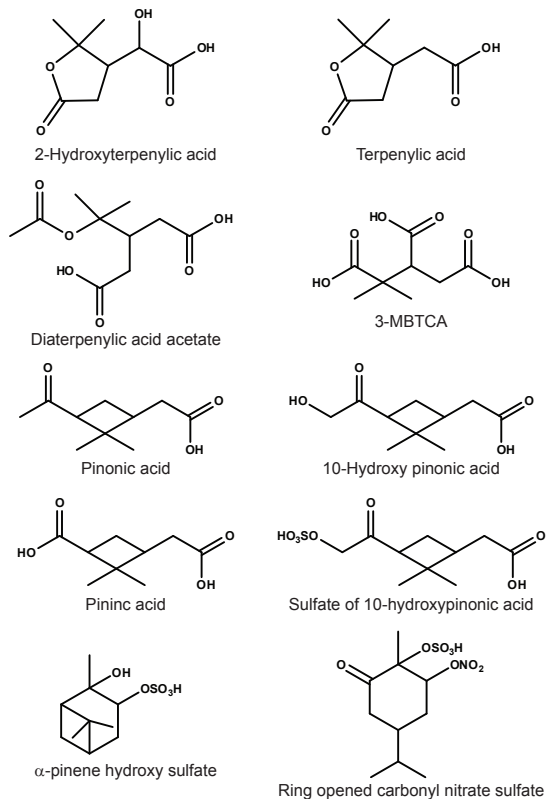


Fig. 4. Structures of identified SOA components detected by UPLC/(-)ESI-TOF.

343), while diaterpenylic acid is a minor peak. In the low- NO_x photooxidation of pinonaldehyde, terpenylic acid was observed, but it is a small contributor to the aerosol mass; diaterpenylic acid was not observed at all. There is a peak in the chromatograms for low- NO_x photooxidation of α -pinene and pinonaldehyde with a molecular ion that corresponds to 2-hydroxy terpenylic acid ($m/z = 187.06$), but it elutes much earlier than found in previous studies (Claeys et al., 2009) or in the high-NO or high- NO_2 studies here. Under high-NO and high- NO_2 photooxidation, diaterpenylic acid acetate is observed to be the dominant peak in the chromatograms. Terpenylic and 10-hydroxy terpenylic acids are also dominant peaks in the chromatograms, with their contribution to the total aerosol greater with higher NO_2 . From this analysis, it appears that terpenylic acid arises from the photooxidation of pinonaldehyde while diaterpenylic acid acetate is from some other channel of α -pinene photooxidation.

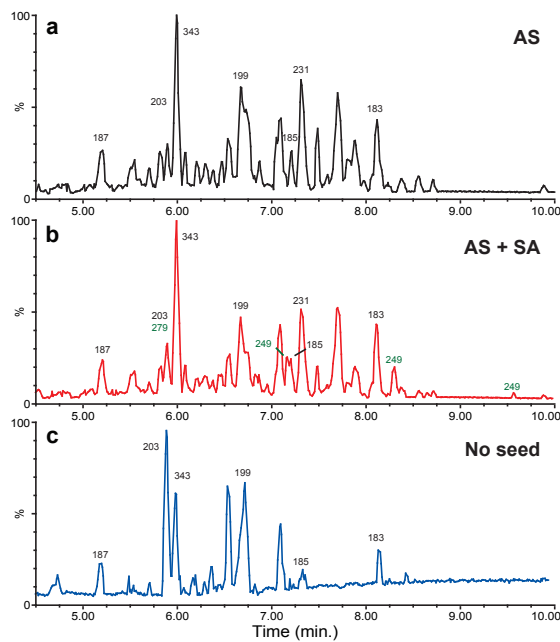


Fig. 5. UPLC/(-)ESI-TOF chromatograms from the filter samples of low- NO_x photooxidation of α -pinene or pinonaldehyde, (a) α -pinene in the presence of AS seed particles (3- H_2O_2) (b) α -pinene in the presence of AS + SA seed particles (5- H_2O_2) and (c) pinonaldehyde. Chromatographic peaks designated with black $[\text{M} - \text{H}]^-$ ions are carboxylic acids and chromatographic peaks designated with green $[\text{M} - \text{H}]^-$ ions are organosulfates. See Table 2 for compound names.

3.2.2 Change in SOA composition in the presence of highly acidic aerosol seed

The composition of the SOA in low- NO_x photooxidation in the presence of AS or AS + SA seed is very similar (see Tables 2 and 3 and Fig. 5). This is consistent with the fact that the SOA yield and mass loading were almost identical between these experiments. In the presence of the acidic seed, four peaks were observed that correspond to organosulfates, one with m/z 279 and three with m/z 249. The organosulfate peak at m/z 279 has been previously identified as the sulfate ester of 10-hydroxy pinonic acid and is thought to originate from the esterification of the hydroxyl group of 10-hydroxy pinonic acid (Surratt et al., 2008). Indeed, the signal for 10-hydroxy pinonic acid decreases in the presence of AS + SA seed (Table 3), while no change in peak area is observed from either pinonic or pinic acid, both of which lack a hydroxyl group. While it has been shown that for simple alcohols, sulfate esterification is too slow to be atmospherically relevant (Minerath et al., 2008), these data indicate that esterification may be sufficiently fast in more complex, acidic alcohols.

The three peaks with m/z 249 are most likely from the reactive uptake of α -pinene oxide, which was observed to be in lower concentration in the gas phase in the presence of an acidic seed. Iinuma et al. (2009) have shown that the uptake of α -pinene oxide results in the formation of three different organosulfates: 2-pinanol-3-hydrogen sulfate, 3-pinanol-2-hydrogen sulfate, and campholenol hydrogen sulfate. The SOA yield is independent of aerosol seed acidity from low- NO_x photooxidation indicating that the gas-phase yield of α -pinene oxide and the resulting organosulfates are minor components.

The SOA composition (and yield) from high-NO photooxidation is substantially different in the presence of AS + SA seed. In the presence of an acidic seed, diaterpenylic acid and 2-hydroxy terpenylic acid were greatly reduced in the aerosol while terpenylic acid was relatively unchanged (see Tables 2 and 3 and Fig. 6). A large number of organosulfates and nitrooxy organosulfates are observed. Both of the organosulfates observed in low- NO_x photooxidation are observed. The source of the m/z 249 is most likely the same, α -pinene oxide. The mechanism for the formation of the sulfate ester of 10-hydroxy pinonic acid is less clear. 10-hydroxy pinonic acid is not observed in the gas phase, is a small fraction of the particle phase mass, and its aerosol concentration is relatively unchanged in the presence of an acidic seed. In addition, 10-hydroxy pinonic acid is more prominent in low- NO_x photooxidation. However, the organosulfate associated with 10-hydroxy pinonic acid is of greater abundance in high-NO and high- NO_2 conditions than in low- NO_x conditions. The sulfate ester of 10-hydroxy pinonic acid coelutes with two other ions and therefore the peak area has greater error. However, even if the peak areas were similar, it would not be consistent with a source from 10-hydroxy pinonic acid under high-NO and high- NO_2 conditions due to the low signal. The peak is observed at the same chromatographic time under all conditions; therefore, either the organosulfates at m/z 279 are formed by different processes depending on NO concentration, or 10-hydroxy pinonic acid is not the source at all. We believe that there must be another mechanism that forms this organosulfate. The nitrooxy organosulfate (m/z = 310) elutes as two peaks in the chromatogram. Under high-NO and high- NO_2 conditions, two species are formed in the gas phase with molecular weight of 231 (CIMS m/z = 316). One of the gas-phase species was assigned to α -pinene dihydroxy nitrate as proposed in previous reports and upon sulfate esterification would produce a nitrooxy organosulfate that would produce the ion of interest (m/z 310) (Aschmann et al., 2002; Surratt et al., 2008). Thus, there is once again evidence for particle-phase sulfate esterification of a hydroxyl group in a poly-functional molecule. The largest sulfate peak was also the dominant peak in the chromatogram corresponding to m/z 247. The identification of the compound is unknown and its overall importance to the SOA yield is not known as no calibrations are available. Tables 2 and 3 list the most likely molecular formula for the ion at m/z 247, along with

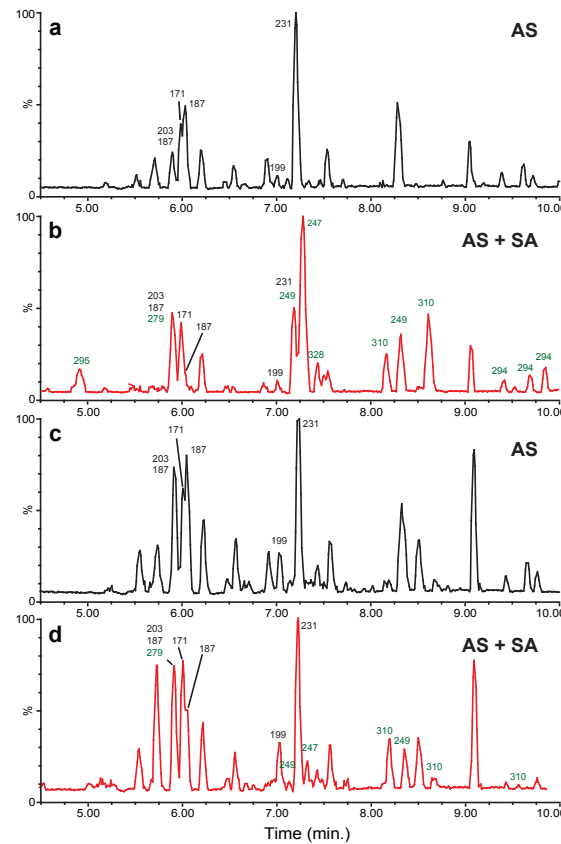


Fig. 6. UPLC/(-)ESI-TOF chromatograms from the filter samples of high- NO_x photooxidation of α -pinene. (a) HONO was the OH source, AS seed particles (4-HONO) (b) HONO was the OH source, AS + SA seed particles (6-HONO), (c) CH_3ONO was the OH source, AS seed particles (10-MeONO), and (d) CH_3ONO was the OH source, AS + SA seed particles (12-MeONO). Chromatographic peaks designated with black $[\text{M} - \text{H}]^-$ ions are carboxylic acids and chromatographic peaks designated with green $[\text{M} - \text{H}]^-$ ions are organosulfates and nitrooxy organosulfates. See Table 2 for compound names.

those from the other observed organosulfates and nitrooxy organosulfates.

Under high- NO_2 conditions, the addition of AS + SA rather than AS seed results in fewer new peaks in the UPLC chromatogram than under high-NO conditions. As with low- NO_x , this result is expected as the SOA yield is insensitive to aerosol acidity. As with high-NO, 2-hydroxy terpenylic acid decreases in concentration in the presence of an acidic seed; however, the concentration of diaterpenylic acid acetate is insensitive to aerosol acidity. We have no explanation for this discrepancy. All of the organosulfates and nitrooxy

organosulfates observed in high-NO₂ photooxidation are observed in high-NO photooxidation, but there are a few additional organosulfates and nitrooxy organosulfates that are unique to the high-NO case (see Tables 2 and 3 and Fig. 6).

Given that the SOA yield and growth curves are so different, it is surprising that the UPLC/(-)ESI-TOFMS data from high-NO or high-NO₂ photooxidation are remarkably similar in the presence of AS seed but substantially different with AS + SA seed (see Fig. 6). This suggests that there must be compositional differences which UPLC/(-)ESI-TOFMS is insensitive. The data also suggest that PANs may play a role in the SOA composition as the amount of PAN was the main difference observed in the gas phase.

3.2.3 Bulk SOA functionality determined by AMS

The aerosol composition in low-NO_x and high-NO₂ OH oxidation of α -pinene in the presence of AS seed particles was further analyzed by HR-ToF-AMS. A description of the results has previously been reported (Chhabra et al., 2011). In Chhabra et al. (2011) the H : C vs. O : C (Van Krevelen diagram) and the ratio of f_{44} (more oxidized species, CO₂⁺ likely from acids) to f_{43} (less oxidized species, C₂H₃O⁺) are compared over the course of the photooxidation experiments. The Van Krevelen diagram can be used to infer the bulk functionality of the organic species within the aerosol. Both the low-NO_x and high-NO₂ photooxidation of α -pinene fall along the -1 slope of the H : C vs. O : C plot (see Fig. 2 of Chhabra et al., 2011), a value indicative of either carboxylic acids and/or hydroxy carbonyls (Heald et al., 2010; Ng et al., 2011; Chhabra et al., 2011). Under both low-NO_x and high-NO₂ OH oxidation, the AMS data indicate the same bulk organic functionality while the gas-phase data show a greater quantity of carboxylic acids in the low-NO_x oxidation. Consistent with the Van Krevelen diagram, f_{44} to f_{43} is very similar between the low-NO_x and high-NO₂ experiments. f_{44} is assigned as an indicator of carboxylic acids and a higher degree of aerosol aging (Ng et al., 2011; Chhabra et al., 2011). Further analysis of AMS data indicates that carboxylic acids are a large fraction (30–40 % of the mass) of the aerosols in low-NO_x and high-NO₂ OH oxidation of α -pinene (see Table 2 of Chhabra et al., 2011).

3.3 Gas-phase composition with injection of inorganic seed after photooxidation

To study how different oxidation products interact with aerosol seed particles of different composition (acidity), experiments were performed in which α -pinene was first photooxidized, followed by introduction of an aerosol seed after the lights had been off for two hours. This results in the exposure of gas-phase compounds, formed later on in the experiment, to fresh inorganic aerosol seed particles. This type of experiment has been used previously to study the SOA produced in the low-NO_x photooxidation of isoprene (Sur-

ratt et al., 2010). Surratt et al. (2010) showed that epoxydiols formed from the photooxidation of isoprene preferentially partition to acidic aerosol by reactive uptake.

Two post-oxidation seed experiments were performed under low-NO_x and two under high-NO₂ conditions. In all experiments, aerosol self-nucleation occurred as soon as the lights were turned on so a substantial amount of aerosol had already formed. Once the oxidation products were formed, the lights were extinguished and the chamber was left in the dark for two hours followed by injection of 15–20 $\mu\text{g m}^{-3}$ of aerosol seed. For low-NO_x, this added about 50 % more aerosol volume into the chamber, while for high-NO₂ the aerosol concentration was doubled.

Figure 7 shows the aerosol growth from each of the photooxidation followed by aerosol injection experiments. Aerosol nucleation and growth occurs as soon as the lights are turned on in all experiments. The difference in SOA volume growth from self-nucleation from both low- and high-NO_x experiments is due to greater gas-phase α -pinene concentration at the beginning of each AS seed experiments compared to the AS + SA experiments. Once the lights are turned off, the aerosol mass remains constant until the addition of the inorganic seed. In the case of low-NO_x, an additional growth of $\sim 8 \mu\text{g m}^{-3}$ of SOA is observed after the addition of AS + SA seed; no growth is observed after the addition of the neutral seed. The difference in the aerosol growth is in contrast to the SOA behavior when the aerosol seed was added prior to photooxidation. Under high-NO₂ conditions, no additional SOA is formed after the addition of either neutral or acidic seed particles in the dark.

When ammonium sulfate seed was added in the dark after photooxidation under low-NO_x or high-NO₂ conditions, no change in any of the gas-phase concentrations was observed. This indicates that the gas-phase molecules were not simply in equilibrium with the total aerosol concentration. It is possible that the gas-phase species were partitioning to the wall as well as to the particles, and were at equilibrium; since the surface area of the chamber walls is two orders of magnitude larger than that of the aerosol, no loss would be observed simply due to the greater surface area. Equilibrium partitioning to the walls does not, however, seem likely as the concentration of nearly all the species in the gas phase did not change when the lights were extinguished, decreasing temperature of $\sim 5^\circ\text{C}$. If the gas-phase molecules were partitioning to the wall, it would be expected that their gas-phase concentration would drop as the temperature decreased.

The gas-phase concentration of a number of oxidation products formed under low-NO_x conditions were noticeably reduced when AS + SA seed particles were introduced after photooxidation (Fig. 8). α -pinene oxide is almost completely lost from the gas phase after introduction of the acidic seed (Fig. 8d). In addition, the highly oxidized products observed at m/z 301 and 303 decrease by $\sim 70\%$. These two compounds probably contain either two hydroperoxy groups or one hydroperoxy group and one bridging peroxy group.

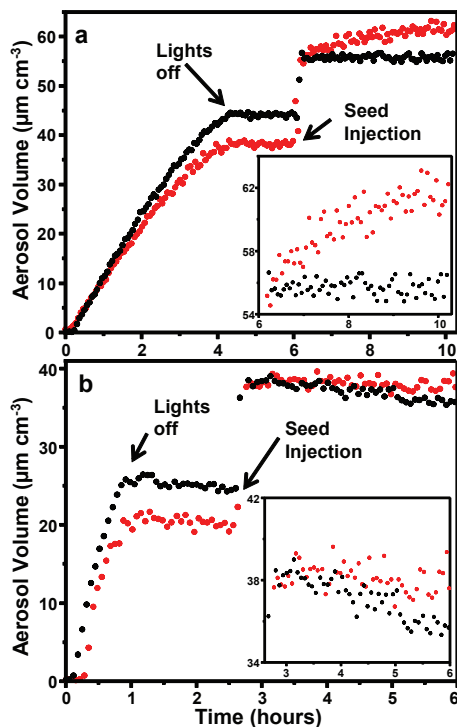


Fig. 7. Time traces of aerosol volume as a result of SOA growth from OH oxidation of α -pinene followed by injection of ammonium sulfate seed (black) or ammonium sulfate and sulfuric acid seed (red) under (a) low- NO_x and (b) high- NO_x (methyl nitrite photolysis) conditions. The difference in the quantity of self-nucleated aerosol volume growth from both (a) low- and (b) high- NO_x experiments is due to greater gas-phase α -pinene concentration at the beginning of each of the AS seed experiments compared to the AS + SA experiments.

Upon addition of the AS + SA seed, the α -pinene hydroxy hydroperoxides also decreased from the gas phase by $\sim 75\%$ (Fig. 8a). This was unexpected, as it has been shown that the hydroxy hydroperoxides formed in the photooxidation of isoprene are not lost from the gas phase due to addition of either AS or AS + SA seed particles (Surratt et al., 2010). In addition, it was unexpected because when aerosol seed was added prior to photooxidation, the only gas-phase product observed to be in lower concentration in the presence of AS + SA seed was α -pinene oxide. It should be noted that the gas-phase mass loss was a factor of two greater than the SOA growth upon addition of AS + SA seed. It is not clear how to interpret the mass balance, as no species were observed to increase substantially in the gas phase after addition of the AS + SA seed.

The loss of additional organics upon addition of AS + SA seed after photooxidation compared to when the seed is in-

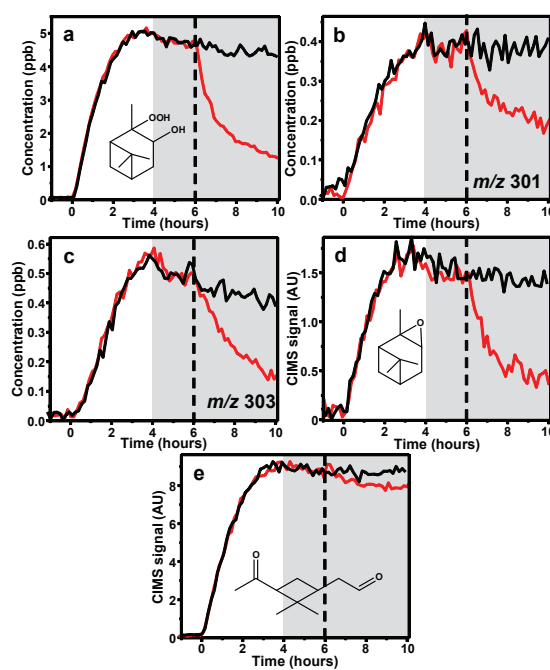


Fig. 8. CIMS traces of α -pinene OH oxidation under low- NO_x conditions, photooxidation for four hours, lights off and contents in the dark for two hours followed by injection of ammonium sulfate seed (black) or ammonium sulfate and sulfuric acid seed (red). Shaded gray area is when the chamber was dark and the dashed line indicates when aerosol seed was added.

jected prior to photooxidation may be related to the composition of the seed when exposed to a given organic. Specifically, perhaps products that are involved in self-nucleation and partition early on in the experiment coat the acidic seed resulting in a hydrocarbon surface rather than an acidic one. If this is the case, loss to the particle would be due to hydrocarbon partitioning rather than acid-catalyzed reactive uptake. Aerosol growth occurs as soon as the lights are turned on, and when a seed is present it takes only about 1.25 h before the aerosol volume has doubled. On the other hand, when the acidic seed is injected after photooxidation has occurred, the products are exposed to the acidic surface allowing reactive uptake to occur from the accumulated products.

Under high- NO_2 conditions, α -pinene oxide is substantially lost from the gas phase when the acidic seed was added (Fig. 9). Besides α -pinene oxide, there are minimal losses of other gas-phase species (Fig. 9). The observed losses include compounds that show up at m/z 215, 301, and 316. The loss of each of these is less than 25 %, as opposed to the low- NO_x case where losses were all greater than 50 %. As mentioned above, multiple species are observed at m/z 316, a first-generation product from the oxidation of α -pinene

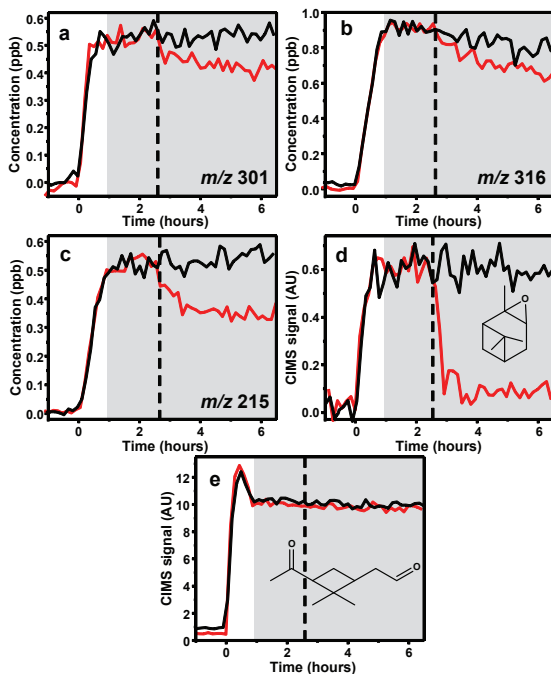


Fig. 9. CIMS traces of α -pinene OH oxidation under high- NO_x conditions, photooxidation for ~ 0.8 h, lights off and contents in the dark for ~ 2 h followed by injection of ammonium sulfate seed (black) or ammonium sulfate and sulfuric acid seed (red). Shaded gray area is when the chamber was dark and the dashed line indicates when aerosol seed was added.

(α -pinene dihydroxy nitrate) and norpinonaldehyde PAN. It is expected that if norpinonaldehyde PAN were to be lost from the gas phase upon addition of an acidic seed then pinonaldehyde PAN would as well. There is no loss of pinonaldehyde PAN from the gas phase, and therefore we conclude that the species lost from the gas phase is the α -pinene oxidation product, which we believe to be α -pinene dihydroxy nitrate. The structures of the molecules at m/z 215 and 301 are not known. Due to the small losses, it appears that under high- NO_2 conditions, acidity will play only a small or negligible effect on SOA growth, as seen in Fig. 7 where no additional growth was observed upon addition of an acidic seed. Consistent with this result, Offenberg et al. (2009) saw only a modest increase in SOA yield with the increase of the aerosol acidity from high- NO_2 photooxidation of α -pinene.

4 Implications

In this study, the aerosol growth and composition from α -pinene OH oxidation were compared in low-NO, high-NO, and high- NO_2 conditions. Aerosol growth from α -pinene OH

oxidation under high- NO_2 conditions behaves more similarly to low- NO_x than high-NO aerosol growth. With low NO, aerosol growth continues well after two lifetime of α -pinene with respect to OH oxidation. This indicates that later generation oxidation products are important for SOA growth, including the products of the oxidation of pinonaldehyde, a major product of both low- and high-NO OH oxidation of α -pinene.

In high-NO conditions the SOA yield is dependent on aerosol acidity. The increase in SOA yield with acidic seed was, however, relatively small ($\sim 22\%$ increase). The composition of the gas phase in high-NO and high- NO_2 OH oxidation was identical with a few notable variations. In high- NO_2 experiments, 1.4 to 2 times greater concentrations of PANs and nitric acid were observed in the gas phase compared to the high-NO experiments. One possible explanation for the difference in SOA growth is that the aerosols formed under high- NO_2 conditions are acidic enough in the presence of a neutral seed, due to the increased nitric acid and PANs, for the SOA yield to be the same in the presence of neutral or acidic particles. Further studies on the effect of NO_2 , PANs, and nitric acid on SOA yield from high- NO_x OH oxidation of α -pinene would aid in elucidating the difference in behavior between using HONO and methyl nitrite as the OH source.

When an acidic seed was added after OH oxidation, the SOA yield under low- NO_x conditions increased with a corresponding loss of species from the gas phase. This acid effect was not observed when the aerosol seed is added prior to oxidation, perhaps due to differences in the composition of the aerosol surface. The hypothesis is that when aerosol seed particles are added prior to oxidation, the surface is coated by organics, suppressing uptake of compounds that are catalyzed by acid. This has potential implications to any system that produces a high SOA yield or systems that start with a high organic VOC concentration. In systems where the seed particles become coated with organics relatively quickly, the acid effect and therefore the SOA yield under acidic conditions might be under represented.

Organic acids are a major component of SOA in both low- and high- NO_x OH oxidation of α -pinene. While AMS data indicate that the total concentration of organic acids in SOA from low- NO_x and high- NO_2 is similar, the individual composition varies depending on the gas-phase conditions. Pinonic and pinic acid are observed in SOA only from low- NO_x OH oxidation of α -pinene. This is consistent with gas-phase data, where pinonic acid was only observed from low- NO_x conditions. It is believed that 3-MBTCA is derived from high- NO_x gas phase oxidation of pinonic acid; however, there must be other mechanism for its formation, as 3-MBTCA is observed in SOA from low- NO_x OH oxidation of α -pinene and high- NO_x OH oxidation of α -pinene where pinonic acid is not observed in the gas or aerosol phase.

Acknowledgements. This work was supported in part by Department of Energy grant DE-SC0006626 and National Science Foundation grant AGS-1057183. N. Eddingsaas was supported by the Camille and Henry Dreyfus Postdoctoral Program in Environmental Chemistry. C. Loza and L. Yee were supported by National Science Foundation Graduate Research Fellowships.

Edited by: R. McLaren

References

Allan, J. D., Delia, A. E., Coe, H., Bower, K. N., Alfara, M. R., Jimenez, J. L., Middlebrook, A. M., Drewnick, F., Onasch, T. B., Canagaratna, M. R., Jayne, J. T., and Worsnop, D. R.: A generalised method for the extraction of chemically resolved mass spectra from aerodyne aerosol mass spectrometer data, *J. Aerosol Sci.*, 35, 909–922, doi:10.1016/j.jaerosci.2004.02.007, 2004.

Anttila, P., Hyotylainen, T., Heikkila, A., Jussila, M., Finell, J., Kulmala, M., and Riekola, M. L.: Determination of organic acids in aerosol particles from a coniferous forest by liquid chromatography-mass spectrometry, *J. Sep. Sci.*, 28, 337–346, doi:10.1002/jssc.200401931, 2005.

Aschmann, S. M., Atkinson, R., and Arey, J.: Products of reaction of OH radicals with alpha-pinene, *J. Geophys. Res.-Atmos.*, 107, 4191, doi:10.1029/2001jd001098, 2002.

Camredon, M., Hamilton, J. F., Alam, M. S., Wyche, K. P., Carr, T., White, I. R., Monks, P. S., Rickard, A. R., and Bloss, W. J.: Distribution of gaseous and particulate organic composition during dark α -pinene ozonolysis, *Atmos. Chem. Phys.*, 10, 2893–2917, doi:10.5194/acp-10-2893-2010, 2010.

Capouet, M., Mueller, J. F., Ceulemans, K., Compernolle, S., Vereecken, L., and Peeters, J.: Modeling aerosol formation in alpha-pinene photo-oxidation experiments, *J. Geophys. Res.-Atmos.*, 113, D02308, doi:10.1029/2007JD008995, 2008.

Chan, M. N., Surratt, J. D., Claeys, M., Edgerton, E. S., Tanner, R. L., Shaw, S. L., Zheng, M., Knipping, E. M., Eddingsaas, N. C., Wennberg, P. O., and Seinfeld, J. H.: Characterization and Quantification of Isoprene-Derived Epoxides in Ambient Aerosol in the Southeastern United States, *Environ. Sci. Technol.*, 44, 4590–4596, doi:10.1021/es100596b, 2010.

Chan, M. N., Surratt, J. D., Chan, A. W. H., Schilling, K., Offenberg, J. H., Lewandowski, M., Edney, E. O., Kleinindst, T. E., Jaoui, M., Edgerton, E. S., Tanner, R. L., Shaw, S. L., Zheng, M., Knipping, E. M., and Seinfeld, J. H.: Influence of aerosol acidity on the chemical composition of secondary organic aerosol from β -caryophyllene, *Atmos. Chem. Phys.*, 11, 1735–1751, doi:10.5194/acp-11-1735-2011, 2011.

Chhabra, P. S., Ng, N. L., Canagaratna, M. R., Corrigan, A. L., Russell, L. M., Worsnop, D. R., Flagan, R. C., and Seinfeld, J. H.: Elemental composition and oxidation of chamber organic aerosol, *Atmos. Chem. Phys.*, 11, 8827–8845, doi:10.5194/acp-11-8827-2011, 2011.

Chung, S. H. and Seinfeld, J. H.: Global distribution and climate forcing of carbonaceous aerosols, *J. Geophys. Res.-Atmos.*, 107, 4407, doi:10.1029/2001JD001397, 2002.

Claeys, M., Iinuma, Y., Szmigelski, R., Surratt, J. D., Blockhuys, F., Van Alsenoy, C., Boge, O., Sierau, B., Gomez-Gonzalez, Y., Vermeulen, R., Van der Veken, P., Shahgholi, M., Chan, A. W. H., Herrmann, H., Seinfeld, J. H., and Maenhaut, W.: Terpenyl Acid and Related Compounds from the Oxidation of alpha-Pinene: Implications for New Particle Formation and Growth above Forests, *Environ. Sci. Technol.*, 43, 6976–6982, doi:10.1021/es9007596, 2009.

Cocker, David R., I., Flagan, R. C., and Seinfeld, J. H.: State-of-the-art chamber facility for studying atmospheric aerosol chemistry, *Environ. Sci. Technol.*, 35, 2594–2601, 2001.

Crounse, J. D., McKinney, K. A., Kwan, A. J., and Wennberg, P. O.: Measurement of gas-phase hydroperoxides by chemical ionization mass spectrometry, *Anal. Chem.*, 78, 6726–6732, 2006.

DeCarlo, P. F., Kimmel, J. R., Trimborn, A., Northway, M. J., Jayne, J. T., Aiken, A. C., Gonin, M., Fuhrer, K., Horvath, T., Docherty, K. S., Worsnop, D. R., and Jimenez, J. L.: Field-deployable, high-resolution, time-of-flight aerosol mass spectrometer, *Anal. Chem.*, 78, 8281–8289, doi:10.1021/ac061249n, 2006.

Eddingsaas, N. C., Loza, C. L., Yee, L. D., Seinfeld, J. H., and Wennberg, P. O.: α -pinene photooxidation under controlled chemical conditions – Part 1: Gas-phase composition in low- and high- NO_x environments, *Atmos. Chem. Phys.*, 12, 6489–6504, doi:10.5194/acp-12-6489-2012, 2012.

Glasius, M., Duane, M., and Larsen, B. R.: Determination of polar terpene oxidation products in aerosols by liquid chromatography-ion trap mass spectrometry, *J. Chromatogr. A*, 833, 121–135, 1999.

Guenther, A., Hewitt, C. N., Erickson, D., Fall, R., Geron, C., Graedel, T., Harley, P., Klinger, L., Lerdau, M., McKay, W. A., Pierce, T., Scholes, B., Steinbrecher, R., Tallamraju, R., Taylor, J., and Zimmerman, P.: A global model of natural volatile organic compound emissions, *J. Geophys. Res.-Atmos.*, 100, 8873–8892, doi:10.1029/94JD02950, 1995.

Heald, C. L., Kroll, J. H., Jimenez, J. L., Docherty, K. S., DeCarlo, P. F., Aiken, A. C., Chen, Q., Martin, S. T., Farmer, D. K., and Artaxo, P.: A simplified description of the evolution of organic aerosol composition in the atmosphere, *Geophys. Res. Lett.*, 37, L08803, doi:10.1029/2010gl042737, 2010.

Hoffmann, T., Odum, J. R., Bowman, F., Collins, D., Klockow, D., Flagan, R. C., and Seinfeld, J. H.: Formation of organic aerosols from the oxidation of biogenic hydrocarbons, *J. Atmos. Chem.*, 26, 189–222, 1997.

Iinuma, Y., Boge, O., Miao, Y., Sierau, B., Gnauk, T., and Herrmann, H.: Laboratory studies on secondary organic aerosol formation from terpenes, *Faraday Discuss.*, 130, 279–294, doi:10.1039/b502160j, 2005.

Iinuma, Y., Boge, O., Kahnt, A., and Herrmann, H.: Laboratory chamber studies on the formation of organosulfates from reactive uptake of monoterpene oxides, *Phys. Chem. Chem. Phys.*, 11, 7985–97, doi:10.1039/B904025K, 2009.

Jaoui, M. and Kamens, R. M.: Mass balance of gaseous and particulate products analysis from alpha -pinene/NO_x/air in the presence of natural sunlight, *J. Geophys. Res.-Atmos.*, 106, 12541–12558, 2001.

Kavouras, I. G., Mihalopoulos, N., and Stephanou, E. G.: Formation of atmospheric particles from organic acids produced by forests, *Nature*, 395, 683–686, 1998.

Kavouras, I. G., Mihalopoulos, N., and Stephanou, E. G.: Formation and gas/particle partitioning of monoterpenes photo-oxidation products over forests, *Geophys. Res. Lett.*, 26, 55–58, doi:10.1029/1998GL900251, 1999.

Keywood, M. D., Varutbangkul, V., Bahreini, R., Flagan, R. C., and Seinfeld, J. H.: Secondary organic aerosol formation from the ozonolysis of cycloalkenes and related compounds, *Environ. Sci. Technol.*, 38, 4157–4164, 2004.

Kourtchev, I., Copolovici, L., Claeys, M., and Maenhaut, W.: Characterization of Atmospheric Aerosols at a Forested Site in Central Europe, *Environ. Sci. Technol.*, 43, 4665–4671, doi:10.1021/es803055w, 2009.

Laaksonen, A., Kulmala, M., O'Dowd, C. D., Joutsensaari, J., Vaattovaara, P., Mikkonen, S., Lehtinen, K. E. J., Sogacheva, L., Dal Maso, M., Aalto, P., Petäjä, T., Sogachev, A., Yoon, Y. J., Lihavainen, H., Nilsson, D., Facchini, M. C., Cavalli, F., Fuzzi, S., Hoffmann, T., Arnold, F., Hanke, M., Sellegrit, K., Umann, B., Junkermann, W., Coe, H., Allan, J. D., Alfarra, M. R., Worsnop, D. R., Riekkola, M. -L., Hyötyläinen, T., and Viisanen, Y.: The role of VOC oxidation products in continental new particle formation, *Atmos. Chem. Phys.*, 8, 2657–2665, doi:10.5194/acp-8-2657-2008, 2008.

Larsen, B. R., Di Bella, D., Glasius, M., Winterhalter, R., Jensen, N. R., and Hjorth, J.: Gas-phase OH oxidation of monoterpenes: Gaseous and particulate products, *J. Atmos. Chem.*, 38, 231–276, 2001.

Librando, V. and Tringali, G.: Atmospheric fate of OH initiated oxidation of terpenes. Reaction mechanism of alpha-pinene degradation and secondary organic aerosol formation, *J. Environ. Manag.*, 75, 275–282, doi:10.1016/j.jenvman.2005.01.001, 2005.

Ma, Y., Russell, A. T., and Marston, G.: Mechanisms for the formation of secondary organic aerosol components from the gas-phase ozonolysis of alpha-pinene, *Phys. Chem. Chem. Phys.*, 10, 4294–4312, doi:10.1039/b803283a, 2008.

Minerath, E. C., Casale, M. T., and Elrod, M. J.: Kinetics Feasibility Study of Alcohol Sulfate Esterification Reactions in Tropospheric Aerosols, *Environ. Sci. Technol.*, 42, 4410–4415, 2008.

Müller, L., Reinnig, M.-C., Naumann, K. H., Saathoff, H., Mentel, T. F., Donahue, N. M., and Hoffmann, T.: Formation of 3-methyl-1,2,3-butanetricarboxylic acid via gas phase oxidation of pinonic acid – a mass spectrometric study of SOA aging, *Atmos. Chem. Phys.*, 12, 1483–1496, doi:10.5194/acp-12-1483-2012, 2012.

Ng, N. L., Chhabra, P. S., Chan, A. W. H., Surratt, J. D., Kroll, J. H., Kwan, A. J., McCabe, D. C., Wennberg, P. O., Sorooshian, A., Murphy, S. M., Dalleska, N. F., Flagan, R. C., and Seinfeld, J. H.: Effect of NO_x level on secondary organic aerosol (SOA) formation from the photooxidation of terpenes, *Atmos. Chem. Phys.*, 7, 5159–5174, doi:10.5194/acp-7-5159-2007, 2007a.

Ng, N. L., Kroll, J. H., Chan, A. W. H., Chhabra, P. S., Flagan, R. C., and Seinfeld, J. H.: Secondary organic aerosol formation from m-xylene, toluene, and benzene, *Atmos. Chem. Phys.*, 7, 3909–3922, doi:10.5194/acp-7-3909-2007, 2007b.

Ng, N. L., Canagaratna, M. R., Jimenez, J. L., Chhabra, P. S., Seinfeld, J. H., and Worsnop, D. R.: Changes in organic aerosol composition with aging inferred from aerosol mass spectra, *Atmos. Chem. Phys.*, 11, 6465–6474, doi:10.5194/acp-11-6465-2011, 2011.

Noziere, B., Barnes, I., and Becker, K.-H.: Product study and mechanisms of the reactions of alpha -pinene and of pinonaldehyde with OH radicals, *J. Geophys. Res.-Atmos.*, 104, 23645–23656, doi:10.1029/1999JD900778, 1999.

Offenberg, J. H., Lewandowski, M., Edney, E. O., Kleindienst, T. E., and Jaoui, M.: Influence of Aerosol Acidity on the Formation of Secondary Organic Aerosol from Biogenic Precursor Hydrocarbons, *Environ. Sci. Technol.*, 43, 7742–7747, doi:10.1021/es901538e, 2009.

Paulot, F., Crounse, J. D., Kjaergaard, H. G., Kroll, J. H., Seinfeld, J. H., and Wennberg, P. O.: Isoprene photooxidation: new insights into the production of acids and organic nitrates, *Atmos. Chem. Phys.*, 9, 1479–1501, doi:10.5194/acp-9-1479-2009, 2009a.

Paulot, F., Crounse, J. D., Kjaergaard, H. G., Kurten, A., St. Clair, J. M., Seinfeld, J. H., and Wennberg, P. O.: Unexpected epoxide formation in the gas-phase photooxidation of isoprene, *Science*, 325, 730–733, doi:10.1126/science.1172910, 2009b.

Presto, A. A., Hartz, K. E. H., and Donahue, N. M.: Secondary organic aerosol production from terpene ozonolysis. 2. Effect of NO_x concentration, *Environ. Sci. Technol.*, 39, 7046–7054, doi:10.1021/es050400s, 2005.

Pye, H. O. T., Chan, A. W. H., Barkley, M. P., and Seinfeld, J. H.: Global modeling of organic aerosol: the importance of reactive nitrogen (NO_x and NO₃), *Atmos. Chem. Phys.*, 10, 11261–11276, doi:10.5194/acp-10-11261-2010, 2010.

Shilling, J. E., Chen, Q., King, S. M., Rosenoern, T., Kroll, J. H., Worsnop, D. R., DeCarlo, P. F., Aiken, A. C., Sueper, D., Jimenez, J. L., and Martin, S. T.: Loading-dependent elemental composition of α -pinene SOA particles, *Atmos. Chem. Phys.*, 9, 771–782, doi:10.5194/acp-9-771-2009, 2009.

Spittler, M., Barnes, I., Bejan, I., Brockmann, K. J., Benter, T., and Wirtz, K.: Reactions of NO₃ radicals with limonene and α -pinene: Product and SOA formation, *Atmos. Environ.*, 40, S116–S127, 2006.

St. Clair, J. M., McCabe, D. C., Crounse, J. D., Steiner, U., and Wennberg, P. O.: Chemical ionization tandem mass spectrometer for the in situ measurement of methyl hydrogen peroxide, *Rev. Sci. Instrum.*, 81, 094102, doi:10.1063/1.3480552, 2010.

Surratt, J. D., Kroll, J. H., Kleindienst, T. E., Edney, E. O., Claeys, M., Sorooshian, A., Ng, N. L., Offenberg, J. H., Lewandowski, M., Jaoui, M., Flagan, R. C., and Seinfeld, J. H.: Evidence for Organosulfates in Secondary Organic Aerosol, *Environ. Sci. Technol.*, 41, 517–527, 2007.

Surratt, J. D., Gomez-Gonzalez, Y., Chan, A. W. H., Vermeylen, R., Shahgholi, M., Kleindienst, T. E., Edney, E. O., Offenberg, J. H., Lewandowski, M., Jaoui, M., Maenhaut, W., Claeys, M., Flagan, R. C., and Seinfeld, J. H.: Organosulfate formation in biogenic secondary organic aerosol, *J. Phys. Chem. A*, 112, 8345–8378, doi:10.1021/jp802310p, 2008.

Surratt, J. D., Chan, A. W. H., Eddingsaas, N. C., Chan, M. N., Loza, C. L., Kwan, A. J., Hersey, S. P., Flagan, R. C., Wennberg, P. O., and Seinfeld, J. H.: Reactive intermediates revealed in secondary organic aerosol formation from isoprene, *P. Natl. Acad. Sci.*, 107, 6640–6645, doi:10.1073/pnas.0911114107, 2010.

Szmigelski, R., Surratt, J. D., Gomez-Gonzalez, Y., Van der Veken, P., Kourtchev, I., Vermeylen, R., Blockhuys, F., Jaoui, M., Kleindienst, T. E., Lewandowski, M., Offenberg, J. H., Edney, E. O., Seinfeld, J. H., Maenhaut, W., and Claeys, M.: 3-methyl-1,2,3-butanetricarboxylic acid: an atmospheric tracer for terpene secondary organic aerosol, *Geophys. Res. Lett.*, 34, L24811, doi:10.1029/2007GL031338, 2007.

Taylor, W. D., Allston, T. D., Moscato, M. J., Fazekas, G. B., Kozlowski, R., and Takacs, G. A.: Atmospheric photo-dissociation

lifetimes for nitromethane, methyl nitrite, and methyl nitrate, *Int. J. Chem. Kinet.*, 12, 231–240, 1980.

Warnke, J., Bandur, R., and Hoffmann, T.: Capillary-HPLC-ESI-MS/MS method for the determination of acidic products from the oxidation of monoterpenes in atmospheric aerosol samples, *Anal. Bioanal. Chem.*, 385, 34–45, doi:10.1007/s00216-006-0340-6, 2006.

Yu, J., Cocker, David R., I., Griffin, R. J., Flagan, R. C., and Seinfeld, J. H.: Gas-phase ozone oxidation of monoterpenes: gaseous and particulate products, *J. Atmos. Chem.*, 34, 207–258, 1999a.

Yu, J., Griffin, R. J., Cocker, David R., I., Flagan, R. C., Seinfeld, J. H., and Blanchard, P.: Observation of gaseous and particulate products of monoterpene oxidation in forest atmospheres, *Geophys. Res. Lett.*, 26, 1145–1148, doi:10.1029/1999GL900169, 1999b.

Zhang, Y. Y., Müller, L., Winterhalter, R., Moortgat, G. K., Hoffmann, T., and Pöschl, U.: Seasonal cycle and temperature dependence of pinene oxidation products, dicarboxylic acids and nitrophenols in fine and coarse air particulate matter, *Atmos. Chem. Phys.*, 10, 7859–7873, doi:10.5194/acp-10-7859-2010, 2010.

Appendix D

Chemical aging of m-xylene secondary organic aerosol: laboratory chamber study¹

¹This chapter is reproduced by permission from "Chemical aging of m-xylene secondary organic aerosol: laboratory chamber study," by C. L. Loza, P. S. Chhabra, L. D. Yee, J. S. Craven, R. C. Flagan, and J. H. Seinfeld, *Atmospheric Chemistry and Physics*, 12, 151–167, doi:10.5194/acp-12-151-2012, 2012. Copyright 2012 Authors. This work is licensed under a Creative Commons License.



Chemical aging of *m*-xylene secondary organic aerosol: laboratory chamber study

C. L. Loza¹, P. S. Chhabra^{1,*}, L. D. Yee², J. S. Craven¹, R. C. Flagan^{1,2}, and J. H. Seinfeld^{1,2}

¹Division of Chemistry and Chemical Engineering, California Institute of Technology, Pasadena, CA, USA

²Division of Engineering and Applied Science, California Institute of Technology, Pasadena, CA, USA

* now at: Aerodyne Research, Inc., Billerica, MA, USA

Correspondence to: J. H. Seinfeld (seinfeld@caltech.edu)

Received: 20 August 2011 – Published in Atmos. Chem. Phys. Discuss.: 7 September 2011

Revised: 8 December 2011 – Accepted: 20 December 2011 – Published: 3 January 2012

Abstract. Secondary organic aerosol (SOA) can reside in the atmosphere for a week or more. While its initial formation from the gas-phase oxidation of volatile organic compounds tends to take place in the first few hours after emission, SOA can continue to evolve chemically over its atmospheric lifetime. Simulating this chemical aging over an extended time in the laboratory has proven to be challenging. We present here a procedure for studying SOA aging in laboratory chambers that is applied to achieve 36 h of oxidation. The formation and evolution of SOA from the photooxidation of *m*-xylene under low-NO_x conditions and in the presence of either neutral or acidic seed particles is studied. In SOA aging, increasing molecular functionalization leads to less volatile products and an increase in SOA mass, whereas gas- or particle-phase fragmentation chemistry results in more volatile products and a loss of SOA. The challenge is to discern from measured chamber variables the extent to which these processes are important for a given SOA system. In the experiments conducted, *m*-xylene SOA mass, calculated under the assumption of size-invariant particle composition, increased over the initial 12–13 h of photooxidation and decreased beyond that time, suggesting the existence of fragmentation chemistry. The oxidation of the SOA, as manifested in the O:C elemental ratio and fraction of organic ion detected at *m/z* 44 measured by the Aerodyne aerosol mass spectrometer, increased continuously starting after 5 h of irradiation until the 36 h termination. This behavior is consistent with an initial period in which, as the mass of SOA increases, products of higher volatility partition to the aerosol phase, followed by an aging period in which gas- and particle-phase reaction products become increasingly more oxidized. When irradiation is stopped 12.4 h into one experiment, and OH generation ceases, minimal loss of SOA is ob-

served, indicating that the loss of SOA is either light- or OH-induced. Chemical ionization mass spectrometry measurements of low-volatility *m*-xylene oxidation products exhibit behavior indicative of continuous photooxidation chemistry. A condensed chemical mechanism of *m*-xylene oxidation under low-NO_x conditions is capable of reproducing the general behavior of gas-phase evolution observed here. Moreover, order of magnitude analysis of the mechanism suggests that gas-phase OH reaction of low volatility SOA precursors is the dominant pathway of aging in the *m*-xylene system although OH reaction with particle surfaces cannot be ruled out. Finally, the effect of size-dependent particle composition and size-dependent particle wall loss rates on different particle wall loss correction methods is discussed.

1 Introduction

Organic aerosol (OA) constitutes 20–90 % of all submicron particles in the atmosphere, and up to 80 % of this is classified as secondary organic aerosol (SOA) (Zhang et al., 2007; Murphy et al., 2006). Aerosol particles in the atmosphere can have lifetimes of 5–12 days (Balkanski et al., 1993), during which they can undergo continuous physical and chemical processing, commonly called aging (Rudich et al., 2007). Laboratory experiments designed to study SOA formation typically have a duration of up to 1 day, during which all processes that cause ambient particle aging may not be captured. Chemical aging of SOA can affect gas-particle partitioning through processes such as vapor-phase oxidation of semivolatiles, heterogeneous oxidation, and reactions within the particle phase, e.g. oligomerization, that take place on

a fairly long timescale (Kroll and Seinfeld, 2008; Hallquist et al., 2009).

Given the potentially large number of organic species in ambient particles, bulk chemical measurements are useful to describe the extent of oxidative aging of SOA. Using aerosol mass spectrometry, changes in O:C (elemental oxygen to carbon ratio) and H:C (elemental hydrogen to carbon ratio) from high-resolution data and f_{44} (ratio of mass-to-charge (m/z) 44 to total signal in the organic component mass spectrum) and f_{43} (ratio of m/z 43 to total signal in the organic component mass spectrum) have been reported for ambient and laboratory-generated particles. The dominant organic ion at m/z 43 is $\text{C}_2\text{H}_3\text{O}^+$, and the dominant organic ion at m/z 44 is CO_2^+ . Ng et al. (2010) evaluated a number of aerosol oxidation data sets in the f_{44} – f_{43} space and found that data for ambient OA tend to occupy a triangular region. As the OA becomes more oxidized, it tends to move from a region of lower f_{44} and a wider range of f_{43} at the base of the triangle toward the apex with higher f_{44} and less variable f_{43} . Heald et al. (2010) used the Van Krevelen diagram to show that the H:C and O:C of total ambient OA tend to fall along a line with a slope of -1 , suggesting, on average, equal additions of carbonyl and alcohol moieties. More recently, Ng et al. (2011) determined a correlation between f_{43} and H:C and, combined with a correlation between f_{44} and O:C (Aiken et al., 2008), mapped the triangular region in f_{44} – f_{43} space onto the Van Krevelen diagram. They found that for ambient OA classified as oxygenated OA (OOA) and laboratory chamber-generated SOA the H:C and O:C evolution toward the apex of the triangle tends to fall along a line with a slope of -0.5 on a Van Krevelen diagram. This difference in slope between the two studies was attributed to the inclusion of primary OA in the study of Heald et al. The evolution of ambient OA can also be represented in terms of saturation concentration (C^*) and O:C (Jimenez et al., 2009). As the OA becomes more oxidized, C^* decreases and O:C increases. In all three of these frameworks, the oxygen content of the organic aerosol increases upon aging.

Laboratory studies have been conducted to probe the mechanisms of chemical aging of SOA. In flow reactor experiments, which have much shorter residence times than chamber experiments, OH concentrations a few orders of magnitude higher than ambient concentrations are used to attain OH exposure similar to that of multiple days of atmospheric processing. Using a flow reactor, Kroll et al. (2009) found that for oxidation of squalane ($\text{C}_{30}\text{H}_{36}$) particles, functionalization reactions (addition of polar functional groups) dominated at low OH exposure, and fragmentation reactions (scission of C–C bonds in the carbon skeleton) dominated as OH exposure increased. They observed an O:C ratio of 0.45 after 35.8 squalene OH oxidation lifetimes. Lambe et al. (2011) also used a flow reactor to attain OH exposures equivalent to 1–20 days of atmospheric aging. Using a range of anthropogenic and biogenic SOA and oxidized primary organic aerosol (OPOA) precursors, they found that as OH ex-

posure increased, the SOA and OPOA followed and extended the progression of ambient SOA in f_{44} – f_{43} space, attaining values of f_{44} higher than ambient SOA. The Van Krevelen diagram slope of the SOA and OPOA was indicative of carboxylic acid formation and carbon–carbon bond fragmentation. In chamber experiments of 16 h oxidant exposure, Qi et al. (2010) found that, starting after 2 h of OH exposure, the volatility of SOA generated from *m*-xylene and α -pinene under high- NO_x conditions decreased slowly for the remainder of the experiment. After this initial 2-h period, the O:C ratio for *m*-xylene SOA increased at a rate of 0.007 h^{-1} ; however, for α -pinene SOA, the O:C ratio decreased at a rate of 0.003 h^{-1} . Chhabra et al. (2010) observed increasing O:C for SOA formed from toluene, *m*-xylene, and naphthalene for irradiation times up to 12 h. The most rapid increase in O:C occurred during the first hour of low- NO_x toluene and *m*-xylene experiments and the first 4 h of low- NO_x naphthalene experiments. Similarly to the results of Qi et al. (2010) that SOA from some precursors exhibits minute aging behavior, no change in O:C was observed for SOA from isoprene photooxidation or α -pinene ozonolysis after initial SOA formation. Chhabra et al. (2011) extended the analysis of the SOA formed from the compounds studied in Chhabra et al. (2010) to assess their behavior in both f_{44} – f_{43} space and Van Krevelen diagram representations. Although the SOA formed from the various precursors occupied different regions in each representation, most systems exhibited a progression similar to aging of ambient SOA.

In this work, we develop and apply to *m*-xylene SOA a procedure to extend to 36 h the experimental duration of a laboratory chamber operated as a batch reactor. Aromatic hydrocarbon emissions are an important contribution (~ 20 –30 %) to the total volatile organic compounds in the urban atmosphere (Calvert et al., 2002). *m*-Xylene SOA yields (ratio of mass concentration of SOA formed to mass concentration of parent hydrocarbon reacted) have been measured previously for initial *m*-xylene concentrations of 10 to 180 ppb and experimental durations up to 10 h (Ng et al., 2007; Song et al., 2007). SOA yields for low- NO_x conditions were found to be higher than those for high- NO_x conditions. In addition, Chhabra et al. (2010) and Qi et al. (2010) observed changes in SOA chemical composition for up to 16 h of oxidation, indicating the potential of aging of *m*-xylene SOA over longer timescales. For a long duration experiment, the initial *m*-xylene concentration can be chosen to produce a sufficient amount of SOA to sample for the duration of the experiment yet remaining close to atmospherically relevant loadings, typically 0.1 – $20 \mu\text{g m}^{-3}$ (Shilling et al., 2009). In the present work, the total amount of SOA formed, its chemical composition, and the composition of the gas phase over 36 h of irradiation are evaluated to infer mechanisms of chemical aging of *m*-xylene SOA. For the first time, the effects of size-dependent particle composition on particle wall loss correction methods are discussed.

2 Materials and methods

2.1 Experimental setup

Experiments were conducted in the Caltech dual 28-m³ Teflon chambers. Details of the facilities are given elsewhere (Cocker et al., 2001; Keywood et al., 2004). Before each experiment, the chambers were flushed with dried, purified air for > 24 h until the particle number concentration < 50 cm⁻³ and the volume concentration < 0.1 $\mu\text{m}^3 \text{ cm}^{-3}$. Experiments were run under low-NO_x conditions using hydrogen peroxide (H₂O₂) as the OH source. With H₂O₂ it is possible to achieve a constant OH concentration for the duration of the experiments. H₂O₂ was injected into the chamber by evaporating 280 μl of 50 % wt aqueous solution into the chamber with 51 min⁻¹ of purified air. Seed particles were injected by atomizing a 0.015 M aqueous ammonium sulfate (AS) solution for neutral seed and a 0.03 M aqueous magnesium sulfate with 0.03 M sulfuric acid (MS + SA) solution for acidic seed. *m*-Xylene (Sigma Aldrich, 99+ %) was introduced into the chamber by injecting the volume of the liquid hydrocarbon required to obtain a concentration of 30 ppb into a glass bulb, and the vapor was carried into the chamber with 51 min⁻¹ of purified air. The chamber contents were allowed to mix for 1 h before beginning irradiation.

A suite of instruments was used to study the evolution of the gas and particle phases. *m*-Xylene was measured using a gas chromatograph with flame ionization detector (GC/FID, Agilent 6890N), equipped with a HP-5 column (15 m \times 0.53 mm ID \times 1.5 μm thickness, Hewlett Packard). Reactive intermediates and H₂O₂ were continuously monitored using a custom-modified Varian 1200 triple-quadrupole chemical ionization mass spectrometer (CIMS). Details of operation can be found elsewhere (Crounse et al., 2006; Paulot et al., 2009; St. Clair et al., 2010). The CIMS was operated in negative mode in which CF₃O⁻ is used as the reagent ion. CF₃O⁻ clusters with the analyte, forming ions at *m/z* MW+85 (R · CF₃O⁻), or, with more acidic species, at *m/z* MW+19 (HF · R₋H). Relative humidity (RH), temperature, NO, NO_x, and O₃ were continuously monitored. The RH of the chamber was < 5%. The initial chamber temperature was \sim 19 °C; however, heating from the blacklights caused a rise in temperature of approximately 5 °C. NO and NO_x concentrations were below the 2 ppb detection limit of the instrument, and initial O₃ concentration was 2 ppb.

Aerosol size distribution and number concentration were measured continuously using a differential mobility analyzer (DMA, TSI, 3081) coupled to a condensation particle counter (CPC, TSI, 3760), henceforth referred to as the DMA. Real-time particle mass spectra were collected continuously by an Aerodyne High Resolution Time-of-Flight Aerosol Mass Spectrometer (DeCarlo et al., 2006; Canagaratna et al., 2007), henceforth referred to as the AMS. The AMS switched once every minute between the high resolution ‘W-mode’ and the lower resolution, higher sensitivity

‘V-mode’. ‘V-mode’ data were analyzed using a fragmentation table to separate sulfate, ammonium, and organic spectra and to time-trace specific *m/z* ratios. ‘V-mode’ and ‘W-mode’ data were analyzed using a separate high-resolution spectra toolbox known as PIKA to determine the chemical formulas contributing to distinct *m/z* ratios (DeCarlo et al., 2006). The signals of organic ions below *m/z* 119 were used to calculate elemental ratios. The ratio of particle-phase CO⁺ to CO₂⁺ was approximately equal to 1, and the contribution of CO⁺ to the organic signal was estimated to equal that of particle-phase CO₂⁺. The intensities of water-derived ions (H₂O⁺, OH⁺, and O⁺) were estimated from particle-phase CO⁺ using the correlation suggested by Aiken et al. (2008). A relative ionization intensity of 1.4 was applied to organic ion signals. AMS data reported in this work are averaged over 10-min intervals.

2.2 Aging experiment protocols

The volume of the reactor limits the duration of experiments in a chamber operated in batch mode; when sampling with all instruments, nearly half of the chamber volume is depleted in 18 h, at which point it is preferable to cease sampling due to deflation of the chamber. To achieve longer OH exposure times with all instruments sampling, sets of experiments were conducted with increasing duration and staggered instrument sampling. Instruments were grouped into two categories based upon their sampling schedule. Group I includes the AMS and a RH and temperature probe. Group II includes the DMA, the CIMS, the GC/FID, the O₃ analyzer, and the NO_x analyzer. All instruments were operated during initial injections before the onset of irradiation. Experimental time began at the onset of irradiation. First, two 18 h experiments were conducted with Group I and II instruments sampling for the entire duration to establish consistency in the gas and particle phases during separate experiments. Subsequent experiments of 24 h, 30 h, and 36 h were conducted to achieve longer OH exposure. The instrument sampling schedule for all experiments is given in Table 1. The entire set of 5 experiments was conducted in the same chamber to avoid any differences between chamber conditions that may arise between the dual chambers. For each of the Group II instruments, the data from all experiments were combined to track the evolution of species for the entire 36 h of OH exposure.

2.3 Total SOA formation

To determine the total SOA mass concentration in the chamber, ΔM_0 , particle wall losses must be taken into account. The extent of interactions between particles deposited on the chamber walls and vapors in the chamber has not been determined completely; therefore, two limiting assumptions are used to bound this interaction. These limits have been described and applied to chamber experiments by Weitkamp et al. (2007) and Hildebrandt et al. (2009, 2011). In one

Table 1. Experiment sampling conditions and instrument sampling protocol.

Experiment Type	Duration (h)	Volume Removed (m ³)	Sampling hours Group I ^a	Sampling hours Group II ^b
Wall loss	23	6.14	N/A ^c	N/A
18 h aging	18	7.92	0–18	0–18
24 h aging	24	3.60	0–24	16–24
30 h aging	30	3.63	0–30	22–30
36 h aging	36	3.66	0–36	28–36

^aGroup I instruments: AMS, RH and temperature probe (total volumetric flow rate = 0.084 L min⁻¹).

^bGroup II instruments: DMA, CIMS, GC/FID, O₃ analyzer, NO_x analyzer (total volumetric flow rate = 7.25 L min⁻¹).

^cInstruments sampling: DMA, O₃ analyzer, NO_x analyzer, RH and temperature probe (total volumetric flow rate = 4.45 L min⁻¹).

limit, particles deposited on the wall are assumed to cease interaction with suspended vapors after deposition. In this case, the amount of organic material in the deposited particles does not change after deposition, and these particles remain at the same size at which they deposited for the remainder of the experiment. In the other limit, particles on the wall are assumed to interact with vapors in the chamber after deposition as if they had remained suspended. Thus, in this case, the amount of organic material in the particles after deposition changes at the same rate as the amount of organic material in the suspended particles, and the deposited particles continue to change size throughout the remainder of the experiment. This limit is analogous in theory to that of a chamber without walls. In either limit, the material on the walls is added to that which remains suspended to obtain the total amount of SOA formed.

During particle growth, the organic mass fraction of the suspended particles increases. In the first limit, the organic mass fraction of deposited particles does not increase after deposition; therefore, this case produces a lower limit for ΔM_o . In the second limit, deposited particles are assumed to continue growing; therefore, this case is an upper limit for ΔM_o . These two limits of wall loss corrected ΔM_o will subsequently be referred to as the lower bound and upper bound, respectively.

The lower bound limit on ΔM_o is calculated from the DMA suspended particle number distribution. For each size bin i at each time step j , the particle number distribution deposited to the wall, $n_{w,ij}$, is calculated using size-dependent wall loss rates, β_i :

$$n_{w,ij} = n_{s,ij} \exp(\beta_i \Delta t) \quad (1)$$

where $n_{s,ij}$ is the suspended particle number distribution in size bin i at time step j , and Δt is the difference between time step j and time step $j+1$. Wall loss rates were determined from calibration experiments performed prior to the start of the aging experiments (methods detailed in Keywood

et al., 2004; Ng et al., 2007). The deposited particle number distribution is added to the suspended particle number distribution to give a wall-loss corrected number distribution, $n_{tot,ij}$, which is then converted to a volume concentration, $V_{tot,j}$, assuming spherical particles:

$$n_{tot,ij} = n_{s,ij} + n_{w,ij} \quad (2)$$

$$V_{tot,j} = \sum_{i=1}^m \frac{n_{tot,ij}}{D_{p,i} \ln 10} \times (D_{p,i+} - D_{p,i-}) \times \frac{\pi}{6} D_{p,i}^3 \quad (3)$$

where m is the total number of size bins, $D_{p,i+}$ is the upper limit diameter for size bin i , and $D_{p,i-}$ is the lower limit diameter for size bin i . A factor of $\ln 10$ is necessary to convert from a log normal distribution. The initial seed volume concentration, V_{seed} , is subtracted from the wall-loss corrected volume concentration to give the volume concentration of SOA, $V_{o,j}$. To convert to SOA mass, $\Delta M_{o,j}$, the SOA volume concentration is multiplied by the SOA density, ρ_{org} :

$$\Delta M_{o,j} = \rho_{org} (V_{o,j} - V_{seed}) \quad (4)$$

For low-NO_x *m*-xylene SOA, $\rho_{org} = 1.33$ g cm⁻³ (Ng et al., 2007). It is possible that ρ_{org} changes as particle age increases, but it was assumed to be constant for the present study, which is consistent with the findings of Qi et al. (2010).

Calculating the lower bound wall-loss corrected mass relies on having continuous number distributions, which were not available for the 24-h, 30-h, and 36-h experiments. To obtain a continuous number distribution, the number distributions for all experiments were combined. The DMA sampling schedule was designed to allow a 2-h overlap period between shorter and longer experiments (i.e. sampling for the 24-h experiment began at 16 h, 2 h prior to the endpoint of the 18-h experiment) to facilitate the comparison of data between shorter and longer experiments. The number distributions from each experiment were combined sequentially. During periods of overlap between two experiments, a weighted average of the number distribution in each size bin was taken giving higher weight to the shorter experiment at the beginning of the overlap period and higher weight to the longer experiment at the end of the overlap period.

Both the number distribution of the seed particles and the initial concentration of *m*-xylene affect the number distribution of the aerosol. In the 24-h experiment, the seed volume was lower than that for the other AS seed experiments (Table 2). Assuming that the SOA produced in this experiment was comparable to that in the other experiments, the suspended particle volume would be lower than that of the other AS seed experiments, and the number distribution would be too small to combine with those of the other AS experiments to obtain a continuous number distribution. Without the data from the 24-h experiment, no number distribution data were available between hours 18 and 22. Number distributions during those 4 h were calculated from the 18- and 30-h experiments by fitting an exponential function to the number

Table 2. Experimental conditions and results.

Seed	Duration (h)	Initial <i>m</i> -xylene (ppb)	Seed vol. ($\mu\text{m}^3 \text{cm}^{-3}$)	Final <i>m</i> -xylene (ppb)	Final ΔM_o^a ($\mu\text{g m}^{-3}$)
AS	18	32.2 \pm 0.7	11.1 \pm 0.3	2.46 \pm 0.66	21.9 \pm 1.7
AS	18	31.8 \pm 0.7	12.3 \pm 0.3	0.84 \pm 0.66	24.7 \pm 1.9
AS	24	29.2 \pm 0.7	9.10 \pm 0.2	< 0.5	N/A
AS	30	29.1 \pm 0.7	12.3 \pm 0.4	< 0.5	N/A
AS	36	28.7 \pm 0.7	13.1 \pm 0.2	< 0.5	N/A
AS	12+8 ^b	25.0 \pm 0.6	10.5 \pm 0.3	2.1 \pm 0.6	20.0 \pm 1.0
MS + SA	18	32.9 \pm 0.7	10.5 \pm 0.4	1.94 \pm 0.66	22.5 \pm 1.8
MS + SA	18	32.4 \pm 0.7	10.8 \pm 0.4	1.15 \pm 0.66	21.7 \pm 1.7
MS + SA	24	32.5 \pm 0.7	10.6 \pm 0.3	< 0.5	N/A
MS + SA	30	29.6 \pm 0.7	10.6 \pm 0.3	< 0.5	N/A
MS + SA	36	30.0 \pm 0.7	10.8 \pm 0.4	< 0.5	N/A

^aLower bound limit^b12.4 h irradiated + 8 h dark

distribution in each size bin during hours 16–18 of the 18-h experiment and hours 22–24 of the 30-h experiment and using the function to interpolate a number distribution at 4-min increments.

Throughout an experiment, the volume of the chamber decreases due to sampling, but the surface area of the walls remains the same. It is possible that the increasing surface-area-to-volume ratio will increase the particle wall loss rates. The duration of a typical wall loss experiment is 18–24 h, shorter than that of the longest aging experiments. The aging experiments were designed to minimize the amount of air sampled from the chamber. Although more instruments sample from the chamber during an aging experiment than during a wall loss calibration experiment, the volume of air removed during an aging experiment is comparable to that of a wall loss calibration experiment (Table 1).

To confirm that wall loss rates do not vary significantly as chamber volume decreases, an additional wall loss calibration experiment was performed in each chamber. These calibration experiments were conducted following the same protocols as a typical wall loss calibration; however, before AS seed aerosol was injected, approximately 8 m³ of air was removed from the chambers to simulate conditions found at the end of an 18 h experiment. The wall loss rates determined from these low-volume experiments were within the range of wall loss rates observed in the chambers since they were installed in 2009 (Fig. 1). Therefore, time-dependence of the wall loss rate constants was assumed to be negligible during these aging experiments.

The upper bound limit on ΔM_o is calculated by combining the AMS and DMA data. The experiments in the present work use seed particles containing sulfate, and the only process that decreases sulfate concentration in the suspended phase is wall loss. The initial sulfate concentration is calculated from the DMA seed volume concentration. There

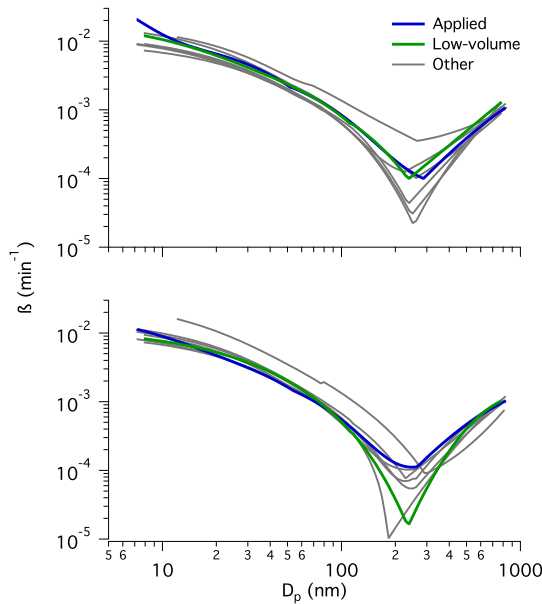


Fig. 1. Particle wall loss rates, β , measured in both chambers from September 2009 to August 2011. The top panel corresponds to near chamber, and the bottom panel corresponds to far chamber. The wall loss rates labeled “applied” were applied to the experiments reported in this manuscript. The wall loss rates labeled “low-volume” were calculated during a wall loss calibration experiment in which the initial chamber volume was decreased by 8 m³ to simulate conditions achieved after 18 h of sampling. The wall loss rates labeled “other” are those calculated from quarterly calibration experiments.

is more uncertainty for the collection efficiency of seed particles in the AMS than in the DMA. Collection efficiency in the AMS increases as organic content of the particles increases, and because the seed particles do not contain organic material, they are more susceptible to bounce in the instrument and have a collection efficiency that is less than unity (Matthew et al., 2008). To calculate the mass of sulfate in the seed, m_{SO_4} , the following equation is used:

$$m_{\text{SO}_4} = V_{\text{seed}} \rho_{\text{seed}} \frac{\text{MW}_{\text{SO}_4}}{\text{MW}_{\text{seed}}} \quad (5)$$

where ρ_{seed} is the density of the seed particles, MW_{SO_4} is the molecular weight of sulfate, and MW_{seed} is the molecular weight of the seed particles. For dry AS seed, ρ_{seed} is 1.77 g cm^{-3} . In the upper bound limit, both suspended and deposited particles gain or lose organic material at the same rate; therefore, the organic-to-sulfate ratio of all particles of the same size is the same, and this ratio is determined from unit mass resolution AMS data. High-resolution analysis of the dominant sulfate ions, m/z 48 and 64, showed less than 1 % contribution of organic signal to the total ion signal; therefore, organic contribution to the unit mass resolution sulfate signal was negligible. Differences in the organic-to-sulfate ratio, r_{OS} , between unit mass resolution and high resolution data are less than 5 %, except during the first 2 h of growth when they are more variable at lower organic loading. To obtain the SOA mass, r_{OS} is multiplied by the initial mass of sulfate in the seed particles:

$$\Delta M_0 = m_{\text{SO}_4} r_{\text{OS}} \quad (6)$$

This equation is valid if the organic-to-sulfate ratio does not vary with particle size or if particle wall loss rates are constant over the particle size range of interest. In the Caltech chambers, particle wall loss rates depend on particle size so the latter assumption is not valid. Depending on the condensation behavior of the SOA, r_{OS} may depend on particle size (Hildebrandt et al., 2009; Riipinen et al., 2011). For the present experiments, data were not available to determine the size dependence of r_{OS} of the particles. For the purpose of calculating the upper bound wall loss corrected organic mass, it is assumed that r_{OS} does not vary with particle size. The implications of this assumption will be discussed in Sect. 3.4.

3 Results and discussion

3.1 SOA formation

Two experiments with the same initial conditions and 18 h of irradiation were performed to assess the reproducibility of initial conditions and SOA production (Table 2). For both AS seed and MS + SA seed, similar concentrations of *m*-xylene reacted and ΔM_0 formed after 18 h of irradiation were achieved. Given the consistency between matched experiments, it was not necessary to sample for the entire duration

of longer experiments. It was assumed that data collected during previous, shorter experiments are adequate to describe the same time period during longer experiments.

Figure 2 shows decay of *m*-xylene and ΔM_0 corrected for wall loss for both the upper and lower bound cases over 36 h of irradiation. The lower bound ΔM_0 and *m*-xylene data are a compilation of the 18-, 30-, and 36-h AS seed experiments (the 24-h experiment was omitted as noted earlier due to low seed particle volume), but the upper bound ΔM_0 data are from only the 36-h experiment because continuous data were available. The variation in the lower bound wall loss corrected mass concentration after peak growth is likely due to differences in number distributions during the 18-, 30-, and 36-h experiments. The peak in SOA formation occurs before all of the *m*-xylene has been reacted. For the lower bound case, ΔM_0 remains relatively stable after its peak, decreasing only slightly over 20 h of irradiation. For the upper bound case, ΔM_0 peaks at approximately the same time as in the lower bound case; however, there is a pronounced decay of ΔM_0 after the maximum is reached. Wall losses result in 43 % of the total volume concentration of particles deposited on the wall for the lower bound case and 56 % of ΔM_0 deposited on the wall for the upper bound case after 36 h. The behavior of ΔM_0 after peak growth will be discussed in Sect. 3.3.

Throughout each experiment, the OH concentration was approximately $2.5 \times 10^6 \text{ molec cm}^{-3}$, as estimated from the decay of *m*-xylene and simulated by a photochemical model (see Appendix A). After 36 h of irradiation, 40 % of the initial 4 ppm of H_2O_2 injected into the chamber remained unreacted.

3.2 SOA composition

Figure 3 shows the evolution in the elemental oxygen-to-carbon ratio (O:C) of the suspended particles for all 5 of the AS seeded experiments. O:C values overlap for all of the experiments with different irradiation durations. O:C decreases during the first 5 h of irradiation in all but the 36-h experiment. During the 36-h experiment, the sensitivity of the AMS sampling in W-mode was lower than that in the other aging experiments, which hindered the detection of initially-formed SOA. The O:C calculated using V-mode data (not shown) decreases during the first 5 h of irradiation for all 5 of the aging experiments. The dominant trend in O:C begins after 5 h. After this time, O:C gradually increases at an average rate of 0.0019 h^{-1} for the remainder of the irradiation period. The minimum in O:C occurs before the maximum ΔM_0 is reached.

The mass spectral parameter f_{44} is commonly used to characterize SOA chemical composition. Aiken et al. (2008) determined a relationship between O:C and f_{44} for ambient aerosol in Mexico City: $\text{O:C} = (3.82 \pm 0.05) \times f_{44} + (0.0794 \pm 0.0070)$ for f_{44} ranging from 0 to 0.25. The SOA in the current set of experiments does not follow the same

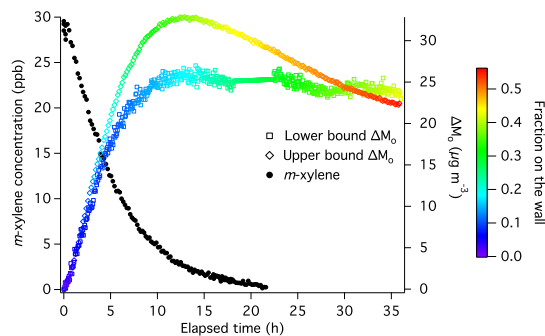


Fig. 2. SOA mass (right axis), corrected for particle wall losses, and *m*-xylene (left axis) for 36 h of OH exposure using AS seed. The lower bound ΔM_0 is calculated assuming that, once deposited, particles on the walls do not interact with gases in the chamber. The upper bound ΔM_0 assumes that, once deposited, particles continue to exhibit the same gas-particle partitioning behavior as suspended particles. The fraction on the wall for the lower bound is the ratio of particle volume on the wall to total particle volume, both suspended and deposited, and includes seed volume. The fraction on the wall for the upper bound is the ratio of organic mass concentration on the wall to the total organic mass concentration.

trend as the Mexico City SOA, and exhibits trendline of $\text{O:C} = (1.42 \pm 0.04) \times f_{44} + (0.439 \pm 0.005)$ over a range of 0.10 to 0.14 of f_{44} . Although the data for *m*-xylene SOA do not follow the same trendline as the Mexico City data, they lie within the scatter of the Mexico City data (Fig. 4). Using the same AMS instrument as the current study, Chhabra et al. (2010) found that the O:C and f_{44} of SOA from aromatics, isoprene, and glyoxal did not lie along the trendline reported in Aiken et al., but the O:C and f_{44} of SOA from α -pinene and naphthalene did. In general, if CO_2^+ contributed most of the oxygen signal in the spectra, then the O:C and f_{44} of the SOA more closely matched those predicted by the trendline from the Mexico City data. The correlation between O:C and f_{44} for *m*-xylene SOA in the present work differs from that of Lambe et al. (2011), who observed that *m*-xylene SOA follows the same trendline as the Mexico City data. The range of f_{44} values observed by Lambe et al. is much larger than that in the present work, initial hydrocarbon loadings are higher, and OH exposure is 2–3 times greater than the maximum OH exposure achieved in the present work ($3.2 \times 10^{11} \text{ molec cm}^{-3} \text{ s}$). Any of these factors could contribute to the different correlations between O:C and f_{44} . The factor most likely to explain the discrepancy between the correlation in the present work and that in Lambe et al. is the difference in OH exposure. At higher OH exposure, the SOA is likely to be more oxidized, and CO_2^+ is likely to be a major contributor to the oxygen signal in the spectra.

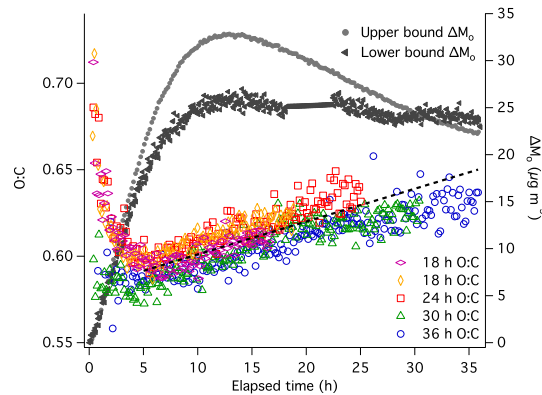


Fig. 3. SOA mass (right axis) and O:C elemental composition (left axis) over 36 h of OH exposure using AS seed. After hour 5, the O:C increases at an average rate of 0.0019 h^{-1} (dashed line).

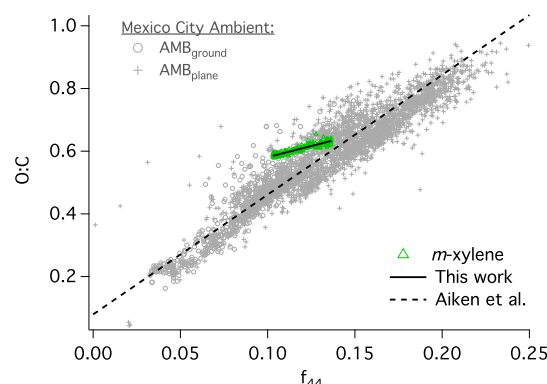


Fig. 4. Correlation of O:C with f_{44} for SOA from *m*-xylene in the present study and Mexico City ambient aerosol from Aiken et al. (2008).

The evolution of *m*-xylene SOA is also represented in f_{44} – f_{43} space (Fig. 5). The change in O:C, derived from the correlation specific to *m*-xylene, is also shown. The marker size is a function of the concentration of suspended organics, normalized to suspended sulfate concentration to account for wall losses. Overall, low- NO_x *m*-xylene SOA exhibits higher f_{43} than the typical range of ambient SOA observed by Ng et al. (2010) and lies to the right of the triangular region derived for ambient SOA. At the beginning of irradiation when the organic mass loading is small, the SOA has a higher f_{44} and a lower f_{43} . As SOA continues to form, f_{44} decreases and f_{43} increases until approximately 5 h of irradiation, at which time the trends reverse. For the remaining duration of irradiation, f_{44} increases and f_{43} decreases, resulting in a progression of the SOA characteristic of the behavior of

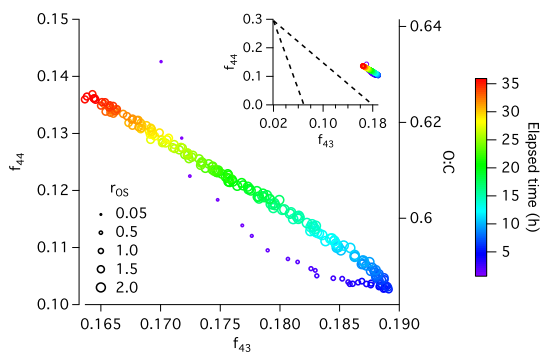


Fig. 5. Evolution of f_{43} , f_{44} , and O:C for 36 h of OH exposure. This system lies to the right of the triangular region in which typical ambient aerosol residues, as shown by the dashed lines in the inset (Ng et al., 2010). Marker size denotes the organic-to-sulfate ratio, r_{OS} , of suspended particles.

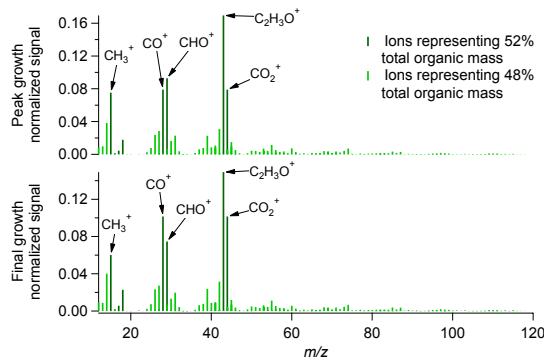


Fig. 6. Average AMS high-resolution organic mass spectra at the time of peak growth and at the end of the experiment (final growth) for the 36-h aging experiment. Prominent peaks are identified. The mass of CO^+ is estimated to equal that of CO_2^+ .

more-aged ambient SOA. The time at which the path reversal in f_{44} – f_{43} space occurs is the same as that at which the minimum in O:C occurs. Curvature in f_{44} – f_{43} space has been observed in other studies (Kroll et al., 2009; Ng et al., 2010; Chhabra et al., 2011; Lee et al., 2011; Lambe et al., 2011). Lambe et al. did not observe curvature in f_{44} – f_{43} space for *m*-xylene SOA, and the curvature observed in the present study occurred for lower OH exposures than the lowest value attained by Lambe et al.. It is possible that the OH exposure levels used to form *m*-xylene SOA in Lambe et al. were too large to observe the curvature.

The high-resolution AMS mass spectra provide clues to the trends in O:C, f_{44} , and f_{43} . The average mass spectra at peak organic growth and at the end of the 36-h aging experiment are shown in Fig. 6. Figure 7 shows the time trends

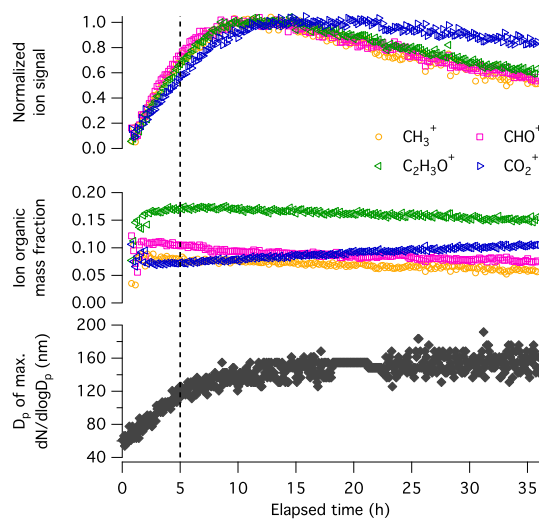


Fig. 7. Evolution of SOA chemical composition from high-resolution AMS measurements and diameter of the maximum number distribution of suspended particles. In the top panel, the ion signal is normalized by sulfate to account for particle wall losses. The sulfate-normalized ion signal is then scaled by the average value at the peak concentration. The middle panel shows the fractional contribution of each ion to the total organic mass signal. A relative ionization efficiency of 1.4 is used when calculating the organic ion concentration. The dashed line at 5 h corresponds to the reversal in trend of O:C.

of the 4 dominant organic ions (CH_3^+ , CHO^+ , $\text{C}_2\text{H}_3\text{O}^+$, and CO_2^+) in the aerosol mass spectra and the maximum of the suspended particle size distribution throughout 36 h of oxidation. Excluding CO_2^+ , these ions account for 30–35 % of the total organic signal throughout the experiment. When organic CO_2^+ and the ions whose organic contributions are assumed to correlate with it (CO^+ , H_2O^+ , OH^+ , and O^+) are included, the mass fraction of the organic signal is approximately 52 %. In the top panel of Fig. 7, the time trends of the normalized, wall-loss corrected ion signals are shown. To obtain this, the ion signal was divided by the sulfate signal to correct for wall losses. The sulfate-normalized ion signal was then scaled by its average value at the peak concentration. In the middle panel, the fractional contribution of each ion to the total organic signal is shown. The bottom panel shows the particle diameter (D_p) of the maximum of the suspended particle size distribution. The most rapid change in D_p occurs during the first 5 h of irradiation. The amount of each of the 4 ions in the particles increases during this time (top panel). After 5 h, D_p changes more slowly, and the contribution of each ion to the spectra begins to peak. CHO^+ reaches a maximum most quickly, followed by CH_3^+ and $\text{C}_2\text{H}_3\text{O}^+$. CO_2^+ peaks later than the other ions. After most of the ions peak, their contribution to the spectra decreases for the remainder

of the experiment; however, the amount of CO_2^+ shows much less of a decrease, suggesting that compounds that contribute to the CO_2^+ signal have a lower tendency to be removed from the particles than those that contribute to the other ion signals.

Shortly after the onset of irradiation, CO_2^+ constitutes the largest fraction of the organic signal, likely from the condensation of low-volatility organics. As irradiation continues, the CO_2^+ fraction of the organic signal decreases as semivolatile material represented by the other ions, especially $\text{C}_2\text{H}_3\text{O}^+$, begins to partition to the particles. Once the rate of particle growth slows, the fraction of CO_2^+ increases because the contribution of CO_2^+ to the mass spectra is still increasing, whereas the amounts of the other ions are beginning to stabilize and then decrease. The increase in the organic fraction of CO_2^+ continues throughout the duration of the experiment caused by a larger decrease in the amounts of the other ions in the particle mass spectra than CO_2^+ .

3.3 Fate of SOA after peak growth

After peak growth, a decrease in most of the major organic ions and the total organic mass is observed (Figs. 2 and 7). The magnitude of the decrease in ΔM_o is much greater for the upper bound wall loss correction than that for the lower bound wall loss correction, suggesting that either the process causing the decrease in ΔM_o has a larger effect on the upper bound wall loss case or that an incorrect assumption was made for one of the wall loss corrections. For the upper bound wall loss correction, r_{OS} was assumed to be constant such that the r_{OS} of the suspended particles was equivalent to that of the deposited particles. If this is not the case, the mass lost to the walls may be over- or underestimated. Implications of the size-dependence of r_{OS} on the upper and lower bound wall loss correction and its effects on the conclusions of the present section will be discussed in Sect. 3.4.

If the organic mass lost to the wall was correctly calculated for both upper and lower bound cases, a possible explanation for the decrease in ΔM_o after peak growth is repartitioning of semivolatiles to the gas phase. As irradiation continues, semivolatiles in the gas phase can undergo reaction with OH or photolysis to form higher-volatility products, or they may be lost to the walls. As the concentration of a semivolatile in the gas phase decreases from fragmentation reactions or wall loss, repartitioning can occur to maintain gas-particle equilibrium. OH can also react with the particle surface, forming higher volatility fragmentation products that evaporate and decrease the particle organic mass. These processes are summarized in Fig. 8. Evaporation of semivolatiles is expected to have a greater effect on ΔM_o in the upper bound limit because all particles are assumed to undergo gas-particle partitioning, opposed to only the suspended particles in the lower bound limit, thus a higher decrease in ΔM_o should be expected in the upper bound limit.

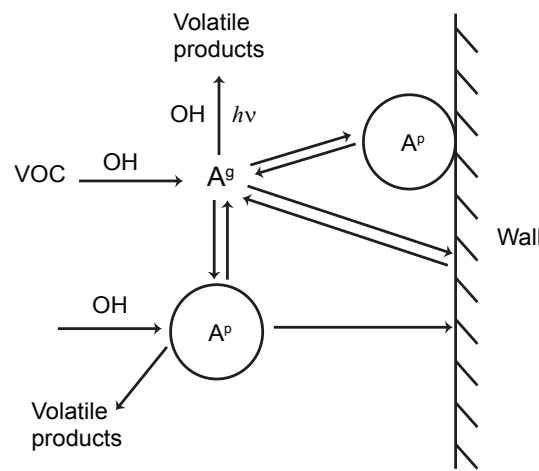


Fig. 8. Sources and sinks of a semivolatile gas-phase species, A^g , and particles containing the condensed semivolatile species, A^p , during SOA aging. We do not explicitly indicate in the sketch processes by which the particle-phase A^p attains a semisolid state, greatly affecting continued exchange with the gas phase (Virtanen et al., 2010; Vaden et al., 2010, 2011; Shiraiwa et al., 2011).

Semivolatile species are expected to repartition from the particle phase more easily than low volatility species. This behavior is observed with the organic ions $\text{C}_2\text{H}_3\text{O}^+$, characteristic of semivolatile oxygenated organic aerosol (SV-OOA), and CO_2^+ , characteristic of low volatility oxygenated organic aerosol (LV-OOA). The amount of $\text{C}_2\text{H}_3\text{O}^+$ in the particle mass spectra increases faster than CO_2^+ and shows a much greater decrease than CO_2^+ as the experiment progresses. There is a slight decrease in CO_2^+ at longer irradiation times, and it is possible that the uptake of low volatility species is not completely irreversible, allowing for some evaporation.

Evaporation of particles is characterized by a shift of the D_p at the maximum of the size distribution to smaller size. This shift was not observed in the aging experiments, as shown in the bottom panel of Fig. 7 where D_p increased slightly after the peak organic loading was attained around 12 h. The two main processes affecting the particle size distribution in chamber experiments are gas-particle partitioning and wall loss. In the Caltech chambers, wall loss rates are at a minimum for particles of diameters between 200 and 300 nm (Fig. 1). During the aging experiments, the D_p at the size distribution maximum is below the 200–300 nm minimum in wall loss. If evaporation is occurring, the rate of wall loss will increase as particles get smaller. As a result, the greater loss of small particles will cause size distribution, characterized by the D_p at its maximum, to shift slightly toward the 200–300 nm minimum in wall loss rate. Both the evaporation and wall loss processes are slow; therefore, the

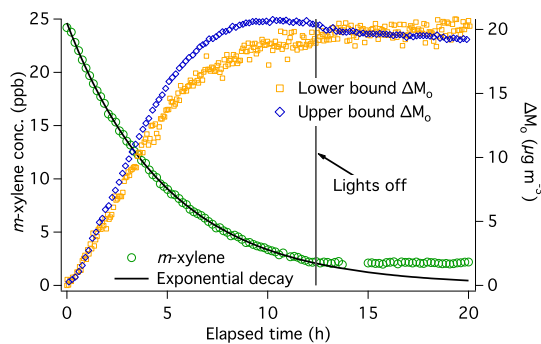


Fig. 9. Trends in *m*-xylene concentration (left axis) and ΔM_0 (right axis) when irradiation is stopped once peak ΔM_0 is attained.

two processes will tend to counteract each other with respect to their effects on the dynamics of the aerosol size distribution, and no change in D_p at the maximum of the size distribution is observed. It is also possible that the upper bound wall loss correction over-predicts the amount of evaporation occurring (see Sect. 3.4). In this case, the D_p at the size distribution maximum would only be expected to increase slightly toward the 200–300 nm minimum in wall loss rate.

To determine the extent to which photochemical processes are affecting the aerosol after peak growth, an experiment was performed in which the lights were turned off after 12.4 h of irradiation (Fig. 9). Production of OH ceases, and shortly thereafter, OH is no longer present in the chambers. The *m*-xylene concentration stabilizes after lights are turned off, and the substantial decrease in the upper bound ΔM_0 is not observed with the lights off. The lower bound ΔM_0 increases after lights are turned off to result in a 5 % change in mass after 8 h. This increase could be the result of uncertainty induced by the wall loss correction or condensation of vapors as the chamber cooled after irradiation stopped from 24 °C to 19 °C during hours 12.4 to 16. The latter process is not observed in the upper bound ΔM_0 , but condensation could be masked by uncertainty in the wall loss correction method, discussed in Sect. 3.4. Despite the potential uncertainties of the wall loss correction and the cooling of the chamber, the decrease observed in the lower bound ΔM_0 in the 36-h aging experiment is not observed after irradiation ceases. After the lights are turned off, the chemical composition of the particles also stops changing significantly. This is shown in f_{44} – f_{43} space in Fig. 10. While the aerosol forms, f_{43} decreases and f_{44} increases; however, after the lights are turned off, the rates of change of both f_{43} and f_{44} decrease substantially. In the absence of irradiation, a semivolatile species in the gas phase, A^g , can partition to and from particles or be lost to the walls (Fig. 8). After irradiation stops, the rate of change in the amount and composition of the particles decreases substantially; therefore, no significant repartitioning is occur-

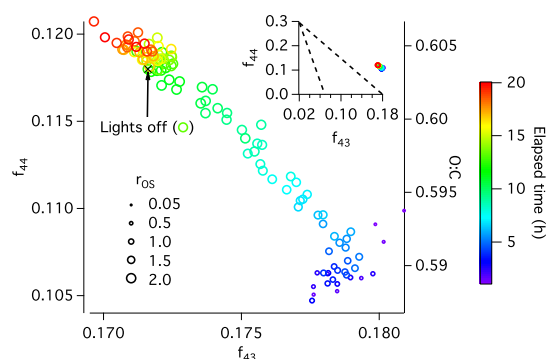


Fig. 10. Evolution of f_{43} , f_{44} , and O:C of *m*-xylene SOA. Irradiation was stopped after 12.4 h, corresponding to the peak of ΔM_0 . This point is denoted by the “x”. Marker size denotes the organic-to-sulfate ratio, r_{OS} , of suspended particles. After irradiation stops, the chemical composition of the SOA does not change significantly. The inset shows the position of the data with respect to the triangular region characteristic of ambient SOA bounded by the dashed lines, as defined by Ng et al. (2010).

ring. Under these conditions, only vapor phase wall loss is expected to cause repartitioning; therefore, vapor phase wall loss is not significant in this system. If minimal repartitioning is observed without irradiation, and if there are no substantial vapor phase wall losses, then repartitioning must be driven by photochemical processes that affect the chemical composition of the gases and SOA.

It was not possible to distinguish among the photochemical process occurring: reaction of OH with semivolatiles; reaction of OH with particles; and photolysis of semivolatiles. The photochemical model described in Appendix A was used to estimate lifetimes for OH against reaction with particles, OH against reaction with semivolatiles, semivolatiles against reaction with OH, and semivolatiles against photolysis. The lifetime of OH against reaction with gas-phase species A^g , τ_{OH+A} (s), is

$$\tau_{OH+A} = \frac{1}{k_{A+OH} c_A} \quad (7)$$

where k_{A+OH} (cm³ molec⁻¹ s⁻¹) is the reaction rate constant and c_A (molec cm⁻³) is the gas-phase concentration of A. Using the combined concentrations of species ROOH, ROHOH, ROHOOH, and EPOXOOH and an average rate constant $k_{OH} = 1 \times 10^{-10}$ cm³ molec⁻¹ s⁻¹ (Table 3), $\tau_{OH+A} \approx 0.2$ s. The heterogeneous reaction of OH with a particle surface is assumed to be pseudo-first order in terms of OH (Seinfeld and Pandis, 2006). The characteristic time for this process, τ_{OH+P} (s), can be calculated by:

$$\tau_{OH+P} = \frac{1}{\frac{1}{4} \gamma \bar{c}_{OH} A_p} \quad (8)$$

Table 3. Rate constants for the photochemical model.

Rate constant ($\text{cm}^3 \text{ molec}^{-1} \text{ s}^{-1}$)	Source
$j_{\text{H}_2\text{O}_2} = 2.9 \times 10^{-6} \text{ (s}^{-1}\text{)}$	Sander et al. (2011)
$k_1 = 1.8 \times 10^{-12}$	Sander et al. (2011)
$k_2 = 2.31 \times 10^{-11}$	Calvert et al. (2002)
$k_3 = 9.8 \times 10^{-13}$	Birdsall et al. (2010)
$k_4 = 1.96 \times 10^{-11}$	MCM (Jenkin et al., 2003, Bloss et al., 2005)
$k_5 = 8.02 \times 10^{-11}$	MCM
$j_{\text{EPOX}} = 1.24 \times 10^{-4} \text{ (s}^{-1}\text{)}$	MCM and Sander et al. (2011)
$k_6 = 9.1 \times 10^{-11}$	MCM
$k_7 = 1.17 \times 10^{-10}$	MCM
$j_{\text{ROOH}} = 2.1 \times 10^{-6} \text{ (s}^{-1}\text{)}$	Sander et al. (2011)
$k_8 = 1.96 \times 10^{-11}$	MCM
$k_9 = 7.41 \times 10^{-11}$	MCM
$k_{10} = 1.96 \times 10^{-11}$	MCM
$k_{11} = 1.13 \times 10^{-10}$	MCM
$k_{12} = 2.05 \times 10^{-10}$	MCM
$k_{13} = 1.4 \times 10^{-12}$	Sander et al. (2011)
$k_{14} = 1.1 \times 10^{-10}$	Sander et al. (2011)

where γ is an uptake coefficient, here assumed to be 1, A_p ($\text{cm}^2 \text{ cm}^{-3}$) is the surface area concentration of the particles, and $\overline{c_{\text{OH}}}$ (cm s^{-1}) is given by

$$\overline{c_{\text{OH}}} = \left(\frac{8RT}{\pi \text{MW}_{\text{OH}}} \right)^{\frac{1}{2}} \quad (9)$$

where T (K) is temperature and MW_{OH} (kg mol^{-1}) is the molecular weight of OH. The particle surface area was calculated from measured particle number distributions. Based on the upper and lower bound wall loss corrections, $\tau_{\text{OH}+\text{P}}$ ranges from 6–13.5 s, corresponding to particle surface areas of $(0.47 - 1.1) \times 10^{-5} \text{ cm}^2 \text{ cm}^{-3}$.

Some of the semivolatile species used to determine $\tau_{\text{OH}+\text{A}}$ can also photolyze. The lifetimes of these species, ROOH, ROHOOH, and EPOXOOH, against OH reaction and photolysis was also calculated to determine if photolysis is expected to be a large sink of gas-phase species. The lifetime of these species against reaction with OH, $\tau_{\text{A}+\text{OH}}$ (s), is

$$\tau_{\text{A}+\text{OH}} = \frac{1}{k_{\text{A}+\text{OH}} c_{\text{OH}}} \quad (10)$$

where c_{OH} (molec cm^{-3}) is the OH concentration, which was estimated to be $2.5 \times 10^6 \text{ molec cm}^{-3}$ from the measured *m*-xylene decay. Under this condition, $\tau_{\text{A}+\text{OH}} = 4.0 \times 10^4 \text{ s}$. The lifetime of these species against photolysis, $\tau_{\text{A}+\text{h}\nu}$, is calculated by:

$$\tau_{\text{A}+\text{h}\nu} = \frac{1}{j_{\text{ROOH}}} \quad (11)$$

where j_{ROOH} is the photolysis rate constant of an organic peroxide, as described in Appendix A. The characteristic lifetime against photolysis is estimated as $4.7 \times 10^5 \text{ s}$. Photolysis is an order of magnitude slower than reaction with OH, and photolysis is not expected to be a major sink of gas-phase species. Changes in particle composition are likely driven by continued oxidation of the gas phase, although OH reaction with particle surfaces cannot be categorically dismissed.

The continued oxidation of semivolatile species is apparent upon examination of possible gas-phase *m*-xylene oxidation products using the CIMS (Fig. 11). The top panel shows the time trace of m/z 207, which has the same m/z as the predicted reagent ion clustering of first-generation oxidation products ROH (MW+85) and ROOH (MW+19) in the model (Table 4). This m/z signal increases rapidly and peaks at 3–4 h of irradiation. When lights are turned off during the experiment, the decay slows significantly. The middle panel shows the time trace of m/z 223, which has the same m/z as the predicted reagent ion clustering of second-generation oxidation products ROHOH (MW+85), ROHOOH (MW+19), and EPOXOOH (MW+19). Again, this m/z signal increases rapidly and peaks slightly later at 4–5 h irradiation. When the lights are turned off, the signal stabilizes. The photochemical model predicts the peak of the first generation product concentrations to occur about an hour before that of the second generation product concentrations, and the time difference between the peak of the CIMS signals at m/z 207 and m/z 223 is consistent with the model output. The bottom panel shows the time trace of m/z 271, which has the same m/z as the predicted reagent ion clustering of third-generation oxidation product (MW+85) formed by the EPOXOOH + OH reaction ($\text{prod}_{\text{EPOXOOH}+\text{OH}}$ in the model). From model predictions, this compound with predicted reagent ion clustering at m/z 271 should form more slowly. The signal at m/z 271 peaks at 13–14 h of irradiation and does not decrease after irradiation ceases. The behavior of these signals is consistent with multiple generations of oxidation. The changes are clearly photochemically driven. Vapor-phase wall loss is not a significant sink of compounds contributing to these signals, indicated by the absence of decay after the lights are turned off.

3.4 Role of organic-to-sulfate ratio in particle wall loss corrections

The partitioning behavior of SOA precursors affects how these species condense onto a particle size distribution (Ripinen et al., 2011). If condensation is limited by diffusion, which is typically the case for essentially non-volatile compounds, the rate of condensation depends on the surface area of the particle size distribution (Seinfeld and Pandis, 2006); in that case the organic growth tends to occur on particles with smaller D_p as this is the particle size regime where the surface area is greatest. For organics exhibiting diffusion-limited behavior, organic condensation on AS seed particles

Table 4. Compounds represented in the photochemical model.

Compound	Structure	Formula
RH		C ₈ H ₁₂
RO ₂		C ₈ H ₁₁ O ₅
EPOX		C ₈ H ₁₀ O ₃
ROH		C ₈ H ₁₀ O
ROOH		C ₈ H ₁₂ O ₅
EPOXO ₂		C ₈ H ₁₁ O ₆
ROHO ₂		C ₈ H ₁₁ O ₆
ROHOH		C ₈ H ₁₀ O ₂
RO		C ₈ H ₉ O
EPOXOOH		C ₈ H ₁₂ O ₆
ROHOOH		C ₈ H ₁₂ O ₆
prodEPOXOOH+OH	e.g.	C ₈ H ₁₂ O ₅

tends to form organic and sulfate mass distributions such that mean D_p of the organic mass distribution is smaller than that of the sulfate distribution. If condensation is controlled by gas-particle partitioning equilibrium, which is typically the case for semi-volatile compounds, these species will tend to condense preferentially into the particle size range where the mass concentration is greatest, i.e. a majority of the organic growth will occur on particles with larger D_p (Zhang et al., 2011). In this case, the organic mass distribution will peak at a larger D_p than the sulfate mass distribution. Because information about the organic and sulfate mass distributions was not available for the present experiments, a simulation was performed to assess the effects of different shapes of organic and sulfate mass distributions on the upper bound wall loss correction method.

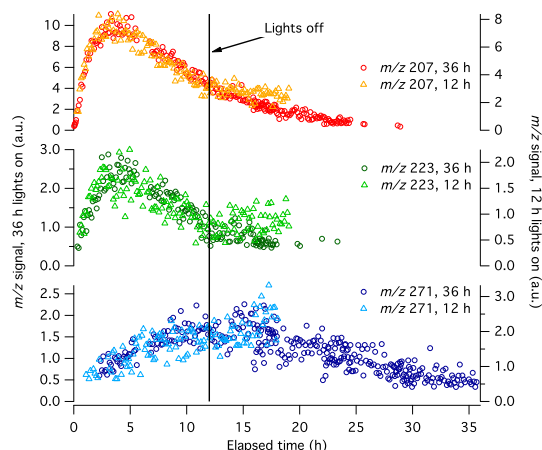


Fig. 11. Time evolution of products formed during *m*-xylene oxidation detected by the CIMS. The signals labeled 36 h were recorded during the set of experiments in which the chamber contents were irradiated for 36 h. The signals labeled 12 h were recorded during the experiment in which the lights were turned off after 12.4 h of irradiation and remained off for the remainder of the experiment.

Three different pairs of organic and sulfate mass distributions consistent with the measured number distribution and r_{OS} were created from the suspended particle number distribution averaged between hours 12 and 12.5 of irradiation from the combined 36 h aging experiment in order to determine the uncertainty in the upper bound wall loss correction induced by size-dependent r_{OS} (Fig. 12). The peak of the measured aerosol number distribution occurs at a D_p smaller than that at which the wall loss rate is at its minimum, and the wall loss rate increases moving from lower D_p to higher D_p across the measured number distribution (not shown). Each of the distributions in Fig. 12 is characterized by the same total particle number distribution, an r_{OS} of 2.00, and an organic mass concentration of 22.7–22.8 $\mu\text{g m}^{-3}$. Case I represents condensation resulting from equilibrium gas-particle partitioning, and Case III represents condensation resulting from diffusion-limited growth. In Case II all particles have the same r_{OS} .

The aerosol size distribution was subjected to 24 h of wall loss at the rates applied to the experimental number distributions, ignoring condensation (growth and evaporation are assumed to cease) and coagulation. For each of the cases, r_{OS} of the suspended particles and the upper bound wall-loss corrected mass concentration were calculated as a function of time (Fig. 13). In Case I, r_{OS} of suspended particles increased by about 10 % over 24 h as particles with a lower r_{OS} were preferentially lost to the walls. Because r_{OS} of suspended particles is higher than that of deposited particles, using r_{OS} of suspended particles to represent deposited

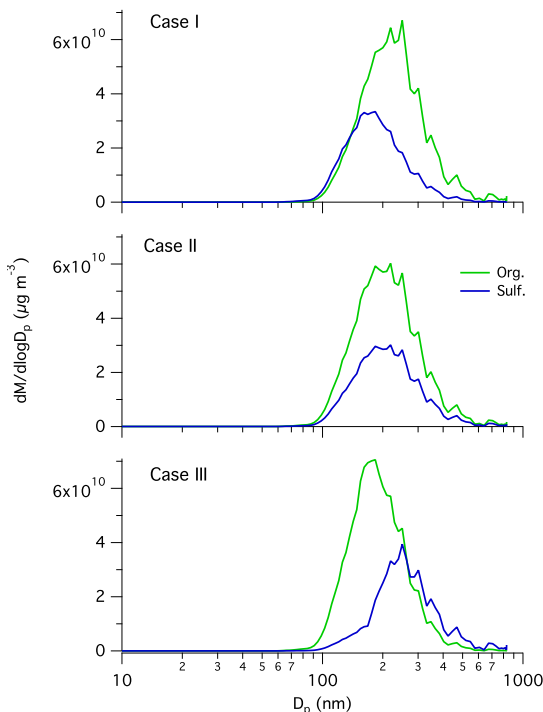


Fig. 12. Organic and sulfate mass distributions used in a simulation to assess the effect of size-dependent r_{OS} on the upper bound organic mass wall loss correction. All mass distributions are derived from the same observed particle number distribution and have r_{OS} of 2.00 and an organic mass concentration of $22.7\text{--}22.8 \mu\text{g m}^{-3}$. Case I is representative of condensation governed by gas-particle equilibrium partitioning (see text), and Case III is representative of condensation governed by diffusion-limited growth (see text). In Case II, r_{OS} is constant for all D_p .

particles leads to an overestimation of organic mass lost to the walls. The over-prediction of wall-loss corrected organic mass concentration is about 10 %. In Case II, r_{OS} of suspended and deposited particles are the same by definition, and the predicted wall-loss corrected organic mass was estimated properly. In Case III r_{OS} of deposited particles is greater than that of suspended particles, and r_{OS} of suspended particles decreased by about 10 % over 24 h because particles with a higher r_{OS} were preferentially lost to the walls. This resulted in an under-prediction of wall-loss corrected organic mass concentration by about 10 %.

Organic and sulfate mass distributions have been reported for toluene SOA condensed onto AS seed and are indicative of diffusion-limited condensation (Hildebrandt et al., 2009). If *m*-xylene SOA formation occurs by processes similar to those of toluene, the mass distributions during the present experiments will most closely resemble Case III, and increase-

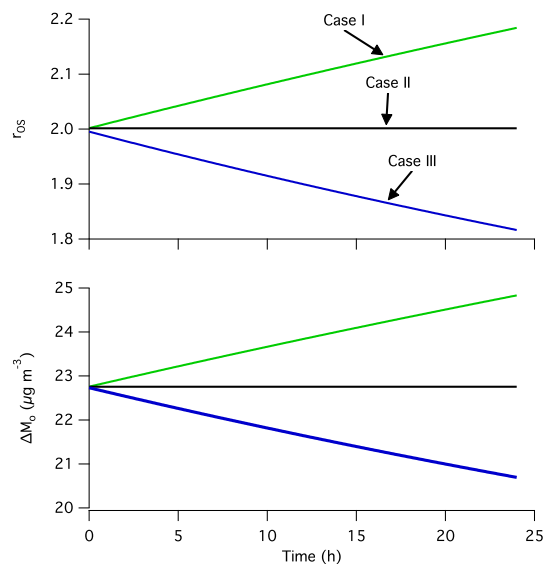


Fig. 13. Effect of 24 h of wall loss on the mass distributions in Fig. 12. The top panel shows the suspended particle organic-to-sulfate ratio, r_{OS} , as a function of time for each case, and the bottom panel shows the upper bound wall-loss corrected organic mass concentration as a function of time for each case.

ing under-prediction of the upper bound wall-loss corrected organic mass concentration may occur with time. During the 36 h combined aging experiments, the measured r_{OS} of suspended particles decreased from 2.1 to 1.9 between hours 12.4 and 20 and continued to decrease linearly to 1.4 at 36 h. Between hours 12.4 and 20, the wall-loss corrected organic mass concentration decreased from 32.8 to $30 \mu\text{g m}^{-3}$. By hour 36, it had decreased to $22.3 \mu\text{g m}^{-3}$. The changes in r_{OS} and mass loss can be compared to those in the experiment in which irradiation ceased after 12 h and in which only particle wall loss occurred after that time. Between hours 12.4 and 20, r_{OS} decreased from 1.50 to 1.42, and the wall-loss corrected mass concentration decreased from 20.5 to $19.2 \mu\text{g m}^{-3}$. The decrease in both organic-to-sulfate ratio and wall-loss corrected mass concentration in the 12-h irradiation experiment are indicative of wall loss of an aerosol size distribution characterized by diffusion-limited growth. The experimental conditions of the 36-h experiment were similar to the 12-h irradiation experiment; however, both the initial *m*-xylene concentration and the seed volume concentration in the 12-h irradiation experiment were lower than those in the combined 36-h aging experiments, and r_{OS} is expected to differ as a result. Despite the differences, it is expected that the size distribution of the suspended particles in hours 12.4–20 during 36-h experiment should behave similarly to the size distribution of particles during hours 12.4–20 of the

12-h irradiation experiment if only particle wall loss is occurring. The fractional decrease in r_{OS} during hours 12.4–20 of the 36-h irradiation experiment is approximately double that of the 12-h irradiation experiment, suggesting that an additional process besides particle wall loss, such as gas-particle repartitioning due to evaporation, affected the suspended particle r_{OS} . The magnitude of evaporation, however, may not be as large as originally thought due to uncertainty in the upper bound wall loss correction method.

The lower bound wall loss correction should be unaffected by size-dependent r_{OS} distributions. The number and size of deposited particles is calculated independently of particle composition and is added back to the number distribution of suspended particles to calculate the total volume of particles. In obtaining the total volume of organics, the volume of seed or other background particles is subtracted from the total volume. This calculation assumes that the seed or background particle volume does not change during an experiment.

3.5 Acidic seed effects

Aging experiments were also performed using acidic MS + SA seed to determine the extent to which particle acidity affects chemical aging of *m*-xylene SOA. Figure 14 shows the elemental ratios for both AS and MS + SA seeded experiments. No difference between the acidic and neutral seeds for *m*-xylene-derived SOA is observed. Ng et al. (2007) did not observe a difference in yields for low-NO_x *m*-xylene SOA with neutral and acidic seed particles; therefore, it is plausible that the chemical composition of the aerosol condensed onto the two types of seed particles is similar.

4 Conclusions

Laboratory chamber studies provide fundamental information on the mechanisms of formation of SOA. The duration of chamber experiments is limited by several factors, including wall loss of particles and vapors and depletion of chamber air through instrument sampling. Laboratory experiments attempt to approach durations of OH radical exposure corresponding to those of particles in the atmosphere, on the order of a week, through enhanced OH radical levels. In the present work we extend the duration of chamber experiments by sampling protocols that minimize the amount of chamber air removed over the course of the experiment. The protocol developed here allows experiments up to 36 h duration. Hydroxyl radical levels in the experiments reported here are roughly at atmospheric levels. We address SOA formation from the photooxidation of *m*-xylene, an important anthropogenic precursor to organic aerosol. The extended duration experiments provide a view into the multi-generational chemistry involved in *m*-xylene SOA formation that can be expected to be occurring in the atmosphere. Although the current work studies only low-NO_x chemistry, the *m*-xylene

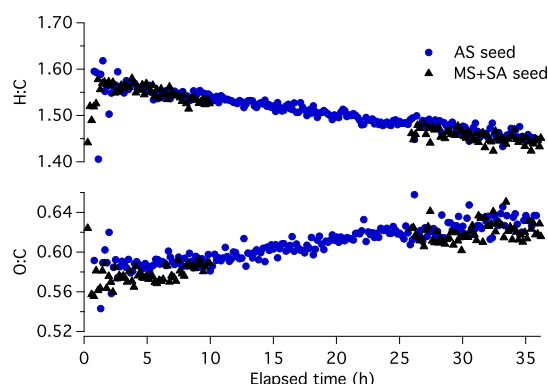


Fig. 14. Elemental ratios of *m*-xylene aerosol condensed onto neutral (AS) and acidic (MS + SA) seed particles.

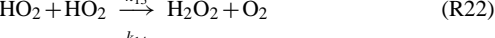
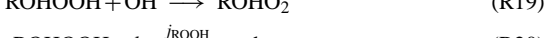
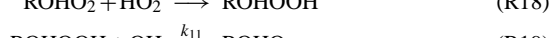
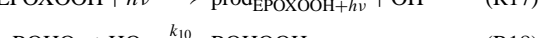
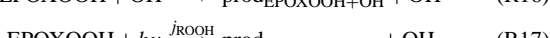
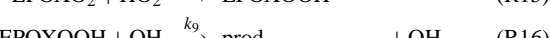
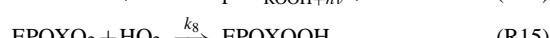
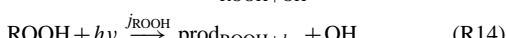
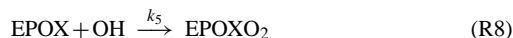
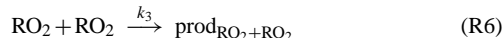
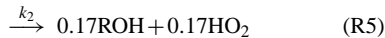
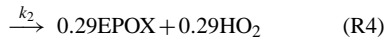
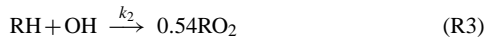
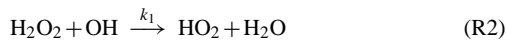
oxidation mechanism leading to SOA formation under high-NO_x conditions is also expected to follow multi-generational chemistry (Kwok et al., 1997; Zhao et al., 2005; Ng et al., 2007; Song et al., 2007; Noda et al., 2009; Birdsall et al., 2010). The generations of oxidation of a precursor volatile organic compound can lead to functionalized products of ever decreasing volatility, characterized by increasing elemental O:C ratio, as well as to products of higher volatility that do not contribute to SOA. Based on CIMS measurements, there is strong evidence of gas-phase loss of higher generation products. That this process involves photooxidation or photolysis is confirmed by the absence of changes in total aerosol amount when irradiation is stopped. Wall loss of vapor can be excluded as the cause of this behavior. Estimates of reaction timescales suggest that gas-phase processes are most likely involved in this latter stage of aging, although direct OH reaction with the surface of the particles cannot be ruled out. Finally, the present work offers a protocol for laboratory chamber experiments to attain times approaching more closely those of atmospheric aerosol residence times.

Appendix A

Photochemical model

To estimate both OH concentration and the importance of OH reaction with later-generation oxidation products, a photochemical model (Reactions R1–R23 below) was constructed. Products through three generations of oxidation are included. Primary oxidation products are those suggested by Birdsall et al. (2010) and Zhao et al. (2005) with product yields and further oxidative pathways as derived from the MCM (Jenkin et al., 2003; Bloss et al., 2005). Values of rate constants are listed in Table 3, and compounds represented in the model are given in Table 4. Photolysis rate constants are calculated using the irradiance spectrum measured for the chamber

lights and absorption cross section values and quantum yields from Sander et al. (2011). The following reactions are included:



Neither gas-particle partitioning nor vapor-phase wall loss was included in the model because there is not sufficient information about either process to accurately represent it in the model. Vapor-phase wall loss is assumed to be minor (Fig. 11) and should not have a large effect on gas species concentrations.

Acknowledgements. This work was supported by the Office of Science (Biological and Environmental Research), US Department of Energy Grant DE-SC 0006626, and National Science Foundation Grant AGS-1057183. The CIMS instrument was purchased as part of a major research instrumentation grant from the National Science Foundation (Grant ATM-0619783); assembly and testing was supported by the Davidow Discovery Fund. We thank Katherine Schilling and ManNin Chan for experimental assistance

and Arthur Chan for helpful discussion. We thank the reviewers for useful feedback on the discussions paper. Christine Loza, Lindsay Yee, and Jill Craven were supported by National Science Foundation Graduate Research Fellowships.

Edited by: N. M. Donahue

References

Aiken, A. C., DeCarlo, P. F., Kroll, J. H., Worsnop, D. R., Huffman, J. A., Docherty, K. S., Ulbrich, I. M., Mohr, C., Kimmel, J. R., Sueper, D., Sun, Y., Zhang, Q., Trimborn, A., Northway, M., Ziemann, P. J., Canagaratna, M. R., Onasch, T. B., Alfarra, M. R., Prevot, A. S. H., Dommen, J., Duplissy, J., Metzger, A., Baltensperger, U., and Jimenez, J. L.: O/C and OM/OC ratios of primary, secondary, and ambient organic aerosols with high-resolution time-of-flight aerosol mass spectrometry, *Environ. Sci. Technol.*, 42, 4478–4485, doi:10.1021/es703009q, 2008.

Balkanski, Y. J., Jacob, D. J., D. J., Gardner, G. M., Graustein, W. C., and Turekian, K. K.: Transport and residence times of tropospheric aerosols inferred from a global 3-dimensional simulation of PB-210, *J. Geophys. Res.–Atmos.*, 98, 20573–20586, doi:10.1029/93JD02456, 1993.

Birdsall, A. W., Andreoni, J. F., and Elrod, M. J.: Investigation of the role of bicyclic peroxy radicals in the oxidation mechanism of toluene, *J. Phys. Chem. A*, 114, 10655–10663, doi:10.1021/jp105467e, 2010.

Bloss, C., Wagner, V., Jenkin, M. E., Volkamer, R., Bloss, W. J., Lee, J. D., Heard, D. E., Wirtz, K., Martin-Reviejo, M., Rea, G., Wenger, J. C., and Pilling, M. J.: Development of a detailed chemical mechanism (MCMv3.1) for the atmospheric oxidation of aromatic hydrocarbons, *Atmos. Chem. Phys.*, 5, 641–664, doi:10.5194/acp-5-641-2005, 2005.

Calvert, J. G., Atkinson, R., H., B. K., Kamens, R. M., Seinfeld, J. H., Wallington, T. J., and Yarwood, G.: *The Mechanisms of Atmospheric Oxidation of Aromatic Hydrocarbons*, Oxford University Press, New York, 2002.

Canagaratna, M. R., Jayne, J. T., Jimenez, J. L., Allan, J. D., Alfarra, M. R., Zhang, Q., Onasch, T. B., Drewnick, F., Coe, H., Middlebrook, A., Delia, A., Williams, L. R., Trimborn, A. M., Northway, M. J., DeCarlo, P. F., Kolb, C. E., Davidovits, P., and Worsnop, D. R.: Chemical and microphysical characterization of ambient aerosols with the Aerodyne aerosol mass spectrometer, *Mass Spectrom. Rev.*, 26, 185–222, doi:10.1002/mas.20115, 2007.

Chhabra, P. S., Flagan, R. C., and Seinfeld, J. H.: Elemental analysis of chamber organic aerosol using an aerodyne high-resolution aerosol mass spectrometer, *Atmos. Chem. Phys.*, 10, 4111–4131, doi:10.5194/acp-10-4111-2010, 2010.

Chhabra, P. S., Ng, N. L., Canagaratna, M. R., Corrigan, A. L., Russell, L. M., Worsnop, D. R., Flagan, R. C., and Seinfeld, J. H.: Elemental composition and oxidation of chamber organic aerosol, *Atmos. Chem. Phys.*, 11, 8827–8845, doi:10.5194/acp-11-8827-2011, 2011.

Cocker, D. R., Flagan, R. C., and Seinfeld, J. H.: State-of-the-art chamber facility for studying atmospheric aerosol chemistry, *Environ. Sci. Technol.*, 35, 2594–2601, doi:10.1021/es0019169, 2001.

Crounse, J. D., McKinney, K. A., Kwan, A. J., and Wennberg, P. O.: Measurement of gas-phase hydroperoxides by chemical ionization mass spectrometry, *Anal. Chem.*, 78, 6726–6732, doi:10.1021/ac0604235, 2006.

DeCarlo, P. F., Kimmel, J. R., Trimborn, A., Northway, M. J., Jayne, J. T., Aiken, A. C., Gonin, M., Fuhrer, K., Horvath, T., Docherty, K. S., Worsnop, D. R., and Jimenez, J. L.: Field-deployable, high-resolution, time-of-flight aerosol mass spectrometer, *Anal. Chem.*, 78, 8281–8289, doi:10.1021/ac061249n, 2006.

Hallquist, M., Wenger, J. C., Baltensperger, U., Rudich, Y., Simpson, D., Claeys, M., Dommen, J., Donahue, N. M., George, C., Goldstein, A. H., Hamilton, J. F., Herrmann, H., Hoffmann, T., Iinuma, Y., Jang, M., Jenkin, M. E., Jimenez, J. L., Kiendler-Scharr, A., Maenhaut, W., McFiggans, G., Mentel, Th. F., Monod, A., Prévôt, A. S. H., Seinfeld, J. H., Surratt, J. D., Szmigielski, R., and Wildt, J.: The formation, properties and impact of secondary organic aerosol: current and emerging issues, *Atmos. Chem. Phys.*, 9, 5155–5236, doi:10.5194/acp-9-5155-2009, 2009.

Heald, C. L., Kroll, J. H., Jimenez, J. L., Docherty, K. S., DeCarlo, P. F., Aiken, A. C., Chen, Q., Martin, S. T., Farmer, D. K., and Artaxo, P.: A simplified description of the evolution of organic aerosol composition in the atmosphere, *Geophys. Res. Lett.*, 37, L08803, doi:10.1029/2010GL042737, 2010.

Hildebrandt, L., Donahue, N. M., and Pandis, S. N.: High formation of secondary organic aerosol from the photo-oxidation of toluene, *Atmos. Chem. Phys.*, 9, 2973–2986, doi:10.5194/acp-9-2973-2009, 2009.

Hildebrandt, L., Henry, K. M., Kroll, J. H., Worsnop, D. R., Pandis, S. N., and Donahue, N. M.: Evaluating the Mixing of Organic Aerosol Components Using High-Resolution Aerosol Mass Spectrometry, *Environ. Sci. Technol.*, 45, 6329–6335, doi:10.1021/es200825g, 2011.

Jenkin, M. E., Saunders, S. M., Wagner, V., and Pilling, M. J.: Protocol for the development of the Master Chemical Mechanism, MCM v3 (Part B): tropospheric degradation of aromatic volatile organic compounds, *Atmos. Chem. Phys.*, 3, 181–193, doi:10.5194/acp-3-181-2003, 2003.

Jimenez, J. L., Canagaratna, M. R., Donahue, N. M., Prevot, A. S. H., Zhang, Q., Kroll, J. H., DeCarlo, P. F., Allan, J. D., Coe, H., Ng, N. L., Aiken, A. C., Docherty, K. S., Ulbrich, I. M., Grieshop, A. P., Robinson, A. L., Duplissy, J., Smith, J. D., Wilson, K. R., Lanz, V. A., Hueglin, C., Sun, Y. L., Tian, J., Laaksonen, A., Raatikainen, T., Rautiainen, J., Vaattovaara, P., Ehn, M., Kulmala, M., Tomlinson, J. M., Collins, D. R., Cubison, M. J., Dunlea, E. J., Huffman, J. A., Onasch, T. B., Alfarra, M. R., Williams, P. I., Bower, K., Kondo, Y., Schneider, J., Drewnick, F., Borrmann, S., Weimer, S., Demerjian, K., Salcedo, D., Cottrell, L., Griffin, R., Takami, A., Miyoshi, T., Hatakeyama, S., Shimono, A., Sun, J. Y., Zhang, Y. M., Dzepina, K., Kimmel, J. R., Sueper, D., Jayne, J. T., Herndon, S. C., Trimborn, A. M., Williams, L. R., Wood, E. C., Middlebrook, A. M., Kolb, C. E., Baltensperger, U., and Worsnop, D. R.: Evolution of organic aerosols in the atmosphere, *Science*, 326, 1525–1529, doi:10.1126/science.1180353, 2009.

Keywood, M. D., Varutbangkul, V., Bahreini, R., Flagan, R. C., and Seinfeld, J. H.: Secondary organic aerosol formation from the ozonolysis of cycloalkenes and related compounds, *Environ. Sci. Technol.*, 38, 4157–4164, doi:10.1021/es035363o, 2004.

Kroll, J. and Seinfeld, J.: Chemistry of secondary organic aerosol: Formation and evolution of low-volatility organics in the atmosphere, *Atmos. Environ.*, 42, 3593–3624, doi:10.1016/j.atmosenv.2008.01.003, 2008.

Kroll, J. H., Smith, J. D., Che, D. L., Kessler, S. H., Worsnop, D. R., and Wilson, K. R.: Measurement of fragmentation and functionalization pathways in the heterogeneous oxidation of oxidized organic aerosol, *Phys. Chem. Chem. Phys.*, 11, 8005–8014, doi:10.1039/b905289e, 2009.

Kwok, E., Aschmann, S., Atkinson, R., and Arey, J.: Products of the gas-phase reactions of *o*-, *m*- and *p*-xylene with the OH radical in the presence and absence of NO_x, *J. Chem. Soc., Faraday Trans.*, 93, 2847–2854, 1997.

Lambe, A. T., Onasch, T. B., Massoli, P., Croasdale, D. R., Wright, J. P., Ahern, A. T., Williams, L. R., Worsnop, D. R., Brune, W. H., and Davidovits, P.: Laboratory studies of the chemical composition and cloud condensation nuclei (CCN) activity of secondary organic aerosol (SOA) and oxidized primary organic aerosols (OPOA), *Atmos. Chem. Phys.*, 11, 8913–8928, doi:10.5194/acp-11-8913-2011, 2011.

Lee, A. K. Y., Herkes, P., Leaitch, W. R., Macdonald, A. M., and Abbatt, J. P. D.: Aqueous OH oxidation of ambient organic aerosol and cloud water organics: Formation of highly oxidized products, *Geophys. Res. Lett.*, 38, L11805, doi:10.1029/2011GL047439, 2011.

Matthew, B. M., Middlebrook, A. M., and Onasch, T. B.: Collection efficiencies in an Aerodyne aerosol mass spectrometer as a function of particle phase for laboratory generated aerosols, *Aerosol Sci. Tech.*, 42, 884–898, doi:10.1080/0278620802356797, 2008.

Murphy, D. M., Cziczo, D. J., Froyd, K. D., Hudson, P. K., Matthew, B. M., Middlebrook, A. M., Peltier, R. E., Sullivan, A., Thomson, D. S., and Weber, R. J.: Single-particle mass spectrometry of tropospheric aerosol particles, *J. Geophys. Res.–Atmos.*, 111, D23S23, doi:10.1029/2006JD007340, 2006.

Ng, N. L., Kroll, J. H., Chan, A. W. H., Chhabra, P. S., Flagan, R. C., and Seinfeld, J. H.: Secondary organic aerosol formation from *m*-xylene, toluene, and benzene, *Atmos. Chem. Phys.*, 7, 3909–3922, doi:10.5194/acp-7-3909-2007, 2007.

Ng, N. L., Canagaratna, M. R., Zhang, Q., Jimenez, J. L., Tian, J., Ulbrich, I. M., Kroll, J. H., Docherty, K. S., Chhabra, P. S., Bahreini, R., Murphy, S. M., Seinfeld, J. H., Hildebrandt, L., Donahue, N. M., DeCarlo, P. F., Lanz, V. A., Prévôt, A. S. H., Dinar, E., Rudich, Y., and Worsnop, D. R.: Organic aerosol components observed in Northern Hemispheric datasets from Aerosol Mass Spectrometry, *Atmos. Chem. Phys.*, 10, 4625–4641, doi:10.5194/acp-10-4625-2010, 2010.

Ng, N. L., Canagaratna, M. R., Jimenez, J. L., Chhabra, P. S., Seinfeld, J. H., and Worsnop, D. R.: Changes in organic aerosol composition with aging inferred from aerosol mass spectra, *Aerosol Sci. Tech.*, 44, 6465–6474, doi:10.5194/acp-11-6465-2011, 2011.

Noda, J., Volkamer, R., and Molina, M. J.: Dealkylation of alkylbenzenes: a significant pathway in the toluene, *o*-, *m*-, *p*-xylene + OH reaction, *J. Phys. Chem. A*, 113, 9658–9666, doi:10.1021/jp901529k, 2009.

Paulot, F., Crounse, J. D., Kjaergaard, H. G., Kurten, A., St Clair, J. M., Seinfeld, J. H., and Wennberg, P. O.: Unexpected epoxide formation in the gas-phase photooxidation of isoprene, *Science*,

325, 730–733, doi:10.1126/science.1172910, 2009.

Qi, L., Nakao, S., Malloy, Q., Warren, B., and Cocker, D. R.: Can secondary organic aerosol formed in an atmospheric simulation chamber continuously age?, *Atmos. Environ.*, 44, 2990–2996, doi:10.1016/j.atmosenv.2010.05.020, 2010.

Riipinen, I., Pierce, J. R., Yli-Juuti, T., Nieminen, T., Häkkinen, S., Ehn, M., Junninen, H., Lehtipalo, K., Petäjä, T., Slowik, J., Chang, R., Shantz, N. C., Abbatt, J., Leaitch, W. R., Kerminen, V.-M., Worsnop, D. R., Pandis, S. N., Donahue, N. M., and Kulmala, M.: Organic condensation: a vital link connecting aerosol formation to cloud condensation nuclei (CCN) concentrations, *Atmos. Chem. Phys.*, 11, 3865–3878, doi:10.5194/acp-11-3865-2011, 2011.

Rudich, Y., Donahue, N. M., and Mentel, T. F.: Aging of organic aerosol: Bridging the gap between laboratory and field studies, *Annu. Rev. Phys. Chem.*, 58, 321–352, doi:10.1146/annurev.physchem.58.032806.104432, 2007.

Sander, S. P., Abbatt, J., Barker, J. R., Burkholder, J. B., Friedl, R. R., Golden, D. M., Huie, R. E., Kolb, C. E., J., K. M., Moortgat, G. K., Orkin, V. L., and Wine, P. H.: Chemical kinetics and photochemical data for use in atmospheric studies, Evaluation No. 17. JPL Publication 10-6, Jet Propulsion Laboratory, Pasadena, <http://jpldataeval.jpl.nasa.gov>, 2011.

Seinfeld, J. H. and Pandis, S. N.: *Atmospheric Chemistry and Physics*, John Wiley and Sons, Inc., Hoboken, NJ, second edn., 2006.

Shilling, J. E., Chen, Q., King, S. M., Rosenoern, T., Kroll, J. H., Worsnop, D. R., DeCarlo, P. F., Aiken, A. C., Sueper, D., Jimenez, J. L., and Martin, S. T.: Loading-dependent elemental composition of α -pinene SOA particles, *Atmos. Chem. Phys.*, 9, 771–782, doi:10.5194/acp-9-771-2009, 2009.

Shiraiwa, M., Ammann, M., Koop, T., and Pöschl, U.: Gas uptake and chemical aging of semisolid organic aerosol particles, *Proc. Natl. Acad. Sci. USA*, 108, 11003–11008, doi:10.1073/pnas.1103045108, 2011.

Song, C., Na, K., Warren, B., Malloy, Q., and Cocker, D. R.: Secondary organic aerosol formation from *m*-xylene in the absence of NO_x , *Environ. Sci. Technol.*, 41, 7409–7416, doi:10.1021/es070429r, 2007.

St. Clair, J. M., McCabe, D. C., Crounse, J. D., Steiner, U., and Wennberg, P. O.: Chemical ionization tandem mass spectrometer for the in situ measurement of methyl hydrogen peroxide, *Rev. Sci. Instrum.*, 81, 094102, doi:10.1063/1.3480552, 2010.

Vaden, T. D., Song, C., Zaveri, R. A., Imre, D., and Zelenyuk, A.: Morphology of mixed primary and secondary organic particles and the adsorption of spectator organic gases during aerosol formation, *P. Natl. Acad. Sci. USA*, 107, 6658–6663, doi:10.1073/pnas.0911206107, 2010.

Vaden, T. D., Imre, D., Beránek, J., Shrivastava, M., and Zelenyuk, A.: Evaporation kinetics and phase of laboratory and ambient secondary organic aerosol, *P. Natl. Acad. Sci. USA*, 108, 2190–2195, doi:10.1073/pnas.1013391108, 2011.

Virtanen, A., Joutsensaari, J., Koop, T., Kannisto, J., Yli-Pirilä, P., Leskinen, J., Mäkelä, J. M., Holopainen, J. K., Pöschl, U., Kulmala, M., Worsnop, D. R., and Laaksonen, A.: An amorphous solid state of biogenic secondary organic aerosol particles, *Nature*, 467, 824–827, doi:10.1038/nature09455, 2010.

Weitkamp, E. A., Sage, A. M., Pierce, J. R., Donahue, N. M., and Robinson, A. L.: Organic Aerosol Formation from Photochemical Oxidation of Diesel Exhaust in a Smog Chamber, *Environ. Sci. Technol.*, 41, 6969–6975, doi:10.1021/es070193r, 2007.

Zhang, Q., Jimenez, J. L., Canagaratna, M. R., Allan, J. D., Coe, H., Ulbrich, I., Alfarra, M. R., Takami, A., Middlebrook, A. M., Sun, Y. L., Dzepina, K., Dunlea, E., Docherty, K., DeCarlo, P. F., Salcedo, D., Onasch, T., Jayne, J. T., Miyoshi, T., Shimono, A., Hatakeyama, S., Takegawa, N., Kondo, Y., Schneider, J., Drewnick, F., Borrmann, S., Weimer, S., Demerjian, K., Williams, P., Bower, K., Bahreini, R., Cottrell, L., Griffin, R. J., Rautiainen, J., Sun, J. Y., Zhang, Y. M., and Worsnop, D. R.: Ubiquity and dominance of oxygenated species in organic aerosols in anthropogenically-influenced Northern Hemisphere midlatitudes, *Geophys. Res. Lett.*, 34, L13801, doi:10.1029/2007GL029979, 2007.

Zhang, X., Pandis, S. N., and Seinfeld, J. H.: Aerosol condensation: Diffusion limited vs quasi-equilibrium growth, *Aerosol Sci. Technol.*, submitted, 2011.

Zhao, J., Zhang, R., Misawa, K., and Shibuya, K.: Experimental product study of the OH-initiated oxidation of *m*-xylene, *J. Photoch. Photobio. A*, 176, 199–207, doi:10.1016/j.jphotochem.2005.07.013, 2005.

Appendix E

Yields of oxidized volatile organic compounds during the OH radical initiated oxidation of isoprene, methyl vinyl ketone, and methacrolein under high- NO_x conditions¹

¹This chapter is reproduced by permission from "Yields of oxidized volatile organic compounds during the OH radical initiated oxidation of isoprene, methyl vinyl ketone, and methacrolein under high- NO_x conditions," by M. M. Galloway, A. J. Huisman, L. D. Yee, A. W. H. Chan, C. L. Loza, J. H. Seinfeld, and F. N. Keutsch, *Atmospheric Chemistry and Physics*, 11, 10779–10790, doi:10.5194/acp-11-10779-2011, 2011. Copyright 2011 Authors. This work is licensed under a Creative Commons License.

Yields of oxidized volatile organic compounds during the OH radical initiated oxidation of isoprene, methyl vinyl ketone, and methacrolein under high-NO_x conditions

M. M. Galloway^{1,*}, A. J. Huisman^{1,***}, L. D. Yee², A. W. H. Chan^{3,***}, C. L. Loza³, J. H. Seinfeld^{2,3}, and F. N. Keutsch¹

¹Department of Chemistry, University of Wisconsin-Madison, Madison, WI, USA

²Division of Engineering and Applied Science, California Institute of Technology, Pasadena, CA, USA

³Division of Chemistry and Chemical Engineering, California Institute of Technology, Pasadena, CA, USA

* now at: Department of Chemistry, Reed College, Portland, OR, USA

** now at: Institute for Atmosphere and Climate, ETH Zurich, Zurich, Switzerland

*** now at: Department of Environmental Science, Policy and Management, University of California, Berkeley, CA, USA

Received: 29 March 2011 – Published in Atmos. Chem. Phys. Discuss.: 6 April 2011

Revised: 20 October 2011 – Accepted: 22 October 2011 – Published: 2 November 2011

Abstract. We present first-generation and total production yields of glyoxal, methylglyoxal, glycolaldehyde, and hydroxyacetone from the oxidation of isoprene, methyl vinyl ketone (MVK), and methacrolein (MACR) with OH under high NO_x conditions. Several of these first-generation yields are not included in commonly used chemical mechanisms, such as the Leeds Master Chemical Mechanism (MCM) v. 3.2. The first-generation yield of glyoxal from isoprene was determined to be 2.1 (± 0.6) %. Inclusion of first-generation production of glyoxal, glycolaldehyde and hydroxyacetone from isoprene greatly improves performance of an MCM based model during the initial part of the experiments. In order to further improve performance of the MCM based model, higher generation glyoxal production was reduced by lowering the first-generation yield of glyoxal from C5 hydroxycarbonyls. The results suggest that glyoxal production from reaction of OH with isoprene under high NO_x conditions can be approximated by inclusion of a first-generation production term together with secondary production only via glycolaldehyde. Analogously, methylglyoxal production can be approximated by a first-generation production term from isoprene, and secondary production via MVK, MACR and hydroxyacetone. The first-generation yields reported here correspond to less than 5 % of the total oxidized yield from isoprene and thus only have a small effect on the fate of isoprene. However, due to the abundance of isoprene, the combination of first-generation yields and reduced higher gen-

eration production of glyoxal from C5 hydroxycarbonyls is important for models that include the production of the small organic molecules from isoprene.

1 Introduction

Isoprene (2-methyl-1,3-butadiene) is emitted into the atmosphere from vegetation in large quantities ($\sim 500 \text{ Tg year}^{-1}$) (Guenther et al., 1995). Globally, the dominant atmospheric sink of isoprene is reaction with the OH radical (Archibald et al., 2010a). Due to its reactivity with the OH radical and high mixing ratios in forested areas, isoprene has important impacts on the oxidative capacity of the atmosphere (Karl et al., 2009). OH oxidation of isoprene has been studied in detail, and there are a number of commonly used explicit chemistry mechanisms such as the Leeds Master Chemical Mechanism (MCM), Mainz Isoprene Mechanism (MIM) or the NCAR Master Mechanism (Madronich and Calvert, 1989; Jenkin et al., 1997; Saunders et al., 2003; Taraborrelli et al., 2009). Oxidation of isoprene initiated by OH is an important source of small carbonyls and hydroxycarbonyls, such as glyoxal, methylglyoxal, and glycolaldehyde. These species are of interest within the context of cloud processing and secondary organic aerosol (SOA) formation (Carlton et al., 2007; Altieri et al., 2008; Ervens et al., 2008; Galloway et al., 2009; Ip et al., 2009; Nozière et al., 2009; Perri et al., 2009; Shapiro et al., 2009; Tan et al., 2009; Volkamer et al., 2009; Sareen et al., 2010; Galloway et al., 2011). To quantify the atmospheric impacts of these compounds, it is important



Correspondence to: F. N. Keutsch
(keutsch@wisc.edu)

Table 1. First-generation yields from high NO_x experiments. All yields and errors are in percent. All uncertainties presented in this work represent the 1σ error. The MCM yields are calculated for the reaction with OH and on the basis that the fate of peroxy radicals is dominated by NO with negligible contribution from reaction with HO_2 or RO_2 .

Compound	MVK	MACR	Glycolaldehyde	Hydroxyacetone	Glyoxal	Methylglyoxal
Isoprene ^a	$30.4 \pm 1.3\%$	$22.01 \pm 0.62\%$	$2.69 \pm 0.82\%$	$2.9 \pm 0.051\%$	$2.10 \pm 1.2\%$	ND
Isoprene ^b	$29 \pm 7\%$	$21 \pm 5\%$				
Isoprene ^c	40 %	26 %	4.2 %	3.8 %	**3.8 %	**4.2 %
Isoprene ^g	41.5 %	26.5 %	NI	NI	NI	NI
Isoprene ^h	NI	NI	NI	NI	0.3–3.0 %	NI
MVK ^a			$67.4 \pm 3.0\%$	*0 %	*0 %	$24.12 \pm 0.14\%$
MVK ^d			$64 \pm 8\%$			$25 \pm 4\%$
MVK ^c			62.5 %			**26.5 %
MVK ^g			70 %	NI	NI	29 %
MACR ^a			*0 %	$39.5 \pm 1.7\%$	*0 %	$8.09 \pm 0.45\%$
MACR ^e				$41 \pm 3\%$		$8.4 \pm 1.6\%$
MACR ^f				$47 \pm 5\%$		<12 %
MACR ^c				20 %		**0 %
MACR ^g		NI		43 %	NI	NI

ND = no data. NI = not included in the MCM. ^a This work ^b Tuazon and Atkinson (1990a). ^c Paulot et al. (2009a). ^d Tuazon and Atkinson (1989). ^e Tuazon and Atkinson (1990b). ^f Orlando et al. (1999). ^g MCM ^h Volkamer et al. (2006). * 0 % within uncertainty of measurement. ** Inferred from the presented mechanism from that study.

to understand their tropospheric production via oxidation of volatile organic compounds (VOCs), isoprene in particular.

Atmospheric isoprene oxidation has long been of interest (Gu et al., 1985; Tuazon and Atkinson, 1990a; Paulson et al., 1992; Miyoshi et al., 1994; Kwok et al., 1995; Sprengnether et al., 2002; Fan and Zhang, 2004; Zhao et al., 2004; Carlton et al., 2009; Karl et al., 2009; Paulot et al., 2009a; Archibald et al., 2010a,b). Tuazon and Atkinson (1990a) studied isoprene oxidation in the presence of OH and NO_x , and determined first-generation formation yields of methyl vinyl ketone (MVK), methacrolein (MACR), and formaldehyde (see Table 1 for all yields). The same authors also determined first-generation photooxidation yields of glycolaldehyde and methylglyoxal from MVK as well as yields of hydroxyacetone, methylglyoxal, and CO from MACR (Tuazon and Atkinson, 1989, 1990b). Orlando et al. (1999) studied OH-initiated MACR oxidation in the presence of NO_x and quantified hydroxyacetone as a product. Based on their detection limit for methylglyoxal, they were able to infer an upper limit of 12 % for the first-generation methylglyoxal yield from MACR.

While all of these studies have added to our mechanistic understanding of isoprene oxidation, recent measurements point to gaps in our understanding of isoprene oxidation (Dibble, 2004a,b; Volkamer et al., 2006; Paulot et al., 2009a). The existing master mechanisms cited above specify glyoxal as a higher generation oxidation product of isoprene, but few studies exist in which glyoxal, methylglyoxal, glycolaldehyde, or hydroxyacetone are measured in isoprene oxidation. One such study compared first-generation MACR and glyoxal to derive a first-generation glyoxal yield of 0.3–

3 % (Volkamer et al., 2006). Theoretical work by Dibble (2004a,b) suggests a mechanism for such first-generation glyoxal and methylglyoxal formation from isoprene under high NO_x conditions, specifically that glyoxal, methylglyoxal, glycolaldehyde, and hydroxyacetone can be formed through rapid isomerisation and double intramolecular hydrogen transfer of alkoxy radical intermediates. Glycolaldehyde and methylglyoxal are produced together in the suggested mechanism, as are glyoxal and hydroxyacetone. Paulot et al. (2009a) also studied isoprene oxidation, focusing on the isoprene δ -hydroxy oxidation channel. They observed first-generation yields of glycolaldehyde and hydroxyacetone and inferred the same yields for methylglyoxal and glyoxal, respectively, based on the work of Dibble (2004a,b) as they had no measurements of the dicarbonyls.

The work presented here studies the formation of a number of first- and higher-generation products formed during OH oxidation of isoprene, MVK, and MACR under high NO_x conditions. First-generation yields from these precursors are incorporated into a zero-dimensional photochemical box model (Huisman et al., 2011) based on the MCM v. 3.2 (Jenkin et al., 1997; Saunders et al., 2003) to evaluate the extent to which the model can represent experimental measurements.

2 Experimental procedures

Experiments were carried out in the Caltech dual 28 m^3 Teflon chambers, described in detail elsewhere (Cocker et al., 2001; Keywood et al., 2004). See Tables 2 and S1 for experimental conditions. Temperature, relative humidity (RH),

Table 2. Experiment list.

Exp. #	Date (mm/dd/yy)	Compound	Initial conc. (ppb)	Initial NO (ppb)	Initial NO ₂ (ppb)	RH (%)	T (K)	Lights	OH source
Chan 1*	02/06/08	Glyoxal	499	3	3	3	298	50 %	None
1	07/21/10	Glyoxal	64	3	21	4	294	50 %	None
2	02/02/08	Isoprene	603	466	606	4	293	10 %	HONO
3	02/04/08	Isoprene	609	465	550	5	294	10 %	HONO
4	10/15/09	Isoprene	187	361	675	8	295	10 %	HONO
5	10/17/09	Isoprene	17	250	403	9	295	10 %	HONO
6	10/19/09	Isoprene	187	307	545	10	294	10 %	HONO
7	07/22/10	Isoprene	60	325	527	4	293	10 %	HONO
8	10/21/09	MVK	25	279	534	10	295	10 %	HONO
9	07/20/10	MVK	20	294	523	4	294	10 %	HONO
10	10/23/09	MACR	42	231	437	7	295	10 %	HONO
11	10/25/09	Blank	None	250	455	8	294	10 %	HONO

* Chan et al. (2009).

O₃, NO, and NO_x were continuously monitored. RH was held at ~10 % throughout the experiments to prevent losses to chamber walls, although the reactions studied here are not sensitive to RH. Therefore the yields determined in this work should be applicable to higher RH. The wavelength of the chamber black lights is centered at 350 nm, and at 50 % power, the lights have a spectral intensity equivalent to $J_{NO_2} = 0.2366 \text{ min}^{-1}$.

Gas-phase isoprene, MVK, and MACR were monitored by gas chromatography with a flame ionization detector (GC-FID, Agilent 6890N). Gas-phase glyoxal was continuously monitored using the Madison laser induced phosphorescence instrument described by Huisman et al. (2008). This instrument was operated at 30 s time resolution, with a limit of detection (3σ) for glyoxal of 2.9 ppt in 30 s. Calibrations are performed with the same methods described for glyoxal by Huisman et al. (2008). Methylglyoxal was also measured with this instrument by subtracting glyoxal and background signals from the total α -dicarbonyl signal to give the methylglyoxal signal and Exps. 7 and 9 (Table 2) also utilized the lifetime methylglyoxal detection method described by Henry et al. (2011). Briefly, this method monitors the phosphorescence decay of glyoxal and methylglyoxal after each laser pulse and uses the known lifetimes of those decays to determine the contribution of each compound to the total signal. More details can be found in the supplemental information.

A chemical ionization mass spectrometer (CIMS) was used for online gas-phase measurement of glycolaldehyde and hydroxyacetone. The CIMS consists of a custom chemical ionization source connected to a Varian 1200 triple quadrupole mass spectrometer, previously described in detail (Crounse et al., 2006; Paulot et al., 2009b; St. Clair et al., 2010). Negative-mode operation utilized CF₃O⁻ ions that cluster with the analyte detected at m/z MW + 85 or via fluoride transfer for more acidic species detected at

m/z MW + 19. Positive-mode operation utilized proton transfer reaction of positively charged water clusters with the analyte.

Experiments typically began with the addition of the reactants into the chamber. A known amount of liquid isoprene, MVK, or MACR was injected into a glass bulb, vaporised into the chamber, and then allowed to mix. Photolysis of nitrous acid (HONO) was used as the OH source. HONO was prepared by adding 1 wt % aqueous NaNO₂ drop wise into 10 wt % sulphuric acid and then introduced into the chamber using an air stream before the experiment started. Additional NO and NO₂ were added to the initial concentrations indicated in Table 2. Experiment time started when the black lights were turned on. No further additions were made to the chamber after the black lights were turned on. Total irradiation times for each experiment were approximately 8 hrs. A representative high-NO_x isoprene experiment is shown in Fig. 1.

3 Determination of first-generation yields

Observed mixing ratios reflect both production and loss of each compound. To calculate total production yields, it is necessary to correct for the amount of product lost via photolysis and reaction with OH and O₃. This requires knowledge of the reaction rates with OH (k_{OH+X}) and O₃ (k_{OH+X}) (taken from the MCM), the O₃ concentration (which was measured), the photolysis rates (inferred from the measured glyoxal photolysis rate, see Sect. 3.1), as well as the OH concentration (inferred from the rate of change of observed VOCs, see Sect. 3.2).

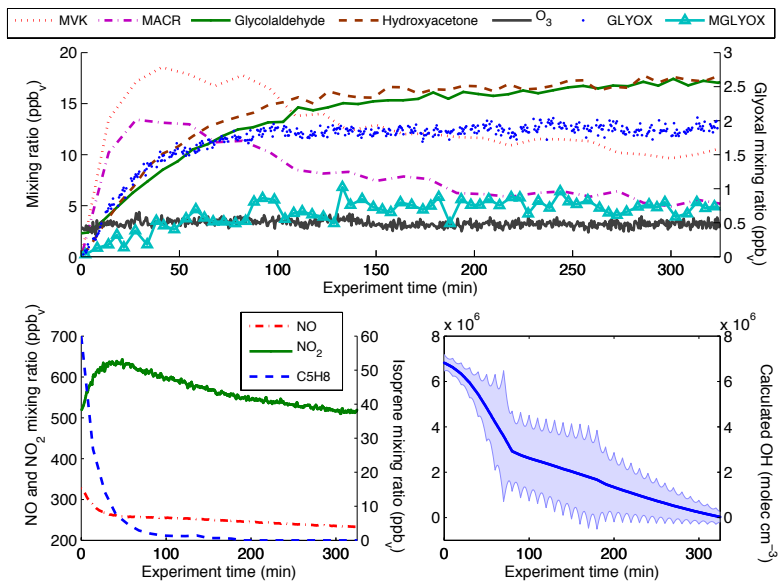


Fig. 1. Timeseries of measured compounds for Exp. 7. OH is the average of that calculated from ISP, MVK, and MACR. See Supplement for details about OH calculations.

3.1 Calculating photolysis rates

The glyoxal photolysis rate was measured during the 2008 experiments (Exp. Chan 1, Table S1, Chan et al., 2009) and again during the 2010 experiments (Exp. 1) to account for changes in blacklight intensity. Glyoxal photolysis in 2010 (0.14 h^{-1}) was 74 % of the value in 2008 (0.19 h^{-1}), so the 2009 photolysis rate was interpolated between these values. The photolysis rates calculated from these experiments were used as a basis to estimate the photolysis rates of all other compounds. Photolysis rates in the MCM are given as a function of solar zenith angle (SZA), so the measured glyoxal photolysis rate was used to calculate an estimated SZA from the MCM; this was then used to calculate the photolysis rates for all other species.

3.2 Determining OH concentrations

OH number densities were estimated from the rate of loss of VOCs. Loss of VOC via reaction with O_3 and photolysis was taken into account by iteratively solving the loss equation for the precursor VOC, rearranged to solve for [OH],

$$[\text{OH}] = -\frac{1}{k_{\text{OH}+\text{X}}} \left(\frac{1}{[\text{X}]_{i-1}} \frac{\Delta[\text{X}]}{\Delta t} + k_{\text{O}_3+\text{X}} [\text{O}_3]_i + J_{\text{X}} \right) \quad (1)$$

where $[\text{X}]_{i-1}$ is the number density of the VOC X of measurement $i-1$, $\frac{\Delta[\text{X}]}{\Delta t}$ is the change in number density per unit time, $k_{\text{OH}+\text{X}}$ and $k_{\text{O}_3+\text{X}}$ are the rate constants for reaction with OH and O_3 , respectively, and J_{X} is the photolysis rate of VOC X. Due to scatter in the precursor VOC

number densities, these data were fit to an exponential or double exponential before calculations. For the isoprene experiments, OH was calculated from isoprene until isoprene number density dropped below the limit of detection of the GC-FID (0.5 ppb, 1–2 h after experiment start), after which MVK and MACR data were used. OH was determined to be the mean of that calculated from MVK and MACR at each step. Due to the small change in VOCs at a 1 min timebase, OH was calculated on a 10 min timebase and then interpolated to a 1 min timebase for use in calculating first-generation yields. In general, OH was calculated to be 1×10^6 – $1 \times 10^7 \text{ molec cm}^{-3}$ at the start of the experiment and decreased to $1 \times 10^4 \text{ molec cm}^{-3}$ towards the end of the experiments. The uncertainty in OH was generally low (near 5 %), at the beginning of the experiments but increased to as high as 250 % as the primary VOC concentrations decreased. Figure S1 shows the calculated OH along with several measured time series for a typical.

3.3 Loss correction

Number densities of each product corrected to account for reaction with OH and O_3 , $[\text{Y}]^{\text{corr}}$, were determined iteratively using the following recursive discrete time equation:

$$[\text{Y}]_i^{\text{corr}} = [\text{Y}]_{i-1}^{\text{corr}} + \Delta[\text{Y}]_i + [\text{Y}]_{i-1} \Delta t (k_{\text{OH}+\text{Y}} [\text{OH}] + k_{\text{O}_3+\text{Y}} [\text{O}_3]_i + J_{\text{Y}}) \quad (2)$$

where $[\text{Y}]_i^{\text{corr}}$ is the corrected number density of the compound at measurement time i , $[\text{Y}]_{i-1}$ is the measured product

concentration of measurement $i - 1$, Δt is time between measurements i and $i - 1$, $\Delta[\text{Y}]_i$ is the observed net change in [Y] that occurs over Δt , $k_{\text{OH}+\text{Y}}$ and $k_{\text{O}_3+\text{Y}}$ are the respective rate constants, and J_{Y} is the photolysis rate constant of the product Y. At any given time during the experiment, $[\text{Y}]^{\text{corr}}$ is equivalent to the total amount of Y which was produced up to that point, neglecting all loss processes. Figure S2 shows the loss corrected glyoxal concentrations for Exp. 3.

3.4 First-generation yields

The relationship between the loss corrected concentrations of reaction products and the amount of precursor VOC consumed via reaction is an indicator of first- versus higher-generation formation. VOCs react with OH, forming peroxy radicals, which then react largely with NO, giving alkoxy radicals and other species. First-generation reactions are those that stem from the initial OH attack and which do not involve another attack by OH, O_3 , or NO_3 on one of the stable products. Therefore, a first generation product is the first stable product which results from one OH reacting with the precursor VOC. This first-generation product is formed at the same rate at which the precursor VOC is lost to reaction, therefore the relationship between these quantities is linear, as can be seen with the first generation formation of glycolaldehyde from 2-methyl-3-buten-2-ol (MBO) in Fig. S3. In contrast, a lag in the appearance of the product demonstrates that the reaction involves intermediates, as production does not depend on the reaction of the primary VOC but rather on that of a first- or later-generation product (Fig. S3). The slope of the line observed for the loss corrected product concentration versus reacted VOC corresponds to the first-generation yield (Fig. 2). This relationship can be expressed with a simple linear relationship:

$$[\text{prod}]_{\text{corr}} = a[\text{VOC}]_{\text{reacted}} + b \quad (3)$$

where $[\text{prod}]_{\text{corr}}$ is the corrected product formed, $[\text{VOC}]_{\text{reacted}}$ is the amount of primary VOC reacted, and a is the first-generation yield.

First-generation yields were determined for each of the measured oxidation products in these experiments using the methods described above (Table 1). A representative isoprene oxidation experiment is shown in Fig. 1; the first-generation glyoxal yield calculated from this experiment is $2.32 (\pm 0.01)\%$. The first-generation yields of MVK and MACR from isoprene presented here agree well with Tuazon and Atkinson (1990a). The first-generation glyoxal yield from isoprene calculated from our work is in the upper range (0.3–3 %) presented by Volkamer et al. (2006). Of the species studied here, the MCM includes only first-generation formation of MVK and MACR from isoprene, for which the yields are also shown in Table 1. Although first-generation formation of the two and three carbon species listed in Table 1 from isoprene is not included in the MCM or other com-

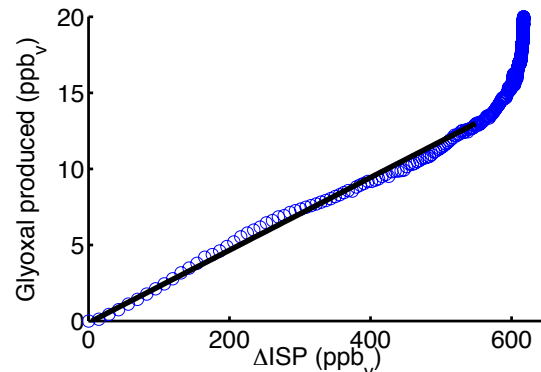


Fig. 2. Glyoxal production as a function of isoprene reacted in Exp. 2. Note the linear relationship between glyoxal and isoprene reacted in the first part of the experiment. The continued upward trend in glyoxal after isoprene is consumed corresponds to the formation of glyoxal as a higher generation oxidation product. The first-generation glyoxal yield for this experiment is $2.4 (\pm 0.013)\%$.

mon mechanisms, Dibble (2004a,b) has presented a possible reaction pathway in a theoretical study. The Dibble mechanism rationalizes first-generation formation of glyoxal together with hydroxyacetone and first-generation formation of methylglyoxal together with glycolaldehyde from isoprene via intramolecular hydrogen shift reactions of the radical intermediates in the presence of NO. The glyoxal, glycolaldehyde and hydroxyacetone observed in the work presented here agree with the Dibble mechanism, as does the work by Paulot et al. (2009a), who also observed first-generation production of glycolaldehyde and hydroxyacetone from reaction of isoprene and OH with similar yields. Due to the time resolution of the methylglyoxal data, we were unable to determine a first-generation methylglyoxal yield from isoprene. However, inclusion of a first-generation yield in the model resulted in good model-measurement agreement (see Sect. 4.3 and Fig. 3).

The first-generation yields of glycolaldehyde and methylglyoxal from MVK in this study agree within error to those found by Tuazon and Atkinson (1989). The same authors also determined a first-generation yield for hydroxyacetone from MACR (Tuazon and Atkinson, 1990b); our yield is on the high end of this range, but is in good agreement with the yield determined by Orlando et al. (1999). The first-generation yield of methylglyoxal from MACR in this work is lower but similar to that determined by Tuazon and Atkinson (1989), whereas the yield inferred by Paulot et al. (2009a) is substantially higher. Overall, the first-generation yields determined in this work agree with previously reported literature values.

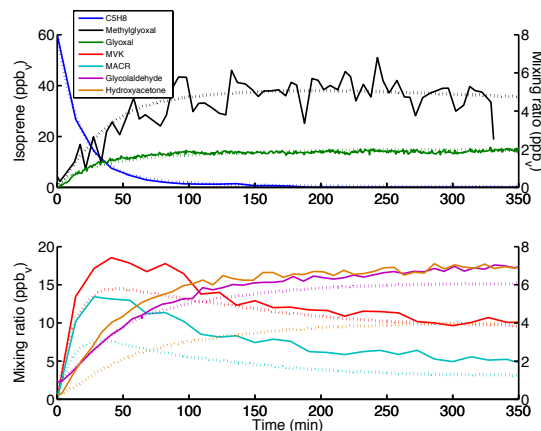


Fig. 3. Model and measurement comparison for high- NO_x isoprene oxidation (Exp. 7) using the modified MCM model. The glycolaldehyde to glyoxal yield was set to 29 %, and first generation yields of glyoxal (2.6 %), methylglyoxal (2.7 %), hydroxyacetone (2.6 %), and glycolaldehyde (2.7 %) were included in this model run. Glyoxal production from C5 hydroxycarbonyls was attenuated to 1/6 of the MCM v. 3.2 values.

4 Comparison of first and higher generation yields with the MCM

4.1 MCM based model parameters

The MCM based photochemical box model described in detail by Huisman et al. (2011) was used to reproduce chamber results with minor modifications to the model parameters. O_3 , NO_2 , and air temperature were constrained to match measurements. However, for these chamber runs, the primary VOC and NO concentrations were not constrained to the measurements but predicted by the model after initialization with the observed initial values. This allowed for validation of the effectiveness of the model and OH calculations. Two features of the box model are the use of an SZA derived from measured photolysis rates (Sect. 3.1) and the use of chamber-derived OH (Sect. 3.2). Raw NO_2 data were corrected for detector saturation ($[\text{NO}_2] > 1000 \text{ ppb}_v$) using a cubic spline fitting routine. In very dry, low aerosol conditions such as those in these experiments, glyoxal has been demonstrated to have negligible wall losses, and wall and aerosol losses are expected to be a minor to negligible sink of the other VOCs as well (Loza et al., 2010). Therefore, wall and aerosol losses are neglected in the model.

4.2 Assessment of unmodified MCM

Model performance is assessed using a quality of fit parameter that takes into account the slope, correlation coefficient (R^2), and absolute residuals between measurement

and model (see Supplement Sect. 2 for details). The fit is evaluated for a short time, usually less than 1 h after experiment start, which reflects primarily first-generation production, and evaluated again for the remainder of the experiment, corresponding to a convolution of first and higher generation production. The MCM based model was able to reproduce chamber results for oxidation of MBO upon inclusion of the 29 % yield of glyoxal from glycolaldehyde found by Chan et al. (2009). For the high- NO_x isoprene oxidation experiments, the model predicted MVK and MACR well. In contrast, the model underpredicted glyoxal (Fig. 5), methylglyoxal, hydroxyacetone, and glycolaldehyde in the primary production regime. This demonstrates that, as expected from Sect. 3, a first-generation yield is necessary to bring the model into agreement with measurements in the early part of the experiments. In contrast, the model overpredicts glyoxal in the later, higher generation production regime by approximately a factor of two.

For the MVK high- NO_x oxidation experiments, predicted glyoxal (Fig. 4a) agrees very well with measurement, and modelled glycolaldehyde and methylglyoxal only slightly exceed the measurements. In the high- NO_x MACR oxidation experiments, measured hydroxyacetone is approx. 75 % of modelled after first generation production, and modelled methylglyoxal is approximately double measured in the later part of the experiment (see Fig. 4b).

4.3 Inclusion of first-generation yields in MCM model

The first-generation yields determined in Sect. 3.2 and Table 1 that are not included in the current version of the MCM were added to the MCM-based model, i.e. first-generation production of glyoxal, glycolaldehyde, hydroxyacetone and methylglyoxal from isoprene and first-generation methylglyoxal production from MACR. As our results for first-generation formation of methylglyoxal from isoprene were inconclusive, we used the same value as that determined for glycolaldehyde following the work of Dibble (2004a,b) and Paulot et al. (2009a). Glyoxal and hydroxyacetone are formed through the same pathway, so the first-generation yield in the model was set to the average of those found in this study. Figure S4 shows the details of the modifications made to the MCM. The yields of hydroxyacetone, glycolaldehyde and glyoxal (see Table 1) are similar to but smaller (by 25–45 %) than those observed (or inferred for the case of glyoxal) by Paulot et al. (2009a) with exception of the first-generation yield of methylglyoxal from MACR, which is substantially lower in our work than the inferred value, but close to the yield determined by Tuazon and Atkinson (1990b). The unaltered MCM based model and a model with the first-generation yields were used to simulate chamber experiments of oxidation of isoprene, MVK, and MACR. Inclusion of the first-generation yields improved the model performance at early times in the isoprene and MACR studies (see Fig. 5 for a representative example), clearly supporting

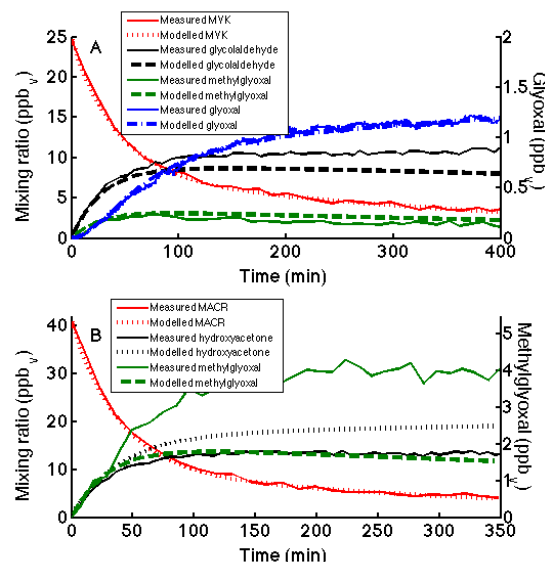


Fig. 4. (A) Modified MCM v. 3.2 Model and measurement comparison for high- NO_x MVK oxidation (Exp. 8). The left axis corresponds to all compounds except glyoxal. The glycolaldehyde to glyoxal yield was set to 0.29 for this model run. (B) MCM v. 3.2 Model and measurement comparison for high- NO_x MACR oxidation (Exp. 10). Note the discrepancy between measurement and model in both the hydroxyacetone and methylglyoxal once secondary production begins to dominate production.

the finding that these first-generation formation pathways should be incorporated into chemical mechanisms. For the best model performance, it was necessary to adjust the first-generation yields of glyoxal, methylglyoxal, glycolaldehyde, and hydroxyacetone to match those determined in each individual experiment. However, using the average of the calculated yields does improve the performance at early times for all experiments.

4.4 Attenuation of higher generation glyoxal production in the MCM

While the inclusion of first-generation production of glyoxal allowed the model to match early experimental results, the model still had a substantial overprediction of glyoxal at later times ($t > 1$ h) when the majority of isoprene had already been processed. This implies that glyoxal as a higher generation oxidation product of isoprene is significantly overexpressed in the MCM for the conditions of our chamber experiments. An overexpression of secondary glyoxal production of an MCM model compared to measurements was also found but not reported in the study by Volkamer et al. (2006) (R. Volkamer, personal communication 2011). There are several channels that produce glyoxal (see Fig. 6); the

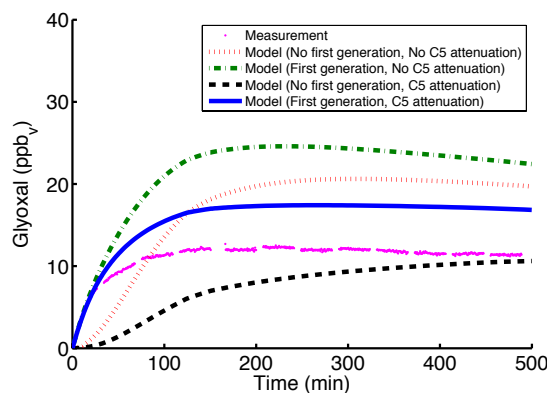


Fig. 5. Comparison of measured glyoxal concentration and MCM prediction for Exp. 2. Attenuation of glyoxal production from C5 hydroxycarbonyls to 1/6 of MCM v. 3.2 values brings the model into closer agreement with measurement during the latter part of the experiment. First-generation glyoxal yield is set to 2.6 %.

glyoxal yield from glycolaldehyde is known and glycolaldehyde was reproduced well in the later part of experiments, first-generation production of glyoxal from isoprene was determined experimentally, and the model is able to adequately reproduce glyoxal from both MVK and MACR oxidation experiments. The discrepancies in glyoxal production from isoprene oxidation are hence unlikely to result from any of these channels (Fig. 6). The majority of glyoxal not produced through these channels is formed through two C5 hydroxycarbonyl pathways (Fig. 6); therefore we adjusted the yield of glyoxal from these carbonyls in the MCM. Berndt and Böge (2007) observed a 17 % yield of glyoxal from the reaction of 4-hydroxy-2-butenal with OH, indicating that the C5 hydroxycarbonyls produce glyoxal, but possibly in lower quantities than predicted by the MCM. Therefore, the yields of glyoxal from the C5 hydroxycarbonyls were reduced in the modified MCM model.

Using the observed first-generation yield for glyoxal in the isoprene experiments, a model variant in which production of glyoxal from C5 hydroxycarbonyls was adjusted improved model performance markedly (Fig. 5). By reducing the higher generation production of glyoxal from C5 hydroxycarbonyls to 1/6 of the value in the MCM v. 3.2, most of the glyoxal production from isoprene oxidation can be modelled through first-generation formation from isoprene and the oxidation of glycolaldehyde. Glyoxal production from C5 hydroxycarbonyls is not necessarily wrong in the MCM; there are several other reasons why this attenuation might improve model performance. These include a missing C5 hydroxycarbonyl sink, such as C5 hydroxycarbonyl wall loss in the chambers, or incorrect reaction rates to form glyoxal. Attenuating the glyoxal production from these compounds is the easiest way to achieve attenuation in this study, and further

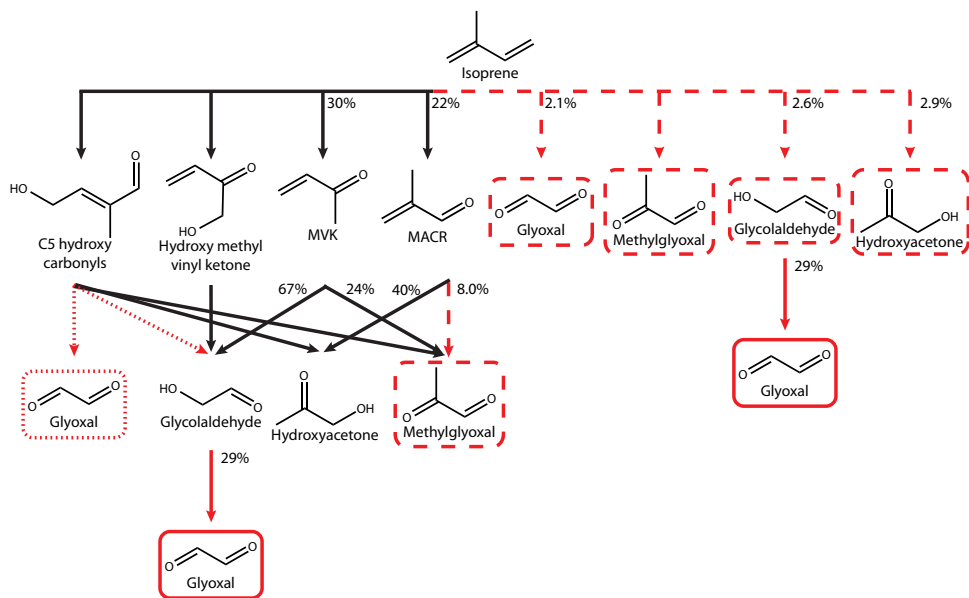


Fig. 6. Isoprene oxidation scheme. Dashed lines indicate first-generation formation pathways not included in the MCM. The dashed MACR to methylglyoxal line was not included in MCM v. 3.1, but is included in MCM v. 3.2 and was confirmed in this study. Dotted lines indicate the modifications to glyoxal production from C5 hydroxycarbonyls to 1/6 of the MCM v. 3.2 yield in our modelling studies. The solid red line indicates a yield verified by measurements with this study and the study by Chan et al. (2009). Yields given are those found in this study. The C5 hydroxycarbonyl shown here is one of multiple isomers in the MCM, which refers to them as HC4CCHO (shown here) and HC4ACHO.

experiments to study C5 hydroxycarbonyl formation and oxidation are necessary to fully understand glyoxal production from isoprene. Even with the complete removal of removing glyoxal production from C5 hydroxycarbonyls, modelled glyoxal is still slightly higher than measurements and the model modifications addressed above do not bring the measurement and model into perfect agreement, the model over-predicts glyoxal measurements by approx. 50 % at the end of experiments (Fig. 5). This could be due to the fact that OH is not measured, but is calculated from the isoprene, MVK, and MACR decay or may indicate that more studies must be done to understand this glyoxal production pathway. However, OH calculated from MVK and MACR is quite low and sensitivity analyses show that lowering it further has little impact, whereas raising it, which is the more likely error, would further increase modelled glyoxal.

4.5 Total product yields from the MCM

Once the model parameters were set to reproduce the measured species of interest, the altered MCM-based model was used to determine total yields of each of the products studied from isoprene, MVK, and MACR. To do this, the OH, O_3 , NO_2 , and air temperature inputs were extended at the final measured value ($[\text{O}_3] = 320 \text{ ppb}$; $\text{OH} = 8.2 \times$

$10^5 \text{ molec cm}^{-3}$) and the model was allowed to run using the modified MCM or unaltered MCM v. 3.2 until all products of interest were consumed. We also performed analogous model runs but with $[\text{O}_3] = 0 \text{ ppb}$, to investigate the effect of the high ozone to OH ratio. The total amount of each compound produced was compared to the total consumption of the precursor VOC. The results of these model runs are shown in Table 3. The exclusion of ozone chemistry increases the glyoxal yields, as glyoxal is primarily formed via OH-driven chemistry and this effect is stronger for the original MCM v. 3.2 than for the modified version. It should be noted that the measured glyoxal yields at the end of the experiment are only about 68 % and 64 % of those modelled with the modified and original MCM v. 3.2, respectively, which correspond to results in column 2 and 3 in Table 3. The fact that the original MCM v. 3.2 overpredicts glyoxal more at the end of the experiment but has a lower total yield results from the fact that it has higher second-generation production (from the C5 hydroxycarbonyls) than the modified MCM, whereas the latter has increased third-(and higher) generation production via glycolaldehyde compared to MCM v. 3.2, due to the increased yield of glyoxal from glycolaldehyde from 20 % to 29 %.

Table 3. Total molar yields from isoprene oxidation calculated with the modified MCM and original MCM v. 3.2 for high NO_x conditions. Total yields are calculated by allowing the model to run until species of interest have reacted away. Columns 2 and 3 are model simulations in which the conditions were held constant at the end of the experiment to determine total yields ([O₃]=320 ppb; OH = 8.2×10^5 molec cm⁻¹). Columns 4 and 5 are for identical runs, except that [O₃] was set to 0 ppb. The observed glyoxal at the end of the experiments was only about 2/3 of the modelled output from columns 2 and 3.

Compound	Total Yield: mod. MCM [O ₃]=320 ppb	Total Yield: MCM v. 3.2 [O ₃]=320 ppb	Total Yield: mod. MCM [O ₃]=0 ppb	Total Yield: MCM v. 3.2 [O ₃]=0 ppb
MVK	40.7 %	40.7 %	41.6 %	41.6 %
MACR	26.8 %	26.8 %	26.6 %	26.6 %
Glycolaldehyde	24.8 %	24.3 %	40.9 %	41.6 %
Hydroxyacetone	23.0 %	22.1 %	22.5 %	22.5 %
Glyoxal	9.6 %	8.0 %	10.3 %	11.0 %
Methylglyoxal	35.0 %	35.2 %	27.1 %	26.4 %

5 Conclusions

We present yields of first-generation oxidation products of isoprene, MVK, and MACR, several of which are not included in current chemical mechanisms, such as the MCM. Inclusion of first-generation production of glyoxal, glycolaldehyde and hydroxyacetone from isoprene and methylglyoxal from MACR greatly improved performance of a MCM based model during the first few hours of oxidation. However, inclusion of the first-generation glyoxal yield degraded the already poor performance of the MCM based model during the higher generation production phase of the isoprene experiments. It was necessary to scale down higher generation glyoxal production from isoprene in order to prevent substantial overprediction in relation to chamber experiments. Reducing the glyoxal production from C5 carbonyls greatly improved model performance, indicating that this pathway could be overexpressed in the MCM. However, further work is needed to determine whether the cause of the over prediction is indeed from the fate of C5 hydroxycarbonyls, which could not be ascertained in this work. The C5 hydroxycarbonyls were detected by the CIMS and the signals were quite low. However, no calibration is available and as no experiments with the C5 hydroxycarbonyls themselves were conducted, no quantitative analysis was possible, demonstrating that further work on these compounds is necessary; in addition, the high glyoxal yield from glycolaldehyde of 29 % in this study should be verified, as an overestimate of this yield could explain part of the discrepancy at later experiment times. In addition, secondary oxidation processes are typically slower and occur at lower OH concentrations, which results in increased uncertainties in the secondary chemistry. Measurements of OH, particularly during the part of experiments dominated by secondary chemistry, would help to better constrain mechanisms.

The results presented here furthermore suggest that glyoxal production from reaction of OH with isoprene under high NO_x conditions can be approximated, e.g. for models requiring simplified mechanisms, by inclusion of only a first-generation production term together with secondary production via glycolaldehyde, which simplifies the MCM isoprene mechanism for glyoxal. Similarly, we propose that methylglyoxal production can be approximated by a first-generation production term from isoprene, and secondary production via MVK, MACR and hydroxyacetone (Fig. 6).

Atmospheric implications

The first-generation yields of glyoxal, methylglyoxal, hydroxyacetone, and glycolaldehyde correspond to less than 5 % of the total isoprene yield and thus only have a small effect on the overall fate of isoprene. However, due to the abundance of isoprene, these findings together with the reduced higher generation production of glyoxal from C5 hydroxycarbonyls are important for models that investigate the production of the small oxidized organic molecules, especially within the context of SOA formation and cloud processing. Fu et al. (2008, 2009) used the GEOS-Chem global model updated with oxidation chemistry from the MCM to determine global aerosol yields from glyoxal and methylglyoxal. The global annual mean yields of glyoxal and methylglyoxal from OH reaction with isoprene as calculated by GEOS-Chem were 8 % and 29 %, respectively. The global glyoxal molar yield from isoprene in the study by Stavrakou et al. (2009) was found to be only slightly (16 %) higher than in the GEOS-Chem model. These glyoxal yields are close to the yields reported in this work (Table 3). However, these studies are missing the first-generation production term. Subtraction of 5/6 of the GEOS-Chem glyoxal yield via C5 hydroxycarbonyls (3.15 %) from the total glyoxal yield predicted by GEOS-Chem results in a higher-generation glyoxal yield from isoprene of 4.85 %. With the addition of the first-generation glyoxal yield from isoprene in this study (2.1 %),

an overall glyoxal yield of 6.95 % from OH reaction with isoprene is predicted, which is lower than that found in our altered and unaltered MCM model runs. However, it should be kept in mind that the modelled glyoxal was about 50 % higher than observed; scaling our total yield of 9.6 % by this amount gives 6.4 %, very close to the modified yields of Fu et al. (2008) and Fu et al. (2009), corrected for direct production and attenuated higher generation production from C5-hydroxycarbonyls. The yields observed in this study suggest that global models discussed above may be overestimating glyoxal production from isoprene by about 15 %, not a large amount. However, comparison of current global models with satellite glyoxal observations actually shows an underestimation of glyoxal over biogenically active regions (Stavrakou et al., 2009). If such discrepancies are true (and not due to satellite observation error or model isoprene emission error), then attenuation of the glyoxal yield from isoprene would aggravate the discrepancy. This, in turn, would mean that the missing biogenic source of glyoxal suggested by Stavrakou et al. (2009) is even larger than previously thought.

In addition, this work demonstrates that even for a molecule that has been as extensively studied as isoprene, its oxidation mechanism remains uncertain. Although the intramolecular rearrangements as proposed by Dibble (2004a,b) are not likely to correspond to the major channels, they can have a substantial impact on species that are produced in lower concentrations. The results presented here support the existence of such intramolecular rearrangements as do the results of (Paulot et al., 2009a) and Volkamer et al. (2006), which has implications for other cases for which similar rearrangements have been proposed, including OH recycling (Peeters et al., 2009).

Supplementary material related to this article is available online at:
<http://www.atmos-chem-phys.net/11/10779/2011/acp-11-10779-2011-supplement.pdf>.

Acknowledgements. The authors would like to thank Sam Henry and Aster Kammrath for instrumental assistance and Beth Kautzman for help with experimental setup and execution as well as Tzung-May Fu and Jenny Stavrakou for assistance with model comparisons. This work was supported by the National Science Foundation grant ATM-0852406, US Environmental Protection Agency STAR grant RD-833749. It has not been formally reviewed by the EPA. The views expressed in this document are solely those of the authors and the EPA does not endorse any products in this publication.

Edited by: V. F. McNeill

References

Altieri, K., Seitzinger, S., Carlton, A., Turpin, B., Klein, G., and Marshall, A.: Oligomers formed through in-cloud methylglyoxal reactions: Chemical composition, properties, and mechanisms investigated by ultra-high resolution FT-ICR mass spectrometry, *Atmos. Environ.*, 42, 1476–1490, doi:10.1016/j.atmosenv.2007.11.015, 2008.

Archibald, A. T., Cooke, M. C., Utembe, S. R., Shallcross, D. E., Derwent, R. G., and Jenkin, M. E.: Impacts of mechanistic changes on HO_x formation and recycling in the oxidation of isoprene, *Atmos. Chem. Phys.*, 10, 8097–8118, doi:10.5194/acp-10-8097-2010, 2010a.

Archibald, A. T., Jenkin, M. E., and Shallcross, D. E.: An isoprene mechanism intercomparison, *Atmos. Environ.*, 44, 5356–5364, doi:10.1016/j.atmosenv.2009.09.016, 2010b.

Berndt, T. and Böge, O.: Atmospheric Reaction of OH Radicals with 1,3-Butadiene and 4-Hydroxy-2-butenal, *J. Phys. Chem. A*, 111, 12099–12105, doi:10.1021/jp075349o, 2007.

Carlton, A., Turpin, B., Altieri, K., Seitzinger, S., Reff, A., Lim, H., and Ervens, B.: Atmospheric oxalic acid and SOA production from glyoxal: Results of aqueous photooxidation experiments, *Atmos. Environ.*, 41, 7588–7602, doi:10.1016/j.atmosenv.2007.05.035, 2007.

Carlton, A. G., Wiedinmyer, C., and Kroll, J. H.: A review of Secondary Organic Aerosol (SOA) formation from isoprene, *Atmos. Chem. Phys.*, 9, 4987–5005, doi:10.5194/acp-9-4987-2009, 2009b.

Chan, A. W. H., Galloway, M. M., Kwan, A. J., Chhabra, P. S., Keutsch, F. N., Wennberg, P. O., Flagan, R. C., and Seinfeld, J. H.: Photooxidation of 2-methyl-3-buten-2-ol (MBO) as a potential source of secondary organic aerosol, *Environ. Sci. Technol.*, 43, 4647–4652, doi:10.1021/es802560w, 2009.

Cocker, D. R., Flagan, R. C., and Seinfeld, J. H.: State-of-the-art chamber facility for studying atmospheric aerosol chemistry, *Environ. Sci. Technol.*, 35, 2594–2601, doi:10.1021/Es0019169, 2001.

Crounse, J., McKinney, K., Kwan, A., and Wennberg, P.: Measurement of gas-phase hydroperoxides by chemical ionization mass spectrometry, *Anal. Chem.*, 78, 6726–6732, doi:10.1021/ac0604235, 2006.

Dibble, T. S.: Intramolecular hydrogen bonding and double H-atom transfer in peroxy and alkoxy radicals from isoprene, *J. Phys. Chem. A*, 108, 2199–2207, doi:10.1021/jp0306702, 2004a.

Dibble, T. S.: Prompt chemistry of alkenoxy radical products of the double H-atom transfer of alkoxyradicals from isoprene, *J. Phys. Chem. A*, 108, 2208–2215, doi:10.1021/jp0312161, 2004b.

Ervens, B., Carlton, A. G., Turpin, B. J., Altieri, K. E., Kreidenweis, S. M., and Feingold, G.: Secondary organic aerosol yields from cloud-processing of isoprene oxidation products, *Geophys. Res. Lett.*, 35, L02816, doi:10.1029/2007gl031828, 2008.

Fan, J. and Zhang, R.: Atmospheric Oxidation Mechanism of Isoprene, *Environ. Chem.*, 1, 140–149, doi:10.1071/EN04045, 2004.

Fu, T.-M., Jacob, D. J., Wittrock, F., Burrows, J., Vrekoussis, M., and Henze, D.: Global budgets of atmospheric glyoxal and methylglyoxal, and implications for formation of secondary organic aerosols, *J. Geophys. Res.*, 113, D15303, doi:10.1029/2007JD009505, 2008.

Fu, T.-M., Jacob, D. J., and Heald, C. L.: Aqueous-phase re-

active uptake of dicarbonyls as a source of organic aerosol over eastern North America, *Atmos. Environ.*, 43, 1814–1822, doi:10.1016/j.atmosenv.2008.12.029, 2009.

Galloway, M. M., Chhabra, P. S., Chan, A. W. H., Surratt, J. D., Flagan, R. C., Seinfeld, J. H., and Keutsch, F. N.: Glyoxal uptake on ammonium sulphate seed aerosol: reaction products and reversibility of uptake under dark and irradiated conditions, *Atmos. Chem. Phys.*, 9, 3331–3345, doi:10.5194/acp-9-3331-2009, 2009.

Galloway, M. M., Loza, C. L., Chhabra, P. S., Chan, A. W. H., Yee, L. D., Seinfeld, J. H., and Keutsch, F. N.: Analysis of photochemical and dark glyoxal uptake: Implications for SOA formation, *Geophys. Res. Lett.*, 38, L17811, doi:10.1029/2011GL048514, 2011.

Gu, C. L., Rynard, C. M., Hendry, D. G., and Mill, T.: Hydroxide radical oxidation of isoprene, *Environ. Sci. Technol.*, 19, 151–155, doi:10.1021/es00132a007, 1985.

Guenther, A., Hewitt, C., Erickson, D., Fall, R., Geron, C., Graedel, T., Harley, P., Klinger, L., Lerdau, M., Mckay, W., Pierce, T., Scholes, B., Steinbrecher, R., Tallamaraju, R., Taylor, J., and Zimmerman, P.: A global model of natural volatile organic-compound emissions, *J. Geophys. Res.-Atmos.*, 100, 8873–8392, doi:10.1029/94JD02950, 1995.

Henry, S. B., Kammrath, A., and Keutsch, F. N.: Quantification of gas-phase glyoxal and methylglyoxal via the Laser-Induced Phosphorescence of (methyl)GlyOxal Spectrometry (LIPGLOS) method, *Atmos. Meas. Tech. Discuss.*, 4, 6159–6183, doi:10.5194/amt-4-6159-2011, 2011.

Huisman, A. J., Hottle, J. R., Coens, K. L., DiGangi, J. P., Galloway, M. M., Kammrath, A., and Keutsch, F. N.: Laser-induced phosphorescence for the in situ detection of glyoxal at part per trillion mixing ratios, *Anal. Chem.*, 80, 5884–5891, doi:10.1021/ac800407b, 2008.

Huisman, A. J., Hottle, J. R., Galloway, M. M., DiGangi, J. P., Coens, K. L., Choi, W. S., Falloona, I. C., Gilman, J. B., Kuster, W. C., de Gouw, J., Bouvier-Brown, N. C., Goldstein, A. H., LaFranchi, B. W., Cohen, R. C., Wolfe, G. M., Thornton, J. A., Docherty, K. S., Farmer, Delphine, K., Cubison, Jimenez, J. L., M. J., Mao, J., Brune, W. H., and Keutsch, F. N.: Photochemical modeling of glyoxal at a rural site: observations and analysis from BEARPEX 2007, *Atmos. Chem. Phys.*, 11, 8883–8897, doi:10.5194/acp-11-8883-2011, 2011.

Ip, H. S. S., Huang, X. H. H., and Yu, J. Z.: Effective Henry's law constants of glyoxal, glyoxylic acid, and glycolic acid, *Geophys. Res. Lett.*, 36, L01802, doi:10.1029/2008GL036212, 2009.

Jenkin, M. E., Saunders, S. M., and Pilling, M. J.: The tropospheric degradation of volatile organic compounds: a protocol for mechanism development, *Atmos. Environ.*, 31, 81–104, doi:10.1016/s1352-2310(96)00105-7, 1997.

Karl, T., Guenther, A., Turnipseed, A., Tyndall, G., Artaxo, P., and Martin, S.: Rapid formation of isoprene photo-oxidation products observed in Amazonia, *Atmos. Chem. Phys.*, 9, 7753–7767, doi:10.5194/acp-9-7753-2009, 2009.

Keywood, M. D., Varutbangkul, V., Bahreini, R., Flagan, R. C., and Seinfeld, J. H.: Secondary organic aerosol formation from the ozonolysis of cycloalkenes and related compounds, *Environ. Sci. Technol.*, 38, 4157–4164, doi:10.1021/es035363o, 2004.

Kwok, E. S. C., Atkinson, R., and Arey, J.: Observation of Hydroxycarbonyls from the OH Radical-Initiated Reaction of Isoprene, *Environ. Sci. Technol.*, 29, 2467–2469, doi:10.1021/es00009a046, 1995.

Loza, C. L., Chan, A. W. H., Galloway, M. M., Keutsch, F. N., Flagan, R. C., and Seinfeld, J. H.: Characterization of vapor wall loss in laboratory chambers, *Environ. Sci. Technol.*, 44, 5074–5078, doi:10.1021/es100727v, 2010.

Madronich, S. and Calvert, J. G.: The NCAR Master Mechanism of the gas phase chemistry-Version 2.0, Rep. NCAR/TN-333+STR, National Center for Atmospheric Research, 1989.

Miyoshi, A., Hatakeyama, S., and Washida, N.: OH radical-initiated photooxidation of isoprene: An estimate of global CO production, *J. Geophys. Res.-Atmos.*, 99, 18779–18787, doi:10.1029/94JD01334, 1994.

Nozière, B., Dziedzic, P., and Cordova, A.: Products and kinetics of the liquid-phase reaction of glyoxal catalyzed by ammonium ions (NH₄⁺), *J. Phys. Chem. A*, 113, 231–237, doi:10.1021/jp0878293, 2009.

Orlando, J. J., Tyndall, G. S., and Paulson, S. E.: Mechanism of the OH-initiated oxidation of methacrolein, *Geophys. Res. Lett.*, 26, 2191–2194, doi:10.1029/1999gl00453, 1999.

Paulot, F., Crounse, J. D., Kjaergaard, H. G., Kroll, J. H., Seinfeld, J. H., and Wennberg, P. O.: Isoprene photooxidation: new insights into the production of acids and organic nitrates, *Atmos. Chem. Phys.*, 9, 1479–1501, doi:10.5194/acp-9-1479-2009, 2009a.

Paulot, F., Crounse, J. D., Kjaergaard, H. G., Kurten, A., St. Clair, J. M., Seinfeld, J. H., and Wennberg, P. O.: Unexpected epoxide formation in the gas-phase photooxidation of isoprene, *Science*, 325, 730–733, doi:10.1126/science.1172910, 2009b.

Paulson, S. E., Flagan, R. C., and Seinfeld, J. H.: Atmospheric photooxidation of isoprene part I: The hydroxyl radical and ground state atomic oxygen reactions, *Int. J. Chem. Kin.*, 24, 79–101, doi:10.1002/kin.550240109, 1992.

Peeters, J., Nguyen, T. L., and Vereecken, L.: HO_x radical regeneration in the oxidation of isoprene, *Phys. Chem. Chem. Phys.*, 11, 5935–5939, doi:10.1039/B908511d, 2009.

Perri, M. J., Seitzinger, S., and Turpin, B. J.: Secondary organic aerosol production from aqueous photooxidation of glycolaldehyde: Laboratory experiments, *Atmos. Environ.*, 43, 1487–1497, doi:10.1016/j.atmosenv.2008.11.037, 2009.

Sareen, N., Schwier, A. N., Shapiro, E. L., Mitroo, D., and McNeill, V. F.: Secondary organic material formed by methylglyoxal in aqueous aerosol mimics, *Atmos. Chem. Phys.*, 10, 997–1016, doi:10.5194/acp-10-997-2010, 2010.

Saunders, S. M., Jenkin, M. E., Derwent, R. G., and Pilling, M. J.: Protocol for the development of the Master Chemical Mechanism, MCM v3 (Part A): tropospheric degradation of non-aromatic volatile organic compounds, *Atmos. Chem. Phys.*, 3, 161–180, doi:10.5194/acp-3-161-2003, 2003.

Shapiro, E. L., Szprengiel, J., Sareen, N., Jen, C. N., Giordano, M. R., and McNeill, V. F.: Light-absorbing secondary organic material formed by glyoxal in aqueous aerosol mimics, *Atmos. Chem. Phys.*, 9, 2289–2300, doi:10.5194/acp-9-2289-2009, 2009.

Sprengnether, M., Demerjian, K. L., Donahue, N. M., and Anderson, J. G.: Product analysis of the OH oxidation of isoprene and 1,3-butadiene in the presence of NO, *J. Geophys. Res.*, 107, 4268, doi:10.1029/2001jd000716, 2002.

St. Clair, J. M., McCabe, D. C., Crounse, J. D., Steiner, U., and Wennberg, P. O.: Chemical ionization tandem mass spectrometry

eter for the in situ measurement of methyl hydrogen peroxide, *Rev. Sci. Instrum.*, 81, 094102–094106, doi:10.1063/1.3480552, 2010.

Stavrakou, T., Müller, J.-F., De Smedt, I., Van Roozendael, M., Kanakidou, M., Vrekoussis, M., Wittrock, F., Richter, A., and Burrows, J. P.: The continental source of glyoxal estimated by the synergistic use of spaceborne measurements and inverse modelling, *Atmos. Chem. Phys.*, 9, 8431–8446, doi:10.5194/acp-9-8431-2009, 2009.

Tan, Y., Perri, M. J., Seitzinger, S. P., and Turpin, B. J.: Effects of precursor concentration and acidic sulfate in aqueous glyoxal-OH radical oxidation and implications for secondary organic aerosol, *Environ. Sci. Technol.* 43, 8105–8112, doi:10.1021/es901742f, 2009.

Taraborrelli, D., Lawrence, M. G., Butler, T. M., Sander, R., and Lelieveld, J.: Mainz Isoprene Mechanism 2 (MIM2): an isoprene oxidation mechanism for regional and global atmospheric modelling, *Atmos. Chem. Phys.*, 9, 2751–2777, doi:10.5194/acp-9-2751-2009, 2009.

Tuazon, E. C. and Atkinson, R.: A product study of the gas-phase reaction of methyl vinyl ketone with the OH radical in the presence of NO_x , *Int. J. Chem. Kinet.*, 21, 1141–1152, doi:10.1002/kin.550211207, 1989.

Tuazon, E. C. and Atkinson, R.: A product study of the gas-phase reaction of isoprene with the OH radical in the presence of NO_x , *Int. J. Chem. Kin.*, 22, 1221–1236, doi:10.1002/kin.550221202, 1990a.

Tuazon, E. C. and Atkinson, R.: A product study of the gas-phase reaction of methacrolein with the OH radical in the presence of NO_x , *Int. J. Chem. Kin.*, 22, 591–602, doi:10.1002/kin.550220604, 1990b.

Volkamer, R., Barnes, I., Platt, U., Molina, L. T., and Molina, M. J.: Remote sensing of glyoxal by differential optical absorption spectroscopy (DOAS): Advancements in simulation chamber and field experiments, in: *Environmental Simulation Chambers: Application to Atmospheric Chemical Processes*, edited by: Barnes, I. and Rudinski, J., 62, Springer, Dordrecht, Netherlands, 2006.

Volkamer, R., Ziemann, P. J., and Molina, M. J.: Secondary organic aerosol formation from acetylene (C_2H_2): seed effect on SOA yields due to organic photochemistry in the aerosol aqueous phase, *Atmos. Chem. Phys.*, 9, 1907–1928, doi:10.5194/acp-9-1907-2009, 2009.

Zhao, J., Zhang, R., Fortner, E. C., and North, S. W.: Quantification of Hydroxycarbonyls from OH Isoprene Reactions, *J. Am. Chem. Soc.*, 126, 2686–2687, doi:10.1021/ja0386391, 2004.

Appendix F

Analysis of photochemical and dark glyoxal uptake: implications for SOA formation¹

¹This chapter is reproduced by permission from "Analysis of photochemical and dark glyoxal uptake: Implications for SOA formation," by M. M. Galloway, C. L. Loza, P. S. Chhabra, A. W. H. Chan, L. D. Yee, J. H. Seinfeld, and F. N. Keutsch, *Geophysical Research Letters*, 38, L17811, doi:10.1029/2011GL048514, 2011. Copyright 2011 by the American Geophysical Union.

Analysis of photochemical and dark glyoxal uptake: Implications for SOA formation

M. M. Galloway,¹ C. L. Loza,² P. S. Chhabra,² A. W. H. Chan,^{2,3} L. D. Yee,⁴
J. H. Seinfeld,^{2,4} and F. N. Keutsch¹

Received 23 June 2011; revised 15 August 2011; accepted 23 August 2011; published 15 September 2011.

[1] The dependence of glyoxal uptake onto deliquesced ammonium sulfate seed aerosol was studied under photochemical (light + hydroxyl radical (OH)) and dark conditions. In this study, the chemical composition of aerosol formed from glyoxal is identical in the presence or absence of OH. In addition, there was no observed OH dependence on either glyoxal uptake or glyoxal-driven aerosol growth for this study. These findings demonstrate that, for the system used here, glyoxal uptake is not affected by the presence of OH. In combination with previous studies, this shows that the exact nature of the type of seed aerosol, in particular the presence of a coating, has a large influence on fast photochemical uptake of glyoxal. Due to the challenge of relating this seed aerosol dependence to ambient conditions, this work highlights the resulting difficulty in quantitatively including SOA formation from glyoxal in models. **Citation:** Galloway, M. M., C. L. Loza, P. S. Chhabra, A. W. H. Chan, L. D. Yee, J. H. Seinfeld, and F. N. Keutsch (2011), Analysis of photochemical and dark glyoxal uptake: Implications for SOA formation, *Geophys. Res. Lett.*, 38, L17811, doi:10.1029/2011GL048514.

1. Introduction

[2] The formation of secondary organic aerosol (SOA) is traditionally explained via uptake of gas-phase species onto aerosol following vapor pressure and partitioning theory [Pankow, 1994a, 1994b; Odum *et al.*, 1996]. Recent work has shown that chemical reactions occurring within the aerosol can increase SOA yields as well as alter both chemical and optical aerosol properties [Carlton *et al.*, 2007; Ervens *et al.*, 2008; Galloway *et al.*, 2009; Nozière *et al.*, 2009; Shapiro *et al.*, 2009; Bones *et al.*, 2010]. Glyoxal has a high effective Henry's Law coefficient, which results in more efficient uptake onto aqueous aerosol droplets than expected for a small carbonyl [Ip *et al.*, 2009]. In the aerosol, glyoxal can react with other species to form acetal oligomers, imidazoles, other high molecular weight compounds, and be oxidized with OH to carboxylic acids [Carlton *et al.*, 2007; De Haan

et al., 2009b; Galloway *et al.*, 2009; Tan *et al.*, 2009]. Due to this potential contribution to SOA, glyoxal has received increasing attention [Kroll *et al.*, 2005; Liggio *et al.*, 2005; Corrigan *et al.*, 2008; Galloway *et al.*, 2009; Volkamer *et al.*, 2009].

[3] Glyoxal uptake onto liquid (deliquesced) aqueous ammonium sulfate (AS) seed aerosol has been studied under dark [Kroll *et al.*, 2005; Liggio *et al.*, 2005; Galloway *et al.*, 2009] and photochemical conditions [Volkamer *et al.*, 2009]. Photochemical conditions will be defined as UV-irradiation with explicit addition of a source of gas-phase OH radicals. Galloway *et al.* [2009] showed that dark uptake is largely reversible except for minor imidazole formation. However, drying of the aerosol results in glyoxal being retained [De Haan *et al.*, 2009a]. Volkamer *et al.* [2009] studied SOA formation from acetylene (C_2H_2) via glyoxal in a photochemical system and dark glyoxal uptake onto different types of seed aerosol. Whereas rapid photochemical uptake was observed for pure AS, pure fulvic acid, and mixed AS/fulvic acid seed, no rapid photochemical uptake was observed in mixed AS/fulvic acid seed that also contained sulfuric or amino acids, highlighting the complex dependence of rapid photochemical uptake on seed composition. SOA yields from the fast photochemical uptake are substantially higher than from slow, dark-type uptake [Ervens and Volkamer, 2010], hence a thorough understanding of the seed dependence of fast photochemical glyoxal uptake and the chemical processes responsible for it are central for models of SOA formation.

[4] In the gas-phase, OH oxidizes glyoxal to form CO, CO_2 , and other high volatility species that do not contribute to aerosol growth (Figure 1). Hence, the gas-phase reaction of glyoxal with OH should not form aerosol. The observed rapid photochemical glyoxal uptake strongly indicates condensed-phase reactions with OH [Volkamer *et al.*, 2009]. Carlton *et al.* [2007] observed oxalic acid production in laboratory studies of photochemical oxidation of glyoxal in bulk aqueous, cloud-processing-like systems with a source of condensed-phase OH radicals. In a related study, Tan *et al.* [2009] demonstrated that transition from cloud to aerosol-processing conditions leads to increased concentrations of larger (C_3 – C_4) carboxylic acids. As the condensed-phase glyoxal-OH reaction produces higher molecular weight compounds, specifically carboxylic acids, any observed increase in aerosol from glyoxal and OH should be a result of carboxylic acid formation within the aerosol. The goals of the work presented here were to investigate these processes within aqueous aerosol and the extent to which photochemical glyoxal uptake affects the chemical composition of the resulting aerosol, in particular

¹Department of Chemistry, University of Wisconsin-Madison, Madison, Wisconsin, USA.

²Division of Chemistry and Chemical Engineering, California Institute of Technology, Pasadena, California, USA.

³Now at Department of Environmental Science, Policy and Management, University of California, Berkeley, California, USA.

⁴Division of Engineering and Applied Science, California Institute of Technology, Pasadena, California, USA.

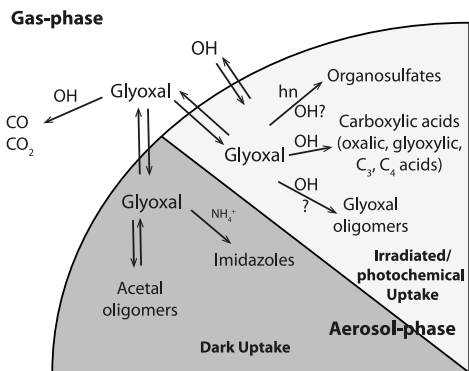


Figure 1. Simplified schematic of glyoxal reactions within aqueous AS aerosol. Glyoxal oligomers formed during photochemical uptake refers to any type of higher molecular weight compound. Whereas dark-type reaction products and kinetics have been extensively studied, photochemical reaction products have only been studied in detail for laboratory bulk samples more similar to cloud processing conditions. These studies show that condensed-phase reactions of glyoxal with OH produce carboxylic acids, leading to oxidized organic aerosol.

the presence of carboxylic acids and higher molecular weight compounds.

2. Experimental Methods

2.1. Preparation and Instrumentation

[5] Experiments were carried out in the Caltech dual 28 m³ Teflon chambers, described in detail elsewhere [Cocker *et al.*, 2001; Keywood *et al.*, 2004]. The chambers were flushed with clean, humidified air for over 40 hrs before each experiment. AS seed particles (~60–80 nm diameter) were generated by atomization of 0.015 M aqueous AS using a constant rate atomizer. Methyl nitrite (CH₃ONO) was used as the OH source, and was prepared following the method described by Chan *et al.* [2010], stored at liquid nitrogen temperatures, and allowed to vaporize into a 500 mL glass bulb before injection into the chamber by a dry air stream. The mixing ratio of injected CH₃ONO was 1 ppm and the initial OH concentration was $\sim 7 \times 10^7$ molec cm⁻³. Gas-phase glyoxal was prepared from glyoxal trimer dihydrate as described by Galloway *et al.* [2009], vaporized into a 2 L glass bulb, and injected using a dry air stream. Temperature, relative humidity (RH), O₃, and NO_x were continuously monitored. Aerosol size distribution, number and volume concentrations were monitored using a differential mobility analyzer (TSI 3081) coupled with a condensation particle counter (TSI 3760). All aerosol volume data are corrected for wall loss, as described by Ng *et al.* [2007]. CH₃ONO was monitored via a gas chromatograph with flame ionization detector (Agilent 6890N). The Madison Laser-Induced-Phosphorescence instrument monitored gas-phase glyoxal [Huisman *et al.*, 2008].

[6] An Aerodyne HR-ToF-AMS operating in “V-mode” continuously collected real-time particle mass spectra [DeCarlo *et al.*, 2006; Canagaratna *et al.*, 2007]. Data were analyzed using a fragmentation table to separate out sulfate,

ammonium, and organic spectra and to allow for monitoring of specific mass-to-charge ratios (see auxiliary material) [Allan *et al.*, 2004].¹ AMS mass fragments *m/z* 58 (C₂H₂O₂⁺) and *m/z* 105 (C₃H₅O₄⁺) are tracers for glyoxal and its oligomers, respectively, and have been used to monitor non-oxidative glyoxal uptake [Galloway *et al.*, 2009]. Their magnitude is only $\sim 10\%$ of the total organic uptake from glyoxal, but these fragments are useful as tracers of glyoxal uptake into aerosol and oligomer formation. The *m/z* 44 fragment (CO₂⁺) is typically used as a tracer for oxidized organics in aerosol, especially carboxylic acids [Canagaratna *et al.*, 2007], the glyoxal condensed-phase oxidation products. During these and previous dark (non-oxidative) glyoxal uptake experiments [Galloway *et al.*, 2009], the magnitude of *m/z* 44 was 8% of *m/z* 58. In the absence of oxidants, this signal cannot be due to OH-driven oxidation and must be directly from glyoxal. To correct for this contribution, 8% of the *m/z* 58 signal was subtracted from the *m/z* 44 signal. The resulting signal corresponds to highly oxidized organics (other than glyoxal but including glyoxal oxidation products, e.g., oxalic acid) and will be referred to as “corrected *m/z* 44” and used as a tracer of condensed-phase reaction products of glyoxal with OH. All AMS data are normalized to sulfate in order to account for aerosol wall loss and changes in collection efficiency (bounce).

2.2. Experimental Procedures

[7] Experimental conditions are summarized in Table 1. AS seed aerosol was injected into the humid chamber and allowed to mix and equilibrate. Then, chamber blacklights were turned on for 2 min to quantify aerosol growth from residual chamber organics without an OH source (1st irradiated period). After this, CH₃ONO and (usually) NO were added (see Table 1), and blacklights were turned on again to quantify aerosol growth from residual chamber organics with an OH source (2nd irradiated period). After ~ 15 min, the total and oxidized organic signals on the AMS started to plateau although less than 15% of initial CH₃ONO had reacted and glyoxal was then injected. After 1 hr, the lights were turned off to allow dark uptake of glyoxal. Blank experiments were run with the same procedures without addition of glyoxal.

3. Results

[8] In all experiments, the 1st irradiated period produced no aerosol volume growth and no increase in the total organic or carboxylic acid tracer fraction (corr. *m/z* 44 to sulfate ratio). At the beginning of the 2nd irradiated period, *t* = 0 in Figure 2, after CH₃ONO but before glyoxal injection, a rapid increase in the carboxylic acid tracer (Figure 2c) and aerosol volume were observed at high RH, but not at low RH. This shows that rapid photochemical growth from residual organics can occur under humid conditions, even after extensive cleaning of the chamber. This chamber-background aerosol (OA) was highly oxidized (O/C ratio of 0.95), typical for water-soluble organic carbon (WSOC), high CCN activity, and aqueous processing [Turpin and Lim, 2001; Massoli *et al.*, 2010]. Figures 2a and 2b show that upon injection of gas-phase glyoxal, the aerosol glyoxal-tracer and total OA fractions increased

¹Auxiliary materials are available in the HTML. doi:10.1029/2011GL048514.

Table 1. Experimental Conditions^a

Experiment	Initial Glyoxal (ppb)	Initial Seed ($\mu\text{m}^3 \text{cm}^{-3}$)	Δ Seed ($\mu\text{m}^3 \text{cm}^{-3}$)	NO (ppb)	RH (%)	T (K)	Lights	OH Precursor
1	None	20	5	625	66	293	5%	CH ₃ ONO
2	38	37	N/A ^b	768	54	294	50%	CH ₃ ONO
3	None	31	-4	278	82	293	50%	CH ₃ ONO
4	131	29	33	1	60	293	10%	None
5	38	19	5	93	76	292	10%	CH ₃ ONO
6	59	18	5	860	76	291	10%	CH ₃ ONO
7	253	19	96	116	67	292	10%	CH ₃ ONO

^a Δ seed volume is calculated at lights off.^bGlyoxal was allowed to equilibrate with the walls before seed injection.

rapidly, whereas the carboxylic acid tracer (corr. m/z 44) was not affected and closely resembled the blanks, demonstrating that formation of carboxylic acids from glyoxal, the expected OH-driven aerosol-processing products, is not observed under our photochemical uptake conditions. In summary, Figure 2 highlights that photochemical aerosol-phase reaction/oxidation products are independent of glyoxal, whereas total organic growth during the photochemical experiments clearly depends on glyoxal but this glyoxal-dependent growth in our photochemical experiments closely resembles that of slow, dark-type uptake.

[9] Figure 3 depicts the change in carboxylic acid, glyoxal, and total OA fractions during the photochemical processing period ($t = 0$ up to vertical lines shown in Figure 2) as a function of gas-phase glyoxal. The glyoxal tracer and the total OA fraction depend on glyoxal, corr. m/z 44 to sulfate ratio is statistically independent of glyoxal concentrations from 0 to 260 ppb. The experimental variability, most readily observed in the difference between the blank experiments

(Figure 3c), does not allow us to fully rule out a small dependence of the carboxylic acid tracer (corr. m/z 44 to sulfate) on glyoxal. However, this contribution must be very small compared to that of the slow, dark-type glyoxal uptake. The fact that no such contribution is observed demonstrates that virtually all uptake from glyoxal can be explained by non-oxidative (dark-type) uptake. Once the blacklights are turned off, OH is quickly depleted. If OH is responsible for an increased glyoxal uptake, the growth in glyoxal and total organic to sulfate ratios should slow down or level off at lights off. This is not the case (Figures 2a and 2b), and glyoxal uptake increases slightly when the blacklights are turned off, likely as a result of the drop in temperature and rise in RH.

4. Discussion

[10] Under all conditions studied here, the observed aerosol growth can be fully explained by slow, dark-type

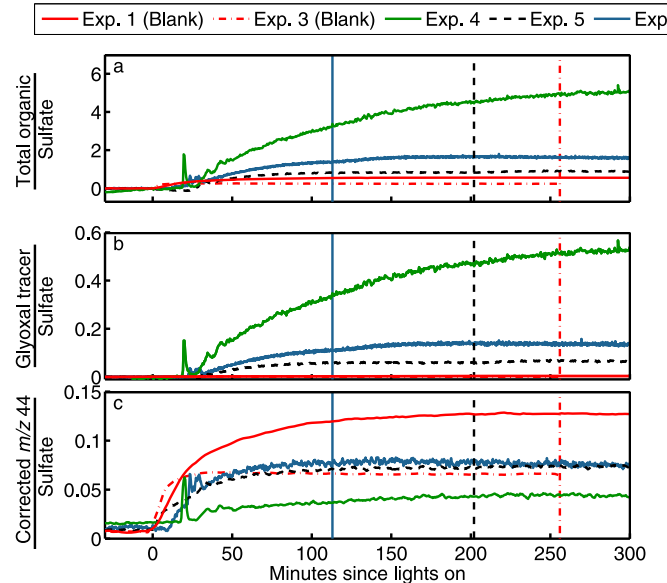


Figure 2. (a) Total organic tracer, (b) m/z 58 and (c) carboxylic acid (corr. m/z 44) tracers, all normalized to sulfate. For experiments with gas-phase glyoxal, glyoxal injections occurred at \sim 15 minutes after lights were turned on. Vertical lines indicate when lights were turned off for each experiment to observe glyoxal uptake in the absence of light and OH. After this time, a slight increase in glyoxal and organic tracer can be seen, while there is no increase in oxidized organic tracer. The growth rate of the oxidized organic fraction does not increase upon addition of glyoxal. After initial fluctuations from glyoxal mixing in the chamber, glyoxal uptake rates are very similar for all experiments.

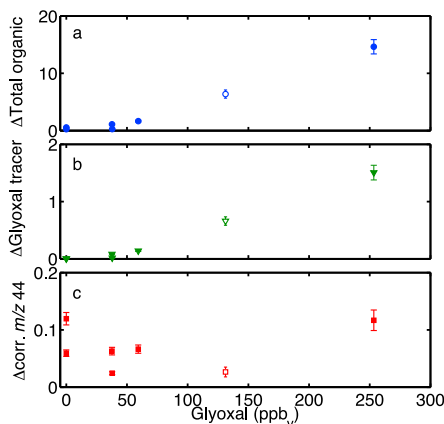


Figure 3. Change in (a) total organic fraction, (b) glyoxal-tracer fraction (m/z 58), and (c) the oxidized fraction (corr. m/z 44) of aerosol during time of OH exposure for all experiments. These data are normalized to sulfate. Solid points indicate experiments with OH source present, open points indicate an irradiated experiment with no OH source present. Error bars reflect precision. Δ organic and Δ glyoxal-tracer increase with increasing glyoxal concentration. The variability in blanks shows that environmental factors and not precision dominate the variability of the corr. m/z 44 to sulfate ratio but not the total organic to sulfate ratio. The trend in oxidized organic with gas-phase glyoxal is statistically not significant, indicating that the contribution to aerosol as a result of oxidized glyoxal uptake is very small.

glyoxal uptake and fast photochemical uptake that results only from residual organics in the chamber. The oxidized OA fraction (carboxylic acids) was not attributable to glyoxal (Figure 3c) in our uptake experiments with glyoxal and a gas-phase OH source. This is in contrast to the laboratory studies of bulk aqueous oxidation of glyoxal by OH with a condensed-phase OH source, which saw photochemical products, specifically carboxylic acids [Carlton *et al.*, 2007; Tan *et al.*, 2009]. The corrected m/z 44 (carboxylic acid) signal indicates the presence of oxidation products, but blank experiments show that this is not a result of glyoxal uptake but from residual chamber organics. With the exception of the oxidized aerosol fraction, which exhibits no dependence on glyoxal, the glyoxal-dependent growth rate and composition of the aerosol as judged by the AMS are identical in the presence and absence of OH. Although the AMS fragments both oligomers and other higher molecular weight compounds, previous experiments have clearly shown that glyoxal oligomers can be detected [Galloway *et al.*, 2009; Liggio *et al.*, 2005]. If OH affected the oxidation or oligomerization chemistry in the aerosol, a shift to higher masses would be evident in the overall AMS mass spectra when compared to dark uptake conditions. Analysis of the m/z 105 to m/z 58 ratio rules out that OH influences the formation of glyoxal (acetal) oligomers. Our analysis also shows that the overall mass spectra of photochemical glyoxal uptake are not shifted to higher molecular weights or do not indicate other changes compared to dark uptake. In addition, analysis with particle-into-liquid-samplers

and analysis of filter extracts of aerosol did not show any higher molecular weight compounds, such as organosulfates or carboxylic acids (see auxiliary material).

[11] The observation of only slow, dark-type uptake in our experiments matches the results for mixed AS/fulvic/amino/sulfuric acid seed particles of Volkamer *et al.* [2009] but disagrees with their AS results that show fast photochemical uptake. This merits further discussion, specifically in the context of the exact nature of the seed, its influence on uptake, and resulting atmospheric implications. The seed introduced into the chamber consisted of pure AS seed aerosol, for which Volkamer *et al.* [2009] saw fast photochemical uptake. However, the seed to which glyoxal was exposed in our study was not pure as it had experienced a small amount of growth from chamber background aerosol, which was unavoidable under humid conditions even after extensive chamber cleaning.

[12] The key question is if and how this small amount of background aerosol or differences in experimental procedure resulted in a barrier for photochemical glyoxal uptake but not dark-type uptake. It was not known if a coating was present on the aerosol, and it is possible that, despite its high O/C ratio, expected high CCN activity, and WSOC-like properties, the chamber-background aerosol formed a coating. This coating may have prevented fast photochemical uptake but not slower dark-type uptake of glyoxal. This could result if dark-type uptake is rate-limited by a bulk-process whereas fast photochemical uptake is rate-limited by surface reactions. It is also possible that direct injection of glyoxal rather than photochemical generation from C_2H_2 could explain the different results. Glyoxal oligomers may have formed in the gas-phase as a result of the high concentrations at the injection port, although it is unclear whether this is a gas-phase or wall/surface process. These oligomers have much lower vapor pressures than glyoxal and should rapidly partition to surfaces, including aerosol, potentially forming a coating. We also conducted experiments in which glyoxal was injected and allowed to equilibrate to the walls before seed was injected and photochemistry initiated (Exp. 2) in which case one might expect the oligomers to rapidly partition to the chamber walls before the seed was present. No fast photochemical uptake was observed, but it is possible that chamber background-aerosol rapidly coated the seed. A coating on our seed from chamber background or glyoxal/glyoxal oligomers could reconcile our results with those of Volkamer *et al.* [2009] if such coatings were not present for the latter experiments.

[13] The atmospheric implications of this work are less dependent on the differences than the similarities between our experimental results for AS and those of Volkamer *et al.* [2009]. Both studies show that fast photochemical uptake does not occur for all types of seed aerosol. The critical question is which type of seed is closest to atmospheric conditions. If the lack of fast photochemical uptake is caused by a coating on the seed, it is important to determine the necessary conditions and types of coatings that are common in the atmosphere to determine when and where ambient aerosol will show fast glyoxal uptake. Answering these questions about ambient aerosol and further elucidating conditions of fast photochemical uptake is required to determine the role of glyoxal in SOA formation from uptake on aerosol. At present, this is unclear and this work high-

lights the difficulty in both quantitatively and accurately including SOA formation from glyoxal in models.

[14] **Acknowledgments.** The authors thank Rainer Volkamer for helpful discussions prior to publication. This work was supported by the National Science Foundation, Division of Atmospheric Sciences, Atmospheric Chemistry Program (grants 1026667, 0852406), US Department of Energy grant DE-FG02-05ER63 983 and US Environmental Protection Agency STAR grant RD-83 374 901. It has not been formally reviewed by the EPA. The views expressed in this document are solely those of the authors and the EPA does not endorse any products in this publication.

[15] The Editor thanks two anonymous reviewers for their assistance in evaluating this paper.

References

Allan, J. D., et al. (2004), A generalised method for the extraction of chemically resolved mass spectra from Aerodyne aerosol mass spectrometer data, *J. Aerosol Sci.*, **35**(7), 909–922, doi:10.1016/j.jaerosci.2004.02.007.

Bones, D. L., D. K. Henricksen, S. A. Mang, M. Gonsior, A. P. Bateman, T. B. Nguyen, W. J. Cooper, and S. A. Nizkorodov (2010), Appearance of strong absorbers and fluorophores in limonene-O₃ secondary organic aerosol due to NH₄⁺-mediated chemical aging over long time scales, *J. Geophys. Res.*, **115**, D05203, doi:10.1029/2009JD012864.

Canagaratna, M. R., et al. (2007), Chemical and microphysical characterization of ambient aerosols with the aerodyne aerosol mass spectrometer, *Mass Spectrom. Rev.*, **26**(2), 185–222, doi:10.1002/mas.20115.

Carlton, A., B. Turpin, K. Altieri, S. Seitzinger, A. Reff, H. Lim, and B. Ervens (2007), Atmospheric oxalic acid and soa production from glyoxal: Results of aqueous photooxidation experiments, *Atmos. Environ.*, **41**(35), 7588–7602, doi:10.1016/j.atmosenv.2007.05.035.

Chan, A. W. H., et al. (2010), Role of aldehyde chemistry and NO_x concentrations in secondary organic aerosol formation, *Atmos. Chem. Phys.*, **10**(15), 7169–7188, doi:10.5194/acp-10-7169-2010.

Cocker, D. R., R. C. Flagan, and J. H. Seinfeld (2001), State-of-the-art chamber facility for studying atmospheric aerosol chemistry, *Environ. Sci. Technol.*, **35**(12), 2594–2601, doi:10.1021/es0019169.

Corrigan, A. L., S. W. Hanley, and D. O. De Haan (2008), Uptake of glyoxal by organic and inorganic aerosols, *Environ. Sci. Technol.*, **42**(12), 4428–4433, doi:10.1021/es7032394.

DeCarlo, P. F., et al. (2006), Field-deployable, high-resolution, time-of-flight aerosol mass spectrometer, *Anal. Chem.*, **78**(24), 8281–8289, doi:10.1021/ac061249n.

De Haan, D. O., A. L. Corrigan, M. A. Tolbert, J. L. Jimenez, S. E. Wood, and J. J. Turley (2009a), Secondary organic aerosol formation by self-reactions of methylglyoxal and glyoxal in evaporating droplets, *Environ. Sci. Technol.*, **43**(21), 8184–8190, doi:10.1021/es902152t.

De Haan, D. O., et al. (2009b), Secondary organic aerosol-forming reactions of glyoxal with amino acids, *Environ. Sci. Technol.*, **43**(8), 2818–2824, doi:10.1021/es803534f.

Ervens, B., and R. Volkamer (2010), Glyoxal processing by aerosol multiphase chemistry: Towards a kinetic modeling framework of secondary organic aerosol formation in aqueous particles, *Atmos. Chem. Phys.*, **10**(17), 8219–8244, doi:10.5194/acp-10-8219-2010.

Ervens, B., A. G. Carlton, B. J. Turpin, K. E. Altieri, S. M. Kreidenweis, and G. Feingold (2008), Secondary organic aerosol yields from cloud-processing of isoprene oxidation products, *Geophys. Res. Lett.*, **35**, L02816, doi:10.1029/2007GL031828.

Galloway, M. M., P. S. Chhabra, A. W. H. Chan, J. D. Surratt, R. C. Flagan, J. H. Seinfeld, and F. N. Keutsch (2009), Glyoxal uptake on ammonium sulphate seed aerosol: Reaction products and reversibility of uptake under dark and irradiated conditions, *Atmos. Chem. Phys.*, **9**(10), 3331–3345, doi:10.5194/acp-9-3331-2009.

Huisman, A. J., J. R. Hottle, K. L. Coens, J. P. DiGangi, M. M. Galloway, A. Kammrath, and F. N. Keutsch (2008), Laser-induced phosphorescence for the in situ detection of glyoxal at part per trillion mixing ratios, *Anal. Chem.*, **80**(15), 5884–5891, doi:10.1021/ac800407b.

Ip, H. S. S., X. H. H. Huang, and J. Z. Yu (2009), Effective Henry's law constants of glyoxal, glyoxyllic acid, and glycolic acid, *Geophys. Res. Lett.*, **36**, L01802, doi:10.1029/2008GL036212.

Keywood, M. D., V. Varutbangkul, R. Bahreini, R. C. Flagan, and J. H. Seinfeld (2004), Secondary organic aerosol formation from the ozonolysis of cycloalkenes and related compounds, *Environ. Sci. Technol.*, **38**(15), 4157–4164, doi:10.1021/es035363o.

Kroll, J. H., N. L. Ng, S. M. Murphy, V. Varutbangkul, R. C. Flagan, and J. H. Seinfeld (2005), Chamber studies of secondary organic aerosol growth by reactive uptake of simple carbonyl compounds, *J. Geophys. Res.*, **110**, D23207, doi:10.1029/2005JD006004.

Liggio, J., S.-M. Li, and R. McLaren (2005), Reactive uptake of glyoxal by particulate matter, *J. Geophys. Res.*, **110**, D10304, doi:10.1029/2004JD005113.

Massoli, P., et al. (2010), Relationship between aerosol oxidation level and hygroscopic properties of laboratory generated secondary organic aerosol (SOA) particles, *Geophys. Res. Lett.*, **37**, L24801, doi:10.1029/2010GL045258.

Ng, N. L., J. H. Kroll, A. W. H. Chan, P. S. Chhabra, R. C. Flagan, and J. H. Seinfeld (2007), Secondary organic aerosol formation from m-xylene, toluene, and benzene, *Atmos. Chem. Phys.*, **7**(14), 3909–3922, doi:10.5194/acp-7-3909-2007.

Nozière, B., P. Dziedzic, and A. Cordova (2009), Products and kinetics of the liquid-phase reaction of glyoxal catalyzed by ammonium ions (NH₄⁺), *J. Phys. Chem. A*, **113**(1), 231–237, doi:10.1021/jp8078293.

Odum, J. R., T. Hoffmann, F. Bowman, D. Collins, R. C. Flagan, and J. H. Seinfeld (1996), Gas/particle partitioning and secondary organic aerosol yields, *Environ. Sci. Technol.*, **30**(8), 2580–2585, doi:10.1021/es950943+.

Pankow, J. F. (1994a), An absorption-model of gas-particle partitioning of organic-compounds in the atmosphere, *Atmos. Environ.*, **28**(2), 185–188, doi:10.1016/1352-2310(94)90093-0.

Pankow, J. F. (1994b), An absorption-model of the gas aerosol partitioning involved in the formation of secondary organic aerosol, *Atmos. Environ.*, **28**(2), 189–193, doi:10.1016/1352-2310(94)90094-9.

Shapiro, E. L., J. Szprengiel, N. Sareen, C. N. Jen, M. R. Giordano, and V. F. McNeill (2009), Light-absorbing secondary organic material formed by glyoxal in aqueous aerosol mimics, *Atmos. Chem. Phys.*, **9**(7), 2289–2300, doi:10.5194/acp-9-2289-2009.

Tan, Y., M. J. Perri, S. P. Seitzinger, and B. J. Turpin (2009), Effects of precursor concentration and acidic sulfate in aqueous glyoxal-OH radical oxidation and implications for secondary organic aerosol, *Environ. Sci. Technol.*, **43**(21), 8105–8112, doi:10.1021/es901742f.

Turpin, B. J., and H. J. Lim (2001), Species contributions to PM_{2.5} mass concentrations: Revisiting common assumptions for estimating organic mass, *Aerosol Sci. Technol.*, **35**(1), 602–610, doi:10.1080/02786820119445.

Volkamer, R., P. J. Zieman, and M. J. Molina (2009), Secondary organic aerosol formation from acetylene (C₂H₂): Seed effect on SOA yields due to organic photochemistry in the aerosol aqueous phase, *Atmos. Chem. Phys.*, **9**(6), 1907–1928, doi:10.5194/acp-9-1907-2009.

A. W. H. Chan, Department of Environmental Science, Policy and Management, University of California, 250C Hilgard Hall, Berkeley, CA 94720, USA.

P. S. Chhabra, C. L. Loza, and J. H. Seinfeld, Division of Chemistry and Chemical Engineering, California Institute of Technology, 1200 E. California Blvd., Pasadena, CA 91125, USA.

M. M. Galloway and F. N. Keutsch, Department of Chemistry, University of Wisconsin-Madison, 1101 University Ave., Madison, WI 53706, USA. (keutsch@chem.wisc.edu)

L. D. Yee, Division of Engineering and Applied Science, California Institute of Technology, 1200 E. California Blvd., Pasadena, CA 91125, USA.

Appendix G

Role of aldehyde chemistry and NO_x concentrations in secondary organic aerosol formation¹

¹This chapter is reproduced by permission from "Role of aldehyde chemistry and NO_x concentrations in secondary organic aerosol formation," by A. W. H. Chan, M. N. Chan, J. D. Surratt, P. S. Chhabra, C. L. Loza, J. D. Crounse, L. D. Yee, R. C. Flagan, P. O. Wennberg, and J. H. Seinfeld, *Atmospheric Chemistry and Physics*, 10, 7169-7188, doi:10.5194/acp-10-7169-2010, 2010. Copyright 2013 Authors. This work is licensed under a Creative Commons License.

Role of aldehyde chemistry and NO_x concentrations in secondary organic aerosol formation

A. W. H. Chan¹, M. N. Chan², J. D. Surratt^{1,*}, P. S. Chhabra¹, C. L. Loza¹, J. D. Crounse¹, L. D. Yee², R. C. Flagan^{1,2}, P. O. Wennberg^{2,3}, and J. H. Seinfeld^{1,2}

¹Division of Chemistry and Chemical Engineering, California Institute of Technology, Pasadena, CA, USA

²Division of Engineering and Applied Science, California Institute of Technology, Pasadena, CA, USA

³Division of Geological and Planetary Sciences, California Institute of Technology, Pasadena, CA, USA

* now at: Department of Environmental Sciences and Engineering, The University of North Carolina at Chapel Hill, Chapel Hill, NC, USA

Received: 7 April 2010 – Published in Atmos. Chem. Phys. Discuss.: 19 April 2010

Revised: 13 July 2010 – Accepted: 16 July 2010 – Published: 4 August 2010

Abstract. Aldehydes are an important class of products from atmospheric oxidation of hydrocarbons. Isoprene (2-methyl-1,3-butadiene), the most abundantly emitted atmospheric non-methane hydrocarbon, produces a significant amount of secondary organic aerosol (SOA) via methacrolein (a C₄-unsaturated aldehyde) under urban high-NO_x conditions. Previously, we have identified peroxy methacryloyl nitrate (MPAN) as the important intermediate to isoprene and methacrolein SOA in this NO_x regime. Here we show that as a result of this chemistry, NO₂ enhances SOA formation from methacrolein and two other α , β -unsaturated aldehydes, specifically acrolein and crotonaldehyde, a NO_x effect on SOA formation previously unrecognized. Oligoesters of dihydroxycarboxylic acids and hydroxynitrooxycarboxylic acids are observed to increase with increasing NO₂/NO ratio, and previous characterizations are confirmed by both online and offline high-resolution mass spectrometry techniques. Molecular structure also determines the amount of SOA formation, as the SOA mass yields are the highest for aldehydes that are α , β -unsaturated and contain an additional methyl group on the α -carbon. Aerosol formation from 2-methyl-3-buten-2-ol (MBO232) is insignificant, even under high-NO₂ conditions, as PAN (peroxy acyl nitrate, RC(O)OONO₂) formation is structurally unfavorable. At atmospherically relevant NO₂/NO ratios (3–8), the SOA yields from isoprene high-NO_x photooxidation are 3 times greater than previously measured at lower NO₂/NO ratios. At sufficiently high NO₂ concentrations, in systems of α , β -

unsaturated aldehydes, SOA formation from subsequent oxidation of products from acyl peroxy radicals+NO₂ can exceed that from RO₂+HO₂ reactions under the same inorganic seed conditions, making RO₂+NO₂ an important channel for SOA formation.

1 Introduction

Organic matter is ubiquitous in atmospheric aerosols and accounts for a major fraction of particulate matter mass (Zhang et al., 2007a). Most particulate organic matter (POM) is secondary in origin, comprising condensable oxidation products of gas-phase volatile organic compounds (VOCs) (Hallquist et al., 2009). Despite the importance of secondary organic aerosol (SOA), its sources and formation processes are not fully understood. Global modeling studies predict that oxidation of biogenic hydrocarbons dominates the global SOA burden owing to high emissions and efficient SOA production (Chung and Seinfeld, 2002; Kanakidou et al., 2005; Henze and Seinfeld, 2006). This is supported by observations of high levels of modern (hence biogenic) carbon in ambient particulate organic matter, even in urban centers such as Nashville, TN, Tampa, FL and Atlanta, GA (Lewis et al., 2004; Lewis and Stiles, 2006; Weber et al., 2007). However, field observations have repeatedly shown that SOA formation is highly correlated with anthropogenic tracers, such as CO and acetylene (de Gouw et al., 2005, 2008).

A considerable body of laboratory chamber studies have investigated the dependence of SOA yields (mass of SOA formed per mass of hydrocarbon reacted) on NO_x level, which can vary greatly between urban and remote



Correspondence to: J. H. Seinfeld
(seinfeld@caltech.edu)

areas. For photooxidation and ozonolysis of monoterpenes (Hatakeyama et al., 1991; Ng et al., 2007a; Zhang et al., 2007b; Presto et al., 2005), monocyclic (Song et al., 2005; Hurley et al., 2001; Ng et al., 2007b) and polycyclic aromatic compounds (Chan et al., 2009b), SOA yields are larger under low- NO_x conditions; for sesquiterpenes, the reverse is true (Ng et al., 2007a). SOA formation from photooxidation of isoprene exhibits especially complex behavior depending on the NO_x level (Kroll et al., 2006). The effect of NO_x level on SOA formation has generally been attributed to the relative reaction rates of peroxy radicals (RO_2) with NO and HO_2 and the difference in volatilities of the products from the respective pathways (Kroll and Seinfeld, 2008). Under high- NO_x conditions, RO_2+NO dominates and leads to formation of fragmentation products or organic nitrates, which are generally volatile (Presto et al., 2005). On the contrary, the RO_2+HO_2 pathway, which is competitive only when $[\text{NO}] \ll 1 \text{ ppb}$, produces less volatile hydroxyhydroperoxides and peroxy acids, leading to higher SOA yields (Johnson et al., 2005). RO_2+NO_2 reactions have not been considered as important for SOA formation due to the short lifetime of peroxy nitrates ($< 1 \text{ s}$); the notable exceptions are acyl peroxy nitrates (PANs) and pernitric acid (PNA). As a result, the so-called “high- NO_x ” yields (corresponding to urban NO_x levels) have typically been measured under high-NO conditions. For example, the overall SOA mass yield for isoprene photooxidation ranges from 0.01–0.05 under low- NO_x conditions (Kroll et al., 2006) to 0.002–0.03 under high- NO_x (high-NO) conditions (Kroll et al., 2005a; Dommen et al., 2006). Owing to the large emissions of isoprene (Guenther et al., 2006), isoprene has been estimated to be the single largest source of SOA globally (Henze and Seinfeld, 2006; Carlton et al., 2009).

In a recent study of the mechanism of SOA formation from isoprene, it was shown that aerosol-phase 2-methylglyceric acid (2-MG) and its oligoesters are produced from methacrolein oxidation through the peroxy methacryloyl nitrate (MPAN) channel, as the SOA from MPAN oxidation is similar in composition to that from high- NO_x oxidation of isoprene and methacrolein (Surratt et al., 2010). Since MPAN is formed from the reversible reaction of methacryloyl peroxy radicals with NO_2 , SOA formation can be highly sensitive to the NO_2 concentration, an effect of gas-phase aldehyde chemistry that had previously not been recognized. Given the large emissions and the substantial fraction of isoprene reacting under high- NO_x conditions (a recent modeling study predicts that globally up to two-thirds of isoprene reacts under high- NO_x conditions (Paulot et al., 2009)), it is essential to understand more generally how gas-phase aldehyde chemistry and both NO and NO_2 affect SOA yield and composition. Here we present the results of a systematic study of the effect of NO_2/NO ratio on SOA formation from methacrolein and two other α, β -unsaturated aldehydes, acrolein and crotonaldehyde. In addition, other structurally similar aldehydes and alcohols are studied to provide insight

Table 1. Hydrocarbons studied.

Name	Structure	OH rate constant, $\text{cm}^3 \text{ molec}^{-1} \text{ s}^{-1}$
isoprene		$1 \times 10^{-10}^a$
methacrolein		$2.9 \times 10^{-11}^a$
acrolein		$2.0 \times 10^{-11}^b$
crotonaldehyde (<i>cis</i> and <i>trans</i>)		$3.5 \times 10^{-11}^b$
2-methyl-2-butenal (2M2B)		unknown
3-methyl-2-butenal (3M2B)		$6.2 \times 10^{-11}^c$
2-pentenal		unknown
4-pentenal		unknown
2-methyl-3-but-en-1-ol (MBO231)		unknown
2-methyl-3-but-en-2-ol (MBO232)		$3.9 \times 10^{-11}^d$

^a Atkinson and Arey (2003); ^b Magneron et al. (2002); ^c Tuazon et al. (2005); ^d Fanuchi et al. (1998).

into the reaction mechanism and to establish the role of PAN-type compounds as important SOA intermediates.

2 Experimental section

2.1 Experimental protocols

Experiments were carried out in the Caltech dual 28- m^3 Teflon chambers. Details of the facilities have been described previously (Cocker et al., 2001; Keywood et al., 2004). Before each experiment, the chambers were flushed with dried purified air for $> 24 \text{ h}$ ($\sim 4\text{--}6$ air changes), until the particle number concentration $< 100 \text{ cm}^{-3}$ and the volume concentration $< 0.1 \text{ } \mu\text{m}^3 \text{ cm}^{-3}$. In all experiments, inorganic seed particles were injected by atomization of a 0.015 M aqueous ammonium sulfate solution. The parent hydrocarbon was then introduced into the chamber by injecting a known volume of the liquid hydrocarbon into a glass bulb, and the vapor was carried into the chamber with 5 L min^{-1} of purified air.

Table 2. Experimental conditions and results.

Date ^a (DD/MM/YY)	Compound	[HC] ₀ , ppb	OH precursor	NO _x addition	[NO] ₀ ^b , ppb	[NO ₂] ₀ ^b , ppb	NO ₂ /NO ^c	V_0^d , $\mu\text{m}^3 \text{cm}^{-3}$	ΔM_o^e , $\mu\text{g m}^{-3}$	SOA Yield
14/07/09	methacrolein	277	HONO	+NO	725	365	0.5	11.4	10.1	0.019
16/07/09	methacrolein	285	HONO	+NO ₂	296	692	1.7	12.3	24.5	0.052
19/07/09	methacrolein	257	HONO	–	527	407	0.7	12.1	14.4	0.030
31/07/09 ^f	methacrolein	232	HONO	+NO	653	394	0.5	11.7	13.3	0.030
12/09/09	methacrolein	255	CH ₃ ONO	+NO+NO ₂	222	799	10.0	13.9	276.3	0.392
15/09/09	methacrolein	67	CH ₃ ONO	+NO+NO ₂	164	549	5.8	14.8	39.9	0.211
17/09/09	methacrolein	20	CH ₃ ONO	+NO+NO ₂	170	602	3.6	16.0	10.8	0.194
19/09/09	methacrolein	48	CH ₃ ONO	+NO+NO ₂	167	582	4.7	13.2	28.8	0.213
21/09/09	methacrolein	32	CH ₃ ONO	+NO+NO ₂	176	657	4.2	14.4	22.4	0.242
16/12/09	methacrolein	32	CH ₃ ONO	+NO+NO ₂	243	444	2.7	13.9	6.8	0.079
17/12/09 ^g	methacrolein	32	CH ₃ ONO	+NO+NO ₂	233	518	2.7	16.2	6.7	0.075
08/08/09	isoprene	523	HONO	–	312	510	7.7	10.8	65.2	0.044
23/09/09	isoprene	228	CH ₃ ONO	+NO+NO ₂	293	825	8.4	16.0	47.4	0.074
24/09/09	isoprene	94	CH ₃ ONO	+NO+NO ₂	271	735	5.0	14.8	16.0	0.061
25/09/09	isoprene	153	CH ₃ ONO	+NO+NO ₂	316	859	6.1	18.7	27.2	0.064
27/09/09	isoprene	44	CH ₃ ONO	+NO+NO ₂	259	715	4.0	15.8	5.2	0.042
30/09/09	isoprene	33	CH ₃ ONO	+NO+NO ₂	289	768	3.4	18.4	2.9	0.031
15/08/09	acrolein	676	HONO	–	214	389	2.5	13.2	21.3	0.022
16/08/09	acrolein	540	HONO	+NO	550	359	0.8	11.2	4.4	0.006
17/08/09	acrolein	611	HONO	+NO ₂	233	630	2.0	13.2	9.9	0.015
28/09/09	acrolein	220	CH ₃ ONO	+NO+NO ₂	313	830	5.5	19.2	16.6	0.035
18/08/09	crotonaldehyde	293	HONO	–	214	371	2.3	12.1	14.0	0.019
19/08/09	crotonaldehyde	297	HONO	+NO	600	416	1.1	12.3	9.0	0.013
20/08/09	crotonaldehyde	361	HONO	+NO ₂	245	625	2.6	12.2	12.9	0.017
29/09/09	crotonaldehyde	74	CH ₃ ONO	+NO+NO ₂	248	664	3.8	16.4	9.2	0.044
26/12/09	2-pentenal	174	CH ₃ ONO	+NO+NO ₂	230	548	6.7	13.9	18.1	0.03
27/12/09	4-pentenal	191	CH ₃ ONO	+NO+NO ₂	243	488	6.5	15.8	8.2	0.012
28/12/09	2M2B	277	CH ₃ ONO	+NO+NO ₂	240	706	9.3	13.8	376.7	0.391
29/12/09	3M2B	207	CH ₃ ONO	+NO+NO ₂	268	747	8.7	16.1	5.6	0.008
31/12/09	MBO231	589	CH ₃ ONO	+NO+NO ₂	308	493	13.2	16.8	87.6	0.042
22/02/10	MBO231	329	CH ₃ ONO	+NO+NO ₂	351	768	7.8	14.5	21.9	0.019
24/02/10	MBO231	300	HONO	+NO	642	514	1.8	14.2	<2	<0.002
25/02/10	MBO231	378	CH ₃ ONO	+NO+NO ₂	346	793	5.5	17.5	10.7	0.008
01/01/10	MBO232	492	CH ₃ ONO	+NO+NO ₂	251	442	11.4	14.8	<2	<0.002
23/02/10	MBO232	388	CH ₃ ONO	+NO+NO ₂	345	809	8.4	17.1	<2	<0.002

^a All experiments carried out at temperatures of 293–295 K and RH of 9–11%. ^b As measured by chemiluminescence NO_x monitor. Note interference on NO₂ signal from HONO and CH₃ONO. ^c Estimated by photochemical modeling (see Appendix). ^d V_0 : volume concentration of ammonium sulfate seed. ^e ΔM_o : mass concentration of SOA. ^f Gas-phase nitric acid added during experiment. ^g Low O₂ experiment.

To study the sensitivity of aerosol yields and composition to relative concentrations of NO and NO₂, different OH precursors were used. Use of nitrous acid (HONO) and methyl nitrite (CH₃ONO) as OH precursors allows for SOA yield measurements over a wide range of NO₂/NO ratios. For “high NO” experiments, OH radicals were generated from photolysis of HONO. We refer to these experiments as “high NO” experiments because NO concentrations are sufficiently high that $\text{RO}_2+\text{NO} \gg \text{RO}_2+\text{NO}_2$, most notably for acyl peroxy radicals, even though NO₂ concentrations are high (>100 ppb). HONO was prepared by adding 15 mL of 1 wt% aqueous NaNO₂ dropwise into 30 mL of 10 wt% sulfuric acid in a glass bulb. A stream of dry air was then passed through the bulb, sending HONO into the chamber. During this process, NO and NO₂ formed as side products and were also introduced into the chamber. To achieve high NO₂

concentrations, CH₃ONO was employed as the OH precursor. These experiments are referred to as “high NO₂” experiments, as NO₂ concentrations are sufficiently higher than NO concentrations such that PAN formation is favored over reaction of acyl peroxy radicals with NO. CH₃ONO was vaporized into an evacuated 500 mL glass bulb and introduced into the chamber with an air stream of 5 L min⁻¹. The mixing ratio of CH₃ONO injected was estimated to be 200–400 ppb, based on the vapor pressure in the glass bulb measured using a capacitance manometer (MKS). In all experiments, varying amounts of NO and NO₂ were also added from gas cylinders (Scott Marrin) both to ensure high-NO_x conditions and to vary the NO₂/NO ratio. For the C₅ unsaturated aldehydes and 2-methyl-3-butene-2-ol (MBO232), only high NO₂ experiments were conducted. Abbreviations, structures, and OH rate constants (Atkinson and Arey, 2003; Magneron et al.,

2002; Tuazon et al., 2005; Fantechi et al., 1998) of the compounds studied are listed in Table 1, and initial conditions of the experiments are summarized in Table 2.

2.2 Materials

The parent hydrocarbons studied and their stated purities are as follows: isoprene (Aldrich, 99%), methacrolein (Aldrich, 95%), acrolein (Fluka, $\geq 99\%$), crotonaldehyde (Aldrich, 98%, predominantly *trans*), trans-2-pentenal (Alfa Aesar, 96%), 4-pentenal (Alfa Aesar, 97%), trans-2-methyl-2-butenal (Aldrich, 96+%), 3-methyl-2-butenal (Sigma-Aldrich, 97%), 2-methyl-3-buten-1-ol (Aldrich, 98%), and 2-methyl-3-buten-2-ol (Aldrich, 98%). CH_3ONO was synthesized following the method described by Taylor et al. (1980). 9 g of NaNO_2 was added to a mixture of 50 mL of methanol and 25 mL of water. 25 mL of 50 wt% sulfuric acid solution was added dropwise into the solution. The CH_3ONO vapor was carried in a small stream of ultra high purity N_2 through a concentrated NaOH solution and an anhydrous CaSO_4 trap to remove any sulfuric acid and water, respectively. The CH_3ONO was then collected in a cold trap immersed in a dry ice/acetone bath (-80°C) and stored under liquid N_2 temperature.

2.3 Measurements

Aerosol size distribution, number and volume concentrations were measured with a differential mobility analyzer (DMA, TSI, 3081) coupled with a condensation nuclei counter (TSI, CNC-3760). The volume concentration was corrected for particle wall loss by applying size-dependent first-order loss coefficients, obtained in a separate seed-only experiment, using methods described in Keywood et al. (2004). Aerosol volume concentrations are converted to mass concentrations assuming a density of 1.4 g cm^{-3} (Kroll et al., 2005a). Concentrations of isoprene, methacrolein, methyl vinyl ketone (MVK), acrolein, and crotonaldehyde were monitored using a gas chromatograph with flame ionization detector (GC/FID, Agilent 6890N), equipped with an HP-PLOT Q column ($15 \text{ m} \times 0.53 \text{ mm ID} \times 30 \mu\text{m}$ thickness, J&W Scientific). For 2M2B, 3M2B, 2-pentenal, 4-pentenal, MBO231 and MBO232 experiments, the GC/FID was equipped with an HP-5 column ($15 \text{ m} \times 0.53 \text{ mm ID} \times 1.5 \mu\text{m}$ thickness, Hewlett Packard). A commercial chemiluminescence NO/NO_x analyzer (Horiba, APNA 360) was used to monitor NO and NO_x . Both HONO and CH_3ONO produce interference on the NO_2 signal from the NO_x monitor. Concentrations of NO and NO_2 are estimated by photochemical modeling (see Appendix). Temperature, RH, and ozone (O_3) were continuously monitored.

A custom-modified Varian 1200 triple-quadrupole chemical ionization mass spectrometer (CIMS) was used to continuously monitor gas-phase species over each experiment. Details of the operation of the CIMS can be found in a num-

ber of previous reports (Crounse et al., 2006; Paulot et al., 2009). The CIMS was operated in negative ion mode, in which CF_3O^- is used as the reagent ion, and in positive ion mode of proton transfer mass spectrometry (PTR-MS). In the negative mode, the reagent ion CF_3O^- clusters with the analyte, R, forming ions at mass-to-charge ratios (m/z) $\text{MW}+85$ ($\text{R} \cdot \text{CF}_3\text{O}^-$), or, with more acidic species, at m/z $\text{MW}+19$ ($\text{HF} \cdot \text{R}_\text{H}^-$). In the positive mode, positively charged water clusters, $n(\text{H}_2\text{O})\text{H}^+$, react via proton transfer with the analyte, R, to form the positively charged ion, $\text{R} \cdot n(\text{H}_2\text{O}) \cdot \text{H}^+$. In some cases, tandem mass spectrometry (MS/MS) was used to separate isobaric compounds. In brief, the parent ions selected in the first quadrupole undergo collision-induced dissociation (CID) in the second quadrupole. The parent ions of isobaric compounds can exhibit different CID patterns and yield different daughter ions. Hence, with the third quadrupole acting as a second mass filter for the daughter ions, this allows for separate measurement of these isobaric compounds (see Supplementary Material). The significance of this separation will be discussed in a later section.

Real-time particle mass spectra were collected continuously by an Aerodyne High Resolution Time-of-Flight Aerosol Mass Spectrometer (DeCarlo et al., 2006; Canagaratna et al., 2007), hereby referred to as the AMS. The AMS switched once every minute between the high resolution “W-mode” and the lower resolution, higher sensitivity “V-mode”. The “V-mode” data were analyzed using a fragmentation table to separate sulfate, ammonium, and organic spectra and to time-trace specific mass-to-charge ratios. “W-mode” data were analyzed using a separate high-resolution spectra toolbox known as PIKA to determine the chemical formulas contributing to distinct m/z ratios (DeCarlo et al., 2006).

Aerosol samples were also collected on Teflon filters and analyzed by offline mass spectrometry. Detailed sample collection and extraction protocol are described in Surratt et al. (2008). Filter extraction using 5 mL of high-purity methanol (i.e., LC-MS Chromasolv Grade) was performed by 45 min of sonication. The filter extracts were then analyzed by a Waters ACQUITY ultra performance liquid chromatography (UPLC) system, coupled with a Waters LCT Premier TOF mass spectrometer equipped with an ESI source operated in the negative (–) mode, allowing for accurate mass measurements (i.e., determination of molecular formulas) to be obtained for each observed ion. Operation conditions and parameters for the UPLC(–)ESI-TOFMS measurement have been described by Surratt et al. (2008).

3 SOA formation

The importance of isoprene as an SOA source was suggested by identification of 2-methyltetrosols and 2-methylglyceric acid (2-MG) in both ambient POM (Claeys et al., 2004; Edney et al., 2005; Ion et al., 2005; Kourtchev et al., 2005)

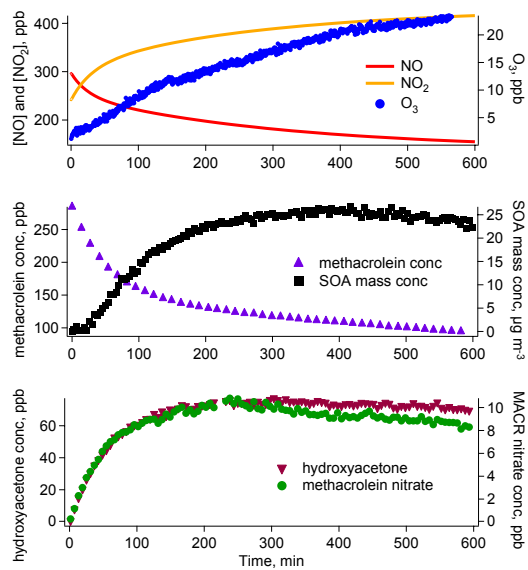


Fig. 1. Concentration profiles of gas-phase species during a typical methacrolein/high-NO experiment (16/07/09). In this experiment, additional NO_2 was injected prior to irradiation. Concentrations of NO and NO_2 shown here are calculated from a photochemical model (see Appendix).

and laboratory aerosol generated from isoprene photooxidation (Edney et al., 2005; Surratt et al., 2006; Szmigielski et al., 2007; Kleindienst et al., 2009). Methacrolein, a first-generation oxidation product of isoprene, has been shown to produce SOA upon further oxidation (Kroll et al., 2006; Surratt et al., 2006) and has been identified as the precursor to aerosol-phase 2-MG and its corresponding oligoester products (Surratt et al., 2006; Szmigielski et al., 2007). A recent study shows aerosol formation from methacrolein oxidation proceeds via subsequent oxidation of MPAN (Surratt et al., 2010). Here we focus our attention on photooxidation of methacrolein under high- NO_x conditions to establish the effect of relative NO and NO_2 concentrations on SOA yields and composition. Acrolein, crotonaldehyde, 2-methyl-2-butenal (2M2B), 3-methyl-2-butenal (3M2B), 2-pentenal, and 4-pentenal differ from methacrolein by one or two methyl groups, and studying their SOA formation provides insight into the mechanism of formation of low-volatility products. Furthermore, aerosol formation from photooxidation of 2-methyl-3-butene-2-ol (MBO232), an atmospherically important unsaturated alcohol (Harley et al., 1998), and structurally similar 2-methyl-3-butene-1-ol (MBO231) is studied to investigate the role of PAN-like compounds in SOA formation.

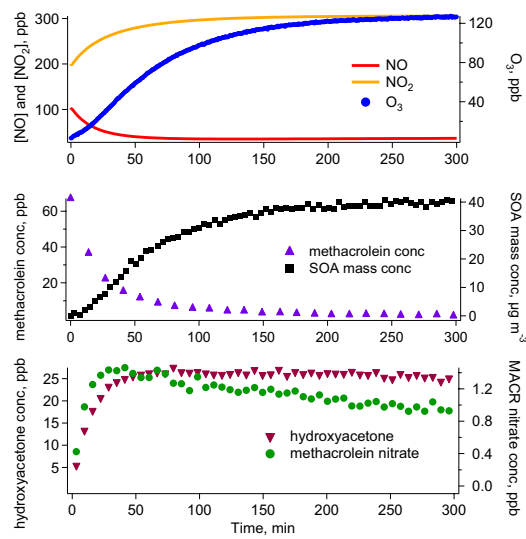


Fig. 2. Concentration profiles of gas-phase species during a typical methacrolein/high- NO_2 experiment (15/09/09). Additional NO (100 ppb) and NO_2 (200 ppb) were injected prior to irradiation. Concentrations of NO and NO_2 shown here are calculated from a photochemical model (see Appendix). As a result of the higher OH concentrations from CH_3ONO than from HONO, more methacrolein was reacted and the concentrations of methacrolein nitrate relative to those of hydroxyacetone were lower than those in high-NO experiments, owing to a more rapid consumption by OH.

3.1 Methacrolein

Figures 1 and 2 show typical concentration profiles of various gas-phase species in methacrolein/HONO (high NO) and methacrolein/ CH_3ONO (high NO_2) photooxidation experiments, respectively. In all experiments, NO concentrations remain above 50 ppb during SOA growth, at which conditions RO_2+HO_2 or RO_2+RO_2 reactions are not competitive with those of RO_2 with NO and NO_2 . Products of these reactions, such as methacrylic acid and methacrylic peracid, are not observed by CIMS. Instead, hydroxyacetone and methacrolein nitrate, products from RO_2+NO reactions, are observed. During these experiments, RO_2 and HO_2 produced from methacrolein oxidation react with NO to produce NO_2 , which photolyses to form ozone. As a result, ozone concentrations reach a maximum of up to 126 ppb. Despite relatively high levels of ozone, reaction rates of methacrolein and peroxy methacryloyl nitrate (MPAN) with ozone are still slow compared to those with OH, as efficient photolysis of HONO or CH_3ONO leads to OH concentrations $>3 \times 10^6$ molec cm^{-3} , estimated from the methacrolein decay. For high-NO experiments, the initial decay of methacrolein slows down after 5 h, consistent with the HONO signal (CIMS $(-) m/z 66$) approaching zero. In

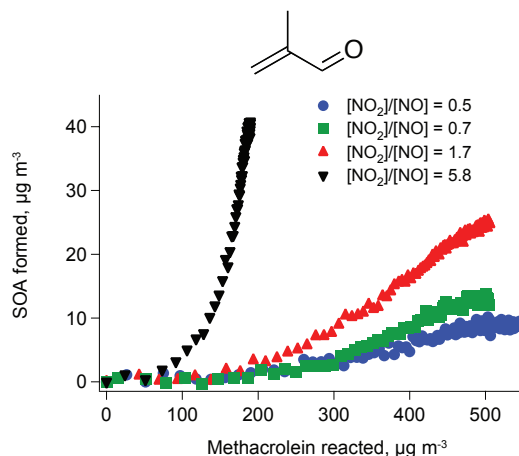


Fig. 3. Time-dependent SOA growth curves for methacrolein photooxidation. NO_2/NO ratios are computed from photochemical modeling (see Appendix). In the high-NO experiments ($\text{NO}_2/\text{NO} < 2$) HONO was used as the OH precursor, and the NO_2/NO ratio was varied by adding different amounts of NO or NO_2 . In the high- NO_2 experiment (black triangles), CH_3ONO was used as the OH precursor.

these experiments, more than 70% of the initial methacrolein is consumed before SOA growth ceases. In the high- NO_2 experiments, more than 90% of the initial methacrolein is consumed before SOA growth ceases.

Mass concentrations of SOA versus the concentration of methacrolein reacted, so-called “time-dependent growth curves”, are shown in Fig. 3. As reported previously, under high-NO conditions (with HONO as the OH precursor), when additional NO is added before irradiation, aerosol formation (mass yield of 0.019) from photooxidation of 277 ppb of methacrolein is suppressed (Surratt et al., 2010). In contrast, SOA yields are higher when no additional NO is added (0.030 from 257 ppb methacrolein), and the highest when 350 ppb of additional NO_2 (instead of NO) is injected (0.052 from 285 ppb methacrolein) (Surratt et al., 2010). In all high-NO experiments, the NO_2/NO ratio remains low (< 2), owing to presence of NO impurity in HONO synthesis and production of NO during HONO photolysis. The observed dependence of SOA yields on NO_2/NO ratio is not a result of condensation of nitric acid from $\text{OH}+\text{NO}_2$, as the experiments were conducted under dry ($< 10\%$ RH) conditions. In confirmation of this conclusion, addition of gas-phase nitric acid in one experiment (31/07/09) did not lead to additional aerosol growth.

In the high- NO_2 experiments, CH_3ONO was used as the OH precursor and lower NO concentrations are expected, owing to relatively pure CH_3ONO synthesis and no net production of NO from CH_3ONO photolysis (see Appendix). Higher SOA yields are observed at higher NO_2/NO ratios;

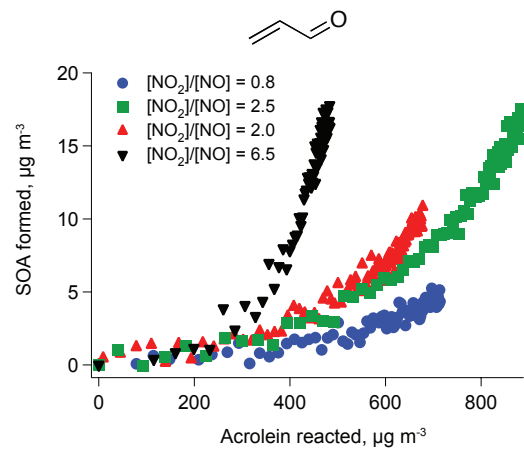


Fig. 4. Time-dependent SOA growth curves for acrolein photooxidation. Similar to methacrolein photooxidation, NO_2/NO ratios are computed from photochemical modeling (see Appendix). In the high-NO experiments ($\text{NO}_2/\text{NO} < 3$), HONO was used as the OH precursor, and the NO_2/NO ratio was varied by adding different amounts of NO or NO_2 . In the experiment in which NO_2 was added (red triangles), high levels of NO_2 depress OH concentrations, resulting in less acrolein reacted. Concentrations of NO did not drop as rapidly as in other high-NO experiments, leading to a lower NO_2/NO ratio. In the high- NO_2 experiment (black triangles), CH_3ONO was used as the OH precursor.

correspondingly, much lower concentrations of methacrolein are required to produce the same amount of SOA (see Fig. 3). Also, owing to the high concentrations of CH_3ONO injected, more than 90% of the initial methacrolein is consumed before CH_3ONO is depleted. For example, when 255 ppb of initial methacrolein is oxidized using CH_3ONO as OH precursor (12/09/09), the SOA yields are more than 5 times larger than when a similar amount of methacrolein is reacted using HONO as OH precursor. This rules out a larger extent of reaction as the cause of the high observed SOA yields. HO_2 concentrations, quantified from the pernitric acid signal on the CIMS ($(-\text{)} m/z 98$) and modelled NO_2 concentrations, do not exceed 60 ppt in all experiments. At organic loadings of $10\text{--}20\text{ } \mu\text{g m}^{-3}$, SOA mass yields of methacrolein/high- NO_2 and methacrolein/high-NO photooxidation are roughly 0.19 and 0.03, respectively.

3.2 Acrolein and crotonaldehyde

Figures 4 and 5 show SOA growth curves for acrolein and crotonaldehyde photooxidation, respectively. The SOA yields of these compounds are lower than those of methacrolein, with maximum yields of roughly 0.08 at the highest loadings ($> 100\text{ } \mu\text{g m}^{-3}$). These compounds exhibit a similar dependence of SOA growth on NO_2/NO ratio to that of methacrolein: SOA formation is suppressed with addition

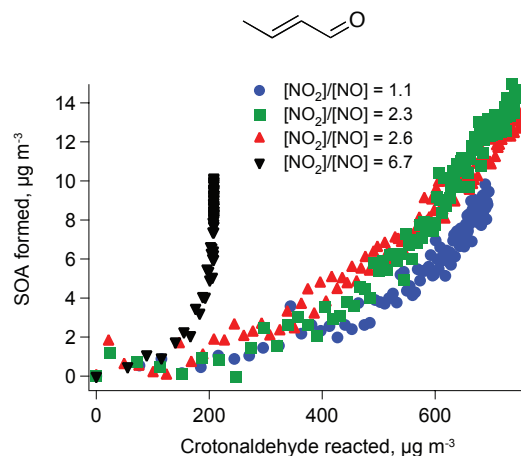


Fig. 5. Time-dependent SOA growth curves for crotonaldehyde photooxidation. Similar to methacrolein photooxidation, NO_2/NO ratios are computed from photochemical modeling (see Appendix). In the high-NO experiments ($\text{NO}_2/\text{NO} < 3$), HONO was used as the OH precursor, and the NO_2/NO ratio was varied by adding different amounts of NO or NO_2 . In the high- NO_2 experiment (black triangles), CH_3ONO was used as the OH precursor.

of NO, and enhanced with addition of NO_2 . SOA yields are highest in the high- NO_2 experiments. Oxidation products analogous to those found in the methacrolein system, such as glycolaldehyde and hydroxynitrates, are observed in the gas phase at similar yields.

3.3 Other aldehydes and methylbutenols (MBO)

The growth curves for 2M2B and 3M2B photooxidation are shown in Fig. 6. Significant SOA growth is observed for 2M2B (277 ppb) photooxidation under high- NO_2 conditions, with mass yields exceeding 0.35. Similar to methacrolein, 2M2B contains a methyl group in the α -position. Interestingly, photooxidation of 3M2B under similar NO_x conditions and hydrocarbon loadings (207 ppb), produces less SOA (mass yield <0.01). 3M2B is a structural isomer of 2M2B with the methyl group in the β -position. The trend in SOA yields between 2M2B and 3M2B is consistent with that observed for methacrolein and crotonaldehyde, their C₄ analogs. The SOA yields from 2-pentenal, a straight-chain α, β -unsaturated aldehyde, are higher than those from 4-pentenal, in which the olefinic bond is not adjacent to the aldehyde group (see Fig. 6).

We also carried out MBO232 and MBO231 photooxidation under high- NO_2 conditions. Both MBO's are structurally similar to isoprene and, upon high- NO_x photooxidation, produce an aldehyde (i.e., hydroxy-methylpropanal, HMPR) analogous to methacrolein. Previous results have shown that aerosol formation from MBO232 photooxidation

under high-NO conditions is negligible, with mass yields of <0.001 (Carrasco et al., 2007; Chan et al., 2009a). Here we do not observe SOA growth even at high NO_2/NO ratios. Gas-phase compounds such as glycolaldehyde and HMPR are observed at molar yields of 0.6 and 0.3, respectively, consistent with those published in previous product studies (Carrasco et al., 2007; Chan et al., 2009a). On the other hand, MBO231, a structural isomer with the hydroxyl group in the 1-position, produces a significant amount of SOA (mass yields of 0.008–0.042) upon oxidation under high- NO_2 conditions, comparable to that of isoprene under similar conditions (see Fig. 6). Under high-NO conditions, no SOA is formed. The dependence of SOA yields from MBO231 on NO_2/NO ratio is therefore consistent with that observed in unsaturated aldehydes.

4 Chemical composition of SOA

4.1 Offline chemical analysis

In previous work, offline chemical analysis of SOA from photooxidation of isoprene, methacrolein, and MPAN by UPLC/(-)ESI-TOFMS has been presented (Surratt et al., 2010). The same compounds are detected in the methacrolein experiments in this work under both high-NO and high- NO_2 conditions, and are summarized in Table 3. Four series of oligoester products from 2-methylglyceric acid (2-MG) and C₄-hydroxynitrooxycarboxylic acid are identified in the SOA. The compounds in the 2-MG oligoester series differ by 102 Da, corresponding to esterification of a 2-MG monomer unit (Surratt et al., 2006). The accurate masses of the identified ions confirm their elemental compositions, and their structures are proposed based on detailed characterization by tandem MS and GC/MS analyses with prior trimethylsilylation (Szmigelski et al., 2007).

All ions detected by UPLC/(-)ESI-TOFMS in acrolein and crotonaldehyde SOA are listed in the Supplementary Material. It is noteworthy that the identities of detected aerosol-phase products are the same regardless of the OH precursor used. The ions detected in acrolein SOA differ from those found in methacrolein SOA by one methyl group for every monomer unit, and those detected in crotonaldehyde SOA have the same exact mass and elemental composition as those in methacrolein SOA. Detected $[\text{M}-\text{H}]^-$ ions in SOA from 2M2B and 2-pentenal can also be found in the Supplementary Material. No filter sample was collected for 3M2B owing to low aerosol loading. Aerosol-phase products of methacrolein, acrolein, crotonaldehyde, 2M2B and 2-pentenal are structural analogs of each other, and the structures for the deprotonated ions are proposed based on those characterized previously in isoprene and methacrolein SOA (Surratt et al., 2006; Szmigelski et al., 2007). Interestingly, SOA produced from 4-pentenal is composed of entirely different products, and hence no structures are proposed at this

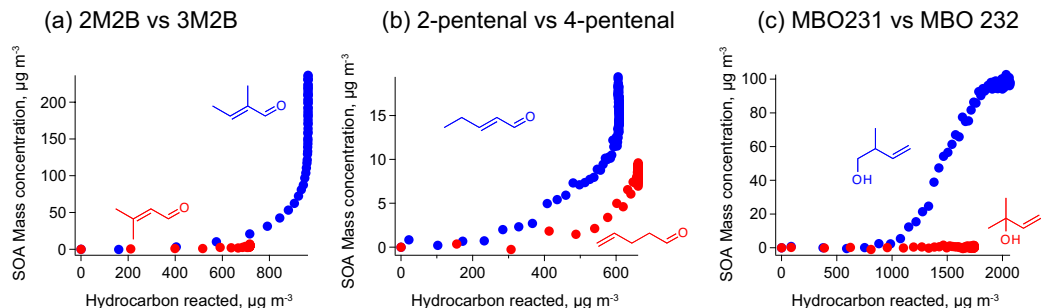


Fig. 6. Comparisons of time-dependent SOA growth from photooxidation of (a) 2M2B and 3M2B, (b) 2-pentenal and 4-pentenal, and (c) MBO231 and MBO 232 under high-NO_x conditions. Within each plot, initial concentrations of parent hydrocarbons are comparable (see Table 2).

Table 3. SOA constituents detected by UPLC/(-)ESI-TOFMS and AMS in methacrolein experiments. All ions were detected in both high-NO and high-NO_x experiments, unless otherwise noted.

	[M - H] ⁻ ^a	UPLC/ESI-TOFMS		TOFMS		# of 2-MG Monomer Units (n)	Structure	AMS Suggested	
		Measured Mass	Suggested Ion Formula	Error (mDa)	i-Fit			[M - OH] ⁺ ^b	Ion Formula ^c
not detected									
Oligoester Series 1	221	221.0661	C ₈ H ₁₃ O ₇ ⁻	1.6	0.3	2		103	C ₄ H ₇ O ₃ ⁺
	323	323.0979	C ₁₂ H ₁₉ O ₁₀ ⁻	0.1	22.6	3		205	C ₈ H ₁₃ O ₆ ⁺
	425	425.1290	C ₁₆ H ₂₅ O ₁₃ ⁻	-0.5	48.0	4		d	--
	527 ^e	527.1609	C ₂₀ H ₃₁ O ₁₆ ⁻	-0.3	3.7	5		d	--
Oligoester Series 2	266	266.0507	C ₈ H ₁₂ NO ₉ ⁻	-0.5	32.8	1		d	--
	368	368.0831	C ₁₂ H ₁₈ NO ₁₂ ⁻	0.2	11.4	2		d	--
	470	470.1149	C ₁₆ H ₂₄ NO ₁₅ ⁻	0.3	56.3	3		d	--
	572	572.1510	C ₂₀ H ₃₀ NO ₁₈ ⁻	4.7	1.0	4		d	--
Oligoester Series 3 ^f	not detected							131	C ₅ H ₇ O ₄ ⁺ ^g
	249	249.0616	C ₉ H ₁₃ O ₈ ⁻	0.6	2.7	2		233	C ₉ H ₁₃ O ₇ ⁺
	351	351.0912	C ₁₃ H ₁₉ O ₁₁ ⁻	-1.5	46.9	3		d	--
	453	453.1248	C ₁₇ H ₂₅ O ₁₄ ⁻	0.4	63.7	4		d	--
Oligoester Series 4 ^h	not detected							145	C ₆ H ₉ O ₄ ⁺
	263	263.0740	C ₁₀ H ₁₆ O ₈ ⁻	-2.7	4.7	2		247	C ₁₀ H ₁₅ O ₇ ⁺
	365	365.1061	C ₁₄ H ₂₁ O ₁₁ ⁻	-2.3	54.9	3		d	--
	467	467.1434	C ₁₈ H ₂₇ O ₁₄ ⁻	3.3	23.7	4		d	--
Oligoester Series 5	569	569.1711	C ₁₈ H ₂₇ O ₁₄ ⁻	-0.7	20.0	5		d	--
	311	311.0333	C ₈ H ₁₁ N ₂ O ₁₁ ⁻	-3.0	58.9	0		d	--
	413	413.0664	C ₁₂ H ₁₇ N ₂ O ₁₄ ⁻	-1.6	71.9	1		d	--
	515 ^e	515.1039	C ₁₆ H ₂₃ N ₂ O ₁₇ ⁻	4.2	3.6	2		d	--
Other Oligoesters	458 ^e	458.0558	C ₁₂ H ₁₆ N ₃ O ₁₆ ⁻	2.7	3.3	n/a		d	--

^a Observed by UPLC/(-)ESI-TOFMS. ^b Observed by AMS V mode. ^c Suggested by AMS high-resolution W mode.

^d Not observed by AMS, most likely due to fragmentation of nitrate group, or below detection limit. ^e Detected in high-NO_x experiments only. ^f This oligoester series involves the esterification with formic acid. ^g C₆H₁₁O₃⁺ also detected. ^h This oligoester series involves the esterification with acetic acid.

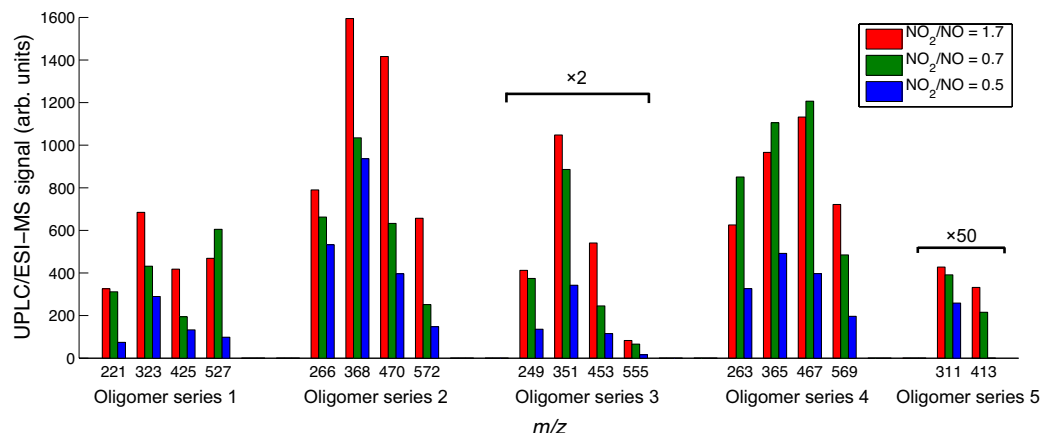


Fig. 7. Absolute peak areas (normalized by sampling volume) of all deprotonated ions detected by UPLC/(-)ESI-TOFMS in methacrolein/high-NO experiments, listed in Table 3. The positive dependence of oligoester abundance on NO_2/NO ratios is consistent with the observed trend in overall SOA growth.

time. The significance of this result will be discussed in a later section.

While the identities of the detected aerosol-phase compounds are independent of the OH precursor, the relative amounts vary greatly and exhibit a strong correlation with NO_2/NO ratio. Figure 7 shows the extracted ion signals for the oligoester products detected by UPLC/(-)ESI-TOFMS in the methacrolein high-NO experiments. The amount of identified aerosol-phase components shows the same dependence on NO_2/NO ratio as the total amount of SOA growth. In general, the abundance of each compound decreases when NO is added and increases when NO_2 is added.

4.2 Online AMS measurements

AMS V-mode organic spectra of SOA from high- NO_2 photooxidation of isoprene and methacrolein are shown in Fig. 8. The mass fragments above m/z 200 likely contain more than 5 carbon atoms, and display a repetitive pattern, indicative of oligomer formation. In addition, 102 Da differences between major peaks were also observed, consistent with previous AMS and LC/MS results (Surratt et al., 2006). Elemental formulas based on accurate mass measurements are determined from high-resolution W-mode data for a number of the major ion peaks observed, as shown in Fig. 9. The ions suggested by these elemental formulas differ from many of the ions detected by UPLC/(-)ESI-TOFMS by an O_2^- group. The observed AMS ions are consistent with loss of a hydroxyl group from the molecular ion (i.e. α -cleavage of a hydroxyl group under electron impact ionization). In UPLC/(-)ESI-TOFMS, these compounds are detected in their deprotonated form (loss of H^+). As shown in Table 3, the oligoesters are detected by both online and offline high-resolution mass

spectrometry, and the agreement between the two techniques confirms that the oligoesters identified are indeed present in the SOA, and that the observations by offline aerosol analysis are not the result of filter sampling artifacts. AMS organic spectra of SOA from oxidation of acrolein and crotonaldehyde show similar features, and accurate mass measurements of a number of the major peaks correspond to the products analogous to those found in the methacrolein system (see Supplementary Material).

5 Effect of NO_2/NO ratios on SOA yield and composition

As mentioned in the Introduction, studies on the effect of NO_x concentrations on SOA formation has shown that for most systems, SOA yields are inversely correlated with NO_x concentrations (Hatakeyama et al., 1991; Hurley et al., 2001; Presto et al., 2005; Song et al., 2005; Zhang et al., 2007b; Ng et al., 2007a,b; Chan et al., 2009b). The “ NO_x effect” on SOA formation has been described as a competition of the chemistries for RO_2 between HO_2 (the high-yield pathway) and NO (the low-yield pathway), such that the ratio of HO_2 to NO is critical in determining the branching ratio between these two pathways (Kroll and Seinfeld, 2008; Henze et al., 2008). Aerosol yields from isoprene photooxidation are also sensitive to HO_2/NO ratios, with higher yields measured under HO_2 -dominated conditions (using H_2O_2 as OH source) (Kroll et al., 2006) than under NO-dominated conditions (using HONO or NO_x cycling as OH source) (Kroll et al., 2005b; Pandis et al., 1991; Dommen et al., 2006). Addition of NO also suppresses SOA growth in low- NO_x experiments, indicating that the RO_2+NO pathway yields

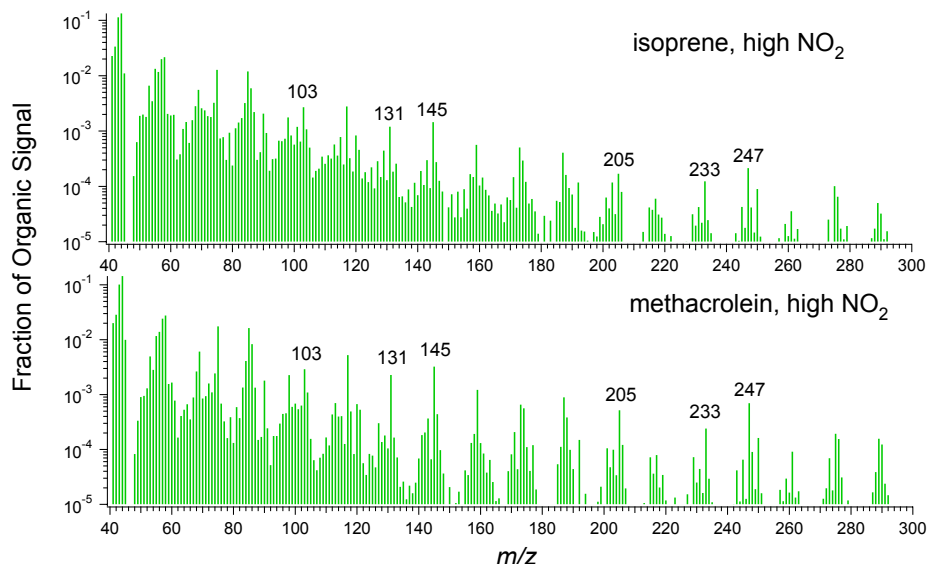


Fig. 8. AMS V-mode organic spectra of SOA from high- NO_2 photooxidation of isoprene and methacrolein. The labelled ion peaks differ from compounds listed in Table 3 by an O_2^- group. The accurate masses are confirmed by W-mode high-resolution analysis, as shown in Fig. 9. Separation of 102 Da between major peaks is consistent with esterification with a 2-MG monomer.

more volatile products, and hence less SOA (Kroll et al., 2006). However, under the experimental conditions in the present study, RO_2+HO_2 reactions are not expected to be significant. Rather, the dependence of SOA yield on the NO_2/NO ratio is consistent with analysis of SOA composition, which is consistent with MPAN, a product of the acyl peroxy radical+ NO_2 reaction, being the intermediate in SOA formation. Although the absolute concentrations of NO_2 in these experiments are a factor of 10 higher than ambient levels, we expect the OH-adduct of alkenes and aldehydes studied here to react predominantly with O_2 to form alkyl peroxy or acyl peroxy radicals. Compounds with nitro functional groups ($\text{R}-\text{NO}_2$), such as those found in the aromatic systems (Calvert et al., 2002), were not detected in these experiments.

Based on the proposed mechanism shown in Fig. 10, the acyl peroxy radical formed from abstraction of the aldehydic hydrogen atom of an unsaturated aldehyde react with either NO or NO_2 . The reversible reaction of RO_2 with NO_2 forms a PAN-type compound (MPAN for methacrolein), which, in the absence of competing reactions, reaches thermal equilibrium. The irreversible reaction of RO_2 with NO leads to fragmentation into CO_2 and a vinyl radical, which subsequently forms volatile gas-phase products, such as formaldehyde and CO (Orlando et al., 1999). At $[\text{OH}] = 2 \times 10^6$ molec cm^{-3} , the reaction of MPAN with OH has a rate comparable to that of thermal decomposition (Orlando et al., 2002), and leads to formation of aerosol products. Hence, the SOA formation potential for this system depends critically on the NO_2/NO

ratio. High NO_2/NO ratios shift the thermal equilibrium towards the unsaturated PAN, and SOA formation increases as the fraction of PAN reacting with OH radicals increases. At low NO_2/NO ratios, acyl peroxy radicals react predominantly with NO, leading to relatively volatile products.

Previous measurements of isoprene SOA yields under high- NO_x conditions have been carried out using photolysis of HONO (Kroll et al., 2005a) or the recycling of HO_x and NO_x to generate OH (so-called classical photooxidation) (Pandis et al., 1991; Dommen et al., 2006). Low SOA yields were observed as NO concentrations remained high during the experiments. In fact, SOA growth occurred only after NO concentrations decreased to less than 10 ppb (Kroll et al., 2005a; Dommen et al., 2006). It was proposed that after NO has been consumed, aerosol formation commences as the RO_2+HO_2 pathway becomes competitive. However, such a mechanism is inconsistent with the major differences in composition observed between high- and low- NO_x SOA products. High- NO_x SOA from isoprene photooxidation is dominated by esterification products of C_4 -carboxylic acids, whereas under low- NO_x conditions, SOA is dominated by peroxides and C_5 -tetros (Surratt et al., 2006). It is more likely that the decrease in NO concentration (and increase in NO_2 concentration) leads to a transition from an RO_2+NO dominated regime to an RO_2+NO_2 dominated regime, resulting in significant SOA formation via the MPAN route.

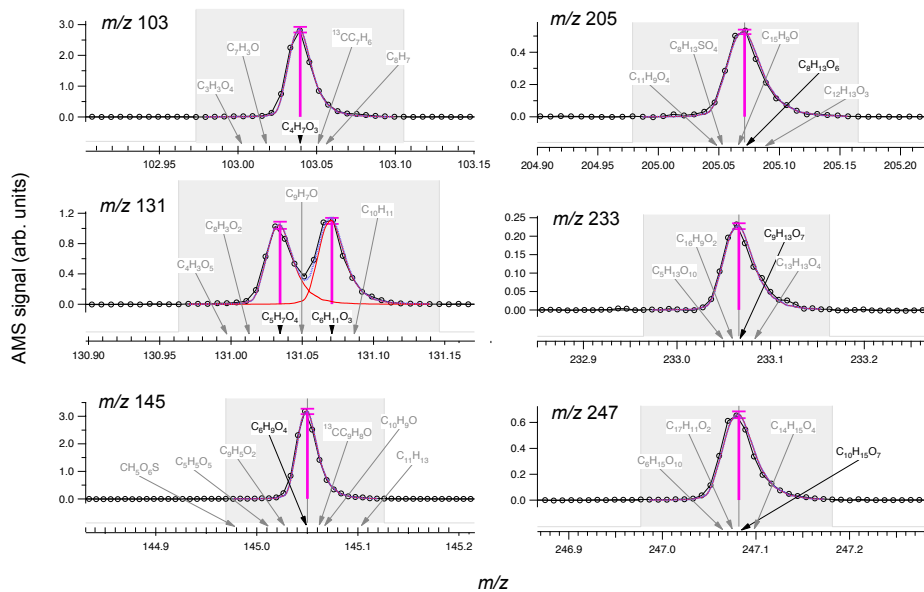


Fig. 9. High-resolution W-mode AMS peaks of a number of the major fragment ions observed in methacrolein/high- NO_2 experiments. Knowledge of the accurate masses allow assignments of molecular formulas, corresponding to loss of hydroxyl groups from compounds detected by offline analysis, suggesting that detection of compounds listed in Table 3 is not a result of sampling artifacts. m/z 131 contains two different ions, only one of which is consistent with compounds detected by offline UPLC/(-)ESI-TOFMS analysis.

At NO_2/NO ratios (between 3 and 8) higher than in previous studies (and more relevant to urban conditions), SOA yields from isoprene are approximately 3 times larger than previously measured. The yields even exceed those under low- NO_x conditions at the same organic aerosol loadings, as shown in Fig. 11. This is, in fact, consistent with observations from Kroll et al. (2006) that at very low NO_x concentrations, addition of NO actually increases SOA yield. It is likely that under very low NO concentrations, the NO_2/NO ratio increases rapidly, as NO is quickly converted to NO_2 . SOA yields are therefore higher than those in the absence of NO, as RO_2 (from methacrolein)+ NO_2 forms SOA more efficiently than RO_2 (from isoprene)+ HO_2 . However, further increasing NO decreases the NO_2/NO ratio. RO_2 (from methacrolein)+NO becomes more dominant, forms volatile products and leads to a decrease in SOA yield. It must be noted that the effect of RO_2 radical chemistry on SOA formation is complex and can be unique to different systems (Kroll and Seinfeld, 2008). Also, the acidity of the inorganic seed can increase SOA yields significantly: Surratt et al. (2010) shows that SOA yields from isoprene low- NO_x photooxidation can be as high as 0.29. Detailed knowledge of the chemical mechanism is required to predict the effect of NO_x conditions on SOA production.

6 Role of PAN in SOA formation

6.1 Unsaturated aldehydes

One can infer from the shapes of the growth curves the relative timescales of the reaction steps of SOA formation. In all high- NO_2 experiments, a greater extent of reaction is achieved than in high-NO experiments, and SOA formation continues after the parent hydrocarbon is completely consumed; this behavior is characterized by a vertical portion (“hook”) at the end of the SOA growth curve. The presence of this vertical portion indicates that SOA formation results from further reaction of first-generation products, which is the rate-limiting step in the mechanism (see Figs. 3–5). This observation is consistent with our previous results showing that first-generation products of methacrolein, such as hydroxyacetone and MPAN, are themselves still volatile (Suratt et al., 2010). SOA is instead formed from the further OH reaction of MPAN, which has a comparable rate coefficient to that of methacrolein (Orlando et al., 2002).

Formation of dihydroxycarboxylic acids (e.g. 2-MG), hydroxynitrooxycarboxylic acids, and corresponding oligoesters appears to be important SOA formation pathways for the five α, β -unsaturated aldehydes studied here (methacrolein, acrolein, crotonaldehyde, 2M2B, 2-pentenal). All of the SOA constituents detected by offline UPLC/(-)ESI-TOFMS in these systems are structural

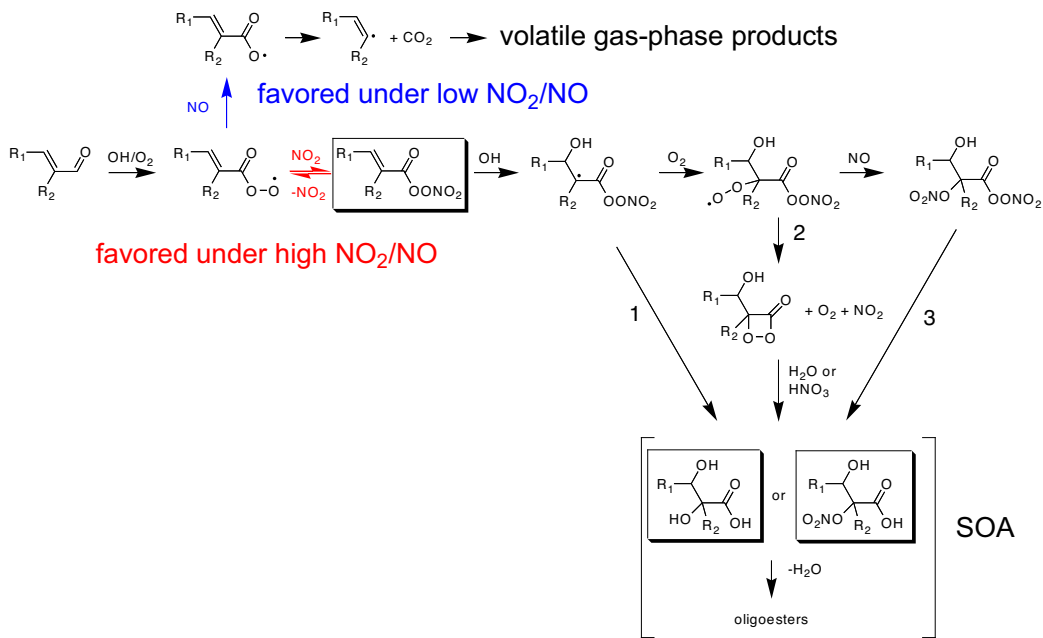


Fig. 10. Proposed mechanism to form aerosol-phase products from α,β -unsaturated aldehydes. The pathways highlighted in red are favored under high NO_2/NO ratios and lead to aerosol formation. The pathways highlighted in blue are favored under low NO_2/NO ratios and lead to fragmentation into volatile products. Aerosol formation from OH-reaction of unsaturated PANs can proceed via 3 possible routes (routes 1–3), and detailed investigation of each route is discussed in the main text.

analogs of each other, as confirmed by the online AMS operated in the high-resolution W-mode. Based on similarities in SOA growth trends and composition, we expect that the formation of SOA products proceeds via pathways similar to those elucidated in Surratt et al. (2010) (see Fig. 10). Although oxidation of these aldehydes can lead to α -dicarbonyls, such as glyoxal and methylglyoxal, which can undergo reactive uptake under humid conditions (Liggio et al., 2005; Kroll et al., 2005b; Volkamer et al., 2009), these compounds are not expected to contribute significantly to SOA formation under dry conditions. In addition, the AMS spectra for acrolein and crotonaldehyde SOA do not show peaks that are characteristic of glyoxal and its oligomers, as described in Liggio et al. (2005) and Galloway et al. (2009).

While MPAN is clearly the intermediate in SOA formation from methacrolein, the exact mechanism by which MPAN leads to such aerosol-phase products as 2-MG and hydroxynitrooxy carboxylic acids has not been established. From the oligoesters observed in the aerosol phase, it appears that the C₄ backbone of MPAN remains intact. Following OH addition to the double bond, the only known gas-phase pathway that would preserve the carbon backbone is formation of hydroxynitrates. (Fragmentation of the MPAN-alkoxy radical would break up the C₄ backbone and yield smaller products.) The nitrooxy functional groups could then be hydrolyzed to

hydroxyl groups (Sato, 2008) to form 2-MG and high-MW oligoesters (Route 3 in Fig. 10). However, gas-phase abundances of C₄- (for methacrolein and crotonaldehyde) or C₅- (for 2M2B, 3M2B and 2-pentenal) hydroxynitrate-PAN, the supposed SOA intermediate in all these systems, do not correlate with the amount of aerosol formed. Substitution of the α -carbon atom by methyl groups (from crotonaldehyde to methacrolein, or from 3M2B to 2M2B) leads to an increase in the amount of SOA formed by more than a factor of 4, but no increase in gas-phase signal of the hydroxynitrate-PAN is observed (see Fig. 12), implying that it is unlikely the SOA-forming channel.

Another possible mechanism is that in which after OH addition to the double bond in MPAN the OH-adduct undergoes intramolecular rearrangement before addition of O₂, leading to formation of 2-MG and oligoesters (Route 1 in Fig. 10). Such isomerization can be competitive with O₂ addition, as the O–O bond in the peroxy nitrate moiety is weak. In one experiment (17/12/09), the chambers were flushed with nitrogen to lower the oxygen content to 2%, thereby slowing down addition of O₂ by a factor of 10. Compared to another experiment with 21% O₂ (16/12/09), no increase in aerosol formation is observed, suggesting that SOA formation likely involves O₂ addition to the MPAN-OH adduct, though it is also possible that the intramolecular rearrangement reaction

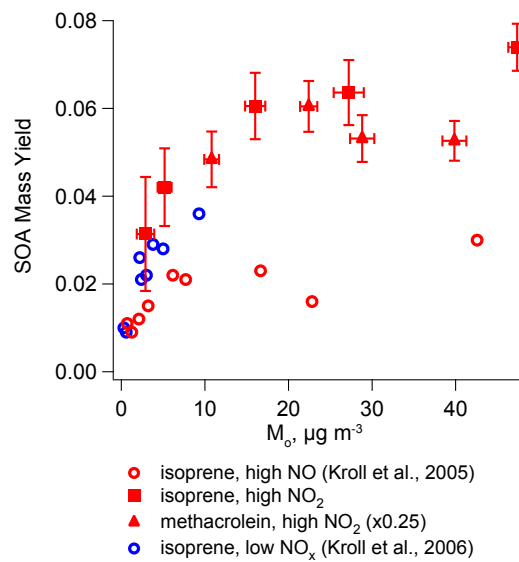


Fig. 11. SOA mass yields from isoprene photooxidation under neutral seed conditions as a function of organic loading. The solid markers indicate SOA yields measured in this study, using CH_3ONO as the OH precursor under high NO_2/NO ratios (between 3 and 8). The SOA yields for methacrolein (solid red triangles) have been multiplied by 0.25 to account for the gas-phase product yield of methacrolein from isoprene high- NO_x oxidation. The SOA yields measured under high- NO_2/NO conditions are higher than both high- NO (open red circles) and low- NO_x conditions (open blue circles) under neutral seed conditions. With an acidified seed, SOA yields can be as high as 0.29 (Surratt et al., 2010).

is sufficiently fast that O_2 addition is not competitive at these O_2 levels.

From the trends of SOA formation observed in the unsaturated aldehyde systems, it appears that the chemical environment of the carbon atom adjacent to the aldehyde group plays an important role in determining the extent of SOA formation. Low-volatility oligoesters are formed only when the α - and β -carbon atoms are unsaturated; SOA yields of 4-pentenal, for which the olefinic bond is in the 4-position, are lower than those of 2-pentenal, and the SOA products are not analogous to those found in SOA from α , β -unsaturated aldehydes (see Fig. 13). SOA formation is correlated with fraction of OH addition to the β -carbon atom, which forms a radical at the α site: SOA yields of crotonaldehyde and 2-pentenal (in which OH addition to the β -carbon is favored) exceed those of 3M2B (in which OH addition to the α -carbon is favored), even though 3M2B has an equal or higher molecular weight. This suggests that an interaction responsible for producing low-volatility species occurs between the peroxy nitrate functional group and the α -carbon (likely a radical species) that our experiments are not able to precisely re-

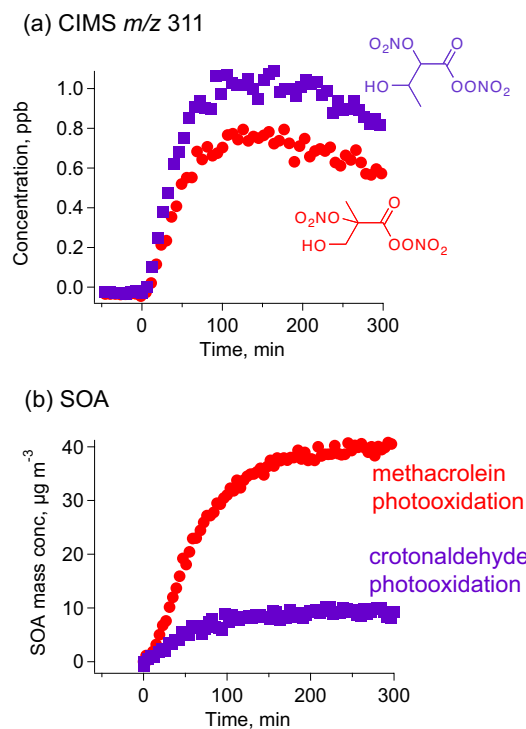


Fig. 12. Time trends of (a) gas-phase CIMS m/z 311 and (b) SOA growth during high- NO_2 photooxidation of methacrolein (red) and crotonaldehyde (purple). m/z 311 corresponds to the unit mass of CF_3O^- adduct of C_4 -hydroxynitrate-PAN. The observed gas-phase signals of C_4 -hydroxynitrate-PAN in both experiments are within 20% of each other, but the amount of SOA formed from methacrolein photooxidation is about a factor of 4 higher. A similar difference was observed between 2M2B and 3M2B photooxidation. This suggests that C_4 - and C_5 -hydroxynitrate-PANs are not precursors to low-volatility aerosol-phase products.

veal. We hypothesize that the peroxy radical undergoes self cyclization to form a highly reactive dioxoketone intermediate, which subsequently reacts with H_2O or HNO_3 heterogeneously to form the low-volatility products observed in the SOA (see Fig. 10). This intermediate is likely short-lived, and further work is required to identify this species and its role in SOA formation.

One possible explanation for the higher SOA yields observed from methacrolein and 2M2B is that for these compounds SOA formation is favored by steric hindrance. With an additional methyl group on the α carbon, steric repulsion causes the methyl group to move away from the neighbouring peroxy nitrate functional group by rotation of the C-C bond. As a result, the intramolecular reaction leading to SOA formation can be enhanced, consistent with the relatively higher SOA yields. For the other α , β -unsaturated

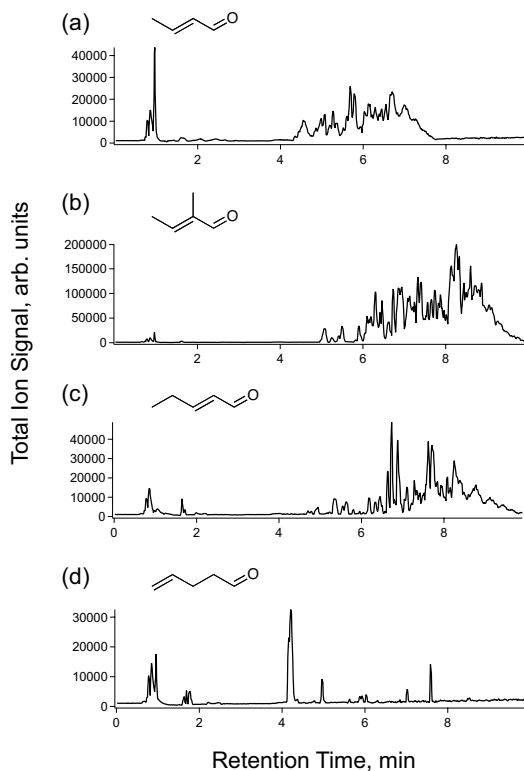
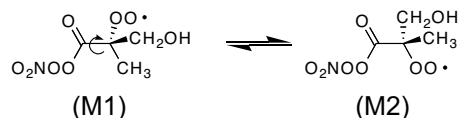


Fig. 13. UPLC/(-)ESI-TOFMS base peak ion chromatograms (BPCs) for high- NO_2 photooxidation of (a) crotonaldehyde (b) 2M2B (c) 2-pentenal and (d) 4-pentenal. The exact masses and elemental composition of detected $[\text{M}-\text{H}]^-$ ions are listed in the Supplementary Material. Compounds detected in crotonaldehyde, 2M2B and 2-pentenal SOA are likely similar. (SOA products from C₅ 2M2B and 2-pentenal are less polar than those from crotonaldehyde, a C₄ compound, and therefore have longer retention times in reverse-phase chromatography.) The chemical composition of 4-pentenal SOA is significantly different from those all 3 other aldehydes, and no oligoester products are detected, suggesting a different SOA formation mechanism.

aldehydes, this interaction is likely not favored, as the hydrogen atom on the α carbon is in plane with the peroxy nitrate group in the most stable rotational conformer (see Fig. 14). The interaction between the peroxy nitrate group and the added functional group is reduced, corresponding to lower SOA formation. Thermodynamic calculations of the relative stabilities of the conformers are required to confirm this hypothesis.

Methacrolein:



Crotonaldehyde:

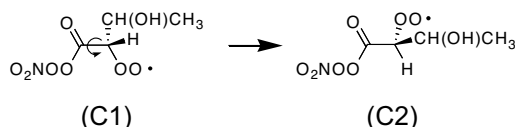


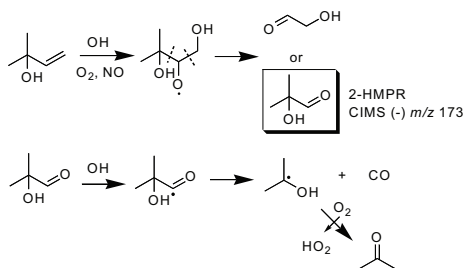
Fig. 14. Rotational conformers of hypothesized SOA intermediate in methacrolein and crotonaldehyde mechanism. For methacrolein, the methyl group on the α -carbon presents significant steric hindrance, which favors the conformer M2. This increases the interaction between the peroxy radical and the peroxy nitrate group, leading to significant SOA formation. For crotonaldehyde, the hydrogen atom presents much smaller steric hindrance, favoring the conformer C2. As a result, the peroxy radical is out of plane with the PAN group, and the reaction to form SOA can be less favorable.

6.2 Methylbutenols (MBO)

MBO232 is a biogenic hydrocarbon potentially important in forest photochemistry (Harley et al., 1998). The SOA yields of MBO232 photooxidation have been shown to be negligible, under both high- and low- NO_x conditions (Carrasco et al., 2007; Chan et al., 2009a). In this study, SOA formation from MBO232 photooxidation is below detection limit, even at high NO_2/NO ratios (which would favor any PAN formation). This is likely linked to the lack of PAN products from MBO232 oxidation. The fate of the alkoxy radical formed from OH-initiated oxidation of MBO232 is shown in Fig. 15. Scission of the C-C bond adjacent to the tertiary carbon is favored, leading to high yields of glycolaldehyde (>0.6). Formation of 2-hydroxymethylpropanal (2-HMPR) following scission of the C-C bond adjacent to the primary carbon is not the favored route, and hence the yields of 2-HMPR are relatively low (<0.4). Furthermore, OH oxidation of 2-HMPR proceeds by OH abstraction of the aldehydic hydrogen, but owing to the neighbouring hydroxyl group, decomposition to acetone and CO is favored over addition of O_2 to form an acyl peroxy radical. Carrasco et al. (2006) found no PAN formation from photooxidation of 2-HMPR, despite high NO_2/NO ratios.

MBO231 photooxidation produces, in contrast, substantial amounts of SOA, at mass yields of 0.008 – 0.042. In MBO231, the hydroxyl group is in the 1-position and is not adjacent to the double bond. Decomposition of the analogous alkoxy radical therefore proceeds by scission of the C-C

MBO232:



MBO231:

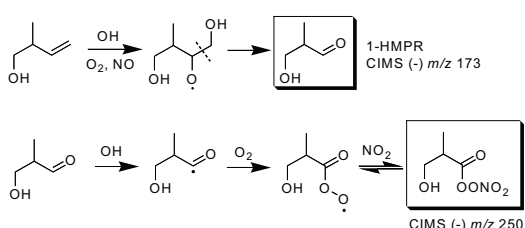


Fig. 15. Mechanism of MBO231 and MBO232 photooxidation under high- NO_x conditions. The dashed lines indicate possible locations of C-C bond scission under decomposition of alkoxy radicals. For MBO232, 2-HMPR formation is relatively small, as scission of the C-C bond with the 4-carbon is not favored. In addition, the acyl radical from H-abstraction of 2-HMPR rapidly decomposes to CO and acetone. As a result, PAN formation is unlikely. For MBO231, 1-HMPR formation is favored from the decomposition of the alkoxy radical. Furthermore, OH reaction of 1-HMPR leads to an acyl peroxy radical, which reacts with NO_2 to form a C4-hydroxy-PAN.

bond adjacent to the primary carbon, favoring the formation of 1-HMPR; observed HMPR (CIMS $(-)m/z$ 173) concentrations in MBO231 photooxidation were twice as high as those in MBO232 photooxidation. Also, following abstraction of the aldehydic hydrogen from 1-HMPR, addition of O_2 to form an acyl peroxy radical is favored over decomposition to CO. Under high- NO_2 conditions, the acyl peroxy radical can react with NO_2 to form a C4-hydroxy-PAN (see Fig. 15). Tandem mass spectrometry was used to distinguish gas-phase C4-hydroxy-PAN from the isobaric C5 dihydroxynitrate, both observed at $(-)m/z$ 250 (see Supplementary Material for details). The C5 dihydroxynitrate is a first generation oxidation product of both MBO231 and MBO232 formed from RO_2+NO at molar yields of 0.10–0.15 (Chan et al., 2009a). In high-NO photooxidation of MBO231 and high- NO_2 photooxidation of MBO232, no C4-hydroxy-PAN was observed in the gas phase, corresponding to negligible aerosol formation. In high- NO_2 photooxidation of MBO231, C4-hydroxy-PAN is a major gas-phase product, and SOA formation is significant. The identification of C4-hydroxy-PAN

is further supported by the ratios of ion signals of m/z 250 to m/z 251, its ^{13}C isotopologue, which indicate that the signal at m/z 250 was dominated by a C4 compound during MBO231 high- NO_2 photooxidation, and by a C5 compound during MBO232 photooxidation. Hence, the low SOA yields from MBO232 are due to the lack of PAN formation, illustrating the potentially important role of PAN compounds as SOA intermediates.

7 Conclusions

In this work, we systematically investigate the effect of relative NO and NO_2 concentrations on SOA formation from aldehyde photooxidation under high- NO_x conditions. A strong positive correlation of SOA yields with NO_2/NO ratio is observed for methacrolein (a major oxidation product of isoprene responsible for SOA formation) and two related α,β -unsaturated aldehydes, acrolein and crotonaldehyde. Oligoester products from dihydroxycarboxylic acids and hydroxynitrooxycarboxylic acids are also observed to depend on NO_2/NO ratio, confirming that PAN chemistry plays an important role in formation of these low-volatility products. Offline high-resolution aerosol mass spectrometry reveals that analogous oligoester products are major constituents in SOA formed from all α,β -unsaturated aldehydes studied here. By comparing SOA formation from structurally similar aldehydes, we establish that SOA formation is favored when the α -carbon is substituted by a methyl group and the olefinic bond is in the 2-position, such as in methacrolein and 2M2B. The experimental data suggest that SOA formation proceeds via an intramolecular reaction involving the peroxy nitrate functional group, following the addition of O_2 to the MPAN+OH adduct. No aerosol formation is observed from MBO232, an atmospherically important unsaturated alcohol, even at high NO_2/NO ratios, as PAN formation is structurally unfavorable.

Understanding the overall effect of NO_x on SOA yields is important, as SOA yields can vary greatly depending on NO_x conditions. In most photooxidation systems, addition of OH, followed by O_2 , to an olefinic bond results in formation of a hydroxyperoxy radical. The competition between the RO_2+HO_2 pathway (which forms low-volatility hydroperoxides) and the RO_2+NO pathway (which forms volatile organic nitrates and fragmentation products) determines the SOA yields. In the isoprene-high- NO_x system, owing to the MPAN chemistry, aerosol formation proceeds via OH abstraction of the aldehydic hydrogen from methacrolein. As a result, a competition exists between reaction of the acyl peroxy radical with NO_2 , leading to formation of MPAN and SOA, and with NO to form volatile fragmentation products. The present work shows the importance of the RO_2+NO_2 pathway of unsaturated aldehyde photooxidation as a route leading to SOA formation. This could have important implications on SOA formation from

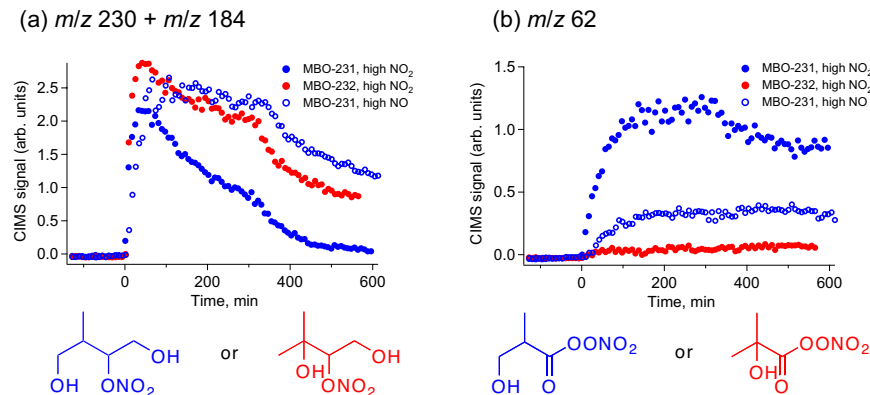


Fig. 16. Gas-phase ion signals of C₄-hydroxy-PAN and C₅-dihydroxynitrate from photooxidation of MBO231 and MBO232, as observed by negative chemical ionization-tandem mass spectrometry of m/z 250. Neutral losses of HF or CF_2O are associated with the C₅-dihydroxynitrate under CID of the parent ion m/z 250, leading to daughter ions of 230 and 184, respectively. The daughter ion m/z 62, most likely NO_3^- , is associated with the C₄-hydroxy-PAN. (See Supplementary Material for more details.) After 300 minutes of irradiation, more OH precursor was added to further react oxidation products. PAN formation was observed only from MBO231 oxidation and is positively correlated with NO_2/NO , similar to unsaturated aldehydes.

other atmospheric compounds, especially those with conjugated double bonds. For example, photooxidation of aromatic compounds (Calvert et al., 2002) can lead to α , β -unsaturated aldehydes, which can form significant amounts of low-volatility products via a PAN intermediate. At atmospherically relevant NO_2/NO ratios, SOA yields from isoprene are 0.031–0.074 at organic aerosol loadings of 3–47 $\mu\text{g m}^{-3}$; these values are 3 times higher than those previously measured under high-NO conditions. The yields exceed even those measured under low- NO_x conditions. An implication of these results is that atmospheric SOA formation from aldehydes may be significantly underestimated in current models, since an appreciable fraction of SOA is generated in areas where NO_2/NO ratios are high.

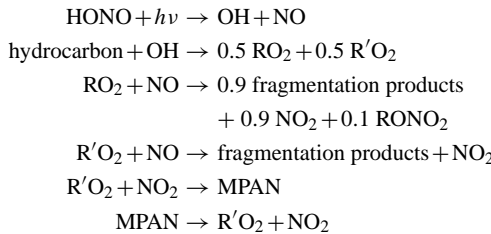
Radiocarbon (¹⁴C) studies have repeatedly shown that ambient organic aerosol is dominated by biogenic carbon, suggesting that biogenic hydrocarbons are an important source of SOA. However, field measurements have shown that organic aerosol levels tend to be correlated with anthropogenic tracers such as CO and acetylene. From satellite observations one can infer that while the source of carbon in many regions is most likely biogenic, the aerosol formation from biogenic hydrocarbons is significantly enhanced by anthropogenic activities (i.e. NO_x and SO_x emissions (Goldstein et al., 2009; Carlton et al., 2010)). The present work moves in the direction of reconciling these two seemingly contradictory observations of biogenic carbon versus anthropogenic enhancement. Here we show that the SOA yields from photooxidation of isoprene under atmospherically relevant NO_2/NO ratios are significantly larger than those previously measured under lower NO_2/NO ratios. Moreover, the SOA yields un-

der these conditions are larger than those under low- NO_x conditions, suggesting that SOA formation from isoprene, the most abundantly emitted non-methane biogenic hydrocarbon, can be more efficient in urban high- NO_x plumes than in remote regions.

Appendix A

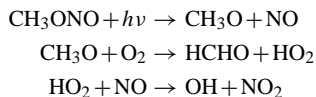
Photochemical modeling to estimate NO and NO_2 concentrations

Owing to interference with the NO_2 signal by HONO and CH_3ONO in the chemiluminescence NO_x monitor, we estimate NO and NO_2 concentrations during chamber experiments by photochemical modeling. In experiments in which HONO is the source of OH , the photolysis rate of HONO is estimated from the first-order decay of the m/z 66 signal on the CIMS, which correspond to the $\text{HF}\cdot\text{ONO}^-$ ion. The initial mixing ratio of HONO was estimated based on the decay of parent hydrocarbon and known rate constants (Atkinson and Arey, 2003; Magneron et al., 2002). Previous comparison to a GC/ NO_2 analyzer allows us to determine the HONO interference on the NO_2 signal, and hence the amount of NO and NO_2 produced during HONO synthesis (Chan et al., 2009b). The initial mixing ratio of NO_2 is therefore the sum of the concentrations of NO_2 impurity from HONO synthesis (calculated by multiplying the NO_2 signal after HONO injection by a known factor) and additional NO_2 injected (the increase in NO_2 signal from direct injection). For unsaturated aldehydes, the photochemical model includes the following reactions:



RO_2 denotes the peroxy radical produced by OH addition to the C=C double bond, followed by O_2 . $\text{R}'\text{O}_2$ denotes the acyl peroxy radical produced by OH abstraction of the aldehydic hydrogen, followed by O_2 addition. These two channels (OH addition and abstraction) have a branching ratio of 1:1 for methacrolein (Tuazon and Atkinson, 1990). Other reactions involving O_3 , HO_x , NO_x are also included in the mechanism. For MBO231 and MBO232, the reactions described in Chan et al. (2009a) are used. The calculated NO_2/NO ratios averaged over the first 200 min of irradiation (the period during which SOA formation occurred, see Fig. 1) are listed in Table 2.

For the high- NO_2 experiments, CH_3ONO was used as the OH precursor:



The photolysis rate of CH_3ONO was estimated by the first-order decay of the CH_3ONO signal on GC/FID. The initial mixing ratio of CH_3ONO was determined from the measured vapor pressure of CH_3ONO in the injection bulb. The modeled decay of the hydrocarbon is consistent with that observed by GC/FID. FTIR analysis shows no NO or NO_2 impurities are produced during CH_3ONO synthesis ($[\text{NO}_2]$ was less than 0.6% of $[\text{CH}_3\text{ONO}]$). In the photochemical calculations, the initial NO and NO_2 concentrations are determined from the increase in NO and NO_2 signals from direct injection. The calculated NO_2/NO ratios averaged over the first 100 min of irradiation are listed in Table 2 (see Fig. 2).

**Supplementary material related to this article is available online at:
<http://www.atmos-chem-phys.net/10/7169/2010/acp-10-7169-2010-supplement.pdf>.**

Acknowledgements. This research was funded by US Department of Energy Biological and Environmental Research Program DE-FG02-05ER63983, US Environmental Protection Agency STAR grant RD-83374901, US National Science Foundation grant ATM-0432377, and the Electric Power Research Institute. This publication has not been formally reviewed by the EPA. The views

expressed in this document are solely those of the authors and EPA does not endorse any products mentioned in this publication. The authors would like to thank K. E. Kautzman and A. J. Kwan for experimental assistance, and F. Pault for helpful discussion.

Edited by: M. Gysel

References

Atkinson, R. and Arey, J.: Atmospheric degradation of volatile organic compounds, *Chem. Rev.*, 103, 4605–4638, 2003.

Calvert, J. G., Atkinson, R., Becker, K. H., Kamens, R. M., Seinfeld, J. H., Wallington, T. J., and Yarwood, G.: The mechanisms of atmospheric oxidation of aromatic hydrocarbons, Oxford University Press, 2002.

Canagaratna, M. R., Jayne, J. T., Jimenez, J. L., Allan, J. D., Alfarra, M. R., Zhang, Q., Onasch, T. B., Drewnick, F., Coe, H., Middlebrook, A., Delia, A., Williams, L. R., Trimborn, A. M., Northway, M. J., DeCarlo, P. F., Kolb, C. E., Davidovits, P., and Worsnop, D. R.: Chemical and microphysical characterization of ambient aerosols with the Aerodyne aerosol mass spectrometer, *Mass. Spec. Rev.*, 26, 185–222, 2007.

Carlton, A. G., Wiedinmyer, C., and Kroll, J. H.: A review of Secondary Organic Aerosol (SOA) formation from isoprene, *Atmos. Chem. Phys.*, 9, 4987–5005, doi:10.5194/acp-9-4987-2009, 2009.

Carlton, A. G., Pinder, R. W., Bhave, P. V. and Pouliot, G. A.: To what extent can biogenic SOA be controlled? *Environ. Sci. Technol.*, 44, 3376–3380, 2010.

Carrasco, N., Doussin, J. F., Picquet-Varrault, B., and Carlier, P.: Tropospheric degradation of 2-hydroxy-2-methylpropanal, a photo-oxidation product of 2-methyl-3-buten-2-ol: Kinetic and mechanistic study of its photolysis and its reaction with OH radicals, *Atmos. Environ.*, 40, 2011–2019, 2006.

Carrasco, N., Doussin, J. F., O'Connor, M., Wenger, J. C., Picquet-Varrault, B., Durand-Jolibois, R., and Carlier, P.: Simulation chamber studies of the atmospheric oxidation of 2-methyl-3-buten-2-ol: Reaction with hydroxyl radicals and ozone under a variety of conditions, *J. Atmos. Chem.*, 56, 33–55, 2007.

Chan, A. W. H., Galloway, M. M., Kwan, A. J., Chhabra, P. S., Keutsch, F. N., Wennberg, P. O., Flagan, R. C., and Seinfeld, J. H.: Photooxidation of 2-methyl-3-buten-2-ol (MBO) as a potential source of secondary organic aerosol, *Environ. Sci. Technol.*, 43, 4647–4652, 2009a.

Chan, A. W. H., Kautzman, K. E., Chhabra, P. S., Surratt, J. D., Crounse, J. D., Kürten, A., Wennberg, P. O., Flagan, R. C., Seinfeld, J. H.: Secondary organic aerosol formation from photooxidation of naphthalene and alkyl naphthalenes: implications for oxidation of intermediate volatility organic compounds (IVOCs), *Atmos. Chem. Phys.*, 9, 3049–3060, doi:10.5194/acp-9-3049-2009, 2009.

Chung, S. H. and Seinfeld, J. H.: Global distribution and climate forcing of carbonaceous aerosols, *J. Geophys. Res.-Atmos.*, 107, doi:10.1029/2001JD001397, 2002.

Claeys, M., Graham, B., Vas, G., Wang, W., Vermeulen, R., Pashynska, V., Cafmeyer, J., Guyon, P., Andreae, M. O., Artaxo, P., and Maenhaut, W.: Formation of secondary organic aerosols through photooxidation of isoprene, *Science*, 303, 1173–1176, 2004.

Cocker, D. R., Flagan, R. C., and Seinfeld, J. H.: State-of-the-art chamber facility for studying atmospheric aerosol chemistry, *Environ. Sci. Technol.*, 35, 2594–2601, 2001.

Crounse, J. D., McKinney, K. A., Kwan, A. J., and Wennberg, P. O.: Measurement of gas-phase hydroperoxides by chemical ionization mass spectrometry, *Anal. Chem.*, 78, 6726–6732, 2006.

de Gouw, J. A., Middlebrook, A. M., Warneke, C., Goldan, P. D., Kuster, W. C., Roberts, J. M., Fehsenfeld, F. C., Worsnop, D. R., Canagaratna, M. R., Pszenny, A. A. P., Keene, W. C., Marchewka, M., Bertman, S. B., and Bates, T. S.: Budget of organic carbon in a polluted atmosphere: Results from the New England Air Quality Study in 2002, *J. Geophys. Res.-Atmos.*, 110, D16305, doi:10.1029/2004JD005623, 2005.

de Gouw, J. A., Brock, C. A., Atlas, E. L., Bates, T. S., Fehsenfeld, F. C., Goldan, P. D., Holloway, J. S., Kuster, W. C., Lerner, B. M., Matthew, B. M., Middlebrook, A. M., Onasch, T. B., Peltier, R. E., Quinn, P. K., Senff, C. J., Stohl, A., Sullivan, A. P., Trainer, M., Warneke, C., Weber, R. J., and Williams, E. J.: Sources of particulate matter in the northeastern United States in summer: 1. Direct emissions and secondary formation of organic matter in urban plumes, *J. Geophys. Res.-Atmos.*, 113, D08301, doi: 10.1029/2007JD009243, 2008.

DeCarlo, P. F., Kimmel, J. R., Trimborn, A., Northway, M. J., Jayne, J. T., Aiken, A. C., Gonin, M., Fuhrer, K., Horvath, T., Docherty, K. S., Worsnop, D. R., and Jimenez, J. L.: Field-deployable, high-resolution, time-of-flight aerosol mass spectrometer, *Anal. Chem.*, 78, 8281–8289, 2006.

Dommen, J., Metzger, A., Duplissy, J., Kalberer, M., Alfarra, M. R., Gascho, A., Weingartner, E., Prevot, A. S. H., Verheggen, B., and Baltensperger, U.: Laboratory observation of oligomers in the aerosol from isoprene/NO_x photooxidation, *Geophys. Res. Lett.*, 33, L13805, doi:10.1029/2006GL026523, 2006.

Edney, E. O., Kleindienst, T. E., Jaoui, M., Lewandowski, M., Offenberg, J. H., Wang, W., and Claeys, M.: Formation of 2-methyl tetros and 2-methylglyceric acid in secondary organic aerosol from laboratory irradiated isoprene/NO_x/SO₂/air mixtures and their detection in ambient PM2.5 samples collected in the eastern United States, *Atmos. Environ.*, 39, 5281–5289, 2005.

Fantechi, G., Jensen, N. R., Hjorth, J., and Peeters, J.: Determination of the rate constants for the gas-phase reactions of methyl butenol with OH radicals, ozone, NO₃ radicals, and Cl atoms, *Int. J. Chem. Kinet.*, 30, 589–594, 1998.

Galloway, M. M., Chhabra, P. S., Chan, A. W. H., Surratt, J. D., Flagan, R. C., Seinfeld, J. H., and Keutsch, F. N.: Glyoxal uptake on ammonium sulphate seed aerosol: reaction products and reversibility of uptake under dark and irradiated conditions, *Atmos. Chem. Phys.*, 9, 3331–3345, doi:10.5194/acp-9-3331-2009, 2009.

Goldstein, A. H., Koven, C. D., Heald, C. L., and Fung, I. Y.: Biogenic carbon and anthropogenic pollutants combine to form a cooling haze over the southeastern United States, *Proc. Natl. Acad. Sci. USA*, 106, 8835–8840, 2009.

Guenther, A., Karl, T., Harley, P., Wiedinmyer, C., Palmer, P. I., and Geron, C.: Estimates of global terrestrial isoprene emissions using MEGAN (Model of Emissions of Gases and Aerosols from Nature), *Atmos. Chem. Phys.*, 6, 3181–3210, doi:10.5194/acp-6-3181-2006, 2006.

Hallquist, M., Wenger, J. C., Baltensperger, U., Rudich, Y., Simpson, D., Claeys, M., Dommen, J., Donahue, N. M., George, C., Goldstein, A. H., Hamilton, J. F., Herrmann, H., Hoffmann, T., Jinuma, Y., Jang, M., Jenkin, M. E., Jimenez, J. L., Kiendler-Scharr, A., Maenhaut, W., McFiggans, G., Mentel, Th. F., Monod, A., Prvt, A. S. H., Seinfeld, J. H., Surratt, J. D., Szmigielski, R., and Wildt, J.: The formation, properties and impact of secondary organic aerosol: current and emerging issues, *Atmos. Chem. Phys.*, 9, 5155–5236, doi:10.5194/acp-9-5155-2009, 2009.

Harley, P., Fridd-Stroud, V., Greenberg, J., Guenther, A., and Vasconcellos, P.: Emission of 2-methyl-3-buten-2-ol by pines: A potentially large natural source of reactive carbon to the atmosphere, *J. Geophys. Res.-Atmos.*, 103, 25479–25486, 1998.

Hatakeyama, S., Izumi, K., Fukuyama, T., Akimoto, H., and Washida, N.: Reactions of OH with alpha-pinene and beta-pinene in air – Estimate of global CO production from the atmospheric oxidation of terpenes, *J. Geophys. Res.-Atmos.*, 96, 947–958, 1991.

Henze, D. K. and Seinfeld, J. H.: Global secondary organic aerosol from isoprene oxidation, *Geophys. Res. Lett.*, 33, L09812, doi: 10.1029/2006GL025976, 2006.

Henze, D. K., Seinfeld, J. H., Ng, N. L., Kroll, J. H., Fu, T.-M., Jacob, D. J., and Heald, C. L.: Global modeling of secondary organic aerosol formation from aromatic hydrocarbons: high- vs. low-yield pathways, *Atmos. Chem. Phys.*, 8, 2405–2420, doi: 10.5194/acp-8-2405-2008, 2008.

Hurley, M. D., Sokolov, O., Wallington, T. J., Takekawa, H., Karasawa, M., Klotz, B., Barnes, I., and Becker, K. H.: Organic aerosol formation during the atmospheric degradation of toluene, *Environ. Sci. Technol.*, 35, 1358–1366, 2001.

Ion, A. C., Vermeylen, R., Kourtchev, I., Cafmeyer, J., Chi, X., Gelencser, A., Maenhaut, W., and Claeys, M.: Polar organic compounds in rural PM_{2.5} aerosols from K-puszta, Hungary, during a 2003 summer field campaign: Sources and diel variations, *Atmos. Chem. Phys.*, 5, 1805–1814, doi:10.5194/acp-5-1805-2005, 2005.

Johnson, D., Jenkin, M. E., Wirtz, K., and Martin-Reviejo, M.: Simulating the formation of secondary organic aerosol from the photooxidation of aromatic hydrocarbons, *Environ. Chem.*, 2, 35–48, 2005.

Kanakidou, M., Seinfeld, J. H., Pandis, S. N., Barnes, I., Dentener, F. J., Facchini, M. C., Van Dingenen, R., Ervens, B., Nenes, A., Nielsen, C. J., Swietlicki, E., Putaud, J. P., Balkanski, Y., Fuzzi, S., Horth, J., Moortgat, G. K., Winterhalter, R., Myhre, C. E. L., Tsigaridis, K., Vignati, E., Stephanou, E. G., and Wilson, J.: Organic aerosol and global climate modelling: a review, *Atmos. Chem. Phys.*, 5, 1053–1123, doi: 10.5194/acp-5-1053-2005, 2005.

Keywood, M. D., Varutbangkul, V., Bahreini, R., Flagan, R. C., and Seinfeld, J. H.: Secondary organic aerosol formation from the ozonolysis of cycloalkenes and related compounds, *Environ. Sci. Technol.*, 38, 4157–4164, 2004.

Kleindienst, T. E., Lewandowski, M., Offenberg, J. H., Jaoui, M., and Edney, E. O.: The formation of secondary organic aerosol from the isoprene + OH reaction in the absence of NO_x, *Atmos. Chem. Phys.*, 9, 6541–6558, doi:10.5194/acp-9-6541-2009, 2009.

Kourtchev, I., Ruuskanen, T., Maenhaut, W., Kulmala, M., and Claeys, M.: Observation of 2-methyltetros and related photo-oxidation products of isoprene in boreal forest aerosols from

Hyttiälä, Finland, *Atmos. Chem. Phys.*, 5, 2761–2770, doi:10.5194/acp-5-2761-2005, 2005.

Kroll, J. H. and Seinfeld, J. H.: Chemistry of secondary organic aerosol: Formation and evolution of low-volatility organics in the atmosphere, *Atmos. Environ.*, 42, 3593–3624, 2008.

Kroll, J. H., Ng, N. L., Murphy, S. M., Flagan, R. C., and Seinfeld, J. H.: Secondary organic aerosol formation from isoprene photooxidation under high-NO_x conditions, *Geophys. Res. Lett.*, 32, L18808, doi:10.1029/2005GL023637, 2005a.

Kroll, J. H., Ng, N. L., Murphy, S. M., Varutbangkul, V., Flagan, R. C., and Seinfeld, J. H.: Chamber studies of secondary organic aerosol growth by reactive uptake of simple carbonyl compounds, *J. Geophys. Res.-Atmos.*, 110, D23207, doi:10.1029/2005JD006004, 2005b.

Kroll, J. H., Ng, N. L., Murphy, S. M., Flagan, R. C., and Seinfeld, J. H.: Secondary organic aerosol formation from isoprene photooxidation, *Environ. Sci. Technol.*, 40, 1869–1877, 2006.

Lewis, C. W. and Stiles, D. C.: Radiocarbon content of PM2.5 ambient aerosol in Tampa, FL, *Aerosol. Sci. Tech.*, 40, 189–196, 2006.

Lewis, C. W., Klouda, G. A., and Ellenson, W. D.: Radiocarbon measurement of the biogenic contribution to summertime PM-2.5 ambient aerosol in Nashville, TN, *Atmos. Environ.*, 38, 6053–6061, 2004.

Liggio, J., Li, S. M., and McLaren, R.: Heterogeneous reactions of glyoxal on particulate matter: Identification of acetals and sulfate esters, *Environ. Sci. Technol.*, 39, 1532–1541, 2005.

Magneron, I., Thevenet, R., Mellouki, A., Le Bras, G., Moortgat, G. K., and Wirtz, K.: A study of the photolysis and OH-initiated oxidation of acrolein and trans-crotonaldehyde, *J. Phys. Chem. A*, 106, 2526–2537, 2002.

Ng, N. L., Chhabra, P. S., Chan, A. W. H., Surratt, J. D., Kroll, J. H., Kwan, A. J., McCabe, D. C., Wennberg, P. O., Sorooshian, A., Murphy, S. M., Dalleska, N. F., Flagan, R. C., and Seinfeld, J. H.: Effect of NO_x level on secondary organic aerosol (SOA) formation from the photooxidation of terpenes, *Atmos. Chem. Phys.*, 7, 5159–5174, doi:10.5194/acp-7-5159-2007, 2007a.

Ng, N. L., Kroll, J. H., Chan, A. W. H., Chhabra, P. S., Flagan, R. C., and Seinfeld, J. H.: Secondary organic aerosol formation from m-xylene, toluene, and benzene, *Atmos. Chem. Phys.*, 7, 3909–3922, doi:10.5194/acp-7-3909-2007, 2007b.

Orlando, J. J., Tyndall, G. S., and Paulson, S. E.: Mechanism of the OH-initiated oxidation of methacrolein, *Geophys. Res. Lett.*, 26, 2191–2194, 1999.

Orlando, J. J., Tyndall, G. S., Bertman, S. B., Chen, W. C., and Burkholder, J. B.: Rate coefficient for the reaction of OH with CH₂=C(CH₃)C(=O)OONO₂ (MPAN), *Atmos. Environ.*, 36, 1895–1900, 2002.

Pandis, S. N., Paulson, S. E., Seinfeld, J. H., and Flagan, R. C.: Aerosol formation in the photooxidation of isoprene and beta-pinene, *Atmos. Environ.*, 25, 997–1008, 1991.

Paulot, F., Crounse, J. D., Kjaergaard, H. G., Kurten, A., St Clair, J. M., Seinfeld, J. H., and Wennberg, P. O.: Unexpected epoxide formation in the gas-phase photooxidation of isoprene, *Science*, 325, 730–733, 2009.

Presto, A. A., Hartz, K. E. H., and Donahue, N. M.: Secondary organic aerosol production from terpene ozonolysis. 2. Effect of NO_x concentration, *Environ. Sci. Technol.*, 39, 7046–7054, 2005.

Sato, K.: Detection of nitrooxypolyols in secondary organic aerosol formed from the photooxidation of conjugated dienes under high-NO_x conditions, *Atmos. Environ.*, 42, 6851–6861, 2008.

Song, C., Na, K. S., and Cocker, D. R.: Impact of the hydrocarbon to NO_x ratio on secondary organic aerosol formation, *Environ. Sci. Technol.*, 39, 3143–3149, 2005.

Surratt, J. D., Murphy, S. M., Kroll, J. H., Ng, N. L., Hildebrandt, L., Sorooshian, A., Szmigelski, R., Vermeylen, R., Maenhaut, W., Claeys, M., Flagan, R. C., and Seinfeld, J. H.: Chemical composition of secondary organic aerosol formed from the photooxidation of isoprene, *J. Phys. Chem. A*, 110, 9665–9690, 2006.

Surratt, J. D., Gomez-Gonzalez, Y., Chan, A. W. H., Vermeylen, R., Shahgholi, M., Kleindienst, T. E., Edney, E. O., Offenberg, J. H., Lewandowski, M., Jaoui, M., Maenhaut, W., Claeys, M., Flagan, R. C., and Seinfeld, J. H.: Organosulfate formation in biogenic secondary organic aerosol, *J. Phys. Chem. A*, 112, 8345–8378, 2008.

Surratt, J. D., Chan, A. W. H., Eddingsaas, N. C., Chan, M. N., Loza, C. L., Kwan, A. J., Hersey, S. P., Flagan, R. C., Wennberg, P. O., and Seinfeld, J. H.: Reactive intermediates revealed in secondary organic aerosol formation from isoprene, *Proc. Natl. Acad. Sci. USA*, 107, 6640–6645, 2010.

Szmigelski, R., Surratt, J. D., Vermeylen, R., Szmigelska, K., Kroll, J. H., Ng, N. L., Murphy, S. M., Sorooshian, A., Seinfeld, J. H., and Claeys, M.: Characterization of 2-methylglyceric acid oligomers in secondary organic aerosol formed from the photooxidation of isoprene using trimethylsilylation and gas chromatography/ion trap mass spectrometry, *J. Mass. Spectrom.*, 42, 101–116, 2007.

Taylor, W. D., Allston, T. D., Moscato, M. J., Fazekas, G. B., Kozlowski, R., and Takacs, G. A.: Atmospheric photo-dissociation lifetimes for nitromethane, methyl nitrite, and methyl nitrate, *Int. J. Chem. Kinet.*, 12, 231–240, 1980.

Tuazon, E. C. and Atkinson, R.: A product study of the gas-phase reaction of methacrolein with the OH radical in the presence of NO_x, *Int. J. Chem. Kinet.*, 22, 591–602, 1990.

Tuazon, E. C., Aschmann, S. M., Nishino, N., Arey, J., and Atkinson, R.: Kinetics and products of the OH radical-initiated reaction of 3-methyl-2-butenal, *Phys. Chem. Chem. Phys.*, 7, 2298–2304, 2005.

Volkamer, R., Ziemann, P. J., and Molina, M. J.: Secondary Organic Aerosol Formation from Acetylene (C₂H₂): seed effect on SOA yields due to organic photochemistry in the aerosol aqueous phase, *Atmos. Chem. Phys.*, 9, 1907–1928, doi:10.5194/acp-9-1907-2009, 2009.

Weber, R. J., Sullivan, A. P., Peltier, R. E., Russell, A., Yan, B., Zheng, M., de Gouw, J., Warneke, C., Brock, C., Holloway, J. S., Atlas, E. L., and Edgerton, E.: A study of secondary organic aerosol formation in the anthropogenic-influenced southeastern United States, *J. Geophys. Res.-Atmos.*, 112, D13302, doi:10.1029/2007JD008408, 2007.

Zhang, Q., Jimenez, J. L., Canagaratna, M. R., Allan, J. D., Coe, H., Ulbrich, I., Alfarra, M. R., Takami, A., Middlebrook, A. M., Sun, Y. L., Dzepina, K., Dunlea, E., Docherty, K., DeCarlo, P. F., Salcedo, D., Onasch, T., Jayne, J. T., Miyoshi, T., Shimojo, A., Hatakeyama, S., Takegawa, N., Kondo, Y., Schneider, J., Drewnick, F., Borrmann, S., Weimer, S., Demerjian, K., Williams, P., Bower, K., Bahreini, R., Cottrell, L., Griffin, K.,

R. J., Rautiainen, J., Sun, J. Y., Zhang, Y. M., and Worsnop, D. R.: Ubiquity and dominance of oxygenated species in organic aerosols in anthropogenically-influenced Northern Hemisphere midlatitudes, *Geophys. Res. Lett.*, 34, L13801, doi:10.1029/2007GL029979, 2007a.

Zhang, Y., Huang, J. P., Henze, D. K., and Seinfeld, J. H.: Role of isoprene in secondary organic aerosol formation on a regional scale, *J. Geophys. Res.-Atmos.*, 112, D20207, doi:10.1029/2007JD008675, 2007b.